frontiers | Research Topics

Women in cardiovascular imaging

Edited by
Adelina Doltra, Sabina Gallina, Claudia Prieto and Anna Vittoria Mattioli

Published in
Frontiers in Cardiovascular Medicine

ISSN 1664-8714
ISBN 978-2-8325-3267-6
DOI 10.3389/978-2-8325-3267-6

About Frontiers

Frontiers is more than just an open access publisher of scholarly articles: it is a pioneering approach to the world of academia, radically improving the way scholarly research is managed. The grand vision of Frontiers is a world where all people have an equal opportunity to seek, share and generate knowledge. Frontiers provides immediate and permanent online open access to all its publications, but this alone is not enough to realize our grand goals.

Frontiers journal series

The Frontiers journal series is a multi-tier and interdisciplinary set of open-access, online journals, promising a paradigm shift from the current review, selection and dissemination processes in academic publishing. All Frontiers journals are driven by researchers for researchers; therefore, they constitute a service to the scholarly community. At the same time, the *Frontiers journal series* operates on a revolutionary invention, the tiered publishing system, initially addressing specific communities of scholars, and gradually climbing up to broader public understanding, thus serving the interests of the lay society, too.

Dedication to quality

Each Frontiers article is a landmark of the highest quality, thanks to genuinely collaborative interactions between authors and review editors, who include some of the world's best academicians. Research must be certified by peers before entering a stream of knowledge that may eventually reach the public - and shape society; therefore, Frontiers only applies the most rigorous and unbiased reviews. Frontiers revolutionizes research publishing by freely delivering the most outstanding research, evaluated with no bias from both the academic and social point of view. By applying the most advanced information technologies, Frontiers is catapulting scholarly publishing into a new generation.

What are Frontiers Research Topics?

Frontiers Research Topics are very popular trademarks of the *Frontiers journals series*: they are collections of at least ten articles, all centered on a particular subject. With their unique mix of varied contributions from Original Research to Review Articles, Frontiers Research Topics unify the most influential researchers, the latest key findings and historical advances in a hot research area.

Find out more on how to host your own Frontiers Research Topic or contribute to one as an author by contacting the Frontiers editorial office: frontiersin.org/about/contact

Women in cardiovascular imaging

Topic editors

Adelina Doltra — Hospital Clinic of Barcelona, Spain
Sabina Gallina — University of Studies G. d'Annunzio Chieti and Pescara, Italy
Claudia Prieto — King's College London, United Kingdom
Anna Vittoria Mattioli — University of Modena and Reggio Emilia, Italy

Citation

Doltra, A., Gallina, S., Prieto, C., Mattioli, A. V., eds. (2023). *Women in cardiovascular imaging*. Lausanne: Frontiers Media SA. doi: 10.3389/978-2-8325-3267-6

Table of contents

frontiers | Frontiers in Cardiovascular Medicine

TYPE Editorial
PUBLISHED 02 August 2023
DOI 10.3389/fcvm.2023.1249983

OPEN ACCESS

EDITED AND REVIEWED BY
Christos Bourantas,
Queen Mary University of London,
United Kingdom

*CORRESPONDENCE
Anna Vittoria Mattioli
annavittoria.mattioli@unimore.it

†These authors have contributed equally to this work

RECEIVED 29 June 2023
ACCEPTED 24 July 2023
PUBLISHED 02 August 2023

CITATION
Mattioli AV, Doltra A, Prieto C and Gallina S (2023) Editorial: Women in cardiovascular imaging.
Front. Cardiovasc. Med. 10:1249983.
doi: 10.3389/fcvm.2023.1249983

Editorial: Women in cardiovascular imaging

Anna Vittoria Mattioli[1*†], Adelina Doltra[2†], Claudia Prieto[3,4†] and Sabina Gallina[5†]

[1]Department of Medical and Surgical Sciences for Children and Adults, University of Modena and Reggio Emilia, Modena, Italy, [2]Non-invasive Imaging Section, Cardiovascular Institute Hospital Clínic, University of Barcelona, Barcelona, Spain, [3]King's College London, London, United Kingdom, [4]Pontificia Universidad Católica de Chile, Santiago, Chile, [5]Department of Neuroscience, Imaging and Clinical Sciences, G. D'Annunzio University, Chieti, Italy

KEYWORDS

women, cardiovascular imaging, gender gap, education, prevention

Editorial on the Research Topic
Women in cardiovascular imaging

To date there is still a great disparity between the sexes in the scientific field and this determines a small number of manuscripts that have a woman as principal investigator and corresponding author. At present, less than 30% of researchers worldwide are women (1). Long-standing biases and gender stereotypes are discouraging girls and women away from science-related fields, and in the area of STEM (Science, Technology, Engineering and Mathematics) research in particular. Analyzing the scientific literature and, specifically clinical trial, it emerges that the number of female Principal Investigators is substantially lower than males (2, 3).

The disparity between the sexes also emerges in careers. A meta-analysis on 218 studies found that men were 2.77 times more likely to be full professors (OR: 2.77, 95% CI: 2.57–2.98). Meta-regression by data collection year demonstrated improvement over time; however, subgroup analysis showed that gender disparities remain significant in the 2010–2020 decade (OR: 2.63, 95% CI: 2.48–2.80). The gender gap was present across all specialties and both within and outside of North America. Men published more papers with a mean difference of 17.2 (95% CI: 14.7–19.7) (3).

The proportion of female medical graduates appears to have increased over time, however, the gender ratio of physicians varies across specialties (4).

Today, women remain a minority in cardiology even though half of the medical school graduates are women over the last decade (49.3% in 2008 and 47.9% in 2018). Despite this, the proportion of women in cardiovascular disease fellowship training remains low (18% in 2008 and 23.4% in 2018), compared with other medical specialties (5).

This underrepresentation of women in cardiology also extends to women in leadership roles within the same community. The representation of women decreases progressively along the career path from medical student to cardiology fellow to practicing cardiologist and, finally, fewer women at leadership roles. The inclusion of women in the authorship guidelines is a good index of this underrepresentation (6, 7).

Science and gender equality are, however, essential to ensure sustainable development as highlighted by UNESCO (1). In order to change traditional mindsets, gender equality must be promoted, stereotypes defeated, and girls and women should be encouraged to pursue STEM careers. Achieving parity in leadership, peer mentorship, and role models can help motivate female medical students devote himself to STEM careers (8).

This special issue has collected 15 manuscripts of the highest quality written by women. The collection focuses on imaging technique from echocardiography, Computed Tomography-scan and Magnetic Resonance Imaging in their most advanced technical applications.

The article "Women physicians in cardiovascular magnetic resonance: Past, present, and future" summarizes the barriers that women in cardiovascular imaging have overcome over the past several years, the positive interventions that have been implemented to better support women in the field of cardiovascular magnetic resonance, and the challenges that still remain, with a special emphasis on women physicians (Sierra-Galan et al.).

Cardiovascular imaging specialty training is prolonged and demanding, consisting of medical school and residency (in either diagnostic radiology or internal medicine), followed by cardiology and dedicated cardiac imaging or cardiovascular fellowship. This long training discourages women from taking this path due to the difficulties in reconciling professional and personal activities above all.

Furthermore, given the well-known under-representation of women participants in cardiovascular studies, the increased recruitment of women demonstrated in trials with female leaders also have practical implications (9, 10).

The limited availability of gender-specific data in clinical research has significant implications for the quality of healthcare provided to women. Historically, medical research has focused predominantly on men, and findings from studies conducted primarily on male participants have been extrapolated to both genders. However, this approach neglects the fact that men and women can have distinct physiological, hormonal, and genetic differences that may influence disease risk, progression, and response to treatments (11, 12).

It is crucial to recognize the importance of including women in clinical trials and conducting adequate sex-specific analyses to gain a comprehensive understanding of women's health and to identify potential gender-specific effects of treatments and interventions (13).

Efforts to bridge the gender gap in medical research and healthcare can lead to more equitable and effective treatments for both women and men, ultimately improving overall health outcomes for all.

To improve the quality of care for women, researchers, healthcare providers, and policymakers should advocate for more inclusive clinical trial designs that prioritize gender representation. Additionally, conducting post-hoc subgroup analyses based on sex and presenting sex-specific results in research publications are essential steps toward advancing gender-specific healthcare.

Although clinical trials often include both sexes, there is often inadequate analysis of sex-based differences. It is important to develop subgroup analyzes and examine potential gender-specific effects within clinical trial data to identify any disparities or considerations unique to women (11, 12). Balancing study recruitment between men and women will help fill some gaps. Including an adequate number of women in clinical trials allows researchers to analyze and address sex-based differences in disease presentation, progression, and treatment response. It helps to identify any disparities or unique considerations that may affect women's health outcomes. Furthermore, the concept of personalized medicine, where medical decisions and treatments are tailored to an individual's specific characteristics, is gaining prominence. Understanding sex-based differences can lead to more tailored and effective healthcare approaches for both men and women (14, 15).

In addition, men and women may respond differently to medications due to variations in metabolism, hormone levels, and other biological factors. Having gender-specific data can help optimize drug dosing and minimize potential side effects in both sexes (16–18).

We believe the time has come for action and the scientific community must encourage women in STEM to write and position themselves as principal investigators.

Author contributions

All authors listed have made a substantial, direct, and intellectual contribution to the work and approved it for publication.

Conflict of interest

The authors declare that the research was conducted in the absence of any commercial or financial relationships that could be construed as a potential conflict of interest.

Publisher's note

References

1. Women in science. UNESCO (2019). Available at: https://uis.unesco.org/en/topic/women-science (Accessed June 24, 2023).

2. Yong C, Suvarna A, Harrington R, Gummidipundi S, Krumholz HM, Mehran R, et al. Temporal trends in gender of principal investigators and patients in cardiovascular clinical trials. *J Am Coll Cardiol.* (2023) 81(4):428–430. doi: 10.1016/j.jacc.2022.10.038

3. Li B, Jacob-Brassard J, Dossa F, et al. Gender differences in faculty rank among academic physicians: a systematic review and meta-analysis. *BMJ Open.* (2021) 11: e050322. doi: 10.1136/bmjopen-2021-050322

4. Balasubramanian S, Pasquali SK, Cousino MK, Lowery RE, Les AS, Yu S, et al. Representation of women and minority faculty and fellows in academic pediatric

cardiology training programs. *J Am Coll Cardiol*. (2023) 81(12):1181–1188. doi: 10.1016/j.jacc.2023.01.022

5. Rai D, Tahir MW, Waheed SH, Kapoor A, Pandey R, Barssoum K, et al. National trends of sex disparity in the American college of cardiology/American heart association guideline writing committee authors over 15 years. *Circ Cardiovasc Qual Outcomes*. (2021) 14(2):e007578. doi: 10.1161/CIRCOUTCOMES.120.007578

6. Rai D, Kumar A, Waheed SH, Pandey R, Guerriero M, Kapoor A, et al. Gender differences in international cardiology guideline authorship: a comparison of the US, Canadian, and European cardiology guidelines from 2006 to 2020. *J Am Heart Assoc*. (2022) 11(5):e024249. doi: 10.1161/JAHA.121.024249

7. Mavedatnia D, Yi G, Wener E, Davidson J, Chan Y, Graham ME. Gender differences in North American and international otolaryngology clinical practice guideline authorship: a 17-year analysis. *Ann Otol Rhinol Laryngol*. (2023) 19:34894231181752. doi: 10.1177/00034894231181752

8. González-Pérez S, Mateos de Cabo R, Sáinz M. Girls in STEM: is it a female role-model thing? *Front Psychol*. (2020) 11:2204. doi: 10.3389/fpsyg.2020.02204

9. Bierer BE, Meloney LG, Ahmed HR, White SA. Advancing the inclusion of underrepresented women in clinical research. *Cell Rep Med*. (2022) 3(4):100553. doi: 10.1016/j.xcrm.2022.100553

10. Bierer BE, Meloney LG. Strategies to optimize inclusion of women in multi-national clinical trials. *Contemp Clin Trials*. (2022) 117:106770. doi: 10.1016/j.cct.2022.106770

11. Gentilin A, Moghetti P, Cevese A, Mattioli AV, Schena F, Tarperi C. Circadian and sex differences in carotid-femoral pulse wave velocity in young individuals and elderly with and without type 2 diabetes. *Front Cardiovasc Med*. (2022) 9:952621. doi: 10.3389/fcvm.2022.952621

12. Cocchi C, Coppi F, Farinetti A, Mattioli AV. Cardiovascular disease prevention and therapy in women with type 2 diabetes. *Future Cardiol*. (2021) 17(3):487–496. doi: 10.2217/fca-2021-0011

13. Göttgens I, Oertelt-Prigione S. Moving beyond gender identity: the need for contextualization in gender-sensitive medical research. *Lancet Reg Health Eur*. (2022) 24:100548. doi: 10.1016/j.lanepe.2022.100548

14. Mattioli AV, Nasi M, Pinti M, Palumbo C. Teaching gender differences at medical school could improve the safety and efficacy of personalized physical activity prescription. *Front Cardiovasc Med*. (2022) 9:919257. doi: 10.3389/fcvm.2022.919257

15. Rebić N, Law MR, Cragg J, Brotto LA, Ellis U, Garg R, et al. What's sex and gender got to do with it? A scoping review of sex and gender-based analysis in pharmacoepidemiologic studies of medication adherence. *Value Health*. (2023): S1098-3015(23)02559-7. doi: 10.1016/j.jval.2023.04.002

16. Mattioli AV, Moscucci F, Sciomer S, Maffei S, Nasi M, Pinti M, et al. Cardiovascular prevention in women: an update by the Italian society of cardiology working group on 'prevention, hypertension and peripheral disease'. *J Cardiovasc Med (Hagerstown)*. (2023) 24(Suppl 2):e147–55. doi: 10.2459/JCM.0000000000001423

17. Woodward M. Cardiovascular disease and the female disadvantage. *Int J Environ Res Public Health*. (2019) 16:1165.

18. Hui K, Sukhera J, Vigod S, Taylor VH, Zaheer J. Recognizing and addressing implicit gender bias in medicine. *CMAJ*. (2020) 192(42):E1269–70. doi: 10.1503/cmaj.200286

frontiers in Cardiovascular Medicine

ORIGINAL RESEARCH
published: 21 January 2022
doi: 10.3389/fcvm.2021.806107

Right Ventricular Flow Vorticity Relationships With Biventricular Shape in Adult Tetralogy of Fallot

*Ayah Elsayed[1], Charlène A. Mauger[1], Edward Ferdian[1], Kathleen Gilbert[2], Miriam Scadeng[1], Christopher J. Occleshaw[3], Boris S. Lowe[3], Andrew D. McCulloch[4], Jeffrey H. Omens[4], Sachin Govil[4], Kuberan Pushparajah[5] and Alistair A. Young[1,5]**

[1] Department of Anatomy and Medical Imaging, University of Auckland, Auckland, New Zealand, [2] Auckland Bioengineering Institute, University of Auckland, Auckland, New Zealand, [3] Department of Cardiology, Auckland District Health Board, Auckland, New Zealand, [4] Department of Bioengineering, University of California, San Diego, La Jolla, CA, United States, [5] Department of Biomedical Engineering, King's College London, London, United Kingdom

Remodeling in adults with repaired tetralogy of Fallot (rToF) may occur due to chronic pulmonary regurgitation, but may also be related to altered flow patterns, including vortices. We aimed to correlate and quantify relationships between vorticity and ventricular shape derived from atlas-based analysis of biventricular shape. Adult rToF ($n = 12$) patients underwent 4D flow and cine MRI imaging. Vorticity in the RV was computed after noise reduction using a neural network. A biventricular shape atlas built from 95 rToF patients was used to derive principal component modes, which were associated with vorticity and pulmonary regurgitant volume (PRV) using univariate and multivariate linear regression. Univariate analysis showed that indexed PRV correlated with 3 modes ($r = -0.55, -0.50$, and 0.6, all $p < 0.05$) associated with RV dilatation and an increase in basal bulging, apical bulging and tricuspid annulus tilting with more severe regurgitation, as well as a smaller LV and paradoxical movement of the septum. RV outflow and inflow vorticity were also correlated with these modes. However, total vorticity over the whole RV was correlated with two different modes ($r = -0.62, -0.69$, both $p < 0.05$). Higher vorticity was associated with both RV and LV shape changes including longer ventricular length, a larger bulge beside the tricuspid valve, and distinct tricuspid tilting. RV flow vorticity was associated with changes in biventricular geometry, distinct from associations with PRV. Flow vorticity may provide additional mechanistic information in rToF remodeling. Both LV and RV shapes are important in rToF RV flow patterns.

Keywords: tetralogy of Fallot, 4D flow, vorticity, shape, atlas

OPEN ACCESS

Edited by:
Giovanni Battista Luciani, University of Verona, Italy

Reviewed by:
Francesco Sturla, IRCCS San Donato Polyclinic, Italy
Jan Brüning, Charité University Medicine Berlin, Germany

***Correspondence:**
Alistair A. Young
alistair.young@kcl.ac.uk

Specialty section:
This article was submitted to Cardiovascular Imaging, a section of the journal Frontiers in Cardiovascular Medicine

Received: *31 October 2021*
Accepted: *27 December 2021*
Published: *21 January 2022*

Citation:
Elsayed A, Mauger CA, Ferdian E, Gilbert K, Scadeng M, Occleshaw CJ, Lowe BS, McCulloch AD, Omens JH, Govil S, Pushparajah K and Young AA (2022) Right Ventricular Flow Vorticity Relationships With Biventricular Shape in Adult Tetralogy of Fallot. Front. Cardiovasc. Med. 8:806107. doi: 10.3389/fcvm.2021.806107

INTRODUCTION

Many patients with repaired Tetralogy of Fallot (rToF) survive to adulthood due to successful primary repair (1). Yet, chronic pulmonary regurgitation is often a consequence, leading to shape, hemodynamic and electrophysiological changes in the right ventricle (RV) (2, 3). Pulmonary valve replacement is often required; however, the timing of this procedure remains controversial (1). Previous studies analyzed the regional three-dimensional (3D) alterations of the RV anatomy in rToF (2–4). RV shape changes have been associated with common clinical metrics such as pulmonary regurgitant volume (PRV), indicating links between PRV and RV dilatation, with

outflow tract bulging and apical dilation (3, 5). Remodeling patterns have been shown to be different in rToF patients compared with pulmonary hypertension patients (6) and quantification of these patterns has been facilitated by shape modeling (7).

3D statistical shape modeling enables quantification of the variation in cardiac shapes and their relationships with disease processes (8–10). RV shape can be represented as morphometric scores based on comparison with an atlas of cardiac shapes. These scores have stronger associations with risk factors such as diabetes and hypertension, giving more powerful quantitative shape measures, than standard measures of mass and volume (9).

Altered blood flow patterns in the heart are also associated with ventricular shape (11). Time-resolved phase-contrast cardiac magnetic resonance imaging, 4D flow MRI, has enabled the qualitative and quantitative measurement of altered flow patterns (12–14). In particular flow vorticity is an index of flow "swirl," including circular, helical or spiral patterns, indicative of high shear in the flow field. These are indicative of higher viscous energy losses, and increased hemodynamic wall shear stress. Although increased vorticity has been described in the LV outflow tract in rToF patients (15), the relationships between biventricular shape and flow vortices is unknown. Application of vorticity estimation in rToF patients is also limited by noise inherent in the data, which is heightened by numerical differentiation required for the calculation of vorticity. Neural networks show promise in enhancing medical imaging data (16), but these methods have not yet been applied in the estimation of vorticity.

We aimed to examine relationships between biventricular geometry and flow vortices in the RV and the right ventricular outflow tract using a processing pipeline including enhancement of velocity vectors using a deep neural network, quantification of vorticity using numerical differentiation, and correlation with morphological scores calculated by projection onto an atlas of rToF patients. To our knowledge, this work is the first study investigating relationships between vorticity and ventricular shape.

METHODS

Research Design and Patient Criteria

This pilot study comprised a prospective, cross-sectional design performed at the Centre for Advanced MRI (CAMRI) at the University of Auckland between 2019 and 2021. Ethics committee approval was obtained from the Health and Disability Ethics Committee New Zealand (17/CEN/226). Informed written consent was obtained for all patients and volunteers. The study group comprised twelve rToF patients recruited from the outpatient cardiology clinic, i.e., patients above 16 years of age attending annual follow-up by cardiovascular magnetic resonance. Ten healthy age- matched volunteers with no known cardiovascular abnormalities were imaged to evaluate flow differences with the study group.

MRI Protocol

Cardiovascular magnetic resonance was performed on a Siemens Magnetom 1.5T Avanto Fit (Siemens Healthcare, Erlangen, Germany) MRI scanner. 2D steady state free precession scans were acquired using a multi-element cardiac coil, with breath-holds and retrospective gating. The typical set of sequence parameters included a repetition time of 2.9 ms, echo time of 1.36 ms, flip angle was 58°, field of view was 400 mm. The slice thickness was 6 mm, image matrix was 192 × 256 and 30 heart phases were reconstructed. Images covered the span of both ventricles. Long-axis slices were obtained through both ventricles and through the four valves. A stack of short-axis slices was acquired parallel to the tricuspid valve, covering all valves, and spanning both ventricles.

4D-flow MRI was acquired during free-breathing, using a navigator gated gradient-echo pulse-sequence with interleaved 3D flow-encoding and retrospective vector cardiogram controlled cardiac gating. Standard acquisition parameters included velocity encoding (VENC) of 150 cm/s, a flip angle of 7°, echo time 2.3 ms and repetition time 38.8 ms. The VENC was chosen to achieve minimal aliasing across all studies. The scan covered the whole heart, the aorta, and the main pulmonary artery at a spatial resolution of 2.4 × 2.4 × 2.4 mm. Parallel imaging was used with an image acceleration factor of 3, with a scanning time of 7.3–10 min. No contrast was used.

Quantitative Measurements of Flow and Vorticity

Flow acquisitions were processed using 4D Flow Demonstrator V2.3 software (Siemens AG, Erlangen, Germany) after antialiasing and background phase correction. Antialiasing allowed for an increase in the range of measurements done to include flow from 0 to 300 cm/sec without the aliasing effects. Forward volume, reverse volume, and the PRV index (PRVi, volume divided by BSA) were measured for the pulmonary flow, and the tricuspid valve was examined for forward flow volume and regurgitant volume.

For vorticity analysis, the phase-contrast images were first denoised using the 4D FlowNet neural network (16). This was done to capture vortices that extended along multiple timeframes and achieve consistent results in the presence of noise, since vorticity requires the calculation of numerical derivatives which are sensitive to noise. Briefly, 4D FlowNet is a noise reduction and super-resolution residual network based on the SRGAN architecture (17). This deep learning network was trained solely using synthetic 4D Flow MR images, generated from computational fluid dynamics simulations. Although 4DFlowNet was designed to perform both denoising and super-resolution, we applied the network with an up sample ratio of 1, which effectively performed denoising without increasing spatial resolution since the flow features (intraventricular vortices) were large relative to the voxel size in our application.

Vorticity was calculated in ParaView (v5.8.0) as the curl of the velocity field (18, 19). Calculation of vorticity was performed by a first-order bilinear interpolation scheme over the chosen

velocity vectors. This property enabled the generation of vorticity magnitude of the computed vector gradient tensor from velocity vector cell data. Subsequently, vorticity vector magnitudes were summed across the region of interest (ROI). Vorticity was reviewed on overlapping timeframes that included only the diastolic phase of the cardiac cycle. Overlapping timeframes were two before and two after the central frame as this allowed visualization of stable vortices that span over more than one time frame, differentiating that from noise and short-term fluid rotations. 3 areas were examined in the RV: 1- the main cavity of RV excluding the right ventricular outflow tract (RVOT), 2- the tricuspid inflow ring and 3- the RVOT. The spherical ROI was placed flush to the opening of the corresponding valve. The area of interest measurements was standardized and calculated in accordance with a normalization factor with the BSA to take into consideration the different sizes of the hearts between groups. Timing in the cardiac cycle was also recorded and standardized between cases so that the timeframes were matched while measuring the vorticity in all cases (**Supplementary Video 1**).

Cardiac Modeling and RToF Atlas Building

Patient-specific biventricular geometries were generated using the Cardiac Image Modeler (CIM) (v8.3.0, University of Auckland, New Zealand) (20). Briefly, CIM is a semi-automatic segmentation software package developed to facilitate segmentation of both RV and LV endocardial and epicardial surfaces from all the short and long axis images. To generate patient-specific geometry, the user first identifies anatomical landmarks (RV insertion points, valve points and LV apex). These landmarks are then automatically tracked throughout the cardiac cycle using non-rigid registration and a 3D biventricular template is then fitted. Guide-points are then placed by the user to deform the model to those points in real-time and end diastolic volume (EDV), end systolic volume (ESV), stoke volume (SV) and ventricular mass are calculated by numerical integration. To identify abnormal patterns and study relationships between shape and clinical parameters, the rToF shape models were projected onto a biventricular atlas generated from 95 rTOF participants without history of valve replacement. The demographics of the atlas cases are shown in **Table 1**. The atlas was constructed using methods described previously (9, 10). Briefly, contours were drawn manually on both long axis and short axis slices by expert analysts using Segment (21). Interobserver errors are reported in (10). The biventricular shape model was then automatically customized to each patient using an iterative registration algorithm (9). Valve locations were customized to the manual landmarks by using landmark registration, and surfaces were customized by using diffeomorphic non-rigid registration to the manual contours. All the end diastolic (ED) mesh points were first aligned to the mean mesh surface points using Procrustes analysis to remove any pose variation (translation and rotation). This transformation was then applied to the end-systolic (ES) mesh. The ED and ES surface points were then concatenated to form a single combined shape and principal component analysis was then applied. The normalized scores of each mode reflected how much each individual differs from the population mean. Using a concatenation of ED and ES phases captured the variation in function as well as shape in the principal components.

TABLE 1 | Demographics and cardiac parameters (mean ± s.d).

Demographics	Volunteers ($n = 10$)	rToF ($n = 12$)	rToF Atlas ($n = 95$)
Age (y)	32.4 ± 11.2	32.3 ± 11.2	19.5 ± 12.7†
Sex Male: Female	5:5	5:7	57:38
Height (cm)	173 ± 8.7	168.6 ± 8.6	154.7 ± 19.7†
Weight (kg)	78 ± 20.6	71 ± 12.2	58 ± 26.0†
BSA (m^2)	1.9 ± 0.27	1.8 ± 0.15	1.5†
PRV (ml/cycle)	1.5 ± 1.70	17.1 ± 21.07*	20.8 ± 11.8
TRV (ml/cycle)	0.11 ± 0.34	1.06 ± 1.36*	NA
LV EDVi (ml/m^2)	85.5 ± 17.2	90.9 ± 23.2	78 ± 14
LV SVi (ml/m^2)	45.3 ± 8.15	44.2 ± 10.3	37.1 ± 8.0
LV mass index (g/m^2)	60.1 ± 8.0	57.9 ± 5.1	76 ± 14†
RV EDVi (ml/m^2)	92.8 ± 13.3	112.6 ± 20.4*	147 ± 14†
RV SVi (ml/m^2)	41.3 ± 8.6	45.7 ± 14.8	52.9 ± 14.8†
RV mass index (g/m^2)	30.5 ± 4.7	36.2 ± 12.7	42 ± 11
RV ESVi (ml/m2)	51.4 ± 7.3	66.8 ± 11.7**	90 ± 27†

*$p < 0.05$, **$p < 0.01$ rToF vs. volunteers, †$p < 0.05$ rToF vs. rToF Atlas; BSA, body surface area; EDVi, indexed end diastolic volume; ESVi, indexed end systolic volume; LV, Left ventricle; PRV, pulmonary regurgitation volume; SD, standard deviation; SVi, indexed stroke volume; TR, tricuspid regurgitation; NA, not available.*

Patient-specific biventricular models were projected onto the first 24 rToF atlas shape modes which captured 90% of the total shape variation. Univariate regression was used to correlate principal component scores with cardiac indices and vorticity to identify shape associations. The main features of the modes with significant correlations were described in a similar manner to previous studies (9, 10). Multiple regression models were used to determine the association between biventricular shape and vorticity, controlling for effects of covariates sex, height, weight, and age. For the multiple regression models, the principal component scores were used as dependent variables and average vorticity and covariates (sex, height, weight, and age) were included as independent variables. A morphometric shape mode was then generated using the regression coefficient associated with vorticity, which quantifies the independent effect of vorticity on biventricular shape as described previously (9, 10). Diagrammatic demonstration of the methodology is shown in **Figure 1**.

Statistics

Statistical analysis was performed using R (22) and SPSS software v. 25 (IBM SPSS, Chicago, IL). All continuous values are reported as mean ± standard deviation for continuous variables and as frequency for categorical variables. Statistical differences were presented by p-values using one-way ANOVA or Kruskal-Wallis test depending on the distribution. Differences were considered significant for $P < 0.05$. Bonferroni correction was used for multiple tests. All variables were standardized before regression.

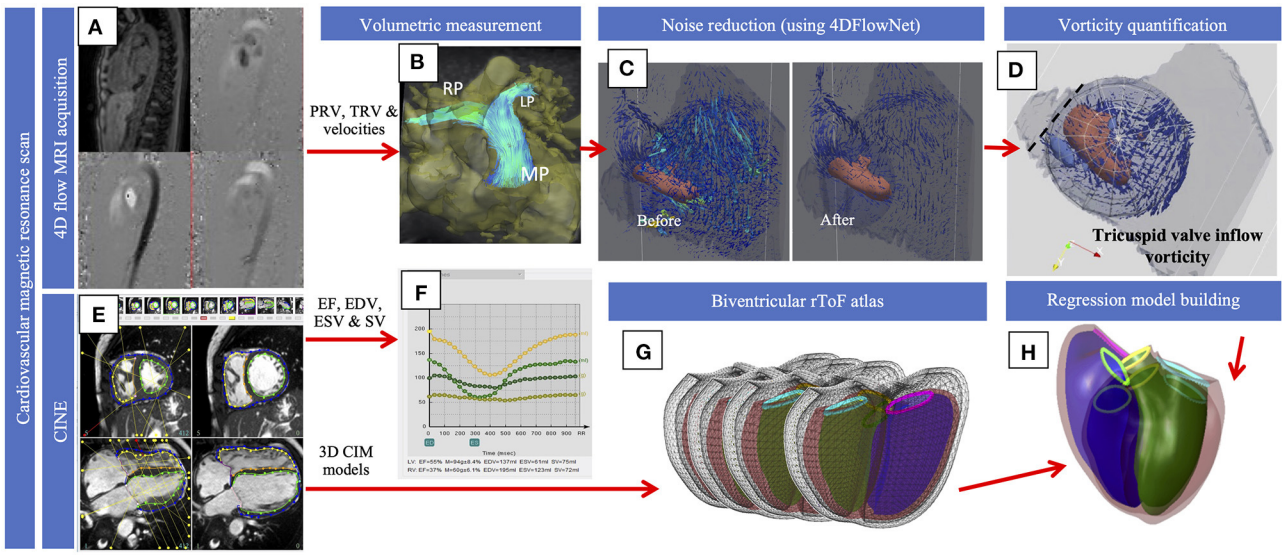

FIGURE 1 | Diagrammatic representation of the methodology. 4D flow **(A)** was used for volumetric quantification of flow in the pulmonary and across the tricuspid valve **(B)** and velocity data was processed with the 4D flow neural network **(C)**. Vorticity **(D)** was quantified and visualized with the vortex core and streamlines that demonstrate velocity within the spherical ROI was shown, and the dotted line represents the opening of the tricuspid valve. Cines **(E)** were used to extract EDV, ESV and SV **(F)**. Cines were also used to build the models for the current population that were projected onto the atlas **(G)**. Regression models **(H)** were used to compute shape variations associated with vorticity. The figure shows an overlapping of the diagrams of a normal biventricular model and the model generated to show the effect of vorticity.

RESULTS

Demographics

12 rToF Patients and 10 Volunteers Were Included in the Study. Volunteers Were Used in Demographic and Vorticity Comparisons Only. Demographics and Cardiac Parameters Are Shown in **Table 1** for Volunteers, Study Group, and Atlas Group. None of the rToF Patients Had Evidence of Pulmonary Stenosis.

Quantitative Vortex Analysis

Isolation of the RV was done with a spherical region of interest considering all the main flow areas. However, some flow outside the ventricle was inevitably included. The amount of error accounted for an average of 1% of the vorticity that was measured, which was considered negligible. This was validated through placement of regions inside the ventricles with exact boundary adjustment, then extension of the boundaries beyond these boundaries to include areas that did not show flow and the difference was calculated. The effect of 4D Flow network in reducing noise is shown in **Figure 2**. Vortex structure was more readily visualized after enhancement, while average vorticity values were in high agreement pre and post enhancement. **Table 2** shows average vorticity in our two groups at different areas of interest.

RV Shape Scores

The absolute point-to-point error between the shapes generated by the 24 shape mode scores and the original shapes was 3.4 ± 0.6 mm at ED and 3.6 ± 0.5 mm at ES, showing that the atlas shape scores formed a good approximation to the study group geometry. The differences in volume were: LVEDV: 4.3 ± 6.1 mL; RVEDV: 2.4 ± 6.2 mL; LVESV:−0.7 ± 4.2 mL; RVESV:−2.2 ± 4.2 mL and the mass differences were: LVM:−3.5 ± 4.9 g; RVM: 0.7 ± 3.5 g (original minus atlas, mean ± s.d.).

RV Shape and PRVi

PRVi showed significant correlation with mode 4, mode 6 and mode 9 ($r = -0.55$, $r = -0.50$ and $r = 0.6$ respectively, $p < 0.05$). Correlations between shape scores and more cardiac metrics are shown in **Figure 3**. **Figure 4** shows the visualization and description of modes associated with PRVi. Greater PRVi was associated with RV dilatation, with an increase in the basal bulging, apical bulging, and an increase in tricuspid annulus tilting. The LV size was reduced with paradoxical movement of the septum toward the RV during systole. RV EDVi, ESVi and SVi correlated with modes 6 and 9, whereas the association with LV size was reversed with respect to mode 9, consistent with reduced LV volume with increased PRVi.

RV Shape and Vorticity

Indexed RV outflow and indexed tricuspid inflow vorticity were both correlated with the same three modes associated with PRVi: mode 4 ($r = -0.63$ and $r = -0.6$ respectively), mode 6 ($r = -0.82$ and $r = -0.78$ respectively) and mode 9 ($r = 0.6$ and $r = 0.62$ respectively). Inflow and outflow vorticity were therefore also associated with an increase in the RV basal bulging, RV apical bulging and tricuspid annulus tilting. Correlations of vorticity and shape scores are shown in **Figure 3**.

In contrast, vorticity over the whole RV was correlated with modes which were not correlated with PRVi. Maximum and

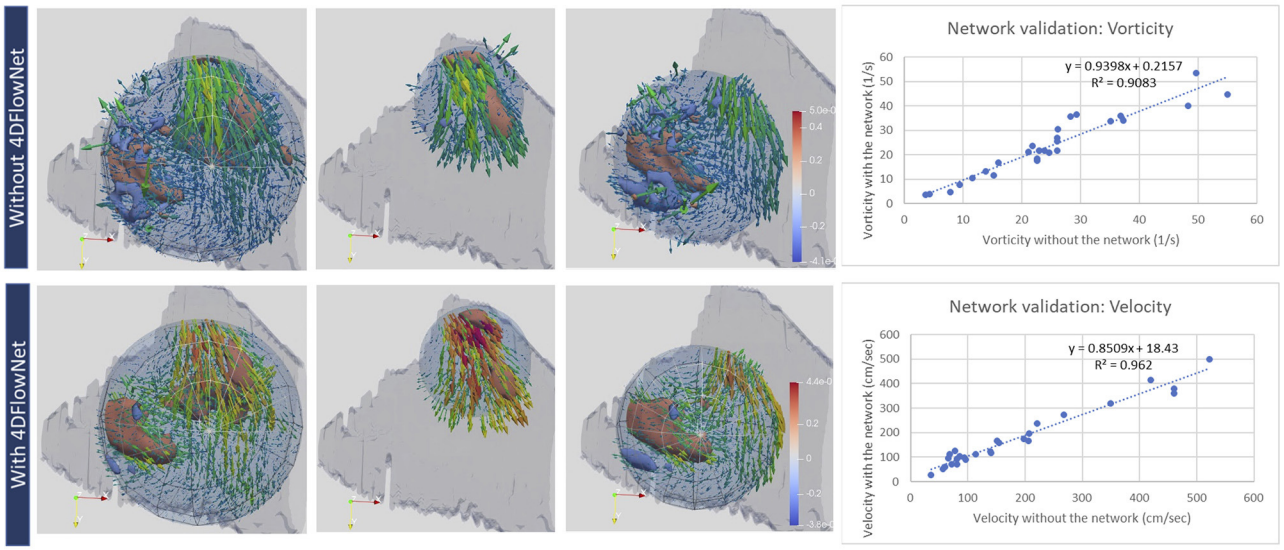

FIGURE 2 | Qualitative (left) and quantitative (right) evaluation of velocity and vorticity with and without the 4DFlownet. The panels show the 3 regions of interest where vorticity was captured (left: whole RV; middle: RVOT; right: tricuspid inflow in diastole. The network reduced noise making the vorticity structure more readily visualized. Right plots show mean vorticity calculated in the region of interest and mean velocity calculated at planes positioned in the RVOT, showing high correlation before and after 4DFlowNet.

TABLE 2 | Vorticity in the volunteer and study groups.

	Volunteer	rToF	*T*-test*
RV vorticity**	23.5 ± 6.5	25.5 ± 5.9	0.59
Tricuspid vorticity	23.5 ± 6.5	20.6 ± 5.4	0.35
RVOT vorticity	5.12 ± 1.9	10.4 ± 5.5	0.006

**t-test is significant at P < 0.05, **vorticity is measured in (1/s)/100. Vorticity was measured across multiple timeframes and averaged over the diastolic phase.*

average RV vorticity correlated with mode 11 ($r = -0.62$ and $r = -0.63$ respectively, $p < 0.05$, **Figure 4**) indicating that higher vorticity was associated with longer ventricular length, bulging beside the tricuspid valve with some abnormal tricuspid tilting. Average RV vorticity was correlated with mode 13 ($r = -0.69$, $p < 0.05$), associated with an increase in tricuspid tilt (**Figure 4**). Through these modes, increased vorticity was associated with increased LV size, rather than the reduction in LV size seen in the modes associated with PRVi.

Multivariate Analysis

Figure 5 shows the results of the multivariate analysis. The model demonstrated the relationship between average vorticity and biventricular shape while controlling for the effects of sex, height, weight and age. The RV enlargement affected the orientation of both the pulmonary outflow tract and tricuspid valves. There was an architectural shift from the normal configuration to an enlarged bulging base. There was an evident effect on the LV as well, showing lengthening of the LV, and change of position of the aortic and mitral valves due to the shift in the RVOT configuration. Increased RV vorticity was associated with an increase in LV size (**Supplementary Video 2**).

DISCUSSION

This study, to the best of our knowledge, is the first to examine RV shape associations with flow vorticity in patients with rToF using statistical shape analysis. A statistical atlas of rToF shape variation was used as a reference to describe shape with relatively few parameters (9, 23, 24). These population-based atlases enable characterization of ventricular shape in a targeted patient or group of related patients. This method enabled evaluation of the change in the regional ventricular anatomy rather than the volume as a whole (5). Individual patient status was quantified using mode scores which showed good agreement with the actual geometry. We found that inflow and outflow RV vorticity was significantly correlated with shape modes which were also significantly correlated with PRVi. However, total RV vorticity was significantly correlated with shape modes which were independent of PRV. These preliminary results suggest that mechanisms of ventricular remodeling may include intra-ventricular flow vorticity.

The application of deep neural network image enhancement to intraventricular vorticity estimation is promising. We found that the network, although trained on computational fluid dynamics simulations in patient specific aortic flow regimes, was able to denoise intraventricular 4D flow data due to its ability to recognize coherent flow patterns. The visualization of the vortex structure was considerably improved, while the average vorticity estimate was not affected (**Figure 2**).

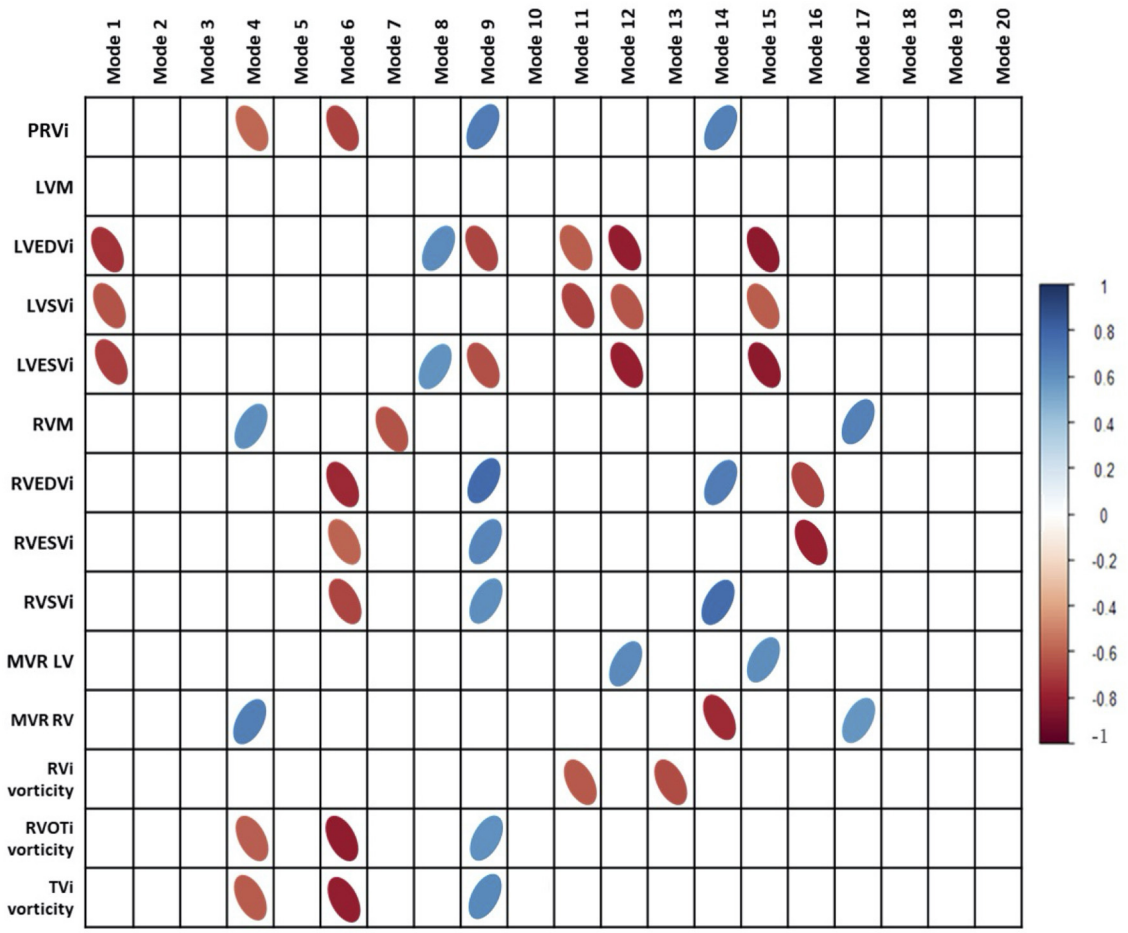

FIGURE 3 | Correlations of cardiac indices and vorticity with principal component analysis modes. PRVi, indexed pulmonary regurgitant volume; LVM, left ventricular mass; LVEDVi, indexed left ventricular end diastolic volume; LVSVi, indexed left ventricular stroke volume; LVESVi, indexed left ventricular end systolic volume; MVR, mass to volume ratio. Modes 9 and 6 Are the most correlated modes with aspects of cardiac metrics and vorticity. Bonferroni correction was done with all correlations.

The RV dilation pattern associated with PRVi was observed as an apical and basal bulging. The outlet also dilated with apical deformation as regurgitation became worse. In addition to RV changes, there was septal paradoxical movement toward the RV and a change in the left ventricular architecture as well. These results agree with previous atlas-based analyses (3, 6) which used 2D flow MRI and color doppler measurement to quantify PVR. 4D flow MRI has been shown to be more accurate for this task (25, 26) leading to higher correlation coefficients in our study compared with (3).

Correlation of vorticity with deformation modes were significant with the same modes that correlated with PRVi, with similar or higher correlation, confirming the interaction between vorticity, PRVi and shape. However, total RV vorticity correlated with 2 modes that did not correlate with PRVi (modes 11 and 13). This suggest that higher total vorticity is also associated with longer ventricular length. Also an increase bulging beside the tricuspid valve was observed with some abnormal tricuspid tilting. This is an interesting finding given that our study group had low to mild tricuspid regurgitation. Both these modes did not correlate with PRVi which indicated that these changes are independent of the amount of PRVi suggesting that the adverse vorticity in the whole ventricle was the influencer of change with these 2 modes. A study on the pulmonary artery (19) suggested that with the dilation of the vessel and a compromised RV function, blood creates shear layers, with differences in the velocity of each layer resulting in the higher vorticity formation. If this is applied to the dilated ventricle, a chaotic flow caused by pulmonary regurgitation would result in an abnormal vorticity affecting the architecture. This would suggest that the consequence of flow variation can have separate effects to the degree of regurgitation. In a study on vorticity in the RV (18) it was suggested that altered vorticity may be a cause for ventricular energy loss and RV dilatation. This was supported by another study (27) on ventricular kinetic energy which indicated a positive correlation between EDV and turbulent kinetic energy. The same study observed the change in kinetic energy to extend toward the apex, not only in the RV outflow tract, which is in line

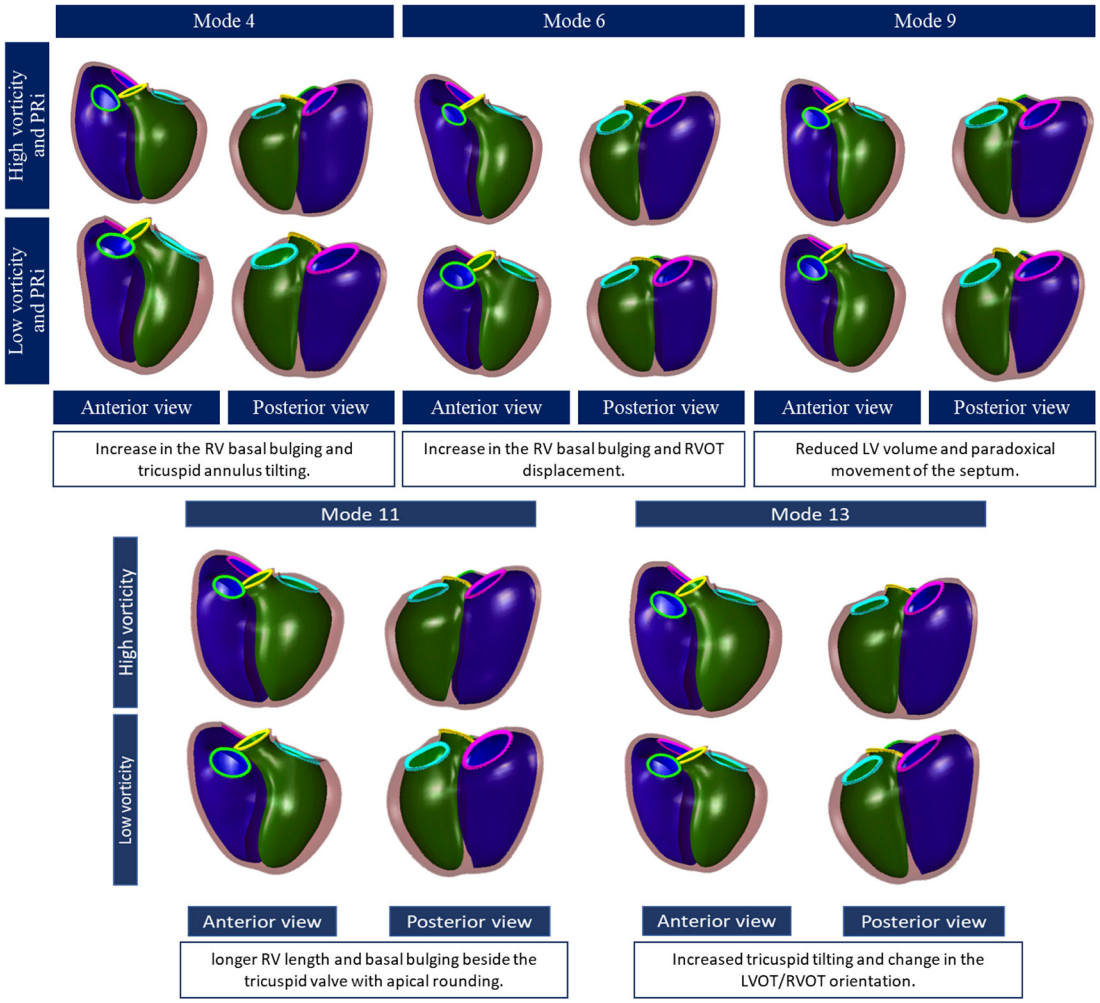

FIGURE 4 | Principal component shape variations associated with pulmonary regurgitant volume (top) and vorticity (bottom). The RV is shown in purple, left ventricle: green, the tricuspid valve: pink, the pulmonary valve: neon green, the aortic valve: yellow and mitral valve: blue. Each mode is shown in an anterior and posterior view with description below.

with our findings on vorticity that differs in behavior between the whole RV compared with inflow and outflow regions. This in turn could explain that abnormal fibrosis induced by changes in flow could affect places that are independent of the degree of pulmonary regurgitation.

There was a correlation between vorticity and modes that described a rounder apex. This could be explained by minimal apical flow observed in volunteers (18) while in patients, marginal flow was a finding and heterogeneous vortex formations were observed. Our study confirms this visual finding by the high correlation with modes that indicated a wider apex. The apical changes had been previously observed by another study (6) that suggested that the apical trabeculations contribute to how the RV adapts to volume overload in rToF. This is also in agreement with previous studies that observed a flatter apex (7, 28).

Our study also shed light on associations between vorticity and the architecture of the RV outflow tract. The pulmonary annulus was displaced anteriorly, and this decreased the concavity that is between the tricuspid valve and the pulmonary valve in mode 6, which was correlated with PRVi and vorticity in the outflow tract. This is in agreement with previous studies that observed a significantly more convex RV outflow tract in rToF (5, 6). The correlation of mode 6 with vorticity and PRVi suggest different remodeling mechanisms than those relating curvature change to postsurgical scarring (29). Furthermore, RV EDVi correlated with mode 6 as well, confirming the relation between volume overload and the outflow tract shape change.

The normal septum is convex toward the right ventricle with the left being a thicker rounder ventricle (30). The systolic motion of the septum to the left happens while the normal configuration is maintained. However, it has been observed in previous studies in patients with right ventricular volume overload that the septum flattens and the convexity may be reversed to be toward the left (30, 31). Vorticity was correlated with mode 4 which expressed the septal paradoxical motion. This is in agreement with previous studies that described the septal curvature (32).

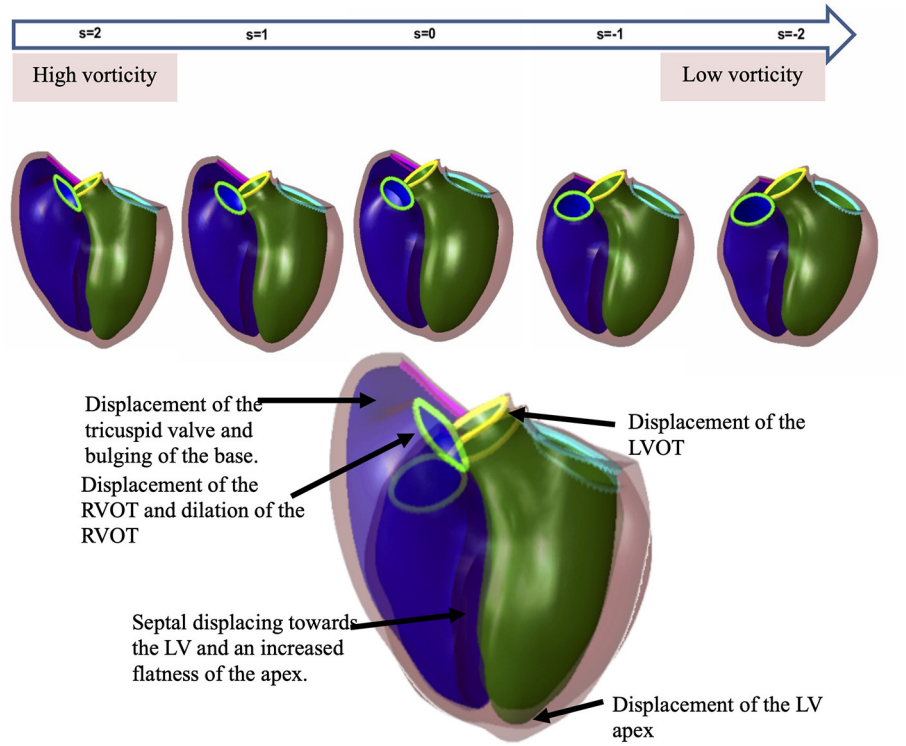

FIGURE 5 | The effect of vorticity on the shape of the RV by a regression model. The spectrum of shapes is demonstrated in the line of shapes above to show the difference between a normal biventricular model (far right) and a model affected by high vorticity (far left). The larger overlapping shapes emphasize the differences. The RV enlargement affects the orientation of both the pulmonary and tricuspid valves. There is an architectural shift from the normal configuration to an enlarged bulging base. There is an evident effect on the LV as well showing the change in wall shape and position of the aortic and mitral valves due to the shift in the RV outflow tract configuration.

Limitations

In this pilot study, our results are limited by a small sample size of patients examined with 4D Flow. RV shape analysis and vorticity extraction relied on segmentation and manually placed areas of interest, which may be automated in the future using machine learning methods. The patients in the atlas were younger than those in the study group, which may lead to differences in shape. However, the shape modes were able to describe the patient-specific geometry with good accuracy, since the atlas covers a wide range of developing disease states. Since we customized the atlas scores to each patient, the mismatch between atlas and 4D flow patients is not critical. Information on type of repair, residual RV obstruction and patient history were not available. More prospective, larger scale, multicenter studies are required to assess the validity and effectiveness of this methodology.

CONCLUSIONS

RV and LV shape features were significantly related to vorticity, and some of these relationships were not explainable by pulmonary regurgitant volumes or volumetric variations alone. Flow vorticity therefore may provide additional mechanistic information about remodeling and developing disease in rToF patients. Both LV and RV shape are important in understanding rToF RV flow vorticity patterns.

DATA AVAILABILITY STATEMENT

The raw data supporting the conclusions of this article will be made available by the authors, without undue reservation.

ETHICS STATEMENT

The studies involving human participants were reviewed and approved by Health and Disability Ethics Committee New Zealand (17/CEN/226). The patients/participants provided their written informed consent to participate in this study.

AUTHOR CONTRIBUTIONS

AE collated the data and performed the analyses. All authors participated in concept and design, revision, and final approval of the submitted manuscript.

FUNDING

This work was supported by the New Zealand Heart Foundation, NIH R01HL121754 from the National Heart, Lung, and Blood Institute USA, the Health Research Council of New Zealand grants 17/234 and 17/608, core funding from the Wellcome/EPSRC Centre for Medical Engineering

[WT203148/Z/16/Z], and a grant from Siemens Healthineers, Erlangen, Germany.

SUPPLEMENTARY MATERIAL

The Supplementary Material for this article can be found online at: https://www.frontiersin.org/articles/10.3389/fcvm.2021.806107/full#supplementary-material

Supplementary Video 1 | Video demonstrating the workflow of vorticity visualization and quantification. 4d Flow velocity data is quantified with Siemens 4D flow software then denoised with 4DFlowNet then visualized on ParaView. CIM is used to create a mask that is superimposed on the velocity data. The final visualization (far right) shows the final result which is visualized with the velocity vector fields, and vorticity cores.

Supplementary Video 2 | The regression model demonstrates each stage of shape evolution during ED and ES with the increase of vorticity and how much it changes the biventricular shape. The shape evolves from normal to what we observe with higher vorticity.

REFERENCES

1. Geva T, Mulder B, Gauvreau K, Babu-Narayan SV, Wald RM, Hickey K, et al. Preoperative predictors of death and sustained ventricular tachycardia after pulmonary valve replacement in patients with repaired tetralogy of fallot enrolled in the INDICATOR Cohort. *Circulation.* (2018) 138:2106–15. doi: 10.1161/CIRCULATIONAHA.118.034740
2. Gatzoulis MA, Till JA, Somerville J, Redington AN. Mechanoelectrical interaction in tetralogy of Fallot. QRS prolongation relates to right ventricular size and predicts malignant ventricular arrhythmias and sudden death. *Circulation.* (1995) 92:231–7. doi: 10.1161/01.CIR.92.2.231
3. Mansi T, Voigt I, Leonardi B, Pennec X, Durrleman S, Sermesant M, et al. A statistical model for quantification and prediction of cardiac remodelling: application to tetralogy of Fallot. *IEEE Trans Med Imaging.* (2011) 30:1605–16. doi: 10.1109/TMI.2011.2135375
4. Zhang H, Wahle A, Johnson RK, Scholz TD, Sonka M. 4-D cardiac MR image analysis: left and right ventricular morphology and function. *IEEE Trans Med Imaging.* (2010) 29:350–64. doi: 10.1109/TMI.2009.2030799
5. Leonardi B, Taylor AM, Mansi T, Voigt I, Sermesant M, Pennec X, et al. Computational modelling of the right ventricle in repaired tetralogy of Fallot: can it provide insight into patient treatment? *Eur Heart J Cardiovasc Imaging.* (2013) 14:381–6. doi: 10.1093/ehjci/jes239
6. Bidviene J, Muraru D, Maffessanti F, Ereminiene E, Kovács A, Lakatos B, et al. Regional shape, global function and mechanics in right ventricular volume and pressure overload conditions: a three-dimensional echocardiography study. *Int J Cardiovasc Imaging.* (2021) 37:1289–99. doi: 10.1007/s10554-020-02117-8
7. Sheehan FH, Ge S, Vick III GW, Urnes K, Kerwin WS, Bolson EL, et al. Three-dimensional shape analysis of right ventricular remodeling in repaired tetralogy of fallot. *Am J Cardiol.* (2008) 101:107–13. doi: 10.1016/j.amjcard.2007.07.080
8. Fonseca CG, Backhaus M, Bluemke DA, Britten RD, Chung J. Do, Cowan BR, et al. The Cardiac Atlas Project–an imaging database for computational modeling and statistical atlases of the heart. *Bioinformatics.* (2011) 27:2288–95. doi: 10.1093/bioinformatics/btr360
9. Mauger C, Gilbert K, Lee AM, Sanghvi MM, Aung N, Fung K, et al. Right ventricular shape and function: cardiovascular magnetic resonance reference morphology and biventricular risk factor morphometrics in UK Biobank. *J Cardiovasc Magn Reson.* (2019) 21:1–13. doi: 10.1186/s12968-019-0551-6
10. Mauger CA, Govil S, Chabiniok R, Gilbert K, Hegde S, Hussain T, et al. Right-left ventricular shape variations in tetralogy of Fallot: associations with pulmonary regurgitation. *J Cardiovasc Magn Reson.* (2021) 23:105. doi: 10.1186/s12968-021-00780-x
11. Föll D, Taeger S, Bode C, Jung B, Markl M. Age, gender, blood pressure, and ventricular geometry influence normal 3D blood flow characteristics in the left heart. *Eur Heart J Cardiovasc Imaging.* (2013) 14:366–73. doi: 10.1093/ehjci/jes196
12. Fenster BE, Browning J, Schroeder JD, Schafer M, Podgorski CA, Smyser J, et al. Vorticity is a marker of right ventricular diastolic dysfunction. *Am J Physiol Heart Circ Physiol.* (2015) 309:H1087–93. doi: 10.1152/ajpheart.00278.2015
13. Stankovic Z, Allen BD, Garcia J, Jarvis KB, Markl M. 4D flow imaging with MRI. *Cardiovasc Diagn Ther.* (2014) 4:173–92. doi: 10.3978/j.issn.2223-3652.2014.01.02
14. Dyverfeldt P, Bissell M, Barker AJ, Bolger AF, Carlhäll C-J, Ebbers T, et al. 4D flow cardiovascular magnetic resonance consensus statement. *J Cardiovasc Magn Reson.* (2015) 17:72. doi: 10.1186/s12968-015-0174-5
15. Schäfer M, Barker AJ, Morgan GJ, Jaggers J, Stone ML, Browne LP, et al. Increased systolic vorticity in the left ventricular outflow tract is associated with abnormal aortic flow formations in tetralogy of fallot. *Int J Cardiovasc Imaging.* (2020) 36:691–700. doi: 10.1007/s10554-019-01764-w
16. Ferdian E, Suinesiaputra A, Dubowitz D, Zhao D, Wang A, Cowan B, et al. 4DFlowNet: super-resolution 4D flow MRI using deep learning and computational fluid dynamics. *Front Phys.* (2020) 8:138. doi: 10.3389/fphy.2020.00138
17. Ledig C, Theis L, Huszar F, Caballero J, Cunningham A, Acosta A, et al. Photo-Realistic Single Image Super-Resolution Using a Generative Adversarial Network. In: *2017 IEEE Conference on Computer Vision and Pattern Recognition (CVPR)*. IEEE (2017). p.105–14. doi: 10.1109/CVPR.2017.19
18. Hirtler D, Garcia J, Barker AJ, Geiger J. Assessment of intracardiac flow and vorticity in the right heart of patients after repair of tetralogy of fallot by flow-sensitive 4D MRI. *Eur Radiol.* (2016) 26:3598–607. doi: 10.1007/s00330-015-4186-1
19. Schäfer M, Barker AJ, Kheyfets V, Stenmark KR, Crapo J, Yeager ME, et al. Helicity and vorticity of pulmonary arterial flow in patients with pulmonary hypertension: quantitative analysis of flow formations. *J Am Heart Assoc.* (2017) 6:e007010. doi: 10.1161/JAHA.117.007010
20. Young AA, Cowan BR, Thrupp SF, Hedley WJ, Dell'Italia LJ. Left ventricular mass and volume: fast calculation with guide-point modeling on MR images. *Radiology.* (2000) 216:597–602. doi: 10.1148/radiology.216.2.r00au14597
21. Heiberg E, Sjögren J, Ugander M, Carlsson M, Engblom H, Arheden H. Design and validation of Segment–freely available software for cardiovascular image analysis. *BMC Med Imaging.* (2010) 10:1. doi: 10.1186/1471-2342-10-1
22. R Core Team. *R: A Language And Environment For Statistical Computing. R Foundation for Statistical Computing*, Vienna, Austria (2019). Available online at: https://www.R-project.org/
23. Gilbert K, Forsch N, Hegde S, Mauger C, Omens JH, Perry JC, et al. Atlas-based computational analysis of heart shape and function in congenital heart disease. *J Cardiovasc Transl Res.* (2018) 11:123–32. doi: 10.1007/s12265-017-9778-5
24. Farrar G, Suinesiaputra A, Gilbert K, Perry JC, Hegde S, Marsden A, et al. Atlas-based ventricular shape analysis for understanding congenital heart disease. *Prog Pediatr Cardiol.* (2016) 43:61–9. doi: 10.1016/j.ppedcard.2016.07.010
25. Isorni MA, Martins D, Ben Moussa N, Monnot S, Boddaert N, Bonnet D, et al. 4D flow MRI versus conventional 2D for measuring pulmonary flow after tetralogy of Fallot repair. *Int J Cardiol.* (2020) 300:132–6. doi: 10.1016/j.ijcard.2019.10.030
26. Nordmeyer S, Riesenkampff E, Crelier G, Khasheei A, Schnackenburg B, Berger F, et al. Flow-sensitive four-dimensional cine magnetic resonance imaging for offline blood flow quantification in multiple vessels: a validation study. *J Magn Reson Imaging.* (2010) 32:677–83. doi: 10.1002/jmri.22280
27. Fredriksson A, Trzebiatowska-Krzynska A, Dyverfeldt P, Engvall J, Ebbers T, Carlhäll C. Turbulent kinetic energy in the right ventricle: Potential MR marker for risk stratification of adults with repaired Tetralogy of Fallot. *J Magn Reson Imaging.* (2018) 47:1043–53. doi: 10.1002/jmri.25830
28. Bodhey NK, Beerbaum P, Sarikouch S, Kropf S, Lange P, Berger F, et al. Functional analysis of the components of the right ventricle in the

setting of tetralogy of Fallot. *Circ Cardiovasc Imaging.* (2008) 1:141–7. doi: 10.1161/CIRCIMAGING.108.783795
29. Oosterhof T, Mulder BJM, Vliegen HW, de Roos A. Corrected tetralogy of Fallot: delayed enhancement in right ventricular outflow tract. *Radiology.* (2005) 237:868–71. doi: 10.1148/radiol.2373041324
30. Kim DH, Choi S Il, Chun EJ, Choi SH, Park JH. The cardiac MR images and causes of paradoxical septal motion. *J Korean Soc Radiol.* (2010) 62:427. doi: 10.3348/jksr.2010.62.5.427
31. Rahman MYA. El, Hui W, Dsebissowa F, Schubert S, Gutberlet M, Hetzer R, et al. Quantitative analysis of paradoxical interventricular septal motion following corrective surgery of tetralogy of fallot. *Pediatr Cardiol.* (2005) 26:379–84. doi: 10.1007/s00246-004-0753-y
32. Moses DA, Axel L. Quantification of the curvature and shape of the interventricular septum. *Magn Reson Med.* (2004) 52:154–63. doi: 10.1002/mrm.20105

Conflict of Interest: This study received working expenses and in-kind support from Siemens Healthineers, Erlangen, Germany. The funder was not involved in the study design, collection, analysis, interpretation of data, the writing of this article or the decision to submit it for publication. AM and JHO are co-founders of and have an equity interest in Insilicomed, Inc., and serves on the scientific advisory board. Some of their research grants, including those acknowledged here, have been identified for conflict of interest management based on the overall scope of the project and its potential benefit to Insilicomed, Inc. The authors are required to disclose this relationship in publications acknowledging the grant support, however the research subject and findings reported here did not involve the company in any way and have no relationship whatsoever to the business activities or scientific interests of the company. The terms of this arrangement have been reviewed and approved by the University of California San Diego in accordance with its conflict of interest policies.

The remaining authors declare that the research was conducted in the absence of any commercial or financial relationships that could be construed as a potential conflict of interest.

Publisher's Note: All claims expressed in this article are solely those of the authors and do not necessarily represent those of their affiliated organizations, or those of the publisher, the editors and the reviewers. Any product that may be evaluated in this article, or claim that may be made by its manufacturer, is not guaranteed or endorsed by the publisher.

frontiers in Cardiovascular Medicine

ORIGINAL RESEARCH
published: 09 March 2022
doi: 10.3389/fcvm.2022.831580

Long-Lasting Myocardial and Skeletal Muscle Damage Evidenced by Serial CMR During the First Year in COVID-19 Patients From the First Wave

Laura Filippetti[1], Nathalie Pace[1], Jean-Sebastien Louis[2,3], Damien Mandry[2,4], François Goehringer[5], Maria-Soledad Rocher[6], Nicolas Jay[6], Christine Selton-Suty[1], Gabriela Hossu[2,3], Olivier Huttin[1,7] and Pierre-Yves Marie[7,8]*

[1] Department of Cardiology, CHRU-Nancy, Nancy, France, [2] Université de Lorraine, INSERM, UMR-1254, Nancy, France, [3] CHRU-Nancy, Université de Lorraine, CIC 1433, Nancy, France, [4] Department of Radiology, CHRU-Nancy, Université de Lorraine, Nancy, France, [5] Department of Infectious Diseases, CHRU-Nancy, Université de Lorraine, Nancy, France, [6] Department of Medical Information, CHRU-Nancy, Université de Lorraine, Nancy, France, [7] Université de Lorraine, INSERM, UMR-1116, Nancy, France, [8] CHRU-Nancy, Université de Lorraine, Nuclear Medicine and Nancyclotep Platform, Nancy, France

OPEN ACCESS

Edited by:
Carlo Gabriele Tocchetti,
University of Naples Federico II, Italy

Reviewed by:
Lu Huang,
Huazhong University of Science and Technology, China
Alessandro Pingitore,
Clinical Physiology Institute, CNR, Italy

***Correspondence:**
Laura Filippetti
l.filippetti@chru-nancy.fr

Specialty section:
This article was submitted to Cardiovascular Imaging, a section of the journal Frontiers in Cardiovascular Medicine

Received: 08 December 2021
Accepted: 15 February 2022
Published: 09 March 2022

Citation:
Filippetti L, Pace N, Louis J-S, Mandry D, Goehringer F, Rocher M-S, Jay N, Selton-Suty C, Hossu G, Huttin O and Marie P-Y (2022) Long-Lasting Myocardial and Skeletal Muscle Damage Evidenced by Serial CMR During the First Year in COVID-19 Patients From the First Wave. Front. Cardiovasc. Med. 9:831580. doi: 10.3389/fcvm.2022.831580

Introduction: This observational CMR study aims to characterize left-ventricular (LV) damage, which may be specifically attributed to COVID-19 and is distant in time from the acute phase, through serial CMR performed during the first year in patients with no prior cardiac disease.

Methods: This study included consecutive patients without any prior history of cardiac disease but with a peak troponin-Ic > 50 ng/ml at the time of the first COVID-wave. All had a CMR in the first months after the acute phase, and some had an additional CMR at the end of the first year to monitor LV function, remodeling, and abnormalities evocative of myositis and myocarditis - i.e., increased T1/T2 relaxation times, increased extracellular volume (ECV), and delayed contrast enhancement.

Results: Nineteen consecutively admitted COVID-19 patients (17 men, median age 66 [57–71] years) were included. Eight (42%) had hypertension, six (32%) were obese, and 16 (84%) had suffered an acute respiratory distress syndrome. The 1st CMR, recorded at a median 3.2 [interquartile range: 2.6–3.9] months from the troponin peak, showed (1) LV concentric remodeling in 12 patients (63%), (2) myocardial tissue abnormalities in 11 (58%), including 9 increased myocardial ECVs, and (3) 14 (74%) increased ECVs from shoulder skeletal muscles. The 2nd CMR, obtained at 11.1 [11.0–11.7] months from the troponin peak in 13 patients, showed unchanged LV function and remodeling but a return to normal or below the normal range for all ECVs of the myocardium and skeletal muscles.

Conclusion: Many patients with no history of cardiac disease but for whom an increase in blood troponin-Ic ascertained COVID-19 induced myocardial damage exhibited signs

of persistent extracellular edema at a median 3-months from the troponin peak, affecting the myocardium and skeletal muscles, which resolved within a one-year time frame. Associations with long-COVID symptoms need to be investigated on a larger scale now.

Clinical Trial Registration: NCT04753762 on the ClinicalTrials.gov site.

Keywords: COVID-19, myocarditis, edema, skeletal muscle, cardiovascular magnetic resonance imaging

INTRODUCTION

COVID-19 induced myocardial damage is complex and exhibits features consistent with inflammation and endothelium dysfunction, and thrombosis (1–3). It has been speculated that this myocardial damage might constitute a risk factor for developing heart failure, given the similarities in the profiles of patients at risk of heart failure with those of severe COVID-19 patients (4). There is, therefore, an urgent need to specify the nature of COVID-19 induced myocardial damage and investigate its impact over time.

Cardiac Magnetic Resonance (CMR) already documented myocardial tissue abnormalities at the acute or sub-acute phase of COVID-19 and, more specifically, increases in myocardial T1 and T2 relaxation times and an increased extracellular volume (ECV) (5, 6). This observation was at the time attributed to inflammatory edema. However, we do not yet know what the clinical consequences of these anomalies are in the long term and whether they correspond to a COVID-19 pathology specifically targeted to the heart or to a more diffuse edematous and inflammatory response (7). Myositis with skeletal muscle edema is also frequently observed during COVID-19 (8).

This observational CMR study aims to characterize the left-ventricular (LV) damage which may be specifically attributed to COVID-19 and distant in time from the acute phase, through serial CMR planned during the first year in patients with no previous history of cardiac disease but with significant increases in blood troponin-Ic during the initial COVID-19 hospitalization.

MATERIALS AND METHODS

Patients and Study Design

The study included consecutive 18- to 80-year-old patients hospitalized in our Regional University Hospital for a COVID-19-related pathology between the 16th and the 31st of March 2020, which corresponded to the peak of the first COVID-19 wave in our region. Patients' COVID-19 status was ascertained by a positive reverse transcriptase-polymerase chain reaction test. Additional inclusion criteria were: (i) a peak troponin Ic $>$ 50 ng/ml measured during hospitalization, (ii) the absence of any prior cardiac disease history, and (iii) health conditions required to endure the CMR-based monitoring which is currently prescribed for myocarditis patients in our center.

Baseline investigations were performed with the 1st CMR within the first months following the acute phase and the follow-up investigations with the 2nd CMR, at the end of the first year, on a 3T PRISMA Magnet (Siemens Medical Solutions, Erlangen, Germany). Echocardiography and blood analysis for routine biomarkers were also performed on the CMR days. Echocardiography data were obtained according to current recommendations (9, 10) with a General Electric® device and the post-processing EchoPAC® software.

CMR Recording

The same CMR protocol was used in all patients and for both the 1st and 2nd CMR. LV function and remodeling were assessed on cine images recorded with a compressed sensing SSFP sequence (11), on contiguous short-axis slices and with the following parameters: 2 x 2 x 8 mm^3 voxel size, 420 x 320 mm^2 field of view (FOV), 60° flip angle (FA), 41 ms repetition time (TR), 2.9 ms interecho time, 1.27 ms echo time (TE), and 14 segments.

According to the "2018 updated Lake Louise Criteria" (12), signs of myocarditis were searched for (i) on longitudinal (T1) and transversal (T2) relaxation maps recorded with short-axis slices and, respectively, precontrast - Modified Look-Locker Inversion Recovery (MOLLI, acquisition scheme 5(3)3) and 2D TurboFlash sequences (12), and (ii) on contiguous late gadolinium enhancement images covering the LV on short-axis, vertical and horizontal long-axis directions with a fast multi-slice phase-sensitive inversion recovery sequence (13), 10 to 15 min after the injection of 0.1 mmol.kg^{-1} body weight of Dotarem®, (GUERBET, France). T1 maps were recorded with the following parameters: 1.4 x 1.4 x 8.0 mm^3 voxel size, 371 x 278 mm^2 FOV, 35° FA, 1 excitation, 180 ms time to inversion (TI), 267 ms TR, 1.11 ms TE, and 63 segments. For the T2 maps, these parameters were: 1.9 x 1.9 x 8.0 mm^3 voxel size, 360 x 360 mm^2 FOV, 12° FA, 201 ms TR, and 1.32/30/50 ms TE. For the LGE images, these parameters were: 2.1 x 2.1 x 8 mm^3 voxel size, 400 x 380 mm^2 FOV, 40° FA, 305 ms TI, 768 ms RT, 2.4 ms interecho time, 1.04 ms TE, and 1 excitation.

CMR Analysis

CMR results were extracted with the Syngovia software (Siemens Medical Solutions, Erlangen, Germany), using a manual adjustment of the ventricular contours applied to determine LV mass, end-diastolic volumes, and ejection fractions (14). Ventricular volumes and LV mass were indexed to body surface area, and the LV mass/end-diastolic volume ratio was used to assess LV concentric remodeling (15, 16). Myocardial T1 and T2 were determined with regions of interest (ROI) drawn on a septal mid-ventricular area (**Figure 1**) (17). The myocardial extracellular volume (ECV), expressed as % myocardium volume, was conventionally computed from: (i) T1-pre values from the pre-contrast MOLLI sequence described above (ii) T1-post values from post-contrast MOLLI sequence (acquisition

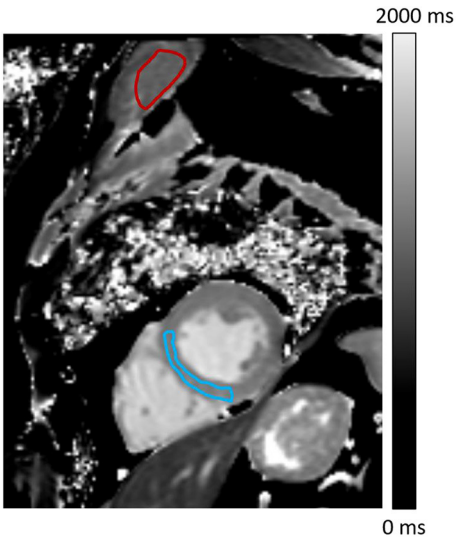

FIGURE 1 | Pre-contrast T1 map showing regions-of-interest (ROIs) drawn to determine ECV and relaxation times on the myocardium (blue) and shoulders skeletal muscle (red).

scheme: 4(1)3(1)2) acquired 10–15 min after the injection and (iii) individual hematocrit values (6, 12). The latter were obtained from blood sampled just before CMR, during placement of the intravenous catheter used for Dotarem® injection.

The cardiac T1 maps were additionally used to determine the T1 and ECV of the shoulder skeletal muscles setting in the field of view (i.e., the pectoralis major, subscapularis, or infraspinatus) with careful exclusion of perimuscular fat and intramuscular tendons from the hand-drawn ROIs (**Figure 1**), as previously described (17).

Criteria Used to Define Abnormal CMR Parameters

Normal limits for the main CMR parameters are summarized in **Table 1**. Most of these normal limits were derived from the 95% confidence intervals and obtained from local control populations with the same operator and extraction methods as the current COVID-19 study.

Normal values of LV ejection fraction, mass, volume, and mass/volume ratio, which are used to assess LV function and remodeling, and which are known to vary according to age and sex, were extracted from a local database of patients without any known cardiovascular disease (14). The final population was further selected according to age to provide a comparable mean and distribution to our COVID-19 population (for mean ± SD: 64.2 ± 7.5 vs. 64.2 ± 8.3 years). There were 74 men and 84 women with respective lower limits of 49% and 51% LV ejection fraction, and respective upper limits of 97 and 88 $mL.m^{-2}$ for LV end-diastolic volume, 73 and 57 $g.m^{-2}$ for LV mass, and 1.11 and 0.90 for LV mass/volume ratio. These limits are within the range of those already defined for ≥ 60 years old normal subjects in previously published CMR studies (18–20).

TABLE 1 | Limits used to define abnormal values for the main CMR parameters obtained from local control populations with the same operator and extraction methods as the current COVID-19 study.

	Women	Men
Lower LV ejection fraction limits	51 %	49 %
Upper LV mass limits	57 g/m^2	73 g/m^2
Upper limits for LV mass/volume ratio	0.90	1.11
Upper myocardial T1 limits	1,293 ms	1,293 ms
Upper myocardial T2 limits	47 ms	47 ms
Upper myocardial ECV limits	28.5 %	28.5 %
Upper skeletal T1 limits	1,206 ms	1,206 ms
Upper skeletal ECV limits	14.9 %	14.9 %

ECV, extracellular volume, LV, left ventricle, T1, longitudinal relaxation time, T2, transversal relaxation time.

Normal T1 and ECV values were determined for both myocardium and shoulders skeletal muscles in a population extracted from a local database of patients who had been initially investigated for a mitral valve prolapse (21). The final selection only included patients without any complicated prolapse (absence of ≥ 2 mitral regurgitation, ventricular arrhythmias, or LV dysfunction) and without any other cardiovascular disease. This group included 30 subjects, 11 women and 19 men, with a mean age of 40 ± 18 years. The normal upper limits of T1 were computed as 1,293 ms for the myocardium and 1,206 ms for the skeletal shoulder muscles. For normal ECV, the respective upper limits were 28.5 and 14.9%. These limits are very similar to those obtained in previous CMR studies performed using a comparable methodology (22, 23).

For myocardial T2, we selected the threshold of 47 ms which corresponds to the upper limit of the 95% confidence interval observed in a study performed with a 3T magnet and with the same methodology as that used in our COVID-19 patients (24).

Late gadolinium enhancement was identified visually by a single observer (PM) as an increase in the signal from myocardial areas clearly distinct from the epicardial fat and cavitary blood. All transmural or sub-epicardial areas of LGE were considered as potentially related to myocarditis (14). This was not the case for the LGE evocative of a mid-wall septal fibrosis and commonly associated with LV hypertrophy and remodeling in the absence of any myocarditis (25).

Statistical Analysis

Statistical analyses were obtained using the SPSS statistical software (IBM Statistics version 20). Qualitative variables were expressed as numbers and percentages and quantitative variables were expressed as medians with interquartile ranges. As the number of cases was not sufficiently large to assume a normal distribution, paired comparisons of quantitative variables between the two CMR visits were assessed using a non-parametric test: the Wilcoxon sum-rank test. Paired comparisons of qualitative variables were planned with Mc Nemar tests. *P* values were not not adjusted for possible multiple comparison

TABLE 2 | Main characteristics of the 19 patients with blood, clinical and CMR data collected on the day of the 1st CMR, at a median of 3.2 months from the troponin peak.

Age (years)	66 [59–71]
Female	2 (11%)
Diabetes	7 (37%)
Dyslipidemia	6 (32%)
Hypertension	8 (42%)
Obesity (BMI > 30 kg/m^2)	7 (37%)
ARDS at acute phase	16 (84%)
Peak troponin Ic at acute phase (ng/ml)	242 [83–896]
Delay time from peak Troponin (months)	3.2 [2.6–3.9]
Heart rate (bpm)	80.0 [64.8–82.1]
Systolic BP (mmHg)	134 [132–155]
Diastolic BP (mmHg)	81 [72–85]
End-diastolic LV volume (mL/m²)	63 [55–72]
LV ejection fraction (%)	58 [52–65]
LV mass (g/m^2)	70 [59–80]
LV mass / volume ratio	1.20 [0.91–1.27]
End-diastolic RV volume (mL/m²)	56 [53–68]
RV ejection fraction (%)	55 [51–59]
Myocardial T1 (ms)	1,257 [1,221–1,270]
Myocardial T2 (ms)	38.0 [36.0–40.2]
Myocardial ECV (%)	27.6 [25.4–31.5]
Delayed retention myocarditis pattern	2 (11%)
Skeletal T1 (ms)	1,149 [1,110–1,149]
Skeletal ECV (%)	16.5 [14.4–22.4]
Hematocrit (%)	42.4 [40.3–43.9]
C Reactive Protein (mg/mL)	4 (4)
Troponin Ic (ng/ml)	6.0 [2.0–13.0]
Nt-pro BNP (pg/mL)	111 [36–259]
Albumin (g/L)	41.5 [39.1–46.4]
eGFR (ml/min/1.73 m^2)	90 [84–90]

ARDS, acute respiratory distress syndrome; BNP, brain natriuretic peptide; BMI, body mass index; BP, blood pressure; ECV, extracellular volume; eGFR, glomerular filtration rate estimated with the CKD-EPI formula and truncated at 90 ml/min/1.73 m^2; LV, left ventricle; RV, right ventricle; T1, longitudinal relaxation time; T2, transversal relaxation time.

TABLE 3 | Changes in clinical, CMR and blood parameters of the 13 patients who underwent the two CMRs at medians of 3 and 11 months from peak troponin respectively.

	1st CMR	2nd CMR	*P*-value
BMI (kg/m^2)	27.4 [25.4–31.9]	30.9 [28.8–33.60]	0.103
Heart rate (bpm)	77.0 [65.4–82.2]	64.1 [57.5–79.3]	0.046
Systolic BP (mmHg)	134 [125–145]	142 [127–156]	0.173
Diastolic BP (mmHg)	81 [72–85]	81 [77–90]	0.166
End-diastolic LV volume (mL/m²)	63 [53–71]	61 [51–69]	0.576
LV ejection fraction (%)	60 [53–65]	56 [52–62]	0.388
LV mass (g/m^2)	70 [60–82]	68 [59–82]	0.419
LV mass/volume ratio	1.23 [1.06–1.26]	1.12 [1.02–1.34]	0.650
End-diastolic RV volume (mL/m²)	63 [53–71]	61 [51–69]	0.576
RV ejection fraction (%)	60 [53–65]	56 [52–62]	0.388
Myocardial T1 (ms)	1,257 [1,225–12,646]	1,233 [1,192–1,256]	0.038
Myocardial T2 (ms)	37.6 [35.9–39.5]	38.0 [36.5–40.5]	0.576
Myocardial ECV (%)	27.4 [25.7–31.1]	25.9 [23.1–27.3]	0.007
Delayed retention myocarditis pattern	2 (14%)	2 (14%)	1.000
Skeletal T1 (ms)	1,122 [1,104–1,173]	1,134 [1,104–1,228]	0.382
Skeletal ECV (%)	15.6 [14.2–19.2]	12.7 [12.2–14.9]	0.001
Hematocrit (%)	42.2 [40.1–43.4]	42.4 [39.2–44.5]	1.000
C Reactive Protein (mg/mL)	4 (4)	4 [4–9.3]	0.028
Troponin Ic (ng/ml)	5.5 [2.0–13.2]	5.0 [2.75–12.25]	0.893
Nt-pro BNP (pg/mL)	111 [41–133]	56 [35–52]	0.285
Albumin (g/L)	42.0 [40.3–47.4]	44.1 [42.7–46.0]	0.388
eGFR (ml/min/1.73 m^2)	90 [87–90]	90 [82–90]	0.221

BMI, body mass index; BNP, brain natriuretic peptide; BP, blood pressure; ECV, extracellular volume; eGFR, glomerular filtration rate estimated with the CKD-EPI formula and truncated at 90 ml/min/1.73 m^2; LV, left ventricle; RV, right ventricle; T1, longitudinal relaxation time; T2, transversal relaxation time.

effects given the exploratory nature of the present study, and $p < 0.05$ were considered to reflect significant differences.

RESULTS

Among the 222 COVID-19 patients hospitalized during the study period, 45 exhibited a peak troponin Ic > 50 ng/ml, and 19 fulfilled all study inclusion criteria. As detailed in **Table 2**, at the 1st CMR, the median age was 66 [59–71] years, and the median from peak troponin was 3.2 [2.6–3.9] months. Seventeen patients (89%) were male, 11 (58%) had previously been identified with hypertension or obesity (6 with obesity and 8 with hypertension), and as many as 16 (84%) had been affected by an acute respiratory distress syndrome (ARDS) requiring mechanical ventilation at the acute phase.

Baseline CMR

The 1st CMR, recorded at a median 3.2 [interquartile range: 2.6–3.9] months from the troponin peak, showed a > 50% LV ejection fraction in all but 2 patients for whom it was only slightly lower (46% and 48%). However, as many as 12 (63%) exhibited LV concentric remodeling (i.e., high LV mass/volume ratio), which was associated with LV hypertrophy (i.e., high LV mass) in 9 cases. Myocardial tissue damage was documented in 11 patients (58%), including 9 increased myocardial ECVs, 3 abnormal T1, 1 abnormal T2, and 2 evocative late gadolinium enhancements (LGE). No pattern suggestive of myocardial infarction was observed (i.e., no sub-endocardial or transmural LGE).

For the shoulder skeletal muscles, abnormal values were observed for T1 in 2 cases (11%) and for ECV in 14 (74%). As detailed in **Table 2**, most plasma analytics were within normal or sub-normal concentration ranges (**Table 2**), including troponin Ic (all ≤ 29 ng/mL), CRP (all ≤ 10 mg/mL), NT-proBNP (all < 450 pg/mL) and eGFR (all but one > 80 ml/min/1.73 m^2).

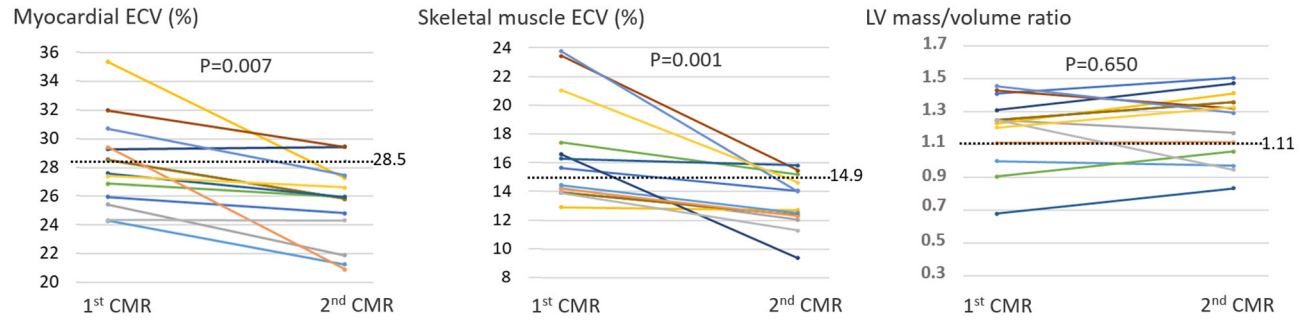

FIGURE 2 | Individual variations between the 1st and 2nd CMR for the ECV from the myocardium and skeletal muscles, as well as for the LV mass/volume ratio, which was used to assess LV concentric remodeling and normalized to male values (i.e., with the values in women increased by 0.21 to compensate for the difference in the normal upper limits between women (0.90) and men (1.11)). The dashed lines represent the normal upper limits.

Follow-Up CMR

The 2nd CMR was performed in 13 out of the 19 patients, at a median of 11.1 [11.0–11.7] months from peak troponin. LV function and remodeling parameters were unchanged between the 1st and 2nd CMR, but significant decreases in heart rate, myocardial T1, and particularly ECV from skeletal muscles and myocardium were observed (**Table 3**, **Figure 2**). Late contrast enhancement was still documented in 2 patients, and as evidenced in **Figure 2**, there was a return to normal or below the normal range for all ECVs of the myocardium and skeletal muscles.

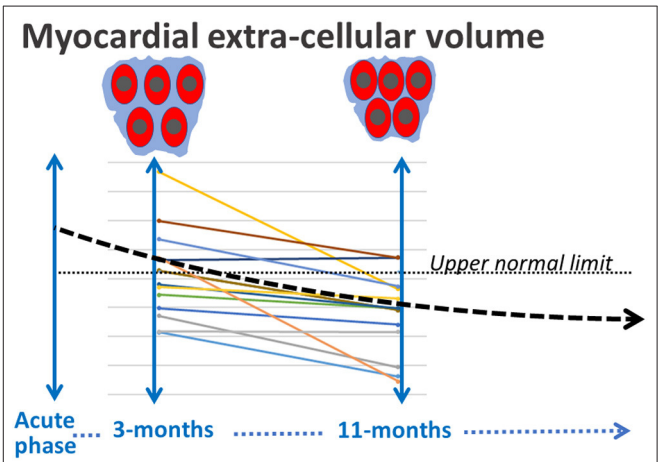

FIGURE 3 | Schematic representation of the progressive decrease during the first year of the myocardial ECV, presumably in line with a delayed resolution of the interstitial edema.

DISCUSSION

As illustrated by a schematic representation in **Figure 3**, a frequent increase in ECV affecting the myocardium and skeletal muscles and which regressed during the first year, constituted the main observation in our consecutive series of patients with no prior history of cardiac disease but for whom COVID-19 induced myocardial damage was ascertained by a significant rise in blood troponin Ic. A COVID-19 etiology of these increased ECV values is supported by their return to normal or below the normal range at 1 year (**Figure 2**), in contrast to the stability observed for other CMR parameters. This ECV evolution likely reflects the resolution of the extracellular interstitial edema, which is commonly observed in the heart and other organs in COVID-19 autopsy studies (26, 27).

CMR already documented an increased myocardial ECV at the acute or sub-acute phase of COVID-19 and associated with increases in myocardial T1 and T2 (5, 6). This observation was attributed to inflammatory edema at the time. Our serial CMR data show that this increased ECV: (i) also affects skeletal muscles, (ii) resolves very progressively, given its common persistence at a median of 3 months from the acute phase (i.e., at the time of the 1st CMR), and (iii) is then no longer associated with any evident signs of active damage or inflammation (i.e., based on the normal or below the normal range of CRP, troponin and myocardial T2 values).

Interestingly, the decrease in ECV at 1 year was observed in our COVID patients irrespective of the presence or absence of an abnormal ECV at 3-months (see **Figure 2**). This decrease might thus be commonly involved in the recovery of severe COVID-19. In addition, a possible role of a non-specific response associated with ARDS needs further investigation. Indeed, 84% of our COVID-19 patients presented an ARDS at the acute phase, and ARDS patients are commonly affected by muscle dysfunction in both early and late stages, constituting a significant morbidity factor (28, 29).

This increased ECV was not associated with any evident deterioration of cardiac function, with LV ejection fractions and volumes remaining normal or below the normal range during follow-up according to the CMR, as well as the echocardiography data (see **Supplementary Data File**). As many as 63% of our patients were affected by LV concentric remodeling, an indicator of increased cardiovascular risk (15, 16). However, this remodeling was unchanged between the two evaluations, and it may constitute an underlying pathology due to the risk factors shared by concentric remodeling and severe COVID-19 (age, obesity, hypertension).

A main limitation is the small sample size of the present study population, and further studies will be required to confirm the results.

Conclusion and Perspectives

The present serial CMR study shows a slow return to normal of the extracellular volume of the myocardium and skeletal muscles in many patients with no history of cardiac disease, but for whom an increase in blood troponin-Ic ascertained COVID-19 induced myocardial damage. This observation is likely due to a delayed resolution of the interstitial edema, which is known to affect severe COVID-19 patients. Associations with long-COVID symptoms (30) need to be investigated on a larger scale. This might help to better understand and perhaps to prevent or treat these symptoms. The potential role of a non-specific response associated with ARDS also requires further investigation.

DATA AVAILABILITY STATEMENT

The raw data supporting the conclusions of this article will be made available by the authors, without undue reservation.

ETHICS STATEMENT

The studies involving human participants were reviewed and approved by Ethics Committee of the Nancy University Hospital. Written informed consent for participation was not required for this study in accordance with the national legislation and the institutional requirements.

AUTHOR CONTRIBUTIONS

Seven authors contributed significantly to the analysis and interpretation of the data (LF, M-SR, NJ, J-SL, GH, OH, and P-YM), and/or to the writing or revision of the manuscript (LF, NP, J-SL, OH, and P-YM), the four others collaborated in the study implementation, and/or management of the included subjects (DM, FG, NP, and CS-S). All authors contributed to the article and approved the submitted version.

FUNDING

This study was funded by CHRU-Nancy, Nancy, France. Hospital's own funds were used for the study organization.

ACKNOWLEDGMENTS

The authors wish to thank Aboubaker Cherifi for his help in the organization of the study and Dr. Petra Neufing for critical review of the manuscript.

SUPPLEMENTARY MATERIAL

The Supplementary Material for this article can be found online at: https://www.frontiersin.org/articles/10.3389/fcvm.2022.831580/full#supplementary-material

REFERENCES

1. Maccio U, Zinkernagel AS, Shambat SM, Zeng X, Cathomas G, Ruschitzka F, et al. SARS-CoV-2 leads to a small vessel endotheliitis in the heart. *EBioMedicine*. (202) 63:103182. doi: 10.1016/j.ebiom.2020.103182
2. Puntmann VO, Carerj ML, Wieters I, Fahim M, Arendt C, Hoffmann J, et al. Outcomes of Cardiovascular Magnetic Resonance Imaging in Patients Recently Recovered From Coronavirus Disease 2019 (COVID-19). *JAMA Cardiol*. (2020) 5:1265-73. doi: 10.1001/jamacardio.2020.3557
3. Filippetti L, Pace N, Marie PY. Cardiac Involvement After Recovering From COVID-19. *JAMA Cardiol*. (2021) 6:243–4. doi: 10.1001/jamacardio.2020.5279
4. Freaney PM, Shah SJ, Khan SS. COVID-19 and Heart Failure With Preserved Ejection Fraction. *JAMA*. (2020) 324:1499–500. doi: 10.1001/jama.2020.17445
5. Chen BH, Shi NN, Wu CW, An DA, Shi YX, Wesemann LD, et al. Early cardiac involvement in patients with acute COVID-19 infection identified by multiparametric cardiovascular magnetic resonance imaging. *Eur Heart J Cardiovasc Imaging*. (2021) 22:844–51. doi: 10.1093/ehjci/jeab042
6. Huang L, Zhao P, Tang D, Zhu T, Han R, Zhan C, et al. Cardiac Involvement in Patients Recovered From COVID-2019 Identified Using Magnetic Resonance Imaging. *JACC Cardiovasc Imaging*. (2020) 13:2330–9. doi: 10.1016/j.jcmg.2020.05.004
7. Doeblin P, Kelle S. Going after COVID-19 myocarditis. *Eur Heart J Cardiovasc Imaging*. (2021) 22:852–4. doi: 10.1093/ehjci/jeab097
8. Ramani SL, Samet J, Franz CK, Hsieh C, Nguyen CV, Horbinski C, et al. Musculoskeletal involvement of COVID-19: review of imaging. *Skeletal Radiol*. (2021) 50:1763–73. doi: 10.1007/s00256-021-03734-7
9. Lang RM, Badano LP, Mor-Avi V, Afilalo J, Armstrong A, Ernande L, et al. Recommendations for cardiac chamber quantification by echocardiography in adults: an update from the American Society of Echocardiography and the European Association of Cardiovascular Imaging. *J Am Soc Echocardiogr*. (2015) 28:1–39. doi: 10.1016/j.echo.2014.10.003
10. Nagueh SF, Smiseth OA, Appleton CP, Byrd BF 3rd, Dokainish H, Edvardsen T, et al. Recommendations for the Evaluation of Left Ventricular Diastolic Function by Echocardiography: An Update from the American Society of Echocardiography and the European Association of Cardiovascular Imaging. *Eur Heart J Cardiovasc Imaging*. (2016) 17:1321–60. doi: 10.1093/ehjci/jew082
11. Vincenti G, Monney P, Chaptinel J, Rutz T, Coppo S, Zenge MO, et al. Compressed sensing single-breath-hold CMR for fast quantification of LV function, volumes, and mass. *JACC Cardiovasc Imaging*. (2014) 7:882–92. doi: 10.1016/j.jcmg.2014.04.016
12. Ferreira VM, Schulz-Menger J, Holmvang G, Kramer CM, Carbone I, Sechtem U, et al. Cardiovascular magnetic resonance in nonischemic myocardial inflammation: expert recommendations. *J Am Coll Cardiol*. (2018) 72:3158–76. doi: 10.1016/j.jacc.2018.09.072
13. Muehlberg F, Arnhold K, Fritschi S, Funk S, Prothmann M, Kermer J, et al. Comparison of fast multi-slice and standard segmented techniques for detection of late gadolinium enhancement in ischemic and non-ischemic cardiomyopathy - a prospective clinical cardiovascular magnetic resonance trial. *J Cardiovasc Magn Reson*. (2018) 20:13. doi: 10.1186/s12968-018-0434-2
14. Marie PY, Mandry D, Huttin O, Micard E, Bonnemains L, Girerd N, et al. Comprehensive monitoring of cardiac remodeling with aortic stroke volume values provided by a phase-contrast CMR sequence. *J Hypertens*. (2016) 34:967–73. doi: 10.1097/HJH.0000000000000889
15. Tsao CW, Gona PN, Salton CJ, Chuang ML, Levy D, Manning WJ, et al. Left Ventricular Structure and Risk of Cardiovascular Events: A Framingham Heart Study Cardiac Magnetic Resonance Study. *J Am Heart Assoc*. (2015) 4:e002188. doi: 10.1161/JAHA.115.002188
16. Bluemke DA, Kronmal RA, Lima JA, Liu K, Olson J, Burke GL, et al. The relationship of left ventricular mass and geometry to incident cardiovascular

events: the MESA (Multi-Ethnic Study of Atherosclerosis) study. *J Am Coll Cardiol.* (2008) 52:2148–55. doi: 10.1016/j.jacc.2008.09.014
17. Huber AT, Bravetti M, Lamy J, Bacoyannis T, Roux C, de Cesare A, et al. Non-invasive differentiation of idiopathic inflammatory myopathy with cardiac involvement from acute viral myocarditis using cardiovascular magnetic resonance imaging T1 and T2 mapping. *J Cardiovasc Magn Reason.* (2018) 20:11. doi: 10.1186/s12968-018-0430-6
18. Aquaro GD, Camastra G, Monti L, Lombardi M, Pepe A, Castelletti S, et al. Reference values of cardiac volumes, dimensions, and new functional parameters by MR: A multicenter, multivendor study. *J Magn Reson Imaging.* (2017) 45:1055–67. doi: 10.1002/jmri.25450
19. Chuang ML, Gona P, Hautvast GL, Salton CJ, Breeuwer M, O'Donnell CJ, et al. CMR reference values for left ventricular volumes, mass, and ejection fraction using computer-aided analysis: the Framingham Heart Study. *J Magn Reson Imaging.* (2014) 39:895–900. doi: 10.1002/jmri.24239
20. Eng J, McClelland RL, Gomes AS, Hundley WG, Cheng S, Wu CO, et al. Adverse Left Ventricular Remodeling and Age Assessed with Cardiac MR Imaging: The Multi-Ethnic Study of Atherosclerosis. *Radiology.* (2016) 278:714–22. doi: 10.1148/radiol.2015150982
21. Constant Dit Beaufils AL, Huttin O, Jobbe-Duval A, Senage T, Filippetti L, Piriou N, et al. Replacement Myocardial Fibrosis in Patients With Mitral Valve Prolapse: Relation to Mitral Regurgitation, Ventricular Remodeling, and Arrhythmia. *Circulation.* (2021) 143:1763–74. doi: 10.1161/CIRCULATIONAHA.120.050214
22. Wang X, Joseph AA, Kalentev O, Merboldt KD, Voit D, Roeloffs VB, et al. High-resolution myocardial T1 mapping using single-shot inversion-recovery fast low-angle shot CMR with radial undersampling and iterative reconstruction. *Br J Radiol.* (2016) 89:20160255. doi: 10.1259/bjr.20160255
23. Thavendiranathan P, Zhang L, Zafar A, Drobni ZD, Mahmood SS, Cabral M, et al. Myocardial T1 and T2 Mapping by Magnetic Resonance in Patients With Immune Checkpoint Inhibitor-Associated Myocarditis. *J Am Coll Cardiol.* (2021) 77:1503–16. doi: 10.1016/j.jacc.2021.01.050
24. van Heeswijk RB, Feliciano H, Bongard C, Bonanno G, Coppo S, Lauriers N, et al. Free-breathing 3 T magnetic resonance T2-mapping of the heart. *JACC Cardiovasc Imaging.* (2012) 5:1231–9. doi: 10.1016/j.jcmg.2012.06.010
25. Soler R, Méndez C, Rodríguez E, Barriales R, Ochoa JP, Monserrat L. Phenotypes of hypertrophic cardiomyopathy. An illustrative review of CMR findings. *Insights Imaging.* (2018) 9:1007–20. doi: 10.1007/s13244-018-0656-8
26. Haslbauer JD, Tzankov A, Mertz KD, Schwab N, Nienhold R, Twerenbold R, et al. Characterisation of cardiac pathology in 23 autopsies of lethal COVID-19. *J Pathol Clin Res.* (2021) 7:326–37. doi: 10.1002/cjp2.212
27. Mondello C, Roccuzzo S, Malfa O, Sapienza D, Gualniera P, Ventura Spagnolo E, et al. Pathological Findings in COVID-19 as a Tool to Define SARS-CoV-2 Pathogenesis A Systematic Review. *Front Pharmacol.* (2021) 12:614586. doi: 10.3389/fphar.2021.614586
28. Files DC, Sanchez MA, Morris PE. A conceptual framework: the early and late phases of skeletal muscle dysfunction in the acute respiratory distress syndrome. *Crit Care.* (2015) 19:266. doi: 10.1186/s13054-015-0979-5
29. Matthay MA, Zemans RL, Zimmerman GA, Arabi YM, Beitler JR, Mercat A, et al. Acute respiratory distress syndrome. *Nat Rev Dis Primers.* (2019) 5:18. doi: 10.1038/s41572-019-0069-0
30. Yan Z, Yang M, Lai CL. Long COVID-19 Syndrome: A Comprehensive Review of Its Effect on Various Organ Systems and Recommendation on Rehabilitation Plans. *Biomedicines.* (2021) 9:966. doi: 10.3390/biomedicines9080966

Conflict of Interest: The authors declare that the research was conducted in the absence of any commercial or financial relationships that could be construed as a potential conflict of interest.

Publisher's Note: All claims expressed in this article are solely those of the authors and do not necessarily represent those of their affiliated organizations, or those of the publisher, the editors and the reviewers. Any product that may be evaluated in this article, or claim that may be made by its manufacturer, is not guaranteed or endorsed by the publisher.

frontiers in Cardiovascular Medicine

ORIGINAL RESEARCH
published: 31 March 2022
doi: 10.3389/fcvm.2022.841776

Right Heart Chambers Longitudinal Strain Provides Enhanced Diagnosis and Categorization in Patients With Pulmonary Hypertension

Nilda Espinola-Zavaleta[1,2†], Neftali Eduardo Antonio-Villa[3†], Enrique C. Guerra[3], Navin C. Nanda[4], Lawrence Rudski[5], Ricardo Alvarez-Santana[1], Gyssele Camacho-Camacho[1,6], Alberto Aranda-Fraustro[7], Jorge Cossio-Aranda[8], Karina Zamora[8], Diego Oregel-Camacho[1,6], Javier Ivan Armenta-Moreno[1], Joaquin Berarducci[1] and Erick Alexanderson-Rosas[1,9]*

[1] Department of Nuclear Cardiology, National Institute of Cardiology Ignacio Chavez, Mexico City, Mexico, [2] Department of Echocardiography, The American British Cowdray Medical Center, Private Assistance Institution, Mexico City, Mexico, [3] MD/Ph.D. (PECEM) Program, Facultad de Medicina, Universidad Nacional Autonoma de Mexico, Mexico City, Mexico, [4] Division of Cardiology, Department of Medicine, University of Alabama, Birmingham, AL, United States, [5] Jewish General Hospital, McGill University, Montreal, QC, Canada, [6] Inter-Institutional Program for Strengthening Research and Postgraduate Studies in the Pacific (Dolphin), Mexico City, Mexico, [7] Department of Pathology, National Institute of Cardiology Ignacio Chavez, Mexico City, Mexico, [8] Out-Patient Clinic, National Institute of Cardiology Ignacio Chavez, Mexico City, Mexico, [9] Department of Physiology, School of Medicine, National Autonomous University of Mexico, Mexico City, Mexico

Background: Increased systolic pulmonary arterial pressure (sPAP) could lead to the mechanical dysfunction and myocardial fibrosis of the right heart chambers. Echocardiographic strain analysis has not been adequately studied in patients with pulmonary hypertension (PH).

Study design and methods: A cross-sectional cohort of patients with suspected PH and echocardiographic strain evaluation was recruited. The cut-off values of peak tricuspid regurgitation velocity (TRV) with the low probability of PH (≤2.8 m/s), intermediate probability (2.9–3.4 m/s, without other echo PH signs), and high probability of PH (2.9–3.4 m/s with other echo PH signs and >3.4 m/s) categories were studied by right ventricular and right atrial (RA) strain analysis in a sample of 236 patients.

Results: The results showed that 58 (56.9%) patients had low, 15 (14.7%) had intermediate, and 29 (28.4%) had a high probability of PH. We observed a negative association between right ventricular free wall strain (RV-FWS) and atrial global strain with sPAP. With the increase in PH severity, RA reservoir, conduit, and contraction (booster) strain values decreased. The identified cut-off values of strain parameters had an adequate ability to detect PH severity categories. In addition, the post-mortem biopsies of right heart chambers from subjects with known severe PH were analyzed to quantify myocardial fibrosis. Our sample of right heart biopsies (n = 12) demonstrated an association between increased sPAP before death and right ventricular and RA fibrosis.

OPEN ACCESS

Edited by:
Salah D. Qanadli,
University of Lausanne, Switzerland

Reviewed by:
Yidan Li,
Capital Medical University, China
John-David Aubert,
Centre Hospitalier Universitaire Vaudois (CHUV), Switzerland

***Correspondence:**
Nilda Espinola-Zavaleta
niesza2001@hotmail.com

[†] These authors have contributed equally to this work

Specialty section:
This article was submitted to Cardiovascular Imaging, a section of the journal Frontiers in Cardiovascular Medicine

Received: 22 December 2021
Accepted: 14 February 2022
Published: 31 March 2022

Citation:
Espinola-Zavaleta N, Antonio-Villa NE, Guerra EC, Nanda NC, Rudski L, Alvarez-Santana R, Camacho-Camacho G, Aranda-Fraustro A, Cossio-Aranda J, Zamora K, Oregel-Camacho D, Armenta-Moreno JI, Berarducci J and Alexanderson-Rosas E (2022) Right Heart Chambers Longitudinal Strain Provides Enhanced Diagnosis and Categorization in Patients With Pulmonary Hypertension. Front. Cardiovasc. Med. 9:841776. doi: 10.3389/fcvm.2022.841776

Conclusion: Mechanical dysfunction and fibrosis in the right chambers are associated with increased sPAP. Right ventricular and atrial strain could provide enhancement in the diagnosis and categorization of subjects with suspected PH.

Keywords: echocardiography, right ventricular free wall longitudinal strain, right atrial global longitudinal strain, pulmonary hypertension, systolic pulmonary arterial pressure

HIGHLIGHTS

- Right heart echocardiographic strain analysis to enhance the diagnosis of pulmonary hypertension (PH) is an area of opportunity.
- We assessed the performance of the deformation parameters of the right heart chambers in characterizing the different severity levels of PH.
- The use of right ventricular and right atrial (RA) strain could provide enhancement in the diagnosis and categorization of subjects with suspected PH.

INTRODUCTION

Echocardiography remains a fundamental clinical imaging tool for the assessment of the right ventricle (RV) in the heart. Conventional echocardiographic parameters used in daily clinical practice that evaluate RV systolic function include tricuspid annular plane systolic excursion (TAPSE), the maximum velocity of the tricuspid lateral annulus during systole or the S wave (S'), and RV fractional area change (RVFAC) (1). All these echocardiographic parameters have well-known limitations (2). The assessment of right ventricular free wall longitudinal strain (RV-FWS) by the two-dimensional echocardiographic speckle tracking analysis has overcome some of these limitations and has emerged as a feasible and reproducible parameter to evaluate RV systolic function (3, 4). RV-FWS has demonstrated a good prognostic value in different clinical scenarios, such as heart failure and congenital heart disease (3). Nonetheless, RV-FWS and right atrial (RA) global strain (RA-GS) have not been fully explored in a broad variety of pathologies (5–8). In patients with pulmonary hypertension (PH), RV-FWS has been shown to be a potential predictor of major cardiovascular events. Moreover, its validation has been assessed with gold-standard methods, such as cardiac MRI (CMR) (9). However, to date, the diagnostic and predictive value of RV-FWS and RA-GS in PH has not been fully explored. The use of the right heart strain parameters in a clinical setting could broaden the stratification and overall, bring relevant information for care providers in patients with PH. Furthermore, the evaluation of the long-standing effect of increased systolic pulmonary arterial pressure (sPAP) and the myocardial fibrosis of the right heart chambers could support the hypothesis that myocardial deformation should be promptly tested in the early stages of patients with PH. Therefore, the main aim of this study is to assess the correlation of RV and RA strain with sPAP parameters. As a secondary objective, we evaluate the ability of strain parameters to predict PH and to categorize its severity compared with other echocardiographic parameters. Furthermore, we extracted post-mortem sample biopsies to measure the degree of myocardial fibrosis in 12 patients classified with severe PH to establish the association of increased sPAP with fibrosis.

Abbreviations: NYHA, New York Heart Association; RVFAC, right ventricular fractional area change; RV, right ventricle; RV-FWS, right ventricular free wall strain; RA-GS, right atrial global strain; TAPSE, tricuspid annular plane systolic excursion; S', velocity of the tricuspid S wave; CMR, cardiac magnetic resonance imaging; sPAP, systolic pulmonary artery pressure; LV, left-ventricle; AUC, area under the curve; ROC, receiver operating characteristic; PPV, positive predictive values; NPV, negative predictive values.

MATERIALS AND METHODS

Study Population Cohorts

We designed a cross-sectional study in which we recruited consecutive patients who were evaluated in the echocardiographic division from the Nuclear Cardiology Department (NCD) at the National Institute of Cardiology Ignacio Chavez, Mexico, between the period of June 2018 and December 2019. The patients attended our institution's outpatient clinic due to dyspnea on exertion, fatigue, and dizziness and were sent for a transthoracic echocardiogram for further evaluation. All patients underwent conventional two-dimensional and Doppler transthoracic echocardiography, along with velocity vector imaging to assess the right heart chamber strain parameters. We excluded subjects with congenital heart diseases, prior myocardial infarction, sarcoidosis, mild or severe valvular disease, or subjects classified with unspecified cardiomyopathies. Patients with low echocardiographic image quality were excluded in the final analysis. We extracted our control group from the same patients who attended our institution's outpatient clinic. The control group was defined by subjects who had normal pulmonary artery pressure values by echocardiographic measurement of peak tricuspid regurgitation velocity (TRV) ($\leq$2.8 m/s) within our cohort sample. To assess the inter-rater reliability and reproducibility of echocardiographic sPAP parameters, 13 selected subjects from our first cohort were assessed at heart catheterization performed 10 days after the echocardiographic study. Written informed consent was obtained from all participants.

Echocardiographic Assessment

We performed a complete conventional transthoracic echocardiogram with subjects in left lateral decubitus using a Siemens Acuson SC 2000 (Mountain View, CA, United States) echocardiographic equipment with a phased array transducer. The right ventricular end-diastolic diameter was measured in

the apical four-chamber view, below the tricuspid valve. The RV wall thickness was measured by 2D echocardiography in the subcostal four-chamber view. RA volume was obtained using a single-plane method of disks in the apical four-chamber view at ventricular end-systole, and it was indexed by body surface area (BSA). The measurements of RVFAC, TAPSE, tricuspid S-wave velocity, Tei index, E, A-wave velocities (rapid filling and atrial contribution, respectively), E/A ratio, and tricuspid E/e′ ratio were obtained according to the guidelines of the American Society of Echocardiography and the European Association of Echocardiography (5, 10, 11).

Pulmonary Arterial Pressure Assessment

The sPAP was calculated by peak TRV with continuous-wave Doppler in the apical four-chamber view, using the simplified Bernoulli equation: $4 \times (\text{maximal TRV})^2$ + right atrial pressure. RA pressure was estimated in the subcostal view according to inferior vena cava (IVC) size and collapsibility following a normal sniff: An IVC diameter <2.1 cm that collapsed >50% with a sniff suggested normal RA pressure of 3 mm Hg (range, 0–5 mmHg), whereas an IVC diameter >2.1 cm that collapsed <50% with a sniff suggested a high RA pressure of 15 mmHg (range, 10–20 mmHg). In scenarios in which the IVC diameter and collapse did not fit this paradigm, an intermediate value of 8 mmHg (range, 5–10 mmHg) might be used, or, preferably, other indices of RA pressure could be integrated to downgrade or upgrade to the standard or high values of RA pressure (5, 11). The echocardiographic probability of PH was classified as (1) low: peak TRV $\leq$ 2.8 m/s, (2) intermediate: peak TRV 2.9–3.4 m/s, without other echo PH signs, and (3) high: peak TRV 2.9–3.4 m/s with other echo PH signs and >3.4 m/s, based on the 2015 European Society of Cardiology (ESC)/European Respiratory Society (ERS) Guidelines for the diagnosis and treatment of PH (12).

Echocardiographic Strain Assessment

Strain assessment was performed offline using velocity vector imaging (Siemens Acuson SC 2000, version 5). All images analyzed were obtained at 50–80 frames/s at end expiration. The region of interest was traced with a point-and-click approach on the endocardium of the RV free wall at end-diastole in the RV-focused apical four-chamber view. A broader region of interest was subsequently generated and manually adjusted if necessary. The program automatically divided the RV free wall into three segments and performed the analysis of the deformation frame by frame. This process allowed an automated confirmation of the contour and generated deformation values. The peak strain values from the three free wall segments were averaged, and the mean value was taken as the right ventricular free wall strain (RV-FWS) (5, 7, 11–13).

For the right atrium (RA), the endocardial border was traced in the apical four-chamber view, excluding the appendage and the Eustachian valve from the RA cavity. RA longitudinal strain curves were generated throughout the cardiac cycle with R-R gating. The accuracy of the automated border tracking was verified and manually adjusted if needed. Tracking was repeated three times, and averages were used for analysis as reported in guidelines (5, 8, 11). The peak RA reservoir strain in ventricular systole, conduit strain in early diastole, and peak contractile phase strain during atrial systole/late diastole were measured and expressed as percentage. The RA total reservoir phase and RA contractile phase were assessed by measuring the corresponding peak strains. The conduit strain was calculated as the difference between RA total reservoir strain and RA contractile strain (**Figure 1**).

To assess the intra- and inter-observer reproducibility of RA reservoir, conduit, and contractile strain, 13 randomly sampled analyses were repeated two times by the same observer and by a second observer without the knowledge of previous findings, respectively.

Postmortem Right Heart Sample Cohort

The second cohort of 12 biopsies of the right heart chambers from the postmortem heart samples of patients diagnosed with severe PH were included. This cohort was created to evaluate the hazardous effect of increased sPAP on the development of fibrosis in the right heart chambers.

The heart was photographed, the macroscopic characteristics were taken, and sections were made for histological study. Samples were taken from the RA and the right ventricular free walls. We took photographs of the longitudinal section from the atrium's anterior wall, from the origin of the appendage to the tricuspid valve, and a transverse section of the ventricle in the middle portion of the free wall, covering the entire thickness of the wall.

The samples were processed with the histological technique of "paraffin inclusion." They were stained with the Masson technique to quantify the percentage of RA and right ventricular fibrous tissue, dividing the field of observation of the microscope into quarters. Two independent observers gave the percentage values, and a consensus value was obtained when there were differences. Microscopic photographs were taken of the most representative areas (**Figures 2**, **3**).

The study was carried out following the Declaration of Helsinki and was approved by the Ethics and Research Committee of the National Institute of Cardiology Ignacio Chavez. Reference number: PT-17-087.

Statistical Analysis

The frequency distribution of categorical variables is reported as frequencies and percentages. Data are presented as mean (SD) or median [interquartile range (IQR)] where appropriate. To compare the differences of echocardiographic parameters among PH categories, we performed a one-way ANOVA or Kruskal–Wallis test wherever it met assumptions of parametric tests or not, and Dunn's *post hoc* test was also assessed to evaluate the differences among groups.

Correlation of Strain Parameters With a Probability of PH

We performed a natural logarithmic transformation in variables with the non-parametric distribution. Afterward, we assessed the correlation of both RV-FWS and RA-GS with sPAP using

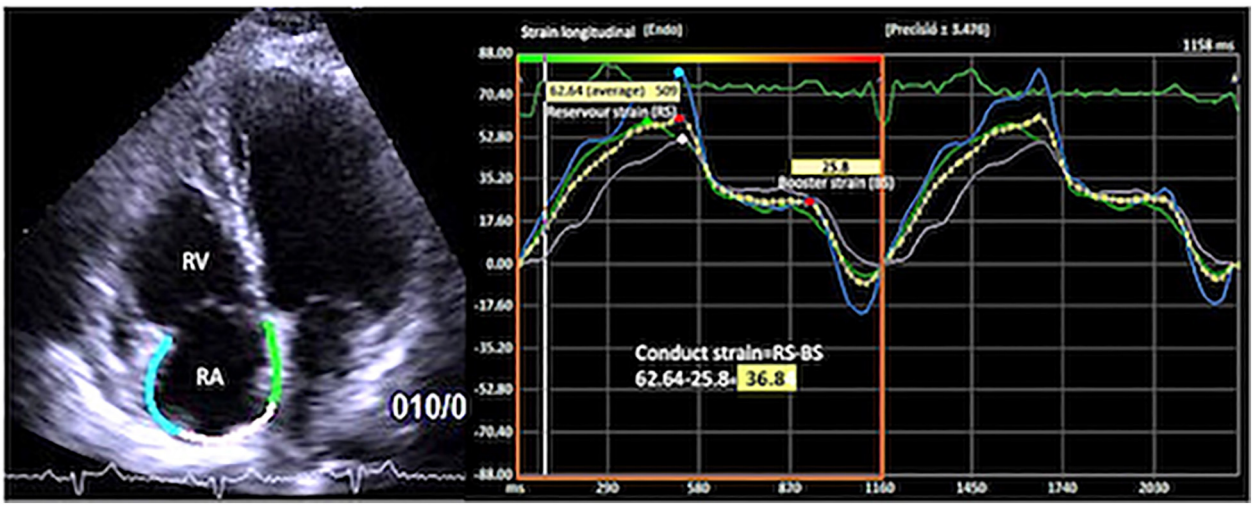

FIGURE 1 | Apical four-chamber view showing the right atrial global longitudinal strain (RA-GS) with the measurement of reservoir, conduit, and contractile strain phases.

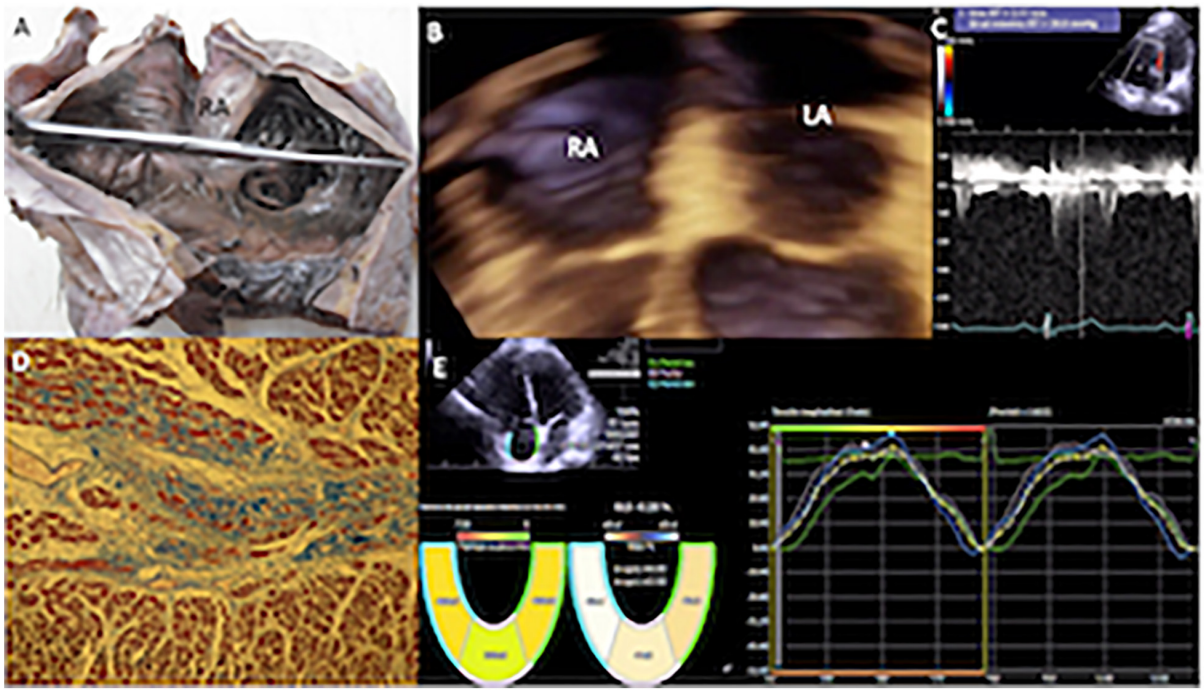

FIGURE 2 | (A) Specimen showing the internal appearance of the dilated right atrium, the pectinate portion that continues with the appendage is observed to the right of the observer, and the anterior leaflet of the tricuspid valve is observed below. **(B)** Transthoracic 3D echocardiogram in four-chamber view with mild enlargement of the right atrium. **(C)** Mild pulmonary hypertension (PH) systolic pulmonary arterial pressure (sPAP) of 44 mmHg. **(D)** Histological study (stained with Masson, 10×) of the atrial myocardium of a patient, with mild PH. The muscle fascicles were mostly cut transversely or obliquely. Two muscle fascicles are replaced by fibrous connective tissue rich in collagen fibers that stain blue, and contrast with the red in which the myocardium is stained. One fascicle is partially replaced by collagen and another almost entirely. The degree of fibrosis in the observed fields was calculated at 25%, since in this image it could reach a little more than a quarter. **(E)** Echocardiography with velocity vector imaging of a patient with a low probability of PH, who had a normal global longitudinal strain of the right atrium (43.5%). RA, right atrium; RV, right ventricle.

Pearson's correlation analysis to obtain the correlation coefficient with our transformed variables. To evaluate the prediction capacity of RV-FWS with sPAP, we performed polynomic adjusted linear regression analysis to assess the association between both parameters. The R^2 was reported to express the variability explained by both variables. As a second step, we

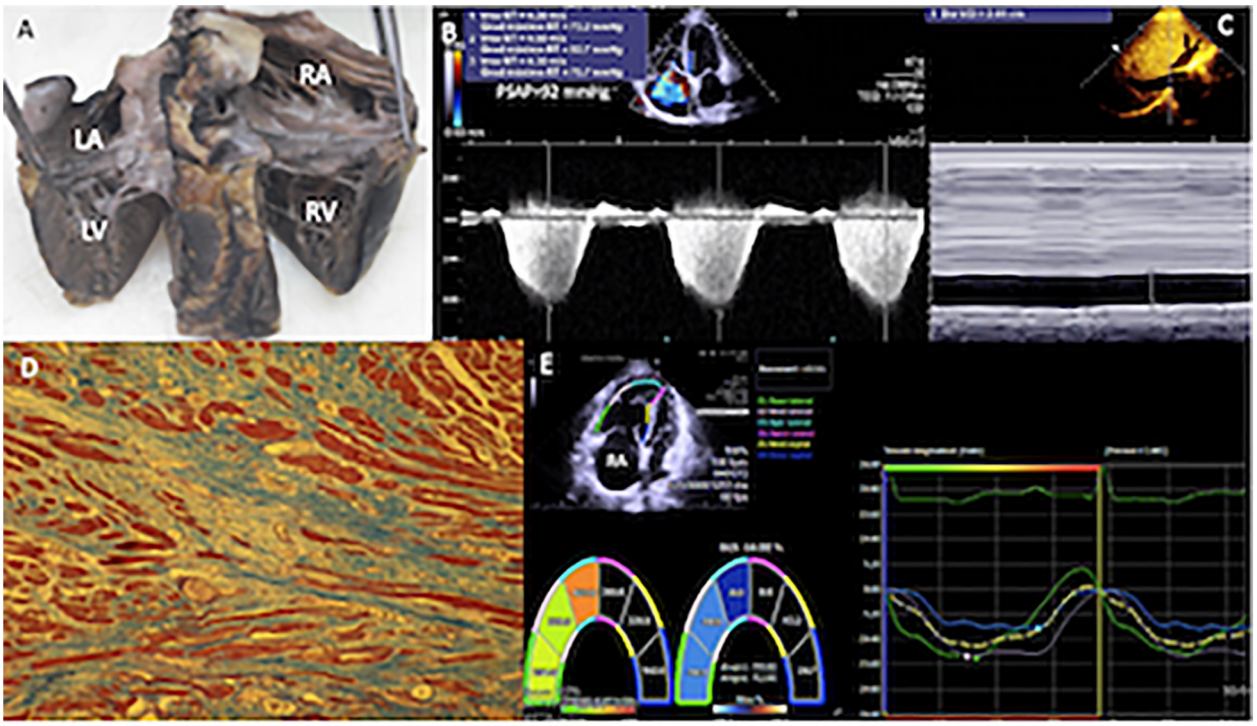

FIGURE 3 | (A) Specimen of the heart of a patient with sPAP of 90 mmHg. Heart cut longitudinally from the atria to the ventricles (entry routes through the posteroinferior aspect) that allow to appreciate the dilation of the right cavities. **(B)** Two-dimensional echocardiogram with Doppler in the apical four-chamber view, with severe tricuspid regurgitation, by means of which an average gradient of 77 mmHg was calculated. **(C)** In the subcostal plane, the dilatation of the inferior vena cava (29.1 mm) and collapse of <50% were detected, calculating a right atrial pressure of 15 mmHg. **(D)** The histological study of right ventricular myocardium, most of the muscle fibers are in longitudinal section in red and the fibrous tissue rich in collagen fibers is observed in blue, it extensively replaces the muscle fascicles, and, in this image, it reaches 75% or three quarters. The muscle fibers embedded in the fibrous connective tissue appear elongated and thinned. Masson 10×. **(E)** The global longitudinal strain of the right ventricle, using velocity vector imaging was −14%, in a patient with a high probability of PH (sPAP = 92 mmHg). RA, right atrium; RV, right ventricle; LA, left atrium; LV, left ventricle.

adjusted these models for age, sex, and BSA as these variables could modify the relationship between RV-FWS and sPAP. As a secondary analysis, we evaluated the association of sPAP with the right heart chamber fibrosis of our second cohort sample, using the methods previously described.

Diagnostic Performance of Right Heart Chambers Strain Parameters

We sought to evaluate the diagnostic performance of RV-FWS and RA-GS to predict categories of PH severity. Receiver operating characteristic (ROC) analysis curves were generated and area under the curve (AUC) derived for RV and RA strain and compared with the Fraction of Shortening, TAPSE, TEI, which are commonly used echocardiographic parameters to evaluate right heart ventricular function. Furthermore, we sought to identify the optimal cut-off value of the strain parameters using the "Youden method" from the R package "*Optimal cut points*" and evaluate the diagnostic test capacity, AUC, sensitivity, specificity, and positive and negative predictive values (VPP and VPN, respectively) to predict PH categories (14). Finally, we performed logistic regression models to assess the likelihood to have each PH category with their respective identified cut-off value. The goodness of fit of the logistic regression model was assessed using the Hosmer–Lemeshow test. All statistical analyses were performed using the R software (version 3.5.1) (15). A value of $p < 0.05$ was considered as our statistically significant threshold.

RESULTS

Study Population

We evaluated 314 patients in our study period, of which 236 had completed clinical and echocardiographic evaluation parameters for our main analyses (**Supplementary Figure 1**). The demographic and echocardiographic assessments of our first cohort sample are presented in **Table 1**. Briefly, our population had a male predominance (52.9%), with a mean age of 55 (±15) years. Arterial hypertension was recorded in 96 (40.7%) patients, followed by obesity in 90 (38.1%), diabetes mellitus in 80 (33.9%), and 42 (17.8%) with dyslipidemia and previous myocardial infarction. The echocardiographic evaluation showed a median peak RV-longitudinal FWS of −26.9% (IQR: −31.2 to −21.2%) and a peak RA-GLS of 42.2% (IQR: 30.6–55.0%). Median sPAP was 33 (IQR: 28–41) mmHg. In our studied sample, 134 (56.8%) had normal sPAP values from peak TR

TABLE 1 | Demographic and echocardiography assessment of study population.

Parameter	*n* = 236
Male (%)	124 (52.9%)
Age (years)	54.6 (±15.6)
Height (cm)	1.62 (±0.1)
Weight (kg)	71.8 (±15.4)
BSA (cm)	1.75 (1.62–1.90)
Obesity (%)	90 (38.1%)
Arterial hypertension (%)	96 (40.7%)
Diabetes (%)	80 (33.9%)
Dyslipidemia (%)	42 (17.8%)
Previous myocardial infarction (%)	42 (17.8)
Tricuspid regurgitation (%)	158 (66.9%)
Mild-TR (%)	138 (58.5%)
Moderate-TR (%)	14 (5.9%)
Severe-TR (%)	6 (2.5%)
Right ventricle	
RVd (mm)	36 (33–40.2)
RVFAC (%)	40.4 (35–48)
TAPSE (mm)	20 (17.4–22)
RV-synchrony (ms), *n* = 141	22 (3.5–44)
TEI index	0.53. (±0.17)
E Wave (cm/s), *n* = 141	9.0 (7–12)
A Wave (cm/s), *n* = 141	13 (9.25–16)
S Wave (cm/s), *n* = 141	11 (9.8–12.4)
E/A, n = 141	0.76 (0.62–0.94)
Right atrium	
Volume (ml/m^2)	31 (21–44)
Area (cm^2)	14 (11.6–17)
Reservoir phase (%)	41.7 (30.3–55)
Conduit phase (%)	22 (13.4–30)
Contractile phase (%)	18.8 (13.3–26.9)
sPAP (mmHg)	33 (28–41)
PH categories	
No-PH (%)	131 (55.5)
With-PH	102 (43.2)
Mild (%)	58 (56.9)
Moderate (%)	15 (14.7)
Severe (%)	29 (28.4)
Ventricular and atrial strain	
RV-FWS (%)	−26.86 (−21.2 to −31.22)
RA-GS (%)	42.2 (30.6–55)

BSA, body surface area; RVd, right ventricle diameter; FAC, fractional area change; TAPSE, tricuspid annular plane systolic excursion; RVS, right ventricular Synchrony; TR: tricuspid regurgitation.

velocity, which represented our control group; 102 (43.2%) were classified with the probability of PH. Of these patients, 58 (56.9%) had low, 15 (14.7%) intermediate and 29 (28.4%) had a high probability of PH. We observed an intraobserver and interobserver variation of 9 and 5%, respectively. Finally, in the 13 patients submitted to cardiac catheterization, we observed an acceptable inter-rater reliability coefficient (IRC: 56.8%) with echocardiographic sPAP parameters and an overall variance with the mean between both parameters ≤30%. The correlation of the echocardiogram with the cardiac catheterization in the determination of pulmonary arterial systolic pressure was of $r = 0.777$ (**Supplementary Figure 2**).

Association of Strain Parameters With Probability of PH

Right ventricular free wall strain absolute values were negatively correlated with sPAP ($r = -0.333$, 95% CI −0.215 to 0.442) as well as with RA-GLS ($r = -0.432$, 95% CI −0.530 to −0.322). RV-FWS and RA-GLS explained 22.2 and 18.3% of the variability of sPAP, respectively. These trends were sustained after adjusting for age, sex, and BSA. Interestingly, we observed that both parameters had a quadratic fit adjustment (**Figure 4**). Regarding the right atrial chamber assessment, the reservoir, conduit, and contractile phases had decreased parameters with advanced PH categories suggesting a functional and structural decline of the RA function. However, when comparing specifically between the intermediate and high probability of PH groups, these changes were not statistically significant (**Figure 5**). This might be related to the small number of subjects classified with intermediate PH.

Association of Probability of PH With Right Chamber Fibrosis

The relationship between increased sPAP values and myocardial fibrosis in right chambers was evaluated in our second cohort of postmortem samples biopsies. Clinical and echocardiographic characteristics are presented in **Supplementary Table 1**. sPAP had a positive correlation with right ventricular fibrosis ($r = 0.671$, 95% CI: 0.118–0.906; $p = 0.024$), but not with atrial fibrosis ($r = 0.416$, 95% CI: −0.246 to 0.81; $p = 0.203$), which explains the 18.3 and 8.1% of the variability of right ventricular and atrial fibrosis, respectively (**Supplementary Figure 3**).

Diagnostic Value of Strain Parameters in the Evaluation of Probability of PH

Finally, as a secondary analysis, we evaluated the ability of strain parameters to predict the presence of PH and to categorize the severity in patients with the probability of PH. Compared with other echocardiographic parameters (RVFAC, TAPSE, and TEI), both RV-FWS and RA-GS showed an adequate AUC to identify the presence of PH and their respective severity categories. RA-GS outperformed other echocardiographic parameters to detect those patients with any degree of PH (AUC: 0.691, 95% CI: 0.621–0.762), while RV-FWS outperformed in those with the high probability of pulmonary hypertension (AUC: 0.886, 95% CI: 0.832–0.940) (**Figure 6**). RV-FWS of −27.30, −22.60, and −22.10% had an optimal AUC and predictive test performance to predict the presence of PH, and to predict the intermediate-to-high probability of PH, and high PH, respectively. Furthermore, our identified cut-off values for RA-GS were 26.30, 34.36, and 37.20% to detect the previously mentioned categories (**Table 2**). Using the previously identified cut-off values in our multivariate logistic regression models, we found a significantly increased likelihood for pulmonary

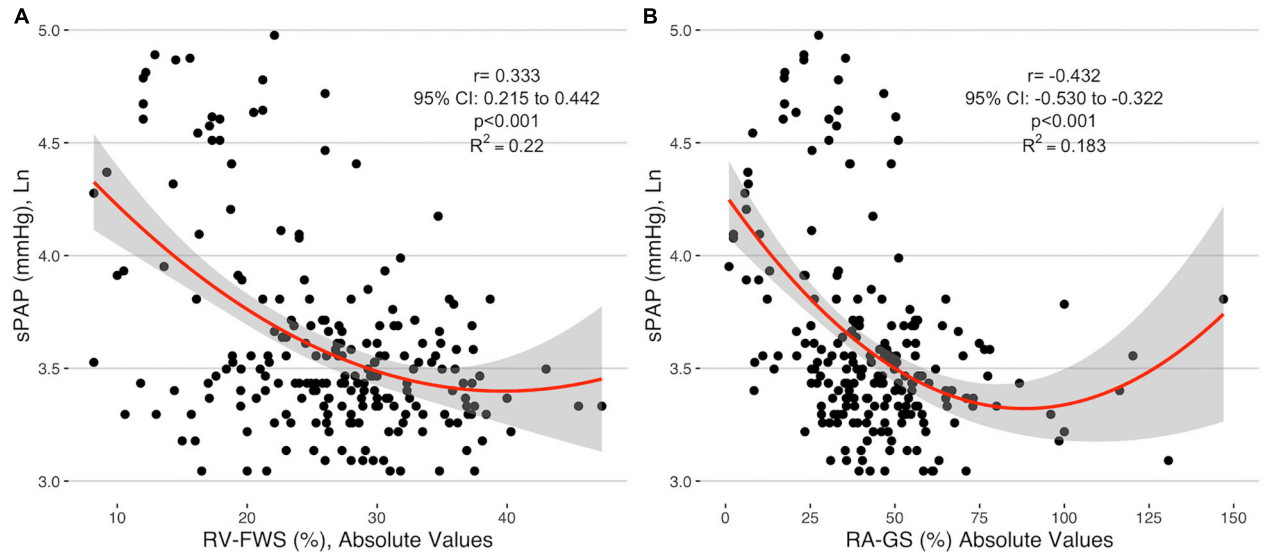

FIGURE 4 | Correlation of the absolute values of RV-FWS **(A)** and RA-GS **(B)** with logarithmical sPAP. sPAP, systolic pulmonary arterial pressure; RV-FWS, right ventricular free wall strain; RA-GS, right atrial global longitudinal strain.

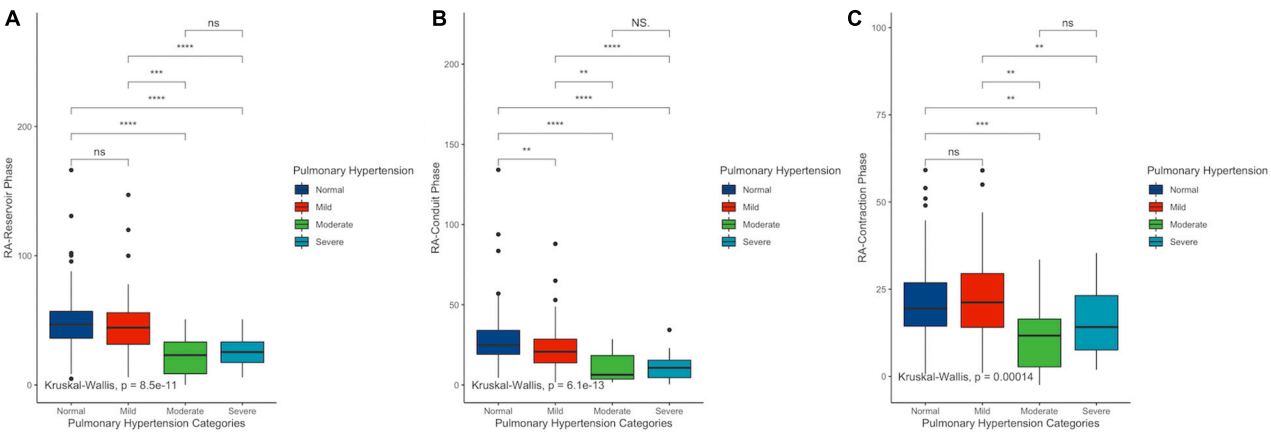

FIGURE 5 | Differences among right atrial reservoir **(A)**, conduit **(B)**, and contractile **(C)** phases in PH categories. sPAP, systolic pulmonary arterial pressure; RV-FWS, right ventricular free wall strain; RA-GS, right atrial global longitudinal strain. $^{**}p < 0.01$, $^{***}p < 0.001$, and $^{****}p < 0.0001$.

hypertension categories, which were maintained after adjustment for covariates (**Table 3**).

DISCUSSION

In this study, we show the association of both right ventricular free wall and global right atrial strain with increased systolic pulmonary artery pressure. Moreover, we demonstrate that pulmonary arterial hypertension could be associated with the myocardial fibrosis of the right heart obtained with histopathological methods. These findings suggest that the association of increased sPAP values with overall ventricular deformation and fibrosis. Finally, we demonstrate that strain parameters contribute to the detection of PH and the assessment of PH severity in patients with a suspected probability of PH.

The relationship between ventricular deformation and sPAP has been previously reported (16–18). A chronic increase in afterload, manifested by an increased pulmonary artery pressure, can cause a decrease in the elastance of myocardial fibers in patients with severe PH (17, 19). This will ultimately cause irreversible myocardial damage with the eventual development of ventricular fibrosis (20). Our physiopathological hypothesis suggests that ventricular strain and atrial strain are modeled as a quadratic function and these patients have an initial period of compensation by increasing contractility, possibly *via* the Frank-Starling mechanism that progressively decreases as the disease advances. This may be more pronounced in the RV, as the chamber

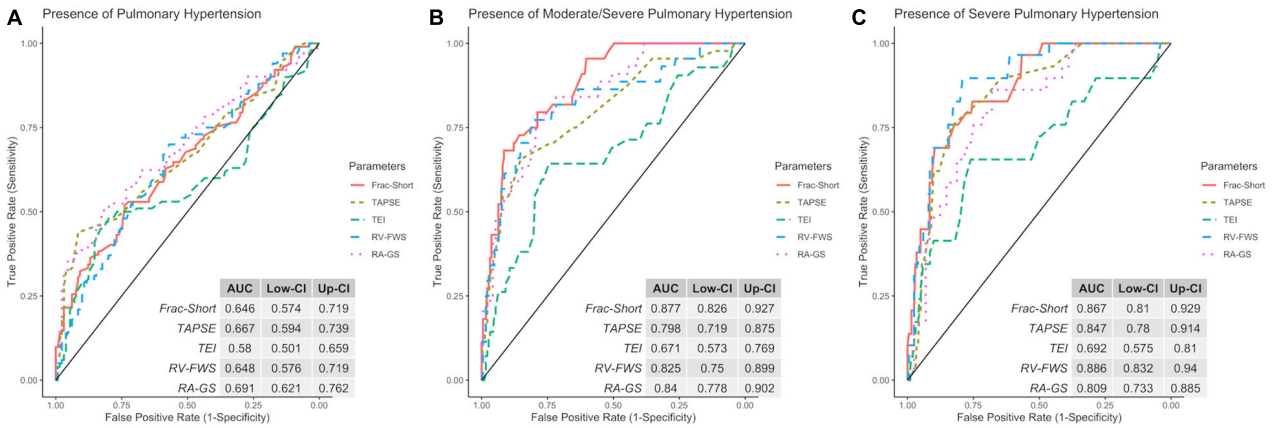

FIGURE 6 | Receiver operating characteristic (ROC) with the area under the curve (AUC) of echocardiographic parameters to identify the discrimination capacity for low **(A)**, intermediate/high **(B)**, and high **(C)** probability of PH. ROC, receiver operator characteristic; Frac-Short, fractional shortening; TAPSE, tricuspid annular plane systolic excursion; TEI, TEI index; RV-FWS, right ventricular free wall strain; RA-GS, right atrial global longitudinal strain.

directly faces the increased afterload, before impairing the right atrium. The atrial function is altered as observed in the evaluation of the various atrial phases. Finally, the degree of fibrosis analyzed in the pathological specimens of a subset of patients with PH was associated with a prolonged decrease in ventricular function.

With the demonstration of fibrosis, usually an irreversible change, early detection, and the stratification of PH is critical. Our data demonstrate the clinical utility of RV-FWS and RA-GS as echocardiographic parameters that aid in this task. Strain parameters have been previously used to predict outcomes in congestive heart failure and myocardial infarction with similar results (21, 22), as well as in PH (23–25). The echocardiographic estimation of sPAP and accordingly the development of the probability of PH is usually predicated on the presence of a complete tricuspid regurgitation envelope by continuous-wave Doppler. Often these envelopes are incomplete and the accuracy of the sPAP estimation is markedly reduced. One usually relies on the secondary signs of PH including RV dilatation, dysfunction by TAPSE or S', or D-shaped septum configuration in systole. Many of these findings are only present in advanced PH. RV strain measurement may permit for earlier detection of dysfunction, as it does in chemotherapy-induced LV cardiomyopathy (26) or in the RV in patients with scleroderma (27). In addition, in the absence of a complete envelope or in the other situations similar to significant regurgitation where stratification into severity categories may not be accurate, strain measurements may similarly assist in this task. In our work, we identified strain cut-off values that demonstrate the differences in PH severity categorization. Overall, RV-FWS offers to be a highly sensitive echocardiographic parameter while RA-GS offers a sufficient specific parameter to detect all the categories of PH. If our cut-off values are validated, they could be used in a clinical setting to aid detection and the categorization of PH. Hence, our results could help the clinicians to further select candidates to be eligible for cardiac catheterization procedures in limited-resource settings.

Strengths and Limitations

Our study has some limitations. Our patients were recruited at a referral hospital, which may represent a population bias in terms of disease prevalence and severity. Despite this, our population had a significant cohort without PH and had various degrees of pulmonary hypertension. We did not recruit an external cohort to define our control group. Instead, the control group was defined by subjects who had normal pulmonary arterial pressure within our same cohort. Moreover, there was, however, only a small number of patients with moderate PH, potentially affecting our ability to see significantly different measurements between the moderate and severe PH categories. Another potential limitation was the restricted number of patients submitted to cardiac catheterization (n = 13), given by the invasive and selective criteria to perform this procedure in all studied population. Furthermore, given the cross-sectional design of our study, we did not assess the etiology of our cases. Nevertheless, according to the evidence published by the "Mexican Registry of Pulmonary Hypertension (REMEHIP)," approximately 43% of all patients with PH in our country had idiopathic PH (28). Additionally, we included a small cohort of patients with PH and with biopsies evaluated postmortem to determine the presence and percentage of fibrosis associated with an increase in sPAP. We did not have strain values in these patients; therefore, the correlation of right heart strain and myocardial fibrosis needs to be further investigated. Accordingly, while fibrosis has been associated with reduced echocardiographic derived strain, we consider the relationship between pathology-derived fibrosis and reduced strain as a measurement of decreased RV function and possibly of fibrosis as exploratory. Finally, the assessment at follow-up to evaluate possible adverse outcomes is left as an area of opportunity for further research.

TABLE 2 | Cut-off values and predictive tests using RV-FWS for pulmonary, intermediate/high, and high probability of pulmonary hypertension (PH).

Outcome	Parameter	Cut-Off	SE	SPE	PPV	NPV	LR+	LR−	AUC
Pulmonary Hypertension	RV-FWS	−27.30	0.700 (0.600–0.787)	0.569 (0.479–0.655)	0.555 (0.465–0.665)	0.711 (0.613–0.780)	1.62 (1.28–2.05)	0.527 (0.37–0.73)	0.648 (0.57–0.72)
Intermediate-High PH		−22.60	0.773 (0.621–0.88)	0.801 (0.736–0.855)	0.479 (0.389–0.676)	0.937 (0.878–0.956)	3.88 (2.79–5.40)	0.284 (0.16–0.49)	0.825 (0.75, 0.9)
High PH		−22.10	0.896 (0.726–0.978)	0.791 (0.728–0.845)	0.382 (0.304–0.761)	0.981 (0.942–0.987)	4.29 (3.19–5.76)	0.131 (0.044–0.38)	0.886 (0.832, 0.94)
Pulmonary Hypertension	RA-FWS	26.30	0.809 (0.731–0.873)	0.515 (0.413–0.615)	0.683 (0.589–0.777)	0.675 (0.572–0.758)	1.67 (1.342–2.072)	0.371 (0.248–0.553)	0.691 (0.621, 0.762)
Intermediate-High PH		34.36	0.793 (0.728–0.848)	0.773 (0.621–0.885)	0.937 (0.878–0.956)	0.466 (0.378–0.664)	3.487 (2.012–6.042)	0.268 (0.194–0.370)	0.84 (0.778, 0.902)
High PH		37.20	0.679 (0.611–0.743)	0.862 (0.683–0.961)	0.972 (0.922–0.979)	0.277 (0.221–0.603)	4.928 (1.97–12.30)	0.371 (0.289–0.476)	0.809 (0.733, 0.885)

RV-FWS, right-ventricular free-wall strain; AUC, area under the curve; SE, sensitivity; SPE, specificity; PLR, positive likelihood ratio; NLR, negative likelihood ratio; PPV, positive predictive value; NPV, negative predictive value.

TABLE 3 | A logistic regression model to predict intermediate/high PH using identified cut-off values for each outcome adjusted for sex, age, and BSA.

Model	Parameter	B	SE	Wald	OR (95% CI)	*P* value
Pulmonary hypertension	RV-FWS > −27.30	1.402	0.311	4.497	4.06 (2.23–7.63)	<0.001
	RA-GS < 26.30	2.701	0.474	5.699	14.90 (6.22–40.66)	<0.001
Intermediate-high probability of pulmonary hypertension	RV-FWS > −22.60	2.687	0.441	6.088	14.69 (6.43–36.74)	<0.001
	RA-GS < 34.36	2.830	0.457	6.18	16.95 (7.23–44.12)	<0.001
High probability of pulmonary hypertension	RV-FWS > −22.10	3.682	0.683	5.391	39.73 (11.96–187.05)	<0.001
	RA-GS < 37.20	2.778	0.599	4.635	16.10 (5.50–60.48)	<0.001

BSA, body surface area; RV, right ventricle; RA, right atrium.

CONCLUSION

Increased pulmonary artery pressure is associated with the dysfunction of the right atrium and RV as shown by decreased RV and RA peak global longitudinal strain. We believe that this chronic dysfunction may be related to an eventual risk for fibrosis. The use of echocardiographic derived strain parameters in clinical practice could be a potential tool for detecting the presence and evaluating the probability of PH as estimated by sPAP. If validated, proposed cut-off values may improve the clinical staging of PH by including a non-invasive marker of dysfunction or fibrosis.

DATA AVAILABILITY STATEMENT

The original contributions presented in the study are included in the article/**Supplementary Material**, further inquiries can be directed to the corresponding author.

ETHICS STATEMENT

The studies involving human participants were reviewed and approved by Ethics and Research Committee of the National Institute of Cardiology Ignacio Chavez. Reference number: PT-17-087. The patients/participants provided their written informed consent to participate in this study.

AUTHOR CONTRIBUTIONS

NE-Z, NA-V, and EA-R contributed to research idea and study design. RA-S, GC-C, AA-F, and DO-C contributed to data acquisition. NE-Z, NA-V, and EG contributed to data analysis/interpretation. NA-V and EG contributed to statistical analysis. NE-Z, NA-V, LR, EA-R, and NN contributed to manuscript drafting. NE-Z, NN, and LR contributed to supervision or mentorship. All authors contributed to important intellectual content during manuscript drafting or revision and

accepts accountability for the overall work by ensuring that questions pertaining to the accuracy or integrity of any portion of the work are appropriately investigated and resolved.

FUNDING

This work was supported by Instituto Nacional de Cardiología Ignacio Chávez.

ACKNOWLEDGMENTS

We would like to acknowledge all the staff of the Nuclear Cardiology Department at Instituto Nacional de Cardiologia Ignacio Chavez, particularly to the nurses and technicians. NA-V and EG are enrolled at the PECEM program of the Faculty of Medicine, and CONACyT supports them.

SUPPLEMENTARY MATERIAL

The Supplementary Material for this article can be found online at: https://www.frontiersin.org/articles/10.3389/fcvm.2022.841776/full#supplementary-material

Supplementary Figure 1 | Algorithm for patients' selection.

Supplementary Figure 2 | Correlation of RV-Fibrosis **(A)** and RA-Fibrosis **(B)** with sPAP. sPAP, systolic pulmonary arterial pressure; RV-FWS, right ventricular free wall strain; RA-GS, right atrial global longitudinal strain.

Supplementary Figure 3 | Correlation of sPAP using echocardiographic and right heart catheterization **(A)** and Bland–Altman plot with observed differences between both the methods of measured sPAP **(B)**. sPAP, systolic pulmonary arterial pressure.

REFERENCES

1. Zaidi A, Knight DS, Augustine DX, Harkness A, Oxborough D, Pearce K, et al. Echocardiographic assessment of the right heart in adults: a practical guideline from the British society of echocardiography. *Echo Res Pract.* (2020) 7:G19–41. doi: 10.1530/ERP-19-0051
2. Habib G, Torbicki A. The role of echocardiography in the diagnosis and management of patients with pulmonary hypertension. *Eur Respir Rev.* (2010) 19:288–99. doi: 10.1183/09059180.00008110
3. Hulshof HG, Eijsvogels TMH, Kleinnibbelink G, van Dijk AP, George KP, Oxborough DL, et al. Prognostic value of right ventricular longitudinal strain in patients with pulmonary hypertension: a systematic review and meta-analysis. *Eur Heart J Cardiovasc Imaging.* (2019) 20:475–84. doi: 10.1093/ehjci/jey120
4. Samarai D, Ingemansson S, Gustafsson R, Thilén U, Hlebowicz J. Global longitudinal strain correlates to systemic right ventricular function. *Cardiovasc Ultrasound.* (2020) 1:18. doi: 10.1186/s12947-020-0186-7
5. Rudski LG, Lai WW, Afilalo J, Hua L, Handschumacher MD, Chandrasekaran K, et al. Guidelines for the echocardiographic assessment of the right heart in adults: a report from the American society of echocardiography: endorsed by the European association of echocardiography, a registered branch of the European society of cardiology, and the Canadian society of echocardiography. *J Am Soc Echocardiogr.* (2010) 23:685–713. doi: 10.1016/j.echo.2010.05.010
6. Hamada-Harimura Y, Seo Y, Ishizu T, Nishi I, Machino-Ohtsuka T, Yamamoto M, et al. Incremental prognostic value of right ventricular strain in patients with acute decompensated heart failure. *Circ Cardiovasc Imaging.* (2018) 11:e007249. doi: 10.1161/CIRCIMAGING.117.007249
7. Lee J-H, Park J-H. Strain analysis of the right ventricle using two-dimensional echocardiography. *J Cardiovasc Imaging.* (2018) 26:111–24. doi: 10.4250/jcvi.2018.26.e11
8. Hasselberg NE, Kagiyama N, Soyama Y, Sugahara M, Goda A, Ryo-Koriyama K, et al. The prognostic value of right atrial strain imaging in patients with precapillary pulmonary hypertension. *J Am Soc Echocardiogr.* (2021) 34:851–61.e1. doi: 10.1016/j.echo.2021.03.007
9. Jones N, Burns AT, Prior DL. Echocardiographic assessment of the right ventricle-state of the art. *Hear Lung Circ.* (2019) 28:1339–50. doi: 10.1016/j.hlc.2019.04.016
10. Sebbag I, Rudski LG, Therrien J, Hirsch A, Langleben D. Effect of chronic infusion of epoprostenol on echocardiographic right ventricular myocardial performance index and its relation to clinical outcome in patients with primary pulmonary hypertension. *Am J Cardiol.* (2001) 88:1060–3. doi: 10.1016/s0002-9149(01)01995-6
11. Lang RM, Badano LP, Mor-Avi V, Afilalo J, Armstrong A, Ernande L, et al. Recommendations for cardiac chamber quantification by echocardiography in adults: an update from the American society of echocardiography and the European association of cardiovascular imaging. *J Am Soc Echocardiogr.* (2015) 28:1–39.e14.
12. Galie N, Humbert M, Vachiery JL, Gibbs S, Lang I, Torbicki A, et al. 2015 ESC/ERS guidelines for the diagnosis and treatment of pulmonary hypertension. *Eur Heart J.* (2016) 37:67–119.
13. Mor-Avi V, Lang RM, Badano LP, Belohlavek M, Cardim NM, Derumeaux G, et al. Current and evolving echocardiographic techniques for the quantitative evaluation of cardiac mechanics: ASE/EAE consensus statement on methodology and indications endorsed by the Japanese society of echocardiography. *J Am Soc Echocardiogr.* (2011) 24:277–313.
14. López-Ratón M, Rodríguez-Álvarez M, Suárez CC, Sampedro FG. OptimalCutpoints: an R package for selecting optimal cutpoints in diagnostic tests. *J Stat Softw.* (2014) 61:1–36. doi: 10.18637/jss.v061.i08
15. Harrell F. *Regression Modeling Strategies: With Applications to Linear Models, Logistic Regression, and Survival Analysis*. New York, NY: Springer-Verlag (2001).
16. Padervinskienė L, Krivickienė A, Hoppenot D, Miliauskas S, Basevičius A, Nedzelskienė I, et al. Prognostic value of left ventricular function and mechanics in pulmonary hypertension: a pilot cardiovascular magnetic resonance feature tracking study. *Medicina (Kaunas).* (2019) 55:73. doi: 10.3390/medicina55030073
17. Yurdakul S, Bingöl Z, Okumuş G, Şahin ŞT, Cengiz B, Bozkurt A, et al. Left ventricular rotational deformation is impaired in pulmonary hypertension: a speckle tracking imaging- based study. *J Am Coll Cardiol.* (2013) 62(18 Suppl. 2):C2.
18. Theres L, Hübscher A, Stangl K, Dreger H, Knebel F, Brand A, et al. Associations of 2D speckle tracking echocardiography-based right heart deformation parameters and invasively assessed hemodynamic measurements in patients with pulmonary hypertension. *Cardiovasc Ultrasound.* (2020) 18:13. doi: 10.1186/s12947-020-00197-z
19. Lan NSH, Massam BD, Kulkarni SS, Lang CC. Pulmonary arterial hypertension: pathophysiology and treatment. *Diseases.* (2018) 6:38.
20. Collum SD, Amione-Guerra J, Cruz-Solbes AS, DiFrancesco A, Hernandez AM, Hanmandlu A, et al. Pulmonary hypertension associated with idiopathic pulmonary fibrosis: current and future perspectives. *Can Respir J.* (2017) 2017:1430350. doi: 10.1155/2017/1430350
21. Di Salvo G, Pergola V, Fadel B, Al Bulbul Z, Caso P. Strain echocardiography and myocardial mechanics: from basics to clinical applications. *J Cardiovasc Echogr.* (2015) 25:1–8. doi: 10.4103/2211-4122.158415
22. Kaufmann D, Szwoch M, Kwiatkowska J, Raczak G, Daniłowicz-Szymanowicz L. Global longitudinal strain can predict heart failure exacerbation in stable outpatients with ischemic left ventricular systolic dysfunction. *PLoS One.* (2019) 14:e0225829. doi: 10.1371/journal.pone.0225829

23. Nathaniel R. Right ventricular strain in pulmonary hypertension. *Circ Cardiovasc Imaging.* (2013) 6:609–11.
24. Fine NM, Chen L, Bastiansen PM, Frantz RP, Pellikka PA, Oh JK, et al. Outcome prediction by quantitative right ventricular function assessment in 575 subjects evaluated for pulmonary hypertension. *Circ Cardiovasc Imaging.* (2013) 6:711–21. doi: 10.1161/CIRCIMAGING.113.000640
25. Shukla M, Park J-H, Thomas JD, Delgado V, Bax JJ, Kane GC, et al. Prognostic value of right ventricular strain using speckle-tracking echocardiography in pulmonary hypertension: systematic review and meta-analysis. *Can J Cardiol.* (2018) 34:1069–78. doi: 10.1016/j.cjca.2018.04.016
26. Thavendiranathan P, Poulin F, Lim KD, Plana JC, Woo A, Marwick TH. Use of myocardial strain imaging by echocardiography for the early detection of cardiotoxicity in patients during and after cancer chemotherapy: a systematic review. *J Am Coll Cardiol.* (2014) 63(25 Pt A):2751–68. doi: 10.1016/j.jacc.2014.01.073
27. Mukherjee M, Mercurio V, Tedford RJ, Shah AA, Hsu S, Mullin CJ, et al. Right ventricular longitudinal strain is diminished in systemic sclerosis compared with idiopathic pulmonary arterial hypertension. *Eur Resp J.* (2017) 50:1701436. doi: 10.1183/13993003.01436-2017
28. Pulido Zamudio T, Sandoval J, Sanchez Z Diaz CJ, Ramirez A, Beltran M, Seoane M, et al. The phenotype of the adult Mexican patient with pulmonary arterial hypertension: baseline characteristics of the REMEHIP registry. The REMEHIP investigators. In pulmonary hypertension. ERS international congress 2018 abstracts. *Eur Respir J.* (2018) 52:A3086. doi: 10.1183/13993003.congress-2018.pa3086

Conflict of Interest: The authors declare that the research was conducted in the absence of any commercial or financial relationships that could be construed as a potential conflict of interest.

Publisher's Note: All claims expressed in this article are solely those of the authors and do not necessarily represent those of their affiliated organizations, or those of the publisher, the editors and the reviewers. Any product that may be evaluated in this article, or claim that may be made by its manufacturer, is not guaranteed or endorsed by the publisher.

frontiers | Frontiers in Cardiovascular Medicine

ORIGINAL RESEARCH
published: 25 April 2022
doi: 10.3389/fcvm.2022.869076

Predictive Value of Left Atrial and Ventricular Strain for the Detection of Atrial Fibrillation in Patients With Cryptogenic Stroke

*Gabriella Bufano[1], Francesco Radico[2], Carolina D'Angelo[2], Francesca Pierfelice[1], Maria Vittoria De Angelis[3], Massimiliano Faustino[4], Sante Donato Pierdomenico[1], Sabina Gallina[5] and Giulia Renda[5]**

[1] Department of Innovative Technologies in Medicine & Dentistry, Institute of Cardiology, G. d'Annunzio University Chieti-Pescara, Chieti, Italy, [2] Department of Cardiology, Renzetti Hospital, Lanciano, Italy, [3] Department of Neurology, Stroke Unit, SS Annunziata Hospital, Chieti, Italy, [4] Department of Cardiology, SS Annunziata Hospital, Chieti, Italy, [5] Department of Neuroscience, Imaging and Clinical Sciences, Institute of Cardiology, G. d'Annunzio University Chieti-Pescara, Chieti, Italy

Background and Aims: Cryptogenic stroke (CS) is associated with a high rate of recurrences and adverse outcomes at long-term follow-up, especially due to its unknown etiology that often leads to ineffective secondary prevention. Asymptomatic atrial fibrillation (AF) could play an important pathophysiological role. Some studies have pointed to left atrial (LA) and left ventricular (LV) systolic and diastolic dysfunction as surrogate markers of AF. The aim of the study is to evaluate the relationship between echocardiographic parameters of LA and LV function, and the occurrence of AF revealed by continuous ECG monitoring in a cohort of patients with CS.

Methods: Single-center prospective cohort study. Seventy-two patients with CS with insertable cardiac monitors (ICM) underwent transthoracic echocardiography (TTE). TTE was focused on LA and LV function, including both standard and longitudinal strain-derived parameters. All detected AF episodes lasting more than 2 min were considered.

Results: Continuous ECG monitoring revealed subclinical AF in 23 patients (32%) at an average of 6.5 months after ICM implantation. Many echocardiographic parameters, indicating LA volume and LV systolic/diastolic function, were significantly associated with the occurrence of AF, suggesting the worst atrial function in the AF group. Furthermore, multivariable regression analysis revealed that peak atrial contraction strain and left ventricular strain were independently associated with AF (adjusted OR = 0.72, CI 95% 0.48–0.90, $p = 0.005$, and adjusted OR = 0.69, CI 95% 0.46–0.95, $p = 0.041$, respectively).

Conclusion: In patients with CS, LA and LV strain analysis add predictive value for the occurrence of AF over clinical and morpho-functional echocardiographic parameters. Impaired booster pump strain and LV longitudinal strain are strong and independent predictors of AF.

Keywords: atrial fibrillation, cryptogenic stroke, insertable cardiac monitor, atrial myopathy, left atrial strain, left ventricular longitudinal strain

OPEN ACCESS

Edited by:
Anna Vittoria Mattioli, University of Modena and Reggio Emilia, Italy

Reviewed by:
Marco Matteo Ciccone, University of Bari Aldo Moro, Italy
Maria Concetta Pastore, Università del Piemonte Orientale, Italy

***Correspondence:**
Giulia Renda
giulia.renda@unich.it

Specialty section:
This article was submitted to Cardiovascular Imaging, a section of the journal Frontiers in Cardiovascular Medicine

Received: *03 February 2022*
Accepted: *21 March 2022*
Published: *25 April 2022*

Citation:
Bufano G, Radico F, D'Angelo C, Pierfelice F, De Angelis MV, Faustino M, Pierdomenico SD, Gallina S and Renda G (2022) Predictive Value of Left Atrial and Ventricular Strain for the Detection of Atrial Fibrillation in Patients With Cryptogenic Stroke. Front. Cardiovasc. Med. 9:869076. doi: 10.3389/fcvm.2022.869076

INTRODUCTION

Cryptogenic stroke (CS) is defined as cerebral ischemia of undetermined origin (1). About 87% of strokes are of ischaemic origin, and 20–30% of ischaemic strokes are estimated to be cryptogenic or of undetermined cause (2). The dominant underlying mechanism of CS seems to be an embolism from an unestablished source. Therefore, the term Embolic Stroke of Undetermined Source (ESUS) was introduced to define such a subset of CS (3). ESUS may account for different embolic sources: atrial cardiopathy, hidden atrial fibrillation (AF), left ventricular (LV) disease, atherosclerotic plaques, patent foramen ovale (PFO), cardiac valvular disease, and cancer (4). Several trials revealed that hidden AF could be detected in up to 30% of patients with ESUS at long term follow-up (5–7). However, its causal association with the index stroke remains a matter of debate (4). Furthermore, two randomized controlled trials (8, 9) failed to demonstrate the superiority of oral anticoagulation over aspirin for the prevention of stroke recurrence in patients with ESUS, probably because of the wide heterogeneity of the patients included in the ESUS definition. Accordingly, early diagnosis of stroke etiology is crucial in order to evaluate the effective strategies in secondary prevention and to particularly identify patients who may best benefit from oral anticoagulation, such as those with hidden AF. For this reason, the use of an Insertable Cardiac Monitor (ICM) has been proposed to enhance the detection of AF and improve the prognosis in patients with CS (10). Specific CS subgroups like older patients (8) or patients with high CHA_2DS_2-VASC score (10) portend a higher probability of hidden AF and could take advantage of long-term ECG monitoring. Since the substrate for AF relates to left atrial (LA) dilation and fibrosis, with subsequent structural and electrophysiological remodeling, dysfunction, and delay in electromechanical conduction (11), echocardiographic parameters investigating LA size and function are gaining growing interest as a surrogate predictor of hidden AF (12, 13), even more so in patients with CS (14, 15). Moreover, the assessment of LV diastolic parameters and compliance, also affecting LA size and function (16–18), can be of relevance in this setting (19, 20).

Some studies have pointed LA dysfunction as a surrogate predictor of hidden AF in patients with CS, but the assessment of incident AF was heterogeneous, mostly based on clinical follow-up, and were more frequently short-term, with a small percentage of patients implanted with cardiac loop recorder (21, 22). This approach could underestimate the incidence of AF after CS, therefore underestimating the relationship between LA dysfunction and AF.

The aim of this study was to evaluate the relationship between echocardiographic parameters, indicating LA and LV function, and the occurrence of AF revealed by continuous ECG monitoring after CS. Particularly, we investigated the predictive value of LA strain and function and LV diastolic function for the detection of AF episodes.

MATERIALS AND METHODS

This is a single-center prospective cohort study. We enrolled consecutive patients from March 2016 to September 2020 who were admitted to the Neurological Clinic of Santissima Annunziata Hospital of Chieti with the diagnosis of CS. The etiology was determined by the neurologist according to Trial of Org 10172 in Acute Stroke Treatment's (TOAST's) classification (1), which states that a stroke was classified as "cryptogenic" if extensive testing failed to reveal a clear etiology. The workup included: 24-h ECG monitoring, standard transthoracic echocardiography, screening for thrombophilic states (in patients under 55 years of age), transcranial and neck Doppler ultrasound, computed tomography (CT) angiography of the head and neck, and magnetic resonance angiography in patients with negative CT findings. We collected clinical parameters such as physical characteristics, medical history, and cardiovascular risks factors. A long-term electrocardiographic monitoring insertable system was planned in all patients with CS, and an echocardiographic assessment, including both standard and strain-derived parameters, was performed. Follow-up clinical events (all-cause death, cardiovascular death, stroke, myocardial infarction, bleeding) were reported by local investigators after verification from clinical records and source documents, or in case of missing data by a phone questionnaire.

Echocardiographic Assessment

Echocardiographic examinations were performed within 30 days from the index stroke using a commercially available ultrasonography system (Philips Affinity 50c). Standard echocardiographic parameters were recorded and measured while blinded to cardiac monitoring findings (G. B.) and according to the recommendations of international guidelines (23), including LA volume, LV mass, and LV systolic/diastolic function. All volumetric measures were indexed to body surface area (BSA). Other echocardiographic parameters included in analysis were as follows: maximum (max), minimum (min), and pre-atrial (Pre-A) LA contraction volume. These parameters were recorded from the apical 4-chamber (A4-C) and 2-chamber (A2-C) views as follows: maximum LA volume (LAV max), measured on the 2D frame just before mitral valve opening, LA pre-atrial contraction volume (LAV pre A), measured on the frame just before the onset of atrial emptying, and LA minimum volume (LAV min) measured on the frame at end-diastole with the smallest LA volume. All measures were computed separately following American Society of Echocardiography guidelines, and using the biplane modified Simpson's method of discs.

Both apical views were optimized in terms of orientation, depth, and gain to avoid LA foreshortening and to visualize the entire LA throughout the cardiac cycle. Five cardiac cycles of each plane were stored in cine loop format in order to subsequently select the images of better quality for off-line speckle-tracking analysis.

With these parameters we then calculated volumetric LA function as follows:

Passive LA emptying fraction (LAPEF) (in %): $100 \cdot [\text{LAV max} \times \text{LAV Pre-A}]/\text{LAV max}$;

Active LA emptying fraction (LAAEF) (in %): 100 · [LAV Pre-A × LAV min]/LAV Pre-A;

Total LA emptying fraction (LATEF) (in %): 100 · [LAV max × LAV min]/LAV max.

Atrial strain was analyzed using A4-C and A2-C views with a frame rate between 70 and 100 frames/s, following European Association of Cardiovascular Imaging (EACVI)/American Society of Echocardiography (ASE)'s consensus document (24). Strain data were digitally stored for offline analysis with Siemens syngo® Vector Velocity Imaging (VVI) Longitudinal version 2.0, with the onset of QRS complex used as the zero-reference point (R-R gating). LA endocardial border was manually traced in both A4-C and A2-C views, delineating a region of interest (ROI) composed by six segments for each view. Then, after the segmental tracking quality analysis and the eventual manual adjustment of the ROI, the longitudinal strain curves were generated by the software for each atrial segment. The resulting atrial strain curve provided 2 peaks consistent with reservoir and contractile strain (24). LA contractile strain was manually calculated from the longitudinal strain mean curve. LA strain pattern consists of a positive wave that peaks at the end of ventricular systole, followed by a decrease after the opening of the mitral valve and, after a plateau, by a second positive wave that corresponds to atrial contraction. From the average of the strain curves, we calculated peak LA strain of A4-C and A2-C view at the end of ventricular systole (peak atrial longitudinal strain, PALS), which is a measure of LA reservoir function (13), and peak atrial contraction strain (PACS), which can be considered a marker of LA pump function, as previously described (13, 16). Passive emptying (conduit) strain was calculated as the difference between PALS and PACS. LV speckle tracking was examined from A4-C, A2-C, and three-chamber (A3-C) view according to EACVI/ASE's position paper (23). In these projections, the software automatically divides each ventricular wall into three segments. From each segment, curves for longitudinal strain were generated (25). In the presence of inadequate view or suboptimal image quality, or when at least one segment of A2-C or A3-C was not correctly visualized, we used only the A4-C view (26).

Patients without interpretable images were excluded from the study. If more than two segments were excluded in a projection, the investigation was deemed unsatisfactory. In all patients, conventional and strain parameters were obtained in sinus rhythm at baseline and without significant valvular heart disease at time of the exam.

Reproducibility of strain measures were confirmed by two physicians (G. B., F. R.) in order to minimize interpersonal variability. The reproducibility was tested while blinded in a random sample of 15 patients, according to a recent practical guideline (27).

Insertable Cardiac Monitor

Long term cardiac monitoring was obtained in all the study patients for up to 3 years by the Reveal LINQ™ (Medtronic, Dublin, Ireland) ICM. The device was implanted subcutaneously on the thoracic surface. We considered for the analysis all detected AF episodes, defined as an irregular supraventricular rhythm with absence of P waves and variable R-R interval lasting more than 2 min. All recorded AF episodes were evaluated and confirmed by an expert cardiologist (M. F.). AF burden was considered as the number of AF episodes recorded by ICM lasting more than 2 min.

Statistical Analysis

Categorical variables are described as absolute frequencies and percentages. Continuous variables are presented as mean values ± standard deviation (SD), their associated 95% confidence intervals (CI), or as median and interquartile range (IQR), as appropriate. Normality of variable distributions was tested by the Kolmogorov–Smirnov test. The unpaired Student's *t*-test and chi-squared test were used to compare means and frequencies of clinical and echocardiographic covariates between groups of subjects with or without AF revealed at ICM. Covariates were screened in univariate models by logistic regression to test AF prediction. Then, a multivariable logistic regression analysis was performed to identify independent predictors by selecting covariates with a p-value <0.10 at univariate analysis. Kaplan-Meier analysis was performed using Log-rank test in order to compare AF probabilities between patients with or without impaired LVLS and PACS, with discriminative cut-off values for each variable deriving from ROC curve analysis. A ROC analysis was also performed by combining LVLS and PACS. At this scope, a binary logistic regression has been run to generate a probability variable of AF with LVLS and PACS as covariates. Then, a ROC curve was generated by using the probability as the test variable and AF as dependent variable.

Inter and intra-operator reproducibility was assessed by Spearman's correlation coefficient (r) and intraclass correlation coefficient (ICC), while agreement was visually assessed by Bland–Altman Plot for inter-operator reproducibility (27).

All probability values were reported as two-sided, and a p-value <0.05 was considered significant. Data were processed using IBM SPSS Statistics, Version 25.0. Armonk, NY: IBM Corp.

The study was conducted according to the guidelines of the Declaration of Helsinki and approved by the Institutional Ethics Committee of G. d'Annunzio University/Santissima Annunziata Hospital of Chieti.

RESULTS

Between March 2016 and September 2020, 1,105 patients were admitted for stroke to the Neurological Clinic of Santissima Annunziata Hospital of Chieti. CS was diagnosed in 76 of these, of which 75 underwent ICM implantation, and 72 completed follow up, constituting the final study population (**Figure 1**).

Mean age was 68 years, and most patients were males (59.4%) (**Table 1**). ICM were implanted, on average, at 3.6 ± 1 months (mean ± SD) after the index stroke. The mean follow-up period was 30.9 ± 1.9 months. Subclinical AF was detected in 23 patients (32%), on average, 6.5 ± 3.5 months after ICM implantation. A median of 10 subclinical AF episodes (IQR 3-234) lasting more than 2 min were recorded in AF group (**Table 2**).

Patients with and without AF at ICM were homogeneous in all baseline characteristics, except for CHA_2DS_2-VASc score, which was significantly higher in AF group (5.8 ±.8 vs. 4.7 ±.4, $p = 0.012$) and for prevalence of hypercholesterolemia, which was significantly higher in no-AF group (84.0 vs. 52.2%, $p = 0.005$)

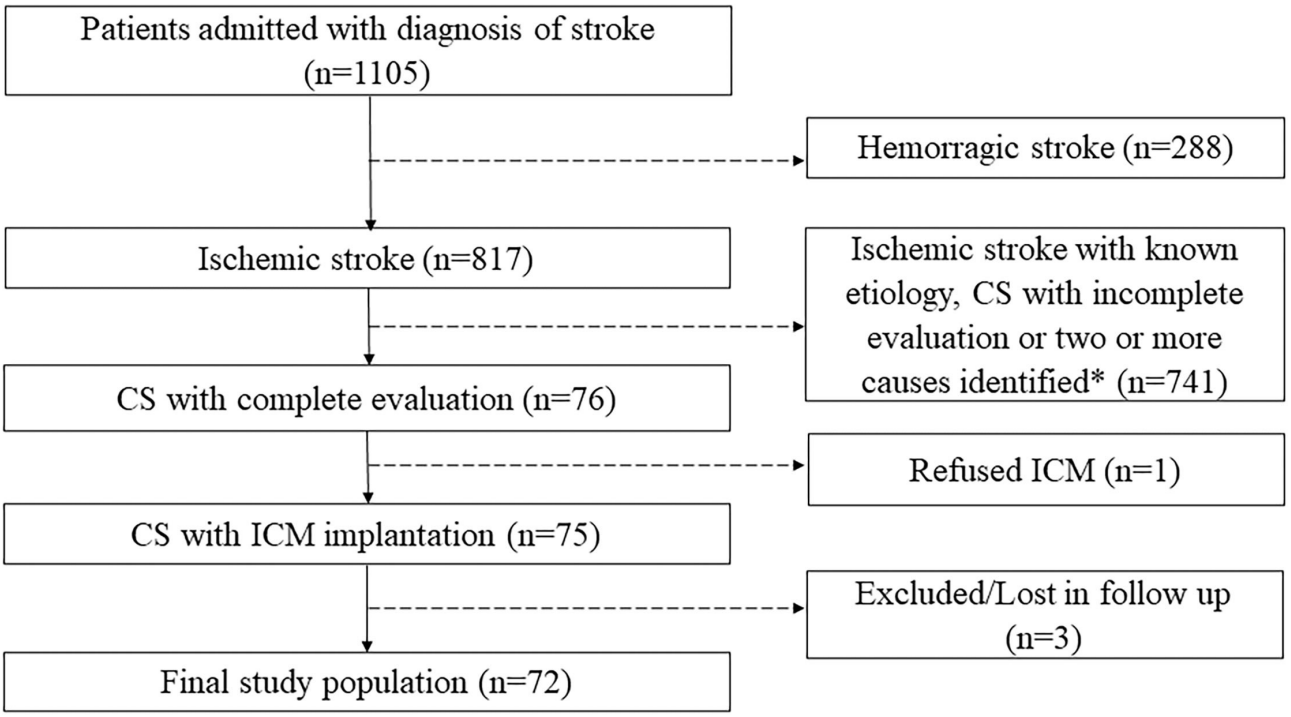

FIGURE 1 | Flow diagram with inclusion and exclusion criteria. *According to Trial of Org 10172 in Acute Stroke Treatment's (TOAST's) classification. CS, cryptogenic stroke; ICM, insertable cardiac monitor.

(**Table 1**). In our cohort, patent foramen ovale (PFO) showed 15% of prevalence without significant differences between AF group and no AF group, although patients with PFO are numerically more frequent in the no-AF group. Furthermore, valvular heart disease (VHD) showed 9.7% of prevalence, without significant differences between the two groups. **Table 3** shows the echocardiographic parameters significantly associated to the occurrence of AF at univariable logistic regression analysis.

A comparison of LA and LV strain between an AF patient and no-AF patient is shown in **Figure 2**.

Multivariable regression analysis revealed that PACS and LV strain were the only parameters independently associated with AF (**Table 3**).

Receiver-operating characteristic (ROC) curve analysis showed that PACS had the best diagnostic performance (area under curve, AUC = 0.91, CI 0.51–0.95, $p = 0.005$; **Figure 3A**) for AF prediction, with a best cut-off value of 10.4% accounting for 86% of sensitivity and 76% of specificity. Also, LVLS showed good diagnostic performance (AUC 0.75, CI 0.48–0.97, $p = 0.041$; **Figure 3B**), with a best cut-off value of 16.9% accounting for 81% of sensitivity and 65% of specificity, and, in addition to PACS, led to significant improvements in AF prediction (AUC 0.92; **Figure 3C**).

Patients with impaired PACS and LVLS showed a much higher probability to develop AF during follow-up with a hazard ratio [HR 10.5 (95% CI 3.8–29.1) and HR 5.6 (95% CI 2.2–14.3) respectively, log-rank $P < 0.001$ for both; **Figure 4**].

PALS and PACS showed good inter and intra-observer correlation. Inter-observer correlation of PALS and PACS were expressed as Spearman's r of 0.70 ($p = 0.003$) and 0.69 ($p = 0.004$), respectively, and ICC was 0.74 and 0.61, respectively. Intra-observer correlation of PALS and PACS were expressed as Spearman's r of 0.7 ($p = 0.004$) and 0.7 ($p = 0.004$), respectively, and ICC was 0.76 and 0.78, respectively.

In our study, all patients presenting subclinical AF at follow-up underwent 12-lead ECG, of which only 3 of them manifested clinical AF in that occasion. However, all patients were prescribed oral anticoagulant therapy, considering their high thromboembolic risk and their preferences.

During a mean follow-up period of 30.9 ± 1.9 months, in the no-AF group, one acute myocardial infarction with persistent ST-segment elevation (STEMI) and one non-cardiovascular death were reported. Two recurrent strokes occurred in the AF group. In the first patient, the second stroke occurred before the implantation of ICM and consequently before the detection of AF. After the beginning of oral anticoagulation, no further strokes were detected. In the second patient, the additional stroke occurred under oral anticoagulation with dabigatran 110 mg bis in die (BID) after a de-escalation from dabigatran 150 mg BID driven by minor bleeding. After the second stroke, dabigatran 150 mg BID was restored, and no further strokes were detected. No major life-threatening or intracranial bleeding were reported in the entire study cohort.

TABLE 1 | Demographic and clinical characteristics in the overall population and according to the occurrence of AF.

	Overall ***n* = 72**	**AF** ***n* = 23**	**No AF** ***n* = 49**	***p*-value**
Age—years, mean ± SD	67.7 ± 11.7	70.6 ± 12.6	66.4 ± 11.2	0.18
Female sex, *n* (%)	30 (41.6)	10 (43.5)	20 (40.8)	0.83
BMI, mean ± SD	27.5 ± 4.3	27.8 ± 4.9	27.4 ± 4.0	0.75
Hypertension, *n* (%)	49 (68)	17 (73.9)	32 (65.3)	0.46
Systolic blood pressure - mmHg, mean ± SD	122 ± 4	123 ± 8	121 ± 5	0.66
Diastolic blood pressure - mmHg, mean ± SD	75 ± 3	76 ± 10	75 ± 4	0.77
Diabetes mellitus, *n* (%)	17 (23.6)	6 (26)	11 (22.4)	0.73
Hypercholesterolemia, *n* (%)	53 (73.6)	12 (52.2)	41 (84)	**<0.01**
Coronary artery disease, *n* (%)	11 (15.3)	6 (23)	5 (10)	0.08
Valvular heart disease, *n* (%)	7 (9.7)	4 (17.4)	3 (6.1)	0.13
Cronic kidney disease, *n* (%)	6 (8)	3 (13)	3 (6)	0.29
Chronic obstructive pulmonary disease *n* (%)	9 (12.5)	3 (13)	6 (12.2)	0.92
Cancer/history of cancer, *n* (%)	11 (15.3)	4 (17.4)	7 (14.3)	0.73
Patent foramen ovale, *n* (%)	11 (15)	2 (8.7)	9 (18.4)	0.29
CHA2DS2-VASc, *n* (%)	5.1 (1.7)	5.8 (0.8)	4.7 (0.4)	**0.01**

BMI, Body Mass Index; CHA2DS2-VASc, Congestive heart failure, Hypertension, Age ≥75 years, Diabetes mellitus, Stroke, Vascular disease, Age 65–74 years, Sex category (female). Statistically significant p-values are reported in bold.

TABLE 2 | Insertable cardiac monitor (ICM) data in the overall population and according to the occurrence of AF.

	Overall ***n* = 72**	**AF** ***n* = 23**	**No AF** ***n* = 49**
Implantation of ICM after the index stroke (months)	3.6 (1)	2.5 (1.1)	4.1 (1.5)
Mean follow-up with ICM (months)	30.9 (1.9)	32.3 (3.6)	30.2 (2.3)
Diagnosis of AF after ICM implantation (months)		6.5 (3.5)	
AF burden (*n*)		10 (3–234)	

Values are expressed as mean (SD), except AF burden expressed as median (IQR). AF, atrial fibrillation; ICM, Insertable Cardiac Monitor; AF Burden, number of AF episodes lasting more than 2 min.

DISCUSSION

There is an increasing interest in the potential role of subclinical AF in patients with CS. After several trials and confirmed by real-world data (10), last Guidelines from the European Society of Cardiology (ESC) on the management of AF (28) have set a Class IIa, level B indication for the use of ICMs after selected ischemic strokes in order to detect subclinical AF. ECG could improve risk stratification, identifying predictive parameters of AF and indicating patients worthy of receiving long-term ICM. In our study, almost one-third of patients with CS developed subclinical AF after on average about 6 months from ICM implantation. Occurrence of AF at long term follow-up was associated in our series by several echocardiographic parameters, including LA volume and LV systolic/diastolic function.

Among them, PACS and LVLS were the strongest and independent predictors of AF occurrence. PACS has been recently associated with AF in patients with CS without LA enlargement and emerged as a new useful echocardiographic parameter for the prediction of AF in this cohort of patients (22).

The value of this parameter, above LA sizing measurements, stands on the capability to detect even initial alteration of LA contractile function (22). Accordingly, in our analysis, LAVI and LA area, and also PALS, were good predictors of AF at univariable analysis, but their relevance was lost after adjustment for functional LA parameters, while PACS remained significantly associated with incident AF. Our findings are in line with previous studies. In fact, some series have shown an association between LA strain parameters and hidden AF in patients with CS (13, 21, 22). Particularly, PACS impairment can be considered a manifestation of atrial myopathy, being less dependent on LV mechanisms (22). This could explain its higher predictive value for the occurrence of AF in a setting of high-risk patients as those with cryptogenic stroke. Among other echocardiographic parameters, LVLS evaluates the deformation of the LV myocardium occurring during the cardiac cycle in the longitudinal plane, and it has been variously correlated to AF development and diastolic dysfunction (22, 29, 30). All conditions leading to diastolic dysfunction, including hypertension, diabetes, ischemic heart disease, and heart failure, could impair LA physiology (12, 17, 18, 31, 32) with a disease

TABLE 3 | Echocardiographic parameters in the overall population and according to the occurrence of AF.

	Overall $n = 72$	AF $n = 23$	No AF $n = 49$	Unadjusted OR	*p*-value	Adjusted OR	*p*-value
LVEF (%)	63.0 (5.5)	60.0 (6.6)	64.4 (4.3)	0.85 (0.76–0.95)	**0.007**		
EDD (mm)	47.6 (5.8)	48.6 (6.0)	47.1 (5.7)		0.330		
SWT (mm)	10.2 (1.5)	10.4 (1.7)	10.2 (1.5)		0.690		
LVMI (g/m^2)	90.6 (24.1)	93.4 (26.6)	89.4 (23.2)		0.560		
TAPSE (mm)	24.4 (3.3)	23.9 (3.1)	24.5 (3.4)		0.450		
LAES Area (cm^2)	21.7 (4.5)	24.1 (5.1)	20.5 (3.8)	1.22 (1.06–1.39)	**0.006**		
LAVI (ml/m^2)	34.5 (11.3)	40.4 (13.4)	31.7 (9.1)	0.01 (0.01–0.37)	**0.008**		
LATEF	0.5 (0.14)	0.4 (0.1)	0.5 (0.1)	0.01 (0.01–0.37)	**0.013**		
LAAEF	0.3 (0.1)	0.2 (0.1)	0.3 (0.1)		0.051		
LAPEF	0.3 (0.1)	0.2 (0.2)	0.3 (0.1)		0.080		
E velocity (cm/s)	76.3 (20.7)	83.7 (20.6)	72.9 (20.1)	1.03 (1.01–1.05)	**0.042**		
A velocity (cm/s)	86.9 (22.0)	89.1 (30.2)	85.9 (17.4)		0.650		
Mitral E velocity DT (ms)	236.2 (50.9)	253.3 (63.8)	228.4 (42.2)		0.100		
Mitral E/A ratio	0.9 (0.3)	1.0 (0.3)	0.9 (0.3)		0.100		
A duration (ms)	170.6 (3.7)	178.3 (31.3)	167.2 (37.3)		0.210		
PV S velocity (cm/s)	62.4 (12.6)	63.2 (12.2)	62.0 (12.9)		0.720		
PV D velocity (cm/s)	42.3 (11.9)	49.2 (15.7)	46.4 (9.7)		0.450		
PV AR velocity (cm/s)	38.1 (8.6)	35.7 (7.0)	39.3 (9.1)		0.100		
PV AR duration (ms)	167.7 (31.6)	182.9 (33.1)	160.6 (28.6)	1.02 (1.01–1.04)	**0.010**		
PV S/D	1.4 (0.4)	1.4 (0.5)	1.4 (0.3)		0.900		
Lateral TDI e'	9.4 (3.0)	9.0 (2.9)	9.6 (3.1)		0.410		
Septal TDI e'	6.6 (1.9)	6.4 (1.8)	6.6 (1.9)		0.570		
Mean TDI e'	8.0 (2.3)	7.7 (2.2)	8.2 (2.3)		0.420		
Lateral TDI E/e'	8.8 (3.5)	10.1 (4.1)	8.3 (3.1)		0.070		
Septal TDI E/e'	12.3 (4.5)	14.1 (5.3)	11.4 (3.9)	1.14 (1.01–1.27)	**0.045**		
Mean TDI E/e'	10.5 (3.8)	12.1 (4.4)	9.8 (3.2)	1.17 (1.02–1.35)	**0.039**		
PALS A4-C (%)	34.3 (14.5)	22.2 (10.7)	39.7 (12.7)	0.85 (0.78–0.92)	**<0.001**		
PALS A2-C (%)	29.0 (13.1)	23.4 (11)	31.8 (13.4)	0.93 (0.87–0.99)	**0.011**		
PACS A4-C* (%)	15.0 (7.8)	8.0 (3.9)	18.2 (6.9)	0.70 (0.58–0.83)	**<0.001**	0.72 (0.48–0.90)	**0.005**
LA Conduit strain A4-C* (%)	19.5 (2.3)	21.6 (2.8)	14.9 (3.5)	0.90 (0.82–0.98)	**0.005**		
LVLS A4-C* (%)	−18.9 (3.9)	−16.6 (3.3)	−19.9 (3.7)	0.76 (0.63–0.91)	**0.001**	0.69 (0.46–0.95)	**0.041**

Values are expressed as mean (SD).

*A4-C, apical four-chambers; A2-C, apical 2-chambers; AF, atrial fibrillation; LVEF, Left Ventricular Ejection Fraction; EDD, End Diastolic Left Ventricular Diameter; SWT, Septal Wall Thickness; LVMI, Left Ventricular Mass Index; LAES Area, Left Atrium End Systolic Area; LAVI, Left Atrial Volume Index; LATEF, Total Left Atrial Emptying fraction; LAAEF, Active Left Atrial Emptying Fraction; LAPEF, Passive Left Atrial Emptying Fraction; DT, Deceleration Time; PV, Pulmonary Vein; AR, Atrial Reversal; TDI, Tissue Doppler Imaging; PALS, Peak Atrial Longitudinal Strain; PACS, Peak Atrial Contractile Strain; LVLS, Left Ventricular Longitudinal Strain. Statistically significant p-values are reported in bold. * For PACS, LA Conduit strain and LVLS, A4-C results are presented because of the better quality of the images.*

progression model that could encompass both atrial fibrosis and atrial mechanical dysfunction (11). Our results are also consistent with current evidence that proves that an impaired diastolic function in AF patients, as an expression of a close interaction between LA and LV function, results in an impaired LVLS (22, 29) and, probably, also reflects an impaired ventricular-arterial coupling (33, 34).

Among clinical parameters, age was not correlated to the occurrence of AF. Thus, suggesting that not the age *per se*, but age-related morpho-functional LA and LV dynamic changes are more important in this setting. CHA_2DS_2-VASc score was higher in patients who developed AF compared with those who did not, as previously observed in a population-based cohort of 22,179 middle-aged individuals (35). However, when adjusted for PACS and LVLS, it lost its predictive value.

We have also found a higher prevalence of hypercholesterolemia in patients without AF at long term follow-up. One may speculate about a non-cardioembolic cause of CS in such patients, with a prevailing atherosclerotic etiology of the stroke. Similarly, the higher number, although not significant, of patients with PFO in the no-AF group could lead to consider this as related to the stroke.

In our study, all patients presenting subclinical AF at follow-up were prescribed oral anticoagulant therapy, considering their high thromboembolic risk and their preferences. Although the routine use of oral anticoagulation (OAC) in subclinical AF

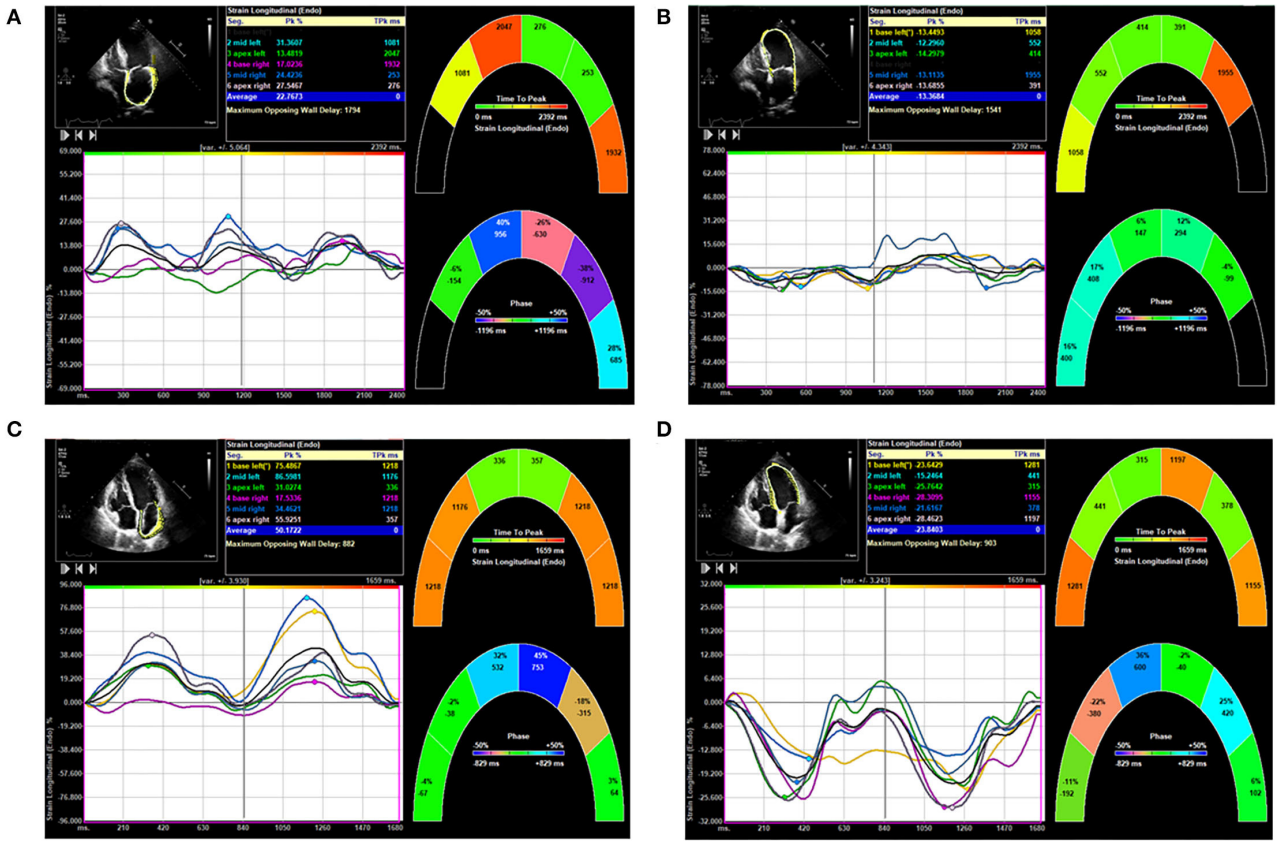

FIGURE 2 | Comparison of left atrial (LA) and left ventricular (LV) strain in patients from atrial fibrillation (AF) group and no-AF group. **(A)** Shows LA strain of a patient of the AF group. **(B)** Shows LV strain of the same patient of the AF group. **(C)** Shows LA strain of a patient of the no-AF group. **(D)** Shows LV strain of the same patient of the no-AF group.

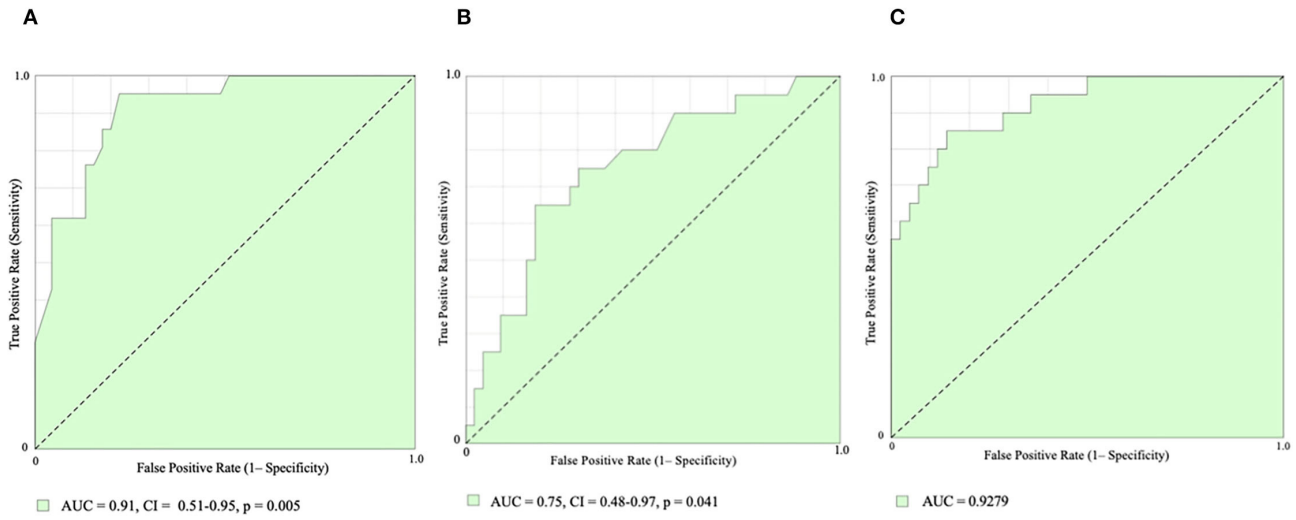

FIGURE 3 | Receiver-operating characteristic (ROC) curve analysis. Peak Atrial Contractile Strain [PACS, **(A)**], Left Ventricular Longitudinal Strain [LVLS, **(B)**], and PACS combined with LVLS **(C)** for AF prediction. AUC, area under curve.

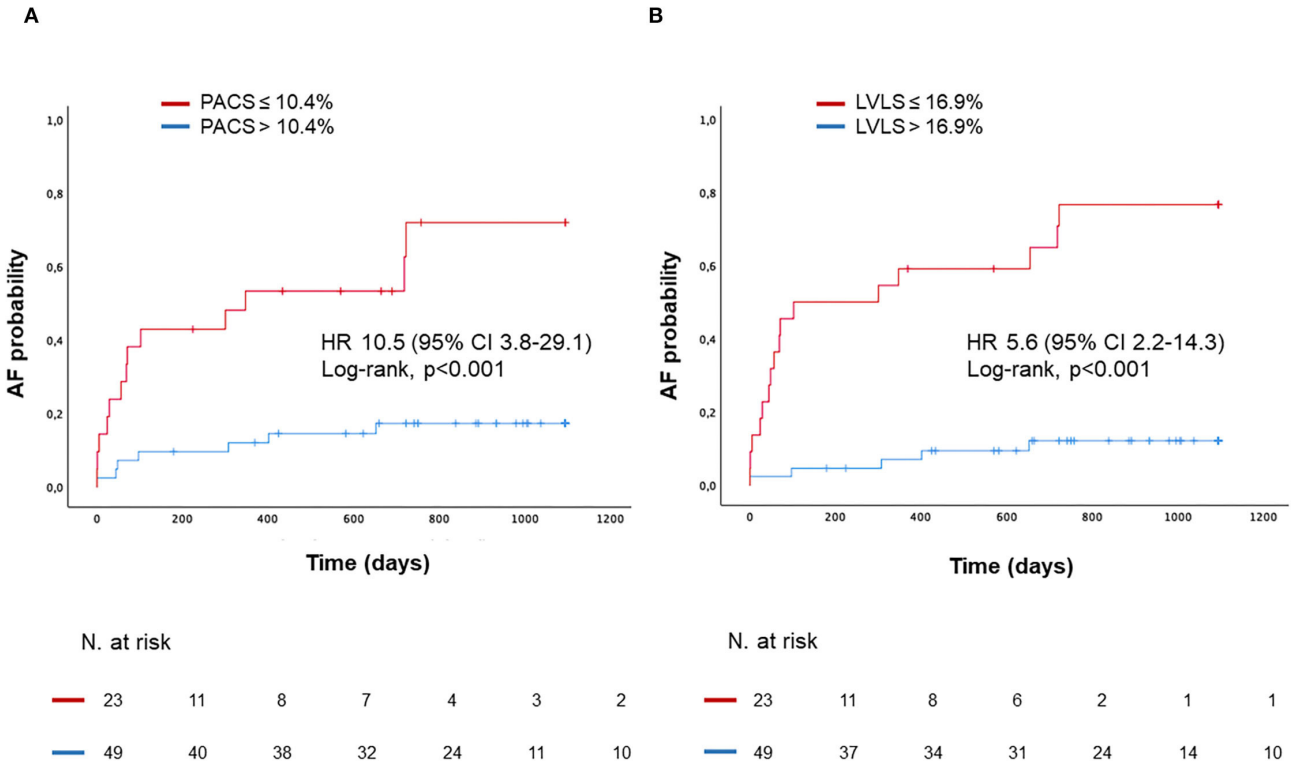

FIGURE 4 | Kaplan–Meyer estimates of AF probability according to PACS **(A)**, or according to LVLS **(B)**. HR, Hazard Ratio.

remains a matter of debate, in the last ESC Guidelines (28), the use of OAC may be considered in selected patients according to AF burden and according to individual risk of stroke, expressed as CHA_2DS_2-VASc score. In our study, the AF group had a mean CHA_2DS_2-VASc score of 5.8. For this reason, the estimated high individual risk of stroke led clinicians to start OAC administration also in presence of subclinical AF.

Further large series studies are needed to address clinical implications of the predictive value of echocardiographic parameters, including PACS and LVLS, for the occurrence of AF. Since the research of hidden AF is crucial in patients with CS and can lead to an adequate therapeutic regimen, availing of predictive parameters of subclinical AF might indicate patients worthy of receiving long-term ICM. Furthermore, LA and LV strain is useful to find out the atrial myopathy and dysfunction related to AF and often preceding the occurrence of the arrhythmia. Therefore, these echocardiographic parameters can be exploited to identify higher risk patients in which the research of AF is strongly recommended, including patients with CS, but also in other high-risk clinical settings.

STRENGTH AND LIMITATIONS

To our knowledge, this is the largest study with the totality of CS population monitored using ICM. In fact, most studies were conducted on patients monitored with conventional methods, while only one enrolled 56 patients with CS monitored with ICM (13).

There are some limitations in this study. First, this is a single-center study with a small sample size. Therefore, a correlation of clinical and echocardiographic variables with hard clinical events was not possible. Moreover, since the ICM here used requires at least 2 min of AF to be detected, episodes <2 min could have been missed, while definition of AF now accounts for episodes lasting more than 30 s with absence of P waves and variable R-R interval. Furthermore, 15 patients were unable to attend a clinical visit, and follow-up data were collected by a phone questionnaire. Finally, for some strain data, only A4-C view results are presented because of the better quality of the images. However, although in most studies, the 2D-global longitudinal strain was calculated as the average of the A4-C, A2-C, and A3-C views, the A4-C view is considered adequate to obtain strain measures when the echocardiographic acoustic window is limited (26).

CONCLUSIONS

In about one-third of patients with CS, ICM revealed subclinical AF episodes. In these patients, LA and LV strain analysis adds predictive value for the occurrence of AF over clinical and other morpho-functional echocardiographic parameters. Impaired booster pump strain and left ventricular longitudinal strain are strong and independent predictors of AF.

DATA AVAILABILITY STATEMENT

The original contributions presented in the study are included in the article/supplementary materials, further inquiries can be directed to the corresponding author/s.

ETHICS STATEMENT

The studies involving human participants were reviewed and approved by Institutional Ethics Committee of G. d'Annunzio University/Santissima Annunziata Hospital of Chieti. The patients/participants provided their written informed consent to participate in this study.

AUTHOR CONTRIBUTIONS

GB and GR contributed to the conception and design of the work. GB, FR, CD'A, and FP contributed to the acquisition and analysis of data for the work. GB, FR, SG, GR, and SP contributed to the interpretation of data. GB and FR drafted the manuscript. MD, MF, SP, SG, and GR critically revised the manuscript. All authors gave final approval and agreed to be accountable for all aspects of work ensuring integrity and accuracy.

ACKNOWLEDGMENTS

We thank Dr. Carmelita Cieri for her help in data collection.

REFERENCES

1. Adams HP Jr, Bendixen BH, Kappelle LJ, Biller J, Love BB, Gordon DL, et al. Classification of subtype of acute ischemic stroke. Definitions for use in a multicenter clinical trial. TOAST. Trial of Org 10172 in Acute Stroke Treatment. *Stroke.* (1993) 24:35–41. doi: 10.1161/01.STR.24.1.35
2. Go AS, Mozaffarian D, Roger VL, Benjamin EJ, Berry JD, Blaha MJ, et al. Heart disease and stroke statistics—2014 update: a report from the American Heart Association. *Circulation.* (2014) 129:e28–e292. doi: 10.1161/01.cir.0000441139.02102.80
3. Hart RG, Diener HC, Coutts SB, Easton JD, Granger CB, O'Donnell MJ, et al. Embolic strokes of undetermined source: the case for a new clinical construct. *Lancet Neurol.* (2014) 13:429–38. doi: 10.1016/S1474-4422(13)70310-7
4. Ntaios G. Embolic stroke of undetermined source: JACC review topic of the week. *J Am Coll Cardiol*. (2020) 75:333–40. doi: 10.1016/j.jacc.2019.11.024
5. Gladstone DJ, Spring M, Dorian P, Panzov V, Thorpe KE, Hall J, et al. Atrial fibrillation in patients with cryptogenic stroke. *N Engl J Med*. (2014) 370:2467–77. doi: 10.1056/NEJMoa1311376
6. Sanna T, Diener HC, Passman RS, Crystal AFSC. Cryptogenic stroke and atrial fibrillation. *N Engl J Med.* (2014) 371:1261. doi: 10.1056/NEJMc1409495
7. Wachter R, Groschel K, Gelbrich G, Hamann GF, Kermer P, Liman J, et al. Holter-electrocardiogram-monitoring in patients with acute ischaemic stroke (Find-AFRANDOMISED): an open-label randomised controlled trial. *Lancet Neurol.* (2017) 16:282–90. doi: 10.1016/S1474-4422(17)30002-9
8. Diener HC, Sacco RL, Easton JD, Granger CB, Bernstein RA, Uchiyama S, et al. Dabigatran for prevention of stroke after embolic stroke of undetermined source. *N Engl J Med*. (2019) 380:1906–17. doi: 10.1056/NEJMoa1813959
9. Hart RG, Sharma M, Mundl H, Kasner SE, Bangdiwala SI, Berkowitz SD, et al. Rivaroxaban for stroke prevention after embolic stroke of undetermined source. *N Engl J Med*. (2018) 378:2191–201. doi: 10.1056/NEJMoa1802686
10. De Angelis MV, Di Stefano V, Franciotti R, Furia N, Di Girolamo E, Onofrj M, et al. Cryptogenic stroke and atrial fibrillation in a real-world population: the role of insertable cardiac monitors. *Sci Rep*. (2020) 10:3230. doi: 10.1038/s41598-020-60180-6
11. Goldberger JJ, Arora R, Green D, Greenland P, Lee DC, Lloyd-Jones DM, et al. Evaluating the atrial myopathy underlying atrial fibrillation: identifying the arrhythmogenic and thrombogenic substrate. *Circulation*. (2015) 132:278–91. doi: 10.1161/CIRCULATIONAHA.115.016795
12. Mondillo S, Cameli M, Caputo ML, Lisi M, Palmerini E, Padeletti M, et al. Early detection of left atrial strain abnormalities by speckle-tracking in hypertensive and diabetic patients with normal left atrial size. *J Am Soc Echocardiogr*. (2011) 24:898–908. doi: 10.1016/j.echo.2011.04.014
13. Olsen FJ, Mogelvang R, Jensen GB, Jensen JS, Biering-Sorensen T. Relationship between left atrial functional measures and incident atrial fibrillation in the general population: the Copenhagen city heart study. *JACC Cardiovasc Imaging.* (2019) 12:981–9. doi: 10.1016/j.jcmg.2017.12.016
14. Pagola J, Gonzalez-Alujas T, Flores A, Muchada M, Rodriguez-Luna D, Sero L, et al. Left atria strain is a surrogate marker for detection of atrial fibrillation in cryptogenic strokes. *Stroke.* (2014) 45:e164–6. doi: 10.1161/STROKEAHA.114.005540
15. Sanchis L, Montserrat S, Obach V, Cervera A, Chamorro A, Vidal B, et al. Left atrial function is impaired in some patients with stroke of undetermined etiology: potential implications for evaluation and therapy. *Rev Esp Cardiol*. (2016) 69:650–6. doi: 10.1016/j.recesp.2015.11.035
16. Blume GG, McLeod CJ, Barnes ME, Seward JB, Pellikka PA, Bastiansen PM, et al. Left atrial function: physiology, assessment, and clinical implications. *Eur J Echocardiogr*. (2011) 12:421–30. doi: 10.1093/ejechocard/jeq175
17. Thomas L, Marwick TH, Popescu BA, Donal E, Badano LP. Left Atrial structure and function, and left ventricular diastolic dysfunction: JACC state-of-the-art review. *J Am Coll Cardiol*. (2019) 73:1961–77. doi: 10.1016/j.jacc.2019.01.059
18. Cameli M, Ciccone MM, Maiello M, Modesti PA, Muiesan ML, Scicchitano P, et al. Speckle tracking analysis: a new tool for left atrial function analysis in systemic hypertension: an overview. *J Cardiovasc Med*. (2016) 17:339–43. doi: 10.2459/JCM.0000000000000073
19. Gupta DK, Shah AM, Giugliano RP, Ruff CT, Antman EM, Grip LT, et al. Left atrial structure and function in atrial fibrillation: ENGAGE AF-TIMI 48. *Eur Heart J*. (2014) 35:1457–65. doi: 10.1093/eurheartj/eht500
20. Mandoli GE, Cameli M, Lisi E, Minardi S, Capone V, Pastore MC, et al. Left atrial fractional shortening: a simple and practical "Strain" for everyone. *J Cardiovasc Echogr*. (2019) 29:52–7. doi: 10.4103/jcecho.jcecho_74_18
21. Deferm S, Bertrand PB, Churchill TW, Sharma R, Vandervoort PM, Schwamm LH, et al. Left atrial mechanics assessed early during hospitalization for cryptogenic stroke are associated with occult atrial fibrillation: a speckle-tracking strain echocardiography study. *J Am Soc Echocardiogr*. (2021) 34:156–65. doi: 10.1016/j.echo.2020.09.009
22. Kawakami H, Ramkumar S, Pathan F, Wright L, Marwick TH. Use of echocardiography to stratify the risk of atrial fibrillation: comparison of left atrial and ventricular strain. *Eur Heart J Cardiovasc Imaging.* (2020) 21:399–407. doi: 10.1093/ehjci/jez240
23. Lang RM, Badano LP, Mor-Avi V, Afilalo J, Armstrong A, Ernande L, et al. Recommendations for cardiac chamber quantification by echocardiography in adults: an update from the American Society of Echocardiography and the European Association of Cardiovascular Imaging. *Eur Heart J Cardiovasc Imaging*. (2015) 16:233–70. doi: 10.1093/ehjci/jev014
24. Badano LP, Kolias TJ, Muraru D, Abraham TP, Aurigemma G, Edvardsen T, et al. Standardization of left atrial, right ventricular, and right atrial deformation imaging using two-dimensional speckle tracking echocardiography: a consensus document of the EACVI/ASE/Industry Task Force to standardize deformation imaging. *Eur Heart J Cardiovasc Imaging*. (2018) 19:591–600. doi: 10.1093/ehjci/jey042
25. Yingchoncharoen T, Agarwal S, Popovic ZB, Marwick TH. Normal ranges of left ventricular strain: a meta-analysis. *J Am Soc Echocardiogr*. (2013) 26:185–91. doi: 10.1016/j.echo.2012.10.008
26. Salaun E, Casalta AC, Donal E, Bohbot Y, Galli E, Tribouilloy C, et al. Apical four-chamber longitudinal left ventricular strain in patients with aortic stenosis and preserved left ventricular ejection fraction: analysis related with

flow/gradient pattern and association with outcome. *Eur Heart J Cardiovasc Imaging*. (2018) 19:868–78. doi: 10.1093/ehjci/jex203
27. Bunting KV, Steeds RP, Slater LT, Rogers JK, Gkoutos GV, Kotecha D. A Practical guide to assess the reproducibility of echocardiographic measurements. *J Am Soc Echocardiogr*. (2019) 32:1505–15. doi: 10.1016/j.echo.2019.08.015
28. Hindricks G, Potpara T, Dagres N, Arbelo E, Bax JJ, Blomstrom-Lundqvist C, et al. 2020 ESC Guidelines for the diagnosis and management of atrial fibrillation developed in collaboration with the European Association for Cardio-Thoracic Surgery (EACTS). *Eur Heart J*. (2021) 42:373–498. doi: 10.1093/eurheartj/ehaa612
29. Bruun Pedersen K, Madsen C, Sandgaard NCF, Hey TM, Diederichsen ACP, Bak S, et al. Left atrial volume index and left ventricular global longitudinal strain predict new-onset atrial fibrillation in patients with transient ischemic attack. *Int J Cardiovasc Imaging*. (2019) 35:1277–86. doi: 10.1007/s10554-019-01586-w
30. Nagueh SF, Appleton CP, Gillebert TC, Marino PN, Oh JK, Smiseth OA, et al. Recommendations for the evaluation of left ventricular diastolic function by echocardiography. *J Am Soc Echocardiogr*. (2009) 22:107–33. doi: 10.1016/j.echo.2008.11.023
31. Morris DA, Belyavskiy E, Aravind-Kumar R, Kropf M, Frydas A, Braunauer K, et al. Potential usefulness and clinical relevance of adding left atrial strain to left atrial volume index in the detection of left ventricular diastolic dysfunction. *JACC Cardiovasc Imaging*. (2018) 11:1405–15. doi: 10.1016/j.jcmg.2017.07.029
32. Santos AB, Kraigher-Krainer E, Gupta DK, Claggett B, Zile MR, Pieske B, et al. Impaired left atrial function in heart failure with preserved ejection fraction. *Eur J Heart Fail*. (2014) 16:1096–103. doi: 10.1002/ejhf.147
33. Saba PS, Cameli M, Casalnuovo G, Ciccone MM, Ganau A, Maiello M, et al. Ventricular-vascular coupling in hypertension: methodological considerations and clinical implications. *J Cardiovasc Med*. (2014) 15:773–87. doi: 10.2459/JCM.0000000000000146
34. Yoon JH, Kim MH, Chung H, Choi EY, Min PK, Yoon YW, et al. Echo-Doppler-derived indexes of ventricular stiffness and ventriculo-arterial interaction as predictors of new-onset atrial fibrillation in patients with heart failure. *Cardiovasc Ultrasound*. (2016) 14:7. doi: 10.1186/s12947-016-0050-y
35. Renda G, Ricci F, Patti G, Aung N, Petersen SE, Gallina S, et al. CHA2DS2VASc score and adverse outcomes in middle-aged individuals without atrial fibrillation. *Eur J Prev Cardiol*. (2019) 26:1987–97. doi: 10.1177/2047487319868320

Conflict of Interest: FR: speaker/consultant fee from Boehringer Ingelheim, Daiichi Sankyo. SP: speaker/consultant fee from Astra Zeneca, Bayer. GR: speaker/consultant fee from Astra Zeneca, Bayer, BMS-Pfizer, Boehringer Ingelheim, Daiichi Sankyo.

The remaining authors declare that the research was conducted in the absence of any commercial or financial relationships that could be construed as a potential conflict of interest.

frontiers | Frontiers in Cardiovascular Medicine

ORIGINAL RESEARCH
published: 28 April 2022
doi: 10.3389/fcvm.2022.880186

End-to-End Deep Learning of Non-rigid Groupwise Registration and Reconstruction of Dynamic MRI

Junwei Yang[1,2], *Thomas Küstner*[3], *Peng Hu*[2], *Pietro Liò*[1] *and Haikun Qi*[2]*

[1] Department of Computer Science and Technology, University of Cambridge, Cambridge, United Kingdom, [2] The School of Biomedical Engineering, ShanghaiTech University, Shanghai, China, [3] Medical Image and Data Analysis (MIDAS.lab), Department of Diagnostic and Interventional Radiology, University Hospital of Tübingen, Tübingen, Germany

Temporal correlation has been exploited for accelerated dynamic MRI reconstruction. Some methods have modeled inter-frame motion into the reconstruction process to produce temporally aligned image series and higher reconstruction quality. However, traditional motion-compensated approaches requiring iterative optimization of registration and reconstruction are time-consuming, while most deep learning-based methods neglect motion in the reconstruction process. We propose an unrolled deep learning framework with each iteration consisting of a groupwise diffeomorphic registration network (GRN) and a motion-augmented reconstruction network. Specifically, the whole dynamic sequence is registered at once to an implicit template which is used to generate a new set of dynamic images to efficiently exploit the full temporal information of the acquired data via the GRN. The generated dynamic sequence is then incorporated into the reconstruction network to augment the reconstruction performance. The registration and reconstruction networks are optimized in an end-to-end fashion for simultaneous motion estimation and reconstruction of dynamic images. The effectiveness of the proposed method is validated in highly accelerated cardiac cine MRI by comparing with other state-of-the-art approaches.

Keywords: dynamic MR imaging, deep learning, reconstruction, registration, multi-task learning

OPEN ACCESS

Edited by:
Adelina Doltra,
Hospital Clínic de Barcelona, Spain

Reviewed by:
Kelvin Kian Loong Wong,
University of Saskatchewan, Canada
Gaspar Delso,
Hospital Clínic de Barcelona, Spain

***Correspondence:**
Haikun Qi
qihk@shangheitech.edu.cn

Specialty section:
This article was submitted to Original Research Article, a section of the journal Frontiers in Cardiovascular Medicine

Received: *21 February 2022*
Accepted: *08 April 2022*
Published: *28 April 2022*

Citation:
Yang J, Küstner T, Hu P, Liò P and Qi H (2022) End-to-End Deep Learning of Non-rigid Groupwise Registration and Reconstruction of Dynamic MRI. Front. Cardiovasc. Med. 9:880186. doi: 10.3389/fcvm.2022.880186

1. INTRODUCTION

Dynamic MRI has found various applications in clinical practice, such as cardiovascular, pulmonary and abdominal imaging. Rapid data acquisition is required in dynamic MRI to provide sufficient spatial and temporal resolution. However, MRI is known to have low acquisition speed, and accelerated data acquisition and reconstruction is an important topic in dynamic MRI.

Parallel imaging (1, 2) and compressed sensing (CS) (3) have achieved great success in accelerating MRI by recovering images from undersampled measurements that are fewer than those required by the Nyquist law. Image reconstruction from undersampled MRI data is an ill-posed inverse problem and regularization on prior information is required to stabilize the solution. For dynamic MRI reconstruction, regularizations have been designed to exploit the spatial and temporal correlation of dynamic images, including sparsity regularization in transformed domains (4–6), low-rank constraint (7), or the combination of sparsity and low-rank priors (8–10).

Attempts have been made to further improve the reconstruction performance through modeling the motion to increase the signal sparsity, which is achieved by exploiting the abrupt signal changes through time caused by inter-frame motion (11–20). The challenge of applying motion estimation (ME) and motion compensation (MC) to dynamic MRI reconstruction is the lack of good quality dynamic images for motion estimation. In k-t FOCUSS with ME/MC (12), each frame is individually registered to a high-quality reference image using a block matching algorithm. However, reference images of good quality are usually not available. The MASTeR algorithm (13) estimates motion between adjacent frames to construct motion-adaptive regularization. Some authors have modeled the reconstruction process as a joint task of motion estimation and reconstruction (19–21), with the two tasks being optimized alternatively, such as MC-JPDAL (19) where the dynamic sequences and the inter-frame motion vectors are estimated jointly by combining an intensity-based optical flow constraint with the traditional CS scheme, and then the reconstructed dynamic images can be further refined with the estimated motion vectors.

However, pairwise registration is performed in the above mentioned approaches, involving only two frames for ME, and consequently additional information in the rest of the frames cannot be exploited, which makes ME sensitive to undersampling artifacts in the dynamic images. To overcome such shortcomings of pairwise ME, Royuela-del Val et al. (16) propose to use groupwise non-rigid registration to register the full set of dynamic images for only once to generate a temporally-aligned dynamic sequence to improve the dynamic reconstruction in a CS framework (GW-CS). Overall, ME/MC can be integrated into the dynamic reconstruction procedure to improve the sparsity of CS reconstruction or provide additional constraints to improve the reconstruction performance. However, the iterative optimization of ME and CS reconstruction is computationally demanding. Especially, the non-rigid registration for ME requires iterative optimization which takes up a lot of the computation time. Although methods have been developed to reduce the non-rigid registration time from hours to minutes, the computation time of registering a sequence of dynamic images using groupwise registration or multiple pairwise registrations can still be considerable. Moreover, the non-rigid registration step has to be performed several times in the motion-compensated reconstruction procedure, so the traditional motion-compensated reconstruction approaches tend to be time-consuming.

Deep learning-based MRI reconstruction methods have been proposed to significantly reduce the reconstruction time and have demonstrated better reconstruction quality than CS-based methods. Deep learning approaches are usually designed to learn the mapping from undersampled images/measurements to fully sampled images/measurements based on the training data (22). Whilst most deep learning reconstruction methods are for static images, networks such as 3D convolutional neural network, 2D/3D+1D convolutional networks and 2D recurrent neural network have been proposed for dynamic reconstruction (23–28). Those state-of-the-art methods can be impaired by spatially unmatched anatomies as they could lead to blurry or temporal inconsistent images for highly undersampled data.

However, so far, only limited works have incorporated motion information into deep learning-based reconstruction. Previously, we have developed an end-to-end trainable framework for motion corrected 3D cardiac image reconstruction (29), but this framework is not applicable to dynamic reconstruction. Huang et al. develop a motion-guided dynamic reconstruction network that utilizes motion estimation and motion compensation to improve the reconstruction quality, which, however, requires a fully sampled reference frame that may not be available (30). The most relevant work is Seegoolam et al. (31), where motion is estimated in each cascade from an intermediate reconstructed image to fuse the full information of acquired data and to aid in improving reconstruction performance. However, this method requires a large number of pairwise registrations to estimate the motion between a specific frame and all the other frames, which are computationally redundant and expensive. A more efficient motion estimation framework is yet to be developed and to be incorporated into the dynamic reconstruction network.

To this end, we propose a novel joint learning approach that performs non-rigid groupwise registration and reconstruction of highly undersampled dynamic MRI. An unrolled deep learning architecture is constructed with each unrolled iteration consisting of a groupwise diffeomorphic registration network (GRN) and a reconstruction network. The GRN is used to efficiently exploit the dynamic information across all frames by estimating the invertible motion fields between the whole sequence and an implicit template, thereby generating a new set of dynamic images by transforming the template with estimated motion fields. The motion-augmented dynamic sequence is then incorporated into the reconstruction network to improve the reconstruction performance. For GRN, we employ the self-supervised deep learning registration model, which is more efficient and robust than traditional motion estimation algorithms in the presence of undersampling artifacts (32, 33). To the best of our knowledge, this is the first work that embeds groupwise registration network into the deep learning reconstruction framework to exploit the full temporal information of the acquired data to aid in the dynamic MRI reconstruction. The contributions of this work are three aspects. Firstly, we design a groupwise diffeomorphic registration network that provides invertible motion fields, and requires no motion ground truth for training and is robust to undersampling artifacts. Secondly, we systemically compare the performance of groupwise registration and pairwise registration in the proposed joint learning approach regarding motion estimation and reconstruction performance. Finally, we devise a composite loss which comprises of a motion estimation loss and an image reconstruction loss to train the joint learning network on an end-to-end basis. The effectiveness of the proposed method is validated in highly accelerated cardiac cine MRI by comparing with other state-of-the-art non-learning-based and learning-based dynamic MRI reconstruction methods.

2. MATERIALS AND METHODS

The proposed groupwise registration and dynamic reconstruction network (GRDRN) consists of several unrolled iterations with each iteration consisting of a groupwise registration network (GRN) to generate motion-augmented dynamic sequence and a dealiasing reconstruction network. Details of each part is introduced as follows.

2.1. Learning-Based Groupwise Registration

Provided a set of dynamic images $X = \{X_1, \cdots, X_N\}$ with N being the number of dynamic frames, the groupwise registration attempts to simultaneously estimate a set of transformations $T = \{T_1, \cdots, T_N\}$ that warp the images X to a common reference image $\bar{X}$, such that the deformed image $T_m \circ X_m$ is similar to $T_n \circ X_n \ \forall m \neq n$ with $\circ$ being the warping operator. To obtain differentiable and invertible deformation fields, and following the conventional diffeomorphic registration that integrates stationary or time-varying velocity fields (34), a set of stationary velocity fields $\upsilon = \{v_1, \cdots, v_N\}$, pointing from the template image $\bar{X}$ to the dynamic images X are estimated. Subsequently, the transformations T and their inverse transformations $T^{-1} = \{T_1^{-1}, \cdots, T_N^{-1}\}$ can be estimated by respectively integrating the velocity field υ and the negative velocity field $-\upsilon$ over unit time (34, 35).

For learning-based groupwise registration (**Figure 1**), we define a network $\mathcal{F}_\theta$ with parameters of θ to simultaneously estimate a set of transformations for a dynamic sequence: $\upsilon = \mathcal{F}_\theta(X)$ and the transformations T is constructed based on υ. The network is optimized via the intensity-based similarity (mean-squared-error, MSE) and velocity field smoothness loss:

$$\mathcal{L}_{\text{reg}}(X, T) = \frac{1}{N}\sum_{n=1}^{N} \|\bar{X} - T_n \circ X_n\|_2^2 + \frac{1}{N}\sum_{n=1}^{N} \|X_n - T_n^{-1} \circ \bar{X}\|_2^2 + \alpha \frac{1}{N}\sum_{n=1}^{N} \|\nabla v_n\|_2^2, \quad (1)$$

where the first term enforces the similarity between the implicit reference image and the warped dynamic images; the second term imposes the intensity similarity between the original dynamic images and the generated dynamic images by transforming the template with the inverse transformations ($T_n^{-1} \circ \bar{X}$); the third term is to encourage the smoothness of the estimated velocity fields and α is the regularization weight. The implicit template image is defined as the average of the warped dynamic images (36, 37):

$$\bar{X} = \frac{1}{N}\sum_{n=1}^{N} T_n \circ X_n. \quad (2)$$

In addition, to enforce the reference image to lie in the geometric center of the group, as proposed in Li et al. (37), the average velocity field is subtracted from each of the estimated velocity fields: $\hat{v}_n = \frac{1}{N}\sum_{n=1}^{N} v_n$, and the sum of all the velocity fields is consequently zero.

2.2. Motion-Augmented Dynamic Reconstruction

We aim to integrate the groupwise registration module, GRN, into an unrolled dynamic MRI reconstruction network (**Figure 2**), where the registration and reconstruction modules are optimized iteratively. In each iteration, the GRN takes as input the magnitude of undersampled or intermediate reconstructed dynamic images and outputs the velocity fields between the implicit template and the dynamic images, from which the sets of transformations and inverse transformations can be obtained. As defined in Equation (2), the implicit template image is the average of all the warped dynamic images so that the full information of dynamic measurements is efficiently fused after motion compensation. Then, a set of dynamic images can be generated by warping the template image $\bar{X}^k$ with the inverse transformations $T^{k-1} = \{T_1^{k-1}, \cdots, T_N^{k-1}\}$ at the k-th iteration:

$$G_n^k = \text{DC}(T_n^{k-1} \circ \bar{X}^k), \quad (3)$$

where $G^k = \{G_1^k, \cdots, G_N^k\}$ is the generated, motion-augmented dynamic images, DC indicates data consistency enforcement which is performed by plugging in the originally acquired data for each frame. The zero-filled reconstructed images are denoted as X^0, and the corresponding template image and generated dynamic images are $\bar{X}^0$ and G^0, respectively.

The motion-augmented dynamic image series which has fused the information along the temporal dimension is used as the input to the dealiasing network to aid the reconstruction. Specifically, two sets of motion-augmented dynamic images are generated with, respectively, the output of the previous iteration and the zero-filling reconstructed images and are stacked together as the input to the reconstruction network, the combination of which was demonstrated to be effective as in Seegoolam et al. (31). Therefore, in the k-th iteration, the dealiased dynamic images Z^k are:

$$Z^k = \mathcal{H}_\Phi(G^{k-1}, G^0, X^{k-1}) + X^{k-1}, \quad (4)$$

where the residual learning strategy is employed and $\mathcal{H}_\Phi$ is the dealiasing network patameterized by Φ. The output of the dealiasing network goes through the DC layer (23) to obtain the reconstruction at the k-th iteration: $X^k = \text{DC}(Z^k)$, which are applied as the input to the next iteration for groupwise registration and motion-augmented reconstruction.

2.3. End-to-End Optimization Framework

The registration loss and reconstruction loss are designed for each unrolled iteration to train the proposed GRDRN. For registration, previous works (32, 33) have demonstrated that by constructing the MSE loss based on the fully sampled ground truth images, it is possible to learn the motion from undersampled images. Therefore, while the input to GRN is the undersampled or intermediate reconstructed images, the registration loss as defined in Equation (1) for the k-th iteration $\mathcal{L}_{\text{reg}}^k(X^{\text{gt}}, T^k)$ is calculated based on the fully sampled ground

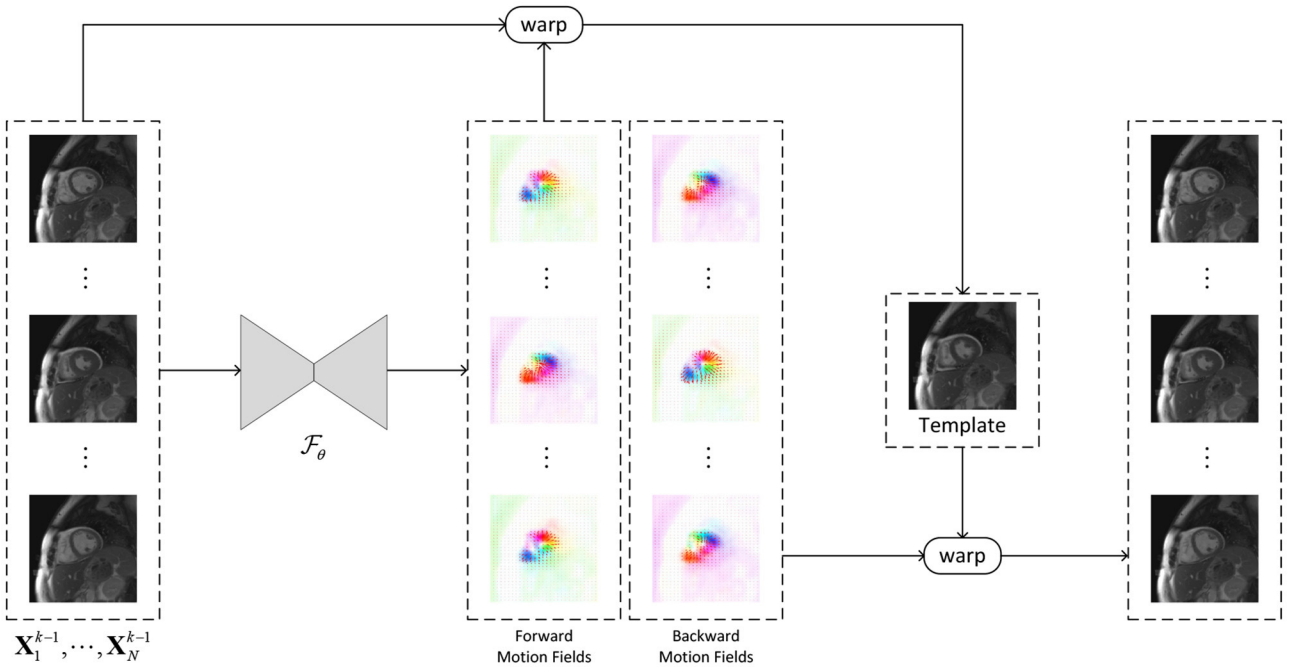

FIGURE 1 | The framework of the learning-based groupwise registration network (GRN, $\mathcal{F}_\theta$). The GRN takes a sequence of images as input and generates the invertible forward and backward motion fields between an implicit template and the dynamic images, where the template is the average of the warped dynamic images with the forward motion. A new sequence of dynamic images can be generated by warping the template using the backward motion fields.

truth dynamic images $X^{\text{gt}} = \{X_1^{\text{gt}}, \cdots, X_N^{\text{gt}}\}$. The reconstruction of each unrolled iteration is compared with the fully sampled ground truth to calculate the reconstruction loss: $\mathcal{L}_{\text{rec}}^k(X^{\text{gt}}, X^k) = \frac{1}{N}\sum_{n=1}^{N} \|X_n^{\text{gt}} - X_n^k\|_2^2$. The joint training loss of each iteration is a weighted combination of the registration loss and reconstruction loss, and the end-to-end optimization problem is formulated as:

$$\arg\min_{\theta,\Phi} \sum_{k=1}^{K} w^k(\mathcal{L}_{\text{rec}}^k(X^{\text{gt}}, X^k) + \lambda \mathcal{L}_{\text{reg}}^k(X^{\text{gt}}, T^k)), \qquad (5)$$

where K is the number of unrolled iterations, $w_k = \exp(k-K)$ is the weighting factor of each unrolled iteration, and λ is the weight controlling the contribution of the registration loss. It is noted that the network parameters are shared for different unrolled iterations to reduce the number of trainable parameters (38).

The UNet architecture (39) is adapted for the registration network $\mathcal{F}_\theta$ and dealiasing network $\mathcal{H}_\Phi$, while the network architecture can be modified for specific applications. We adopt the 2D UNet for $\mathcal{F}_\theta$ with the magnitude of the dynamic images stacked along the channel dimension, and employ the 3D UNet for $\mathcal{H}_\Phi$ with the real and imaginary components of the complex images stacked along the channel dimension. The convolution layers produce a set of C feature maps by individually convolving the input with C kernels. In this work, we use $C = [32, 64, 128, 256, 128, 64, 32]$ for both $\mathcal{F}_\theta$ and $\mathcal{H}_\Phi$. Each convolution layer is of kernel size $(3, 3)$ and $(3, 3, 3)$ for $\mathcal{F}_\theta$ and $\mathcal{H}_\Phi$ respectively, followed by a leaky ReLU layer for nonlinear activation except for the last convolution layer where no activation function is used. Max-pooling and transposed convolution is respectively used for the downscale and upscale layers. The whole model has a total number of around 7M trainable parameters.

2.4. Experiments

We evaluate our method on the dataset of breath-held 2D cardiac cine MRI, where repeated breath-holds are usually required to cover the whole left ventricle. During the acquisition, acceleration is essential to reduce the scan time and the number of breath-holds, and highly accelerated MRI acquisition may enable the scan of whole-heart cine in a single breath-hold. We therefore target for high acceleration factors of 8×, 12×, and 16×. We evaluate the motion estimation and reconstruction performance of the proposed method in retrospectively undersampled cardiac cine MRI data. We compare GRDRN with state-of-the-art conventional dynamic reconstruction methods with ME/MC and learning-based dynamic reconstruction approaches with pairwise registration or without motion estimation. The compared methods are detailed in the Section of 2.4.3.

2.4.1. Dataset and Preprocessing

We use a dataset of 56 cardiac cine MRI scans including 34 healthy volunteers and 22 patients with suspected cardiovascular diseases acquired using a commercially available 2D balanced steady-state free precession cine imaging technique. Multiple

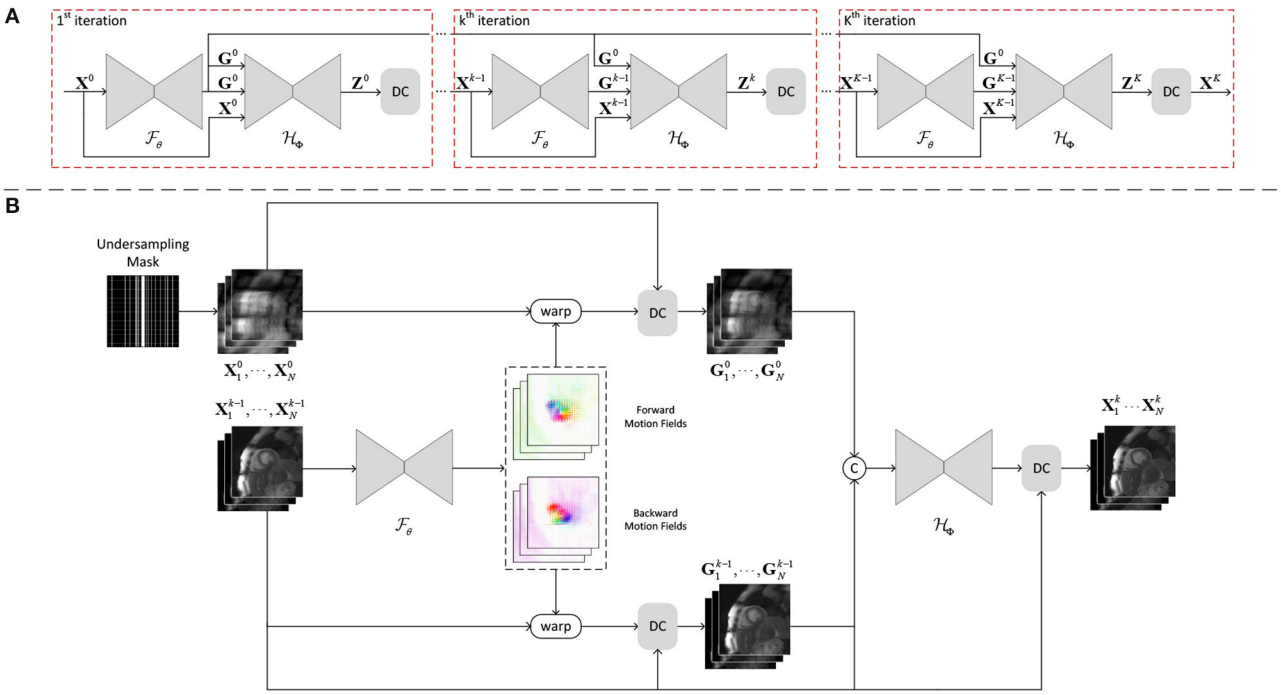

FIGURE 2 | (A) The unrolled architecture of GRDRN for K iterations, where $\mathcal{F}_\theta$ and $\mathcal{H}_\Phi$ is the groupwise registration and dynamic reconstruction network respectively. **(B)** The detailed framework of the k-th iteration in GRDRN. The groupwise registration network $\mathcal{F}_\theta$ takes as input the reconstructed dynamic images from the previous iteration and outputs the invertible motion fields between the implicit template and dynamic images. The reconstruction network $\mathcal{H}_\Phi$ denoises the dynamic images with additional inputs of the motion augmented dynamic sequences. After the data consistency layer (DC), the denoised dynamic images will be inputted to the next iteration.

short-axis slices are acquired in 6–8 breath-holds of around 12-s duration (2 slices per breath-hold) each with 20 s pause in between, which results in an acquisition time of 3–4 min. The imaging parameters are: in-plane spatial resolution = 1.9 × 1.9 mm; matrix size = 176 × 144; slice thickness = 8 mm; TR/TE = 2.12/1.06; flip angle = 52°; bandwidth = 915 Hz/pixel; 25 dynamic frames with temporal resolution of 40 ms; parallel imaging factor = 2.

The 2-fold accelerated data is firstly reconstructed using a k-space based parallel imaging method GRAPPA (2). The reconstructed multi-coil k-space data is coil combined into single-coil k-space data and regarded as the "fully sampled" reference in this work. The image reconstructed by inverse Fourier Transform of the single-coil k-space is thus considered as the ground truth image for training and evaluation of the reconstruction methods. We have randomly selected 35 subjects for training, 3 subjects for validation and 18 subjects for testing. For each subject, 6–8 central slices are selected resulting in 263, 23, and 128 slices for training, validation and testing, respectively.

We consider Cartesian undersampling in this work, where the data is fully sampled along the frequency-encoding dimension and is randomly undersampled along the phase-encoding dimension. The sampling density conforms to a zero-mean Gaussian distribution, and five central k-space lines are always sampled for each frame. We follow the implementation in Schlemper et al. (23) to generate undersampling masks for 8×, 12×, and 16× acceleration factors.

2.4.2. Implementation Details

The number of unrolled iterations in the proposed GRDRN is set to 4. The weighting factor α and λ was, respectively, optimized to be 0.05 and 1 by a limited number of searches. The network performance reaches a plateau within 60 epochs. The training samples are shuffled at the beginning of each epoch and the undersampling masks are generated on-the-fly during training to reduce overfitting. We train the network with Adam optimizer with the initial learning rate of $1e-4$, which is reduced by half every 20 epochs. The network is trained on a single NVIDIA GeForce RTX 3090 graphics card. With batch size of 1, the network training took around 12 h and 19 GB GPU memory.

2.4.3. Baseline Methods

The reconstruction performance of the proposed method is compared with state-of-the-art non-learning-based and learning-based dynamic MRI reconstruction methods. Specifically, for conventional methods, we consider two reconstruction approaches that modeled cardiac motion during reconstruction. One is GW-CS (16), which adopts a B-spline based groupwise registration approach to register the

whole sequence to a common template to generate temporally aligned dynamic images, which are highly sparse in temporally transformed domains and can benefit the compressed sensing reconstruction. The other is MC-JPDAL (19) which combines intensity-based optical flow constraint with the compressed sensing scheme to jointly reconstruct the dynamic sequence and estimate the motion fields between adjacent frames. Then, the dynamic reconstruction is further refined through motion compensation with the estimated motion fields in MC-JPDAL. We have used the codes provided by the authors: GW-CS, https://www.lpi.tel.uva.es/node/609; MC-JPDAL, https://github.com/ning22/Motion-Compensated-Dynamic-MRI-Reconstruction-with-Local-Affine-Optical-Flow-Estimation. The relevant reconstruction parameters are optimized for our dataset.

For the learning-based methods, the motion-estimation groupwise registration network is removed from the joint learning approach to understand its benefits. This thus results in a classic unrolled deep learning reconstruction framework which alternates between network-based dealiasing and data consistency enforcement (23), which is termed as CNN-DC in this work. Furthermore, we hypothesize that the groupwise registration should perform better than pairwise registration in registering a group of dynamic images. To validate this point, we replace the groupwise registration network with a pairwise registration network where the dynamic images are registered to a selected frame instead of the learned implicit template. For the considered cardiac cine MRI, the diastolic phase which is the first frame in the dynamic sequence is selected as the registration reference. The pairwise registration-based motion estimating dynamic reconstruction framework is called PRDRN in this work. Other components are kept the same for GRDRN and PRDRN except for the registration scheme. The CNN-DC and PRDRN are trained with the same data and training settings to GRDRN for fair comparison.

2.4.4. Evaluations

We analyze the reconstruction performance quantitatively by calculating the peak signal-to-noise ratio (PSNR) and the image structure similarity (SSIM) (40) between the ground truth images and the reconstructed images with each reconstruction method.

We evaluate the motion estimation performance for the pairwise and groupwise registration adopted in the deep learning dynamic reconstruction task, PRDRN and GRDRN. The motion estimation error cannot be calculated directly as motion ground truth is not available. We propose to evaluate the registration performance by evaluating the similarity between the generated dynamic images with estimated motion fields and the original dynamic ones. All learning-based registration methods in this work are able to produce invertible motion fields, where backward motion fields point from the dynamic images to the reference image, and forward motion fields point from the reference image to the dynamic images. For GRDRN, we use the estimated forward motion fields to warp the fully sampled dynamic images to obtain the implicit template, and then warp the template image with the backward motion fields to generate a new set of dynamic images. For PRDRN, we warp the designated reference image with the backward motion for the motion augmented dynamic images. We then calculate PSNR and SSIM between the generated dynamic images and the original fully sampled dynamic images with the assumption that better registration performance should result in higher PSNR and SSIM metrics.

3. RESULTS

3.1. Dynamic Reconstruction

We have a total of 128 slices from 18 testing subjects to evaluate the reconstruction and motion estimation performance. **Figure 3** shows the example reconstructions of GW-CS, MC-JPDAL, CNN-DC, PRDRN and the proposed GRDRN as well as the fully sampled and zero-filled reconstructed images for 12× acceleration, where five representative frames (frame 1, 6, 11, 16, and 21 ranging from systole to end-diastole) are demonstrated. The error map of frame 21 for each reconstruction method is shown in the last column to better visualize the reconstruction difference. Comparing between the reconstruction methods with ME/MC, over-smoothness and/or residual undersampling artifacts can be observed in MC-JPDAL and GW-CS reconstructions for this high acceleration factor, while the learning-based PRDRN and GRDRN performs better in removing artifacts and preserving image details. Quantitatively, the groupwise registration-based reconstruction approach GW-CS and GRDRN results in higher PSNR than the pairwise registration-based reconstruction method MC-JPDAL and PRDRN, respectively (GW-CS vs. MC-JPDAL: 36.89 vs. 31.46; GRDRN vs. PRDRN: 37.10 vs. 36.86), suggesting that groupwise registration works better than pairwise registration in improving the reconstruction quality. Comparing between the learning-based methods, more obvious residual undersampling artifacts can be observed in the CNN-DC reconstruction than PRDRN and GRDRN, indicating that incorporating motion estimation benefits reconstruction.

Figure 4 shows the representative cardiac cine images and temporal profiles reconstructed with the five reconstruction approaches for 8×, 12×, and 16× acceleration factors. The image quality of PRDRN and GRDRN degrades less than other reconstruction methods with the increasing of acceleration factors. The proposed GRDRN results in the best visual image quality for all acceleration factors among all the compared methods.

The PSNR and SSIM of all the five reconstruction methods for 8×, 12× and 16× accelerated cardiac cine MRI are shown in the box plots in **Figure 5**. The quantitative metrics agree with the visual assessment that the proposed GRDRN consistently performed the best among the testing methods. Notably, the PSNR and SSIM of GRDRN and PRDRN at 16× are similar to those of other reconstruction methods at 12×. We then emphasize the strength of the deep learning-based motion-estimating dynamic reconstruction approaches of producing good reconstruction quality even with high acceleration factors. The average computation times per slice of different reconstruction methods are: GRDRN 2.44s; PRDRN 2.38s; CNN-DC 0.29s; GW-CS 506.11s; and MC-JPDAL 298.59s. It can be seen that deep learning-based methods operate much

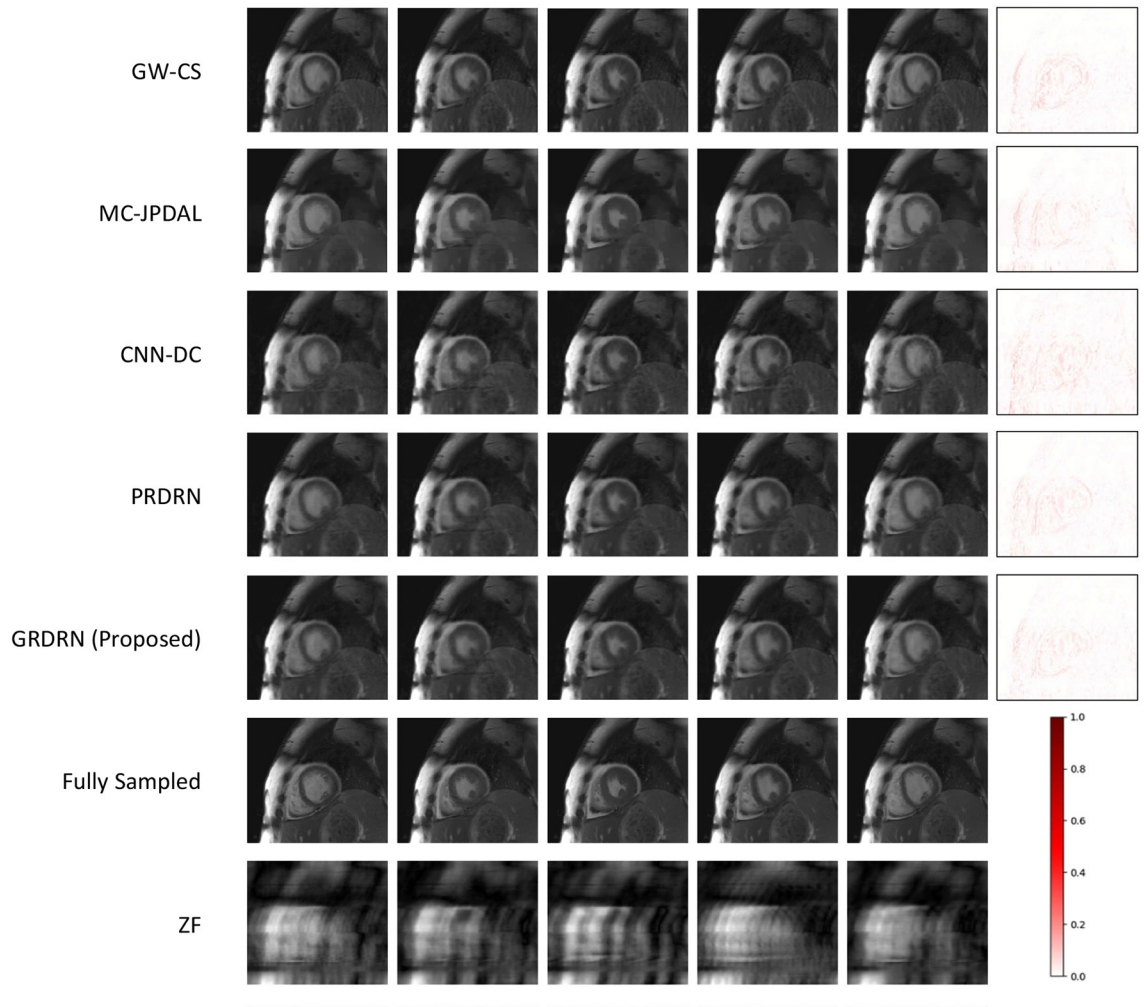

FIGURE 3 | Visualization of reconstructed images as well as the fully sampled and zero-filling (ZF) reconstructed images for five representative frames (systolic to end-diastolic) in the case of acceleration rate 12×. The last column shows the difference maps between the reconstructed and ground-truth images for the frame in the fifth column. The color bar represents the magnitude of the error in the difference maps.

faster than the traditional methods. Among the deep learning-based methods, CNN-DC is the fastest as it does not have the ME component, while the reconstruction times of GRDRN and PRDRN are similar.

3.2. Motion Estimation

Following the scheme described in the section of Evaluations, we evaluate the registration performance by assessing the dynamic images generated using the invertible motion fields. Animated images showing motion fields for a whole dynamic sequence with 8×, 12× and 16× accelerations are provided in **Supplementary Figure S1**. It is noted that the learned motion is smooth and reasonable, and is mostly in the cardiac region. **Figure 6** illustrates two frames (one diastolic and one systolic frame) of the generated cardiac cine images with motion fields estimated with PRDRN and GRDRN models trained in 12× accelerated cardiac cine MRI. By visualizing the error maps, GRDRN achieves similar registration accuracy for both diastolic and systolic frames, while the error level of the systolic frame is obviously higher than the diastolic frame for PRDRN which uses the end-diastolic frame as the registration reference. Overall, the groupwise registration-based GRDRN has better registration than the pairwise registration-based PRDRN regarding PSNR (41.46 vs. 37.90) and SSIM (0.985 vs. 0.972) in this subject. **Figure 7** provides the PSNR and SSIM of the generated cine images for 8×, 12×, and 16× acceleration factors. The higher PSNR of SSIM of GRDRN than PRDRN indicates the groupwise registration gives better motion estimation than pairwise registration, leading to better reconstruction of GRDRN as demonstrated in the previous section.

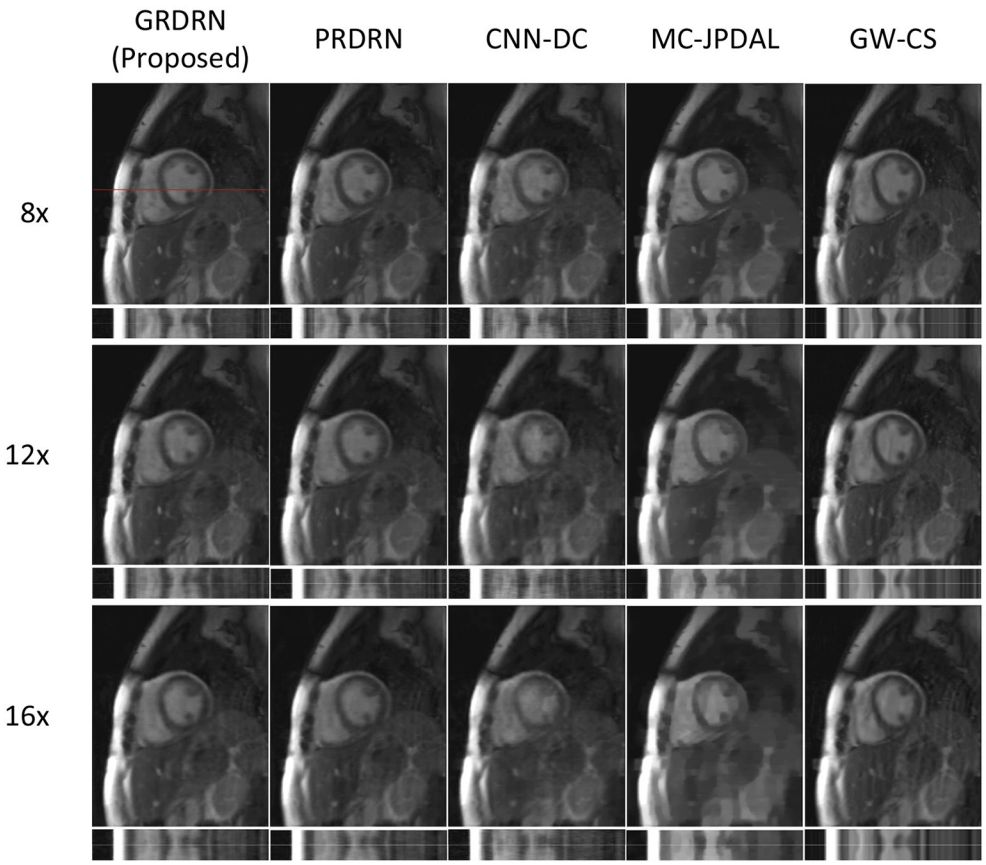

FIGURE 4 | Visual comparison of reconstructions with different reconstruction approaches for 8×, 12×, and 16× acceleration rates. The temporal profile at the location indicated by the red line is shown for each reconstruction.

4. DISCUSSION

We propose an end-to-end trainable joint learning approach which performs groupwise registration-based motion estimation and dynamic reconstruction, denoted as GRDRN. We construct an unrolled network architecture where the registration and reconstruction are optimized alternatively, and the two tasks are beneficial to each other as accurate motion estimation contributes to improving the reconstructed image quality and good image quality in turn helps to improve the motion estimation accuracy. We evaluate GRDRN in breath-hold cardiac cine MRI for aggressive undersampling rates of 8×, 12× and 16×, aiming to reduce the number of breath-holds substantially and ultimately to achieve whole-heart cine MRI in a single breath-hold. The proposed method consistently achieves improved reconstruction performance compared with deep learning dynamic reconstruction with pairwise registration PRDRN or without exploiting motion information CNN-DC, and the conventional state-of-the-art dynamic MRI reconstruction methods with ME/MC, confirming the superiority of GRDRN.

A common strategy for registration is to register a moving image to a reference image. When there are multiple images to be registered, another strategy that can be beneficial is to register multiple images to a common space instead of in pairs, the process of which is termed as groupwise registration. There are in general three different types of groupwise registration: sum-of-pairs approach that attempts to reduce the registration loss among all image pairs; reference-based approach that requires the designation of one image as reference; implicit template approach that implicitly determines the template image during registration, and can avoid the bias caused by selecting one particular image as reference while being more computationally efficient than the sum-of-pairs method (41). Deep learning groupwise registration has been adopted in several recent studies (36, 37, 42) and has demonstrated superior performance over pairwise registration. For example, Zhang et al. propose an one-shot learning groupwise registration network to register respiratory motion-resolved 3D CT images (36). Martín-González et al. (42) develop a deep learning framework to achieve groupwise registration of 2D dynamic sequence, in which the implicit template deep learning groupwise registration approach is adopted to estimate the nonrigid motion across the dynamic sequence.

The motion estimation performance is evaluated by employing the estimated invertible motion fields to generate a new sequence of cine images to be compared with the original

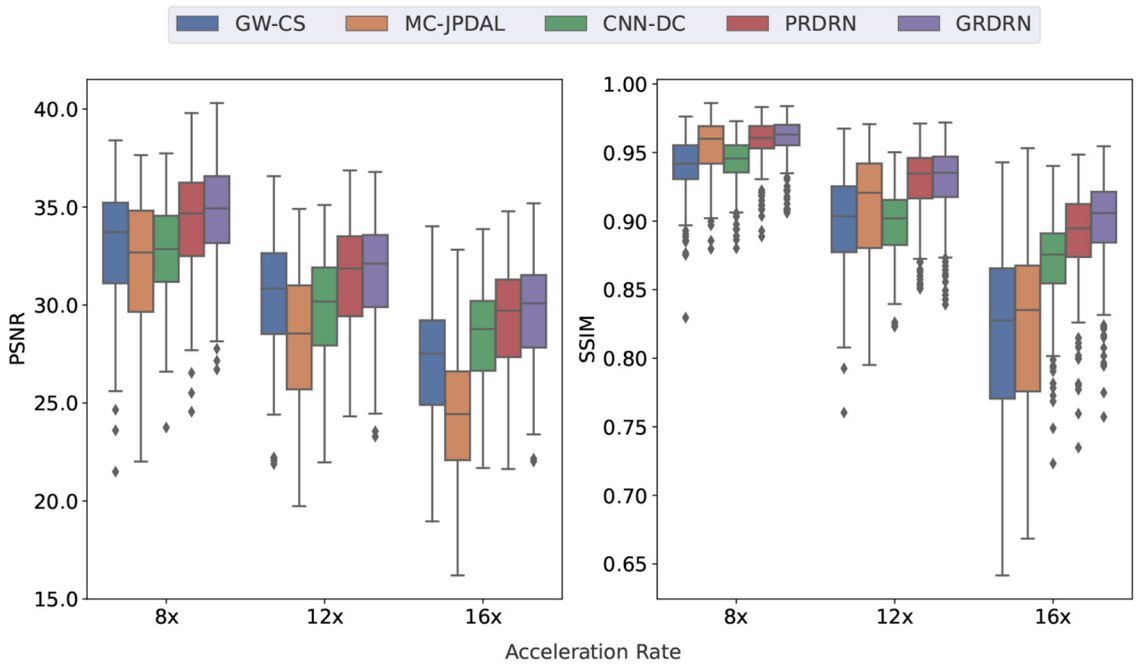

FIGURE 5 | Box plots of PSNR and SSIM values of the reconstructed dynamic images with different reconstruction methods for 8×, 12×, and 16× acceleration rates. Boxes depict the 25 and 75% percentile, horizontal line shows the median, whiskers show the standard deviation and dots represent the outliers.

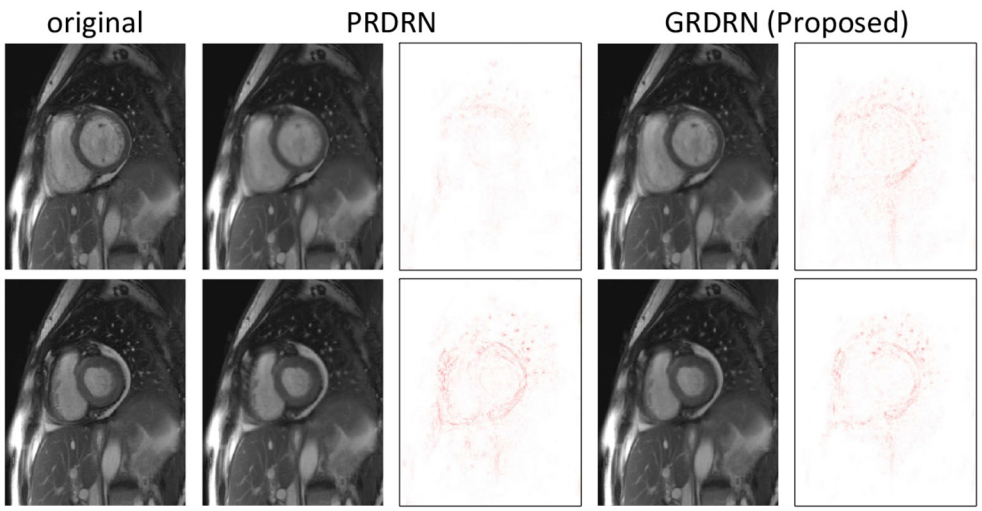

FIGURE 6 | Visualization of generated dynamic images with motion fields estimated with PRDRN (pairwise registration) and proposed GRDRN (groupwise registration) models trained in 12× accelerated data. Two representative frames at diastole and systole are shown with the corresponding error maps.

dynamic images. The joint motion estimation and reconstruction model achieves similarly good quantitative metrics for a range of acceleration factors, indicating that the motion estimation in GRDRN is robust to undersampling artifacts. Moreover, the results indicate that groupwise registration performs better than pairwise registration in registering a set of dynamic images by finding a template image that lies in the geometric center of the group. Besides aiding in improving the reconstruction performance, cardiac motion estimation is an important step in myocardial strain analysis. The applicability of the estimated motion with the proposed joint learning approach to myocardial strain analysis will be investigated in the future work.

In GRDRN, motion-augmented dynamic images are generated based on both the intermediately reconstructed and

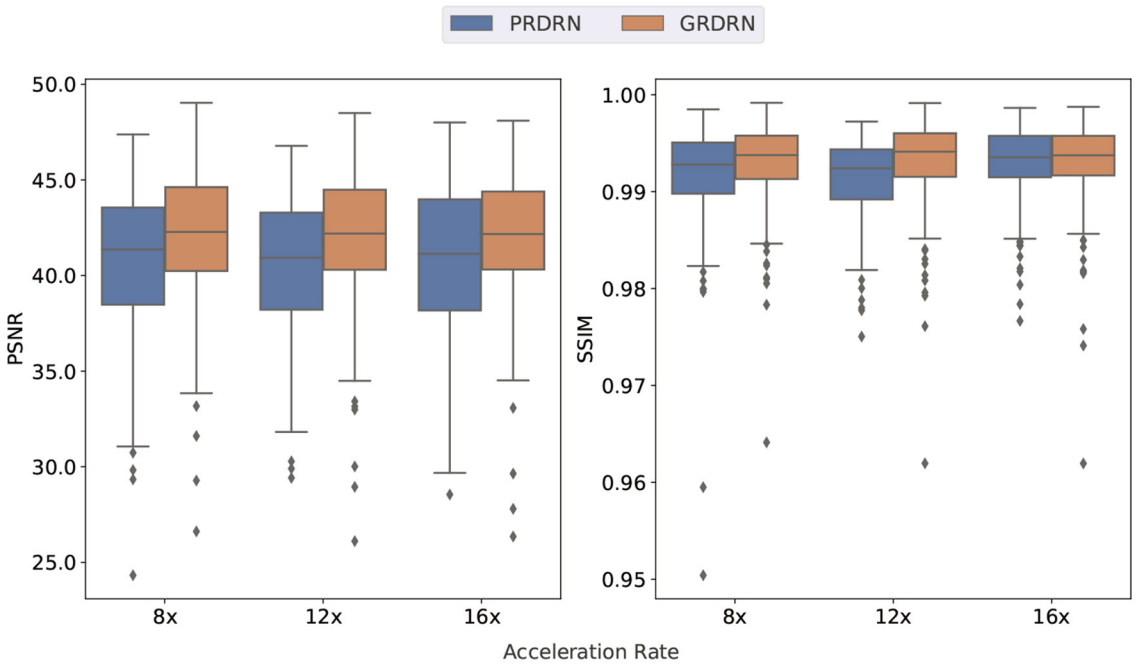

FIGURE 7 | Box plots of PSNR and SSIM for the registration task with pairwise (PRDRN) and groupwise (GRDRN) registrations, where the metrics are reported between generated dynamic image sequences and the original ones.

the zero-filling reconstructed images as additional inputs to the reconstruction network. In our initial experiments, we have tried to use motion-augmented dynamic images generated from the intermediate reconstruction only, which leads to a decrease of the reconstruction PSNR of 1-2dB compared to reconstruction with both sets of motion-augments images. The possible reason could be that the undersampling artifacts are gradually removed in the unrolled iterations. However, the images of intermediate reconstructions tend to get smooth and may lose some fine details. On the other hand, the zero-filling motion-augmented images though being more undersampled, may contain more image details than the motion-augmented images generated from the intermediate reconstructions. Consequently, adding the zero-filling motion-augmented images will allow the reconstruction network to exploit such details at all stages of the cascade, and can ultimately improve the reconstruction performance. It is noted that similar strategy has been employed in a previous study (31) that adopts pairwise registration to augment the reconstruction.

The appearance of the heart and the motion pattern may be heterogeneous in the short-axis cardiac cine MR images from the base to the apex of the heart, which may lead to heterogeneous reconstruction performance for the basal, middle and apical slices. We then analyze the 128 testing slices thoroughly and find that reconstruction and motion estimation metrics of apical slices are similar to those of middle slices. However, for some basal slices where the myocardium is not intact we do observe the performance drop for all the reconstruction methods, indicating the basal slices are more challenging to be reconstructed. Specifically, there is a total of 17 basal slices, and the reconstruction PSNR of 8× accelerated cine MRI of the basal slices is 32.46 ± 3.46, 31.84 ± 3.24, 30.89 ± 2.94, 30.81 ± 3.34, and 30.06 ± 4.08 for the methods of GRDRN, PRDRN, CNN-DC, GW-CS and MC-JPDAL respectively, compared with PSNR of 34.82 ± 2.73, 34.19 ± 2.94, 32.90 ± 2.44, 33.30 ± 3.00, and 32.34 ± 3.29 of non-basal slices. We can see that the proposed GRDRN still outperforms other testing methods in the challenging basal slices.

The single-coil acquisition scenario is simulated in this work to reduce computation complexity and memory consumption, while the proposed GRDRN can be extended to multi-coil reconstruction by adapting the data consistency layer. It is noted that the applicability of the proposed method needs to be further tested in prospectively undersampled data.

In conclusion, we propose an end-to-end trainable joint learning approach which performs groupwise registration-based motion estimation and dynamic reconstruction. The groupwise registration network GRN, predicts invertible motion fields between all dynamics and an implicit template. Taking advantage of the estimated motion, all measurements along the temporal dimension are fused to the implicit template, from which a new sequence of dynamic images with lower undersampling can be generated to assist in the reconstruction. We evaluate the proposed approach on cardiac cine MRI datasets for aggressive acceleration factors and demonstrate that the proposed GRDRN can achieve state-of-the-art reconstruction

performance benefiting from the motion information from the groupwise registration.

DATA AVAILABILITY STATEMENT

The original contributions presented in the study are included in the article/**Supplementary Materials**, further inquiries can be directed to the corresponding author/s.

AUTHOR CONTRIBUTIONS

The manuscript was written by HQ and revised by JY, TK, PH, and PL. The study was designed by JY and HQ. The experiments were performed by JY. Research funds were offered by HQ. All authors contributed to the article and approved the submitted version.

FUNDING

This work was supported in part by the National Natural Science Foundation of China under Grant No. 82102027.

ACKNOWLEDGMENTS

We greatly appreciate and acknowledge the facilities and support provided by the University of Cambridge and ShanghaiTech University.

SUPPLEMENTARY MATERIAL

The Supplementary Material for this article can be found online at: https://www.frontiersin.org/articles/10.3389/fcvm.2022.880186/full#supplementary-material

Supplementary Figure S1 | Animated visualization of generated motion fields estimated by PRDRN and GRDRN for a whole dynamic sequence with 8x, 12x and 16x accelerations.

REFERENCES

1. Pruessmann KP, Weiger M, Scheidegger MB, Boesiger P. SENSE: sensitivity encoding for fast MRI. *Magn Reson Med*. (1999) 42:952–62. doi: 10.1002/(SICI)1522-2594(199911)42:5<952::AID-MRM16>3.0.CO;2-S
2. Griswold MA, Jakob PM, Heidemann RM, Nittka M, Jellus V, Wang J, et al. Generalized autocalibrating partially parallel acquisitions (GRAPPA). *Magn Reson Med*. (2002) 47:1202–10. doi: 10.1002/mrm.10171
3. Lustig M, Donoho D, Pauly JM. Sparse MRI: the application of compressed sensing for rapid MR imaging. *Magn Reson Med*. (2007) 58:1182–95. doi: 10.1002/mrm.21391
4. Jung H, Sung K, Nayak KS, Kim EY, Ye JC. k-t FOCUSS: a general compressed sensing framework for high resolution dynamic MRI. *Magn Reson Med*. (2009) 61:103–16. doi: 10.1002/mrm.21757
5. Knoll F, Clason C, Bredies K, Uecker M, Stollberger R. Parallel imaging with nonlinear reconstruction using variational penalties. *Magn Reson Med*. (2012) 67:34–41. doi: 10.1002/mrm.22964
6. Feng L, Axel L, Chandarana H, Block KT, Sodickson DK, Otazo R. XD-GRASP: golden-angle radial MRI with reconstruction of extra motion-state dimensions using compressed sensing. *Magn Reson Med*. (2016) 75:775–88. doi: 10.1002/mrm.25665
7. Miao X, Lingala SG, Guo Y, Jao T, Usman M, Prieto C, et al. Accelerated cardiac cine MRI using locally low rank and finite difference constraints. *Magn Reson Imaging*. (2016) 34:707–14. doi: 10.1016/j.mri.2016.03.007
8. Lingala SG, Hu Y, DiBella E, Jacob M. Accelerated dynamic MRI exploiting sparsity and low-rank structure: kt SLR. *IEEE Trans Med Imaging*. (2011) 30:1042–54. doi: 10.1109/TMI.2010.2100850
9. Otazo R, Candes E, Sodickson DK. Low-rank plus sparse matrix decomposition for accelerated dynamic MRI with separation of background and dynamic components. *Magn Reson Med*. (2015) 73:1125–36. doi: 10.1002/mrm.25240
10. Trémoulhéac B, Dikaios N, Atkinson D, Arridge SR. Dynamic MR image reconstruction-separation from undersampled (k, t)-space via low-rank plus sparse prior. *IEEE Trans Med Imaging*. (2014) 33:1689–701. doi: 10.1109/TMI.2014.2321190
11. Prieto C, Batchelor PG, Hill D, Hajnal JV, Guarini M, Irarrazaval P. Reconstruction of undersampled dynamic images by modeling the motion of object elements. *Magn Reson Med*. (2007) 57:939–49. doi: 10.1002/mrm.21222
12. Jung H, Ye JC. Motion estimated and compensated compressed sensing dynamic magnetic resonance imaging: what we can learn from video compression techniques. *Int J Imaging Syst Technol*. (2010) 20:81–98. doi: 10.1002/ima.20231
13. Asif MS, Hamilton L, Brummer M, Romberg J. Motion-adaptive spatio-temporal regularization for accelerated dynamic MRI. *Magn Reson Med*. (2013) 70:800–812. doi: 10.1002/mrm.24524
14. Usman M, Atkinson D, Odille F, Kolbitsch C, Vaillant G, Schaeffter T, et al. Motion corrected compressed sensing for free-breathing dynamic cardiac MRI. *Magn Reson Med*. (2013) 70:504–16. doi: 10.1002/mrm.24463
15. Lingala SG, DiBella E, Jacob M. Deformation corrected compressed sensing (DC-CS): a novel framework for accelerated dynamic MRI. *IEEE Trans Med Imaging*. (2014) 34:72–85. doi: 10.1109/TMI.2014.2343953
16. Royuela-del Val J, Cordero-Grande L, Simmross-Wattenberg F, Martín-Fernández M, Alberola-López C. Nonrigid groupwise registration for motion estimation and compensation in compressed sensing reconstruction of breath-hold cardiac cine MRI. *Magn Reson Med*. (2016) 75:1525–36. doi: 10.1002/mrm.25733
17. Rank CM, Heußer T, Buzan MT, Wetscherek A, Freitag MT, Dinkel J, et al. 4D respiratory motion-compensated image reconstruction of free-breathing radial MR data with very high undersampling. *Magn Reson Med*. (2017) 77:1170–83. doi: 10.1002/mrm.26206
18. Tolouee A, Alirezaie J, Babyn P. Nonrigid motion compensation in compressed sensing reconstruction of cardiac cine MRI. *Magn Reson Imaging*. (2018) 46:114–20. doi: 10.1016/j.mri.2017.11.004
19. Zhao N, O'Connor D, Basarab A, Ruan D, Sheng K. Motion compensated dynamic MRI reconstruction with local affine optical flow estimation. *IEEE Trans Biomed Eng*. (2019) 66:3050–9. doi: 10.1109/TBME.2019.2900037
20. Aviles-Rivero AI, Debroux N, Williams G, Graves MJ, Schönlieb CB. Compressed sensing plus motion (CS+ M): a new perspective for improving undersampled MR image reconstruction. *Med Image Anal*. (2021) 68:101933. doi: 10.1016/j.media.2020.101933
21. Odille F, Vuissoz PA, Marie PY, Felblinger J. Generalized reconstruction by inversion of coupled systems (GRICS) applied to free-breathing MRI. *Magn Reson Med*. (2008) 60:146–57. doi: 10.1002/mrm.21623
22. Liang D, Cheng J, Ke Z, Ying L. Deep magnetic resonance image reconstruction: inverse problems meet neural networks. *IEEE Signal Process Mag*. (2020) 37:141–51. doi: 10.1109/MSP.2019.2950557
23. Schlemper J, Caballero J, Hajnal JV, Price AN, Rueckert D. A deep cascade of convolutional neural networks for dynamic MR image reconstruction. *IEEE Trans Med Imaging*. (2017) 37:491–503. doi: 10.1109/TMI.2017.2760978
24. Qin C, Schlemper J, Caballero J, Price AN, Hajnal JV, Rueckert D. Convolutional recurrent neural networks for dynamic MR image reconstruction. *IEEE Trans Med Imaging*. (2018) 38:280–90. doi: 10.1109/TMI.2018.2863670

25. Küstner T, Fuin N, Hammernik K, Bustin A, Qi H, Hajhosseiny R, et al. CINENet: deep learning-based 3D cardiac CINE MRI reconstruction with multi-coil complex-valued 4D spatio-temporal convolutions. *Sci Rep*. (2020) 10:1–13. doi: 10.1038/s41598-020-70551-8
26. Sandino CM, Lai P, Vasanawala SS, Cheng JY. Accelerating cardiac cine MRI using a deep learning-based ESPIRiT reconstruction. *Magn Reson Med*. (2021) 85:152–67. doi: 10.1002/mrm.28420
27. Qin C, Duan J, Hammernik K, Schlemper J, Küstner T, Botnar R, et al. Complementary time-frequency domain networks for dynamic parallel MR image reconstruction. *Magn Reson Med*. (2021) 86:3274–91. doi: 10.1002/mrm.28917
28. Qin C, Schlemper J, Duan J, Seegoolam G, Price A, Hajnal J, et al. k-t NEXT: dynamic MR image reconstruction exploiting spatio-temporal correlations. In: *International Conference on Medical Image Computing and Computer-Assisted Intervention*. Shenzhen: Springer (2019). p. 505–13. doi: 10.1007/978-3-030-32245-8_56
29. Qi H, Fuin N, Cruz G, Pan J, Kuestner T, Bustin A, et al. Non-rigid respiratory motion estimation of whole-heart coronary MR images using unsupervised deep learning. *IEEE Trans Med Imaging*. (2020) 40:444–54. doi: 10.1109/TMI.2020.3029205
30. Huang Q, Xian Y, Yang D, Qu H, Yi J, Wu P, et al. Dynamic MRI reconstruction with end-to-end motion-guided network. *Med Image Anal*. (2021) 68:101901. doi: 10.1016/j.media.2020.101901
31. Seegoolam G, Schlemper J, Qin C, Price A, Hajnal J, Rueckert D. Exploiting motion for deep learning reconstruction of extremely-undersampled dynamic MRI. In: *International Conference on Medical Image Computing and Computer-Assisted Intervention*. Shenzhen: Springer (2019). p. 704–12. doi: 10.1007/978-3-030-32251-9_77
32. Qi H, Hajhosseiny R, Cruz G, Kuestner T, Kunze K, Neji R, et al. End-to-end deep learning nonrigid motion-corrected reconstruction for highly accelerated free-breathing coronary MRA. *Magn Reson Med*. (2021) 86:1983–96. doi: 10.1002/mrm.28851
33. Qin C, Bai W, Schlemper J, Petersen SE, Piechnik SK, Neubauer S, et al. Joint motion estimation and segmentation from undersampled cardiac MR image. In: *International Workshop on Machine Learning for Medical Image Reconstruction*. Granada: Springer (2018). p. 55–63.
34. Ashburner J. A fast diffeomorphic image registration algorithm. *Neuroimage*. (2007) 38:95–13. doi: 10.1016/j.neuroimage.2007.07.007
35. Dalca AV, Balakrishnan G, Guttag J, Sabuncu MR. Unsupervised learning of probabilistic diffeomorphic registration for images and surfaces. *Med Image Anal*. (2019) 57:226–36. doi: 10.1016/j.media.2019.07.006
36. Zhang Y, Wu X, Gach HM, Li H, Yang D. GroupRegNet: a groupwise one-shot deep learning-based 4D image registration method. *Phys Med Biol*. (2021) 66:045030. doi: 10.1088/1361-6560/abd956
37. Li B, Niessen WJ, Klein S, Ikram MA, Vernooij MW, Bron EE. Learning unbiased group-wise registration (LUGR) and joint segmentation: evaluation on longitudinal diffusion MRI. In: *Medical Imaging 2021: Image Processing. vol. 11596. International Society for Optics Photonics*. (2021). p. 115960L. doi: 10.1117/12.2580928
38. Aggarwal HK, Mani MP, Jacob M. MoDL: model-based deep learning architecture for inverse problems. *IEEE Trans Med Imaging*. (2018) 38:394–405. doi: 10.1109/TMI.2018.2865356
39. Ronneberger O, Fischer P, Brox T. U-net: Convolutional networks for biomedical image segmentation. In: *International Conference on Medical Image Computing and Computer-Assisted Intervention*. Munich: Springer (2015). p. 234–41.
40. Wang Z, Bovik AC, Sheikh HR, Simoncelli EP. Image quality assessment: from error visibility to structural similarity. *IEEE Trans Image Process*. (2004) 13:600–12. doi: 10.1109/TIP.2003.819861
41. Wu G, Wang Q, Lian J, Shen D. Estimating the 4D respiratory lung motion by spatiotemporal registration and super-resolution image reconstruction. *Med Phys*. (2013) 40:031710. doi: 10.1118/1.4790689
42. Martín-González E, Sevilla T, Revilla-Orodea A, Casaseca-de-la Higuera P, Alberola-López C. Groupwise non-rigid registration with deep learning: an affordable solution applied to 2D cardiac cine MRI reconstruction. *Entropy*. (2020) 22:687. doi: 10.3390/e22060687

Conflict of Interest: The authors declare that the research was conducted in the absence of any commercial or financial relationships that could be construed as a potential conflict of interest.

Publisher's Note: All claims expressed in this article are solely those of the authors and do not necessarily represent those of their affiliated organizations, or those of the publisher, the editors and the reviewers. Any product that may be evaluated in this article, or claim that may be made by its manufacturer, is not guaranteed or endorsed by the publisher.

frontiers | Frontiers in Cardiovascular Medicine

ORIGINAL RESEARCH
published: 05 July 2022
doi: 10.3389/fcvm.2022.901902

CT-Based Analysis of Left Ventricular Hemodynamics Using Statistical Shape Modeling and Computational Fluid Dynamics

Leonid Goubergrits[1,2†], Katharina Vellguth[1†], Lukas Obermeier[1], Adriano Schlief[1], Lennart Tautz[3], Jan Bruening[1], Hans Lamecker[4], Angelika Szengel[4], Olena Nemchyna[5], Christoph Knosalla[5,6,7], Titus Kuehne[1,6] and Natalia Solowjowa[5]*

[1] Institute of Computer-Assisted Cardiovascular Medicine, Charité-Universitätsmedizin Berlin, Berlin, Germany, [2] Einstein Center Digital Future, Berlin, Germany, [3] Fraunhofer Institute for Digital Medicine MEVIS, Bremen, Germany, [4] 1000shapes, Berlin, Germany, [5] Department of Cardiothoracic and Vascular Surgery, German Heart Center Berlin, Berlin, Germany, [6] German Centre for Cardiovascular Research (DZHK), Partner Site Berlin, Berlin, Germany, [7] Charité-Universitätsmedizin Berlin, Corporate Member of Freie Universität Berlin, Humboldt-Universität zu Berlin and Berlin Institute of Health, Berlin, Germany

OPEN ACCESS

Edited by:
Sabina Gallina,
University of Studies G. d'Annunzio Chieti and Pescara, Italy

Reviewed by:
Rajiv Rampat,
William Harvey Hospital, United Kingdom
Elias Karabelas,
University of Graz, Austria

***Correspondence:**
Natalia Solowjowa
solowjowa@dhzb.de

[†] These authors share first authorship

Specialty section:
This article was submitted to Cardiovascular Medicine, a section of the journal Frontiers in Cardiovascular Medicine

Received: 22 March 2022
Accepted: 07 June 2022
Published: 05 July 2022

Citation:
Goubergrits L, Vellguth K, Obermeier L, Schlief A, Tautz L, Bruening J, Lamecker H, Szengel A, Nemchyna O, Knosalla C, Kuehne T and Solowjowa N (2022) CT-Based Analysis of Left Ventricular Hemodynamics Using Statistical Shape Modeling and Computational Fluid Dynamics. Front. Cardiovasc. Med. 9:901902. doi: 10.3389/fcvm.2022.901902

Background: Cardiac computed tomography (CCT) based computational fluid dynamics (CFD) allows to assess intracardiac flow features, which are hypothesized as an early predictor for heart diseases and may support treatment decisions. However, the understanding of intracardiac flow is challenging due to high variability in heart shapes and contractility. Using statistical shape modeling (SSM) in combination with CFD facilitates an intracardiac flow analysis. The aim of this study is to prove the usability of a new approach to describe various cohorts.

Materials and Methods: CCT data of 125 patients (mean age: 60.6 ± 10.0 years, 16.8% woman) were used to generate SSMs representing aneurysmatic and non-aneurysmatic left ventricles (LVs). Using SSMs, seven group-averaged LV shapes and contraction fields were generated: four representing patients with and without aneurysms and with mild or severe mitral regurgitation (MR), and three distinguishing aneurysmatic patients with true, intermediate aneurysms, and globally hypokinetic LVs. End-diastolic LV volumes of the groups varied between 258 and 347 ml, whereas ejection fractions varied between 21 and 26%. MR degrees varied from 1.0 to 2.5. Prescribed motion CFD was used to simulate intracardiac flow, which was analyzed regarding large-scale flow features, kinetic energy, washout, and pressure gradients.

Results: SSMs of aneurysmatic and non-aneurysmatic LVs were generated. Differences in shapes and contractility were found in the first three shape modes. Ninety percent of the cumulative shape variance is described with approximately 30 modes. A comparison of hemodynamics between all groups found shape-, contractility- and MR-dependent differences. Disturbed blood washout in the apex region was found in the aneurysmatic cases. With increasing MR, the diastolic jet becomes less coherent, whereas energy dissipation increases by decreasing kinetic energy.

The poorest blood washout was found for the globally hypokinetic group, whereas the weakest blood washout in the apex region was found for the true aneurysm group.

Conclusion: The proposed CCT-based analysis of hemodynamics combining CFD with SSM seems promising to facilitate the analysis of intracardiac flow, thus increasing the value of CCT for diagnostic and treatment decisions. With further enhancement of the computational approach, the methodology has the potential to be embedded in clinical routine workflows and support clinicians.

Keywords: cardiac computed tomography, intraventricular hemodynamics, statistical shape modeling, fluid-structure interaction, computational fluid dynamics, left ventricle aneurysms, mitral regurgitation

1. INTRODUCTION

Disorders of intraventricular hemodynamics are proposed to serve as an early biomarker for diagnosis of heart diseases, as they are associated with progressive remodeling of the left ventricle (LV) toward heart failure (1). A broad range of parameters has been proposed to quantitatively as well as qualitatively analyze *in vivo* blood flow by means of visualization techniques for various imaging techniques (2). Echocardiography is clinically the most used imaging modality and has been employed for the investigation of a wide spectrum of cardiac pathologies (3, 4), guidance of interventional procedures (5) or assessing the success of treatments (6, 7). However, echocardiography depends on an exact geometric alignment and is highly dependent on the operator. 4D flow magnetic resonance imaging (MRI) provides a higher spatial resolution with time-averaged assessment of intracardiac flow. Intraventricular kinetic energy has therewith been investigated (8) and large-scale flow patterns as well as vortex behavior have been topic of research (6, 9, 10). Downsides of 4D flow MRI are long acquisition times and limitations with implantable devices. Cardiac computed tomography (CCT) has the highest spatial resolution (11) but does not allow to capture intracardiac flow quantities.

Despite progressive developments in imaging modalities in recent years, a profound intraventricular blood flow analysis has not yet translated into clinical workflows. One major reason is the insufficient spatial and temporal resolution of echocardiography and MRI combined with intolerably long acquisition times of detailed 4D flow imaging. Another crucial factor impeding this translation from research to clinic is, that as for today, no consensus has been found regarding hemodynamic parameters or features distinguishing normal from pathological cases. Since pathological cases appear with a huge variety of changes in anatomy and heart function, it is challenging to compare inter-individual differences on the one hand, and on the other hand to identify characteristics by which patients can be sorted in groups to compare inter-group differences.

To overcome the first issue of limited resolution of imaging modalities, various research groups have proposed to use image-based computational fluid dynamics (CFD) to gain information about ventricular flow fields in combination with decreased patient scan times. Detailed reviews on different modeling approaches in cardiovascular medicine are provided by Quarteroni et al. (12), Doost et al. (13), and Hirschhorn et al. (14). Such image-based CFD frameworks can also be employed to investigate post-operative outcomes after virtual treatment (5, 15, 16). Furthermore, CFD can complement cardiac computed tomography (CCT) by functional analysis of patient-specific intraventricular hemodynamics via so-called CCT-based CFD (17). Despite being time-consuming and demanding high computational resources, CCT-based CFD may be an alternative to 4D flow MRI due to a higher possible spatial resolution and a reduction of scan times (18).

A combination of CFD simulations with a representation of clinical image data by means of statistical shape models (SSMs) can help to improve several aspects of image-based CFD models of the LV, as recently demonstrated by Khalafvand et al. (19). First, the integration and automation of medical image data and segmentations into the pre-processing workflow can be improved since it allows for description of complex shapes in a reduced manner. Further, SSMs can be used to analyze characteristics of different individuals or patient groups, e.g., using hierarchical cluster analysis (20) and may thus be a tool to find correlations between SSM shape parameters and biomechanical risk score (21), hemodynamic parameters (22, 23) or cardiac electromechanics (24). Eventually, SSMs are also used to generate synthetic cases in order to train machine learning algorithms (21, 25) or to investigate simulated blood flow in representative shapes of specific groups of patients (26–28).

In this work, we complement our previously introduced workflow for the comprehensive Fluid-Structure-Interaction CFD simulations of the LV of an entire heart cycle (29) by a SSM representation of LV geometry and motion. A cohort of 125 CCT examinations of heart failure patients after myocardial infarction, partly combined with mitral regurgitation (MR), is used for an extensive statistical shape analysis and clustering into seven subcohorts. For each subcohort, a mean shape representing the respective pathological state is derived from SSMs and used in the image-based CFD framework. Consequences of myocardial infarction (scar formation, disturbed contractility, and a dilation of LVs causing MR and an increase of the LV shape sphericity) are likely to alter the intracardiac flow. Our focus was therefore to investigate the intraventricular hemodynamics of the seven mean cases, each representing a different pathological state, and to reveal differences between the groups.

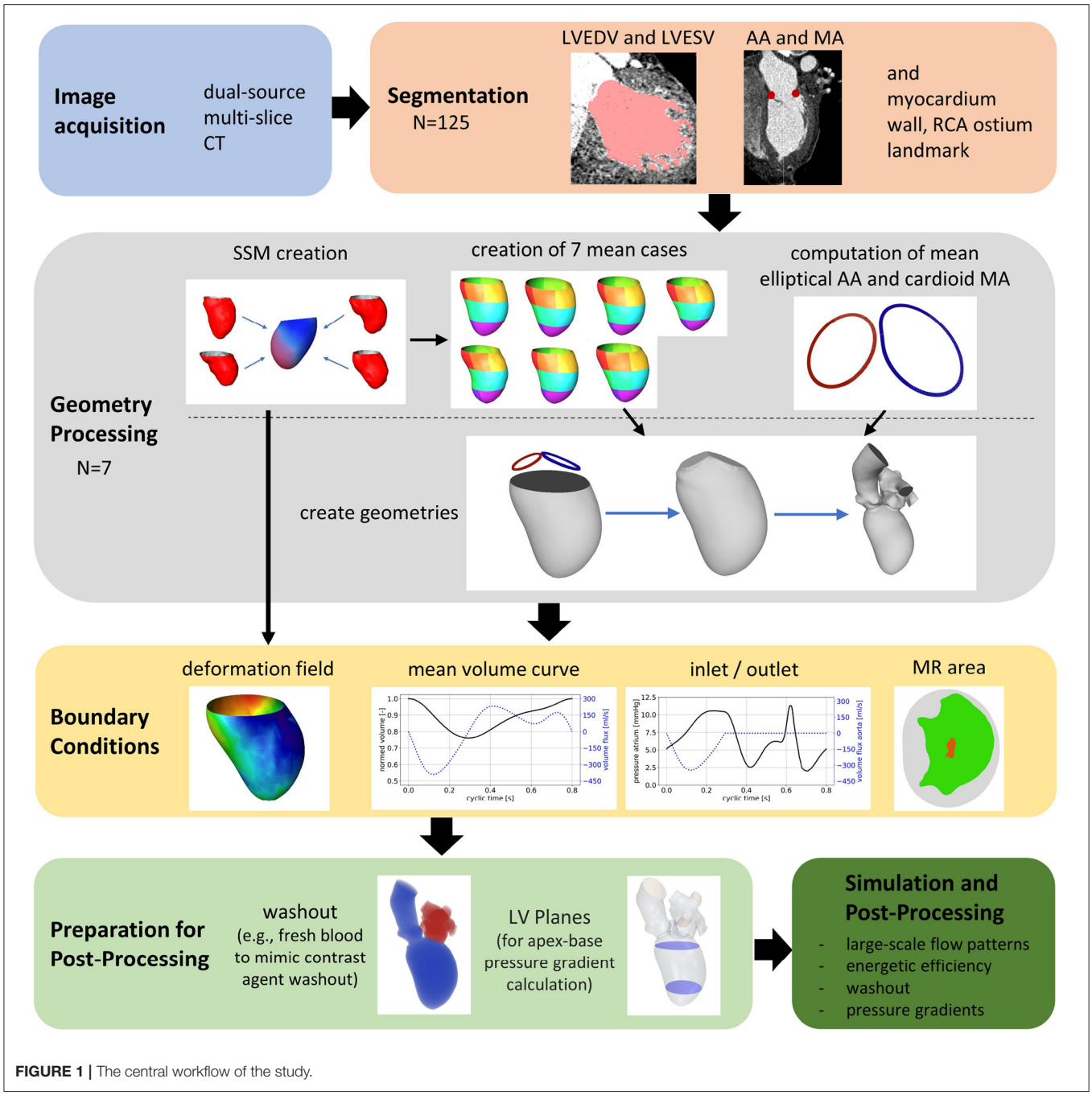

FIGURE 1 | The central workflow of the study.

2. MATERIALS AND METHODS

The general workflow of the numerical framework is displayed in **Figure 1**. Based on the acquired CCT images, left ventricular end-diastolic (LVEDV) and left ventricular end-systolic (LVESV) geometries as well as the end-diastolic myocardial wall, both annuli, and the ostium of the right coronary artery (RCA) are segmented. The data are used to create SSMs of the LV, including the ventricular contraction. Then, seven representative shapes of different groups of patients each representing a pathological state are generated using the SSMs. The generated cases are used as input of a recently developed computational framework for patient-specific simulations of the intraventricular flow. Finally, relevant hemodynamic parameters for the analysis of intracardiac flow are selected, calculated, and evaluated per case.

2.1. Study Cohort

Retrospective CCT data of heart failure patients after myocardial infarction (n=125, mean age of 60.6 ± 10.0 years, 16.8 %

TABLE 1 | Clinical and demographic data of the seven subcohorts.

Parameters	A0ML	A0MH	A1ML	A1MH	A1T	A1I	A1HK
Nr. of cases	40	32	35	18	10	22	16
Age (years)	60 ± 10.2	63 ± 9.2	59 ± 9.7	60 ± 11.2	59±12.0	60 ± 10.0	58 ± 10.7
Sex (m/f)	34/6	28/4	27/8	15/3	6/4	17/5	14/2
BSA (m^2)	1.99 ± 0.22	1.97 ± 0.16	1.91 ± 0.25	1.92 ± 0.20	1.91 ± 0.26	1.91 ± 0.22	1.89 ± 0.24
MR (grade)	1.0 [0.5]	2.5 [0.5]	1.0 [0.5]	2.25 [1.0]	1.0 [1.0]	1.0 [2.0]	1.25 [1.5]
NYHA class	III [0.5]	III [0.0]	III [0.0]	III [0.0]	III [0.0]	III [0.0]	III [0.25]
RV (ml)	7.8	29.8	8.1	25.8	11.9	15.8	10.3

Values are shown as median [interquartile range] for both cohorts if a parameter is not normally distributed. Otherwise, values are displayed as mean ± standard deviation. The Shapiro-Wilk test was used to test normality. The Dubois formula (31) was used to calculate the BSA. LV, left ventricle; BSA, body surface area; MR, mitral regurgitation; NYHA, New York Heart Association; RV, regurgitation volume.

women) collected in the German Heart Center Berlin were used in this study. The patients are grouped into subcohorts in two ways: first, all 125 patients were subdivided into four groups, separating into patients without and with anterior LV aneurysm. Each of these two groups was further subdivided into patients with low MR (MR grade $<$ II) and high MR (MR grade $\geq$ II). The different subcohorts are denominated via A (with 0 for non-aneurysmatic and 1 for aneurysmatic cases) and via M (with L indicating low MR grade $<$ II and H indicating high MR grade $\geq$ II), resulting in the four subcohorts: A0ML, A0MH, A1ML, and A1MH. As second grouping, all cases with LV aneurysm were further subdivided into the three groups denoted via A1 [T = true aneurysms; I = intermediate aneurysms; HK = globally hypokinetic, which is also referred to as ischemic cardiomyopathy (30)]: A1T, A1I, A1HK. The definition of three LV aneurysm types was done according to Di Donato et al. (30). Briefly, true aneurysm cases are characterized by two changes in curvature in the LV geometry, intermediate aneurysms incorporate solely one such border, and globally hypokinetic cases have none. In five cases, the shape of the LV aneurysm was not evaluated. These cases were thus not classified and included into one of the subcohorts of different aneurysm types. The LV aneurysms were primarily diagnosed by echocardiography. The MR grade was quantified entirely by echocardiography. **Table 1** summarizes clinical and demographic data of the seven subcohorts.

2.2. Computed Tomography

CCT examinations were performed using a dual-source multi-slice spiral computed tomography scanner (Somatom Definition Flash, Siemens Healthcare GmbH, Erlangen, Germany). A spiral modus using retrospective electrocardiogram-gating was used to reduce motion artifacts from the heart. A tube voltage of 100 kV and an individually adapted tube current were applied to retrieve a multiphase data set resolving the heart cycle by 10 phases. This allows to assess LVEDV and LVESV. For image reconstruction, a standard soft-tissue convolution kernel and a dedicated noise reduction software were employed. Spatial resolution of the CCT images varied in the range of (0.390–0.648 mm) × (0.390–0.648 mm) for in-plane resolution and (0.5–1.85 mm) for the slice thickness. Temporal resolution varied between 70 and 140 ms, depending on the patient's heart rate.

2.3. Segmentation

Segmentations are required to generate the SSMs of the LV. The segmentations were carried out using a recently developed in-house tool based on the MeVisLab platform (32) as described in detail by Tautz et al. (33). Briefly summarized, the LV in end-diastolic and end-systolic state is segmented semi-automatically building on an adaptive 3D region growing approach and contextual information of the heart topology. Where necessary, e.g., due to artifacts caused by metallic implants or uneven distribution of contrast agent, manual corrections were made. The segmented LV in end-diastolic state is used to manually segment the end-diastolic myocardial wall. Subsequently, both annuli were segmented by rotating 18 planes around the valvular axis, which was manually defined by setting two landmarks defining the LV apex and the respective center of the valve orifice. The annuli landmarks are used to interpolate the aortic annulus to an ellipse and the mitral annulus to a cardioid, which were used to define major geometric parameters of the annuli. As last, a landmark is set manually to define the RCA ostium. It is used for the registration of the segmented LVs, which is necessary to generate the SSM, which requires a similar orientation of input data. Furthermore, this allows a 17-segment analysis according to Cerqueira et al. (34), as well as visualizations of the myocardial wall thickness and wall movement during contraction. **Figure 2** shows the 17-segment visualizations of the myocardial wall movement and wall thickness as well as wire-frame representations of the representative LVs for four subcohorts (which were defined based on MR and presence of an aneurysm), subdividing the whole study cohort of 125 cases. **Figure 3** shows three subcohorts, subdividing the entire cohort into different aneurysm types. The segmentations were saved as DICOM files and used to generate triangulated surfaces required for the generation of the SSM and the measurement of the key geometric parameters: LVEDV, LVESV, LV sphericity index calculated according to (35), stroke volume (SV), ejection fraction (EF), and the areas of both annuli. **Table 2** summarizes the averaged geometric parameters for all seven subcohorts.

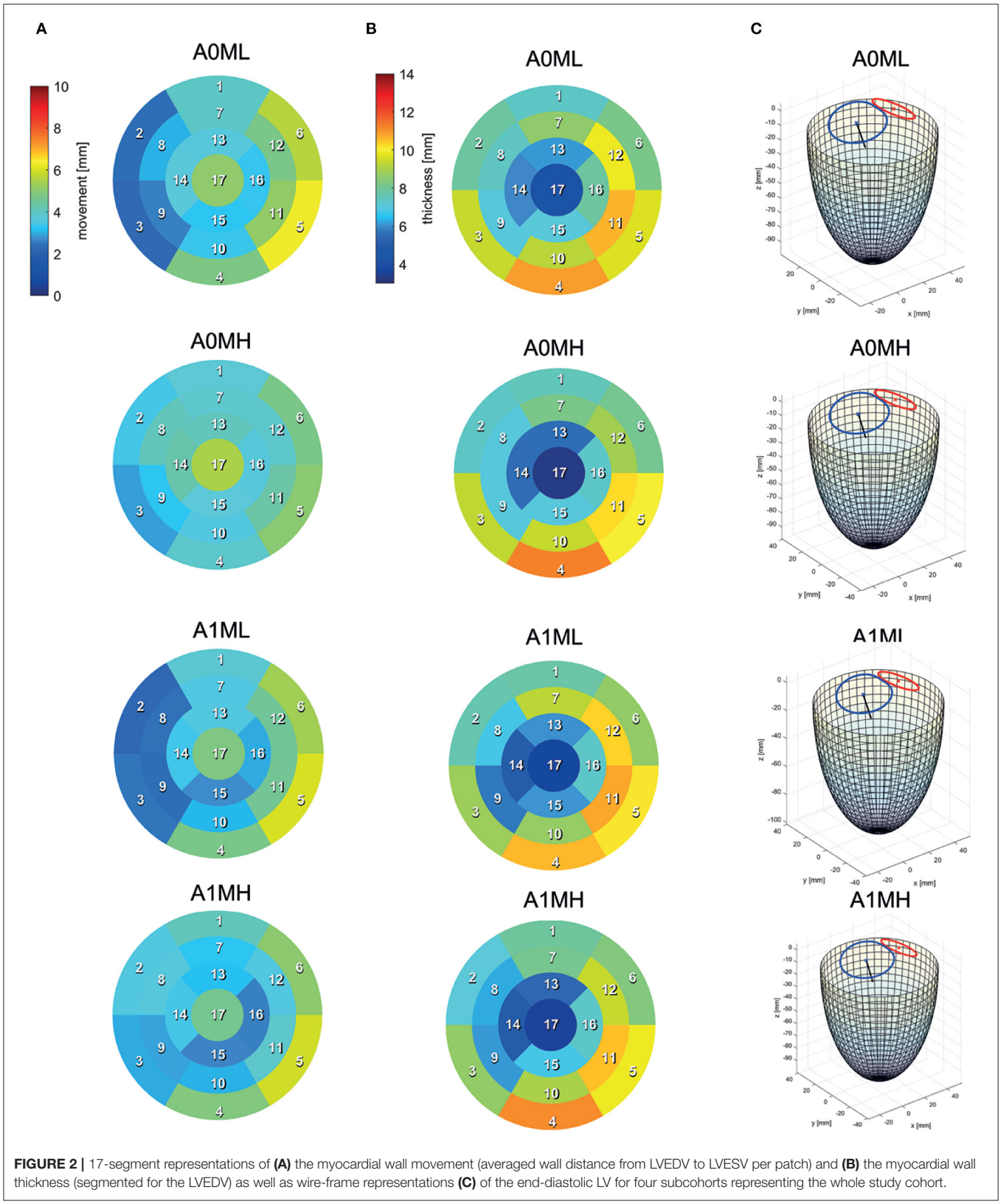

FIGURE 2 | 17-segment representations of **(A)** the myocardial wall movement (averaged wall distance from LVEDV to LVESV per patch) and **(B)** the myocardial wall thickness (segmented for the LVEDV) as well as wire-frame representations **(C)** of the end-diastolic LV for four subcohorts representing the whole study cohort.

Two SSMs were generated to separate cases with and without LV aneurysms.

2.4. Statistical Shape Model

Prior to the actual SSM computation of the LVs, the segmentations need to go through a pre-processing step that subdivides the surfaces into areas, so-called patches. These patches are projected on a circular disc, so-called reference. Subsequently, a point correspondence can be computed between each individual surface geometry and the reference. In this SSM, we decided to design the patches according to the 17-segment heart model (34). This way, the patch-wise information can be later used for further analysis according to clinical routine workflows. To define the borders on the surface, the segmented landmarks are used to define separating planes, as follows. The plane defined through the RCA and apex is used to define all vertical borders of the 17 segments by rotating. A plane which is fitted to the annuli landmarks is used to cut the LV open right below the annuli landmarks. The plane is then displaced horizontally to 1/3 and 2/3 of the LV's height to add the horizontal borders. Apart from the end-diastolic surface information, a displacement field between end-diastolic and end-systolic surfaces is created by computing the closest points between the two surfaces. The displacement field can be used to recreate the end-systolic surface by displacing the end-diastolic vertices along the field while also preserving the patch information from the end-diastolic surface. Additionally, the surface distance is computed between the end-diastolic and the myocardium to store the myocardial thickness in a scalar field, which can be displayed as a color map on the end-diastolic surface. Our SSM approach is able to combine the end-diastolic surface, the displacement field to the end-systolic surface, the vector field of the myocardial thickness as well as the RCA landmark in one single model and is computed as follows. First, all training data is aligned to the first input training case. A data matrix with rows for features and n columns containing the training cases, is constructed. Most of the features are related to the m vertices of the end-diastolic surface and are encoded in the data matrix as shown in Equation 1.

$$M = \begin{pmatrix} s_{1,1} & s_{1,2} & \cdots & s_{1,n} \\ s_{2,1} & s_{2,2} & \cdots & s_{2,n} \\ \vdots & \vdots & \ddots & \vdots \\ s_{3*m,1} & s_{3*m,2} & \cdots & s_{3*m,n} \\ d_{1,1} & d_{1,2} & \cdots & d_{1,n} \\ d_{2,1} & d_{2,2} & \cdots & d_{2,n} \\ \vdots & \vdots & \ddots & \vdots \\ d_{3*m,1} & d_{3*m,2} & \cdots & d_{3*m,n} \\ v_{1,1} & v_{1,2} & \cdots & v_{1,n} \\ v_{2,1} & v_{2,2} & \cdots & v_{2,n} \\ \vdots & \vdots & \ddots & \vdots \\ v_{m,1} & v_{m,2} & \cdots & v_{m,n} \\ p_{1,1} & p_{1,2} & \cdots & p_{1,n} \\ p_{2,1} & p_{2,2} & \cdots & p_{2,n} \\ p_{3,1} & p_{3,2} & \cdots & p_{3,n} \end{pmatrix} \quad (1)$$

Therein, s represents the surface vertex coordinates, d the elements of the displacement field vectors, v the scalar values of the myocardial thickness per vertex, and p the coordinates for the RCA landmark. Using principal component analysis (PCA), the covariance matrix can be computed. The SSM is then described according to Equation 2.

$$S_i = \overline{S} + X \cdot b_i \quad (2)$$

Therein, $\overline{S}$ is the mean shape, X the eigenvector matrix of the covariance matrix, and b_i the shape parameters of the modes. The method is based on previous work as described in more detail by Lamecker et al. (36).

Making use of the described procedure, two SSMs are computed: the first one using all cases with LV aneurysm, the latter one considering only cases without LV aneurysm. These two SSMs are then evaluated, e.g., in terms of mode analysis: the first three modes are compared visually and the cumulative variance of modes is calculated in order to assess the dimensionality reduction. Furthermore, seven mean cases are computed based on the respective differentiation into subcohorts as pointed out in Section 2.1. Each mean case represents a different pathological configuration.

2.5. CFD Simulation Setup

The mean shapes of all seven subcohorts are used to set up the simulation. A detailed description of the workflow can be found in our recently published work (29). Average shapes are computed for the cardioid mitral annulus and the elliptical aortic annulus which are used to reconstruct the entire LVEDV via a Poisson Surface Reconstruction algorithm. Non-case-specific reconstructions of a left atrium (LA) and an aorta are attached at the respective annulus of all seven representative SSM-based LV shapes. The SSM-based vector field prescribing the LV endomyocardial surface motion is scaled by a time-dependent factor to obtain a grid velocity vector allowing the ventricular volume to follow a specified volume curve at given EF. A grid velocity vector field results, which is prescribed as motion in the STAR-CCM+ (version 2021.2.1, Siemens Industries Digital Software, Plano, TX, USA) simulation.

The volumetric change of the LVs in time is described by a mean volume curve which was obtained from another cohort. This mean volume curve is scaled to a heart rate of 75 bpm (0.8 s per cycle) and the respective EF per case. At all walls, no-slip boundary conditions (BCs) in terms of relative movement of wall to fluid are posed. At the pulmonary veins, a physiological pressure BC is applied, whereas at the aorta, the respective mass flow rate is set, taking into consideration the blood that regurgitates into the LA. The MR grade determines the regurgitation fractions by correlating regurgitation fractions of 15, 30, and 50% to MR grades of I, II, and III (37) and interpolating linearly in between. The resulting regurgitation volumes are shown in **Table 1**. The valves are positioned in the annuli planes in a 2D-planar modeling approach (38, 39). For the aortic valve (AV), an elliptical opening area and for the mitral valve (MV) a projected orifice area, taken

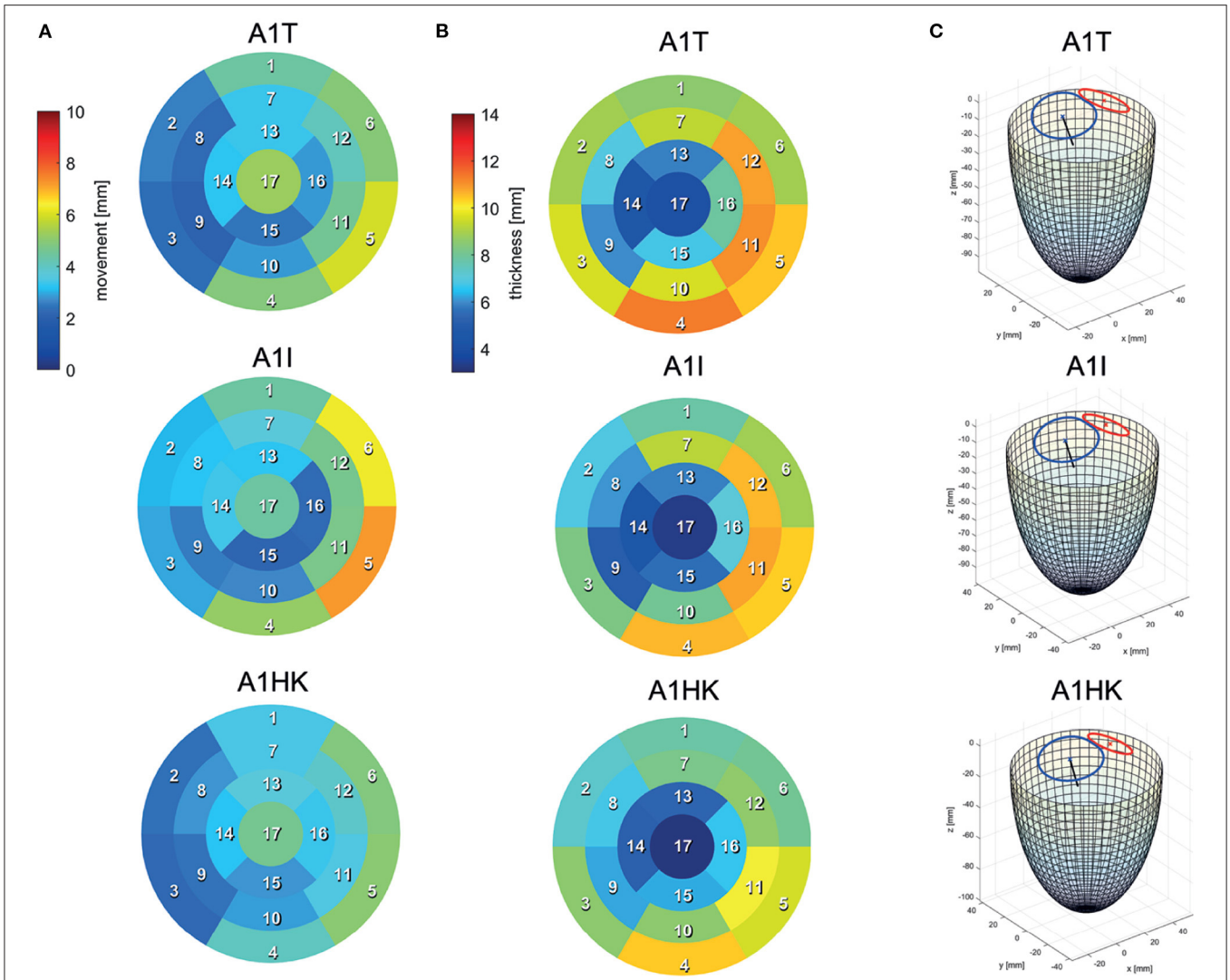

FIGURE 3 | 17-segment representations of **(A)** the myocardial wall movement (averaged wall distance from LVEDV to LVESV per patch) and **(B)** the myocardial wall thickness (segmented for the LVEDV) as well as wire-frame representations **(C)** of the end-diastolic LV for three subcohorts representing cases with different LV aneurysm types.

TABLE 2 | Averaged geometric parameters for the seven investigated subcohorts.

Parameters	A0ML	A0MH	A1ML	A1MH	A1T	A1I	A1HK
LVEDV (ml)	275 [108]	304 [126]	313 [113]	279 [220]	222 [96]	324 [149]	324 [182]
LVESV (ml)	200 [102]	223 [97]	218 [98]	214 [187]	180 [74]	250 [127]	250 [166]
EF (%)	26.3 ± 7.8	25.3 ± 6.0	23.9 ± 6.7	23.4 ± 6.5	24.9 ± 6.9	24.1 ± 7.2	21.5 ± 5.2
SI	0.79 ± 0.16	0.87 ± 0.20	0.80 ± 0.20	0.88 ± 0.17	0.70 ± 0.14	0.88 ± 0.21	0.89 ± 0.15
MWT (mm)	8.3 ± 1.67	8.1 ± 1.37	8.0 ± 1.58	7.9 ± 1.04	8.5 ± 1.94	7.8 ± 1.39	7.7 ± 0.89
WM (mm)	3.86 ± 1.18	3.88 ± 1.13	3.60 ± 1.13	3.64 ± 1.24	3.51 ± 1.26	3.82 ± 1.01	3.36 ± 1.18
AVAA (cm^2)	5.7 ± 1.05	5.9 ± 0.93	5.5 ± 0.99	5.6 ± 0.92	5.6 ± 1.22	5.7 ± 0.85	5.4 ± 1.02
MVAA (cm^2)	10.2 ± 2.18	11.4 ± 2.13	9.9 ± 2.23	12.0 ± 2.90	9.0 ± 2.21	10.7 ± 2.50	11.2 ± 2.97

Values are shown as median [interquartile range] for both cohorts if a parameter is not normally distributed. Otherwise, values are displayed as mean ± standard deviation. The Shapiro-Wilk test was used to test normality. LVEDV, left ventricular end-diastolic volume; LVESV, left ventricular end-systolic volume; EF, ejection fraction; SI, end-diastolic sphericity index; MWT, end-diastolic mean myocardial wall thickness; WM, mean wall movement; AVAA, end-diastolic aortic valve annulus area; MVAA, end-diastolic mitral valve annulus area.

from Schenkel et al. (38), are used. Valve opening and closing is modeled via a porous baffle interface. Modeling moving obstacles as e.g., heart valves via porous media theory enables to model a surface movement via a spatio-temporal adaption of permeability parameters, being computationally efficient and easy to implement (40). To mimic valve opening and closing, a pressure drop according to Darcy's law is impressed onto the fluid via the porous baffle interface, as shown in Equation 3 (41).

$$\Delta p = -\rho(\alpha|v_n| + \beta)v_n \tag{3}$$

Therein, Δp is the induced pressure drop over the interface, ρ the fluid density, α the user-specified porous inertial resistance, v_n the fluid velocity normal to the interface, and β the user-specified porous viscous resistance. By varying this pressure drop in time and space, smooth 2D valve openings can be realized. The AV is opened elliptically, keeping the aspect-ratio of the AV in opened state. For the MV, an intermediate state, also taken from Schenkel et al. (38), is applied. For the MV, orifice areas of 5.65 cm^2 and for the AV orifice areas of 4 cm^2 are chosen. Based on the studies by Leyh et al. (42), the AV opening and closing time intervals are set to 57 and 39 ms. For the MV, opening and closing times of 48 ms and 60 ms were chosen. The regurgitation areas on the MV are chosen such that reasonable pressure losses over the MV result. A detailed description of the BCs as well as their detailed motivation can be found in Obermeier et al. (29).

STAR-CCM+ is used to create a polyhedral volume mesh at a base size of 1 mm with a refinement to 0.25 mm in valve regions where the highest velocity gradients are expected. The number of cells results in approximately 650,000. To retrieve reasonable initial conditions, two cycles were computed in advance. As results in a previous study suggested, a sufficiently swung-in state can be assumed after two cycles for such dilated LVs with reduced EF (29). In the same study, mesh convergence was shown for the specified mesh dimensions. Blood is modeled as incompressible with a density of 1,050 kgm^{-3} and as non-Newtonian Fluid according to the Carreau-Yasuda model. The model is parameterized with an infinity shear rate of 0.0035 Pas, a zero shear rate of 0.16 Pas, a relaxation time of 8.2 s, a power constant of 0.2128 and a = 0.64 (43). An arbitrary Lagrangian-Eulerian discretization method from STAR-CCM+ is used to solve the 3D incompressible Navier-Stokes equations with moving mesh for unsteady flow with no body-forces and source terms (Equations 4 and 5) (41).

$$\frac{\partial}{\partial t}\int_V \rho \mathrm{d}V + \int_\Omega \rho(\mathbf{v} - \mathbf{v}_g)\cdot \mathbf{n}\mathrm{d}\Omega = 0 \tag{4}$$

$$\frac{\partial}{\partial t}\int_V \rho \mathbf{v}\mathrm{d}V + \int_\Omega [\rho\mathbf{v}(\mathbf{v} - \mathbf{v}_g) + p\mathbf{I} - \mathbf{T}]\cdot \mathbf{n}\mathrm{d}\Omega = \mathbf{0} \tag{5}$$

Here, t denotes time, V the control volume, Ω is the boundary of the control volume, $\mathbf{n}$ is the outwardly directed vector normal to $d\Omega$, $\mathbf{v}$ is velocity, $\mathbf{v}_g$ is the grid velocity, p is pressure, ρ is density, $\mathbf{I}$ is the unit tensor of second order, and $\mathbf{T}$ is the viscous stress tensor. A RANS k-omega SST turbulence model and an implicit second order time-stepping scheme are applied.

In comparison to our previous work (29), we further automated the pre-processing procedures and optimized the time-consuming numerical framework. Pre-processing now required 4–8 h, whereas the cyclic blood flow computation took 12–13 h on 4 nodes at 40 cores (Intel Skylake 6,148, 2.3 GHz) on the Emmy system of the North-German Supercomputing Alliance. Due to an adaption of the deformation scaling factor into an implicit formulation (considering previous time steps), the pre-processing step of deformation computation is now omitted.

2.6. Post-processing of the LV Hemodynamics

The hemodynamics analysis is based on pressure and velocity fields as well as a passive scalar to investigate the blood washout process. A passive scalar is a passive tracer that can be placed in the fluid and moves according to the velocity field, without influencing the fluid motion itself (only convective transport is considered, herein). Therewith, a transport equation is solved to track the passive scalar motion, bypassing the need to consider multi-phase flow. To analyze the washout, the blood domain is separated into old and new blood with identical rheological properties by using two passive scalars. This modeling approach enables to mimic the clinically used blood washout behavior analysis by injecting contrast agent. The passive scalar for the old blood is placed in the LV in the initial state at $t = 0$ s, as e.g., done by Grünwald et al. (44). It is being washed out in the subsequent considered eight cycles. The passive scalar for fresh blood is placed in the LA at the onset of diastole of the first cycle at $t = 0.29$ s and mimics a contrast agent washout.

For an energetic evaluation, beside the normalized kinetic energy (normalized with the ventricular volume) called specific kinetic energy (SKE), the dissipation function Φ is used to quantify energetic losses. It is computed via the double-dot product of the velocity gradient vector $\nabla\mathbf{v}$ and the stress tensor σ (45, 46) as shown in Equation 6.

$$\Phi = \sigma \cdot\cdot \nabla\mathbf{v} \tag{6}$$

For the investigation of intraventricular pressure gradients, two horizontal planes are positioned in the LV: one in basal and one in apical region. The intraventricular pressure gradient is then computed by the difference of the average pressure per plane.

3. RESULTS

First, both SSMs as well as the seven mean geometries and contractions are analyzed. Subsequently, the hemodynamics are evaluated by means of large-scale flow patterns, energetic performance, blood washout behavior, and intraventricular pressure gradients. Therein, differences between the pathological states are emphasized by comparing two particular LV groups. The first group consists of cases A0ML, A0MH, A1ML and A1MH, separating cases with and without LV aneurysm as well

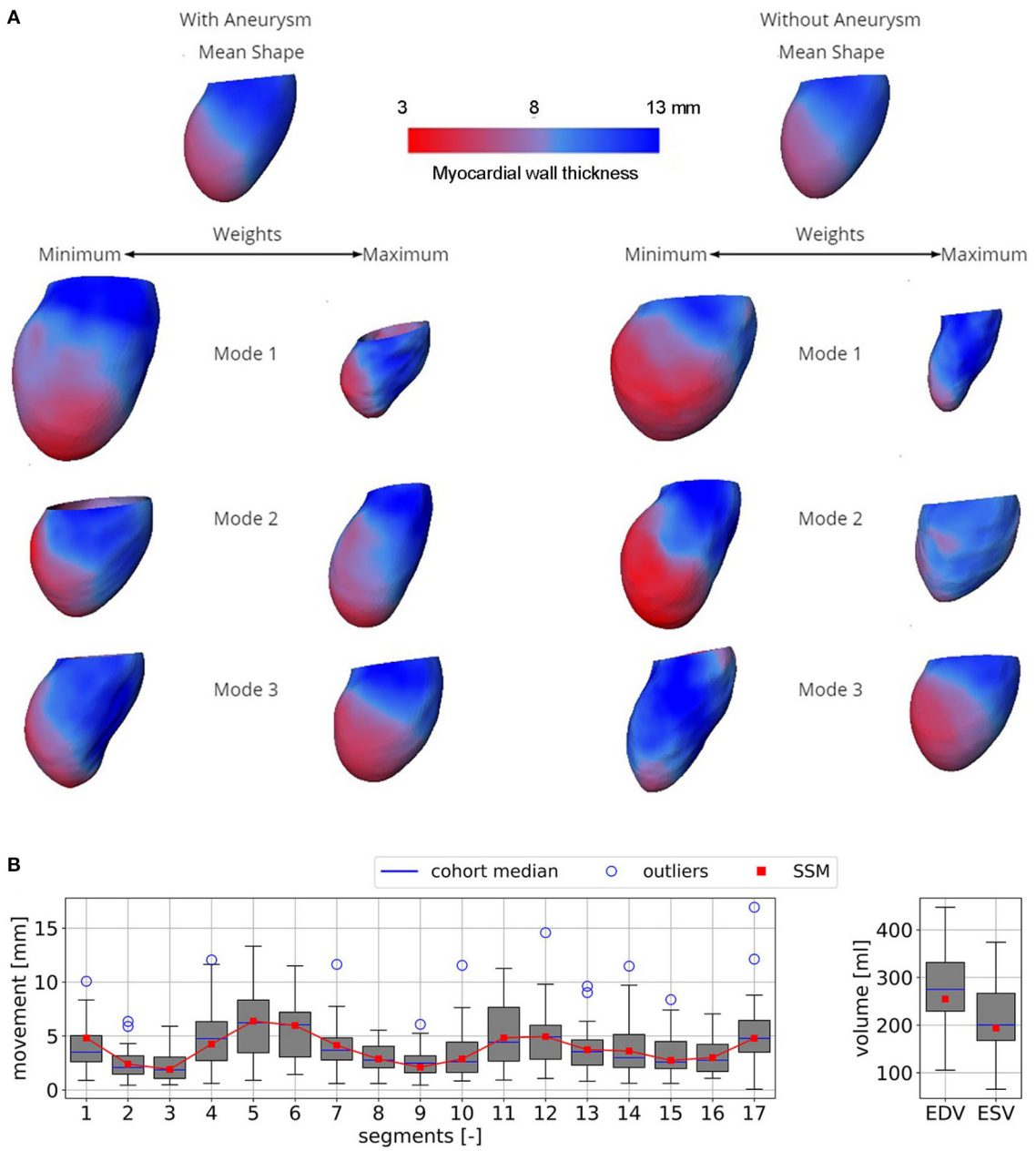

FIGURE 4 | (A) Both SSMs of the LV with and without aneurysm represented by mean end-diastolic shapes colored by the myocardial wall thickness. Three first most descriptive shape modes, representing the variance of the models, are shown. When changing the weight of a mode, certain features of the model are altered as well. **(B)** Boxplots of the mean segment-wise movement (left) and boxplots of EDV and ESV (right) exemplary shown for case A0ML.

as different degrees of MR (low and high). The second group is composed of cases with different characteristics of the LV aneurysm, i.e., A1MT, A1MI, and A1HK, all being accompanied by a medium MR grade.

3.1. Statistical Shape Model

The two developed SSMs aim to describe pathological LVs of patients with and without LV aneurysms, including a description of shape, deformation due to contraction, and myocardial wall thickness. Identification of principal modes allows for a reduction of complexity and dimensionality. Note, that the MR degree was not included into the SSM but is directly defined through the computational model via the MR area during systole.

Figure 4A shows the resulting SSMs. Visually, both mean shapes are very similar. However, comparison of the first three modes and their variances by weights shows remarkable differences. Mode 1 of the non-aneurysmatic SSM reveals a higher sphericity by comparing minimum weights, whereas the

maximum weight of the aneurysmatic shape clearly indicates the LV aneurysm: a bulge left from the apex associated with relatively low myocardial thickness can be observed. Mode 2 of both SSMs shows a variance in the shape sphericity of the LV with higher variability of the myocardial wall thickness in the non-aneurysmatic SSM in the apex region. The third modes are similar but show a higher variability for the myocardial wall thickness in the non-aneurysmatic SSM. In the process of dimension reduction by identifying principal modes, the aneurysmatic SSM requires 35 modes to include 95% of the cumulative variance, whereas the non-aneurysmatic SSM requires 38 modes.

Figure 4B exemplary compares the 17-segment-wise wall movement during contraction as well as LVEDV and LVESV values of the A0ML cohort (40 cases) as a boxplot vs. the values of the representative mean shape of the cohort, created by the SSM. The values of the mean case are close to the median values of the cohort. Similar results are found for the other 6 representative mean cases. Comparing the deformations of the mean cases in **Figures 5**, **6** to the cohort-wise averaged ones as shown in **Figures 2**, **3** also reveals a good match of the myocardial wall movement.

The last point to address is to what extent the seven mean shapes represent the respective pathological state. Concerning the first group of cases (A0ML, A0MH, A1ML, and A1MH), less deformation can be seen in segments 13, 15, and 16 in the aneurysmatic cases A1ML and A1MH due to the anterior aneurysm (**Figure 5** bottom). Furthermore, the non-aneurysmatic and high MR grade case reveals a more homogeneous myocardial wall deformation as respectively the aneurysmatic and low MR degree case. The three aneurysm types in cases A1T, A1I, and A1HK as defined by Di Donato et al. (30) can also be observed in the red marked regions in **Figure 6** at t_1. Case A1T shows two changes in curvature in systolic state, case A1I only one and case A1HK shows no change in curvature.

3.2. Large-Scale Flow Patterns

Figure 5 visualizes differences between major flow features of cases A0ML, A0MH, A1ML, and A1MH during peak systole (t_1) and diastasis (t_3). At peak systole, the majority of blood flows into the ascending aorta in all cases. The other portion regurgitates into the LA in form of a high velocity jet, impinging on the upper LA wall (**Figure 5** t_1). In the low MR grade cases, higher velocities appear in the left ventricular outflow tract (LVOT). The AV velocities at peak systole are between 0.69 and 1.03 m/s. The regurgitation jet velocities are between 3.84 and 4.38 m/s at pressure drops of 53–77 mmHg. During diastole, a blood jet enters the LVs from the LAs, causing the formation of commonly observed ring vortices. During diastasis, the jets become less coherent, especially in the cases with high MR. In cases A0MH, A1ML, and A1MH, the jets travel along the LV axis toward the apex. In case A0ML, it is directed at the lateral to anterior wall, where it impinges (**Figure 5** t_3). In these lateral and anterior regions in basal and mid LV regions, (i.e., segments 1, 5, 6, 7, 11, and 12), also a distinct LV movement is visible in case A0ML (**Figure 5** bottom). In the other non-aneurysmatic case A0MH, a rather homogeneous contraction is present. In the aneurysmatic cases A1ML and A1MH, little movement is observed in the apical inferior and lateral region (i.e., segments 15 and 16) due to the development of aneurysms.

Figure 6 identifies differences in flow structures of cases A1T, A1I, and A1HK with different types of LV aneurysm and similar MR grades. A likewise systolic flow is observed in all three cases, consisting of an aortic outflow with velocities between 0.67 and 1.00 m/s as well as regurgitating jets at velocities from 3.88 to 4.44 m/s, resulting in MV pressure gradients of 66 to 73 mmHg (**Figure 6** t_1). Case A1I has a higher SV at comparable regurgitation volume, thus showing higher velocities in the aorta during systole as well as higher velocities of the diastolic jet (**Figure 6** t_3). The diastolic jets are accompanied by ring vortices. When reaching diastasis, the diastolic jet in case A1I traveled further and is directed toward the lateral to anterior wall, where it impinges. In cases A1T and A1HK, the jets move along the LV axis. Cases A1T and A1I show almost no movement in segments 15 and 16, while being characterized by a strong deformation in segments 5, 6, 11, and 12 in lateral and anterior regions (**Figure 6** bottom). Case A1HK reveals a distinctively different deformation with the strongest contraction in apex region and less movement elsewhere.

3.3. Energetic Performance

The specific kinetic energy (SKE) and specific energy dissipation (SED) take a qualitatively similar temporal course for all cases: the SKE has local maxima in peak systole, in the middle between peak E-wave and diastasis as well as during A-wave (**Figures 7A,C**). The SKE during systole is within the same order of magnitude as in diastole. Local minima can be observed as blood inside the LV decelerates and stagnates shortly after beginning of systole, at the end of the systolic phase, and in the middle of the A-wave deceleration phase. Comparing the four cases with and without LV aneurysms (**Figure 7A**), where SVs are similar, the cyclic mean of SKE reveals lower values in the aneurysmatic cases (A0ML: 12.2 J/mm^3, A0MH: 10.3 J/mm^3, A1ML: 9.8 J/mm^3 and A1MH: 9.0 J/mm^3). Furthermore, higher MR grades can be associated with lower SKE for both groups, with and without LV aneurysms. Comparing the three cases with different LV aneurysms (**Figure 7C**), case A1I with the largest SV (see **Table 3**) is characterized by a remarkable larger SKE if compared to A1I and A1HK. Regarding SED, a five-fold higher maximum in systole than in diastole is observed (**Figures 7B,D**). Furthermore, the SED during systole reveals inverse trends if compared with SKE: higher SED in the non-aneurysmatic cases as well as higher SED at higher MR. Comparing the three aneurysmatic cases, case A1I, which was associated with the highest SKE, is also associated with the highest SED. Finally, during systole there is a noteworthy difference in SED between A1T and A1HK, which show similar values for SKE.

3.4. Intraventricular Washout

The intraventricular blood washout is quantified by relative and absolute volumetric fractions of fresh and old blood (**Table 3**)

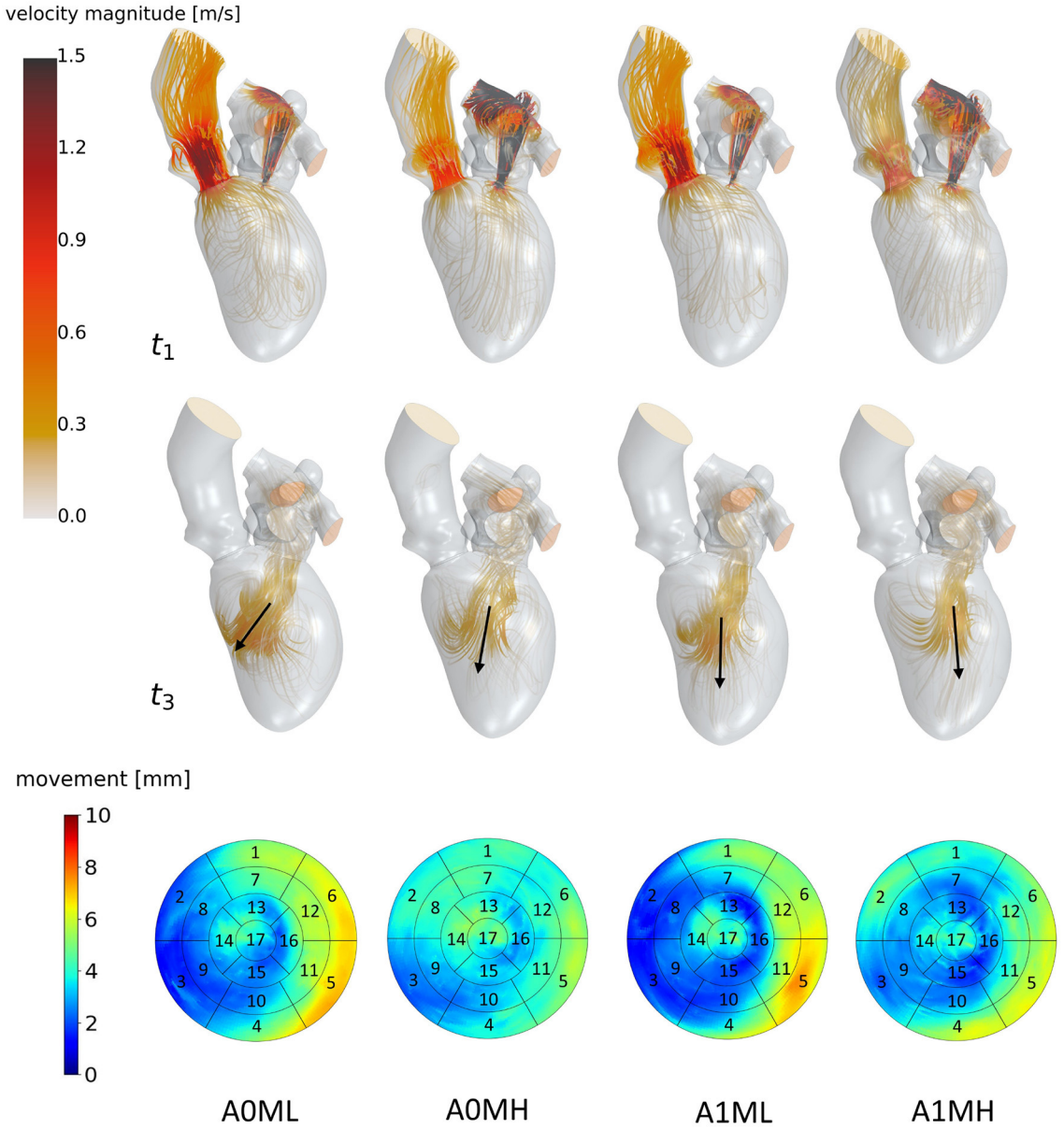

FIGURE 5 | Streamlines of cases A0ML, A0MH, A1ML and A1MH from left to right at t_1: peak systole (top) and t_3: diastasis (mid) of the seventh cycle. At low velocity regions, streamlines are made transparent to underline the major flow features. Black arrows indicate the diastolic jet orientation. The bottom row shows the LV deformations at the surfaces. The black boxes and numbers display the regions corresponding to the 17-segment model.

and qualitatively analyzed via the washout of fresh blood (**Figures 8**, **9**).

Comparison of the four aneurysmatic vs. non-aneurysmatic cases shows a reduced blood washout in the aneurysmatic cases, reaching the half-life of fresh blood approximately one heart cycle later (3 cycles vs. 4 cycles). Interestingly, the difference in the half-life between cases with low and high MR is relatively small, despite the lower direct flow rates in the high MR cases. After eight cycles, there is a larger percentage of old blood being still present in the aneurysmatic LVs. **Figure 8** visualizes the blood washout behavior over a period of three heart cycles represented by four time steps: peak E-wave of the first cycle (0.42 s), end diastole of the first cycle (0.8 s), peak systole of the second cycle (0.92 s), and the end of the third cycle (2.4 s). The first and last represented time steps are very similar for all four cases. Time points at 0.8 s and 0.92 s appear to be most suitable for the visual differentiation between cases. At the end of the first cycle, the fresh blood did penetrate toward the apex in all cases (**Figure 8** at 0.8 s). In case A0ML, the jet is directed toward the lateral to anterior wall. In the opposite regions (i.e., inferior and septal), a region with poor mixing appears, being still visible in peak systole of the second cycle (**Figure 8** at 0.92 s). In the aneurysmatic cases

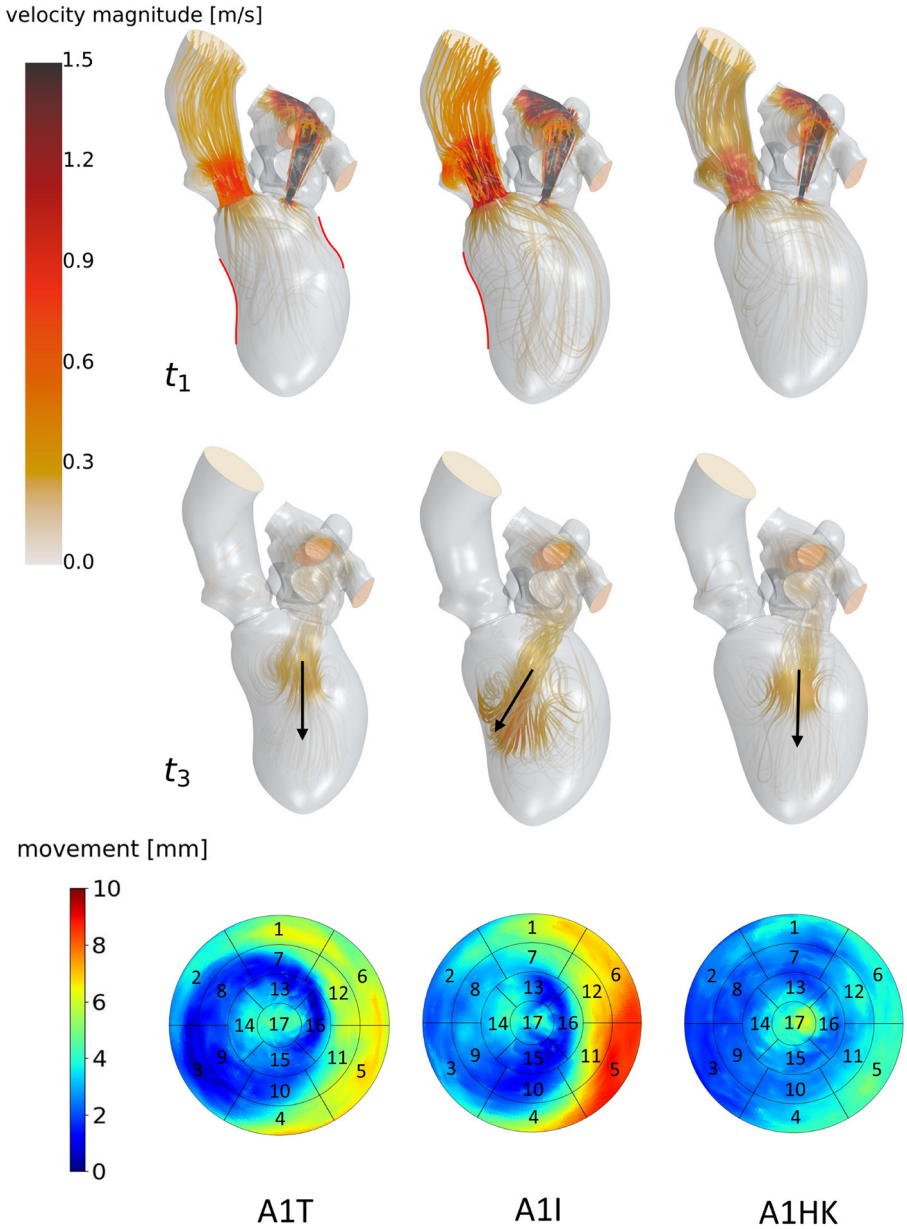

FIGURE 6 | Streamlines of cases A1T, A1I and A1HK from left to right at t_1: peak systole (top) and t_3: diastasis (mid) of the seventh cycle. At low velocity regions, streamlines are made transparent and velocities above 1.5 m/s are clipped. Black arrows indicate the diastolic jet orientation. Red contours at t_1 show changes in curvature to distinguish between different aneurysm types. The bottom row shows the LV deformation at the surfaces. The black boxes and numbers display the regions corresponding to the 17-segment model.

A1ML and A1MH, regions with poor mixing can be observed at that time as well: inferior and septal near-wall region in the A1ML case and central LV region in the A1MH case. In case A0MH, the most homogeneous mixing seems to be present.

A comparison of the washout behavior between the three cases with different characteristics of the LV aneurysm (i.e., A1T, A1I, and A1HK) reveals the by far highest direct flow rate in case A1T. Yet, the half-lives of fresh blood are similar in cases A1T and A1I, whereas it is significantly longer in case A1HK. In terms of old blood washout, the analysis found that cases A1T and A1HK are related to the worst washout, still having 20 % of the old blood inside the LVs after eight cycles. In the qualitative washout analysis (**Figure 9**), a poor mixing of fresh blood especially at 0.8 s and 0.92 s in cases A1T and A1HK can be observed. In case A1T, the jet of fresh blood does not penetrate all the way to the apex and remains in the area below the AV,

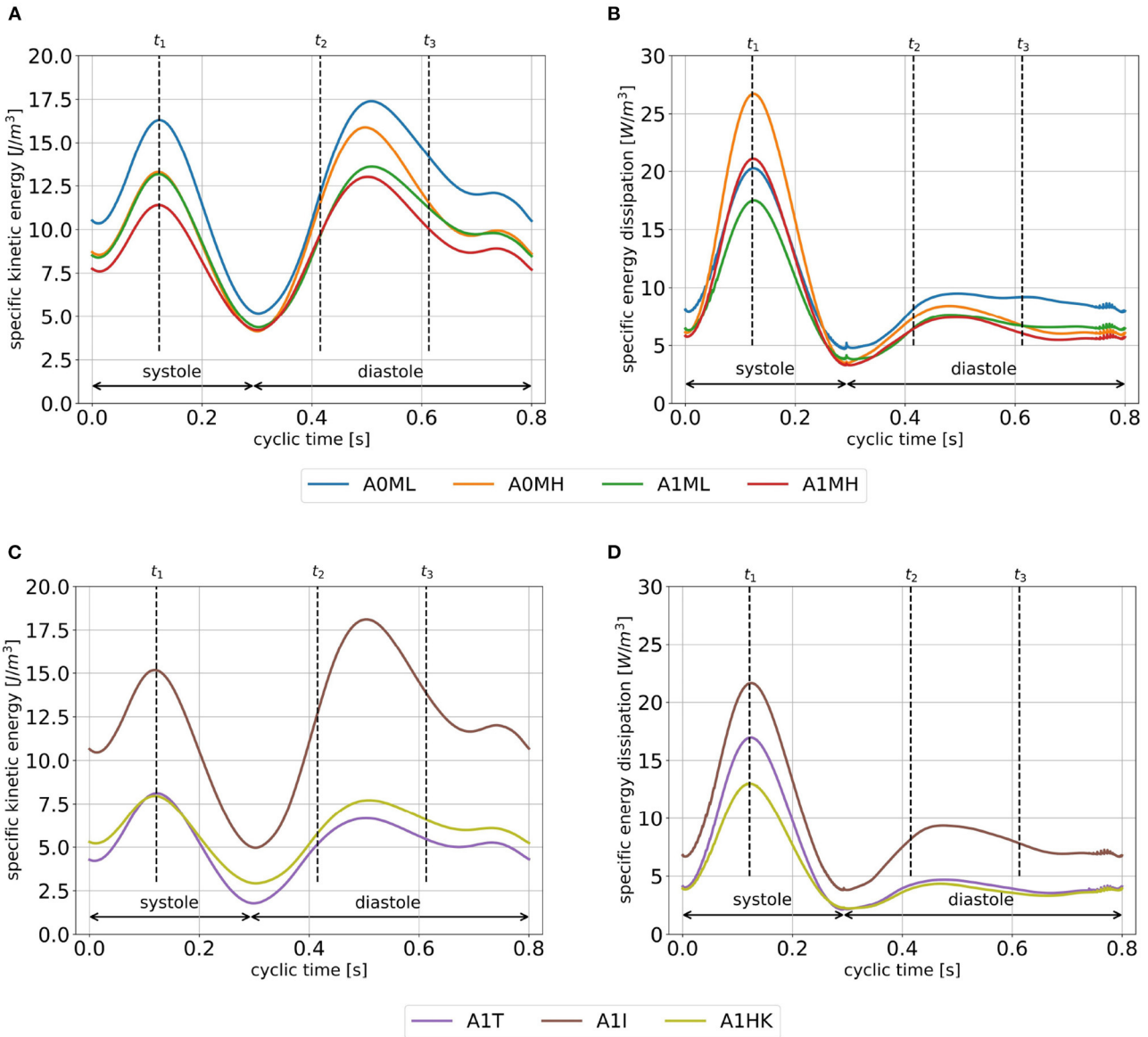

FIGURE 7 | SKE **(A,C)** and SED **(B,D)** averaged over cycles one to seven. Time points t_1, t_2 and t_3 mark peak systole, peak E-wave, and diastasis.

TABLE 3 | Intraventricular blood washout measures of the seven cases.

Parameters	A0ML	A0MH	A1ML	A1MH	A1T	A1I	A1HK
direct flow F.B. relative (%)	25.5	15.9	18.0	14.1	30.8	12.9	5.9
direct flow F.B. absolute (ml)	18.1	11.6	12.1	9.6	16.3	10.0	3.3
half-life F.B. (s)	2.60	2.65	3.27	3.33	2.46	2.61	4.87
half-life F.B. (cycles)	3.2	3.3	4.1	4.2	3.1	3.3	6.1
O.B. after 8 cycles (%)	11.52	10.17	13.87	15.02	19.00	10.04	21.47
SV (ml)	70.73	72.80	67.31	68.23	52.91	77.38	56.29

The half-life marks the time when 50% of fresh blood are ejected. SV: stroke volume. F.B., fresh blood; O.B., old blood.

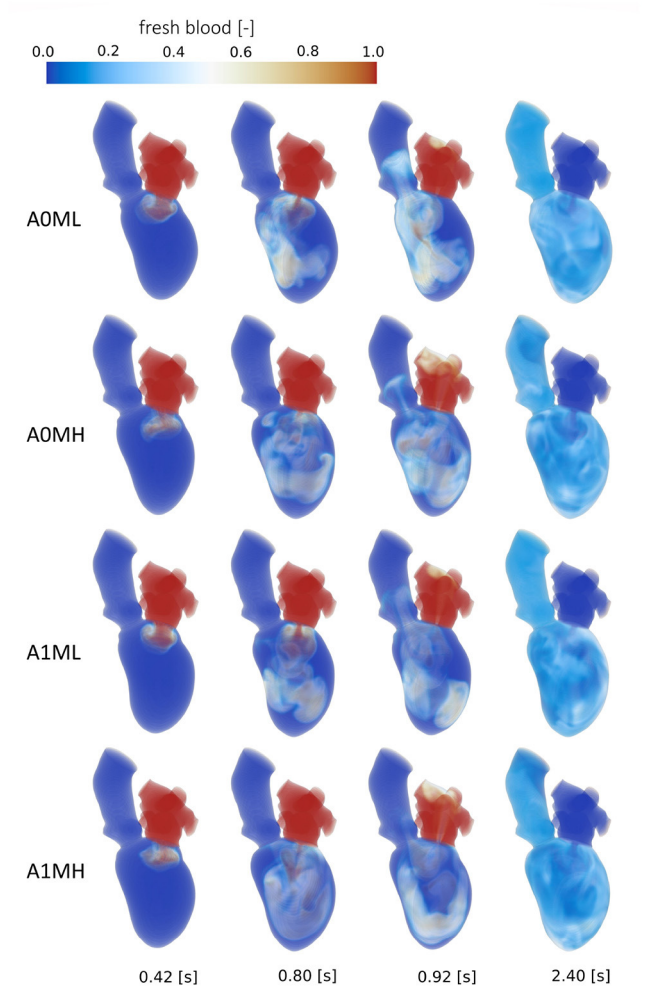

FIGURE 8 | Washout of fresh blood of cases A0ML, A0MH, A1ML and A1MH from top to bottom at, from left to right, peak E-wave of the first cycle (0.42 s), end diastole of the first cycle (0.8 s), peak systole of the second cycle (0.92 s) and the end of the third cycle (2.4 s).

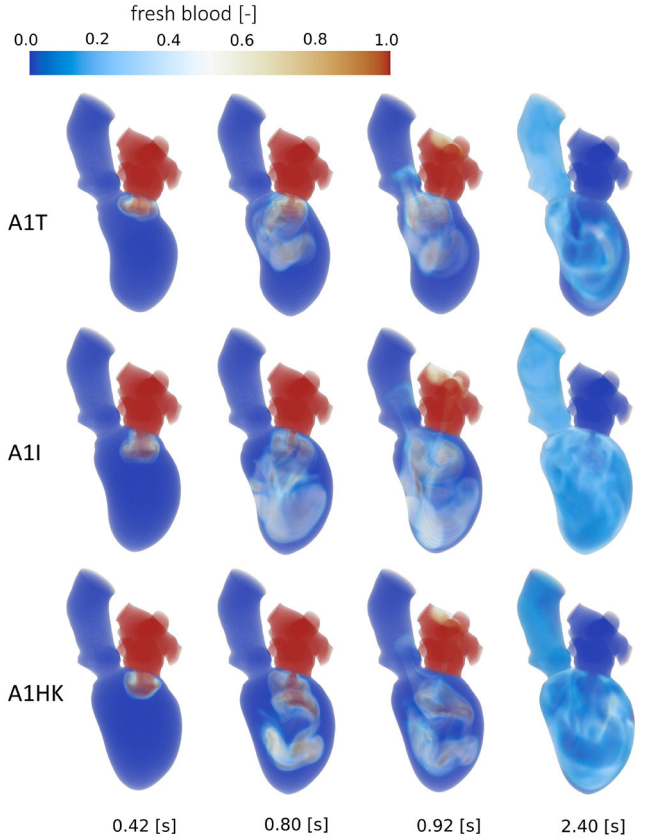

FIGURE 9 | Washout of fresh blood of cases A1T, A1I and A1HK from top to bottom at, from left to right, peak E-wave of the first cycle (0.42 s), end diastole of the first cycle (0.8 s), peak systole of the second cycle (0.92 s) and the end of the third cycle (2.4 s).

mixing poorly. In case A1HK, the jet reaches the apex, but rarely mixes with the rest of the blood. In both cases, unmixed regions are still visible at the end of the third cycle at 2.4 s.

3.5. Intraventricular Pressure Gradients

Figures 10A,B show the pressure gradient from apex to base for all seven cases, whereas **Figures 10C–E** exemplary show the relative static pressure field in a three-chamber view of case A0MH for three representative time steps. The temporal course of the pressure gradients is similar in all cases with two maxima and two minima: the first flat maximum (**Figures 10A,B** at t_4) at the onset of systole lasts for approximately 50 ms. The resulting intraventricular pressure gradient inside the LV accelerates blood toward the LVOT (**Figure 10C**). During systole, the pressure gradient decreases and achieves a minimum at the onset of diastole (**Figures 10A,B,D** at t_5). This negative pressure gradient pointing from base to apex supports the early diastolic filling (**Figure 10D**). During early diastole, the pressure gradient shifts its sign a second time, reaching the second maximum after E-wave (**Figures 10A,B** at t_6). The positive pressure gradient decelerates inflowing blood from the LA (**Figure 10E**). During diastasis, the pressure gradient decreases again, reaching the second minimum approximately at atrial contraction, when the A-wave is accelerated into the LV. Comparing the cases among each other, the major differences can be seen in the magnitudes of the second maximum in the pressure difference with higher values found for both cases with lower MR (A0ML and A1ML) as well as in case A1I.

4. DISCUSSION

In this study, two SSMs were developed in order to describe two populations of patients after myocardial infarction: patients with and without LV aneurysms. Despite advances in drug and device therapy, heart failure subsequent to myocardial infarction remains a frequent cause of death. Thus, e.g., enhancement of therapeutic approaches that address LV remodeling following scar formation is highly desired to improve life expectancy

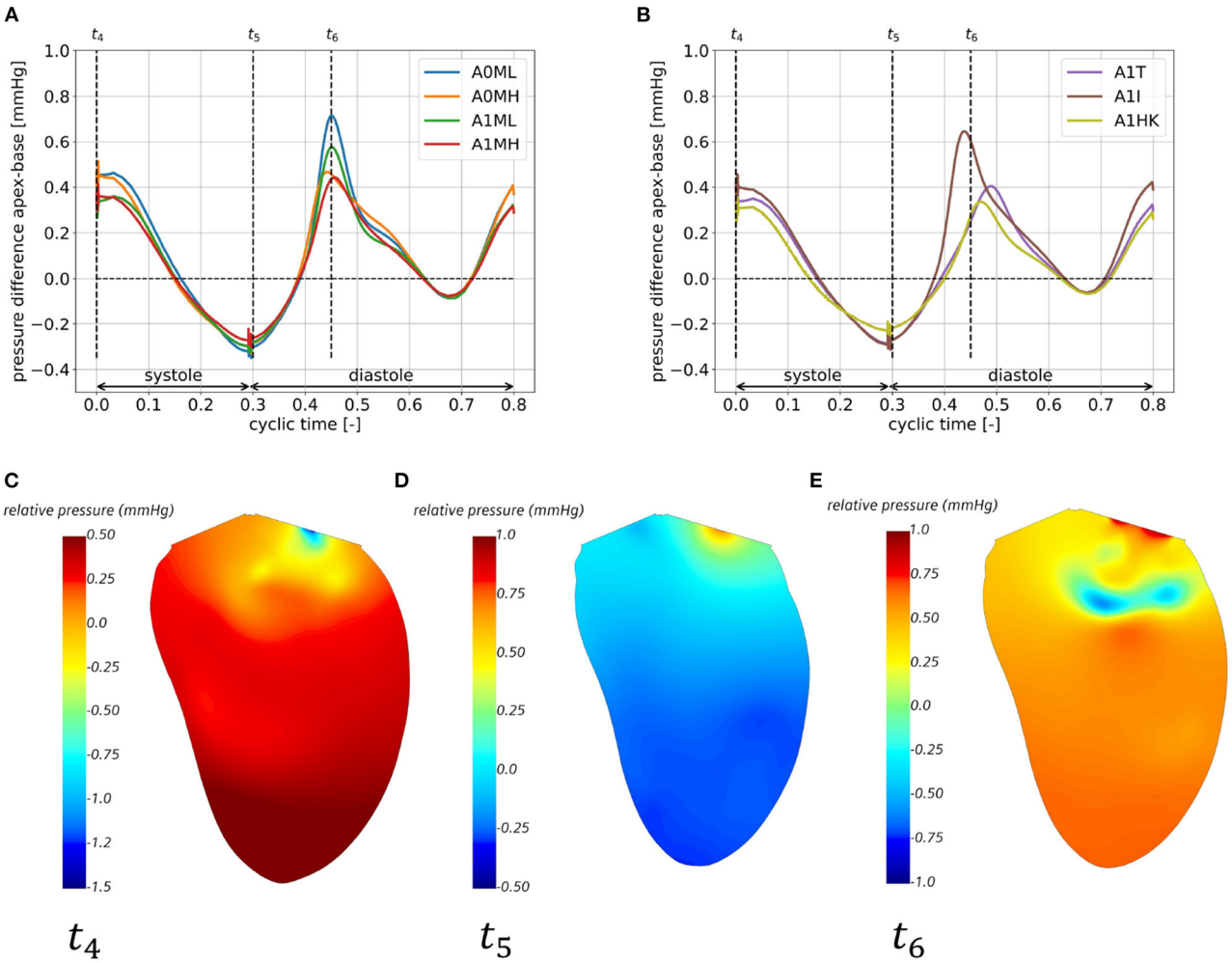

FIGURE 10 | Apex-base pressure difference for cases A0ML, A0MH, A1ML, and A1MH **(A)** and cases A1T, A1I, A1HK **(B)** in the eighth cycle and relative pressure field in a half cut along the LV long axis, exemplary for case A0MH at the onset of systole at t_4 **(C)**, the onset of diastole at t_5 **(D)** and shortly after peak E-wave at t_6 **(E)**.

and quality for patients with heart failure. Image-based CFD could thereby play a supportive role by modeling and predicting post-operative states. All the here considered patients are characterized by enlarged LVs, a condition which is often accompanied by MR, low EF, abnormalities in myocardial wall motion as well as myocardial wall thinning. Using these SSMs, seven mean cases are created, each representing a respective pathological configuration of MR grade and LV aneurysm. For each case, a mean end-diastolic shape is generated via the SSM together with the deformation field of the contraction from end diastole to end systole. This serves as a basis for an analysis of intraventricular hemodynamics via CFD. The numerical hemodynamic study was done using a recently proposed CCT-based CFD methodology, which was improved with respect to the earlier study in terms of physiological complexity and toward clinical translation. For a detailed discussion on the computational model, the reader is referred to Obermeier et al. (29). In order to improve the potential of the methodology toward clinical translation, the level of automation in pre-processing procedures was increased and solver settings were optimized, resulting in a 30 % reduction of the total required time for pre-processing, simulation, and post-processing. To investigate the potential of the CCT-based CFD model to reveal differences in hemodynamics between the different pathological states, various hemodynamic parameters were analyzed with the aim of identifying the best suitable biomarkers to characterize pathological features of intraventricular flow.

4.1. Statistical Shape Model

The two developed SSMs, which are based on multi-phase CCT data of 125 patients after myocardial infarction, aimed at providing BCs for numerical modeling of intraventricular hemodynamics. This aim was successfully realized. Additionally, the SSMs allow to analyze LV shapes by comparison of modes identified by PCA. A comparison of the first three modes

showed differences in shapes and myocardial wall movement between the SSMs that are associated with presence of the LV aneurysm. The SSMs successfully represent the major features of the investigated pathology, including local shape changes due to aneurysm development and LV volume enlargement with sphericity change as well as an ability to represent hypokinetic segments caused by antero-apical, or antero-apical and basal LV aneurysms and/or scar formation. This affirms the potential ability of the SSM to be used as a diagnostic tool on its own as it was also proposed in other studies (47). However, our major aim was to describe the complex shape and contraction of the LVs in a simple way.

There is a set of earlier developed SSMs or so-called atlases for the LV (19, 47–50). Bai et al. (49) and Gilbert et al. (48) also give an overview of studies in which LV SSMs were developed. These SSMs were based on different imaging modalities including CT (19), MRI (47, 49), and echocardiography (50), which are - depending on spatial and temporal resolution - better or less suitable for subsequent use in numerical simulations. An SSM based on CCT can, however, be assumed to exhibit a robust quality regarding spatial resolution and independence of image quality from user-biases.

All of the SSMs, as well as ours, show a rather smooth ventricular shape neglecting the details of papillary muscles and trabeculae carneae. Also, the size of datasets used for SSM generation varies between approximately 100 as used in our study and several thousands. Both SSMs developed in our study describe 90 % shape variance with approximately 30 modes. Thus, the number of cases used to generate these SSMs as well as the representative cases A0ML, A0MH, and A1ML can be considered sufficient. However, the number of cases used to generate the representative cases A1MH, A1T, A1I, and A1HK seems to be low and should be increased in the future. The required number of modes to represent the shape variance is much larger than the number of modes describing the variance of normal subjects [e.g., eight in Bai et al. (49)]. A similar behavior can be noted by a SSM describing normal subjects as well as patients with dilated cardiomyopathy or with heart valve diseases, requiring 92 modes to describe 99 % shape variance (50). Beside the limited number of cases used in the development of the SSMs, the SSM methodology used in this study is limited to linear PCA. Nonlinear PCA (51) should be investigated in the future. Since SSMs simplify the shape and the contraction motion, these simplifications could be associated with uncertainties or bias in CFD results. This impact also requires to be investigated separately. Finally, it is desired in the future to extend the current SSM of the LV by shape models describing LA, ascending aorta as well as AV and MV.

Looking closer at the ventricular shape of the SSM-created mean shapes A1T, A1I, and A1HK (see **Figure 6** at t_1), one can see the curving and the characteristic neck resulting from myocardial thickening in case of A1T and the curving near the mid-LV anteroseptal and inferoseptal segment (segments 8 and 9) as described by Di Donato et al. (30). Regarding the mean shapes of cases A1T, A1I, and A1HK, less movement is observed in the aneurysmatic regions. We thus conclude the created mean shapes to represent the respective pathology in an adequate manner.

4.2. Left Ventricular Hemodynamics

The comparison of intraventricular flow features between SSM-based mean cases represents the major focus of this study. To analyze the intraventricular hemodynamics, a set of qualitative and quantitative measures were used, including large-scale flow features, energetic aspects, washout behavior as well as flow driving forces using pressure field information. These markers allow to identify differences between the investigated groups.

In an earlier study (29), we investigated four patient-specific cases each originating from one of the here presented cohorts A0ML, A0MH, A1ML, and A1MH. We found similar large-scale flow patterns in the representative and individual cases, with diastolic jets becoming less coherent with rising MR grade. This finding also correlates well with MRI-based observations (8) and is likely to be caused by the highly disturbed flow in the LA due to the regurgitation jet (29, 52). However, the individual cases showed a higher shape variability and complexity compared to the mean cases that results in higher individual differences regarding diastolic jet direction and regions of blood stagnation. Considering the impact of the MR on the intraventricular hemodynamics, we found increased systolic SED with rising MR grade in both individual and mean cases. This could be associated with an energy loss on small scales due to the regurgitation jet. This results in a lower energetic maximum of the SKE during systole and probably in a rising ratio of SKE at peak diastole to peak systole as also reported in the MRI study by Al-Wakeel et al. (8). Note, that the results associated with the regurgitation jet should be considered with caution due to a simplified modeling of the MV shape and generic valve opening and closing.

Considering differences in SKE between non-aneurysmatic and aneurysmatic cases A0ML, A0MH, A1ML, and A1MH, where SVs are comparable, the lower cyclic-mean of the aneurysmatic cases indicates a less energetic redirection of blood through these LVs, which may be caused by pathological contractions in aneurysm regions. This may lead to higher loads the LVs have to overcome to ensure a stable cardiac output and may in turn favor further remodeling (1).

Concerning the intraventricular pressure field, our results are in agreement with published pressure field distributions in a three-chamber view and the temporal course of apex-base pressure gradients (53). In the future, the pressure field analysis could be extended by an analysis of hemodynamic forces as described by Vallelonga et al. (54). Note, that the current numerical framework considers the LV as an isolated organ, thus impeding assessment of absolute pressure values. Extending the current model by a Lumped Parameter Model [e.g., a three-element Windkessel model as done by Gao et al. (55)] is a necessary next step to include an LA-LV and LV-arterial coupling.

Comparing the blood washout of the four mean cases (aneurysmatic and non-aneurysmatic with high and low MR), a better blood washout is observed in the non-aneurysmatic cases, matching clinical observations (56). As LVEDVs, SVs, and EFs of these four cases are comparable, the reason is likely to be found in the mean shapes and ventricular contraction. In the aneurysmatic cases, less movement is seen in the apex region (i.e., segments 13–17), possibly interfering with a suction effect and mixing in

this area. When we investigated the four patient-specific cases in Obermeier et al. (29), we contra-intuitively found a slightly better washout in the aneurysmatic-cases. Yet, the SVs of these cases were 25–30 % higher than those of the non-aneurysmatic cases. This may indicate SSM-based mean shapes to be less affected by individual variations and provide more generalizable results. However, such a statement must be tested in depth by comparing the mean cases to a variety of patient-specific cases.

Considering the washout, focus should be attended on the apex region because this is a region of high thrombus formation risk after myocardial infarction (57–59). These clinical studies also note thrombus formation occurring preferably in patients with anterior myocardial infarction, whereas thrombus formation in patients with inferior infarction or anterior infarction without severe apical-wall-motion abnormality is rare. This correlates well with our results, showing regions with poor washout behavior (especially in the apex region) as visible in **Figures 8**, **9** at 0.92 s.

Interesting observations are also made when comparing the washout of different aneurysm types (i.e., cases A1T, A1I, and A1HK). While the direct flow rate of fresh blood in case A1T (30.8 %) is in the same range as observed in healthy LVs (44 $\pm$ 11 %) (60), there is still 20 % of old blood present after eight cycles, which is high even in comparison to the other pathological states. This underlines the necessity in washout analysis to evaluate fresh as well as old blood. To emphasize is furthermore the extremely poor washout in case A1HK, in terms of fresh and old blood. A connection to the contraction field seems likely. In this case, less movement in basal and mid LV regions is visible, whereas the strongest movement is present in the apex. When viewing the pathway of blood (**Figure 9**) of case A1HK, movement and mixing can primarily be observed in longitudinal direction toward the apex, whereas mixing in radial direction is small. From these observations, a hypokinetic movement can be linked to an increased risk of thrombus formation in comparison to other aneurysm types.

Summing up, the SSM-created mean cases are able to represent characteristic flow features that were previously observed in patient-specific investigations of the respective pathology (higher systolic SED and less coherent diastolic jets in MR) and are in line with clinical observations (worse washout in aneurysmatic cases). Our findings show differences in intraventricular hemodynamics associated with different LV remodeling changes caused by myocardial infarction: local (aneurysm development) and global (volume and sphericity index increase) changes in shape as well as development of an MR of varying severity and abnormalities of the myocardial wall movement with hypokinetic segments. In combination with further model developments and investigations toward the selection of best suitable hemodynamic biomarkers assessing heart illnesses, the proposed numerical framework may support treatment decisions by distinguishing different pathological states from healthy states and among each other.

4.3. Model Discussion and Limitations

Modeling the complex LV anatomy and physiology in a way that points toward translation into clinical routine induces some simplifications, which are emphasized in the following.

The incorporation of valves with their complex shape and motion poses a major challenge in a detailed numerical modeling of the LV (39, 61). We modeled the valves in 2D via a porous baffle interface. This is a simplified approach, which delivered reasonable results in recent studies (38, 39). In our study, the 2D valve representation induced the formation of ring vortices below the MV during both E-wave and A-wave, as visible in the visualization of Q-criterion isosurfaces provided as **Supplementary Material**. These ring vortices were observed, e.g., in Ebbers et al. (53) and discussed in detail by Pedrizzetti et al. (1). In the Q-criterion visualizations it furthermore becomes visible, that with rising MR grade, vortex decay in diastole starts earlier, an observation that correlates well with the study of Al-Wakeel et al. (8).

In the MR-cases, a generic planar regurgitation area is applied, such that a reasonable pressure loss over the MV results and the case-specific MR grade (regurgitation volume in % of the SV) is met. Following this approach, the 3D character of the valves cannot be accounted for and the projected orifice area in diastole as well as during MR cannot be realized in a case-specific manner. This also includes the modeling of a regurgitation jet angle, which could not be obtained from our data base. As the here investigated cases are SSM-based and non-patient-specific, including these characteristics would, e.g., require an additional SSM per valve. As the valves and their movement could not be accurately captured in the available CCT data, this was not possible at current development state. The same applies for case-specific modeling of LA, aorta, papillary muscles, and trabeculae. Extending the model by these aspects is planned in future development steps. For a detailed discussion on the impact of these simplifications onto the intraventricular hemodynamics, the reader is referred to Obermeier et al. (29).

The LV motion is derived based on end-diastolic and end-systolic states. Temporal resolution of the CCT data did not allow for an accurate tracking of intermediate states. Consequently, phenomena as the torsional motion of the LV cannot be implemented. During systole, apex and base are rotating in opposite directions. This twisting mechanism is associated with a momentum change of blood, which may affect intraventricular flow patterns (62). Yet, the influence of LV torsional motion onto flow and energy dynamics was investigated via image-based CFD by Vasudevan et al. (63) and concluded to be insignificant. Similar results are reported from the image-based CFD model of Canè et al. (64), where torsional motion did not influence energy loss and only slightly affected velocity, vorticity and wall shear stress. Our approach of two-state-based deformation derivation is motivated by a minimization of data requirements of the computational model in the sense of a possible translation of the model to clinical routine workflows. Yet, the influence of neglecting intermediate states remains to be clarified in depth, e.g., via a study on the impact of different deformations on flow parameters like inflow orientation and vortex formation.

Last to discuss is the incorporated model for small scale flow features. In the context of turbulence analysis, a Large Eddy Simulation (LES) is more appropriate than RANS, due to the transitional flow regime (65, 66). Yet, the present study

does not focus turbulence on analysis. Further, the increasing requirements on the computational mesh as well as the need to compute a significantly larger number of cells when using LES does not align with the goal of a development toward clinical translation. Furthermore, in the context of ventricular assist devices, Zhang et al. (67) compared several turbulence models to experimental data, and all models reasonably replicated the fluid flow. A study opposing RANS and LES models in LV hemodynamics might, however, provide further insights.

5. CONCLUSION

The proposed CCT-based analysis of hemodynamics combined with SSM-based description of the heart shape and contraction pattern for subcohorts of patients seems to be a promising approach facilitating an analysis of intracardiac flow. Modeling of hemodynamics of mean shapes as a kind of reduced order modeling instead of patient-specific simulations could accelerate intracardiac flow analysis and reduce requirements in computational power that is necessary to translate the modeling-based analysis of intraventricular flow into the clinic. The proposed approach has the potential to increase the significance of CCT for diagnosis and treatment decisions. However, further enhancement of the computational framework, identification of suitable hemodynamic parameters as well as a clarification of the reduced order modeling level and its representativeness are necessary to embed the approach in clinical routine workflows to support clinicians.

DATA AVAILABILITY STATEMENT

The data sets (geometries and applied boundary conditions) presented in this study are provided as open data in an online repository. The name of the repository and accession number can be found at: doi: 10.6084/m9.figshare.19328687.

ETHICS STATEMENT

The studies involving human participants were reviewed and approved by the Ethics Committee - Charité Universitätsmedizin Berlin (EA2/177/20). The study was performed according to the principles of the Declaration of Helsinki.

AUTHOR CONTRIBUTIONS

LG, NS, CK, and TK: conceptualization. LO, ASz, NS, ON, and CK: data curation. LO, LT, KV, JB, HL, and ASc: formal analysis and methodology. LG and TK: funding acquisition and supervision. LO and ASc: visualization. LO, NS, ON, CK, and LG: investigation. LO, KV, ASz, LG, and NS: writing original draft. All authors: review and editing. All authors contributed to the article and approved the submitted version.

FUNDING

This study was funded by the Einstein Center Digital Future and by the DFG grants for the project Nr. 465178743 in frames of the SPP2311.

ACKNOWLEDGMENTS

The work was supported by the North-German Supercomputing Alliance (HLRN).

SUPPLEMENTARY MATERIAL

Visualizations of Q-criterion isosurfaces of all cases throughout the cardiac cycle are provided as Supplementary Material and can be found online at: https://www.frontiersin.org/articles/10.3389/fcvm.2022.901902/full#supplementary-material

REFERENCES

1. Pedrizzetti G, La Canna G, Alfieri O, Tonti G. The vortex–an early predictor of cardiovascular outcome? *Nat Rev Cardiol*. (2014) 11:545–53. doi: 10.1038/nrcardio.2014.75
2. Mele D, Smarrazzo V, Pedrizzetti G, Capasso F, Pepe M, Severino S, et al. Intracardiac flow analysis: techniques and potential clinical applications. *J Am Soc Echocardiogr*. (2019) 32:319–32. doi: 10.1016/j.echo.2018.10.018
3. Poh KK, Lee LC, Shen L, Chong E, Tan YL, Chai P, et al. Left ventricular fluid dynamics in heart failure: echocardiographic measurement and utilities of vortex formation time. *Eur Heart J Cardiovasc Imaging*. (2011) 13:385–93. doi: 10.1093/ejechocard/jer288
4. Abe H, Caracciolo G, Kheradvar A, Pedrizzetti G, Khandheria BK, Narula J, et al. Contrast echocardiography for assessing left ventricular vortex strength in heart failure: a prospective cohort study. *Eur Heart J Cardiovasc Imaging*. (2013) 14:1049–60. doi: 10.1093/ehjci/jet049
5. Vellguth K, Brüning J, Goubergrits L, Tautz L, Hennemuth A, Kertzscher U, et al. Development of a modeling pipeline for the prediction of hemodynamic outcome after virtual mitral valve repair using image-based CFD. *Int J Comput Assist Radiol Surg*. (2018) 13:1795–805. doi: 10.1007/s11548-018-1821-8
6. Faludi R, Szulik M, D'hooge J, Herijgers P, Rademakers F, Pedrizzetti G, et al. Left ventricular flow patterns in healthy subjects and patients with prosthetic mitral valves: an *in vivo* study using echocardiographic particle image velocimetry. *J Thorac Cardiovasc Surg*. (2010) 139:1501–10. doi: 10.1016/j.jtcvs.2009.07.060
7. Witschey WRT, Zhang D, Contijoch F, McGarvey JR, Lee M, Takebayashi S, et al. The influence of mitral annuloplasty on left ventricular flow dynamics. *Ann Thorac Surg*. (2015) 100:114–21. doi: 10.1016/j.athoracsur.2015.02.028
8. Al-Wakeel N, Fernandes JF, Amiri A, Siniawski H, Goubergrits L, Berger F, et al. Hemodynamic and energetic aspects of the left ventricle in patients with mitral regurgitation before and after mitral valve surgery. *J Mag Reson Imaging*. (2015) 42:1705–12. doi: 10.1002/jmri.24926
9. Su B, San Tan R, Le Tan J, Guo KWQ, Zhang JM, Leng S, et al. Cardiac MRI based numerical modeling of left ventricular fluid dynamics with mitral valve incorporated. *J Biomech*. (2016) 49:1199–205. doi: 10.1016/j.jbiomech.2016.03.008
10. Töger J, Kanski M, Carlsson M, Kovács SJ, Söderlind G, Arheden H, et al. Vortex ring formation in the left ventricle of the heart: analysis by 4D flow MRI and lagrangian coherent structures. *Ann Biomed Eng*. (2012) 40:2652–62. doi: 10.1007/s10439-012-0615-3
11. Lin E, Alessio A. What are the basic concepts of temporal, contrast, and spatial resolution in cardiac CT? *J Cardiovasc Comput Tomogr*. (2009) 3:403–8. doi: 10.1016/j.jcct.2009.07.003

12. Quarteroni A, Veneziani A, Vergara C. Geometric multiscale modeling of the cardiovascular system, between theory and practice. *Comput Methods Appl Mech Eng*. (2016) 302:193–252. doi: 10.1016/j.cma.2016.01.007
13. Doost SN, Ghista D, Su B, Zhong L, Morsi YS. Heart blood flow simulation: a perspective review. *Biomed Eng Online*. (2016) 15:101. doi: 10.1186/s12938-016-0224-8
14. Hirschhorn M, Tchantchaleishvili V, Stevens R, Rossano J, Throckmorton A. Fluid-structure interaction modeling in cardiovascular medicine - a systematic review 2017-2019. *Med Eng Phys*. (2020) 78:1–13. doi: 10.1016/j.medengphy.2020.01.008
15. Hellmeier F, Brüning J, Sündermann S, Jarmatz L, Schafstedde M, Goubergrits L, et al. Hemodynamic modeling of biological aortic valve replacement using preoperative data only. *Front Cardiovasc Med*. (2021) 7:1–10. doi: 10.3389/fcvm.2020.593709
16. Khalafvand SS, Zhong L, Ng EYK. Three-dimensional CFD/MRI modeling reveals that ventricular surgical restoration improves ventricular function by modifying intraventricular blood flow. *Int J Numer Method Biomed Eng*. (2014) 30:1044–56. doi: 10.1002/cnm.2643
17. Lantz J, Gupta V, Henriksson L, Karlsson M, Persson A, Carlhäll CJ, et al. Intracardiac flow at 4D CT: comparison with 4D flow MRI. *Radiology*. (2018) 289:51–58. doi: 10.1148/radiol.2018173017
18. Schoepf UJ, Varga-Szemes A. 4D flow meets CT: can it compete with 4D flow MRI? *Radiology*. (2018) 289:59–60. doi: 10.1148/radiol.2018181210
19. Khalafvand SS, Voorneveld JD, Muralidharan A, Gijsen FJH, Bosch JG, van Walsum T, et al. Assessment of human left ventricle flow using statistical shape modelling and computational fluid dynamics. *J Biomech*. (2018) 74:116–25. doi: 10.1016/j.jbiomech.2018.04.030
20. Bruse JL, Zuluaga MA, Khushnood A, McLeod K, Ntsinjana HN, Hsia TY, et al. Detecting clinically meaningful shape clusters in medical image data: metrics analysis for hierarchical clustering applied to healthy and pathological aortic arches. *IEEE Trans Biomed Eng*. (2017) 64:2373–83. doi: 10.1109/TBME.2017.2655364
21. Liang L, Liu M, Martin C, Elefteriades JA, Sun W. A machine learning approach to investigate the relationship between shape features and numerically predicted risk of ascending aortic aneurysm. *Biomech Model Mechanobiol*. (2017) 16:1519–33. doi: 10.1007/s10237-017-0903-9
22. Cosentino F, Raffa GM, Gentile G, Agnese V, Bellavia D, Pilato M, et al. Statistical shape analysis of ascending thoracic aortic aneurysm: correlation between shape and biomechanical descriptors. *J Pers Med*. (2020) 10:28. doi: 10.3390/jpm10020028
23. Hoeijmakers MJMM, Huberts W, Rutten MCM, van de Vosse FN. The impact of shape uncertainty on aortic-valve pressure-drop computations. *Int J Numer Method Biomed Eng*. (2021) 37:e3518. doi: 10.1002/cnm.3518
24. Rodero C, Strocchi M, Marciniak M, Longobardi S, Whitaker J, O'Neill MD, et al. Linking statistical shape models and simulated function in the healthy adult human heart. *PLoS Comput Biol*. (2021) 17:1–28. doi: 10.1371/journal.pcbi.1008851
25. Thamsen B, Yevtushenko P, Gundelwein L, Setio AAA, Lamecker H, Kelm M, et al. Synthetic database of aortic morphometry and hemodynamics: overcoming medical imaging data availability. *IEEE Trans Med Imaging*. (2021) 40:1438–49. doi: 10.1109/TMI.2021.3057496
26. Gambaruto AM, Taylor DJ, Doorly DJ. Decomposition and description of the nasal cavity form. *Ann Biomed Eng*. (2012) 40:1142–59. doi: 10.1007/s10439-011-0485-0
27. Keustermans W, Huysmans T, Danckaers F, Zarowski A, Schmelzer B, Sijbers J, et al. High quality statistical shape modelling of the human nasal cavity and applications. *R Soc Open Sci*. (2018) 5:181558. doi: 10.1098/rsos.181558
28. Brüning J, Hildebrandt T, Heppt W, Schmidt N, Lamecker H, Szengel A, et al. Characterization of the airflow within an average geometry of the healthy human nasal cavity. *Sci Rep*. (2020) 10:3755. doi: 10.1038/s41598-020-60755-3
29. Obermeier L, Vellguth K, Schlief A, Tautz L, Bruening J, Knosalla C, et al. CT-based simulation of left ventricular hemodynamics: a pilot study in mitral regurgitation and left ventricle aneurysm patients. *Front Cardiovasc Med*. (2022) 9:828556. doi: 10.3389/fcvm.2022.828556
30. Di Donato M, Castelvecchio S, Kukulski T, Bussadori C, Giacomazzi F, Frigiola A, et al. Surgical ventricular restoration: left ventricular shape influence on cardiac function, clinical status, and survival. *Ann Thoracic Surg*. (2009) 87:455–61. doi: 10.1016/j.athoracsur.2008.10.071
31. Du Bois D, Du Bois EF. Clinical calorimetry: tenth paper a formula to estimate the approximate surface area if height and weight be known. *Arch Intern Med*. (1916). XVII:863–71. doi: 10.1001/archinte.1916.00080130010002
32. Ritter F, Boskamp T, Homeyer A, Laue H, Schwier M, Link F, et al. Medical image analysis. *IEEE Pulse*. (2011) 2:60–70. doi: 10.1109/MPUL.2011.942929
33. Tautz L, Neugebauer M, Hüllebrand M, Vellguth K, Degener F, Sündermann S, et al. Extraction of open-state mitral valve geometry from CT volumes. *Int J Comput Assist Radiol Surg*. (2018) 13:1741–54. doi: 10.1007/s11548-018-1831-6
34. Cerqueira MD, Weissman NJ, Dilsizian V, Jacobs AK, Kaul S, Laskey WK, et al. Standardized myocardial segmentation and nomenclature for tomographic imaging of the heart. *J Cardiovasc Mag Reson*. (2002) 4:203–10. doi: 10.1081/JCMR-120003946
35. Di Donato M, Dabic P, Castelvecchio S, Santambrogio C, Brankovic J, Collarini L, et al. Left ventricular geometry in normal and post-anterior myocardial infarction patients: sphericity index and 'new' conicity index comparisons. *Eur J Cardiothoracic Surg*. (2006) 29:S225–30. doi: 10.1016/j.ejcts.2006.03.002
36. Lamecker H, Seebaß M, Hege HC, Deuflhard P. A 3D statistical shape model of the pelvic bone for segmentation. In: Fitzpatrick JM, Sonka M, editors. *Medical Imaging 2004: Image Processing. Vol. 5370. International Society for Optics and Photonics*. San Diego, CA: SPIE (2004). p. 1341–51.
37. Ricciardi MJ, Beohar N, Davidson CJ. Cardiac catheterization and coronary angiography. In: Rosendorff C, editor. *Essential Cardiology: Principles and Practice*. Totowa, NJ: Humana Press (2006). p. 197–219.
38. Schenkel T, Malve M, Reik M, Markl M, Jung B, Oertel H. MRI-Based CFD analysis of flow in a human left ventricle: methodology and application to a healthy heart. *Ann Biomed Eng*. (2009) 37:503–15. doi: 10.1007/s10439-008-9627-4
39. Daub A, Kriegseis J, Frohnapfel B. Replication of left ventricular haemodynamics with a simple planar mitral valve model. *Biomed Eng Biomed Technik*. (2020) 65:595–603. doi: 10.1515/bmt-2019-0175
40. Fuchsberger J, Aigner P, Niederer S, Plank G, Schima H, Haase G, et al. On the incorporation of obstacles in a fluid flow problem using a Navier-Stokes-Brinkman penalization approach. *J Comput Sci*. (2022) 57:101506. doi: 10.1016/j.jocs.2021.101506
41. Siemens Digital Industries Software. *Simcenter STAR-CCM+ User Guide v. 2021. 2.1*. Plano, TX: Siemens (2021).
42. Leyh RG, Schmidtke C, Sievers HH, Yacoub MH. Opening and closing characteristics of the aortic valve after different types of valve-preserving surgery. *Circulation*. (1999) 100:2153–60. doi: 10.1161/01.CIR.100.21.2153
43. Karimi S, Dabagh M, Vasava P, Dadvar M, Dabir B, Jalali P. Effect of rheological models on the hemodynamics within human aorta: CFD study on CT image-based geometry. *J Nonnewton Fluid Mech*. (2014) 207:42–52. doi: 10.1016/j.jnnfm.2014.03.007
44. Grünwald A, Korte J, Wilmanns N, Winkler C, Linden K, Herberg U, et al. Intraventricular hemodynamics in pediatric patients with single right ventricles reveal deteriorated washout and low vortex formation times: an in silico study. *bioRxiv*. (2020) doi: 10.1101/2020.12.13.422573
45. Dimasi A, Cattarinuzzi E, Stevanella M, Conti CA, Votta E, Maffessanti F, et al. Influence of mitral valve anterior leaflet in vivo shape on left ventricular ejection. *Cardiovasc Eng Technol*. (2012) 3:388–401. doi: 10.1007/s13239-012-0105-7
46. Durst F. *Grundlagen der Strömungsmechanik: eine Einführung in die Theorie der Strömungen von Fluiden*. Berlin; Heidelberg: Springer (2006).
47. Marciniak M, van Deutekom AW, Toemen L, Lewandowski AJ, Gaillard R, Young AA, et al. A three-dimensional atlas of child's cardiac anatomy and the unique morphological alterations associated with obesity. *Eur Heart J Cardiovasc Imaging*. (2021) 21:jeab271. doi: 10.1093/ehjci/jeab271
48. Gilbert K, Mauger C, Young AA, Suinesiaputra A. Artificial intelligence in cardiac imaging with statistical atlases of cardiac anatomy. *Front Cardiovasc Med*. (2020) 7:102. doi: 10.3389/fcvm.2020.00102
49. Bai W, Shi W, de Marvao A, Dawes TJ, O'Regan DP, Cook SA, et al. A bi-ventricular cardiac atlas built from 1000+ high resolution MR images of

healthy subjects and an analysis of shape and motion. *Med Image Anal*. (2015) 26:133–45. doi: 10.1016/j.media.2015.08.009
50. Carminati MC, Piazzese C, Pepi M, Tamborini G, Gripari P, Pontone G, et al. A statistical shape model of the left ventricle from real-time 3D echocardiography and its application to myocardial segmentation of cardiac magnetic resonance images. *Comput Biol Med*. (2018) 96:241–51. doi: 10.1016/j.compbiomed.2018.03.013
51. Brandt C, von Tycowicz C, Hildebrandt K. Geometric flows of curves in shape space for processing motion of deformable objects. *Comput. Graphics Forum*. (2016) 35:295–305. doi: 10.1111/cgf.12832
52. Le TB, Sotiropoulos F. On the three-dimensional vortical structure of early diastolic flow in a patient-specific left ventricle. *Eur J Mech B/Fluids*. (2012) 35:20–4. doi: 10.1016/j.euromechflu.2012.01.013
53. Ebbers T, Wigström L, Bolger AF, Wranne B, Karlsson M. Noninvasive measurement of time-varying three-dimensional relative pressure fields within the human heart. *J Biomech Eng*. (2002) 124:288–93. doi: 10.1115/1.1468866
54. Vallelonga F, Airale L, Tonti G, Argulian E, Milan A, Narula J, et al. Introduction to hemodynamic forces analysis: moving into the new frontier of cardiac deformation analysis. *J Am Heart Assoc*. (2021) 10:e023417. doi: 10.1161/JAHA.121.023417
55. Gao H, Feng L, Qi N, Berry C, Griffith BE, Luo X. A coupled mitral valve–left ventricle model with fluid-structure interaction. *Med Eng Phys*. (2017) 47:128–136. doi: 10.1016/j.medengphy.2017.06.042
56. Konishiike A, Mihata S, Matsumori Y, Nishian K, Ikeoka K, Yasutomi N, et al. [Blood flow patterns in the left ventricle in patients with myocardial infarction and ventricular aneurysm: evaluation using real-time two-dimensional Doppler echocardiography]. *J Cardiol*. (1987) 17:671–82.
57. Pöss J, Desch S, Eitel C, de Waha S, Thiele H, Eitel I. Left ventricular thrombus formation after st-segment-elevation myocardial infarction: insights from a cardiac magnetic resonance multicenter study. *Circ Cardiovasc Imaging*. (2015) 8:e003417. doi: 10.1161/CIRCIMAGING.115.003417
58. Delewi R, Nijveldt R, Hirsch A, Marcu CB, Robbers L, Hassell ME, et al. Left ventricular thrombus formation after acute myocardial infarction as assessed by cardiovascular magnetic resonance imaging. *Eur J Radiol*. (2012) 81:3900–4. doi: 10.1016/j.ejrad.2012.06.029
59. Asinger RW, Mikell FL, Elsperger J, Hodges M. Incidence of left-ventricular thrombosis after acute transmural myocardial infarction. Serial evaluation by two-dimensional echocardiography. *N Engl J Med*. (1981) 305:297–302. doi: 10.1056/NEJM198108063050601
60. Bolger A, Heiberg E, Karlsson M, Nordenmark L, Engvall J, Sigfridsson A, et al. Transit of blood flow through the human left ventricle mapped by cardiovascular magnetic resonance. *J Cardiovasc Magn Reson*. (2007) 9:741–7. doi: 10.1080/10976640701544530
61. Khalafvand SS, Xu F, Westenberg J, Gijsen F, Kenjeres S. Intraventricular blood flow with a fully dynamic mitral valve model. *Comput Biol Med*. (2019) 104:197–204. doi: 10.1016/j.compbiomed.2018.11.024
62. Codreanu I, Robson MD, Golding SJ, Jung BA, Clarke K, Holloway CJ. Longitudinally and circumferentially directed movements of the left ventricle studied by cardiovascular magnetic resonance phase contrast velocity mapping. *J Cardiovasc Mag Reson*. (2010) 12:48. doi: 10.1186/1532-429X-12-48
63. Vasudevan V, Wiputra H, Yap CH. Torsional motion of the left ventricle does not affect ventricular fluid dynamics of both foetal and adult hearts. *J Biomech*. (2019) 96:109357. doi: 10.1016/j.jbiomech.2019.109357
64. Canè F, Selmi M, De Santis G, Redaelli A, Segers P, Degroote J. Mixed impact of torsion on LV hemodynamics: A CFD study based on the Chimera technique. *Comput Biol Med*. (2019) 112:103363. doi: 10.1016/j.compbiomed.2019.103363
65. Chnafa C, Mendez S, Nicoud F. Image-based large-eddy simulation in a realistic left heart. *Comput Fluids*. (2014) 94:173–187. doi: 10.1016/j.compfluid.2014.01.030
66. Zingaro A, Dede' L, Menghini F, Quarteroni A. Hemodynamics of the heart's left atrium based on a Variational Multiscale-LES numerical method. *Eur J Mech B Fluids*. (2021) 89:380–400. doi: 10.1016/j.euromechflu.2021.06.014
67. Zhang J, Zhang P, Fraser KH, Griffith BP, Wu ZJ. Comparison and experimental validation of fluid dynamic numerical models for a clinical ventricular assist device. *Artif Organs*. (2013) 37:380–9. doi: 10.1111/j.1525-1594.2012.01576.x

Conflict of Interest: HL and ASz were employed by 1000shapes GmbH, which received funds from Charité-Universitätsmedizin Berlin to create the statistical shape model and perform the presented research in relation to the statistical shape model.

The remaining authors declare that the research was conducted in the absence of any commercial or financial relationships that could be construed as a potential conflict of interest.

Publisher's Note: All claims expressed in this article are solely those of the authors and do not necessarily represent those of their affiliated organizations, or those of the publisher, the editors and the reviewers. Any product that may be evaluated in this article, or claim that may be made by its manufacturer, is not guaranteed or endorsed by the publisher.

frontiers | Frontiers in Cardiovascular Medicine

ORIGINAL RESEARCH
published: 11 July 2022
doi: 10.3389/fcvm.2022.924899

Peripheral Microangiopathy Changes in Pulmonary Arterial Hypertension Related to Systemic Sclerosis: Data From a Multicenter Observational Study

Dilia Giuggioli[1], Valeria Riccieri[2], Edoardo Cipolletta[3], Nicoletta Del Papa[4], Francesca Ingegnoli[4], Amelia Spinella[1], Greta Pellegrino[2], Anna Maria Risa[3], Marco de Pinto[1], Silvia Papa[2], Giuseppe Armentaro[4] and Rossella De Angelis[3]*

[1] Scleroderma Unit, Rheumatology Unit, University Hospital of Modena and Reggio Emilia, Modena, Italy, [2] Scleroderma Clinic, Rheumatology Unit, Sapienza University of Rome, Rome, Italy, [3] Rheumatology Unit, Department of Clinical and Molecular Sciences, Polytechnic University of Marche, Ancona, Italy, [4] Clinical Rheumatology Unit, ASST Pini-CTO, Department of Clinical Science and Community Health, Università degli Studi di Milano, Milan, Italy

OPEN ACCESS

Edited by:
Sabina Gallina,
University of Studies G. d'Annunzio Chieti and Pescara, Italy

Reviewed by:
Francesco Bianco,
Azienda Ospedaliero Universitaria Ospedali Riuniti, Italy
Marco Matteo Ciccone,
University of Bari Aldo Moro, Italy

***Correspondence:**
Dilia Giuggioli
dilia.giuggioli@unimore.it

Specialty section:
This article was submitted to Cardiovascular Imaging, a section of the journal Frontiers in Cardiovascular Medicine

Received: 20 April 2022
Accepted: 22 June 2022
Published: 11 July 2022

Citation:
Giuggioli D, Riccieri V, Cipolletta E, Del Papa N, Ingegnoli F, Spinella A, Pellegrino G, Risa AM, de Pinto M, Papa S, Armentaro G and De Angelis R (2022) Peripheral Microangiopathy Changes in Pulmonary Arterial Hypertension Related to Systemic Sclerosis: Data From a Multicenter Observational Study.
Front. Cardiovasc. Med. 9:924899.
doi: 10.3389/fcvm.2022.924899

Systemic sclerosis (SSc) is a connective tissue disease characterized by immune-system alterations, fibrosis involving the skin and internal organs and diffuse microangiopathy. Pulmonary arterial hypertension (PAH) is a severe complication of SSc affecting about 10–15% of the patients and it is a leading cause of mortality. Due to the devastating nature of SSc-PAH, there is a clear need to systematically adopt appropriate screening programs. Nail fold videocapillaroscopy (NVC) studies have shown a more severe peripheral microvascular dysfunction in SSc patients with PAH suggesting that abnormalities in peripheral microcirculation may correlate with pulmonary microangiopathy. This is a cross-sectional study involving four tertiary University Rheumatology Units in the Center-North of Italy. Seventy patients, 35 adults with SSc and PAH confirmed by RHC (F/M 34/1; median age 65.2 ± 8.9 SD yrs), and 35 SSc patients without PAH were enrolled (F/M 3471; median age 63.3 ± 10.3 SD yrs). Clinical, laboratoristic and instrumental data were collected and NVC was performed in all patient. Specific NVC parameters were evaluated and a semi-quantitative rating scale was adopted to score these changes. Finally, patients were distributed into the suitable NVC pattern belonging to the scleroderma pattern. Our aim was to compare the peripheral microangiopathy changes in SSc patients with and without PAH, and to investigate the relationship between NVC findings and the main hemodynamic parameters of pulmonary vasculopathy. Patients with SSc-PAH+ showed a significant higher frequency of interstitial lung disease (ILD). No significant differences regarding clinical and laboratoristic parameters were observed. NVC abnormalities, avascular areas were more frequent in SSc patients with PAH, respect to those without ($p = 0.03$), and capillary density was significantly lower when considering grade 3 ($p = 0.02$). A higher NVC semiquantitative mean was found in SSc-PAH+ patients and a greater rate of the "late" pattern was detected in SSc-PAH+ subjects in respect to PAH- (57.1% vs. 25.7%) ($p = 0.03$). A significant correlations between pulmonary pressure values (sPAP by TTE and mPAP by RHC) and the capillary density (Spearman's rho 0.35, $p = 0.04$ for both).

Our findings provide additional evidence to the literature data, confirming that a higher degree of peripheral nailfold microangiopathy is more common in SSc-PAH patients, and further strengthening the concept that NVC changes may run parallel with similar abnormalities inside pulmonary microcirculation.

Keywords: systemic sclerosis, nailfold capillaroscopy, pulmonary arterial hypertension, echocardiography, right heart catheterization

INTRODUCTION

Pulmonary arterial hypertension (PAH) is a life-threatening and progressive disease characterized by vasoconstriction and remodeling of the pulmonary vasculature leading to increased pulmonary vascular resistance (PVR) that may result in right heart failure and death (1, 2).

According to the 6th World Symposium on Pulmonary Hypertension Task Force and the current Guidelines of the European Society of Cardiology/European Respiratory Society (ESC-ERS) (3, 4). PAH is defined by an elevated mean pulmonary arterial pressure (mPAP) >20 mmHg, normal pulmonary artery wedge pressure (PAWP) ≤15 mmHg, and elevated pulmonary vascular resistance (PVR) ≥3 Wood Units at rest. Some of the pathological changes involved with PAH are pulmonary endothelial dysfunction and inflammation promoting the remodeling of small- and medium-sized pulmonary arterioles thrombosis and obstruction of pulmonary blood vessels with proliferation of the vascular endothelium that may lead to the formation of the obstructive plexiform lesions (5). Recently, the possibility of a co-existing peripheral microangiopathy has been reported in idiopathic PAH (6, 7) and the peripheral microvascular changes play a decisive role also in systemic sclerosis (SSc). SSc is a challenging immune-mediated connective tissue disease (CTD) affecting skin and internal organs (8–11). SSc represents the main CTD associated with PAH occurring in approximately 10–15% of SSc patients (12–15). Despite the possibility of having new-targeted therapies, slowing down the progression of PAH, this condition is still a leading cause of death in SSc (16, 17). Therefore, an early accurate diagnosis should be mandatory to improve the survival of SSc patients (18). Nailfold video-capillaroscopy (NVC) is a well-known, validated, non-invasive imaging technique, which allows assessing peripheral microcirculation and diagnosing different diseases affecting peripheral microcirculation (19). Some NVC studies have shown a more severe peripheral microvascular dysfunction in SSc patients with PAH compared to those without PAH, suggesting that abnormalities in peripheral microcirculation may correlate with pulmonary microangiopathy (7, 20–24).

The aim of the present study was to compare the peripheral microangiopathy changes in SSc patients with and without PAH, and to investigate the relationship between NVC findings and the main hemodynamic parameters of pulmonary vasculopathy.

PATIENTS AND METHODS

This was a cross-sectional, case-control study involving four tertiary University Rheumatology Units in the Center-North of Italy with expertise in SSc diagnosis and management, as well as in NVC (19–21, 25, 26). PAH assessment was made by the local Cardiology Units with experience in right heart catheterization (RHC). All patients satisfied the ACR/EULAR 2013 classification criteria for SSc (27).

The DETECT-PAH algorithm (17, 18) was used to screen SSc patients and identify those with a high-risk of PAH. Briefly, the DETECT algorithm is a tool to identify patients with PAH in the asymptomatic stages, through the study of clinical variables, pulmonary function tests, immunological, biological, electrocardiographic and finally echocardiographic parameters. Those with a high PAH probability underwent RHC. On the contrary, RHC was not performed in those with a low probability of PAH due to ethical reasons.

Patients with SSc were divided into "cases," those with a high probability of PAH by DETECT-PAH algorithm and a RHC-confirmed diagnosis of PAH (mPAP>20 mmHg+PAWP≤15 mmHg + PVR≥3 Wood Units at rest) (3, 4) and "controls," those with a low probability of PAH by DETECT-PAH algorithm. Controls were matched for sex, age, and disease duration.

Written informed consent was obtained from all participants and data were collected in a general database. The study received approval from the local Ethical Committees and performed according to the Declaration of Helsinki.

The patients' demographic and clinical findings were carefully considered. Data collected at registration included: age, disease duration, type of skin subset (limited/diffuse), presence of Raynaud's phenomenon (RP), modified Rodnan skin score, other skin involvement (subcutaneous calcinosis, telangiectasia), digital ulcers-DUs, lung involvement, gastro-intestinal symptoms (dysphagia, reflux), cardiopulmonary signs and symptoms (heart failure, pericardial effusion, dilated cardiomyopathy), sicca syndrome (xerostomia/xeropthalmia), and joint involvement (tenosynovitis, arthritis, tendon friction rubs), as previously described (20, 21, 28). Laboratory and instrumental evaluations included antinuclear antibodies (ANA), anti-extractable nuclear antigens (anti-ENA), SSc-related antibodies (mainly anti-centromere/CENP-B and anti-topoisomerase I/Scl-70), diffusion capacity for carbon monoxide (DLCo) and high-resolution computed tomography-HRCT were reported (17, 18, 20, 21, 28).

Nailfold Videocapillaroscopy and Image Analysis

NVC was performed in all patients during their regular assessment (within 3-months before and after the RHC) using a videocapillaroscope with a 200x magnification optical contact probe. All fingers of both hands, excluding thumbs, were examined for each patient. Two adjacent fields of 1 mm in the middle of the nailfold were captured from all fingers at least, according to the current method (21, 25, 26). The derived digital

images were stored and the same experienced investigator for each Unit (FI, DG, RDA, VR), blinded to the clinical data, was responsible for reviewing and scoring the NVC images.

The following parameters were considered, according to previous categorizing methods: presence of enlarged/giant capillaries, micro-hemorrhages, loss of capillaries (avascularity), disorganization of the vascular bed, morphology (tortuous, ramified/bushy capillaries, bizarre loops). Altered capillary flow, appearing as granular/sludge and loops' length (normal/short/elongated loops), were evaluated.

A semi-quantitative rating scale was adopted to score these changes: grade 0 = no changes; 1 = < 33%; 2 = 33–66% 3 =>66% of changes on the total number of capillaries/mm. The mean score for each subject was obtained from the analysis of all fingers assessed (19, 26).

The degree of capillary density was considered to be 0 when capillaries were >9/mm, 1 for 7–9 capillaries/mm, 2 for 4–6 capillaries/mm and 3 for <4 capillaries/mm.

The rating system for avascular areas (avascularity of the capillary bed) was classified as follows: grade 0 = no obvious avascular areas; grade 1 = mild (one or two discrete areas of vascular deletion); grade 2 = moderate (more than two discrete areas of vascular deletion); grade 3 = severe (presence of large, confluent avascular areas). Finally, patients were distributed into the suitable NVC pattern belonging to the scleroderma pattern: (i) early (few giant capillaries, few hemorrhages, relatively preserved capillary distribution, not obvious loss of capillaries). (ii) active (frequent giant capillaries, frequent hemorrhages, moderate loss of capillaries with some avascular areas, mild disorganization of the capillary bed, absent or some ramified capillaries). (iii) late (irregular enlargement of the capillaries, few or absent giant capillaries, absence of hemorrhages, severe loss of capillaries with confluent avascular areas, severe disorganization of the capillary array, frequent ramified/bushy capillaries) (19).

Statistical Analysis

Qualitative variables (e.g., sex, clinical phenotype, organ involvement, laboratory data, medication use, and NVC findings) were reported using the absolute frequency and/or its corresponding percentage. Quantitative variables (e.g., age, diseases duration, echocardiographic and hemodynamic data) were reported using the mean ± the standard deviation (SD).

Baseline demographic, laboratory, and disease-related data were compared among cases and controls using the Chi-Square test (for qualitative variables) and Mann-Whitney U test (for quantitative variables). NVC findings were compared among those with and without a RHC-confirmed diagnosis of PAH using the Cochran-Armitage test for trend.

The correlation between hemodynamic and NVC findings was evaluated using the Spearman's rank correlation coefficient. A p value <0.05 was considered significant. The analyses were carried out using STATA v.14.

RESULTS

70 patients, 35 adults with SSc and PAH confirmed by RHC, and 35 disease controls, matched for sex, age, and disease duration were enrolled in the study. Demographic, clinical, laboratory and hemodynamic parameters of SSc patients, with and without PAH, are given in **Table 1**.

As regards NVC abnormalities, avascular areas were more frequent in SSc patients with PAH, respect to those without ($p = 0.03$), and capillary density was significantly lower when considering grade 3 ($p = 0.02$). Moreover, a higher NVC semiquantitative mean score (percentage of all abnormalities >66%) was found in SSc-PAH+ patients (**Table 2**). Finally, a greater rate of the "late" pattern was detected in SSc-PAH+ subjects in respect to PAH- (57.1% vs. 25.7%) ($p = 0.03$). When comparing the hemodynamic parameters in the group with PAH, we found significant correlations between pulmonary pressure values (mPAP by RHC) and the capillary density (Spearman's rho 0.35, $p = 0.04$ for both) (**Table 3**). No correlation between other abnormalities was detected, particularly regarding avascular areas (**Table 3**). **Figure 1** highlights the correlations between mPAP by RHC along with the capillary density scores, knowing that scores 0–1 and 2–3 have been paired to better illustrate the statistical difference.

DISCUSSION

The main result of our study was that a higher degree of peripheral nailfold microangiopathy, mainly avascular areas and low capillary density is more common in SSc-PAH patients.

Microvascular dysfunction plays a key role in SSc pathogenesis, leading to the typical clinical manifestations of the disease, such as RP, DUs, skin and internal organs involvement (9–11). Furthermore, endothelial disfunction and vascular inflammation in SSc result in accelerated atherosclerosis and macrovascular damage, as demonstrated by Ciccone et al. (29), which observed an increased carotid intima-media thickness values in SSc compared to NoSSc patients and controls.

Hearth is frequently affected, and the burden of cardiac complications leads to a reduction in life expectancy of these patients (12–15). In particular PAH is characterized by increased resistance of pulmonary vessels because of remodeling and obstruction of pulmonary arterioles with subsequent increase of the mean pulmonary artery pressure and is usually diagnosed 10 to 15 years after the onset of the disease, so the majority of the SSc patients are usually presented with serious manifestations, severe hemodynamic impairment and associated with poor prognosis and increased mortality especially in male subjects (18, 28, 30). Early screening through systematic evaluation of asymptomatic SSc patients could diagnose PAH at an early stage with a consequent better prognosis of the disease (17).

NVC is a safe, inexpensive, simple, and non-invasive imaging technique used to analyze the morphology of capillaries mainly in the nailfold area (19), providing a potential early screening tool for the diagnosis of otherwise asymptomatic organ involvement, such as PAH (31, 32).

Previous studies demonstrated some correlations between NVC abnormalities and the severity of internal organs involvement, including PAH (20, 23, 24, 30, 31). In a 3-year prospective study, the sequential loss of capillaries was

TABLE 1 | Demographic, clinical, laboratory and hemodynamic parameters of SSc patients, with and without pulmonary hypertension.

		SSc PAH+ ($n = 35$)	SSc PAH- ($n = 35$)	p-value
	Sex (F. %)	34 (97.1%)	34 (97.1%)	0.99
	Age (years. mean ± SD	65.2 ± 8.9	63.3 ± 10.3	0.38
	Disease duration (months)	166.7 ± 121.3	168.3 ± 13.4	0.61
Clinical phenotype	Limited	28 (80.0%)	24 (68.6%)	0.27
	Diffuse	7 (20.0%)	11 (31.4%)	
Organ involvement	Raynaud's phenomenon	35 (100.0%)	35 (100.0%)	0.99
	Interstitial lung disease	20 (57.1%)	11 (31.4%)	0.03*
	Digital ulcers	9 (25.7%)	18 (51.4%)	0.03*
	Joint involvement	8 (22.9%)	12 (34.3%)	0.29
	Teleangectasias	24 (68.6%)	19 (54.3%)	0.22
	Subcutaneous calcinosis	8 (22.9%)	7 (20.0%)	0.77
	Xerostomia	12 (34.3%)	15 (42.9%)	0.46
	Xerophtalmia	11 (31.4%)	16 (45.7%)	0.22
	Gastrointestinal involvement	23 (65.7%)	25 (71.4%)	0.61
	Cardiac involvement	17 (48.6%)	12 (34.3%)	0.23
	Skin Score	8.7 ± 9.4	7.5 ± 5.2	0.39
Treatments	PGAs	12 (34.3%)	16 (45.7%)	0.33
	ERAs	23 (65.7%)	12 (34.3%)	0.01
	PDE5Is	14 (40.0%)	7 (20.0%)	0.07
Laboratory data	Antinuclear antibodies	29 (82.9%)	35 (100.0%)	0.01*
	Anti-Scl70	8 (22.9%)	14 (40.0%)	0.12
	Anti-centromere	17 (48.6%)	17 (48.6%)	0.99
Echocardiographic and hemodynamic findings	Right atrial area	24.6 ± 4.6	/	/
	Tricuspid regurgitation gradient	49.9 ± 13.1	/	/
	sPAP	59.9 ± 18.3	/	/
	mPAP	36.0 ± 9.4	/	/
	PAWP	10.4 ± 4.1	/	/
	TPR (Wood units)	8.6 ± 4.7	/	/

PGAs, Prostacyclins and prostaglandins.
ERAs, Endothelin receptor antagonists.
PDE5Is, Phosphodiesterase inhibitors.
sPAP, Systolic pulmonary arterial pressure.
mPAP, Mean pulmonary arterial pressure.
PAWP, Pulmonary Artery Wedge Pressure.
TPR, Total Pulmonary Resistance.
$^*p < 0.05$.

recognized as a marker for the occurrence of PAH (31). SSc-PAH patients have also been associated with higher scores of capillary loss and disorganization of the nailfold capillary bed (32) and among observational studies, that employed RHC for PAH diagnosis, capillary density was found significantly reduced in SSc-PAH+ patients (21, 22, 32). In our study, the largest group of SSc-PAH+ patients so far investigated, we observed a significant extremely low degree of capillary density (<4 loops/mm) in PAH-SSc patients, in agreement with the finding of the previous studies. Our data confirmed the higher NVC rating scores more frequent in the SSc using the semi-quantitative assessment, in SSc-PAH group (**Table 2**) while, using the same scoring method for avascular area, we reported the higher frequency of capillary dropout in SSc-PAH+ patients (21) as reported in the literature studies (21, 22, 32). We also evaluated the different qualitative patterns across studies (21–24, 32). Corrado et al. (22) found that the percentage of patients presenting the more severe NVC patterns (active/late) was overall significantly greater in SSc-PAH+ compared to SSc-PAH- (73.2% vs. 50% respectively. Hofstee et al. (33) reported a lower capillary density in SSc with PAH, although loop dimensions were comparable. Finally, Riccieri et al. described more severe NVC patterns (active/late) in 11 (92%) and only in 5 (42%) patients, respectively (21). Our data are almost overlapping, confirming a higher significant percentage of the active/late pattern in our SSc-PAH+ patients ($p = 0.03$) (**Table 2**). It should be emphasized that both "active" and "late" patterns are characterized by the presence of discrete/large areas of capillary loss (19), reflecting a greater internal organs involvement in respect to the presence of the "early" pattern (34).

Our study confirmed even the relationship between echo and/or RHC detected mPAP, and capillary density, in particular the increase of PAP was related to the decrease of the

TABLE 2 | Capillaroscopic findings in patients with or without pulmonary hypertension (PAH).

	PAH+ (n° 35)				PAH- (n° 35)				
	Grade 0	**Grade 1**	**Grade 2**	**Grade 3**	**Grade 0**	**Grade 1**	**Grade 2**	**Grade 3**	***P-value***
Avascular areas	4 (11.4%)	7 (20.0%)	12 (34.3%)	12 (34.3%)	12 (34.3%)	11 (31.4%)	6 (17.1%)	6 (17.1%)	<0.01*
Loops' morphology	-	6 (17.1%)	13 (37.1%)	16 (45.7%)	-	14 (40.0%)	13 (37.1%)	8 (22.9%)	0.01
Capillary density	1 (2.9%)	3 (8.8%)	19 (55.9%)	11 (32.4%)	5 (14.3%)	9 (25.7%)	18 (51.4%)	3 (8.6%)	<0.01*
Loops' length	-	17 (48.6%)	18 (51.4%)	-	1 (2.9%)	17 (48.6%)	17 (48.6%)	-	0.63
Loops' dilatation	3 (8.6%)	11 (31.4%)	21 (60.0%)	-	6 (17.1%)	14 (40.0%)	14 (40.0%)	1 (2.9%)	0.19
Microhaemorrhages	9 (25.7%)	19 (54.3%)	7 (20.0%)	-	9 (25.7%)	11 (31.4%)	13 (31.7%)	5 (12.2%)	0.57
Loops' distribution	1 (2.9%)	2 (5.7%)	23 (65.7%)	9 (25.7%)	3 (8.6%)	4 (11.4%)	13 (37.1%)	11 (31.4%)	0.57
Capillary flow	1 (2.9%)	6 (17.1%)	16 (45.7%)	12 (34.3%)	-	11 (31.4%)	13 (37.1%)	11 (31.4%)	0.54
Mean NVC score	3 (8.6%)	17 (48.6%)	15 (42.9%)	-	9 (25.7%)	22 (62.9%)	4 (11.4%)	-	<0.01*
Scleroderma pattern	*NS*	*Early*	*Active*	*Late*	*NS*	*Early*	*Active*	*Late*	
	-	5 (14.3%)	10 (28.6%)	20 (57.1)	2 (5.7%)	12 (34.3%)	9 (25.7%)		<0.01*

NVC, Nailfold Videocapillary.
NS, Non specific pattern.
P < 0.05.

TABLE 3 | Correlation between capillaroscopic parameters and the main haemodynamic/echocardiographic findings regarding 35 SSc patients with pulmonary hypertension.

	mPAP		sPAP		Wood score		PAWP	
Scleroderma pattern	**Rho** 0.08	**p** 0.66	**Rho** 0.11	**p** 0.56	**Rho** 0.14	**p** 0.41	**Rho** 0.16	**P** 0.36
Loop length	0.09	0.63	0.16	0.38	0.14	0.43	0.30	0.08
Architectural distribution	0.00	0.99	0.10	0.60	0.07	0.68	0.23	0.18
Capillary density	0.35	0.04*	0.35	0.04*	0.14	0.42	0.10	0.56
Loops' morphology	0.15	0.48	0.29	0.11	0.14	0.43	0.06	0.75
Loops' dilatation	0.10	0.56	0.04	0.81	0.18	0.29	0.02	0.91
Avascular areas	0.03	0.85	0.10	0.60	0.15	0.38	0.07	0.67
Microhaemorrhages	0.04	0.84	0.09	0.73	0.05	0.78	0.20	0.06
Capillary flow	0.08	0.66	0.20	0.27	0.07	0.70	0.15	0.37
Mean NVC score	0.20	0.26	0.23	0.21	0.01	0.94	0.04	0.83

sPAP, Systolic pulmonary arterial pressure.
mPAP, Mean pulmonary arterial pressure.
PAWP, Pulmonary arterial wedge pressure.
NVC, Nailfold videocapillary.
**p< 0.05.*

number of nailfold capillaries. Preliminary data reported that increasing echocardiographically estimated sPAP correlates with the severity of the scleroderma pattern (34), particularly with the late pattern. Our data more consistently support the idea that a lower capillary density of the peripheral microcirculation reflects increased pressures at the pulmonary artery level (35). The NVC capillaries changes might reveal what is going on in the pulmonary circulation, supporting the possible hypothesis that nailfold microangiopathy may be related to those vascular abnormalities presenting in the pulmonary circulation with reduced capillary density and broad avascular areas. Another valuable observation of the study was the female prevalence in our PAH patients' cohort, confirming the registries worldwide PAH data showing a female predominance of pulmonary hypertension. Dysregulation of estrogen synthesis and metabolism seems to play a major role in these sex-related differences (28, 35), so further analyses on larger sample size are needed to better understand the penetrance of PAH in SSc women in order to translate to a better prognosis and/or a better quality of life. Finally, if the association between PAH and ILD is expected in SSc (17, 18), even together with NVC alterations (36), the lack of association with DU's is conflicting and needs of further investigation (37).

The study has also a few limitation. Although this was the largest multicentric study on this topic so far, the sample size is relatively small and it does not allow us to take into

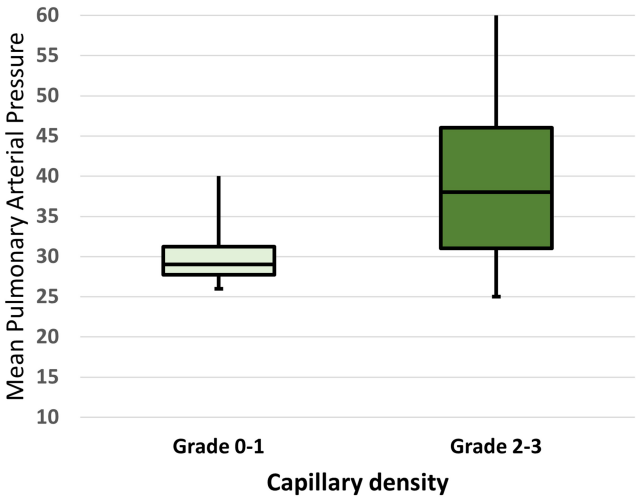

FIGURE 1 | Mean pulmonary arterial pressure (mPAP) in SSc patients with a capillary density score of 0–1 vs. 2–3. The horizontal line in the box represents the median, lower and upper boundaries of the box represent the 25th (Q1) and the 75th (Q3) percentiles. Whiskers represent the minimum and the maximum value. The minimum, 25th, 50th (median) and 75th percentile and maximum values were 26.0, 27.5, 29.0, 31.5, and 48.5 in those with capillary density score of 0–1. The minimum, 25th, 50th (median) and 75th percentile and maximum values were 25.0, 31.0, 38.0, 46.0, 60.0 in those with capillary density score of 2–3. *P*-value for comparison: 0.01.

account other potential confounders. Second, a formal reliability exercise among cardiologists performing echocardiographic examinations was not carried out before the study's start. However, the participating centers have a great experience in the diagnosis and management of SSc and followed shared procedural protocols.

In conclusion, we found precise NVC changes using both a specific evaluation system of avascular areas and capillary density, as well as a semi-quantitative evaluation scale of overall scores. More specifically, a clear association emerged between scores referring to low capillary density/avascular areas and the presence of PAH, also with respect to the qualitative assessment, through the scleroderma pattern late. In addition, low capillary density correlates directly with mean pulmonary pressure. Overall, our findings provide additional evidence to the literature data, confirming that a higher degree of peripheral nailfold microangiopathy is more common in SSc-PAH patients, and further strengthening the concept that NVC changes may run parallel with similar abnormalities inside pulmonary microcirculation (23, 24). If confirmed by further investigations in larger patients' series, NVC microvascular alterations could be included in the armamentarium of PAH early detection and so to contribute to a better survival of the patients. There is a need for prospective, multicenter, possibly cross-national studies to validate capillaroscopic findings in the early recognition of this life-threatening condition.

DATA AVAILABILITY STATEMENT

The original contributions presented in the study are included in the article/supplementary material, further inquiries can be directed to the corresponding author.

ETHICS STATEMENT

The studies involving human participants were reviewed and approved by Local Ethical Committees. The patients/participants provided their written informed consent to participate in this study.

AUTHOR CONTRIBUTIONS

All authors listed have made a substantial, direct, and intellectual contribution to the work and approved it for publication.

REFERENCES

1. Stamm JA, Risbano MG, Mathier MA. Overview of current therapeutic approaches for pulmonary hypertension. *Pulm Circ.* (2011) 1:138–59. doi: 10.4103/2045-8932.83444
2. Frumkin LR. The pharmacological treatment of pulmonary arterial hypertension. *Pharmacol Rev.* (2012) 64:583–620. doi: 10.1124/pr.111.005587
3. Galiè N, Humbert M, Vachiery J-L, Gibbs S, Lang I, Torbicki A, et al. 2015 ESC/ERS Guidelines for the diagnosis and treatment of pulmonary hypertension: the joint task Force for the Diagnosis and Treatment of Pulmonary Hypertension of the European Society of Cardiology (ESC) and the European Respiratory Society (ERS): Endorsed by: Association for European Pediatric and Congenital Cardiology (AEPC), International Society for Heart and Lung Transplantation (ISHLT). *Eur Respir J.* (2015) 46:90375. doi: 10.1183/13993003.01032-2015
4. Giuggioli D, Bruni C, Cacciapaglia F, Dardi F, De Cata A, Del Papa N, et al. Pulmonary arterial hypertension: guidelines and unmet clinical needs. *Reumatismo.* (2021) 72:228–46. doi: 10.4081/reumatismo.2020.1310
5. Firth AL, Mandel J, Juan J X-J. Idiopathic pulmonary arterial hypertension. *Dis Model Mech.* (2010) 3:268–73. doi: 10.1242/dmm.003616
6. Arvanitaki A, Giannakoulas G, Triantafyllidou E, Feloukidis C, Boutou AK, Garyfallos A, et al. Peripheral microangiopathy in precapillary pulmonary hypertension: a nailfold video capillaroscopy prospective study. *Respir Res.* (2021) 22:27. doi: 10.1186/s12931-021-01622-1
7. Arvanitaki A, Giannakoulas G, Triantafyllidou E, Karvounis H, Garyfallos A, Kitas G, et al. Nailfold videocapillaroscopy: a novel possible surrogate marker for the evaluation of peripheral microangiopathy in pulmonary arterial hypertension. *Scand J Rheumatol.* (2021) 50:85–94. doi: 10.1080/03009742.2020.1786854
8. Hachulla E, Launay D. Diagnosis and classification of systemic sclerosis. *Clin Rev Allergy Immunol.* (2011) 40:78–83. doi: 10.1007/s12016-010-8198-y
9. Denton CP, Khanna D. Systemic sclerosis. *Lancet.* (2017) 390:1685–99. doi: 10.1016/S0140-6736(17)30933-9
10. Varga J, Trojanowska M, Kuwana M. Pathogenesis of systemic sclerosis: recent insights of molecular and cellular mechanisms and therapeutic opportunities. *J Scleroderma Relat Disord.* (2017) 2:137–52. doi: 10.5301/jsrd.5000249
11. Ferri C, Arcangeletti MC, Caselli E, Zakrzewska K, Maccari C, Calderaro A, et al. Insights into the knowledge of complex diseases: environmental infectious/toxic agents as potential etiopathogenetic factors of systemic sclerosis. *J Autoimmun.* (2021) 124:102727. doi: 10.1016/j.jaut.2021.102727

12. Elhai M, Meune C, Avouac J, Kahan A, Allanore Y. Trends in mortality in patients with systemic sclerosis over 40 years: a systematic review and meta-analysis of cohort studies. *Rheumatology.* (2012) 51:1017–26. doi: 10.1093/rheumatology/ker269
13. Tyndall AJ, Bannert B, Vonk M, Airò P, Cozzi F, Carreira PE, et al. Causes and risk factors for death in systemic sclerosis: a study from the EULAR Scleroderma Trials and Research (EUSTAR) Database. *Ann Rheum Dis.* (2010) 69:1809–15. doi: 10.1136/ard.2009.114264
14. Steen VD, Medsger TA. Changes in causes of death in systemic sclerosis, 1972-2002. *Ann Rheum Dis.* (2007) 66:940–4. doi: 10.1136/ard.2006.066068
15. Elhai M, Meune C, Boubaya M, Avouac J, Hachulla E, Balbir-Gurman A, et al. Mapping and predicting mortality from systemic sclerosis. *Ann Rheum Dis.* (2017) 76:1897–905. doi: 10.1136/annrheumdis-2017-211448
16. Phung S, Strange G, Chung LP, Leong J, Dalton B, Roddy J, et al. Prevalence of pulmonary arterial hypertension in an australian scleroderma population: screening allows for earlier diagnosis. *Intern Med J.* (2009) 39:682–91. doi: 10.1111/j.1445-5994.2008.01823.x
17. Weatherald J, Montani D, Jevnikar M, Jaïs X, Savale L, Humbert M. Screening for pulmonary arterial hypertension in systemic sclerosis. *Eur Respir Rev.* (2019) 28:190023. doi: 10.1183/16000617.0023-2019
18. Humbert M, Yaici A, de Groote P, Montani D, Sitbon O, Launay D, et al. Screening for pulmonary arterial hypertension in patients with systemic sclerosis: clinical characteristics at diagnosis and long-term survival. *Arthritis Rheum.* (2011) 63:3522–30. doi: 10.1002/art.30541
19. Smith V, Herrick AL, Ingegnoli F, Damjanov N, De Angelis R, Denton CP, et al. EULAR study group on microcirculation in rheumatic diseases and the scleroderma clinical trials consortium group on capillaroscopy standardisation of nailfold capillaroscopy for the assessment of patients with Raynaud's phenomenon and systemic sclerosis. *Autoimmun Rev.* (2020) 19:102458. doi: 10.1016/j.autrev.2020.102458
20. Ingegnoli F, Ardoino I, Boracchi P, Cutolo M, Airò P, Ananieva LP. et. Nailfold capillaroscopy in systemic sclerosis: data from the EULAR Scleroderma Trials and Research (EUSTAR). *Database Microvasc Res.* (2013) 89:122–8. doi: 10.1016/j.mvr.2013.06.003
21. Riccieri V, Vasile M, Iannace N, Stefanantoni K, Sciarra I, Vizza CD, et al. Systemic sclerosis patients with and without pulmonary arterial hypertension: a nailfold capillaroscopy study. *Rheumatology (Oxford).* (2013) 52:1525–8. doi: 10.1093/rheumatology/ket168
22. Corrado A, Correale M, Mansueto N, Monaco I, Carriero A, Mele A, et al. Nailfold capillaroscopic changes in patients with idiopathic pulmonary arterial hypertension and systemic sclerosis-related pulmonary arterial hypertension. *Microvasc Res.* (2017)114:46–51. doi: 10.1016/j.mvr.2017.06.005
23. Smith V, Vanhaecke A, Vandecasteele E, Guerra M, Paolino S, Melsens K, et al. Nailfold videocapillaroscopy in systemic sclerosis-related pulmonary arterial hypertension: a systematic literature review. *J Rheumatol.* (2020) 1 47:888–95. doi: 10.3899/jrheum.190296
24. Minopoulou I, Theodorakopoulou M, Boutou A, Arvanitaki A, Pitsiou G, Doumas M, et al. Nailfold capillaroscopy in systemic sclerosis patients with and without pulmonary arterial hypertension: a systematic review and meta-analysis. *J Clin Med.* (2021) 10:1528. doi: 10.3390/jcm10071528
25. Gutierrez M, Bertolazzi C, Tardella M, Becciolini A, Di Carlo M, Dottori M, et al. Interreader reliability in assessment of nailfold capillary abnormalities by beginners: pilot study of an intensive videocapillaroscopy training programme. *J Rheumatol.* (2012) 39:1248–55. doi: 10.3899/jrheum.111299
26. Del Papa N, Pignataro F, Maglione W, Minniti A, Sambataro D, Valentini G, et al. High Nemo score values in nailfold videocapillaroscopy are associated with the subsequent development of ischemic digital ulcers in patients with systemic sclerosis. *Arthritis Res Ther.* (2020) 22:237. doi: 10.1186/s13075-020-02342-5
27. Van Den Hoogen F, Khanna D, Fransen J, Johnson SR, Baron M, Tyndall A, et al. 2013 classification criteria for systemic sclerosis: an American College of Rheumatology/European League against Rheumatism collaborative initiative. *Arthritis Rheum Dis.* (2013) 72:1747–55. doi: 10.1136/annrheumdis-2013-204424
28. De Angelis R, Giuggioli D, Bajocchi G, Dagna L, Zanframundo G, Foti R, et al. Sex-related differences in systemic sclerosis: a multicentre cross-sectional study from the National registry of the Italian Society for Rheumatology. *J Rheumatol.* (2022) 49:176–85. doi: 10.3899/jrheum.210794
29. Ciccone MM, Scicchitano P, Zito A, et al. Evaluation of differences in carotid intima-media thickness in patients affected by systemic rheumatic diseases. *Intern Emerg Med.* (2015) 10:823–30. doi: 10.1007/s11739-015-1250-4
30. Ruaro B, Confalonieri M, Salton S, Wade B, Baratella E, Geri P, et al. The relationship between pulmonary damage and peripheral vascular manifestation in systemic sclerosis patients. *Pharmaceuticals (Basel).* (2021) 14:403. doi: 10.3390/ph14050403
31. Avouac J, Lepri G, Smith V, Toniolo E, Hurabielle C, Vallet A, et al. Sequential nailfold videocapillaroscopy examinations have responsiveness to detect organ progression in sistemic sclerosis. *Semin Arthritis rheum.* (2017) 47:86–94. doi: 10.1016/j.semarthrit.2017.02.006
32. Sulli A, Pizzorni C, Smith V, Zampogna G, Ravera F, Cutolo M. Timing of transition between capillaroscopic patterns in systemic sclerosis. *Arthritis Rheum.* (2012) 64:821–25. doi: 10.1002/art.33463
33. Hofstee H, Noordegraaf AV, Voskuyl AE, Dijkmans B, Postmus P, Smulders Y, et al. Nailfold capillary density is associated with the presence and the severity of pulmonary arterial hypertension in systemic sclerosis. *Ann Rheum Dis.* (2009) 68:191–5. doi: 10.1136/ard.2007.087353
34. Sulli A, Paolino S, Pizzorni C, Ferrari G, Pacini G, Pesce G, et al. Progression of nailfold capillaroscopy patterns and correlation with organ involvement in systemic sclerosis. a 12-year study. *Rheumatology.* (2020) 59:105-—8. doi: 10.1093/rheumatology/kez374
35. Xia Z, Wang G, Xiao H, Guo S, Liu Y, Meng F, et al. Diagnostic value of nailfold videocapillaroscopy in systemic sclerosis secondary pulmonary arterial hypertension: a meta-analysis. *Intern Med J.* (2018) 48:1355–59. doi: 10.1111/imj.13968
36. Lemmers JMJ,Velauthapillai A, van Herwaarden N, Vonk MC. Change of microvascularization in systemic sclerosis, a matter of air. *Best Pract Res Clin Rheumatol.* (2021) 35:101683. doi: 10.1016/j.berh.2021.101683
37. Hughes M, Herrick A. Digital ulcers in systemic sclerosis. *Rheumatology.* (2017) 56:14–25. doi: 10.1093/rheumatology/kew047

Conflict of Interest: The authors declare that the research was conducted in the absence of any commercial or financial relationships that could be construed as a potential conflict of interest.

frontiers | Frontiers in Cardiovascular Medicine

REVIEW
published: 12 July 2022
doi: 10.3389/fcvm.2022.940560

Combined MitraClip and Left Atrial Appendage Occlusion: Is It Still a Utopia?

Martina Belli[1], Federico Zanin[1], Massimiliano Macrini[2], Lucy Barone[2], Massimo Marchei[2], Saverio Muscoli[2], Francesca Romana Prandi[1], Domenico Sergi[2], Marco Di Luozzo[2], Francesco Romeo[3†] and Francesco Barillà[1†]*

[1] Department of Systems Medicine, University Tor Vergata, Rome, Italy, [2] Division of Cardiology, University Hospital Tor Vergata, Rome, Italy, [3] Department of Departmental Faculty of Medicine, Unicamillus-Saint Camillus International, University of Health and Medical Sciences, Rome, Italy

Atrial fibrillation (AF) is the most common cardiac arrhythmia, affecting 32 million individuals worldwide, particularly the elderly. It is the main cause of ischemic strokes. Oral anticoagulation (OAC) is the gold standard strategy for stroke prevention. Still, there is a not negligible share of patients who have contraindications to this therapy, more frequently due to an increased risk of bleeding. AF is often associated with moderate-severe mitral regurgitation (MR), the second most frequent valvular disease in elderly patients. Data from the literature reported that more than half of patients with severe mitral regurgitation are not suitable candidates for cardiac surgery. Given the progressive aging of the population and the simultaneous increase in the number of patients with comorbidities, the advent of new therapeutic strategies, such as the combined approach of Left Atrial Appendage Occlusion (LAAO) and MitraClip procedure, is acquiring great interest. At present, the category of patients who may benefit from combined percutaneous therapies and the long-term risks and benefits might not have been identified. Despite the efforts of researchers, the correct selection of patients is a very important clinical need that has not yet been met to avoid committing human and financial resources to interventions that may be unnecessary. It is conceivable that the most modern and recent innovations in cardiovascular imaging, particularly three-dimensional echocardiography and new methods of volume imaging, could improve our ability to select patients appropriately. Since data in the literature are scarce, future studies will be needed to evaluate the efficacy and safety of combined MitraClip and LAA occlusion.

Keywords: MitraClip, Left Atrial Appendage Occlusion, percutaneous transcatheter mitral valve repair, atrial fibrillation, combined percutaneous procedures

OPEN ACCESS

Edited by:
Anna Vittoria Mattioli, University of Modena and Reggio Emilia, Italy

Reviewed by:
Pradyumna Agasthi, Mayo Clinic, United States
Tetsu Tanaka, University Hospital Bonn, Germany

***Correspondence:**
Francesco Barillà
francesco.barilla@uniroma2.it

[†] These authors share senior authorship

Specialty section:
This article was submitted to Cardiovascular Imaging, a section of the journal Frontiers in Cardiovascular Medicine

Received: *10 May 2022*
Accepted: *17 June 2022*
Published: *12 July 2022*

Citation:
Belli M, Zanin F, Macrini M, Barone L, Marchei M, Muscoli S, Prandi FR, Sergi D, Di Luozzo M, Romeo F and Barillà F (2022) Combined MitraClip and Left Atrial Appendage Occlusion: Is It Still a Utopia? Front. Cardiovasc. Med. 9:940560. doi: 10.3389/fcvm.2022.940560

INTRODUCTION

Population aging brings to the attention of cardiologists more and more complex patients with multiple comorbidities; therefore, the need for combined percutaneous procedures is affirming in the field of interventional cardiology. Atrial fibrillation (AF) is the most common cardiac arrhythmia, affecting 32 million individuals worldwide, and has a high impact on the costs of the health system (1). Its incidence increases with age, reaching about 6% in people over 60 (2). It is

characterized by grossly disorganized atrial electrical activity and an increased thromboembolic risk. It is responsible for 15–20% of cerebrovascular accidents of ischaemic origin. In non-valve atrial fibrillation (NVAF), 90% of blood clots form at the level of the left appendage, a small, ear-shaped sac in the muscle wall of the left atrium (3, 4). Anticoagulant therapy is the gold standard in reducing the risk of stroke, but about 1 in 10 patients do not receive anticoagulant therapy due to contraindications: previous bleeding, anemia, chronic renal failure, and liver cirrhosis (5). The current guidelines recommend anticoagulant therapy in patients with CHA2DS2-VASc score $\geq$2. Direct-Acting Oral Anticoagulants (DOACs) are recommended as first-line therapy in patients with NVAF, while Vitamin K Antagonist (VKAs) are used in AF patients with mechanical valve prosthesis or moderate-to-severe mitral stenosis. Lifelong dependence on anticoagulation in patients with AF is inevitably associated with an increased risk of bleeding complications as well as cardioembolic events in the event of inadequate therapy and, ultimately, significant lifestyle changes (e.g., consulting with the doctor before taking medications, certain vegetables, or supplements, regular blood tests and avoiding major dietary changes when taking VKAs) (6). Consequently, real-world data has demonstrated that the adherence to the therapy is poor, and up to 25–30% of patients stop OAC on long-term follow-up (7). AF in about 30% of cases is associated with mitral valve disease, more frequently with moderate-severe mitral regurgitation (MR) (8). MR is, after degenerative aortic stenosis, the second most frequent valvular disease in elderly patients, which, if not properly treated, has a very high mortality. More than half of patients with severe mitral regurgitation are not suitable candidates for cardiac surgery. Percutaneous transcatheter closure of the LAA and percutaneous transcatheter mitral valve repair with the MitraClip system are new therapeutic strategies in patients at high risk of hemorrhagic and cardioembolic events. The percutaneous repair procedure with the "edge to edge" technique using MitraClip is a procedure based on the same principle of surgical correction proposed by Alfieri in the early 90s: a double orifice valve is created through a permanent suture between the free margin of the two mitral flaps (9). Compared to conventional surgery, using a transcatheter antegrade approach, the MitraClip System (Abbott Vascular, Abbott Park, IL, USA) is less invasive. Percutaneous occlusion of LAA consists of the positioning of a device in the site where thrombi are most frequently allocated. Since 1949, heart surgeons have performed the combination of mitral valve repair and LAA exclusion in patients with MR and AF; the LAA occlusion is recommended in patients with AF who undergo heart surgery (10). These important clinical findings have prompted interventional cardiologists to start this combined approach percutaneously. The last ESC guidelines recommended the MitraClip procedure for symptomatic patients with severe primary or secondary MR, who are judged inoperable or at high risk for surgical repair and LAA closure, for stroke prevention, in patients with AF and contraindications for long-term anticoagulant treatment. Therefore, the purpose of this review is to evaluate the clinical aspects and advantages that can derive from performing the two procedures in the same session in selected groups of patients.

MITRACLIP

The MitraClip (Abbott Vascular Santa Clara, CA, USA) is a percutaneous mitral regurgitation repair procedure that consists of the insertion of one or more clips between the anterior and posterior mitral leaflets with the formation of a double orifice valve and subsequent reduction of the degree of regurgitation. The data of the EVEREST trials (11, 12). and results of registries (13) demonstrated that the MitraClip procedure was feasible and safer than surgical mitral-valve repair but was not as effective in reducing the severity of mitral regurgitation. More recently two trials, MITRA-FR (Percutaneous Repair with the MitraClip Device for Severe Functional/Secondary Mitral Regurgitation) and COAPT (Cardiovascular Outcomes Assessment of the MitraClip Percutaneous Therapy for Heart Failure Patients with Functional Mitral Regurgitation) assessed the efficacy and safety of MitraClip in patients with systolic heart failure and severe secondary MR (14, 15). A priori, these two trials targeted the different patient populations with the same disease using the same device but the results of these trials were diametrically opposed: MITRA-FR being neutral and COAPT being highly positive with respect to the efficacy of the MitraClip procedure. MITRA-FR and COAPT targeted the same disease entity with the same device, the MitraClip. However, COAPT enrolled a subset of patients who had more severe MR and less advanced LV disease (dilation/dysfunction) compared to patients with MITRA-FR. These differences may explain the different outcomes observed in COAPT vs. MITRA-FR. Indeed, patients with too severe LV (Left ventricle), or right ventricle, dilation/dysfunction (i.e., too extensive LV myocardial damage) may not benefit from the MitraClip procedure. In view of the results of the studies MITRA-FR and COAPT, it, therefore, seems reasonable to conclude that the MitraClip procedure reduces hospitalization of patients with heart failure and mortality in patients who fulfill the following criteria: (1) $\geq$ moderate-to-severe (3+) secondary MR, defined as EROA $\geq$30 mm^2 and/or regurgitant volume >45 ml; (2) LVEF between 20 and 50% and LV end-systolic diameter <70 mm) despite optimal (maximally tolerated) guideline-directed medical therapy (GDMT) with cardiac resynchronization and coronary revascularization if appropriate. Furthermore, the goal of the procedure should be to obtain an acute reduction of the MR severity to $\leq$ mild (1+) and the implantation of additional clips should be considered to achieve this goal (16). This procedure is currently indicated in patients affected by severe MR and prohibitive surgical risk, namely patients deemed not good surgical candidates for MitraClip after the discussion about the potential its feasibility (17). So the 2021 European Society of Cardiology Guidelines for the management of valvular heart disease recommended transcatheter edge-to-edge repair (TEER) with MitraClip, for patients with symptomatic, severe primary mitral regurgitation, that fulfill the echocardiographic criteria of eligibility and judged inoperable or at high surgical risk by

the Heart Team (class of recommendation IIb, level of evidence B). For patients with severe secondary mitral regurgitation, the ESC Guidelines recommended MitraClip procedure for selected symptomatic patients, not eligible for surgery and fulfilling criteria suggesting an increased chance of responding to the treatment (class of recommendation IIa, level of evidence B). At the same time, in high-risk symptomatic patients not eligible for surgery and not fulfilling the criteria suggesting an increased chance of responding to TEER, the Heart Team may consider in selected cases a MitraClip procedure (or other transcatheter valve therapy if applicable), after careful evaluation for ventricular assist device or heart transplant (18). Anatomical evaluation of the mitral valve, particularly in the degenerative form, is of fundamental importance for the feasibility of the MitraClip. The main contraindications are extensive calcifications on free margins of leaflets, area <3 cm^2, mean gradient >5 mmHg, perforation of leaflets, active endocarditis, rheumatic mitral valve disease.

PATIENT SELECTION AND IMAGING GUIDED MITRACLIP IMPLANTATION

The patient selection and pre-procedural echocardiographic evaluation, in particular, to diagnose the pathoanatomic mechanism, the severity of the mitral regurgitation, the right and left ventricular size and function, the left atrial size, pulmonary hypertension, and severity of tricuspid regurgitation are crucial to identify ideal candidates for MitraClip. We describe the procedure's steps in detail, stressing the importance of collaboration between the echocardiographer and the interventional cardiologist. Two-dimensional transesophageal echocardiography (2D TEE) is the primary imaging modality for the guidance of the procedure. Realtime three-dimensional (3D) TEE has recently been introduced as an additional imaging modality (**Figure 1**). In comparison with 2D TEE, 3D TEE provides additional information in some procedure steps, such as precise positioning of the clip delivery system into the left atrium, and correct alignment of the clip arms perpendicular to the coaptation line, and confirmation of the right grasping location (19). Biner et al. demonstrated that using 2D and 3D TEE in combination is associated with a remarkable 28% reduction in procedure times (20). Fluoroscopy provides additional helpful information on the positioning and distance for delivery catheter advancement and MitraClip positioning. Fluoroscopy provides good spatial and temporal resolution over a wide field of view with continuous monitoring and easy identification of devices. Still, it can only provide monoplane information, does not allow visualization of soft tissue, and is related to the use of ionizing radiation and contrast medium. The two methods are therefore complementary, and the most recent innovation, such as fluoroscopic-echocardiographic fusion imaging with the new EchoNavigator (Philips Medical System, Best, The Netherlands) and TrueFusion (Siemens Healthinners, Erlangen, Germany) systems, allows simultaneous acquisition of both fluoroscopic and echocardiographic images and co-registration, thus overcoming the limitations of the two methods. The coordinates of the two images are integrated into the same reference system, thus obtaining a hybrid image, which has the advantage of being easily interpretable by the interventional cardiologist since the echocardiographic images in which the soft tissues and the functional aspect (e.g., valve regurgitation jets) are well-visualized, are integrated in real-time in the standard fluoroscopic projections where the catheters and devices are easily identifiable (21).

MITRACLIP PROCEDURE

The procedure can be divided into six steps:

- Trans-septal puncture (after cannulation of femoral vein);
- Introduction of the steerable guide catheter (SGC) into the left atrium;
- Advancement of the clip delivery system (CDS) into the left atrium and positioning of the MitraClip below the mitral valve leaflets;
- Crossing the valve and advancing the CDS into the left ventricle;
- Grasping the leaflets;
- Assessment of the result.

Trans-Septal Puncture

The trans-septal approach and puncture are crucial; the latter is one of the most important aspects of the MitraClip procedure. The optimal puncture has to be superior and posterior across the interatrial septum. In degenerative MR, 4–5 cm are required from the exit point in the left atrium to the mitral annulus to allow good mobility of the system; in functional MR, the line of coaptation is usually below the plane of the mitral annulus due to extensive tethering. Therefore, the puncture site in these patients needs to be inferior and closer to the annular plane (about 3.5 cm above the annular plane). To establish the exact position of the puncture, the TEE is indispensable. The two-dimensional picture shows the so-called "tenting", i.e., the deformation that the pressure of the catheter exerts on the fossa ovalis before the tissue is passed through. To determine the exact point where the septum is perforated, three planes are needed with the 2D TEE: the bicaval view for superior-caudal orientation, the short-axis view for anteroposterior direction, and the four-chamber view to measure the height between the exit point and the annulus plane. In contrast, the 3D TEE provides all this information in a single image: a projection of the interatrial septum similar to the fluoroscopic left anterior oblique projection, including the mitral valve, allows a realistic visualization of the "tenting" and, in the same image, easily measures the distance between the puncture site and the mitral valve annulus.

Introduction of the Steerable Guide Catheter Into the Left Atrium

Once the septum is punctured, the guidewire is commonly positioned into the left upper pulmonary vein with care to avoid entering the left atrial appendage and the risk of perforation under fluoroscopic and TEE guidance.

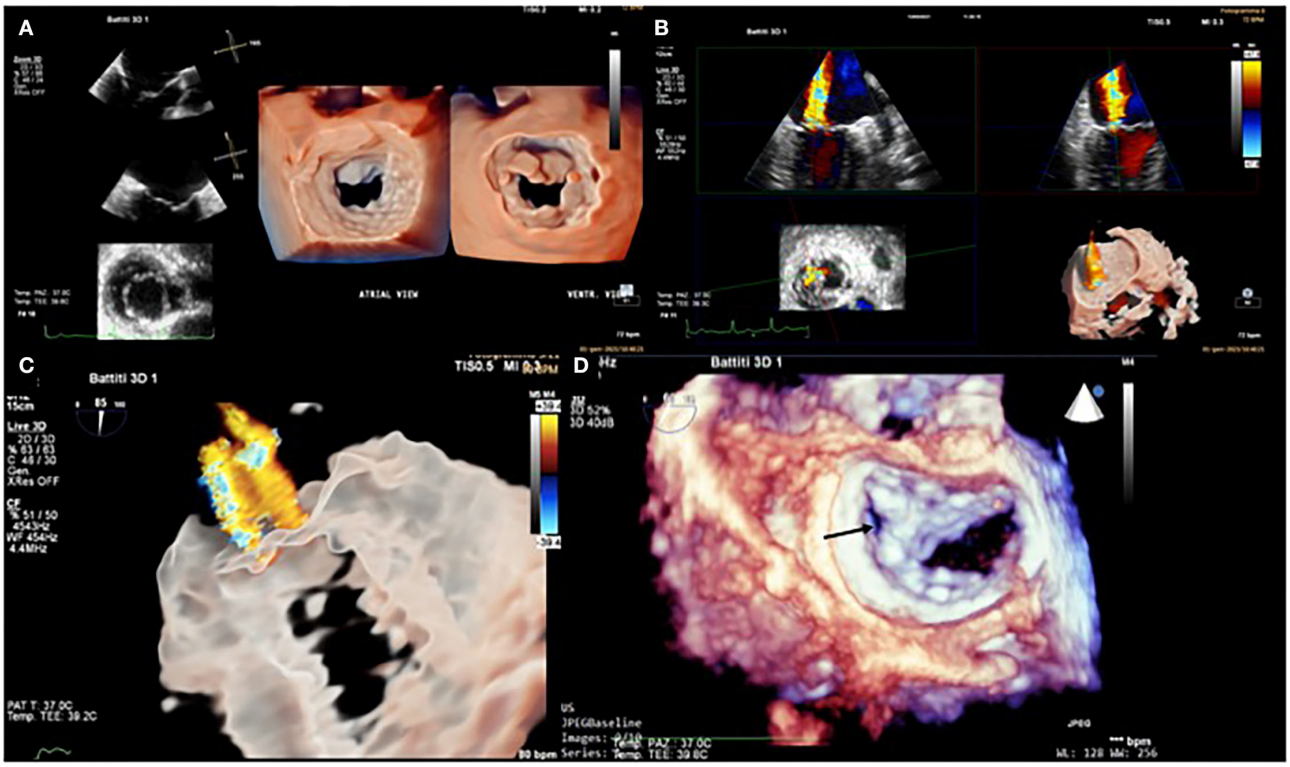

FIGURE 1 | Transesophageal echocardiogram. 3D mitral valve reconstruction with atrial view (or "surgeon's view") and ventricular view sergi **(A)**. Severe mitral regurgitation (MR) was documented with 3D color Doppler acquisition **(B)**. 3D Glass image of MR **(C)**. 3D mitral valve reconstruction (atrial view) after Mitra-Clip system placement in the lateral paracommissural region (black arrow) **(D)**.

Advancement of the Clip Delivery System Into the Left Atrium and Positioning of the MitraClip Below the Mitral Valve Leaflets

When the SGC is stably positioned in the left atrium, the guide wire is replaced by CDS. Then the catheter and clip are oriented toward the mitral valve by rotating the catheter 90°. For correct orientation, 2D ETE is essential, which uses two echocardiographic views: a 2-chamber view to establish the latero-medial position of the catheter and a long axis on the left ventricular outflow tract to establish its anteroposterior position. ETE 3D, on the other hand, allows real-time monitoring of maneuvers that position the catheter perfectly perpendicular to the line of mitral valve coaptation using a single 3D en face view.

Crossing the Valve and Advancing the CDS Into the Left Ventricle

Routinely, when the catheter is perpendicular to the valve plane, operators open the clip arms and orient them perpendicularly to the coaptation line of the leaflets. This step is critical as it will allow easier and faster grasping. In the routine practice, it is recommended to pass the opened clip into the left ventricle (22), many operators prefer to advance the clip closed, like Sherif et al. (23) at the site of the regurgitant jet under the mitral leaflets in the LVOT view under breath holding, because crossing the mitral valve with an open clip can cause it to rotate during translation from the left atrium to the left ventricle, prolonging the procedure.

Grasping the Leaflets

When the MitraClip is in a satisfactory position, the gripper is opened so as to grasp the leaflets between the grippers and the arms. This phase of the procedure is driven by the 2D ETE: identifying valve leaflets trapped between the grippers and the arms requires a high spatial and temporal resolution that 3D ETE does not yet possess. Once captured, the 3D ETE displays the clip attached to the two leaflets from a ventricular view, from which it is possible to evaluate the new morphology of the valve with the two neo-orifices. The presence of significant regurgitation may require a second clip. If the mean gradient is >5 mmHg and valve area <2 cm^2, this is contraindicated due to the risk of mitral stenosis.

Assessment of the Result

Residual mitral regurgitation with color Doppler is performed by rotating the TEE probe medially (clockwise) and laterally (anticlockwise) relative to the view showing the MitraClip. The pulmonary vein flow pattern is assessed with the aim of achieving a systolic dominant pattern. Intraprocedural monitoring of left atrial pressure and the presence of V waves is also commonly performed to assess the success of reducing or

eliminating significant mitral regurgitation (17). The mitral regurgitation quantification is dependent on pre and after-load of the left ventricle, general anesthesia, and whether inotropic or vasopressor drugs are used. This is especially the case for functional mitral regurgitation. In routine practice, 2D color Doppler imaging allows visual detection of residual mitral jets. The exact quantification of the grade of mitral regurgitation due to these multiple jets has yet to be validated, but their extension into the left atrium is routinely used. Then, an anatomical assessment of the valve using 3D echocardiography is performed to confirm that both leaflets are correctly and symmetrically joined by the clip or clips. If the result is satisfactory the clip is released, the delivery sheath is withdrawn back and the procedure is completed. At this point, it is essential to assess the size and the direction of shunting of the iatrogenic atrial sept defect because it appears that persistent interatrial shunting is associated with worse clinical outcomes and mortality (24).

LAA ANATOMY AND INDICATION FOR CLOSURE

Left Atrial Appendage (LAA) is mainly responsible for the formation of a thrombus that can cause strokes by embolization of the cerebral circulation (3). LAA is a structure derived from the primordial left atrium (LA), which develops during the third to sixth week of fetal cardiac development from the pulmonary venous bud and it has unique physiological characteristics (25). First of all, LAA is more compliant than the left atrium and has an important role in LA decompression during overload. The occlusion of LAA determined an improvement in the LA reservoir and conduit function. Moreover, LAA has an endocrine role. It accounts for the production of atrial natriuretic peptides (ANP) that contribute to natriuresis and diuresis. The distension of LAA is directly correlated with the production of ANP rather than elevation in the LA pressure or distension of the body of LA. For this reason, LAA closure can downregulate Renin-Angiotensin-Aldosterone System and Adrenergic Input (26). There are several morphological LAA classifications. The most commonly adopted one consists of four shapes: chicken-wing (∼48%; presence of a significant bend), windsock (∼19%; single dominant lobe without a significant bend), cactus (∼30%; dominant central lobe with multiple secondary lobes), and cauliflower (∼3%; short LAA without a dominant lobe that branches into several lobes) (27). The shape of the LAA may affect stroke risk. In particular, the presence of extensive trabeculations is correlated to higher risk. Furthermore, the LAA shape can increase the technical challenge for percutaneous LAA closure. Therefore, imaging is essential to pre-plan equipment selection and implantation strategy, to guide procedural device implantation, and also for device surveillance post implantation. The transesophageal echocardiography 2D (2D TOE) is routinely used in assessing LAA morphology, and recent 3D innovations such as multiplanar reconstruction (3D TOE MPR) and 3D TOE TrueView Glass rendering (**Figure 2**), have increased its accuracy. However, the gold standard in defining the morphology of the LAA remains the computed tomography (CT). LAA occlusion provides an alternative to oral anticoagulation for thromboembolic risk reduction in patients with nonvalvular atrial fibrillation (28). The earliest study was made by Madden et al. in 1948, which showed that the LAA was a source of thrombus formation in patients with AF and that its removal could prevent systemic thromboembolism (29). Subsequently, surgeons started to exclude progressively, the LAA during mitral valve intervention, in patients with AF. Over the years, many devise has been developed for the closure of the LAA by percutaneous interventional techniques. The first device designed for percutaneous LAA occlusion was the PLAATO device (Appriva Medical, Sunnyvale, California) (30). The device is made by a self-expanding nitinol cage covered by a polytetrafluoroethylene membrane. Despite the promising results, this device was taken off the market in 2016 (31). Currently, many percutaneous LAA closure devices have obtained CE mark. Watchman (Boston Scientific, Marlborough, MA, USA) and the Amplatzer Cardiac Plug (ACP) (Abbott, St Paul, MN, USA) are the most commonly used devices for mechanical orifice obstruction, and the Lariat device (SentreHEART, Redwood City, CA, USA) for epicardial suture ligation. The Watchman device is approved in many countries worldwide and is the only device studied in randomized trials, as well as in multicenter prospective non-randomized studies. The PROTECT AF (Watchman Left Atrial Appendage Closure Device for Embolic Protection in Patients with atrial Fibrillation) trial, a multicenter prospective RCT, established that the percutaneous LAA closure device was non-inferior to warfarin for the combined primary efficacy endpoint of cardiovascular mortality, all-cause mortality, and systemic thromboembolism (32). The PREVAIL (Prospective Randomized Evaluation of the Watchman Left Atrial Appendage Closure Device in Patients With Atrial Fibrillation vs. Long Term Warfarin Therapy) trial, was conducted to assess the safety and efficacy of LAA occlusion raised from the PROTECT AF study. The study concluded that LAA occlusion was non-inferior to warfarin for ischemic stroke prevention (33). For ACP and its second-generation, Amulet, multiple retrospective and prospective registries have reported successful device implantation in 95–100% of patients, with a low rate of major periprocedural adverse events. A recently published, industry-initiated, large, randomized, multi-center, trial (Amulet IDE trial), evaluating the safety and effectiveness of the Amulet occluder compared with the Watchman™ device, has shown that the Amulet occluder was non-inferior to safety and effectiveness of stroke prevention compared with the Watchman device (34). In light of the results of these trials, ESC guidelines suggest LAA closure, for stroke prevention, in patients with AF and contraindications for long-term anticoagulant treatment, e.g., intracranial bleeding without a reversible cause (class of recommendation IIb, level of evidence B) (35).

LAA IMPLANTATION TECHNIQUE

The LAA closure is implanted by a percutaneous procedure and is typically performed under general anesthesia or conscious sedation. Is reasonable to perform closure under general

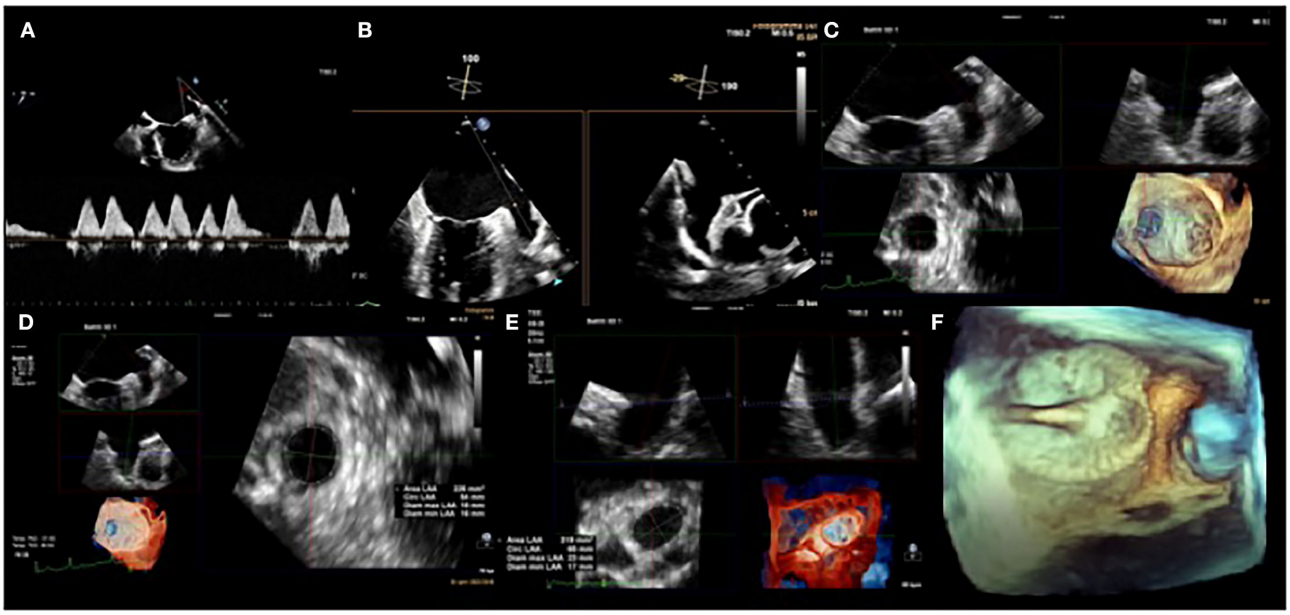

FIGURE 2 | Transesophageal echocardiogram. Left atrial appendage (LAA) flow velocity pattern by pulsed-wave Doppler **(A)**. 2D TEE biplane LAA assessment. Note how the appearance of the appendage varies in the different views **(B)**. 3D TEE evaluation of the LAA landing zone **(C)**, with post-processing analysis measurements of the diameters and the area of the LAA **(D,E)**. 3D colorized depth map of LAA occluder device using peri-operative TEE **(F)**.

anesthesia to ensure patient immobility and transesophageal monitoring. Intravenous or oral antibiotic prophylaxis is administered once before and also after the procedure. Right femoral access, under ultrasound or fluoroscopic guidance to avoid vascular complications, is recommended. It is preferred over left access, to give more stability to transeptal puncture. One of the most critical parts of the procedure is the transeptal puncture. It can be performed with traditional transseptal systems such as an SL-1 sheath and Brockenbrough (BRK) needle. It can be guided under fluoroscopy guidance but it is strongly recommended to perform under echographic (ICE or TEE) vision; as for the other procedures "fusion" could provide an added value: the preferred site is the postero-inferior portion of the fossa ovalis which ensures maximum co-axiality between the long axis of the auricle and the catheter. This ensures the best orientation of the catheter during device release to avoid as much as possible movement of the catheter within the LAA, a potential cause of wall damage. If a patent foramen ovale (PFO) or an atrial septal defect is present is reasonable to use that access to the left atrium. In this case, the access will be more anterior and the approach to the LAA can be more difficult. It is crucial to administer heparin (before or upon transseptal crossing for a target activated clotting time (ACT) of >250 s.

Once access to the left atrium is obtained, a wire is advanced into the left superior pulmonary vein and subsequently, a 14F access sheath is exchanged and it is advanced into the left atrium.

A pigtail catheter is advanced in the access sheath to reach LAA and perform angiography. Is important to position the pigtail catheter tip into the deepest lobe of LAA. A two orthogonal views angiography can be used to confirm the sizing of the device. It is advisable to oversize by 20% the diameter of the device to larger than the largest size to decrease the risk of leaks.

Once a device has been chosen, the pigtail catheter remains in the LAA to maintain its position and prevent the advancement of the sheath. Once the device is prepared and ready for insertion, the pigtail catheter can be removed and the delivery catheter can be inserted. The procedure is followed under fluoroscopy usually using the cranial RAO projection on which a 3D volume or 2D images TEE can be superimposed. This allows appreciation of the long axis of the LAA, the Coumadin ridge, and the left superior pulmonary vein, and the movement of the guidewire as it passes from the left superior pulmonary vein into the LAA. The delivery catheter and the access sheath will be connected and then both are pulled to unfold the device. During the deployment of the device is recommended to hold the breath or the ventilation to find the best position. Then the device is opened and the correct anchorage is verified with the "tug test". When the device is fully unfolded four elements (PASS criteria: P = position, A = anchor, S = size, S = seal), will be checked in fluoroscopy and TEE. If all four PASS criteria are met, the device can be released by rotating the delivery cable counterclockwise. A contract angiography of the left atrium can be performed to find the peri-device leak. Then the delivery cable can be retracted into the access sheath and removed. Femoral access can be closed by compression or vascular closure devices (36).

COMBINED INTERVENTION OF MITRACLIP AND LAA CLOSURE

The interest in combined percutaneous procedures is increasing in the field of interventional cardiology, especially in complex

patients with multiple comorbidities. Percutaneous transcatheter mitral valve repair with the MitraClip system and left appendage occlusion (LAAO), are new therapeutic strategies in older patients with severe mitral insufficiency and atrial fibrillation that are at both high-risk of cardioembolic events and bleeding.

Currently, limited evidence exists regarding the combined procedure of MitraClip and LAAO and is mainly derived from single clinical cases or small sample trials (maximum 25 patients enrolled) (37, 38), showing the technical feasibility and safety of the combined procedure.

The two combined procedures could have important advantages: first of all, a single trans-septal approach can reduce the risk of complications compared to double puncture, although at different sites. Furthermore, the use of large sheaths in two different positions may increase the risk of significant residual septal shunting (39). In addition, single venous access would be required with less risk of bleeding; the procedure and fluoroscopy times would be reduced as the initial steps are the same and this could also reduce the length of hospital stay. Certainly, there are some doubts about the position of the trans-septal puncture, since for the MitraClip it is indicated in the postero-superior position, but for LAAO it is indicated in the postero-inferior position of the fossa ovalis, so there is a risk of not having a correct alignment for the second procedure. Previous reports have demonstrated the feasibility and safety of LAAO in combination with MitraClip (40). The MitraClip procedure is generally performed before LAAO because it is more technically demanding. In addition, the device's presence in the LAA could lead to technical difficulties in the introduction of the MitraClip, especially in the phase of steering and rotation of the device in the left atrium. In the LAAO procedure, dedicated deflectable catheters can help overcome the lack of alignment and allow correct positioning of the prosthesis. However, if the coaxial LAA approach is impossible, a second transeptal should be performed to achieve an optimal LAAO. Another tricky aspect is femoral venous access, as a 24F delivery sheath is required for the MitraClip, and a 14F for LAAO, so if the MitraClip is done first, effective hemostasis must be ensured e.g., with Proglide systems to close the orifice around the sheath and reduce the risk of bleeding. So, in what order should the two procedures be carried out? Francisco et al. (39) suggested performing the LAAO first rather than the MitraClip which would require an exchange for a shorter sheath compatible with the 14F Watchman delivery sheath, to avoid massive bleeding at the access site and they found that the presence of the device in left appendage served as a useful anatomical reference during manipulation of the MitraClip delivery system. On the contrary, D'Amico et al. (41), performed the MitraClip first, favoring transseptal puncture, and then to ensure effective hemostasis by switching from a larger to a smaller caliber guide catheter, completed the intervention with LAAO previous an eight-lumen suture. Therefore, from a clinical standpoint, patients referred for MitraClip implantation frequently present a profile suitable for LAA occlusion and conversely. The combined approach has advantages: a single procedure involves a single transseptal puncture and single vascular access reducing the risk of complications, finally, overall fluoroscopy time may be reduced compared to two individual procedures. On the other hand, there are disadvantages: the high trans-septal puncture for the MitraClip is less well-suited for LAA occlusion and the overall procedure time may be prolonged, with an added risk of volume overload or hemodynamic instability, especially considering the severely depressed systolic function of many of these patients. A combined MitraClip and LAAO procedure appear to be feasible and safe, with a favorable medium-term outcome of thromboembolism, bleeding, and heart failure hospitalization. The positioning of embolic brain protection systems *via* trans-radial would also allow reducing complications associated with prolongation of the combined procedure (42).

CLINICAL IMPLICATIONS

The combined approach of MitraClip and LAAO is a great stimulating innovation in interventional cardiology, as through a minimally invasive approach and with relatively acceptable risk, it allows to treat elderly patients with both diseases in which the intervention of reparative surgery is contraindicated and in which due to high bleeding risk, there's a contraindication for systemic anticoagulation. In most cases, these are complex patients with chronic diseases, with important comorbidities and therefore in polypharmacy, in whom ischaemic and hemorrhagic risk assessment is essential. However, patient selection is of crucial importance for the success of the two combined interventional procedures.

CONCLUSION

Percutaneous MitraClip intervention and LAA closure are generally recommended procedures for patients with severe mitral insufficiency and AF, who are at high risk of both surgical valve repair and bleeding during anticoagulation treatment. Certainly, it is a very interesting area that could offer opportunities to treat fragile patients, guaranteeing an improvement in symptoms, functional capacity, and quality of life. Thanks to the latest imaging innovations and more sophisticated interventional techniques, combined treatments in the same session would not seem utopian and could be the best strategy for selected high-risk patients. However, there are still insufficient data in the literature; therefore, further studies and maybe RCT will be needed to evaluate the safety and the long-term efficacy of the MitraClip and LAAO combined approach.

AUTHOR CONTRIBUTIONS

MB and FB contributed to manuscript conceiving and revision. FZ, MMac, LB, MMar, SM, MD, DS, and FP contributed to data collection and literature review. All authors contributed to the article and approved the submitted version.

REFERENCES

1. Benjamin EJ, Muntner P, Alonso A, Bittencourt MS, Callaway CW, Carson AP et al. Heart disease and stroke statistics-2019 update: a report from the American Heart Association. *Circulation.* (2019) 139:e56–528. doi: 10.1161/CIR.0000000000000659
2. Morillo C, Banerjee A, Perel P, Wood D, Jouven X, et al. Atrial fibrillation: the current epidemic. *J Geriatr Cardiol.* (2017) 14:195–203.
3. Blackshear JL, Odell JA. Appendage obliteration to reduce stroke in cardiac surgical patients with atrial fibrillation. *Ann Thorac Surg.* (1996) 61:755–9. doi: 10.1016/0003-4975(95)00887-X
4. Crystal E, Connolly SJ. Role of oral anticoagulation in management of atrial fibrillation. *Heart*. (2004) 90:813–7. doi: 10.1136/hrt.2003.021642
5. Lowres N, Giskes K, Hespe C, Freedman B. Reducing stroke risk in atrial fibrillation: adherence to guidelines has improved, but patient persistence with anticoagulant therapy remains suboptimal. *Korean Circ J.* (2019) 49:883–907. doi: 10.4070/kcj.2019.0234
6. Cullen MW, Jonathan S, Piccini JP, Ansell JE, Fonarow GC, Hylek EM, et al. Risks and benefits of anticoagulation in atrial fibrillation: Insights from the Outcomes Registry for Better Informed Treatment of Atrial Fibrillation (ORBIT-AF) registry. *Circ Cardiovasc Qual Outcomes.* (2013) 6:461–9. doi: 10.1161/CIRCOUTCOMES.113.000127
7. Yao X, Abraham NS, Alexander GC, Crown W, Montori VM, Sangaralingham LR, et al. Effect of adherence to oral anticoagulants on risk of stroke and major bleeding among patients with atrial fibrillation. *J Am Heart Assoc.* (2016) 5:e003074. doi: 10.1161/JAHA.115.003074
8. Nieuwlaat R, Capucci A, Camm AJ, Olsson SB, Andresen D, Davies DW, et al. Atrial fibrillation management: a prospective survey in ESC member countries: the Euro Heart Survey on Atrial Fibrillation. *Eur Heart J.* (2005) 26:2422–34. doi: 10.1093/eurheartj/ehi505
9. Alfieri O, Maisano F, De Bonis M. P L Stefano, L Torracca, M Oppizzi, et al. The double-orifice technique in mitral valve repair: a simple solution for complex problems. *J Thorac Cardiovasc Surg.* (2001) 122:674–81. doi: 10.1067/mtc.2001.117277
10. Danna P, Sagone A, Proietti R, Arensi A, Viecca M, Santangeli P, et al. New technology for prevention of embolic events in atrial fibrillation: a systematic review on percutaneous endovascular left atrial appendage closure. *Giornale Ital Cardiol.* (2012) 13:571–82. doi: 10.1714/1133.12485
11. Glower DD, Kar S, Trento A, Lim DS, Bajwa T, Quesada R, et al. Percutaneous mitral valve repair for mitral regurgitation in high-risk patients: results of the EVEREST II study. *J Am Coll Cardiol.* (2014) 64:172–81. doi: 10.1016/j.jacc.2013.12.062
12. Feldman T, Wasserman HS, Herrmann HC, Gray W, Block PC, Whitlow P, et al. Percutaneous mitral valve repair using edge-to-edge technique: six month results of the EVEREST phase I Clinical Trial. *J Am Coll Cardiol.* (2005) 46:2134–40. doi: 10.1016/j.jacc.2005.07.065
13. Baldus S, Schillinger W, Frazen O, Bekeredjian R, Sievert H, Schofer J, et al. Mitraclip therapy in daily clinical practice: initial results from German transcatheter mitral valve interventions (TRAMI) registry. *Eur J Keart Fail.* (2012) 14:1050–5. doi: 10.1093/eurjhf/hfs079
14. Obadia JF, Messika-Zeitoun D, Leurent G, Iung B, Bonnet G, Piriou N, et al. Percutaneous repair or medical treatment for secondary mitral regurgitation. *N Engl J Med.* (2018) 379:2297–306. doi: 10.1056/NEJMoa1805374
15. Stone GW, Lindenfeld J, Abraham WT, Kar S, Lim DS, Mishell JM, et al. Transcatheter mitral-valve repair in patients with heart failure. *N Engl J Med.* (2018) 379:2307–18. doi: 10.1056/NEJMoa1806640
16. Pibarot P, Delgado V, Bax J. MITRA-FR vs. COAPT: lessons from two trials with diametrically opposed results. *Eur Heart J Cardiovasc Imaging.* (2019) 20:620–4. doi: 10.1093/ehjci/jez073
17. Katz WE, Smith AJ, Crock FW, Cavalcante JL. Echocardiographic evaluation and guidance for MitraClip procedure. *Cardiovasc Diagn Therapy*. (2017) 7:616–32. doi: 10.21037/cdt.2017.07.04
18. Vahanian A, Beyersdorf F, Pratz F, Milojevic M, Baldus S, Bauersachs J, et al. 2021 ESC/EACTS Guidelines for the management of valvular heart disease. *Eur Heart J.* (2022) 43:561–632. doi: 10.1093/ejcts/ezac209
19. Faletra FF, Leo LA, Murzilli R, Pedrazzini G, Pasotti E, Moccetti T. The emerging role of three-dimensional transesophageal echocardiography in guiding the MitraClip procedure. *Giornale Ital Cardiol.* (2015) 16:549–54. doi: 10.1714/2028.22038
20. Biner S, Perk G, Kar S, Rafique AM, Slater J, Shiota T, et al. Utility of combined two-dimensional and three-dimensional transesophageal imaging for catheter-based mitral valve clip repair of mitral regurgitation. *J Am Soc Echocardiogr.* (2011) 24:611–7. doi: 10.1016/j.echo.2011.02.005
21. Melillo F, Ancona F, Romano V, Ingallina G, Capogrosso C, Stella S, Montorfano M, Agricola E. Fusion imaging in structural heart interventions. *Giornale Ital Cardiol.* (2020) 21(4 Suppl. 2):34S—41S. doi: 10.1714/3336.33072
22. Wunderlich NC, Siegel RJ. Peri-interventional echo assessment for the MitraClip procedure. *Eur Heart J Cardiovasc Imaging.* (2013) 14:935–49. doi: 10.1093/ehjci/jet060
23. Sherif M A, Paranskaya L, Yuecel S, Kische S, Thiele O, D'Ancona G, et al. MitraClip step by step; how to simplify the procedure. *Neth Heart J.* (2017) 25:125–30. doi: 10.1007/s12471-016-0930-7
24. Schueler R, Öztürk C, Wedekind JA, Werner N, Stöckigt F, Mellert F, et al. Persistence of iatrogenic atrial septal defect after interventional mitral valve repair with the MitraClip system: a note of caution. *JACC Cardiovasc Interv.* (2015) 8:450–9. doi: 10.1016/j.jcin.2014.10.024
25. Al-Saady NM, Obel OA, Camm AJ. Left atrial appendage: structure, function, and role in thromboembolism. *Heart.* (1999) 82:547–54. doi: 10.1136/hrt.82.5.547
26. Tabata T, Oki T, Yamada H, Abe M, Onose Y, Thomas JD. Relationship between left atrial appendage function and plasma concentration of atrial natriuretic peptide. *Eur J Echocardiogr.* (2000) 1:130–7. doi: 10.1053/euje.2000.0019
27. Glikson M, Wolff R, Hindricks G, Mandrola J, Camm AJ, Lip GYH, et al. EHRA/EAPCI expert consensus statement on catheter-based left atrial appendage occlusion – an update. *Europace.* (2020) 22:184. doi: 10.1093/europace/euz258
28. Kar S, Doshi SK, Sadhu A, Horton R, Osorio J, Ellis C, et al. Primary outcome evaluation of a next-generation left atrial appendage closure devie. *Circulation.* (2021) 143:1754–62. doi: 10.1161/CIRCULATIONAHA.120.050117
29. Madden JL. Resection of the left auricular appendix: a prophylaxis for recurrent arterial emboli. *J Am Med Assoc.* (1949) 140:769–72. doi: 10.1001/jama.1949.02900440011003
30. Sievert H, Lesh MD, Trepels T. Omran h, Bartorelli A, Della Bella P, et al. Percutaneous left atrial appendage transcatheter occlusion to prevent stroke in high-risk patients with atrial fibrillation: early clinical experience. *Circulation.* (2002) 105:1887–9. doi: 10.1161/01.CIR.0000015698.54752.6D
31. Park JW, Leithäuser B, Gerk U, Vrsansky M, Jung F. Percutaneous left atrial appendage transcatheter occlusion (PLAATO) for stroke prevention in atrial fibrillation: 2-year outcomes. *J Invasive Cardiol.* (2009) 21:446–50.
32. Reddy VY, Doshi SK, Sievert H, Buchbinder M, Neuzil P, Huber K, et al. Percutaneous left atrial appendage closure for stroke prophylaxis in patients with atrial fibrillation: 23-Year Follow-up of the PROTECT AF (Watchman Left Atrial Appendage System for Embolic Protection in Patients With Atrial Fibrillation). *Trial Circ.* (2013) 127:720–9. doi: 10.1161/CIRCULATIONAHA.112.114389
33. Holmes DR, Kar S, Price MJ, Whisenant B, Sievert H. Doshi SK, et al. Prospective randomized evaluation of the Watchman Left Atrial Appendage Closure device in patients with atrial fibrillation versus long-term warfarin therapy: the PREVAIL trial. *J Am Coll Cardiol.* (2014) 64:1–12. doi: 10.1016/j.jacc.2014.04.029
34. Saad M, Risha O, Sano M, Fink T, Heeger CH, Vogler J, et al. Comparison between Amulet and Watchman left atrial appendage closure devices: a real-world, single center experience. *Int J Cardiol Heart Vasc.* (2021) 37:100893. doi: 10.1016/j.ijcha.2021.100893
35. Hindricks G, Potpara T, Dagres N, Arbelo E, Bax JJ, Blomström-Lundqvist C, et al. 2020 ESC Guidelines for the diagnosis and management of atrial fibrillation developed in collaboration with the European Association for Cardio-Thoracic Surgery (EACTS): The Task Force for the diagnosis and management of atrial fibrillation of the European Society of Cardiology (ESC) Developed with the special contribution of the European Heart Rhythm Association (EHRA) of the ESC. *Eur Heart J.* (2021) 42:373–498. doi: 10.1093/eurheartj/ehab648

36. Di Biase L, Santangeli P, Anselmino M, Mohanty P, Salvetti I, Gili S, et al. Does the left atrial appendage morphology correlate with the risk of stroke in patients with atrial fibrillation? Results from a multicenter study. *J Am Coll Cardiol.* (2012) 60:531–8. doi: 10.1016/j.jacc.2012.04.032
37. Kuwata S, Taramasso M, Zuber M, Guetsch G, Attinger-Toller A, Wicki D, et al. Feasibility of concomitant MitraClip and left atrial appendage occlusion. *EuroIntervention.* (2017) 12:1940–5. doi: 10.4244/EIJ-D-16-00784
38. Tichelbäcker T, Puls M, Jacobshagen C, Hasenfuß G, Schillinger W, Hünlich M, et al. MitraClip® and Amplatzer® cardiac plug implantation in a single procedure: a reasonable approach? *Int J Cardiol.* (2016) 220:107–11. doi: 10.1016/j.ijcard.2016.06.170
39. Francisco AR, de Oliveira EI, Menezes MN, Ferreira PC, da Silva PC, Nobre A, et al. Pinto Combined MitraClip implantation and left atrial appendage occlusion using the Watchman device: A case series from a referral center. *Rev Port Cardiol.* (2017) 36:525–32. doi: 10.1016/j.repc.2016.11.012
40. D'Amico G, Estèvez-Loureiro R, Rofastes XF, Ronco F, Nombela-Franco L, Melica B, et al. Combined procedure of percutaneous mitral valve repair and left atrial appendage occlusion: a multicenter study. *JACC Cardiovasc Intervent.* (2021) 14:590–2. doi: 10.1016/j.jcin.2020.11.030
41. D'Amico G, Fabris T, Fraccaro C, Tarantini G. Combined percutaneous procedure of mitral valve repair with the edge-to-edge technique and left atrial appendage occlusion. *Giornale Ital Cardiol.* (2019) 20(3 Suppl. 1): 35S–9S. doi: 10.1714/3121.31040
42. Cammalleri V, Ussia GP, Muscoli S, De Vico P, Romeo F. Transcatheter occlusion of left atrial appendage with persistent thrombus using a trans-radial embolic protection device. *J Cardiovasc Med.* (2016) 17(Suppl. 2):e224. doi: 10.2459/JCM.0000000000000323

Conflict of Interest: The authors declare that the research was conducted in the absence of any commercial or financial relationships that could be construed as a potential conflict of interest.

Publisher's Note: All claims expressed in this article are solely those of the authors and do not necessarily represent those of their affiliated organizations, or those of the publisher, the editors and the reviewers. Any product that may be evaluated in this article, or claim that may be made by its manufacturer, is not guaranteed or endorsed by the publisher.

frontiers | Frontiers in Cardiovascular Medicine

TYPE Original Research
PUBLISHED 24 August 2022
DOI 10.3389/fcvm.2022.915074

OPEN ACCESS

EDITED BY
Anna Vittoria Mattioli,
University of Modena and Reggio Emilia, Italy

REVIEWED BY
Giuseppe De Nisco,
Polytechnic University of Turin, Italy
Francesco Sturla,
IRCCS San Donato Polyclinic, Italy

*CORRESPONDENCE
Katharina Vellguth
katharina.vellguth@charite.de

†These authors share last authorship

SPECIALTY SECTION
This article was submitted to Cardiovascular Imaging, a section of the journal Frontiers in Cardiovascular Medicine

RECEIVED 07 April 2022
ACCEPTED 12 July 2022
PUBLISHED 24 August 2022

CITATION
Vellguth K, Barbieri F, Reinthaler M, Kasner M, Landmesser U, Kuehne T, Hennemuth A, Walczak L and Goubergrits L (2022) Effect of transcatheter edge-to-edge repair device position on diastolic hemodynamic parameters: An echocardiography-based simulation study.
Front. Cardiovasc. Med. 9:915074.
doi: 10.3389/fcvm.2022.915074

Effect of transcatheter edge-to-edge repair device position on diastolic hemodynamic parameters: An echocardiography-based simulation study

Katharina Vellguth [1]*, Fabian Barbieri[2], Markus Reinthaler[2,3], Mario Kasner[2], Ulf Landmesser[2,4,5], Titus Kuehne[1,4,6], Anja Hennemuth[1,7], Lars Walczak[1,7†] and Leonid Goubergrits[1,8†]

[1]Institute of Computer-Assisted Cardiovascular Medicine, Charité—Universitätsmedizin Berlin, Corporate Member of Freie Universität Berlin and Humboldt-Universität zu Berlin, Berlin, Germany, [2]Department of Cardiology, Charité—Universitätsmedizin Berlin, Corporate Member of Freie Universität Berlin and Humboldt-Universität zu Berlin, Berlin, Germany, [3]Institute of Active Polymers and Berlin-Brandenburg Center for Regenerative Therapies, Helmholtz-Zentrum Hereon, Teltow, Germany, [4]German Center for Cardiovascular Research (DZHK), Berlin, Germany, [5]Berlin Institute of Health at Charité—Universitätsmedizin Berlin, Berlin, Germany, [6]Deutsches Herzzentrum der Charité—Medical Heart Center of Charité and German Heart Institute Berlin, Berlin, Germany, [7]Fraunhofer MEVIS, Bremen, Germany, [8]Einstein Center Digital Future, Berlin, Germany

Background: Transcatheter edge-to-edge repair (TEER) has developed from innovative technology to an established treatment strategy of mitral regurgitation (MR). The risk of iatrogenic mitral stenosis after TEER is, however, a critical factor in the conflict of interest between maximal reduction of MR and minimal impairment of left ventricular filling. We aim to investigate systematically the impact of device position on the post treatment hemodynamic outcome by involving the patient-specific segmentation of the diseased mitral valve.

Materials and methods: Transesophageal echocardiographic image data of ten patients with severe MR (age: 57 ± 8 years, 20% female) were segmented and virtually treated with TEER at three positions by using a position based dynamics approach. Pre- and post-interventional patient geometries were preprocessed for computational fluid dynamics (CFD) and simulated at peak-diastole with patient-specific blood flow boundary conditions. Simulations were performed with boundary conditions mimicking rest and stress. The simulation results were compared with clinical data acquired for a cohort of 21 symptomatic MR patients (age: 79 ± 6 years, 43% female) treated with TEER.

Results: Virtual TEER reduces the mitral valve area (MVA) from 7.5 ± 1.6 to 2.6 ± 0.6 cm^2. Central device positioning resulted in a 14% smaller MVA than eccentric device positions. Furthermore, residual MVA is better predictable for central than for eccentric device positions (R^2 = 0.81 vs. R^2 = 0.49). The MVA

reduction led to significantly higher maximal diastolic velocities (pre: 0.9 ± 0.2 m/s, post: 2.0 ± 0.5 m/s) and pressure gradients (pre: 1.5 ± 0.6 mmHg, post: 16.3 ± 9 mmHg) in spite of a mean flow rate reduction by 23% due to reduced MR after the treatment. On average, velocities were 12% and pressure gradients were 25% higher with devices in central compared to lateral or medial positions.

Conclusion: Virtual TEER treatment combined with CFD is a promising tool for predicting individual morphometric and hemodynamic outcomes. Such a tool can potentially be used to support clinical decision making, procedure planning, and risk estimation to prevent post-procedural iatrogenic mitral stenosis.

KEYWORDS

mitral valve, mitral regurgitation, transcathether edge-to-edge repair, iatrogenic mitral stenosis, patient-specific, therapy planning, computational fluid dynamics

1. Introduction

Mitral regurgitation (MR) is one of the leading acquired valvular heart diseases in western societies with an increasing prevalence in people over 65 years of age (1, 2). The overall number of cases will rise further with increasing life expectancy and a growing population. While the gold standard for therapy is still found in surgical mitral valve repair, patients with high or prohibitive surgical risk may also be treated by transcatheter edge-to-edge repair (TEER) (3). The general principle of this treatment is to permanently connect the anterior and posterior leaflet at their tips. In case of a primary MR, e.g., due to a prolapse or flail leaflet, the device is supposed to catch the failing part of the leaflet and hold it back in position during systole. In the case of secondary MR, TEER is slightly narrowing the mitral annulus by applying a strain on the mitral leaflets, pulling them toward the orifice center and obtaining an improved coaptation.

The technique has first been proposed about 30 years ago by the Italian surgeon Ottavio Alfieri (4) as the Alfieri-stitch, performed as open heart surgery, and has resulted in two device series for TEER therapy to date. The MitraClip™ (Abbott Laboratories, Abbot Park, IL, USA) was the first CE marked TEER device to be certified in 2013 and was investigated broadly in the two EVEREST studies (5, 6). In 2019, the PASCAL device (Edwards Lifesciences, Irvine, CA, USA) received a CE mark as the second device system on the market. Up to now, there are several generations and sizes of each device available (7). Comparison in the literature between MitraClip™ and PASCAL regarding clinical usage aligns with our own experience: a higher flexibility in adaptation to patient specific valve characteristics is reached with PASCAL, while the MitraClip™ system is more likely to allow shorter intervention times (7, 8).

However, recurrence of MR and the risk of iatrogenic mitral stenosis (MS) are major issues and reduce the therapeutic effect (9–12). The opinions on residual and recurrent MR are rather concordant (13, 14), whereas the risk of iatrogenic MS is discussed controversially. Early studies and case studies did not find evidence of an increased risk of post-op stenosis (5, 6, 15), while more recent studies witnessed cases of the high mitral gradient at diastolic filling after TEER in spite of seemingly normal pressure gradients during the intervention (9, 16). The challenge of balancing between residual regurgitation and increased mitral pressure gradient (MPG) after TEER is mentioned by several researchers (11, 14, 17, 18). Singh et al. (19) state an overall underestimated risk of iatrogenic MS and further call the best choice for measuring the MPG an "unanswered question." An algorithm for estimating the required pre-interventional mitral valve area (MVA) to avoid an iatrogenic MS was developed by Kassar et al. (20). It is based on 3D ultrasound data and takes into account the amount of TEER devices and their position.

TEER procedures, in contrast to surgical interventions, are performed on the beating heart and thus allow for real-time monitoring of hemodynamic parameters, such as left atrial pressure, residual regurgitation, and MPG. Since the hemodynamic characteristics under anesthesia or sedation might not be comparable to hemodynamics in an awake state or even under physical stress, drug-induced stress testing represents a valuable option to test hemodynamics with a TEER device in place. This is, however, only done if necessary in cases of very low stroke volume (21) and not recommended to be used routinely as it bears potential side effects.

A clinical routine of TEER interventions lacks planning tools for device placing and risk assessment, particularly for borderline cases. Planning tools should ideally not only take individual patient characteristics into account but be also able to predict post-interventional residual MVA and MPGs under different activity levels to estimate the risk of MS.

Computational methods and image-based modeling provide tools to investigate several hemodynamic parameters on the basis of patient specific input data. Such approaches have, for instance, been applied to investigate left ventricular hemodynamic flow structures (22–24), the outcome after implantation of biological and mechanical aortic valve prostheses (25), MV tissue properties (26), as well as mitral hemodynamics with and without simulation of diseases and treatment (27). Caballero et al. (18) and Errthum et al. (28) were the first to use advanced computational methods to systematically investigate post-interventional hemodynamic characteristics for one case and several TEER strategies, as well as for specific devices. Lately, Dabiri et al. (29) analyzed a bigger cohort with regard to residual MR by means of finite element modeling and smoothed particle hydrodynamics.

In this work, we want to investigate the influence of the device position on diastolic hemodynamic parameters with regard to iatrogenic stenosis at an individual level of treatment planning. Therefore, we systematically apply virtual TEER treatment in a cohort of 10 patients at three different positions with position based dynamics. Diastolic hemodynamic parameters at conditions of rest and moderate stress are subsequently simulated by means of a low-complexity computational fluid dynamics (CFD) approach (30). The simulation results are further compared to clinical routine data of mitral TEER patients for a plausibility check.

2. Materials and methods

The workflow of this study is displayed in Figure 1. Patient-specific geometries of LV and MV obtained from 3D transesophageal echocardiography (TEE) data are virtually treated by using a position based dynamics approach. Pre- and post-treatment diastolic hemodynamic parameters are further simulated with CFD.

2.1. Patient data

A cohort of 10 patients (age: 57 ± 8 years, BSA: 1.96[1.94–2.13], $n = 2$ female, MR grade III, NYHA class III), diagnosed with severe primary mitral regurgitation, was retrospectively analyzed. An aspired share of 50% female cases within the cohort could not be achieved due to a limited database. All patients showed a primary mitral insufficiency without any further heart valve pathology and underwent surgical mitral valve repair since they were not considered high-risk patients. As no suitable 3D TEE data of a patient cohort receiving TEER data was available at the time of this study, we developed this workflow on a cohort with the same pathology but different treatment. Table 1 lists the patient data of the cohort. Written consent was obtained from all of these 10 patients, and the procedures were approved by the local Ethical Committees (Ethikkommission Charité—Universitätsmedizin Berlin: EA2/093/16).

For plausibility check, the simulation results are compared to clinical routine data of 21 patients (age: 79 ± 6 years, BSA: 1.83[1.72–2.00], $n = 9$ female, MR grade II–IV) who received mitral TEER to treat MR of various causes (primary, secondary, and mixed). Mitral orifice areas were evaluated by planimetric measurements from 3D TEE images. Maximum and mean velocity and mitral pressure gradients were measured using continuous wave Doppler echocardiography images. All TEE images were acquired peri-operatively in routine practice with a GE Vivid E95 Ultrasound machine (GE Healthcare, Chicago, Illinois, USA).

2.2. Image processing

Pre-operative TEE images of the simulation cohort acquired with a GE Vivid E9 Ultrasound machine (GE Healthcare, Chicago, Illinois, USA) were processed using the software TOMTEC ARENA (TOMTEC Imaging Systems GmbH, Unterschleissheim, Germany). Imaging was performed with a synchronized electrocardiogram. Volumetric TEE sequences that were used for segmentation had a time resolution of 23 ± 5.5 frames per cycle. The automated LV-Analysis tool of TOMTEC ARENA was used to segment the LV over an entire cycle from 4D TEE images. Manual corrections were applied at the end-diastolic phase to improve the accuracy of the automated segmentation. A segmentation of the mitral valve in the early diastolic phase was obtained by manual adaptation of the automated valve segmentation during systole by means of the 4D MV-Assessment tool (TOMTEC ARENA). The MV commissure definition results from the automated systolic segmentation of Tomtec and was not changed during manual adaption. Only the leaflet reconstruction of the initial segmentation was adapted to the open state in a frame during diastole by moving the segmentation spline until it overlapped the leaflets.

Both MV and LV segmentation were exported as triangulated surface meshes in the STL format. The initial segmentation of Tomtec has a low spatial resolution. To enhance surface quality, the MV geometries are remeshed and smoothed, after which they have an average edge length of 1.3–1.8 mm. Detailed mesh statistics can be found in the Supplementary material. The manual adaptation may be associated with uncertainties in the resulting valve geometries. We investigated the effect of inter-user variability on manual valve segmentation by experts and its influence on CFD-computed hemodynamic results in our previous work (31, 32). Results showed that the proportional variation in pressure drop and maximal velocities is smaller than the expected uncertainty of ultrasound measurements of these parameters (33).

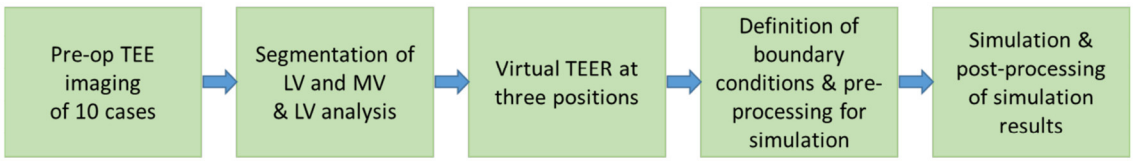

FIGURE 1
Workflow of this *in silico* study to investigate the effect of trans-catheter edge-to-edge repair (TEER) device position on mitral valve area (MVA) and hemodynamic parameters.

TABLE 1 Clinical and demographic data of study cohort.

Patient	1	2	3	4	5	6	7	8	9	10	Mean ± std/Median [IQR]
Sex	F	M	M	M	M	M	F	M	M	M	–
Age [years]	65	63	64	66	53	65	52	44	60	46	57 ± 8
Body surface area [m^2]	1.68	2.34	2.17	3.4	1.94	1.89	1.97	1.94	1.95	2.02	1.96 [1.94–2.13]
Heart rate [bpm]	57	70	55	59	70	63	72	68	75	84	67 ± 8.9
Ejection fraction [%]	61	33	30	26	35	22	38	24	49	18	34 ± 13.1
Stroke volume [ml]	91	76	55	52	70	34	69	53	104	45	65 ± 21.5
EDV [ml]	150	229	184	199	202	158	183	224	212	245	199 ± 20.5
ESV [ml]	59	153	130	147	132	124	114	171	108	201	134 ± 38.3
Mitral regurgitation (MR) fraction [%]	64	62	47	50	56	30	34	55	47	65	51 ± 12.0
E-wave flow [ml/s]	456	490	311	494	586	344	368	425	610	664	475 ± 118.0

2.3. Virtual TEER of the mitral valve

To perform an automated virtual TEER at comparable positions, commissure points of the segmentation were added as landmarks to each valve data set. This information was used to divide the reconstructed valve surface into anterior and posterior segments and into sectors A1, A2, A3, P1, P2, and P3 (see Figure 2A). For this, the vertex positions of the valve mesh were transformed into a cylindrical coordinate system (r, φ, z) in which the height axis (z-component) was aligned with the normal vector of the annulus plane (blue vector in Figure 2). The origin of the new coordinate system was set to the center of gravity of the annulus (blue sphere in Figure 2). The zero angle component $\varphi_{al} = 0$ was aligned with the anterolateral commissure position (red sphere in Figure 2), and the angle component of the posteromedial commissure position φ_{pm} was determined (green sphere in Figure 2). Using this definition, the valve surface was segmented into anterior (all vertices with coordinates $\in \{(r, \varphi, z) \mid \varphi \in [0, \varphi_{pm}]\}$) and posterior leaflets (vertices $\in \{(r, \varphi, z) \mid \varphi \in [\varphi_{pm}, 2\pi]\}$) and into the six sectors $\{A,P\}\{1, 2, 3\}$. The boundaries between the sectors were located at $\frac{1}{3}$ and $\frac{2}{3}$ arc length of the respective leaflet segment (Figure 2A). Three device positions were defined to be at $\{\frac{1}{3}, \frac{1}{2}, \frac{2}{3}\}$ arc length of the respective leaflet segment (left to right in Figure 2). Oriented at measurements of a commercially available TEER device, we defined the diameter of the grasped leaflet area to be 5 mm. Using the three arc length positions and the diameter, device placing areas were defined at the free ends of the leaflets.

The virtual TEER process is simulated by means of our previously developed approach (34–36). The approach simulates mitral valve dynamics with position-based dynamics (PBD), which is an efficient simulation technique designed for real time computer graphics applications. It uses a mass-constraint system to model elastic deformations where mesh vertices are represented as point masses with position and velocity. The elastic material behavior of mitral valves can be approximated by multiple constraints modeling distance, bending, and area conservation constraints. Dirichlet boundary conditions, external forces, and collision constraints model the final dynamics, e.g., simulating the closing of the mitral valve during systole. To model virtual TEER, we needed to relate the opposite device placing areas to each other. For this, we used ray casting. Rays originating from one of the device placing areas cast in the direction of the other leaflet were used to define springs between opposite device placing areas. In PBD, springs are modeled as positional constraints between two mesh vertices. For virtual device closure, spring rest lengths were set to zero. Using the zero rest length modeling for the springs, the opposite leaflets were deformed

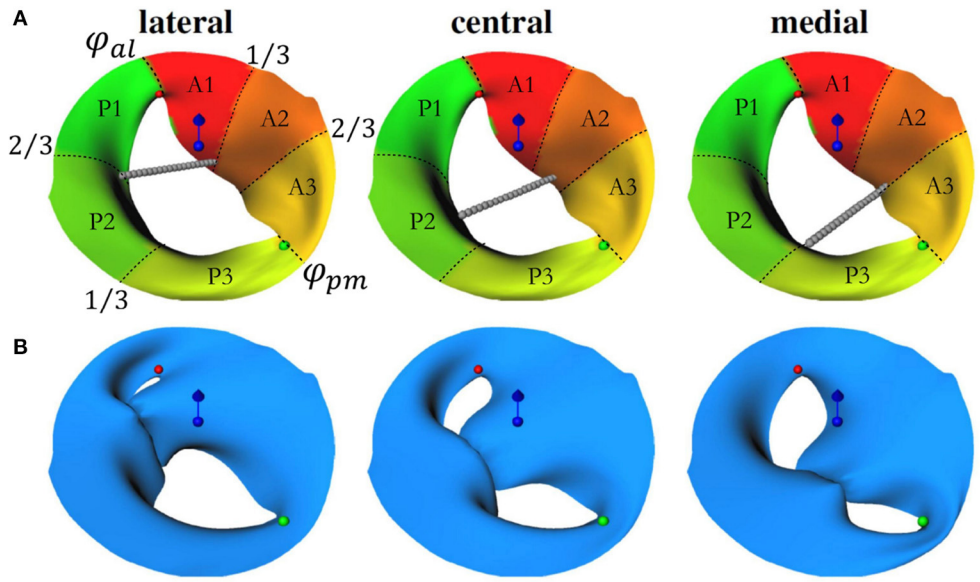

FIGURE 2
(A) Visualization of the automated setup for the device positioning. Red and green spheres depict the anterolateral (at $\varphi_{al} = 0$) and posteriomedial commissures (at φ_{pm}). Sectors in red-yellow mark the anterior leaflet segments ($\varphi \in [0, \varphi_{pm}]$), yellow-green sectors mark the posterior leaflet segments ($\varphi \in [\varphi_{pm}, 2\pi]$). The center of gravity of the annulus is marked by the blue sphere while the blue vector shows the annulus plane normal. The gray chains of spheres indicate lateral, central, and medial device positions and depict which sectors are to be connected in the simulation. **(B)** Geometries after virtual TEER and slight postprocessing. Similar to **(A)**, commissure positions, annulus plane normal, and center of gravity are depicted.

toward and opposite device placing areas were mapped onto each other in the simulation (see Figure 2B). We applied the same material parameterization as previously published in Walczak et al. (36) for simulating the closing of healthy and pathological mitral valves. No fiber directions, non-linearities, calcifications, chordae tendineae, papillary muscles, or trabeculae were modeled. Collision constraints prevented self-intersections. No external forces were applied. The annulus contour was kept fixed.

2.4. CFD simulations

A total of 70 CFD simulations were performed in Simcenter STAR-CCM+ (Siemens Industries Digital Software. Simcenter STAR-CCM+, version 2020.1, Siemens 2020) using a quasi-stationary approach to mimic peak diastolic flow, according to the same principles as in our previous work (30, 32). Continuity equation for incompressible fluids (Equation 1) and momentum equations (Equation 2) were discretized by means of a finite volume formulation and an implicit second-order scheme with $\Delta t = 10^{-4}$ s was applied for temporal discretization. Blood was modeled as an incompressible non-Newtonian generalized Carreau-Yasuda fluid with dynamic viscosity (Equation 3) with $\eta_\infty = 0.0035$ Pa·s, $\eta_0 = 0.16$ Pa·s, $\lambda = 8.2$ s, $n = 0.2128$, $a = 0.64$ [see (37)].

$$\nabla \cdot \vec{v} = 0 \tag{1}$$

$$\rho\left(\frac{\partial \vec{v}}{\partial t} + (\vec{v} \cdot \nabla)\,\vec{v}\right) = -\nabla p + \eta \Delta \vec{v} + \vec{f} \tag{2}$$

$$\eta(\dot{\gamma}) = \eta_\infty + (\eta_0 - \eta_\infty)\left(1 + (\lambda\dot{\gamma})^a\right)^{\frac{n-1}{a}} \tag{3}$$

Mesh base size was set to 1.0 mm with a refinement in the MVA down to 0.25 mm to ensure sufficient spatial resolution of expected detachment phenomena and acceleration at the leaflet tips. The conducted mesh independence study can be found in the Supplementary material. The atrium was modeled as a funnel with a single inlet which was set to a zero pressure boundary condition while the funnel wall, as well as the mitral valve, were assigned with a no-slip boundary condition and kept fixed. According to the referenced wall model (30), the ventricle serves as a velocity outlet representing the instantaneous LV movement at peak diastole.

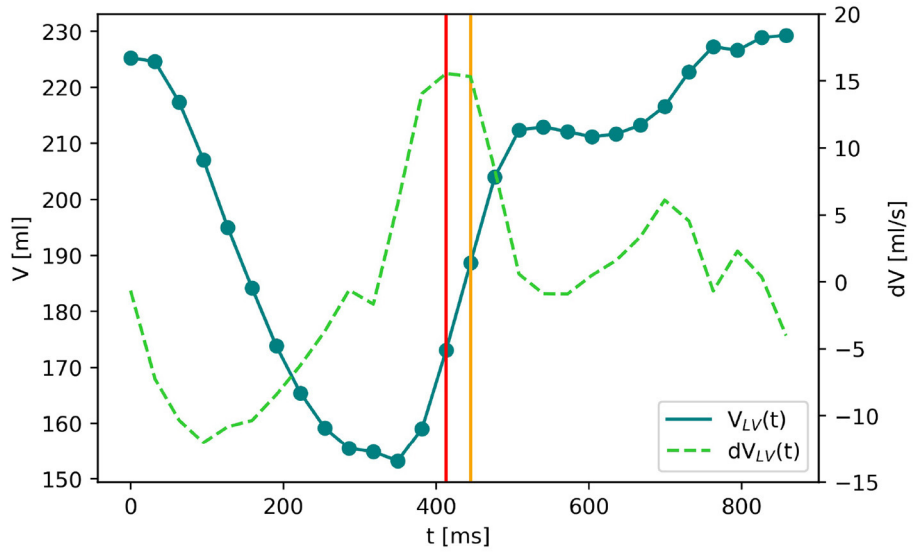

FIGURE 3
The blue solid line shows the volume curve $V_{LV}(t)$ of the left ventricle of Patient 2 over the time of one heartbeat. The dots are the time frames of echocardiographic imaging. $dV_{LV}(t)$ (green dashed line) denotes the LV volume change between two subsequent time frames. The biggest positive volume change (marked by the red vertical line) indicates the E-wave which is the moment of maximal blood flow through the mitral valve during diastole. The LV segmentations at this and the following time point (yellow vertical line) are chosen to create the surface distance map for the boundary condition of the computational fluid dynamics (CFD) simulation.

2.5. Patient-specific boundary condition and modeling of hemodynamic parameters

For the quasi-stationary simulations at the peak-E wave, a boundary condition is required to represent the instantaneous wall movement and therewith induced volume change of the LV, which results in the peak E-wave flow rate (474.9 ± 117.9 ml/s, listed for each case in Table 1). The above mentioned automated LV analysis performed in TOMTEC ARENA was used to obtain the volume curve as exemplarily shown for Patient 2 in Figure 3. These image data were also taken to receive end-diastolic and end-systolic LV volume, resulting in stroke volume and ejection fraction as listed in Table 1. The peak diastolic time point was identified by the largest positive volume difference ΔV between two consecutive segmentations Δt (note the two vertical lines in Figure 3). Segmented LV geometries of these two time points were used to derive a patient specific boundary condition for the quasi-stationary CFD simulations by mapping the flow rate at peak E-wave by means of a distance map of the LV geometries at the respective time points. Therefore, the LV segmentations were exported as triangulated meshes in the STL format, and both geometries were aligned with the annulus center in the global origin by means of the software Blender (38). This step simplifies further alignment of the mitral valve and definition of internal coordinate systems in the CFD simulation setup. A surface distance map was calculated containing the distances in the normal direction from the LV with a smaller volume toward the other. In the CFD simulations, a velocity outlet boundary condition was applied at the LV wall. A surface distance map between the two chosen time steps was used to weight the fluid velocity at the walls such that the resulting volume flow in the simulations matched the instantaneous blood flow at peak E-wave (compare Figure 4).

The peak E-wave flow rate of the clinical comparison data was estimated by multiplying the echo Doppler measured maximal velocity with the MVA, measured by planimetry: $\dot{V}_{E-wave} = v_{max} \cdot MVA$. This delivered similar results as for the simulation cohort (447.6 ± 107.6 ml/s). After TEER, the clinical data had a residual MR of trace to mild and showed in average a drop of peak E-wave flow rate by 23%, resulting in 372.9 ± 115.9 ml/s. However, no significant linear regression was found between pre- and post-interventional flow rate values. Since the post-interventional simulations after virtual TEER are based on pre-interventional data only, we assume the same average drop in flow rates as observable in the clinical data. Hence, the post-interventional flow rates of the simulation cohort under the conditions of rest are 77% of the pre-interventional flow rates. With the observation, that the heart was capable of affording a higher flow rate pre-interventionally, we further presume the pre-interventional flow rate to serve as a reasonable estimation to mimic conditions of moderate stress after virtual TEER.

During TEER interventions, three of the basic hemodynamic surveillance parameters are the MVA, mean and maximum velocities, which are measured by ultrasound, and mean and

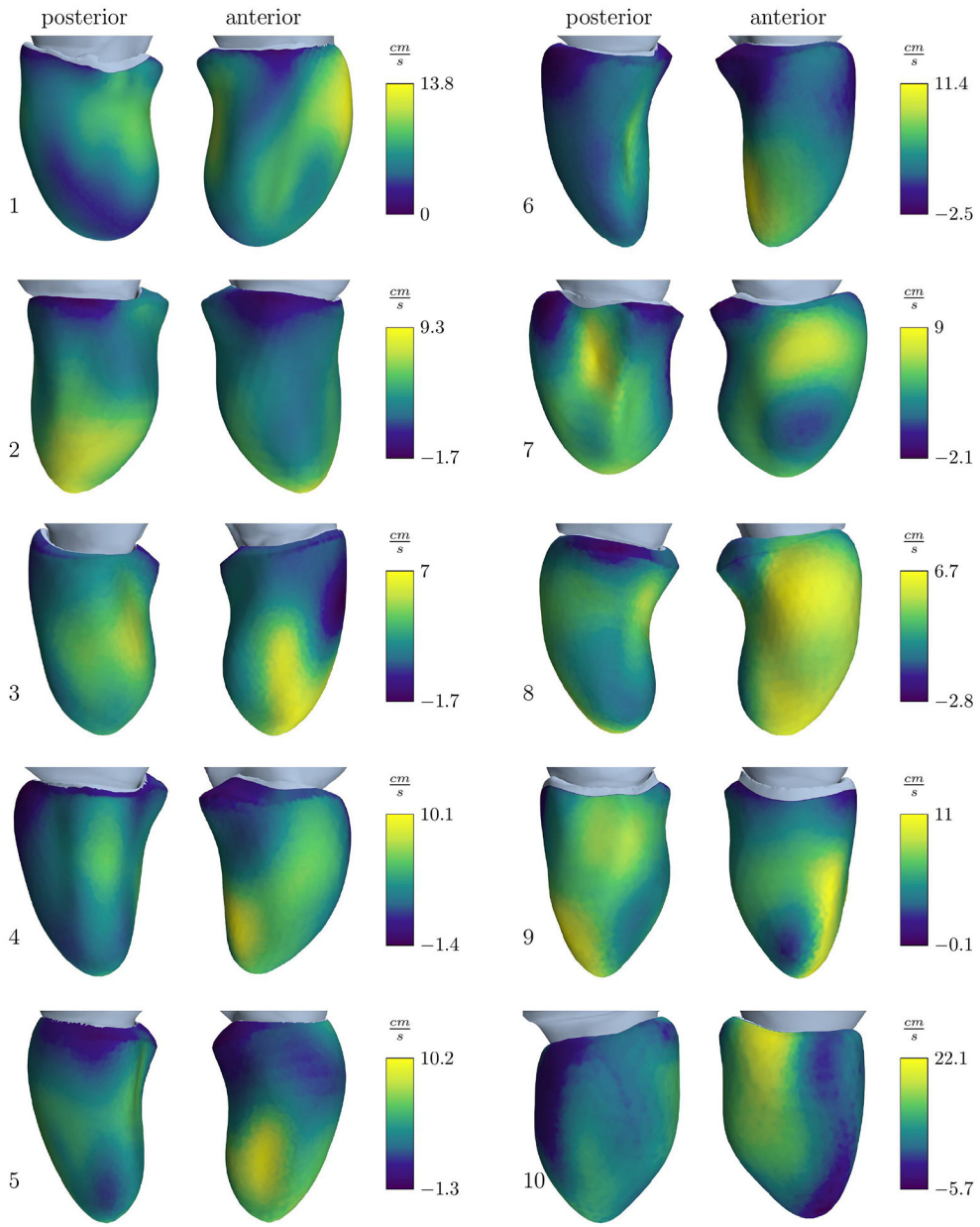

FIGURE 4
Velocity outlet boundary condition for the simulation cohort resulting to obtain the E-wave flow measured by volumetric analysis. Positive values stand for an outward directed flow representing wall movement away from the center, while negative values represent a movement toward the center.

maximum MPG, which are estimated by means of the simplified Bernoulli Equation (Equation 4). The MVA is an important indicator for assessing the suitability of a TEER procedure for a patient since guidelines recommend to only consider patients with a MVA>4 cm^2 for TEER (14). During and after the procedure, MVA and MPG are used to judge the risk of MS. These parameters were also analyzed in the simulation cases of this study. Thereby, the effective MVA before and after virtual TEER was measured by means of the shrink-wrap approach developed by Razafindrazaka et al. (39). Maximum velocities were monitored during the simulation time. They occured at the shear layer of the leaflet tips during early simulation time and travelled with the vortex structures toward the mid ventricle. The static pressure was numerically calculated by solving the Poisson-Equation within STAR-CCM+ since the simulations work with an incompressible fluid. It was extracted along a

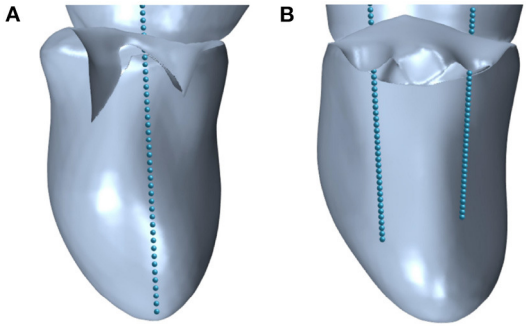

FIGURE 5
Line probes defined in STAR-CCM+ to extract the pressure in **(A)** pre-interventional geometries with single orifice and **(B)** post-interventional geometries with double orifice.

line probe that is set between the annulus center and the apex for all cases before virtual TEER as shown in Figure 5A. After virtual TEER, a line probe was placed in each opening of the double orifice (Figure 5B) and the results of both probes were averaged. Note that in clinical routine mean and maximum of both velocity and MPG are available. The simulations performed with the presented setup, however, only allow for the assessment of maximum values of velocities and pressure gradients.

$$\Delta P[mmHg] = 4\left[\frac{mmHg \cdot s^2}{m^2}\right] \cdot v_{max}^2 \left[\frac{m^2}{s^2}\right] \quad (4)$$

2.6. Statistical analysis

Statistical analysis of simulated and clinical data was performed using IBM SPSS Statistics 28 software (IBM Company, USA). Mean and SD were reported for normally distributed parameters as assessed by the Shapiro-Wilk test due to the high statistical power of the test and due to the small size of both cohorts. Otherwise, median and interquartile [IQR] ranges were used. The two-tailed student's *t*-test was used to test for significant differences within normally distributed parameter differences, while the Mann–Whitney U and Wilcoxon signed-rank tests were used for testing non-normally distributed parameter differences. Paired tests were used to compare differences between pre- and post-treatment and between different device positions. All tests used a standard significance level of 0.05.

3. Results

In the following, results of the simulations before and after virtual TEER under conditions of rest and stress are presented and compared to clinical routine data. First, the influence of virtual TEER on the MVA was analyzed. Furthermore, the results of image data analysis delivering the boundary conditions for CFD and hemodynamic results of the CFD simulations themselves were investigated. Table 2 summarizes the results.

3.1. Mitral valve area

Placing a TEER device, virtually or in a real procedure, has the two effects of both reducing the mitral orifice area and usually converting the single orifice of the native valve into a double orifice. The projected MVAs of the segmented mitral valve geometries measure a mean and SD of 7.50 ± 1.62 cm^2 and reduce to 2.56 ± 0.63 cm^2 after virtual TEER when averaging over all device positions. Comparison of the remaining MVA after virtual device placement at different positions shows that central positions lead to a significantly stronger reduction of MVA than eccentric positioning of the device (paired *t*-test) at either lateral ($p = 0.002$) or medial ($p = 0.035$) segments of the leaflets. A virtual TEER at the A1-P1 segments (lateral) leads to a mean MVA of 2.65 ± 0.68 cm^2 and A3-P3 (medial) leads to a mean MVA of 2.72 ± 0.62 cm^2. This is a reduction of MVA to 35 and 36% of the original MVA, respectively. Central device positioning at segments A2-P2 reduces the MVA to 31%, measuring 2.30 ± 0.58 cm^2. This leads to an average difference of 0.35–0.42 cm^2 between central and eccentric device positions (see Figure 7A). Having a closer look at the MVAs of the single patient cases after virtual TEER, two of them get close to the clinical definition of severe stenosis (MVA<1.5 cm^2) according to (3). Patient 3, e.g., shows a pre-interventional MVA of 5.58 cm^2 which reduces to 1.54 cm^2 after central device placement while lateral and medial positions lead to 2.02 and 1.79 cm^2, respectively. With a pre-interventional MVA of 5.92 cm^2, Patient 6 exhibits remaining MVAs of 1.67 and 1.69 cm^2 after central and medial device position, while lateral positioning entails a much bigger MVA of 2.43 cm^2. All other cases maintain MVAs of >1.7 cm^2, independent of the device position, and would therefore not be judged as severe stenosis cases according to the guidelines (3). A brief comparison to clinical routine data shows good agreement regarding measurements of post-interventional MVA, which are 2.53 ± 0.79 cm^2. Pre-interventional MVA, on the contrary, measures significantly smaller values of 4.75 ± 0.99 cm^2.

Figure 6 depicts respective changes of MVAs in the simulation cohort for each patient after virtual TEER at central or eccentric (lateral and medial) positions in a scatter plot. Regressions for central and eccentric positions show a low coefficient of determination ($R_e^2 = 0.49$), hence large scattering for eccentric device positions. In contrast, MVA after central virtual TEER shows lower

TABLE 2 Hemodynamic results after virtual trans-catheter edge-to-edge repair (TEER) at rest and stress conditions for different device positions.

		Pre	$Post_{all}$	Lateral	Central	Medial
MVA [cm^2]	Simulation	7.50 ± 1.62	2.56 ± 0.63	2.65 ± 0.68	2.30 ± 0.58	2.72 ± 0.62
	Clinical routine	4.75 ± 1.00	2.81 ± 0.80	–	–	–
v_{max} [m/s]	Simulation rest	0.90 ± 0.16	2.04 ± 0.45	1.94 ± 0.60	2.20 ± 0.38	1.97 ± 0.32
	Simulation stress	–	2.59 ± 0.57	2.41 ± 0.57	2.78 ± 0.48	2.59 ± 0.63
	Clinical routine	0.96±0.21	1.33±0.21	–	–	–
MPG [mmHg]	Simulation rest	1.46 ± 0.63	16.30 ± 9.0	14.92 ± 11.65	19.51 ± 8.54	14.47 ± 5.90
	Simulation stress	–	27.36 ± 13.34	23.01 ± 13.48	32.14 ± 12.31	26.94 ± 14.23
	Clinical routine	3.85 ± 1.72	7.24 ± 2.28	–	–	–

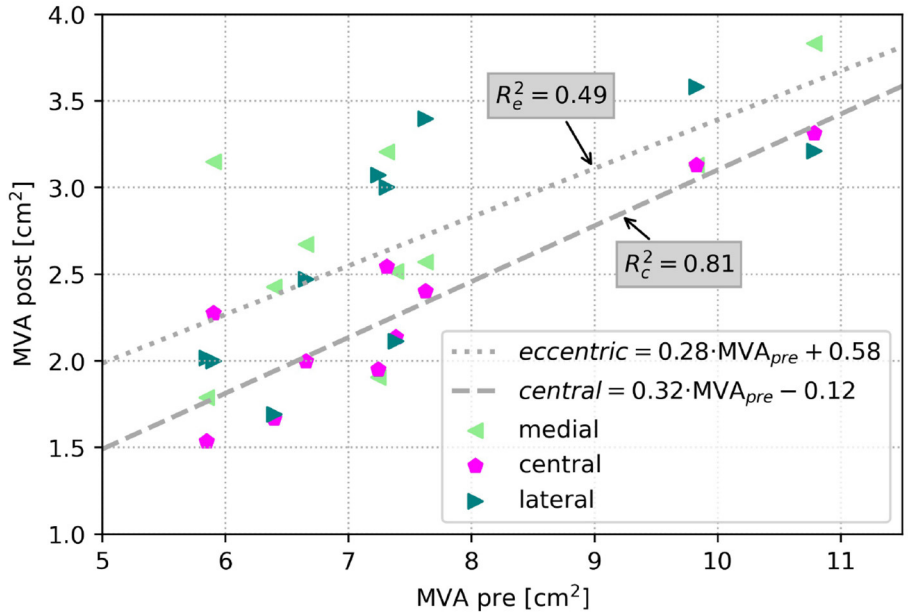

FIGURE 6
Scatter plot of MVA in the simulation cohort after virtual TEER at all positions respective to MVA before virtual treatment. The dashed line shows a regression of central device positions ($R_c^2 = 0.81$), and the dotted line shows the regression for eccentric device positions ($R_e^2 = 0.49$).

scattering with $R_c^2 = 0.81$. For an illustration of the mitral valve geometries and detailed MVA results of all cases at all device positions the reader is referred to the Supplementary material.

3.2. Hemodynamic parameters

The quantitative analysis of hemodynamic parameters is focused on the simulations results of maximal velocities and pressure gradients at peak E-wave flow. Further, the intraventricular flow structures evolving at different device placement locations are looked at qualitatively for exemplary cases.

3.2.1. Maximum velocity and pressure gradient

Prior to virtual TEER, the maximal velocities in the simulation cohort were 0.90 ± 0.16 m/s. The simulations after virtual TEER at all positions showed that maximal velocities rise to 2.04 ± 0.45 m/s at rest conditions and significantly higher to 2.59 ± 0.57 m/s under conditions of light stress. This is an increase of 127% at rest and 188% under stress in relation to the pre-interventional simulations. In the clinical data, on the contrary, the maximal velocities only rose by 38% from 0.96 ± 0.21 m/s before to 1.33 ± 0.21 m/s after the TEER therapy.

Figure 7B shows that central device positions lead to a significantly higher rise in maximal velocities than eccentric device positions. At rest, maximal velocities show a larger increase of 0.23–0.27 m/s after central virtual TEER, than after eccentric device placement at the lateral or medial position.

Stress boundary conditions in combination with a central device position, averagely resulted in 0.19–0.37 m/s higher maximal velocities than stress simulations with eccentric device positions. These results are listed in detail in Table 2.

Similar tendencies are seen for the MPG. It increased from 1.46 ± 0.63 mmHg before virtual TEER to 16.30 ± 9.00 mmHg at rest and 27.36 ± 13.34 under stress considering all device positions. Pre-interventional MPGs of the clinical comparison data were significantly higher with 3.85 ± 1.72 mmHg and lower after the procedure with 7.24 ± 2.28 mmHg. Figure 7C shows a stronger increase of MPG at central compared to eccentric device position. In detail, the MPG rose on average roughly 5 mmHg higher after central device positioning than after eccentric virtual TEER at rest and about 5–9 mmHg higher under stress (Table 2). The stronger spread in measured velocities and pressure differences under conditions of stress is visible in Figures 7B,C. Regarding the objective of providing tools to support clinical therapy planning and decision making by predicting possible patient outcomes after treatment, it is important to consider habits of estimating hemodynamic parameters in clinical routine when comparing results of clinical and simulation outcomes. Therefore, simulated results are plotted over estimations, that can be drawn from easily accessible parameters, such as volume flow ($\dot{V}$) and MVA (Figure 8). The simulated values of velocity were, apart from few outliers, above the estimated values and regression of the point cloud is almost parallel to the angle bisector but shifted upward by 0.5 cm/s with $R^2 = 0.72$ (Figure 8A). Estimations of the MPG and simulated values corresponded well for the pre-interventional cases, which are directly on the angle bisector of the plot (Figure 8B). Post-interventional cases, on the contrary, revealed considerably higher MPGs in simulations than estimated with the Bernoulli-Equation based on volume flow and MVAs.

3.2.2. Ventricular flow structures

Intraventricular flow structures can, in contrast to velocity and pressure gradients, only be compared qualitatively among different simulation setups since ultrasound data do not capture them. Figure 9 shows streamlines of the early diastolic inflow jet of Patients 1 and 2. Pre-interventional flow (left) is opposed to post-interventional flow after medial, central, and lateral device positions, respectively. At the leaflet tips, the jet is rolling up at the shear layer of the tips, developing the diastolic vortex ring. The velocity maxima are located in the center of the jet. All device positions cause a division of the pre-interventional single orifice area into a double orifice. Under identical boundary conditions, the device positions have a strong influence on the vortex formation and jet direction. For example in Patient 1, a medial device position leads to a stronger vortex than central or lateral device positions, whereas lateral positioning directs the diastolic jet more towards the inerolateral LV wall. In this case, the maximum velocities differ only weakly between the device positions. For Patient 2, however, the effect of stronger acceleration after central compared to eccentric device position is more clearly exhibited than the effect on the jet direction. Nevertheless, after lateral device placement, the jet at the anterior LV wall turns out stronger, while a medial device positioning enhances the jet at the inferior LV wall. Illustrations of the flow structures of all patients can be found in the Supplementary material. Considering all patient cases, it becomes clear, that the device position has various effects, not only on changes in velocity and MPG but also on redirecting the diastolic jet and acting on the vortex formation and development.

4. Discussion

In this study, we established a workflow of virtual TEER device placement in patient-specific mitral valve geometries and modeled the impact of the device position on diastolic hemodynamics under rest and stress conditions. Our key findings are that MVA reduces most at central device positions, which leads to a stronger increase in hemodynamic parameters associated with iatrogenic mitral stenosis. Vortex structures are highly dependent on individual valve morphology and boundary conditions. Results and clinical application of the workflow are discussed in the following.

4.1. Mitral valve area

Virtual TEER treatment simulations allow an estimation of post-treatment MVA. We found that central device positions lead to a stronger reduction of MVA (Figure 7A). On average, central device positions led to a 0.36–0.42 cm^2 smaller residual MVA after virtual TEER than eccentric device positions. This diverges from the results of Kassar et al. (20), who found the biggest reduction of MVA in a slightly eccentric position. Focusing on individual cases of the cohort, two out of ten can be considered borderline cases. They reach or come close to the cut-off range for severe mitral stenosis of MVA$<$1.5 cm^2 (3) after central virtual device placement, whereas eccentric device positions result in MVAs above that limit. A virtual treatment tool as presented here could both help to identify such borderline cases and support the careful planning of device positioning with regard to residual MVA.

Furthermore, we were able to show that residual MVA in the simulated cases is also better predictable after central than after eccentric virtual device placement by exhibiting a stronger linear correlation with the pre-interventional MVA (compare Figure 6). This leads to the assumption that residual MVA after eccentric device

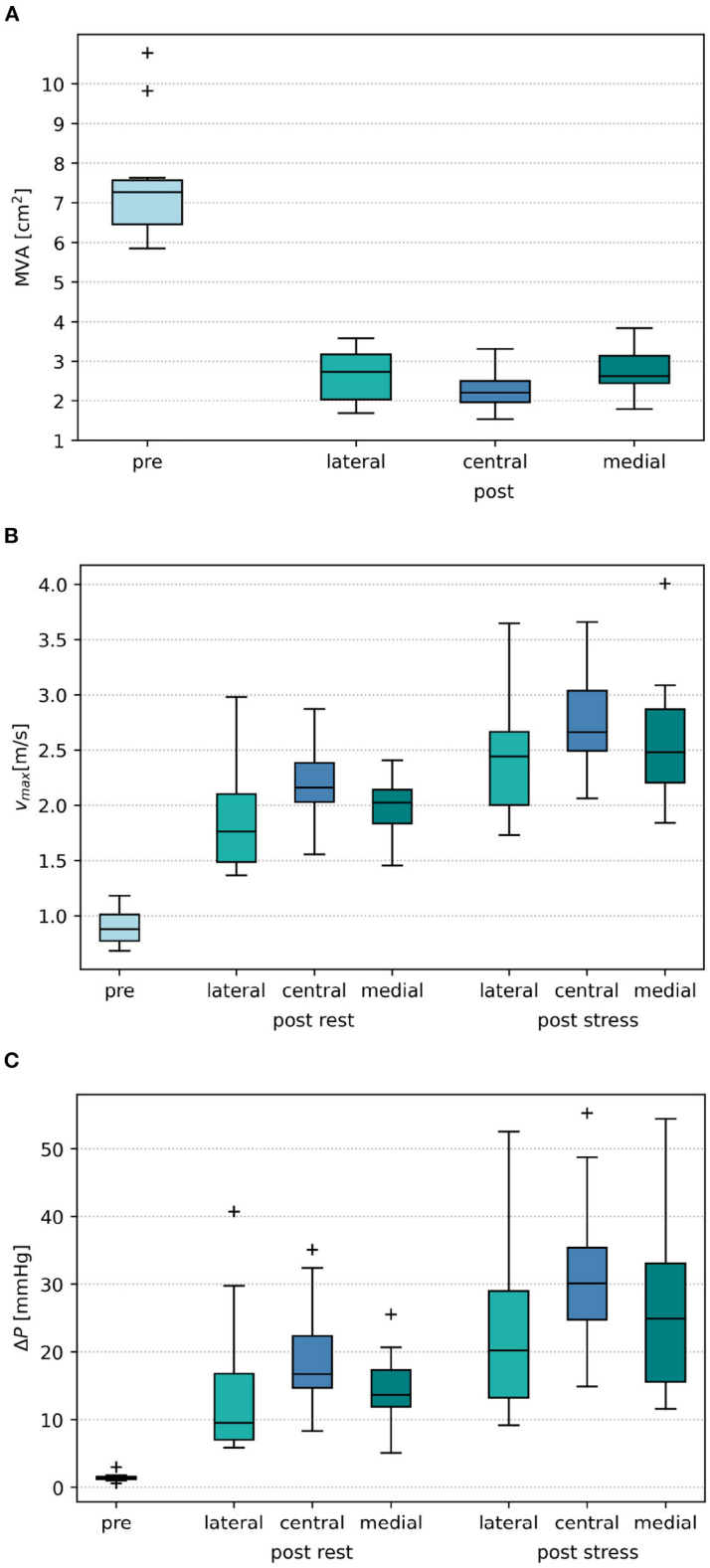

FIGURE 7
(A) Boxplot of mitral orifice area (MVA) before virtual treatment (pre) and after virtual TEER placement at the lateral, central, and medial position, respectively. **(B)** Boxplot of pre- and post-interventional maximal velocities v_{max}. **(C)** Boxplot of pre- and post-interventional mitral pressure gradient ΔP.

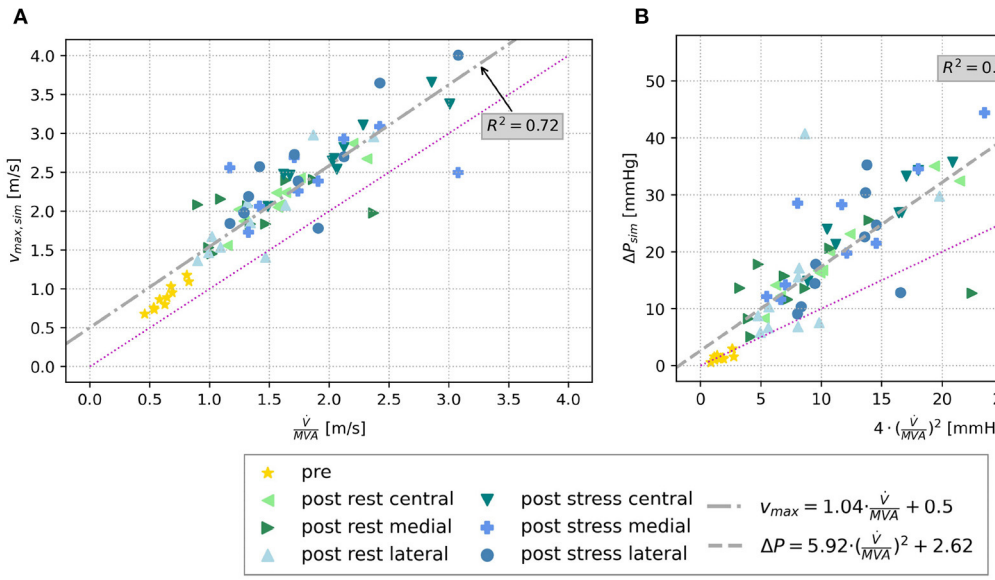

FIGURE 8
(A) Scatter plot of simulated maximal velocities pre and post virtual TEER at rest and stress, respectively, over the estimated maximal velocity using volume flow and MVA. **(B)** Scatter plot of simulated MPG (ΔP) over the estimated MPG by means of the simplified Bernoulli-Equation (Equation 4). The bisector is indicated by the magenta line in both plots, and a regression line is drawn in gray.

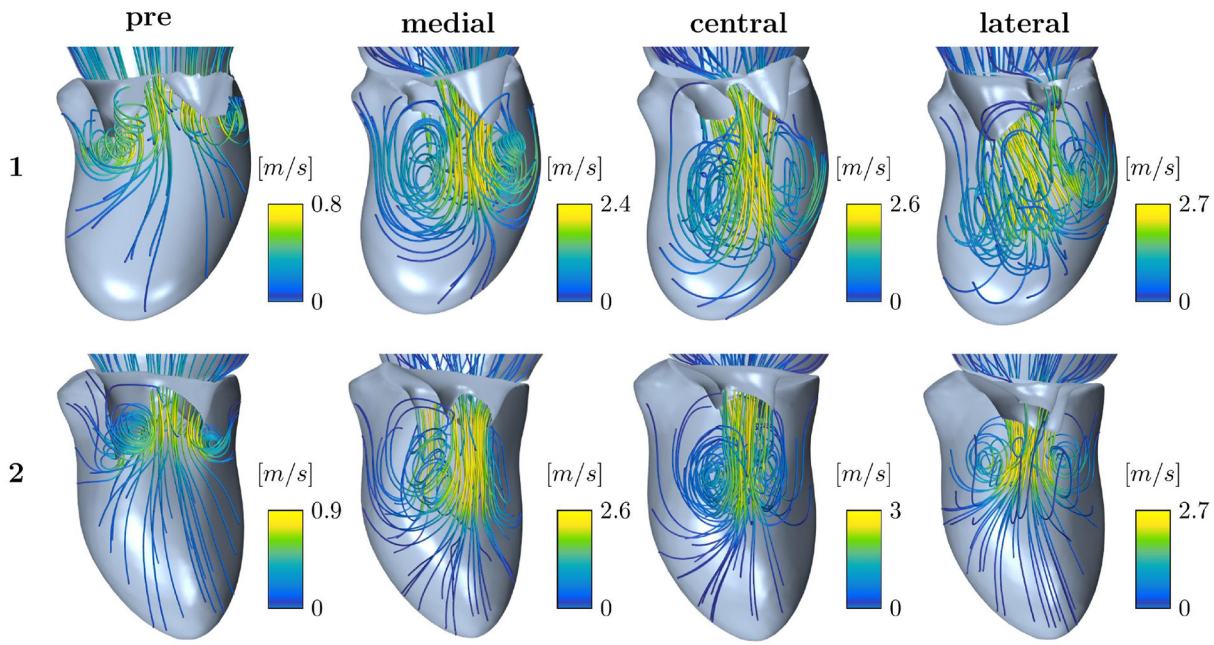

FIGURE 9
Streamline representation of the flow field for pre-interventional conditions and after virtual TEER at medial, central, and lateral device positions, respectively, for Patients 1 and 2.

positioning is more dependent on individual valve morphology, such as annulus area, leaflet length, and coaptation area.

While post-interventional MVAs of the simulated cases align well with the clinically measured MVA after TEER, the pre-interventional MVAs are significantly

bigger in the simulation data, even though the planimetric measurement is suspected to overestimate the MVA (20). This may be caused by an overestimation of MVA by the shrink-wrap algorithm (39), which is stronger for single than for double orifices. Systematic studies on the difference in MVA measurements from ultrasound and segmented valve geometries are therefore vital.

4.2. Hemodynamics after virtual TEER

Analysis of pre- and post-treatment hemodynamics found that maximal velocities and MPG increased more after central than after eccentric virtual device placement (see Figure 7). This corresponds to the findings of smaller MVA for central device positions. However, a wide spread in the data is observed suggesting a strong dependence on individual factors. With regard to clinical applicability, we tested whether the maximal velocity and MPG could be predicted by the individual volume flow and MVA only and observed good correlations (see Figure 8). The ratio of peak E-wave volume flow and MVA is a simple estimation for the average velocity necessary to obtain a certain flow rate through an orifice area. In the diastolic flow, maximal velocities appear first at the rolled up shear layer close to the leaflet tips. After formation and progression of the diastolic jet, maximal velocities are found in the center of the jet. This also explains the discrepancy between pre- and post-interventional MPG. Since the pre-interventional vortex ring and jet are not fully developed yet, pressure measurements taken at the centerline do not capture maximal velocities at the leaflet tips (Figure 9). On the contrary, clinical pressure gradients are estimated by using the Bernoulli equation.

Intraventricular flow structures are discussed to act on cardiac efficiency (40) and CFD provides a quantitative tool for further investigations toward this question in cohorts of MR patients receiving mitral TEER treatment. Our results show that flow patterns vary widely between the simulated cases and are not only influenced by the device position but also by the valve morphology and the boundary conditions including LV shape and LV contraction patterns (Figure 4).

It can be summarized, that simple considerations allow estimating the resulting maximal velocities and MPG from MVA and peak-E wave flow rate. CFD may therefore not be necessary. However, when investigating the impact of a TEER device on the flow structures, which have been shown to be very individual, CFD is a suitable tool to use. The need for a more complex CFD modeling, assessing the whole heart cycle or the whole diastolic phase instead of modeling the peak E-wave should be evaluated in future studies.

4.3. Clinical application

Therapy planning tools for TEER interventions are tremendously needed when it comes to device positioning, choice of device, and outcome prediction on an individual patient level. Ideally, such tools do not only help in procedure planning but also identify borderline cases and assess the risk of iatrogenic MS. This may be approached on the level of MVA estimation regarding geometric changes after TEER only or in combination with the consideration of hemodynamic parameters. To prevent an underestimation of MS, e.g., in patients with low-flow/low-gradient characteristics (21), outcome scenarios could be simulated by taking into account the following factors:

- Ventricular recovery, a potential improvement of left ventricular function, and a corresponding increase in diastolic blood flow.
- A reduction or absence or regurgitating volume, resulting in a decrease of the absolute stroke volume and counteracting rises in MPG.

Furthermore, intra-procedural stress testing might be replaced by simulation approaches, thus preventing the exposure of patients to additional risks.

Our workflow is based on data that can easily be acquired in clinical routine. TOMTEC ARENA used for valve segmentation is broadly available and integrated into clinical systems. The virtual TEER treatment with PBD is fast and easy to use. Further steps of the analysis could be automatized for better usability. CFD is considered to be a valuable method for development of prediction tools and to investigate academic questions rather than being used in clinical routine.

When considering the translation of simulation results into clinically interpretable data, it must be taken into account that ultrasound-measured velocity data is likely to underestimate velocities and pressure gradients compared to catheter-based measurements (41). A similar phenomenon is to be expected whenever checking clinical data against our simulation results. Since velocity acquisition with ultrasound is physically only possible for the component along the beam direction, an underestimation will increase with a rising inclination of the jet direction respective to the ultrasound beam as observable in case of double orifices after TEER treatment. It is further to mention that our simulations only allow for representation of maximum values of velocity and MPG, whereas clinical judgment is mostly based on mean values of those quantities. Riegel et al. (42) state however, that both mean and peak values of velocity and MPG are suitable for judging relevant iatrogenic MS after MR treatment.

Finally, it is important to point out that a general statement regarding the suitability of a certain device position is not possible. It highly depends on the etiology, the individual morphology of the MV, and potential adaptation to the treatment. The necessity of a patient-individual focus in systematic treatment planning tools is thereby underlined. Future work could enhance the understanding of relations between the number and position of TEER devices in combination with specific MR etiologies.

4.4. Limitations

Although there are not many simulation studies regarding TEER treatment with cohorts containing more than 10 cases, we still acknowledge the limitation of power and its related effects on statistical analysis. Furthermore, we have only examined deployment of one virtual TEER device, while many patients receive more than one device for the treatment of MR (43). We have refrained from simulating specific device products as a part of our simplified methodology. The quasi-stationary modeling approach means that all meshes are fixed. Detailed structures of the LV and MV apparatus, such as chordae, papillary muscles, and trabeculae, are neglected. Note that LV torsion has, according to the work of Vasudevan et al. (44) and Canè et al. (45), no crucial influence on the investigated parameters and has not been included in the model. Manual interaction in the segmentation process can moreover lead to user-dependent uncertainties which may influence the CFD results. Results of our previous investigation (32) show, however, that the proportional variation in pressure drop and maximal velocities is smaller than the expected uncertainty of ultrasound measurements of these parameters (33). Furthermore, the estimation of rest and stress boundary conditions have to be understood as estimations rather than validated relations. Finally, a direct validation with clinical data of the simulated cohort was not possible since the included patients did not receive the simulated treatment. Our comparison with the clinical cohort could be considered a plausibility check or feasibility proof.

5. Conclusion

High inter-individual and device location-dependent variability between morphometric and hemodynamic parameters before and after virtual TEER treatment was found in our study. Virtual TEER treatment using a position based dynamics approach combined with CFD seems to be a promising tool for predicting residual MVA and hemodynamic outcomes for varying device positions. Post-interventional scenarios can be simulated for varying flow conditions, associated with rest or stress. Once these flow conditions are validated, this enables stress testing without any additional risks for patients. The method could hence be used in the future to support treatment decision making and procedure planning. However, in order to translate the proposed approach into the clinical workflow, a clinical validation study is vital.

Data availability statement

The data sets (geometries and applied boundary conditions) presented in this study are provided as open data on figshare: https://doi.org/10.6084/m9.figshare.19535047.v1.

Ethics statement

The studies involving human participants were reviewed and approved by Ethics Committee of Charité—Universitätsmedizin Berlin. The patients/participants provided their written informed consent to participate in this study.

Author contributions

KV and LG: conceptualization. KV and FB: data curation. KV, LW, and LG: formal analysis, methodology, and writing original draft. LG, UL, TK, and AH: funding acquisition and supervision. KV and LW: visualization. KV, FB, MR, and MK: investigation. All authors: review and editing, contributed to the article, and approved the submitted version.

Funding

This work was part of the projects EurValve (funded by the European Union's Horizon 2020 research program, grant no. 689617), DSSMitral, and MINIMAKI, each funded by the German Federal Ministry of Education and Research (Grant nos. 03VP00851 and 16SV8649).

Conflict of interest

Author FB received grant support from Abbott Laboratories (Chicago, USA).

The remaining authors declare that the research was conducted in the absence of any commercial or financial relationships that could be construed as a potential conflict of interest.

Publisher's note

All claims expressed in this article are solely those of the authors and do not necessarily represent those

of their affiliated organizations, or those of the publisher, the editors and the reviewers. Any product that may be evaluated in this article, or claim that may be made by its manufacturer, is not guaranteed or endorsed by the publisher.

Supplementary material

The Supplementary Material for this article can be found online at: https://www.frontiersin.org/articles/10.3389/fcvm.2022.915074/full#supplementary-material

References

1. Iung B, Baron G, Tornos P, Gohlke-Bärwolf C, Butchart EG, Vahanian A. Valvular heart disease in the community: a European experience. *Curr Probl Cardiol.* (2007) 32:609–61. doi: 10.1016/j.cpcardiol.2007.07.002

2. Iung B, Vahanian A. Epidemiology of acquired valvular heart disease. *Can J Cardiol.* (2014) 30:962–70. doi: 10.1016/j.cjca.2014.03.022

3. Vahanian A, Beyersdorf F, Praz F, Milojevic M, Baldus S, Bauersachs J, et al. 2021 ESC/EACTS Guidelines for the management of valvular heart disease: developed by the Task Force for the management of valvular heart disease of the European Society of Cardiology (ESC) and the European Association for Cardio-Thoracic Surgery (EACTS). *Eur Heart J.* (2021) 43:561–632. doi: 10.1093/eurheartj/ehac051

4. Maisano F, Torracca L, Oppizzi M, Stefano PL, D'Addario G, La Canna G, et al. The edge-to-edge technique: a simplified method to correct mitral insufficiency. *Eur J Cardio-Thorac Surg.* (1998) 13:240–6. doi: 10.1016/S1010-7940(98)00014-1

5. Herrmann HC, Rohatgi S, Wasserman HS, Block P, Gray W, Hamilton A, et al. Mitral valve hemodynamic effects of percutaneous edge-to-edge repair with the mitraclip™ device for mitral regurgitation. *Catheter Cardiovasc Intervent.* (2006) 68:821–8. doi: 10.1002/ccd.20917

6. Herrmann HC, Kar S, Siegel R, Fail P, Loghin C, Lim S, et al. Effect of percutaneous mitral repair with the MitraClip device on mitral valve area and gradient. *EuroIntervention.* (2009) 4:437–42. doi: 10.4244/EIJV4I4A76

7. Corpataux N, Winkel MG, Kassar M, Brugger N, Windecker S, Praz F. The PASCAL device-early experience with a leaflet approximation device: what are the benefits/limitations compared with the MitraClip? *Curr Cardiol Rep.* (2020) 22:1–7. doi: 10.1007/s11886-020-01305-1

8. Barth S, Hautmann MB, Arvaniti E, Kikec J, Kerber S, Zacher M, et al. Mid-term hemodynamic and functional results after transcatheter mitral valve leaflet repair with the new PASCAL device. *Clin Res Cardiol.* (2021) 110:628–39. doi: 10.1007/s00392-020-01733-7

9. Boerlage-Van Dijk K, Van Riel ACMJ, De Bruin-Bon RHACM, Wiegerinck EMA, Koch KT, Vis MM, et al. Mitral inflow patterns after mitraclip implantation at rest and during exercise. *J Am Soc Echocardiogr.* (2014) 27:24–31.e1. doi: 10.1016/j.echo.2013.09.007

10. Nita N, Scharnbeck D, Schneider LM, Seeger J, Wöhrle J, Rottbauer W, et al. Predictors of left ventricular reverse remodeling after percutaneous therapy for mitral regurgitation with the MitraClip system. *Catheter Cardiovasc Intervent.* (2020) 96:687–97. doi: 10.1002/ccd.28779

11. Neuss M, Schau T, Isotani A, Pilz M, Schöpp M, Butter C. Elevated mitral valve pressure gradient after MitraClip implantation deteriorates long-term outcome in patients with severe mitral regurgitation and severe heart failure. *Cardiovasc Intervent.* (2017) 10:931–9. doi: 10.1016/j.jcin.2016.12.280

12. Schnitzler K, Hell M, Geyer M, Kreidel F, Münzel T, von Bardeleben RS. Complications following MitraClip implantation. *Curr Cardiol Rep.* (2021) 23:131. doi: 10.1007/s11886-021-01553-9

13. Singh K, Raphael J, Colquhoun D. A rare case of mitral stenosis after MitraClip placement: transesophageal echocardiography findings and examination. *Anesth Anal.* (2013) 117:777–9. doi: 10.1213/ANE.0b013e3182a4afa9

14. Feldman T, Guerrero M. Assessing the balance between less mitral regurgitation and more residual transmitral pressure gradient after MitraClip. *JACC Cardiovasc Intervent.* (2017) 10:940–1. doi: 10.1016/j.jcin.2016.12.273

15. Paranskaya L, Kische S, Bozdag-Turan I, Nienaber C, Ince H. Mitral valve with three orifices after percutaneous repair with the MitraClip system: the triple-orifice technique. *Clin Res Cardiol.* (2012) 101:847–9. doi: 10.1007/s00392-012-0451-3

16. Osswald A, Al Jabbari O, Abu Saleh WK, Barker C, Ruhparwar A, Karmonik C, et al. Development of a severe mitral valve stenosis secondary to the treatment of mitral regurgitation with a single MitraClip. *J Cardiac Surg.* (2016) 31:153–5. doi: 10.1111/jocs.12692

17. Cilingiroglu M. Mitral stenosis following MitraClip procedure: is it preventable? *Catheter Cardiovasc Intervent.* (2014) 83:303–4. doi: 10.1002/ccd.25316

18. Caballero A, Mao W, McKay R, Hahn RT, Sun W. A Comprehensive engineering analysis of left heart dynamics after MitraClip in a functional mitral regurgitation patient. *Front Physiol.* (2020) 11:432. doi: 10.3389/fphys.2020.00432

19. Singh GD, Smith TW, Rogers JH. Mitral stenosis due to dynamic clip-leaflet interaction during the MitraClip procedure: case report and review of current knowledge. *Cardiovasc Revascul Med.* (2017) 18:287–94. doi: 10.1016/j.carrev.2016.12.009

20. Kassar M, Praz F, Hunziker L, Pilgrim T, Windecker S, Seiler C, et al. Anatomical and technical predictors of three-dimensional mitral valve area reduction after transcatheter edge-to-edge repair. *J Am Soc Echocardiogr.* (2022) 35:96–104. doi: 10.1016/j.echo.2021.08.021

21. El Sabbagh A, Reddy YNV, Barros-Gomes S, Borlaug BA, Miranda WR, Pislaru SV, et al. Low-gradient severe mitral stenosis: hemodynamic profiles, clinical characteristics, and outcomes. *J Am Heart Assoc.* (2019) 8:1–12. doi: 10.1161/JAHA.118.010736

22. Mele D, Smarrazzo V, Pedrizzetti G, Capasso F, Pepe M, Severino S, et al. Intracardiac flow analysis: techniques and potential clinical applications. *J Am Soc Echocardiogr.* (2019) 32:319–32. doi: 10.1016/j.echo.2018.10.018

23. Obermeier L, Vellguth K, Schlief A, Tautz L, Bruening J, Knosalla C, et al. CT-based simulation of left ventricular hemodynamics: a pilot study in mitral regurgitation and left ventricle aneurysm patients. *Front Cardiovasc Med.* (2022) 9:828556. doi: 10.3389/fcvm.2022.828556

24. Lantz J, Henriksson L, Persson A, Karlsson M, Ebbers T. Patient-specific simulation of cardiac blood flow from high-resolution computed tomography. *J Biomech Eng.* (2016) 138:1–9. doi: 10.1115/1.4034652

25. Hellmeier F, Brüning J, Sündermann S, Jarmatz L, Schafstedde M, Goubergrits L, et al. Hemodynamic modeling of biological aortic valve replacement using preoperative data only. *Front Cardiovasc Med.* (2021) 7:593709. doi: 10.3389/fcvm.2020.593709

26. Rego BV, Khalighi AH, Drach A, Lai EK, Pouch AM, Gorman RC, et al. A non-invasive method for the determination of *in vivo* mitral valve leaflet strains. *Int J Numer Methods Biomed Eng.* (2018) 34:e3142. doi: 10.1002/cnm.3142

27. Sacks MS, Drach A, Lee CH, Khalighi AH, Rego BV, Zhang W, et al. On the simulation of mitral valve function in health, disease, and treatment. *J Biomech Eng.* (2019) 141:070804. doi: 10.1115/1.4043552

28. Errthum R, Caballero A, McKay R, Sun W. Comparative computational analysis of PASCAL and MitraClip implantation in a patient-specific functional mitral regurgitation model. *Comput Biol Med.* (2021) 136:104767. doi: 10.1016/j.compbiomed.2021.104767

29. Dabiri Y, Mahadevan VS, Guccione JM, Kassab GS. A Simulation study of the effects of number and location of mitraclips on mitral regurgitation. *JACC Adv.* (2022) 1:100015. doi: 10.1016/j.jacadv.2022.100015

30. Vellguth K, Brüning J, Goubergrits L, Tautz L, Hennemuth A, Kertzscher U, et al. Development of a modeling pipeline for the prediction of hemodynamic outcome after virtual mitral valve repair using image-based CFD. *Int J Comput Assist Radiol Surg.* (2018) 13:1795–805. doi: 10.1007/s11548-018-1821-8

31. Tautz L, Neugebauer M, Hüllebrand M, Vellguth K, Degener F, Sündermann S, et al. Extraction of open-state mitral valve geometry from CT volumes. *Int J Comput Assist Radiol Surg.* (2018) 13:1741–54. doi: 10.1007/s11548-018-1831-6

32. Vellguth K, Brüning J, Tautz L, Degener F, Wamala I, Sündermann S, et al. User-dependent variability in mitral valve segmentation and its impact on CFD-computed hemodynamic parameters. *Int J Comput Assist Radiol Surg.* (2019) 14:1687–96. doi: 10.1007/s11548-019-02012-1

33. Quiñones MA, Otto CM, Stoddard M, Waggoner A, Zoghbi WA. Recommendations for quantification of Doppler echocardiography: a report from

the Doppler Quantification Task Force of the Nomenclature and Standards Committee of the American Society of Echocardiography. *J Am Soc Echocardiogr*. (2002) 15:167–84. doi: 10.1067/mje.2002.120202

34. Walczak L, Georgii J, Tautz L, Neugebauer M, Wamala I, Sündermann S, et al. Using position-based dynamics for simulating the mitral valve in a decision support system. In: Kozlíková B, Linsen L, Vázquez PP, Lawonn K, Raidou RG, editors. *Eurographics Workshop on Visual Computing for Biology and Medicine*. The Eurographics Association (2019).

35. Walczak L, Tautz L, Neugebauer M, Georgii J, Wamala I, Sündermann S, et al. Interactive editing of virtual chordae tendineae for the simulation of the mitral valve in a decision support system. *Int J Comput Assist Radiol Surg*. (2020) 16:125–32. doi: 10.1007/s11548-020-02230-y

36. Walczak L, Georgii J, Tautz L, Neugebauer M, Wamala I, Sündermann S, et al. Using position-based dynamics for simulating mitral valve closure and repair procedures. *Comput Graph Forum*. (2022) 41:270–87. doi: 10.1111/cgf.14434

37. Karimi S, Dabagh M, Vasava P, Dadvar M, Dabir B, Jalali P. Effect of rheological models on the hemodynamics within human aorta: CFD study on CT image-based geometry. *J Non-Newtonian Fluid Mech*. (2014) 207(Suppl. C):42–52. doi: 10.1016/j.jnnfm.2014.03.007

38. Blender Online Community. *Blender - a 3D Modelling and Rendering Package*. Amsterdam: Blender Institute. Available online at: http://www.blender.org

39. Razafindrazaka FH, Vellguth K, Degener F, Suendermann S, Kühne T. Mesh based approximation of the left ventricle using a controlled shrinkwrap algorithm. In: *Lecture Notes in Computer Science (including subseries Lecture Notes in Artificial Intelligence and Lecture Notes in Bioinformatics)*. Vol. 11504. Cham: Springer (2019). p. 230–9. Available online at: http://link.springer.com/10.1007/978-3-030-21949-9_25

40. Pierrakos O, Vlachos PP. The effect of vortex formation on left ventricular filling and mitral valve efficiency. *J Biomech Eng*. (2006) 128:527. doi: 10.1115/1.2205863

41. Moro E, Nicolosi G, Burelli C, Rellini G, Grenci G, Zanuttini D. [Determination of the transvalvular gradient using continuous wave Doppler in patients with mitral stenosis. Correlation with the hemodynamic method]. *Giornale Ital Cardiol*. (1987) 17:306–10.

42. Riegel AK, Busch R, Segal S, Fox JA, Eltzschig HK, Shernan SK. Evaluation of transmitral pressure gradients in the intraoperative echocardiographic diagnosis of mitral stenosis after mitral valve repair. *PLoS ONE*. (2011) 6:e26559. doi: 10.1371/journal.pone.0026559

43. Besler C, Noack T, von Roeder M, Kitamura M, Kresoja KP, Flo Forner A, et al. Transcatheter edge-to-edge mitral valve repair with the PASCAL system: early results from a real-world series. *EuroIntervention*. (2020) 16:824–32. doi: 10.4244/EIJ-D-20-00216

44. Vasudevan V, Wiputra H, Yap CH. Torsional motion of the left ventricle does not affect ventricular fluid dynamics of both foetal and adult hearts. *J Biomech*. (2019) 96:109357. doi: 10.1016/j.jbiomech.2019.109357

45. Canè F, Selmi M, De Santis G, Redaelli A, Segers P, Degroote J. Mixed impact of torsion on LV hemodynamics: a CFD study based on the Chimera technique. *Comput Biol Med*. (2019) 112:103363. doi: 10.1016/j.compbiomed.2019.103363

frontiers | Frontiers in Cardiovascular Medicine

TYPE Review
PUBLISHED 13 September 2022
DOI 10.3389/fcvm.2022.970438

OPEN ACCESS

EDITED BY
Sabina Gallina,
University of Studies G. d'Annunzio Chieti and Pescara, Italy

REVIEWED BY
Saverio Muscoli,
Policlinico Tor Vergata, Italy
Federica Moscucci,
Sapienza University of Rome, Italy

*CORRESPONDENCE
Christian Cadeddu Dessalvi
cadedduc@unica.it

SPECIALTY SECTION
This article was submitted to Cardiovascular Imaging, a section of the journal Frontiers in Cardiovascular Medicine

RECEIVED 15 June 2022
ACCEPTED 25 July 2022
PUBLISHED 13 September 2022

CITATION
Onnis C, Cadeddu Dessalvi C, Cademartiri F, Muscogiuri G, Angius S, Contini F, Suri JS, Sironi S, Salgado R, Esposito A and Saba L (2022) Quantitative and qualitative features of carotid and coronary atherosclerotic plaque among men and women. *Front. Cardiovasc. Med.* 9:970438. doi: 10.3389/fcvm.2022.970438

Quantitative and qualitative features of carotid and coronary atherosclerotic plaque among men and women

Carlotta Onnis[1], Christian Cadeddu Dessalvi[2]*, Filippo Cademartiri[3], Giuseppe Muscogiuri[4], Simone Angius[2], Francesca Contini[2], Jasjit S. Suri[5], Sandro Sironi[4], Rodrigo Salgado[6], Antonio Esposito[7,8] and Luca Saba[1]

[1]Department of Radiology, Azienda Ospedaliero-Universitaria (A.O.U.), di Cagliari—Polo di Monserrato, Cagliari, Italy, [2]Department of Medical Sciences and Public Health, Università Degli Studi di Cagliari, Cagliari, Italy, [3]Department of Radiology, Fondazion Monasterio/CNR, Pisa, Italy, [4]Department of Radiology, San Luca Hospital, Istituto Auxologico Italiano IRCCS, University of Milano-Bicocca, Milan, Italy, [5]Stroke Diagnostic and Monitoring Division, AtheroPoint™, United States and Advanced Knowledge Engineering Centre, Global Biomedical Technologies Inc. (GBTI), Roseville, CA, United States, [6]Department of Radiology, Antwerp University Hospital, Antwerp, Belgium, [7]Experimental Imaging Center, Istituto di Ricovero e Cure a Carattere Scientifico (IRCCS) Ospedale San Raffaele, Milan, Italy, [8]School of Medicine, Vita-Salute San Raffaele University, Milan, Italy

Cardiovascular diseases (CVDs), particularly ischemic heart disease (IHD) and stroke, present epidemiologically in a different way among sexes. The reasons of these sex-based differences should be delved into sex-specific cardiovascular (CV) risk factors and different mechanisms of atherosclerotic progression. Imaging techniques of both carotid and coronary atherosclerotic plaques represent a tool to demonstrate sex-related features which might be used to further and better assess CV risk of male and female population. The aim of this review is to evaluate current knowledge on sex-specific qualitative and quantitative plaque features of coronary and carotid atherosclerosis. We also discuss the clinical implication of a sex-based plaque phenotype, evaluated with non-invasive imaging techniques, such as CT-angiography and MRI-angiography, to stratify CV risk.

KEYWORDS

atherosclerosis, sex-based differences, coronary imaging, carotid imaging, MRA (magnetic resonance angiography), CTA (computed tomographic angiography), gender

Introduction: Patho-physiology of sex-related differences in atherosclerosis

Atherosclerosis is a progressive disease that affects arteries, characterized by the accumulation of lipids, macrophages, fibrous elements and smooth muscle cells within the vessel, forming the atherosclerotic plaque. Atherosclerosis is a chronic inflammatory condition that can lead to acute clinical events by plaque rupture and/or thrombosis, thus causing major events such as acute myocardial infarction (AMI), heart failure (HF), within the galaxy of ischemic heart disease (IHD), and stroke (1). These two cardiovascular diseases (CVDs) together represent the most common cause of death globally, with IHD and stroke responsible for 16 and 11% of the world's total deaths, respectively, and that is why atherosclerosis is a condition of global interest (2, 3).

In the past decades, several studies have proven that atherosclerosis is strongly associated with several risk factors, such as hypertension, smoking, dyslipidemia, diabetes, obesity, age and family history, leading to the concept of vulnerable patient, at higher risk of developing acute CV events in the near future (4–6). Nonetheless, it is well known that CVDs presents differently among men and women: IHD in women develops after 7–10 years compared to men, in fact men are three times more likely to develop acute coronary syndromes (ACS) under the age of 60, while this tendency decreases with age and the likelihood among sexes equalizes over 75 years. With regards to cerebrovascular events, women over the age of 85 have a higher risk of developing stroke than men, leading to greater disability, mortality and case fatality in this group (7). Additionally, stroke is more likely to be the first manifestation of CVD in women, while IHD tends to be the first in men.

This knowledge has progressively led to the establishment of sex-specific CV risk assessment (8, 9), with sex referring to the biological characteristics of individuals as opposed to gender which indicates a broader concept rooted into society. Even though gender can influence health by reflecting the economic resources and healthcare access of the population, and despite the impossibility to define sex and gender in a binary way, the literature offers very few examples of non-binary trials or gender-related studies (10, 11). Thus, in this review we will use the term sex, but we emphasize its limitations.

Regarding sex-specific CV risk-factors, attention should be paid also to the modern role of women in the Western society: nowadays working patterns and activities are similar among sexes, but with women often having family responsibilities on top of time- and energy-consuming working roles. This joint social burden led to increased psychosocial stressors which further increase CV risk (12). Thus, modern female lifestyle and under-recognized risk factors, such as anxiety, depression, physical and psychological abuse, socioeconomic status and health literacy should be taken into consideration when adopting CV risk prevention strategies, especially during and after Sars-CoV-2 pandemic which exacerbated these risk factors (13).

The mechanisms underlying sex as a variable in atherosclerosis are constantly under-study, but the main finding is that until menopause women are protected by estrogens which seem to have an athero-protective role. In particular, estrogens have a pluripotent effect on the cardiovascular system, affecting the endothelium, coagulation, inflammation and adhesion (14). 17beta-estradiol (E2) is the most common form of circulating estrogen and by binding with estrogen receptors (ERs) it triggers a signaling cascade that alter gene expression affecting atherogenesis: For example, in hepatocytes the ER signaling activation is crucial to reverse cholesterol transport and protects against lipid accumulation in women. Furthermore, ER inhibits the proliferation of vascular smooth muscle cells in case of high level of glucose and, considering that those cells are a source of reactive oxygen species (ROS), which advances atherosclerosis, estrogen-ER complex performs its protective role. Finally, ER decreases differentiation of vascular muscle cells in osteoblastic-like cells, thus reducing occurrence of calcification within atherosclerotic lesions (15).

The important role of sex hormones also drove attention to sex hormone-binding globulin (SHBG), a protein that binds to and regulates available testosterone and estradiol. SHBG seems to be a potential risk stratification tool for predicting CV risk. In particular, there is an inverse association between serum SHBG levels and vascular risk factors (insulin resistance, diabetes, metabolic syndrome for example) and outcomes (IHD and stroke), which might be linked to either high free testosterone with consequent downstream pro-androgenic effects, or activation of inflammatory pathways (16, 17).

Moreover, proteomic studies have shown that female and male endothelial cell secretome responds differently to cellular stress induced by the same injury. Endothelial cells seem to adopt different strategies: in male more commonly apoptosis, while in female cells autophagy. Among the proteins secreted during apoptosis, PTX3 was found to have a crucial role in male-specific endothelial response to stressors. These results suggest a novel mechanism for sex-specific pathophysiological responses and identify PTX3 as a possible pharmacological target, considering its role as regulator of pro- and anti-inflammatory signals at the vascular bed, which should be further studied (18).

Female-specific risk factors, both modifiable and not, should also be taken into consideration. Adverse pregnancy outcomes (i.e., gestational hypertension, preterm delivery, preeclampsia/eclampsia) are associated with increased long-term CV risk of the mother and the mechanism seems to be an altered inflammatory state which affects maternal vasculature (19, 20). Lifetime estrogen exposure, early menarche and short reproductive life span in particular, represent another

unmodifiable risk factor, as shown in a recent meta-analysis that highlights how a reproductive life span < 33 years is associated with higher rate of CVD events in midlife (21). Among the modifiable female-specific risk factors use of combined oral contraceptive and menopausal hormone therapy play an important role that is still under study (22). Even though systemic autoimmune disease is not a sex-specific risk factor, it should be taken into consideration that females are disproportionally affected, accounting for the 78% of patients (23). On one hand, chronic inflammation caused by autoimmune disease is associated with endothelial dysfunction and atherosclerosis progression, on the other hand steroid used to treat these conditions worsen hyperglycemia and dyslipidemia (24).

Clinical and pathological evaluation has revealed that males develop atherosclerotic plaque earlier, with the atherogenesis starting at a younger age in men than women; intima-media thickness (IMT) is usually greater in men until the age of 75, when we assist to the late catch-up phenomenon in women. Plaque inflammatory state seems to be greater in males than females and more vulnerable/unstable features are seen in non-invasive imaging of the male population. Moreover, plaque burden is greater in males while individual stenosis is greater in females, but plaque burden, associated with vulnerability, better predicts adverse ischemic events (25).

In this setting, non-invasive imaging techniques such as ultrasound, computed tomography angiography (CTA) and magnetic resonance angiography (MRA) can provide a useful tool to analyze plaque features among men and women. Thus, the aim of this review is to evaluate the current knowledge on sex-related differences of atherosclerosis in order to better stratify CV risk and target a preventive and effective therapy to the sub-population.

State of the art: Quantitative and qualitative aspects of carotid and coronary atherosclerotic plaque among men and women

Sex-related features in coronary atherosclerosis

CTA has proven to be a valid technology that can easily identify patients at risk of subsequent CV events, and it can guide treatment management, improving outcome (**Table 1**). Recent studies have shown that a quantitative analysis of atherosclerotic plaque burden on cardiac-CTA (CCTA) can stratify the risk of future events better than traditional CV risk factors, coronary artery calcification (CAC) and coronary artery stenosis severity (26). In particular, low-attenuation plaque burden proved to be the strongest predictor of fatal or non-fatal myocardial infarction and with a low-attenuation plaque burden greater than 4% the risk of having a myocardial infarction is 5 times higher. Thus, CCTA adds important prognostic information but whether this assessment has an equal prognostic value in men and women is still under study. In fact, as Williams et al.(27) hypothesized based on the SCOT-HEART multicenter randomized controlled trial, sex differences in CAD may be explained by CT plaque assessment, which included evaluation of adverse plaque characteristics: positive remodeling, low-attenuation plaque, spotty calcification and the "napkin ring" sign (**Figure 1**). They discovered that women had lower CAC score, less frequent adverse plaque features, less obstructive CAD and overall lower quantitatively assessed plaque burden, leading to fewer subsequent MI compared to men. These findings, in agreement with the CONFIRM registry (28) and the ICONIC (29) study results, suggest that, while women presenting with stable chest pain have a specific, sex-based, plaque phenotype, symptomatic patients presenting with ACS have no sex difference in quantitative plaque features in culprit lesions. Indeed, there was no difference in necrotic core volume despite women having lower fibrous/fibrofatty plaque volume compared to men. Thus, even though women with stable angina presents with a different set of plaque features, when it comes to culprit lesions causing MI, both sexes seem to have similar plaque characteristics. Recent studies also showed that, within a given CAC score group, women tend to have smaller number, but larger size and density of calcified plaques compared to men, reflecting a more advanced atherosclerotic state/higher levels of inflammation, in line with less frequent obstructive disease but higher CVD mortality among women (mean age: 56.2 years) compared with men (30) (**Figure 2**).

Additionally, El Mahdiui et al. (31) in their study evaluated plaque composition by serial CTA taking into consideration the influence of menopause. What they demonstrated is that men had more fibrofatty percentage atheroma volume (PAV), but pre-menopausal women, younger than 55 years, had greater regression of fibrous and non-calcified PAV over time compared to men of the same age, and given the positive association between non-calcified plaques with ischemia and ACS, these findings are in agreement with the lower risk of symptomatic CAD in young women (32). On the contrary, the lack of this regression in post-menopausal women suggests a progressive match to the non-calcified PAV of men with consequent increased risk of CAD in accordance with epidemiological data.

The PARADIGM study (33), a dynamic multinational observational registry of patients who underwent clinically indicated serial CCTA, also showed that total and compositional plaque volume (PV) progression rate differed among sexes: women had lower overall atherosclerotic burden in all age groups, reduced development of high-risk plaques and a PV progression mainly driven by calcified PV (faster calcified and slower non-calcified progression) while men had more non-calcified PV progression. The study demonstrated a 9-year delay in women for developing the total coronary atherosclerotic burden of men. The protective role of estrogen,

TABLE 1 Studies regarding coronary atherosclerosis.

Authors	Number (patients)	Date published	Research objectives	Main results
Williams et al. (26) babi	1,769	2020	Role of non-calcified low-attenuation plaque burden assessed by coronary-CTA as a predictor of future risk of myocardial infarction (MI)	Low-attenuation plaque burden the strongest predictor of fatal or non-fatal MI (low-attenuation burden > 4% = nearly 5 times higher risk to have subsequent MI)
Williams et al. (27) babi	1,769	2021	Role of CCTA plaque assessment in explaining prognostic differences among men and women presenting with chest pain	Women (58 ± 9 years) less likely to have adverse plaque features compared to men and lower risk of subsequent MI
Schulman-Marcus et al. (28) babi	5,632	2016	Sex-specific associations between per-vessel CAD and major adverse CV events (MACE) over a 5-year period	Obstructive CAD more prevalent in men. Strong association between increased MACE risk and extent of per-vessel obstructive CAD
Conte et al. (29) babi	468	2021	Investigate sex and age differences in atherosclerotic features assessed by CCTA prior to acute coronary syndrome	Females had lower total plaque volume and fibrous/fibrofatty plaque volume within both the age groups
Shaw et al. (30) babi	63,215	2018	Sex differences in calcified plaque assessed by Agatson score and other CAC measures	Within CAC subgroups women had fewer calcified lesions and greater lesion size; CAC was associated with 1.3-fold higher risk for CV death among women; women with larger sized and more numerous CAC lesions had 2.2-fold higher CV mortality compared to men
El Mahdiui et al. (31) babi	211	2021	Role of sex and menopause on long-term plaque progression and evolution of plaque composition	Women had less fibrofatty atheroma volume on a per-lesion analysis; women < 55 years had more regression of fibrous and non-calcified atheroma volume over time compared to men
Lee et al. (33) babi	1,255	2020	Role of sex in total and compositional plaque volume progression in patients with CAD	9-year delay in women in developing total PV than in men; high-risk plaques more prevalent in men; women had greater calcified PV progression, slower non-calcified PV progression and less development of high-risk plaques
Xie et al. (36) babi	5,166	2017	Prognostic significance of non-obstructive left main CAD among sexes	Presence of non-obstructive LM plaque increased the risk for composite outcome and adverse events in women
Langabeer et al. (52) babi	16,861	2019	Gender differences in non-STEMI acute coronary syndrome	At baseline women were older and more often with history of prior CVD; women had higher in-hospital mortality, 23 min longer stay at ED, less likely to receive early invasive strategy compared to men
Langabeer et al. (53) babi	9,674	2018	Sex-related effects in outcomes in a large regional STEMI system of care	Length of stay was longer for women; females were less likely to survive at discharge and to be discharged to home

until menopause, on development and progression have been suggested, especially taken into consideration the inhibitory effect of estrogen on vascular calcification (34). However, estrogen influence seems to be over-taken by the presence of risk factors resulting in worse outcome and prognosis for young women presenting with acute coronary syndrome compared to young men (35).

Finally, Xie et al. (36) found that non-obstructive left-main plaque was associated with 50% higher risk for adverse events among women, independently of CAD burden in other vessels, whereas this association was not significantly present among men; similarly, they found that women had a risk for future events 1.8-fold higher than men. Finding these sex-specific differences in prognosis provides an important risk and prognostic marker that should be considered during risk stratification of women. Thus, when evaluating prognosis, location of non-obstructive plaque should be considered.

New insights have been given by arterial and plaque characterization through intravascular ultrasound (IVUS), particularly concerning endothelial shear stress (ESS) which, with lower values, induces endothelial cell dysfunction and plaque progression. As Wentzel et al. (37) suggested in their study, which analyzed data from the PREDICTION study, coronary arteries and plaques were significantly smaller in females compared to males but ESS and ESS-related plaque progression were similar in both sexes. Only after stratifying for age they found that ESS-related plaque growth was more marked in women < 55 years and that female population showed a continuous reduction in magnitude of ESS-dependent plaque progression until 75 years of age, partially explaining the "catch up phenomenon" in female atherosclerosis.

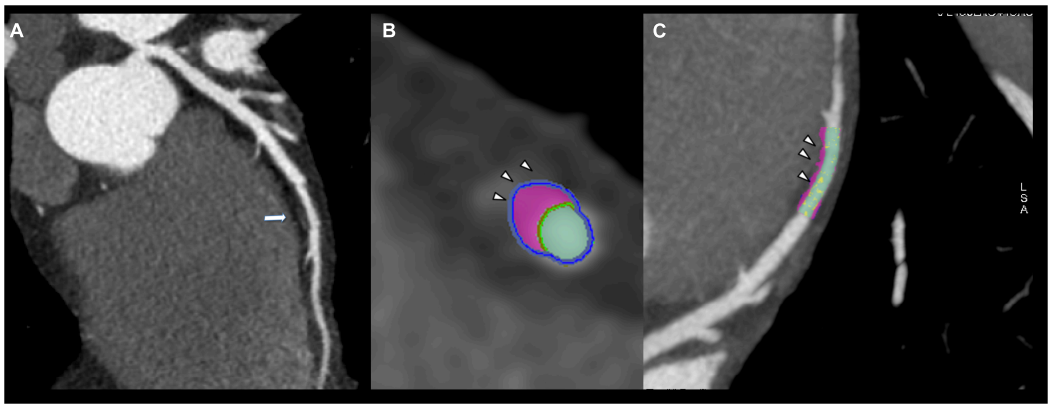

FIGURE 1
Thirty-six years old male showing fibrofatty plaque with positive remodeling on mid-lef anterior descending artery (arrow, **A**). Plaque analysis confirmed the fibrofatty composition of coronary plaque demonstrating the positive remodeling (arrowhead, **B,C**).

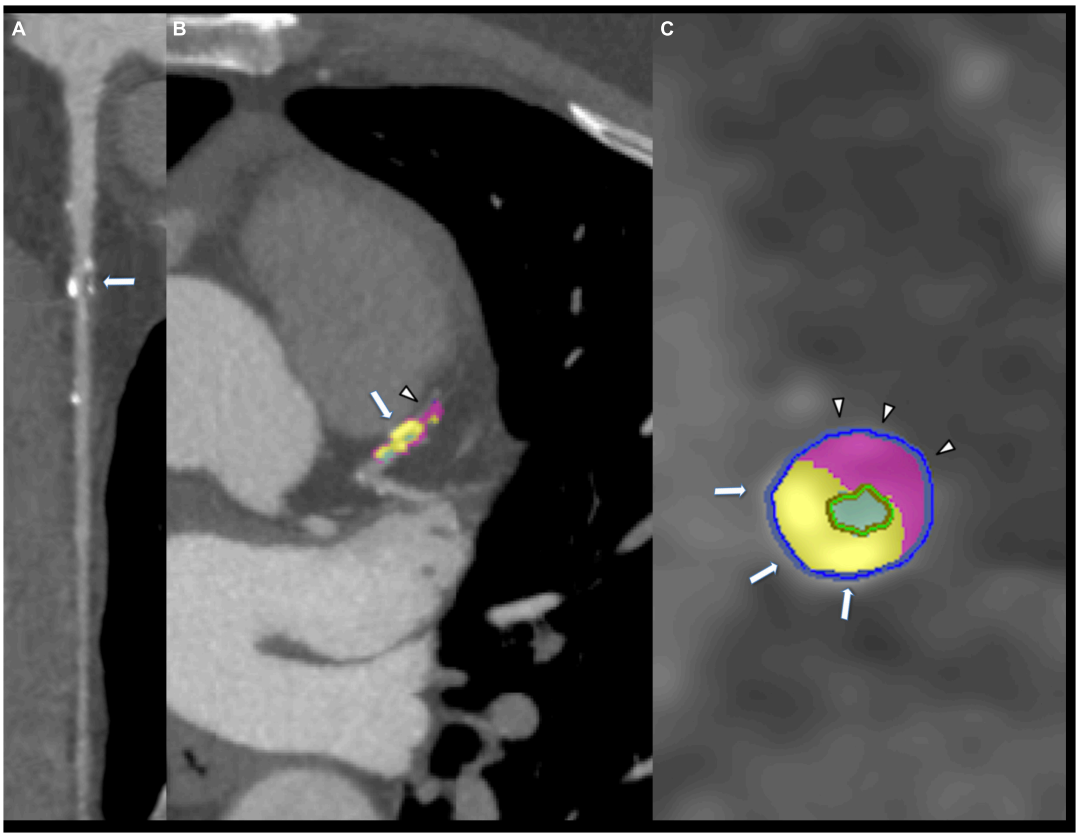

FIGURE 2
Eighty-five years old male showing mixed coronary plaque on proximal left anterior descending artery (arrow, **A**). Composition of plaque was composed by calcium (arrow, **B,C**) and fibrofatty portion (arrowhead **B,C**).

Sex-related features in carotid atherosclerosis

Epidemiology tells us that men have higher lifetime risk of stroke than women, but if women suffer from a stroke it is usually more severe, leading to greater disability (38). These epidemiological dissimilarities may have root in a sex-based pattern of carotid atherosclerosis, which is constantly under study especially through plaque imaging, including ultrasound and CTA, but mainly MRI (**Table 2**). It is well known that

10.3389/fcvm.2022.970438

TABLE 2 Studies regarding carotid atherosclerosis.

Authors	Number (patients)	Date published	Research	Main results
Van den Bouwhuijsen et al. (42) babi	1,006	2012	Carotid plaque components as determinants of plaque progression and destabilization	Intraplaque hemorrhage (IPH) and lipid core (indicators of unstable plaque) more prevalent in men than women
Ota et al. (43) babi	131	2010	MRI carotid plaque assessment as a tool to demonstrate sex differences indicative of higher-risk plaque	Presence of thin/ruptured fibrous cap and lipid-rich necrotic core (LRNC) were more common in men; men had larger volumes of percent hemorrhage and necrotic core
Zhang et al. (44) babi	567	2021	To compare carotid atherosclerotic features among sexes	In both symptomatic and asymptomatic arteries, men had greater lumen, wall and total vessel area, higher mean wall thickness, higher prevalence of LRNC
Van Dam-Nolen et al. (45) babi	224	2022	To investigate sex differences in carotid plaque composition and morphology in patients with stroke	Total plaque volume was higher in men; IPH and LRNC more prevalent in men; men had more often coexistence of calcifications, LRNC and IPH, of thin/ruptured fibrous cap, LRNC and IPH and of all plaque features
Van Dam-Nolen et al. (46) babi	182	2021	To investigate the relation of lipoprotein(a) levels and carotid atherosclerotic plaque features	In women increased plasma Lp(a) was associated with IPH, in men with degree of stenosis
Schreiner et al. (47) babi	15,124	1996	To study the association of lipoprotein(a) with preclinical atherosclerotic disease in different race and gender groups	Lp(a) was associated with increased wall thickness in men while in women the association was stronger when smoking and diabetes were present
Song et al. (48) babi	189	2021	Sex differences in non-stenotic carotid plaque composition in patients with embolic stroke of undetermined source (ESUS)	Men had higher calcified plaque volume and IPH/LRNC ratio in carotid ipsilateral to stroke side; control cohort showed no sex difference in plaque volumes ipsilateral to stroke
Singh et al. (50) babi	906	2017	Age-specific sex differences in the presence of IPH	IPH was more prevalent in men for all ages; male sex modified the effect of age on the presence of IPH; with increasing age post-menopause, the odds of IPH in women become closer to that of men

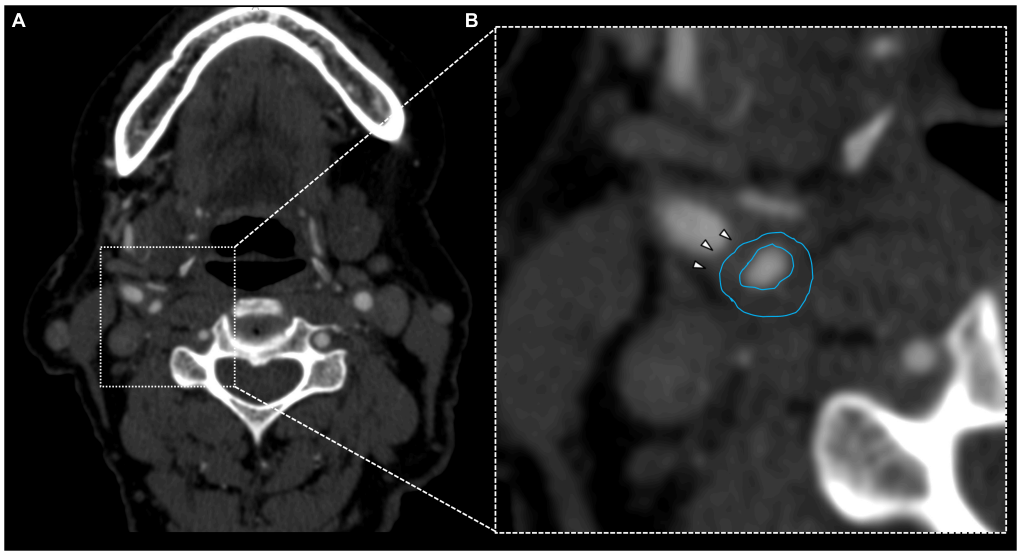

FIGURE 3
Fifty-six years old female showing fibrofatty plaque with concentric remodeling on right ICA **(A)**. Plaque analysis confirmed the fatty composition of the plaque (**B**, white arrowheads).

imaging biomarkers of vulnerability exist and that they predict stroke risk: intraplaque hemorrhage (IPH), best seen with MRI (39) but recently studied with CT as well (40); lipid-rich necrotic core (LRNC) either on CT and MRI; thin-rupture fibrous cap (TRFC), with contrast-enhanced MRI; carotid plaque thickness and surface morphology with all three imaging modalities;

10.3389/fcvm.2022.970438

TABLE 3 Difference between men and women of high-risk plaque features in carotid and coronary arteries.

High-risk features	Prevalence	References
Carotid arteries		
IPH	Men > Women	(42)
LRNC	Men > Women	(42–43)
Thin/ruptured fibrous cap	Men > Women	(43)
Wall thickness	Men > Women	(44)
Total vessel area	Men > Women	(45)
Total plaque volume	Men > Women	(46)
Calcified plaque volume	Men > Women	(48)
Coronary arteries		
Low-attenuation burden > 4%	Men > Women	(26–27)
Extent of per-vessel obstructive CAD	Men > Women	(28)
Total plaque volume	Men > Women	(29)
Fibrous/fibrofatty plaque volume	Men > Women	(29–31)
Larger sized and number of calcified lesions	Men < Women	(30)

plaque volume with CT because of its high spatial resolution (41). These imaging features of vulnerability present differently among men and women. Indeed, men tend to have vulnerable plaques more frequently than women, as seen in the Rotterdam study (42) where they demonstrated that in a population with carotid wall thickening, IPH and LRNC, indicating plaque vulnerability, are highly frequent and more prevalent in men (**Figure 3**).

Similarly, Ota et al. (43) assessed plaque characteristics in asymptomatic patients using 3-T MRI and they discovered that men present more frequently with LRNC, TRFC, larger percent volume of lipid core and IPH compared to women. With this features, atherosclerotic plaque is more prone to rupture, leading to subsequent ischemic events: hence, in their study Ota et al. suggested that 3-T carotid plaque MRI can identify high-risk phenotype and patients, and that their findings are consistent with epidemiological data, explaining why men age < 75 years have higher incidence of stroke than women.

Recently, in a study by Zhang et al. (44), both asymptomatic and symptomatic patients underwent 3-T carotid MRI. While in symptomatic carotid arteries, men showed similar plaque burden, despite larger vessel size, higher prevalence of LRNC and IPH compared to women, in asymptomatic carotid arteries men had more vulnerable features, such as higher percent LRNC and TRFC. Their findings are in agreement with the previous studies, indicating that asymptomatic male population tend to have vulnerable plaque features more frequently than women while plaque burden is similar in both sexes.

New insights have been given by the Plaque At Risk (PARISK) study (45), a prospective multicenter cohort study of patients with a high recurrent stroke risk with < 70% carotid stenosis. In particular, van Dam-Nolen et al. (46) examined patients with recent ischemic cerebrovascular symptoms and ipsilateral carotid stenosis < 70%, who underwent carotid MRI and CTA. They confirmed that men tend to have larger plaque volume, more vulnerable plaque composition (IPH, LRNC, TRFC) and more frequent coexistence of vulnerable features. They also suggested that sex-based plaque differences may not be related just to larger plaque burden in men: in fact, after adjusting the findings for total plaque volume, the prevalence of IPH and LRNC remained higher in men than in women, while the difference in IPH and LRNC volume disappeared, indicating that plaque burden does not fully explain the sex differences in carotid atherosclerosis and that sex plays an important role in the development of a vulnerable plaque rather than in the size of its components. This knowledge may lead to a sex-specific management of stroke and transient ischemic attack, with men benefitting from a carotid endarterectomy more than women (45).

Moreover, another work of van Dam-Nolen et al. (46) on the PARISK study, further evaluated the known importance of lipoprotein(a) as an independent risk factor for CVD and recurrent stroke (47). Not only they confirmed the positive association between Lp(a) levels and atherosclerosis, but also they suggested that Lp(a) distribution, as well as carotid plaque composition, differ between men and women and that Lp(a) levels peak during late perimenopause/postmenopause. Notably, they identified new associations between Lp(a) concentrations and plaque features: in male population elevated Lp(a) levels were associated with higher degree of stenosis, whilst in female population high Lp(a) levels tend to be associated with higher prevalence of IPH. This difference suggests that Lp(a) levels in women might be a stronger risk indicator for developing severe carotid atherosclerosis.

Additionally, Song et al. (48) examined sex differences in non-stenotic carotid plaque composition in patients with embolic stroke of undetermined source (ESUS) who underwent CTA. What they discovered is that in the atrial fibrillation cohort, used as control population, there was no significant sex difference in plaque volume and features, while among the ESUS cohort men had significantly higher IPH volume and IPH/LRNC ratio ipsilateral to stroke side compared to women, suggesting a differential contribution of atheroembolism from carotid plaque among men and women presenting with ESUS. Furthermore, they suggested IPH/LRNC ratio as a possible predictor of plaque rupture, stronger than LRNC alone, which may not always progress to rupture. In fact, IPH and increased neovascularity within a lipid-rich necrotic core can facilitate inflammation and core expansion, leading to greater rupture risk. Similarly, Saba et al. (49) observed that the ratio between IPH, indicated by Hounsfield units < 25 on CTA, and lipid volume is significantly associated with cerebrovascular events, hence representing a strong parameter for future events. Another study, by Singh et al. (50), also revealed that in patients with low-grade carotid stenosis the presence of IPH occurs more frequently with age, affecting less than 1% of patients before the age of 55 until a maximum of 12% by the age of 75 years,

and with sex, affecting more men than women. An interesting result of this study was also the absence of IPH in females before the age of 65 years, which was progressively replaced with age, indicating that sex modifies the effect of age on carotid IPH. Hence, the infrequency of IPH in women before the age of 75 might explain the lower incidence of stroke among women of this age group when compared to men.

Discussion

Atherosclerosis differs among sexes, both from a physio-pathological point of view and clinically as well. Epidemiology shows that women presents with IHD after an average of 7–10 years compared to men; men under the age of 60 are three times more likely to present with ACS, ST-segment elevation myocardial infarction (STEMI) and NSTEMI (51); while this tendency decreases over 75 years, we see an increase of morbidity and mortality rate in women, with 7.4% in-hospital mortality for STEMI in women vs. 4.6% in men and 4.8 vs. 3.9%, respectively, for NSTEMI (52, 53). Moreover, women over the age of 85 have a higher risk of developing stroke than men, with 55,000 more females having a stroke than males every year, indicating that women might be treated less aggressively in primary and secondary prevention for this disease (7). Other data from the Heart Disease and Stroke Statistics—2022 Update (54) revealed that stroke is more prevalent in men until the age of 80 years, but over 80 this tendency inverts, and that more females than men die of stroke each year, indicating that the cause might be this higher prevalence in elderly women.

What the literature reveals is that these epidemiological disparities have a physio-pathological counterpart which can be studied histologically and with invasive methods, but also with non-invasive techniques. In this context, radiology with CTA, MRA and ultrasound provides useful tools that may be used not only for academic purposes but also for clinical ones, giving information regarding plaque characteristics that can be linked to outcome and prognosis (**Table 3**). Indeed, CTA provides information regarding plaque features of vulnerability (positive remodeling, low-attenuation plaque, spotty calcification, "napkin ring" sign) and thus prognosis. In fact, low-attenuation plaque volume (26) and IPH/LRNC ratio (49) appeared to be two strong prognostic markers that can predict fatal and non-fatal future MI the former, and cerebrovascular events the latter. In addition, through CCTA it is possible to understand the female-specific coronary plaque phenotype, which partially explains the epidemiological data mentioned above. Women before menopause tend to have lower CAC score, less high-risk plaque features, less plaque volume, less obstructive CAD (27) and greater fibrous and non-calcified PAV regression (31). After menopause, the literature seems to identify a different female-specific coronary plaque phenotype, which tends to be more similar to that one of men: Less non-calcified PAV regression (31) and smaller number but larger size and higher density of calcified plaque (30), progressively matching, with a 9-year delay, the total coronary atherosclerotic burden of men (33). Additionally, taken into consideration that non-calcified PV seems to be influenced mainly by environmental factors, while CAC and calcified PV are linked to genetics (55), CCTA might be a useful tool to early detect non-calcified plaque in order to start an early lifestyle intervention, thus preventing coronary plaque formation.

Notably, the literature (27) shows that women presents with this specific, sex-based plaque phenotype more evidently when they are asymptomatic or in case of stable angina. Indeed, the above-mentioned sex-based features tend to flatten when ACS occurs, and no significant difference among men and women can be found in culprit lesions causing MI. The necrotic core volume is in fact similar among sexes. This finding might suggest the role of CCTA for risk stratification, before ACS occur, and the importance of primary prevention in order to treat aggressively those women presenting with high-risk features or markers of worse prognosis. With this regard, an interesting insight has been given by Xie et al. (36) who suggested that location of CAD should be assessed with CCTA in order to stratify the risk of future events in women: particularly, they found that non-obstructive left main plaque has a great prognostic implication, with a 50% higher risk for females of having adverse events, independently from CAD burden in other vessels.

Finally, a female-specific plaque phenotype can be seen in CT/MRI evaluation of carotid atherosclerosis as well. Women tend to have less features of vulnerability compared to men: less IPH, LRNC and calcified PV in particular, in accordance with a less frequent tendency to rupture compared to male carotid plaques (42, 43). Thus, CT and MRI represent valid techniques that can detect high-risk features, in order to discriminate which group of patients might benefit from an aggressive primary prevention therapy. Moreover, the ratio of IPH/LRNC seems to be a predictive marker of future plaque rupture and consequent cerebrovascular events, and various studies showed that the ratio is usually higher in the male population (48, 49). Ultrasound is worth mentioning because of its availability and cost feasibility; in addition, it offers accurate and reproducible imaging evaluation of lumen and vessel wall, particularly IMT. However, it has a low sensitivity and specificity for detection of other plaque features, such as fibrous cap, ulceration, plaque inflammation, IPH and LRNC (56). Ultrasound does not distinguish IPH and LRNC because they both appear hypoechogenic, making it difficult to evaluate the ratio, and it is affected by calcified components that create acoustic shadow. For these reasons, ultrasound is not useful for the assessment of most quantitative measurements of carotid

plaque and it is not considered the imaging modality of choice (41).

As suggested by Nasir et al. (57) the question is how and if this information will modify medical management, especially if the assessment of plaque phenotype will lead to consideration of a lipid-lowering therapy of various intensities and/or whether the presence of high-risk plaque characteristics will influence the decision-making process of starting antiplatelet treatment.

Further studies should be carried forward in order to fully comprehend how these insights can impact the clinical management of atherosclerosis in men and women, but what we know so far from the literature is that there are undeniable differences among sexes in atherosclerotic presentation, that these phenotypes can be successfully evaluated throughout non-invasive imaging techniques and that this type of plaque assessment should be strengthened and enhanced because of its prognostic implication.

Author contributions

LS, CCD, and AE contributed to the conception and design of the study. CO and FCa wrote the first draft of the manuscript. GM, SA, JS, FC, SS, and RS wrote sections of the manuscript. All authors contributed to the manuscript revision, read, and approved the submitted version.

Conflict of interest

JS was employed by company Global Medical Technologies Inc.

The remaining authors declare that the research was conducted in the absence of any commercial or financial relationships that could be construed as a potential conflict of interest.

Publisher's note

References

1. Lusis AJ. Atherosclerosis. *Nature.* (2000) 407:233–41. doi: 10.1038/35025203

2. GBD 2019 Diseases and Injuries Collaborators. Global burden of 369 diseases and injuries in 204 countries and territories, 1990-2019: A systematic analysis for the global burden of disease study 2019. *Lancet.* (2020) 396:1204–22. doi: 10.1016/S0140-6736(20)30925-9

3. World Health Organization. *The top 10 causes of death*. Geneva: World Health Organization (2020).

4. Naghavi M, Libby P, Falk E, Casscells SW, Litovsky S, Rumberger J, et al. From vulnerable plaque to vulnerable patient: A call for new definitions and risk assessment strategies: Part I. *Circulation.* (2003) 108:1664–72. doi: 10.1161/01.CIR.0000087480.94275.97

5. Naghavi M, Libby P, Falk E, Casscells SW, Litovsky S, Rumberger J, et al. From vulnerable plaque to vulnerable patient: A call for new definitions and risk assessment strategies: Part II. *Circulation.* (2003) 108:1772–8. doi: 10.1161/01.CIR.0000087481.55887.C9

6. Yusuf S, Hawken S, Ounpuu S, Dans T, Avezum A, Lanas F, et al. Effect of potentially modifiable risk factors associated with myocardial infarction in 52 countries (the INTERHEART study): Case-control study. *Lancet.* (2004) 364:937–52. doi: 10.1016/S0140-6736(04)17018-9

7. Persky RW, Turtzo LC, McCullough LD. Stroke in women: Disparities and outcomes. *Curr Cardiol Rep.* (2010) 12:6–13. doi: 10.1007/s11886-009-0080-2

8. SCORE2 Working Group and ESC Cardiovascular Risk Collaboration. SCORE2 risk prediction algorithms: New models to estimate 10-year risk of cardiovascular disease in Europe. (2021) 42:2439–54. doi: 10.1093/eurheartj/ehab309

9. Maffei S, Guiducci L, Cugusi L, Cadeddu C, Deidda M, Gallina S, et al. Women-specific predictors of cardiovascular disease risk – new paradigms. *Int J Cardiol.* (2019) 286:190–7. doi: 10.1016/j.ijcard.2019.02.005

10. Pelletier R, Khan NA, Cox J, Daskalopoulou SS, Eisenberg MJ, Bacon SL, et al. Sex versus gender-related characteristics: Which predicts outcome after acute coronary syndrome in the young? *J Am Coll Cardiol.* (2016) 67:127–35. doi: 10.1016/j.jacc.2015.10.067

11. Norris CM, Johnson NL, Hardwicke-Brown E, McEwan M, Pelletier R, Pilote L. The contribution of gender to apparent sex differences in health status among patients with coronary artery disease. *J Womens Health (Larchmt).* (2017) 26:50–7. doi: 10.1089/jwh.2016.5744

12. Sciomer S, Moscucci F, Maffei S, Gallina S, Mattioli AV. Prevention of cardiovascular risk factors in women: The lifestyle paradox and stereotypes we need to defeat. *Eur J Prev Cardiol.* (2019) 26:609–10. doi: 10.1177/2047487318810560

13. Vogel B, Acevedo M, Appelman Y, Bairey Merz CN, Chieffo A, Figtree GA, et al. The lancet women and cardiovascular disease commission: Reducing the global burden by 2030. *Lancet.* (2021) 397:2385–438. doi: 10.1016/S0140-6736(21)00684-X

14. Baker L, Meldrum KK, Wang M, Sankula R, Vanam R, Raiesdana A, et al. The role of estrogen in cardiovascular disease. *J Surg Res.* (2003) 115:325–44. doi: 10.1016/s0022-4804(03)00215-4

15. Aryan L, Younessi D, Zargari M, Banerjee S, Agopian J, Rahman S, et al. The role of estrogen receptors in cardiovascular disease. *Int J Mol Sci.* (2020) 21:4314. doi: 10.3390/ijms21124314

16. Madsen TE, Luo X, Huang M, Park KE, Stefanick ML, Manson JE, et al. Circulating SHBG (sex hormone-binding globulin) and risk of ischemic stroke: Findings from the WHI. *Stroke.* (2020) 51:1257–64. doi: 10.1161/STROKEAHA.120.028905

17. Rexrode KM, Manson JE, Lee IM, Ridker PM, Sluss PM, Cook NR, et al. Sex hormone levels and risk of cardiovascular events in postmenopausal women. *Circulation.* (2003) 108:1688–93. doi: 10.1161/01.CIR.0000091114.36254.F3

18. Cattaneo MG, Banfi C, Brioschi M, Lattuada D, Vicentini LM. Sex-dependent differences in the secretome of human endothelial cells. *Biol Sex Differ.* (2021) 12:7. doi: 10.1186/s13293-020-00350-3

19. Søndergaard MM, Hlatky MA, Stefanick ML, Vittinghoff E, Nah G, Allison M, et al. Association of adverse pregnancy outcomes with risk of atherosclerotic cardiovascular disease in postmenopausal women. *JAMA Cardiol.* (2020) 5:1390–8. doi: 10.1001/jamacardio.2020.4097

20. O'Kelly AC, Michos ED, Shufelt CL, Vermunt JV, Minissian MB, Quesada O, et al. Pregnancy and reproductive risk factors for cardiovascular disease in women. *Circ Res.* (2022) 130:652–72. doi: 10.1161/CIRCRESAHA.121.319895

21. Rexrode KM, Madsen TE, Yu AYX, Carcel C, Lichtman JH, Miller EC. The impact of sex and gender on stroke. *Circ Res.* (2022) 130:512–28. doi: 10.1161/CIRCRESAHA.121.319915

22. Mishra SR, Chung HF, Waller M, Dobson AJ, Greenwood DC, Cade JE, et al. Association between reproductive life span and incident nonfatal cardiovascular disease: A pooled analysis of individual patient data from 12 studies. *JAMA Cardiol.* (2020) 5:1410–8. doi: 10.1001/jamacardio.2020.4105

23. Fairweather D, Frisancho-Kiss S, Rose NR. Sex differences in autoimmune disease from a pathological perspective. *Am J Pathol.* (2008) 173:600–9. doi: 10.2353/ajpath.2008.071008

24. Young L, Cho L. Unique cardiovascular risk factors in women. *Heart.* (2019) 105:1656–60. doi: 10.1136/heartjnl-2018-314268

25. Man JJ, Beckman JA, Jaffe IZ. Sex as a biological variable in atherosclerosis. *Circ Res.* (2020) 126:1297–319. doi: 10.1161/CIRCRESAHA.120.315930

26. Williams MC, Kwiecinski J, Doris M, McElhinney P, D'Souza MS, Cadet S, et al. Low-attenuation noncalcified plaque on coronary computed tomography angiography predicts myocardial infarction: Results from the multicenter SCOT-HEART trial (Scottish computed tomography of the heart). *Circulation.* (2020) 141:1452–62. doi: 10.1161/CIRCULATIONAHA.119.044720

27. Williams MC, Kwiecinski J, Doris M, McElhinney P, D'Souza MS, Cadet S, et al. Sex-Specific computed tomography coronary plaque characterization and risk of myocardial infarction. *JACC Cardiovasc Imaging.* (2021) 14:1804–14. doi: 10.1016/j.jcmg.2021.03.004

28. Schulman-Marcus J, Hartaigh BÓ, Gransar H, Lin F, Valenti V, Cho I, et al. Sex-specific associations between coronary artery plaque extent and risk of major adverse cardiovascular events: The CONFIRM long-term registry. *JACC Cardiovasc Imaging.* (2016) 9:364–72. doi: 10.1016/j.jcmg.2016.02.010

29. Conte E, Dwivedi A, Mushtaq S, Pontone G, Lin FY, Hollenberg EJ, et al. Age- and sex-related features of atherosclerosis from coronary computed tomography angiography in patients prior to acute coronary syndrome: Results from the ICONIC study. *Eur Heart J Cardiovasc Imaging.* (2021) 22:24–33. doi: 10.1093/ehjci/jeaa210

30. Shaw LJ, Min JK, Nasir K, Xie JX, Berman DS, Miedema MD, et al. Sex differences in calcified plaque and long-term cardiovascular mortality: Observations from the CAC Consortium. *Eur Heart J.* (2018) 39:3727–35. doi: 10.1093/eurheartj/ehy534

31. El Mahdiui M, Smit JM, van Rosendael AR, Neglia D, Knuuti J, Saraste A, et al. Sex differences in coronary plaque changes assessed by serial computed tomography angiography. *Int J Cardiovasc Imaging.* (2021) 37:2311–21. doi: 10.1007/s10554-021-02204-4

32. Chang HJ, Lin FY, Lee SE, Andreini D, Bax J, Cademartiri F, et al. Coronary atherosclerotic precursors of acute coronary syndromes. *J Am Coll Cardiol.* (2018) 71:2511–22. doi: 10.1016/j.jacc.2018.02.079

33. Lee SE, Sung JM, Andreini D, Al-Mallah MH, Budoff MJ, Cademartiri F, et al. Sex differences in compositional plaque volume progression in patients with coronary artery disease. *JACC Cardiovasc Imaging.* (2020) 13:2386–96. doi: 10.1016/j.jcmg.2020.06.034

34. Osako MK, Nakagami H, Koibuchi N, Shimizu H, Nakagami F, Koriyama H, et al. Estrogen inhibits vascular calcification via vascular RANKL system: Common mechanism of osteoporosis and vascular calcification. *Circ Res.* (2010) 107:466–75. doi: 10.1161/CIRCRESAHA.110.216846

35. Chandrasekhar J, Mehran R. Sex-based differences in acute coronary syndromes: Insights from invasive and noninvasive coronary technologies. *JACC Cardiovasc Imaging.* (2016) 9:451–64. doi: 10.1016/j.jcmg.2016.02.004

36. Xie JX, Eshtehardi P, Varghese T, Goyal A, Mehta PK, Kang W, et al. Prognostic significance of nonobstructive left main coronary artery disease in women versus men: Long-term outcomes from the CONFIRM (coronary CT angiography evaluation for clinical outcomes: An international multicenter) registry. *Circ Cardiovasc Imaging.* (2017) 10:e006246. doi: 10.1161/CIRCIMAGING.117.006246

37. Wentzel JJ, Papafaklis MI, Antoniadis AP, Takahashi S, Cefalo NV, Cormier M, et al. Sex-related differences in plaque characteristics and endothelial shear stress related plaque-progression in human coronary arteries. *Atherosclerosis.* (2022) 342:9–18. doi: 10.1016/j.atherosclerosis.2021.12.013

38. Appelros P, Stegmayr B, Terént A. Sex differences in stroke epidemiology: A systematic review. *Stroke.* (2009) 40:1082–90. doi: 10.1161/STROKEAHA.108.540781

39. Schindler A, Schinner R, Altaf N, Hosseini AA, Simpson RJ, Esposito-Bauer L, et al. Prediction of stroke risk by detection of hemorrhage in carotid plaques: Meta-analysis of individual patient data. *JACC Cardiovasc Imaging.* (2020) 13:395–406. doi: 10.1016/j.jcmg.2019.03.028

40. Saba L, Francone M, Bassareo PP, Lai L, Sanfilippo R, Montisci R, et al. CT attenuation analysis of carotid intraplaque hemorrhage. *AJNR Am J Neuroradiol.* (2018) 39:131–7. doi: 10.3174/ajnr.A5461

41. Saba L, Saam T, Jäger HR, Yuan C, Hatsukami TS, Saloner D, et al. Imaging biomarkers of vulnerable carotid plaques for stroke risk prediction and their potential clinical implications. *Lancet Neurol.* (2019) 18:559–72. doi: 10.1016/S1474-4422(19)30035-3

42. van den Bouwhuijsen QJ, Vernooij MW, Hofman A, Krestin GP, van der Lugt A, Witteman JC. Determinants of magnetic resonance imaging detected carotid plaque components: The Rotterdam Study. *Eur Heart J.* (2012) 33:221–9. doi: 10.1093/eurheartj/ehr227

43. Ota H, Reeves MJ, Zhu DC, Majid A, Collar A, Yuan C, et al. Sex differences in patients with asymptomatic carotid atherosclerotic plaque: In vivo 3.0-T magnetic resonance study. *Stroke.* (2010) 41:1630–5. doi: 10.1161/STROKEAHA.110.581306

44. Zhang L, Zhu L, Lu M, Zhao X, Li F, Cai J, et al. Comparison of carotid plaque characteristics between men and women using magnetic resonance vessel wall imaging: A Chinese atherosclerosis risk evaluation study. *J Magn Reson Imaging.* (2021) 54:646–54. doi: 10.1002/jmri.27576

45. van Dam-Nolen DHK, van Egmond NCM, Dilba K, Nies K, van der Kolk AG, Liem MI, et al. Sex differences in plaque composition and morphology among symptomatic patients with mild-to-moderate carotid artery stenosis. *Stroke.* (2022) 53:370–8. doi: 10.1161/STROKEAHA.121.036564

46. van Dam-Nolen DHK, van Dijk AC, Crombag GAJC, Lucci C, Kooi ME, Hendrikse J, et al. Lipoprotein(a) levels and atherosclerotic plaque characteristics in the carotid artery: The plaque at RISK (PARISK) study. *Atherosclerosis.* (2021) 329:22–9. doi: 10.1016/j.atherosclerosis.2021.06.004

47. Schreiner PJ, Heiss G, Tyroler HA, Morrisett JD, Davis CE, Smith R. Race and gender differences in the association of Lp(a) with carotid artery wall thickness. The atherosclerosis risk in communities (ARIC) study. *Arterioscler Thromb Vasc Biol.* (1996) 16:471–8. doi: 10.1161/01.atv.16.3.471

48. Song JW, Cao Q, Siegler JE, Thon JM, Woo JH, Cucchiara BL. Sex differences in carotid plaque composition in patients with embolic stroke of undetermined source. *J Am Heart Assoc.* (2021) 10:e020143. doi: 10.1161/JAHA.120.020143

49. Saba L, Micheletti G, Brinjikji W, Garofalo P, Montisci R, Balestrieri A, et al. Carotid intraplaque-hemorrhage volume and its association with cerebrovascular events. *AJNR Am J Neuroradiol.* (2019) 40:1731–7. doi: 10.3174/ajnr.A6189

50. Singh N, Moody AR, Zhang B, Kaminski I, Kapur K, Chiu S, et al. Age-specific sex differences in magnetic resonance imaging-depicted carotid intraplaque hemorrhage. *Stroke.* (2017) 48:2129–35. doi: 10.1161/STROKEAHA.117.017877

51. Vakhtangadze T, Singh Tak R, Singh U, Baig MS, Bezsonov E. Gender differences in atherosclerotic vascular disease: From lipids to clinical outcomes. *Front Cardiovasc Med.* (2021) 8:707889. doi: 10.3389/fcvm.2021.707889

52. Langabeer JR II, Champagne-Langabeer T, Fowler R, Henry T. Gender-based outcome differences for emergency department presentation of non-STEMI acute coronary syndrome. *Am J Emerg Med.* (2019) 37:179–82. doi: 10.1016/j.ajem.2018.05.005

53. Langabeer JR II, Henry TD, Fowler R, Champagne-Langabeer T, Kim J, Jacobs AK. Sex-based differences in discharge disposition and outcomes for ST-segment elevation myocardial infarction patients within a regional network. *J Womens Health (Larchmt).* (2018) 27:1001–6. doi: 10.1089/jwh.2017.6553

54. Tsao CW, Aday AW, Almarzooq ZI, Alonso A, Beaton AZ, Bittencourt MS, et al. Heart disease and stroke statistics-2022 update: A report from the American heart association. *Circulation.* (2022) 145:e153–639. doi: 10.1161/CIR.0000000000001052

55. Drobni ZD, Kolossvary M, Karady J, Jermendy AL, Tarnoki AD, Tarnoki DL, et al. Heritability of coronary artery disease: Insights from a classical twin study. *Circ Cardiovasc Imaging.* (2022) 15:e013348. doi: 10.1161/CIRCIMAGING.121.013348

56. Spanos K, Tzorbatzoglou I, Lazari P, Maras D, Giannoukas AD. Carotid artery plaque echomorphology and its association with histopathologic characteristics. *J Vasc Surg.* (2018) 68:1772–80. doi: 10.1016/j.jvs.2018.01.068

57. Nasir K, Sharma G, Blumenthal RS. Sex differences in coronary plaque composition and progression: Will it influence clinical management? *JACC Cardiovasc Imaging.* (2020) 13:2397–9. doi: 10.1016/j.jcmg.2020.05.040

frontiers | Frontiers in Cardiovascular Medicine

TYPE Original Research
PUBLISHED 31 October 2022
DOI 10.3389/fcvm.2022.928090

OPEN ACCESS

EDITED BY
Anna Vittoria Mattioli,
University of Modena and Reggio Emilia, Italy

REVIEWED BY
Ana Teresa Timoteo,
Hospital de Santa Marta, Portugal
Alberto Guido Pozzoli,
Ospedale Regionale di Lugano, Switzerland
Vincenzo Santinelli,
IRCCS San Donato Polyclinic, Italy

*CORRESPONDENCE
Sílvia Montserrat
smontser@clinic.cat

SPECIALTY SECTION
This article was submitted to Cardiovascular Imaging, a section of the journal Frontiers in Cardiovascular Medicine

RECEIVED 25 April 2022
ACCEPTED 12 October 2022
PUBLISHED 31 October 2022

CITATION
Montserrat S, Gabrielli L, Borràs R, Cascos E, Castellá M, Sanchis L, Bijnens B, Mont L and Sitges M (2022) Percutaneous or mini-invasive surgical radiofrequency re-ablation of atrial fibrillation: Impact on atrial function and echocardiographic predictors of short and long-term success.
Front. Cardiovasc. Med. 9:928090.
doi: 10.3389/fcvm.2022.928090

Percutaneous or mini-invasive surgical radiofrequency re-ablation of atrial fibrillation: Impact on atrial function and echocardiographic predictors of short and long-term success

Sílvia Montserrat[1,2]*, Luigi Gabrielli[3], Roger Borràs[1], Enric Cascos[1], Manel Castellá[1], Laura Sanchis[1], Bart Bijnens[4], Lluís Mont[1] and Marta Sitges[1]

[1]Hospital Clínic, IDIBAPS, Institut Clinic Cardiovascular (ICCV), Centro de Investigación Biomédica en Red (CIBER), Cardiovascular Instituto de Salud Carlos III, University of Barcelona, Barcelona, Spain, [2]Department of Cardiology, Consorci Hospitalari de Vic, Universitat Central de Catalunya, Barcelona, Spain, [3]Advanced Center for Chronic Diseases, Escuela de Medicina, Pontificia Universidad Católica de Chile, Santiago, Chile, [4]Department of Engineering, Institució Catalana de Recerca i Estudis Avançats (ICREA)—Universitat Pompeu Fabra, Barcelona, Spain

Objectives: The aim of this study was to compare percutaneous catheter ablation vs. minimally invasive surgical ablation, evaluating the impact of repeated ablation on atrial function, and evaluating predictors of atrial fibrillation (AF) recurrence.

Background: When AF ablation fails, re-ablations are required in up to 40% of patients to treat recurrent arrhythmia; surgical ablation is more effective than catheter ablation.

Methods: Thirty-two patients with failed prior catheter ablation and referred for a second ablation (18 catheter and 14 surgical) were included in a descriptive observational study. Left atrial volumes, strain, and strain rate were measured with 2D speckle tracking echocardiography at baseline and 6 months after the procedures to assess left atrial functions. Patients received up to 1 year of clinical and Holter follow-up.

Results: At the 12-month follow-up, catheter ablation was effective in 56% and surgical ablation in 72% of patients (OR 2 (CI 0.45–8.84), *p* 0.36). Left atrial booster function was similar in all patients, but left atrial reservoir function was more impaired in those patients who underwent surgical ablation. Left atrial booster function was predictive of arrhythmia recurrence after both catheter and surgical ablation: late diastolic strain rate (LASRa) cut-off $\leq$ -0.89 s^{-1} (sensitivity 88%, specificity 70%, AUC 0.82) and $\leq$ -0.85 s^{-1} (sensitivity 60%, specificity 100%, AUC 0.82), respectively.

10.3389/fcvm.2022.928090

Conclusion: Surgical ablation has a more negative impact on LA reservoir function despite being slightly more effective in arrhythmia suppression. LA booster function is not significantly impaired by either procedure. LA booster function predicts arrhythmia elimination after a re-ablation (catheter or surgical).

KEYWORDS

LA function after catheter/surgical re-AF ablation atrial fibrillation, atrial function, echocardiography, catheter ablation, surgical ablation, strain and strain rate

Introduction

After an initial radiofrequency catheter ablation, both percutaneous catheter (CA) and minimally invasive surgical (SA) ablation are accepted therapeutic options for the treatment of patients with recurrent atrial fibrillation (AF) (1). A second procedure is required in up to 40% of patients undergoing AF ablation. Indeed, the efficacy of a second ablation in patients with AF recurrence after a first ablation is reported to be approximately 58%, while antiarrhythmic drugs are only effective in 27% of these patients (2). The efficacy of AF ablation increases with the number of procedures: arrhythmia-free survival rate at 5 years after CA is reported to be around 29% with one procedure and can increase to 63% with two or more procedures (3). In addition, AF ablation with minimally invasive surgery has shown excellent short- and mid-term results. Data suggests that SA more effectively eliminates the arrhythmia in patients with recurrent AF after a failed CA, although CA is associated with fewer complications (4).

Nonetheless, the impact of such procedures on left atrial (LA) function is not well known. Additionally, guidelines on candidate selection for either procedure have not been well established due to lack of data regarding potential factors predicting procedural success, particularly for SA. Despite evidence that LA size, function and fibrosis (as surrogates of the underlying atrial AF substrate) are all related to the success of a first AF ablation procedure, no studies have specifically compared these parameters in the setting of redo CA and SA procedures.

Therefore, the aim of this study was to evaluate, first, the impact of redo CA and SA on atrial function and second, to analyze the potential role of LA size and function in selecting the best candidates for each technique, in order to optimize the rate of long-term success in eliminating the arrhythmia.

Abbreviations: AF, atrial fibrillation; CA, percutaneous Catheter ablation; LA, left atrial; LASs $_{I}$, LA systolic longitudinal strain; LASRa $_{I}$, LA late diastolic longitudinal strain rate; SA, Surgical ablation.

Materials and methods

Study population and study protocol

A descriptive observational study analyzed two cohorts of patients undergoing SA or CA. The study included 32 patients (81% men, 53 ± 7 years old) with symptomatic, antiarrhythmic, drug-refractory AF treated with at least one antiarrhythmic drug and with a failed prior percutaneous ablation. All patients had symptoms before the intervention: palpitations, shortness of breath, and anxiety for the possibility of a symptomatic AF episode. **Table 1** shows the clinical [age, hypertension, BSA, paroxysmal or persistent AF, AF duration (84–72 months), and antiarrhythmic drugs] (2) and the echocardiographic characteristics of the studied population before CA and SA.

Eighteen participants underwent repeated CA while fourteen subjects underwent a redo SA. We excluded patients with significant valve disease (more than mild regurgitation), severe ventricular hypertrophy (wall thickness in end-diastole > 14 mm), or major ventricular dysfunction (left ventricular ejection fraction ≤ 35%) and patients in AF during echocardiography at follow-up. A repeated procedure was indicated when patients persisted with symptomatic AF after a blanking period of 3 months after the first ablation, despite appropriate pharmacologic treatment. In all patients, two transthoracic echocardiographies were performed before the redo procedure, either CA or SA, and at the 6-month follow-up. All patients were in sinus rhythm when the echocardiogram was registered The Ethics Committee of our institution approved the study and all patients signed an informed consent.

Percutaneous radiofrequency catheter ablation

The LA and pulmonary veins were explored using a transseptal approach. A 3-dimensional map was constructed using an electroanatomic mapping system (CARTO®, Biosense-Webster, Diamond Bar, CA, USA) to support the creation and validation of radiofrequency lesions. Continuous radiofrequency lesions surrounding

10.3389/fcvm.2022.928090

TABLE 1 Baseline clinical and echocardiographic parameters.

	Catheter ablation (n = 18)	Surgical ablation (n = 14)	p-value
Age (years)	52[49–59]	55 [47–57]	0.94
Hypertension (%)	11p (61%)	3p (21%)	0.04
Body surface area (BSA) (m^2)	1.99 [1.92–2.07]	2.15 [1.81–2.17]	0.50
Antiarrhythmic drugs (number)	2 [1–2]	2 [1.5–2]	0.37
AF duration (month)	84 [36–114]	72 [48–133]	0.69
Paroxysmal AF n (%)	10 (56%)	11 (79%)	0.27
LV hypertrophy n (%)	6 (33%)	3 (21%)	0.69
LV EF (%)	60 [60–60]	60 [59–65]	0.67
LV end-diastolic diameter (mm)	55 [49–57]	52 [50–55]	0.19
LV end-systolic diameter (mm)	33 [31–36]	32 [27–34]	0.34
LA anteroposterior diameter (mm)	41 [34–44]	40 [37–42]	0.77
LA anteroposterior diameter/BSA (mm/m^2)	21 [18–22]	20 [18–21]	0.45
LA maximum volume (ml)	68 [50–78]	52 [46–61]	0.25
LA maximum volume/BSA (ml/m^2)	36 [22–42]	27 [24–35]	0.87
$LASs_l$ (%)	17 [12–19]	15 [13–18]	0.63
$LASRs_l$ (s^{-1})	0.71 [0.67–1.10]	0.90 [0.72–1.40]	0.89
$LASRe_l$ (s^{-1})	−1.19 [−1.58/−1.03]	−1.20 [−1.65/0.90]	0.97
$LASRa_l$ (s^{-1})	−0.80 [−1.07/−0.59]	−0.80 [−1.02/−0.52]	0.73

Data expressed as number of patients (n) and percentage or median and interquartile range, as appropriate. AF, atrial fibrillation; BSA, body surface area; EF, ejection fraction; LA, left atrium; LV, left ventricle; Ss_l, systolic strain; SRa_l, late diastolic strain rate, SRe_l, early diastolic strain rate; SRs_l, systolic strain rate.

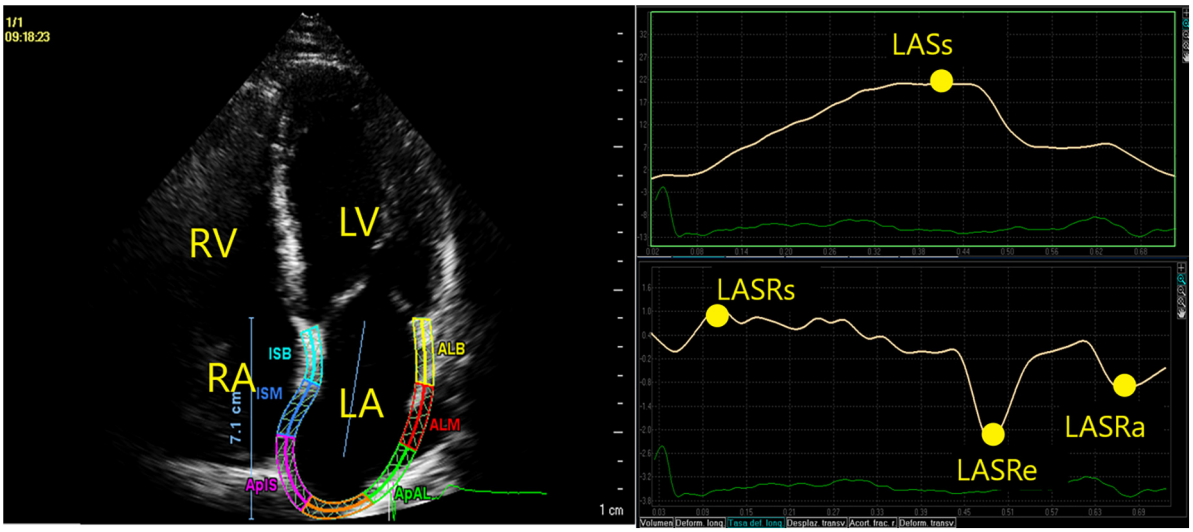

FIGURE 1
Endocardial border was automatically traced with speckle tracking. $LASs_l$, representing LA reservoir function, was identified as the peak positive strain value during LV systole. In the LA strain rate curve, we identified the peak positive strain rate ($LASRs_l$) at the beginning of LV systole, the peak negative strain rate during early diastolic ($LASRe_l$) strain rate, representing conduction function and late diastolic ($LASRa_l$) strain rate after the P-wave on the electrocardiogram, representing LA active contraction.

ipsilateral were delivered as previously described (5, 6). In patients with persistent AF, additional radiofrequency applications were made along the LA roof (between superior pulmonary veins), LA posterior wall, and mitral isthmus (between inferior pulmonary veins) at the discretion of the operator. Radiofrequency was delivered through an irrigated-tip thermocouple-equipped catheter, using a target temperature of 45°C at 40 W. The endpoint was a reduction of local electrogram to < 0.15 mV and the establishment of a bidirectional

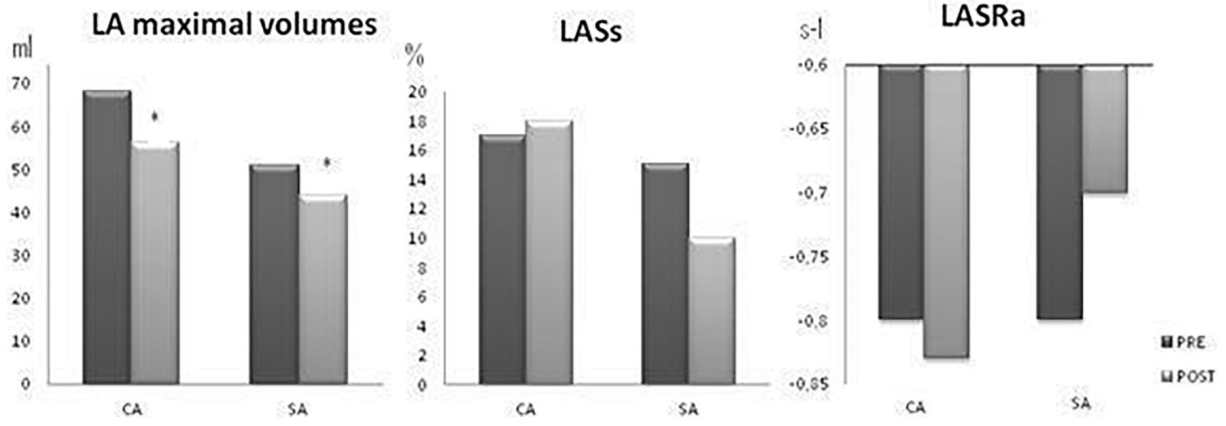

FIGURE 2
Effect of catheter (CA) and surgical ablation (SA) on LA size (LA 2D maximum volume) and LA reservoir ($LASs_l$) and LA booster function ($LASRa_l$). PRE, pre-ablation (black bars) and POST, post-ablation (gray bars). CA, Catheter ablation; SA, surgical ablation. *$p < 0.05$ POST vs. PRE.

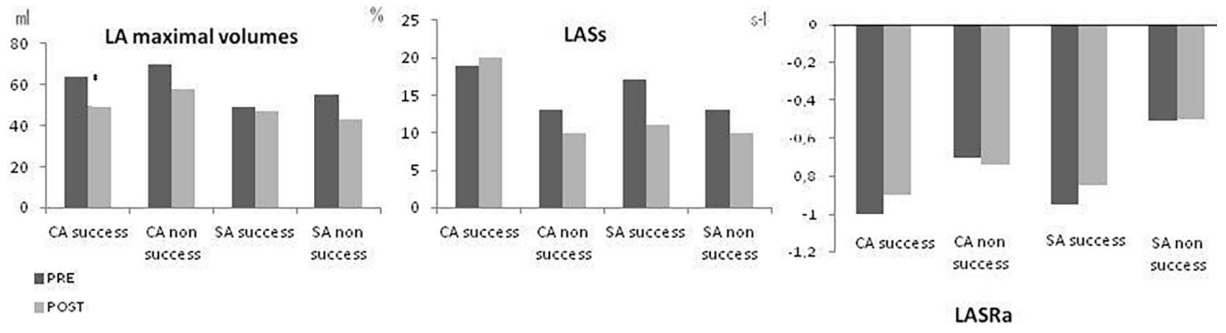

FIGURE 3
Effect of catheter (CA) and surgical ablation (SA) on LA size (LA maximum volume), LA reservoir function ($LASs_l$) and LA booster function ($LASRa_l$) depending of the success of the procedure in eliminating AF. PRE: pre-ablation and POST: post-ablation. CA, Catheter ablation; SA, surgical ablation. *$p < 0.05$ PRE vs. POST.

conduction block between the LA and pulmonary veins (6).

Surgical ablation

Patients were treated with a minimally invasive surgery protocol (4) using video-assisted thoracoscopy, under general anesthesia. Pulmonary vein isolation was performed from the epicardial side with a bipolar RF ablation clamp (Nasdaq:ATC, AtriCure, Inc., Ohio, USA). At least 2 overlapping applications around each of the ipsilateral veins were performed, and isolation was confirmed by the absence of pulmonary vein potentials and exit block during pacing. Ablation of ganglionic plexi was also performed, with an additional application in the interatrial Waterston groove on the right side, while Marshal's ligament was cut on the left side. In all patients, the LA appendage was excluded by stapling and then cutting.

Clinical follow-up

After CA and SA, all patients continued oral anticoagulation to maintain an international normalized ratio between 2.0 and 3.0 for a minimum of 3 months; therapy was continued at the discretion of the treating cardiologist on the basis of the CHA2DS2-VASc score (1). Previous antiarrhythmic therapy was maintained for at least 1 month and then discontinued if there were no arrhythmia recurrences 3 months after ablation, except in two patients previously prescribed beta-blockers due to ischemic heart disease and ventricular extrasystolia. Clinical follow-up consisted of outpatient check-ups with serial ECG ambulatory monitoring to evaluate the recurrence and frequency of any potential arrhythmia. All patients underwent a 7-day continuous ECG recording to detect asymptomatic AF episodes at 6 and 12 month follow up. In symptomatic patients but with sinus rhythm in the ECG, ECG monitoring was limited to 48 h.

The ablation procedure was considered successful if no recurrences of atrial tachycardia lasting > 30 s were present during follow-up, after a blanking period of 3 months (1). Also, clinical improvement, defined as fewer clinical palpitations and hospitalizations due to arrhythmia, was evaluated.

Echocardiography

All patients underwent transthoracic and transesophageal echocardiography prior to the CA or SA procedure, including conventional 2-dimensional echocardiography to detect predictors of success for CA and SA. Echocardiographic follow-up was performed at 6 months to detect the effect of CA and SA. All images were obtained using the IE33 Philips ultrasound system (Philips, Andover, MA, USA), digitally stored, and transferred to a workstation for off-line analysis using dedicated software (Qlab, version 7.1, Philips Medical Systems).

The LA anteroposterior diameter and left ventricular dimensions were measured in the long parasternal axis; left ventricular ejection fraction was determined using the biplane Simpson method using biplane apical views. LA volumes were measured *via* the disc summation method from apical 4-chamber views, in LA and right atrium. LA function was assessed using myocardial deformation imaging derived from 2D speckle tracking (7, 8) by offline analysis of standard apical 4-chamber views. Special care was taken at the time of image acquisition to focus on the LA and to have a frame rate in the range of 50–70 fps. After selecting 3 points (8) (the inferior part of the LA septum, the inferior part of the LA lateral wall, and the LA roof), an endocardial border trace was generated by the software (**Figure 1**). The reference point for the initiation of 2D speckle tracking is QRS. The LA strain and strain rate traces were calculated and depicted. The left atrium was divided into 7 segments. The strain and strain rate curves were measured for each segment and the results represent the average value. From the average strain curves, myocardial LA longitudinal systolic strain (LASs $_l$) was calculated, representing LA reservoir function. LA systolic strain rate (LASRs $_l$) also represents LA reservoir function; early diastolic strain rate (LASRe $_l$) represents conduit function; and late diastolic strain rate (LASRa $_l$) represents LA booster function (**Figure 1**).

Statistical analysis

Data is reported as median and interquartile range. Continuous variables were tested by the U Mann-Whitney test, and paired data by Wilcoxon analysis where appropriate. Categorical variables are presented in proportions, and were compared *via* the Fisher exact test. We used ROC methodology to evaluate the optimal cut-off value for predicting recurrence in our sample. Classification trees (9) were constructed in order to select the best LA parameters for predicting ablation success (AF recurrence or non-recurrence). A P-value $\leq$ 0.05 was considered statistically significant. The Lin concordance coefficient was calculated to study the reproducibility of the measured variables (8). Statistical analysis was performed using R software for Windows version 3.1.1 (R project for Statistical Computing; Vienna, Austria).

Results

Baseline characteristics and clinical follow-up at 1 year

Table 1 shows the clinical and echocardiographic characteristics of the population studied pre-CA and SA. There were no significant echocardiographic differences between groups undergoing CA or SA, including LA size and function parameters. Hypertension was more frequent in CA patients compared with patients undergoing SA. At the 1-year follow-up, SA was slightly more effective, achieving success in 72% of patients compared with 56% of CA patients [OR 2 (CI 95% 0.45–8.84), $p = 0.36$].

Of the SA failures, 4/14 patients (28%) occurred before 6 months follow-up without any other recurrences between 6 and 12 month follow. Of the CA failures, 4/18 patients (22%) occurred before 6 months and increased to 8/18 patients (44%) before 12-month visits. Clinical improvement, defined as fewer clinical palpitations and hospitalizations due to arrhythmia, was observed in 16 of 18 (89%) patients from the CA group and in 13 of 14 (93%) from the SA group ($p = 0.99$).

Impact of successful repeated atrial ablation on LA function at 6 months

Figure 2 shows the effect of CA and SA on LA size and function [reservoir (LASs$_l$) and booster LA functions (LASRa$_l$)] as studied with deformation imaging of the LA wall (pre- and 6 months after ablation). Both procedures reduced the LA maximum volumes, but did not significantly impair LASs$_l$ or LASRa$_l$. Comparison between CA and SA only showed a difference in the reservoir function effect. First, LA size showed a similar decrease after both procedures: in patients undergoing CA, maximum LA volume decreased by a median Δ -12 [-2/-21] ml and, for SA, this decrease was Δ -8 [-1/-13] ml ($p = 0.59$). Second, LA reservoir function was more impaired after SA [LASs$_l$ decreased by Δ -4.65 (-0.02/-9)%], than after CA [LASs$_l$ increased by Δ + 0.75% (-1.1/ + 2.8) (p 0.04)]. Third, LA booster function was similarly affected in patients undergoing SA (LASRa$_l$ decreased by Δ -0.03 (-0.55/ + 0.29)s^{-1}] and in those treated with CA [LASRa$_l$ decreased by Δ -0.10^{-1} (-0.23/ + 0.20)]s^{-1} ($p = 0.83$).

TABLE 2 Baseline characteristics of patients undergoing CA according to the success of the procedure.

	Successful CA (n = 10)	Non-successful CA (n = 8)	p-value
Age (years)	53 [50–56]	52 [46–69]	0.86
Hypertension n (%)	4 (40%)	7 (88%)	0.07
AF duration (months)	66 [24–126]	84 [36–96]	0.85
Paroxysmal AF n (%)	7 (70%)	3 (38%)	0.34
Antiarrhythmic drugs (number)	1.5[1–2]	2 [1–2]	0.61
LV hypertrophy n (%)	4 (40%)	2 (25%)	0.64
LV EF (%)	60 [59–62]	60 [60–60]	0.87
LA anteroposterior diameter (mm)	41 [32–44]	42 [36–46]	0.48
LA AP diameter/BSA (mm/m^2)	20 [17–22]	22 [18–23]	0.49
LA maximum volume (ml)	64 [36–92]	70 [56–73]	0.79
LA maximum volume/BSA (ml/m^2)	36 [17–44]	35 [29–37]	0.87
LASs$_l$ (%)	18 [15–22]	13 [7–17]	**0.03**
LASRs$_l$ (s^{-1})	0.98 [0.83–1.17]	0.73 [0.58–0.95]	**0.02**
LASRe$_l$ (s^{-1})	−1.20 [−1.53/−1.01]	−1.18 [−1.75/−1.02]	0.86
LASRa$_l$ (s^{-1})	−1.01 [−1.42/−0.78]	−0.69 [−0.80/−0.54]	**0.02**
RA maximum volume (ml)	30 [19–54]	43 [42–51]	0.43
A wave (cm/s)	51 [42–62]	43 [42–51]	0.53

Data expressed as number of patients (n) and percentage or median and interquartile range as appropriate. Bold values indicate statistical significance. AF, atrial fibrillation; AP: anteroposterior; A wave, late diastolic transmitral wave; BSA, body surface area; EF, ejection fraction; LA, left atrium; LV, left ventricle; RA, right atrium; Ss$_l$, systolic strain; SRa$_l$, late diastolic strain rate, SRe$_l$, early diastolic strain rate; SRs$_l$, systolic strain rate.

TABLE 3 Baseline characteristics of patients undergoing SA according to the success of the procedure.

	Successful SA (n = 10)	Non-successful SA (n = 4)	p-value
Age (years)	50 [50–57] 8 (80%)	47 [38–58]3 (75%)	0.26
Hypertension n (%)	2 (20%)	1 (25%)	1
AF duration (months)	72 [48–120]	72 [48–150]	0.92
Paroxysmal AF n (%)	7 (70%)	4 (100%)	0.51
Antiarrhythmic drugs (number)	2 [1.25–2]	2 [2–2]	0.60
LV hypertrophy n (%)	2 (20%)	1 (25%)	1
LV EF (%)	63 [60–65]	58 [40–60]	0.05
LA anteroposterior diameter (mm)	40 [37–42]	39 [37–44]	0.88
LA AP diameter/BSA (mm/m^2)	20 [18–21]	20 [18–24]	1
LA maximum volume (ml)	49 [44–61]	55 [49–71]	0.36
LA maximum volume/BSA (ml/m^2)	25 [23–35]	31 [23–36]	0.81
LASs$_l$ (%)	17 [13–20]	13 [13–15]	0.22
LASRs$_l$ (s^{-1})	0.95 [0.79–1.77]	0.70 [0.57–0.92]	0.17
LASRe$_l$ (s^{-1})	−1.15 [−2.02/−0.87)]	−1.30 [−1.92/−1.13]	0.39
LASRa$_l$ (s^{-1})	−0.95 [−1.47/−0.52)]	−0.50 [−0.73/−0.39]	0.04
RA maximum volume (ml)	49 [41–59]	53 [50–75]	0.41
A wave (cm/s)	58 [41–66]	37 [27–43]	0.05

Data expressed as number of patients (n) and percentage or median and interquartile range as appropriate. AF, atrial fibrillation; AP, anteroposterior; A wave, late diastolic transmitral wave; BSA, body surface area; EF, ejection fraction; LA, left atrium; LV, left ventricle; RA, right atrium; Ss$_l$, systolic strain; SRa$_l$, late diastolic strain rate, SRe$_l$, early diastolic strain rate; SRs$_l$, systolic strain rate.

Figure 3 shows the effect of CA and SA on LA size and function, according to the success of the procedure in eliminating the arrhythmia. LA size was reduced in all subgroups (CA/SA, successful/non-successful) but the reduction was significant only in patients with successful CA. Compared to preprocedure imaging, LA booster function showed no significant changes and was stable after both CA and SA, independently of the success of the ablation. LA reservoir

10.3389/fcvm.2022.928090

function slightly improved after successful CA (p = 0.47) and slightly decreased after non-successful CA (p = 0.09). However, LA reservoir function slightly worsened after SA whether successful (p = 0.26) or not (p = 0.07).

Predictors of success after repeated atrial ablation

Tables 2, 3 show the baseline characteristics of patients undergoing CA and SA, respectively, according to the success of the procedure. Despite similar LA size, LA reservoir and booster function were significantly more preserved, as shown by higher LASs$_l$, LASRs$_l$ and LASRa$_l$, in patients undergoing a successful redo CA (Table 2). A similar trend was observed in the SA group, with better LA booster function in patients with a successful SA (Table 3).

The LA booster function (LARSa $_l$) predicted the success of second procedures, whether CA or SA. The patients with LASRa$_l$ < -0.85 s^{-1}, 93% (13/14) had no AF recurrence (54% in the CA group, 7 patients; 46% in the SA group, 6 patients). Among patients with impaired LA booster function (LASRa$_l$ ≥ -0.85 s^{-1}), the arrhythmia was eliminated after the second procedure in 39% (7/18): 3 CA patients and 4 SA patients. The remaining 61% (11/18) had a non-successful second procedure [64% (7/11) CA patients and 36% (4/11) SA patients] (Figure 4).

In the ROC (Receiver operating characteristic) analysis, LA booster function (LASRa$_l$ cut-off ≤ -0.89 s^{-1}) predicted arrhythmia elimination after CA (sensitivity 88%, specificity 70%, AUC 0.82). LA reservoir function also predicted CA success (LASs$_l$ cut-off > 15%; sensitivity 71%, specificity 80%, AUC 0.79). Among patients undergoing SA, the LA booster function was the only predictor of ablation success: LASRa$_l$ cut-off ≤ -0.85 s^{-1} (sensitivity 60%, specificity 100%, AUC 0.82).

Of the CA failures, 4/18 patients (22%) occurred before 6 months and increased to 8/18 patients (44%) before 12-month visits." LASs (not LA size) post CA at 6 months predicts the recurrence at 12 month (OR 0.64, IC 0.44–0.92; p 0.02).

Reproducibility study

The reproducibility of LASRa$_l$ measurements was excellent: Both inter-observer and intra-observer Lin concordance was 0.97 (Figure 5). The concordance value is classified as Poor (< 0.90), Moderate (0.90–0.95), Substantial (0.95–0.99), and Almost perfect (> 0.99) (9).

Discussion

The main finding of the study was that LA booster function is preserved after repeated CA and SA, suggesting that repeated ablation is useful for avoiding AF complications and increasing the success of ablation procedures without further harm to LA function induced by ablation lesions and potential induced scarring. In a previous meta-analysis (10), successful CA in AF patients significantly decreased LA size and did not appear to adversely affect LA function, as studied *via* 3D echocardiography and magnetic resonance. This finding was also reported in the subgroup of patients undergoing repeated CA ablation (11). In our study, LA remodeling (reduction of LA size) was observed in both CA and SA.

A previous study also suggested that minimally invasive surgical AF ablation (12) (first and repeated procedures) improves LA function as measured *via* 2D speckle-tracking echocardiography. In our study we evaluated the impact of SA on LA size and function, and compared it with that seen in patients undergoing repeated CA where previous CA had failed. We found that, at the 6-month follow-up, LA reservoir function had decreased more in patients treated with SA than in those receiving repeated CA. The LA reservoir function depends on left ventricular systolic function and LA compliance. In our patients, left ventricular systolic function was preserved, but the impairment of LA compliance was higher in the SA group of patients than in CA patients. This finding might be secondary to several factors: a more extensive ablation, more wall fibrosis due to the epicardial approach, superior transmurality of the

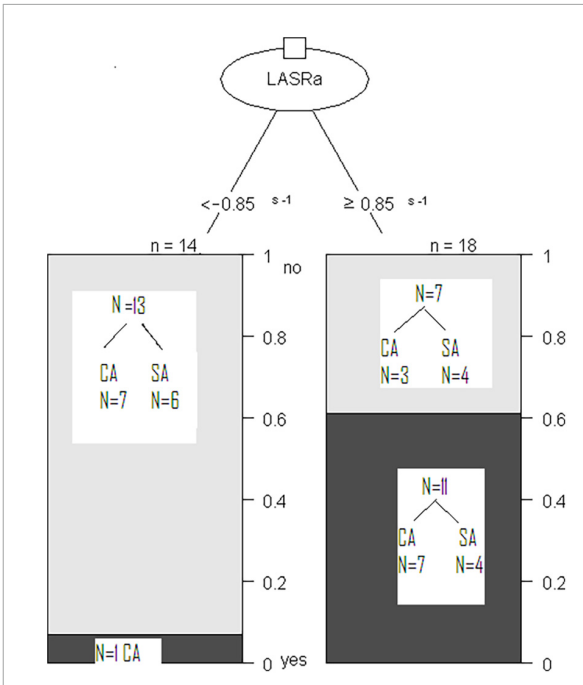

FIGURE 4
Classification Tree Model to predict arrhythmia elimination with repeated procedures (CA or SA) based on LA contractile function as determined by LASRa$_l$. Patients with non-recurrence of AF are represented by gray bars **(Top)** and those with recurrence of AF by black bars **(Bottom)**.

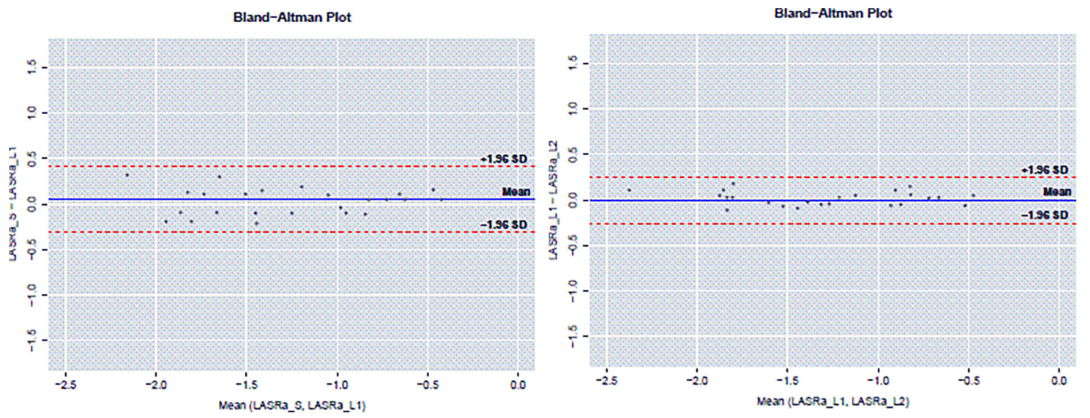

FIGURE 5
Reproducibility of LASRa$_l$ measurements: inter-observer Lin concordance and intra-observer concordance.

bipolar radiofrequency lesion, concomitant ablation of ganglia, and the elimination of LA appendage by SA. All these factors might influence LA compliance, and consequently, LA reservoir function. However, LA booster function was not significantly impaired by ablation after either the CA or SA procedure.

While electrical restoration is mandatory, restoration of LA contraction, and mechanical function is also important after CA and SA. Long-term cardiovascular events could depend on the evolution of LA function in these patients, as they could potentially maintain sinus rhythm after ablation, but with reduced LA function, and consequently, an increased risk of embolism and AF recurrence.

Enlarged LA and impaired ResF (LA ResF [emptying fraction (LAEF) and expansion index (LAEI)]) at 3-month post-ablation for AF are strongly associated with long-term outcomes (cardiac hospitalization for heart failure or acute ischemic events, stroke/TIA, and all-cause death), independent of LV function or cardiac rhythm at follow-up (13).

Indeed, the continuation of the anticoagulation treatment currently depends on the CHA2DS2-VASc score; however, knowing the status of LA function might have therapeutic implications in the future management of these patients. Some studies report that LA strain is reduced in patients with AF, stroke, and low risk CHADS 2 scores (14). Finally, this is important in terms of the strong cardiovascular prognostic implication of LA contractile function in patients with chronic hypertension and diastolic dysfunction (15) frequently underlying AF.

Actually LA function determined by 2D Speckle tracking appears to be a promising technique for diagnosis and therapeutic decision-making (16).

It is a powerful biomarker for adverse events in different cardiovascular diseases. Recent review describes the methodology, benefits, and pitfalls of measuring LA longitudinal strain function by echocardiography (17).

Predictors of success after repeated atrial ablation

Another finding in our study was that the LA function status predicts the success of a second ablation procedure (CA and SA) in eliminating arrhythmia after 1-year follow-up. LA function measured *via* 3D echocardiography failed to detect predictors of a second CA (18). Some studies have aimed to assess factors related to the success of a second CA. Wójcik et al. (19) studied 42 patients after a second ablation procedure (5 of them undergoing SA) and identified 3 predictors of success: paroxysmal AF, normalized LA area $\geq$ 10.25, and a high score with a combination of the AF type, LA size, renal insufficiency, presence of metabolic syndrome or cardiomyopathy (ALARMEc score). Similarly, Tang et al. (20) studied patients before undergoing a second AF ablation procedure. Increased anteroposterior LA diameter, measured by M-mode after the first procedure, was the only independent predictor of AF recurrence after the second procedure. Interest in understanding atrial fibrillation substrate is growing as a predictor for the success of repeated procedures of CA (21). Finally, *via* myocardial deformation imaging techniques, we previously demonstrated that LA reservoir function (LASs $_l$) is the best predictor of AF recurrence described to date. After repeated CA, at the 6-month follow-up, the sensitivity, and specificity were high (LASs$_l$ cut-off > 12%, sensitivity 84%, specificity 90%, AUC 0.89) (8). The present study confirms the importance of LA reservoir function in predicting AF recurrence, but extends its prognostic utility up to 12 months after CA (LASs$_l$ cut-off > 15%; sensitivity 71%, specificity 80%, AUC 0.79). The LA reservoir function, as measured by myocardial deformation imaging techniques, inversely correlates with fibrosis in the atrial wall, detected using cardiac magnetic resonance (22), and also with fibrosis detected by histology in atrial wall

samples extracted during cardiac surgery in patients with severe mitral insufficiency (23). Therefore, $LASs_I$ can be considered as a surrogate of atrial wall fibrosis measurement. Finally, the data we present shows the relevance of LA booster function ($LASRa_I$) in predicting the success of CA after a 12-month follow-up.

Only one study has addressed the identification of factors that might predict the success of SA after a failed percutaneous ablation (24). In this study, > 1-year persistent AF and non-dilated LA (anteroposterior diameter < 45 mm) were related to the success of SA in eliminating the arrhythmia. In contrast, our present study, which only included patients in sinus rhythm, demonstrated the value of LA booster function, in addition to LA size, in predicting the success of SA.

New LA functional parameters derived from 2D speckle tracking are of great utility in detecting effect and predictors of second AF procedures (CA vs. SA). From the clinical point of view, patients treated with CA have a less impaired LA reservoir function than patients treated with SA, thus, CA seems to be the best option for patients with more preserved LA booster and reservoir function. However, patients that require a second procedure and with more advanced atrial disease (greater LA reservoir impairment), but preserved booster function might benefit more from SA, while those with very advanced LA disease (greater LA booster impairment) could potentially be treated just with antiarrhythmic and rate-control drugs. Certainly, further studies on a larger population are required to confirm this recommendation. However, our findings provide data that could generate hypotheses for future research.

One limitation of our study was the relatively small sample size. Only patients in sinus rhythm could be studied, so the effect of ablation and predictors found in this study only relates to this subgroup of patients. Another limitation involves the technique itself, as the platform used was designed for the analysis of the ventricle. Special care in LA tracking must be taken into account; pulmonary veins, and LA appendage could be a problem with tracking, so these structures must be avoided during the delineation of the endocardial border. In our study, we obtained acceptable tracking in all segments in 95% of the patients and our reproducibility was good, as reported elsewhere (20). The translation to other commercially available platforms and vendors of our proposed cut-off values in strain and strain rate measurements requires further validation. Another limitation is that we only performed the analysis in the 4-chamber view; valuable information could also be acquired by adding and averaging LA analysis in the 2-chamber view. Also as chronic hypertension can affect atrial function, the different prevalence of hypertension in the two groups could be a limitation to compare baseline LA function in the CA and SA groups. However, it should not impact on the effect of the intervention in each group.

Conclusion

The present study proved the efficacy of adding LA function values to LA size to improve the selection of candidates for repeated procedures of AF ablation, whether CA or SA. The analysis of LA function allows a more accurate selection of patients that could suffer an AF recurrence after CA or SA. The surgical procedure does not further impair LA booster function, which must be preserved to avoid dyspnea and improve symptoms in patients with mild hypertrophy or diastolic dysfunction. This could result in improvements in the efficiency of repeated ablation and reduced complications from these procedures. Finally, the clinical impact of these findings in the long-term warrants further investigation.

Data availability statement

The raw data supporting the conclusions of this article will be made available by the authors, without undue reservation.

Ethics statement

The studies involving human participants were reviewed and approved by the Comitè Ètic Hospital Clínic de Barcelona. The patients/participants provided their written informed consent to participate in this study.

Author contributions

All authors listed have made a substantial, direct, and intellectual contribution to the work, and approved it for publication.

Conflict of interest

The authors declare that the research was conducted in the absence of any commercial or financial relationships that could be construed as a potential conflict of interest.

Publisher's note

References

1. Hindricks G, Potpara T, Dagres N, Arbelo E, Bax JJ, Blomström-Lundqvist C, et al. ESC Guidelines for the diagnosis and management of atrial fibrillation developed in collaboration with the European association of cardio-thoracic surgery (EACTS). *Eur Heart J.* (2020) 42:373–98.

2. Calkins H, Reynolds MR, Spector P, Sondhi M, Xu Y, Martin A, et al. Treatment of atrial fibrillation with antiarrhythmic drugs or radiofrequency ablation. Two systematic literature reviews and meta-analyses. *Circ Arrhythm Electrophysiol.* (2009) 2:349–61.

3. Weerasooriya R, Khairy P, Litalien J, Macle L, Hocini M, Sacher F, et al. Catheter ablation for atrial fibrillation: are results maintained at 5 years of follow-up? *J Am Coll Cardiol.* (2011) 57:160–6.

4. Boersma LV, Castella M, van Boven W, Berruezo A, Yilmaz A, Nadal M, et al. Atrial fibrillation catheter ablation versus surgical ablation treatment (FAST): a 2-center randomized clinical trial. *Circulation.* (2012) 125:23–30. doi: 10.1161/CIRCULATIONAHA.111.074047

5. Pappone C, Oreto G, Lamberti F, Vicedomini G, Loricchio ML, Shpun S, et al. Catheter ablation of paroxysmal atrial fibrillation using a 3D mapping system. *Circulation.* (1999) 100:1203–8.

6. Calvo N, Nadal M, Berruezo A, Andreu D, Arbelo E, Tolosana JM, et al. Improved outcomes and complications of atrial fibrillation catheter ablation over time: learning curve, techniques, and methodology. *Rev Esp Cardiol.* (2012) 65:131–8.

7. Voigt JU, Pedrizzetti G, Lysyansky P, Marwick TH, Houle H, Baumann R, et al. Definitions for a common standard for 2D speckle tracking echocardiography: consensus document of the EACVI/ASE/industry task force to standardize deformation imaging. *J Am Soc Echocardiogr.* (2015) 28:183–93.

8. Montserrat S, Gabrielli L, Bijnens B, Borras R, Berruezo A, Poyatos S, et al. Left atrial deformation predicts success of first and second percutaneous atrial fibrillation ablation. *Heart Rhythm.* (2015) 12:11–8. doi: 10.1016/j.hrthm.2014.08.032

9. James G, Witten D, Hastie T, Tibshirani R. *An Introduction to Statistical Learning.* New York, NY: Springer Texts (2013).

10. Zhuang Y, Yong Y, Chen M. Updating the evidence for the effect of radiofrequency catheter ablation on left atrial volume and function in patients with atrail fibrillation: a meta-analysis. *JRSM Open.* (2014) 5:1–18.

11. Montserrat S, Sitges M, Calvo N, Silva E, Tamborero D, Vidal B, et al. Effect of repeated radiofrequency catheter ablation on left atrial function for the treatment of atrial fibrillation. *Am J Cardiol.* (2011) 108:1741–6.

12. Gelsomino S, Lucà F, Rao C, Parise O, Pison L, Francis W, et al. Improvement of left atrial function and left atrial reverse remodeling after surgical treatment of atrial fibrillation. *Ann Cardiothorac Surg.* (2014) 3:70–4.

13. Wen S, Pislaru SV, Lin G, Scott CG, Lee AT, Asirvatham SJ, et al. Association of post-procedural left atrial volume and reservoir function with outcomes in patients with atrial fibrillation undergoing catheter ablation. *J Am Soc Echocardiogr.* (2022) 35:818.e–28.e. doi: 10.1016/j.echo.2022.03.016

14. Azemi T, Rabdiya VM, Ayirala SR, McCullough LD, Silvermana DI. Left atrial strain is reduced in patients with atrial fibrillation, stroke or TIA, and low risk CHADS 2 scores. *J Am Soc Echocardiogr.* (2012) 25:1327–32.

15. Kaminski M, Steel K, Jerosch-Herold M, Khin M, Tsang S, Hauser T, et al. Strong cardiovascular prognostic implication of quantitative left atrial contractile function assessed by cardiac magnetic resonance imaging in patients with chronic hypertension. *J Cardiovasc Magn Reson.* (2011) 13:42. doi: 10.1186/1532-429X-13-42

16. Yuda S. Current clinical applications of speckle tracking echocardiography for assessment of left atrial function. *J Echocardiogr.* (2021) 19:129–40. doi: 10.1007/s12574-021-00519-8

17. Thomas L, Muraru D, Popescu BA, Sitges M, Rosca M, Pedrizzetti G, et al. Evaluation of left atrial size and function: relevance for clinical practice. *J Am Soc Echocardiogr.* (2020) 33:934–52.

18. Montserrat S, Gabrielli L, Borras R, Poyatos S, Berruezo A, Bijnens B, et al. Left atrial size and function by three-dimensional echocardiography to predict arrhythmia recurrence after first and repeated ablation of atrial fibrillation. *Eur Heart J Cardiovasc Imaging.* (2014) 15:515–22. doi: 10.1093/ehjci/jet194

19. Wójcik M, Berkowitsch A, Greiss H, Zaltsberg S, Pajitnev D, Deubner N, et al. Repeated catheter ablation of atrial fibrillation: how to predict outcome? *Circ J.* (2013) 77:2271–9.

20. Tang RB, Yanl XL, Dong JZ, Kalifa J, Long DY, Yu RH, et al. Predictors of recurrence after a repeat ablation procedure for paroxysmal atrial fibrillation: role of left atrial enlargement. *Europace.* (2014) 16:1569–74. doi: 10.1093/europace/euu013

21. Sitges M, Montserrat S. Understanding atrial fibrillation substrate: the case of repeated procedures of catheter ablation. *Europace.* (2014) 16:1541–2.

22. Kuppahally SS, Akoum N, Burgon NS, Badger TJ, Kholmovski EG, Vijayakumar S, et al. Left atrial strain and strain rate in patients with paroxysmal and persistent atrial fibrillation: relationship to left atrial structural remodeling detected by delayed-enhancement MRI. *Circ Cardiovasc Imaging.* (2010) 3:231–9. doi: 10.1161/CIRCIMAGING.109.865683

23. Cameli M, Lisi M, Righini FM, Massoni A, Natali BM, Focardi M, et al. Usefulness of atrial deformation analysis to predict left atrial fibrosis and endocardial thickness in patients undergoing mitral valve operations for severe mitral regurgitation secondary to mitral valve prolapse. *Am J Cardiol.* (2013) 111:595–601. doi: 10.1016/j.amjcard.2012.10.049

24. Castellá M, Pereda D, Mestres CA, Gómez F, Quintana E, Mulet J. Thoracoscopic pulmonary vein isolation in patients with atrial fibrillation and failed percutaneous ablation. *J Thorac Cardiovasc Surg.* (2010) 140:633–8.

frontiers | Frontiers in Cardiovascular Medicine

TYPE Original Research
PUBLISHED 11 November 2022
DOI 10.3389/fcvm.2022.1015983

OPEN ACCESS

EDITED BY
Sabina Gallina,
University of Studies G. d'Annunzio Chieti and Pescara, Italy

REVIEWED BY
Neftali Eduardo Antonio-Villa,
Instituto Nacional de Cardiologia Ignacio Chavez, Mexico
Hermann Körperich,
Heart and Diabetes Center North Rhine-Westphalia, Germany

*CORRESPONDENCE
Zhi-Gang Yang
yangzg666@163.com

SPECIALTY SECTION
This article was submitted to Cardiovascular Imaging, a section of the journal Frontiers in Cardiovascular Medicine

RECEIVED 10 August 2022
ACCEPTED 24 October 2022
PUBLISHED 11 November 2022

CITATION
Huang S, Shi K, Jiang L, Ren Y, Wang J, Yan W-F, Qian W-L, Li Y and Yang Z-G (2022) Adverse association of epicardial adipose tissue accumulation with cardiac function and atrioventricular coupling in postmenopausal women assessed by cardiac magnetic resonance imaging.
Front. Cardiovasc. Med. 9:1015983.
doi: 10.3389/fcvm.2022.1015983

Adverse association of epicardial adipose tissue accumulation with cardiac function and atrioventricular coupling in postmenopausal women assessed by cardiac magnetic resonance imaging

Shan Huang[1], Ke Shi[1], Li Jiang[1], Yan Ren[2], Jin Wang[1], Wei-Feng Yan[1], Wen-Lei Qian[1], Yuan Li[1] and Zhi-Gang Yang[1]*

[1]Department of Radiology, West China Hospital, Sichuan University, Chengdu, Sichuan, China, [2]Department of Endocrinology, West China Hospital, Sichuan University, Chengdu, Sichuan, China

Background: This study aims to investigate the association of epicardial adipose tissue (EAT) accumulation with cardiac function and atrioventricular coupling in a cohort of postmenopausal women assessed by cardiac magnetic resonance imaging (CMR).

Materials and methods: Overall, 283 postmenopausal women (mean age 61.5 ± 9.1 years) who underwent CMR examination were enrolled. Participants were classified into four groups by the quartile of EAT volume. EAT volume was quantified on short-axis cine stacks covering the entire epicardium. CMR-derived cardiac structure and function, including left atrial (LA)- volume, emptying fraction, deformation, and left ventricular (LV)- mass, volume, ejection fraction, and deformation, were compared among the four groups of graded EAT volume.

Results: Left ventricular mass (LVM) and LV remodeling index were both increased in the group with the highest EAT volume, compared to those in the lowest quartile ($p = 0.016$ and $p = 0.003$). The LV global longitudinal strain (LV-GLS), circumferential strain (LV-GCS), and LA- reservoir strain (LA-RS), conduit strain (LA-CS), and booster strain (LA-BS), were all progressively decreased from the lowest quartile of EAT volume to the highest (all $p < 0.05$). Multivariable linear regression analyses showed that EAT was independently associated with LV-GLS, LA-RS, LA-CS, and LA-BS after adjusting for body mass index and other clinical factors.

Conclusion: Epicardial adipose tissue accumulation is independently associated with subclinical LV and LA function in postmenopausal women. These associations support the role of EAT in mediating deleterious effects on cardiac structure and function.

KEYWORDS

epicardial adipose tissue, left atrial strain, left ventricular strain, cardiac magnetic resonance imaging, postmenopausal women

Introduction

During menopausal transition, women are susceptible to metabolic alterations. Redistribution of body fat from the subcutaneous area to the intra-abdominal visceral area is an important metabolic change for women after menopause. Previous studies have shown that epicardial adipose tissue (EAT) volume tends to be expanded particularly in postmenopausal women (1, 2). EAT was indicated to be associated with hypertension, coronary microvascular dysfunction, and diastolic filling restriction in women but not in men (1, 3, 4). In addition, studies have shown that in the presence of hemodynamic stress, women tend to present more frequently with left ventricular (LV) hypertrophy, smaller LV volumes, and preserved ejection fraction, compared to age-matched men (5, 6). These notable sex differences indicate that estrogen deficiency and EAT might play a role in mediating cardiac abnormalities in postmenopausal women.

Cardiac magnetic resonance (CMR) imaging has been widely used in the evaluation of heart structure and function. CMR tissue tracking has been validated to have excellent producibility and reproducibility in evaluating LV myocardial deformation. Recently, the importance of left atrial (LA) phasic function and feature tracking strain has been increasingly recognized. A prior study indicated that LA dysfunction preceded the onset of heart failure (7). CMR-derived phasic LA function and strain have been suggested to be able to serve as sensitive imaging biomarkers in the assessment and stratification of diastolic dysfunction (8, 9). Furthermore, CMR has been validated to be able to quantify the epicardial fat tissue using a simple volumetric technique on a standard clinical steady-state free-precession sequence (10).

To the best of our knowledge, few studies on this subject have assessed EAT volume and cardiac structure and function by using CMR. Therefore, we aimed to investigate the association of EAT accumulation with cardiac function and atrioventricular coupling in a cohort of postmenopausal women by CMR.

Abbreviations: EAT, epicardial adipose tissue; LV, left ventricular; CMR, cardiac magnetic resonance; LA, left atrial; LVEF, left ventricular ejection fraction; eGFR, estimated glomerular filtration rate; EDV, end-diastolic volume; ESV, end-systolic volume; LVM, LV mass; GRS, global radial strain; GCS, global circumferential strain; GLS, global longitudinal strain; RS, reservoir strain; CS, conduit strain; BS, booster strain; LAV_{max}, maximum LA volume; LAV_{min}, minimum LA volume; LAV_{ac}, pre-atrial contraction LA volume; LAEFT, total LA emptying fraction; LAEFP, passive LA emptying fraction; LAEFB, booster LA emptying fraction; BSA, body surface area; BMI, body mass index; ICC, intraclass correlation coefficient; PAT, pericardial adipose tissue.

Materials and methods

Study population

This study was approved by the Biomedical Research Ethics Committee of our hospital and conducted in accordance with the Declaration of Helsinki. Written informed consent was waived due to the retrospective nature of this study.

In this cross-sectional study, we included a cohort of 283 postmenopausal women who underwent CMR examination between January 2015 and June 2021. The menopausal status of the participants was recorded according to self-report. Women with both natural menopause and surgical menopause were included. The demographic and clinical characteristics of the included individuals were recorded according to digital medical records. Triglyceride-to-high density lipoprotein cholesterol ratio (TG/HDL) was calculated to indicate insulin resistance level (11).

Exclusion criteria were as follows: (a) patients with pericardial effusion; (b) atrial fibrillation; (c) obstructive coronary artery disease and myocardial infarction, (d) myocarditis and pericarditis, (e) moderate to severe valvular disease, (f) primary and secondary cardiomyopathies, and (g) poor image quality and unavailable to derive CMR parameters.

Cardiac magnetic resonance protocol

All CMR scans were performed using a 3.0T scanner (Siemens Healthcare, Erlangen, Germany). Balanced steady-state free-precession sequence was used to obtain cine images. Three long-axis views (2-chamber, 3-chamber, 4-chamber)

and consecutive short-axis slices covering the entire LV were obtained with the following parameters: temporal resolution, 33.22 ms; repetition time, 2.77 ms; echo time, 1.31 ms; field of view, 234 mm × 280 mm and slice thickness, 8 mm.

Imaging analysis

Measurement of left ventricular structure and function

All CMR parameters were assessed using a commercially available software (CVI[42]; Circle Cardiovascular Imaging, Inc., Calgary, AB, Canada). LV structural parameters, including LV end-diastolic volume (LV-EDV), LV end-systolic volume (LV-ESV), and LV mass (LVM), were attained by manually tracing the endocardial and epicardial contours of the left ventricle at the end-diastolic and end-systolic phases on the short-axis stacks. LV functional parameters included LVEF and LV myocardial strain. LV myocardial strain indices were acquired by loading the short-axis stacks and the two-chamber and four-chamber long-axis images into the feature tracking module. The software then computes the LV global radial (LV-GRS), circumferential (LV-GCS), and longitudinal peak strain (LV-GLS) (12).

Measurement of left atrial structure and function

Left atrial parameters were obtained as previously described (13). LA structural parameters included maximum LA volume (LAV_{max}), minimum LA volume (LAV_{min}), and pre-atrial contraction LA volume (LAV_{ac}). LA functional parameters included phasic volumetric-based LA emptying fractions and LA strain-based indices. LA endocardial and epicardial borders were manually delineated in the two- and four-chamber long-axis images using LV end-diastole as a reference phase. LA appendage and pulmonary veins were excluded from the LA volume. Then, the software automatically traced the atrial border in the subsequent phases. Manual adjustments were performed to obtain optimal tracking of the LA border. The software then computes the LA peak longitudinal reservoir strain (LA-RS), conduit strain (LA-CS), and booster strain (LA-BS). Total LA emptying fraction (LAEFT), a measure of reservoir function, was calculated as (LAV_{max}–LAV_{min})/LAV_{max}. Passive LA emptying fraction (LAEFP), a measure of conduit function, was calculated as (LAV_{max}–LAV_{ac})/LAV_{max}. Booster LA emptying fraction (LAEFB), a measure of atrial contractile pump function, was calculated as (LAV_{ac}–LAV_{min})/LAV_{ac}. Representative images of LV and LA longitudinal strain are shown in **Figure 1**.

Measurement of epicardial adipose tissue volume

The measurement of EAT volume has been previously described (10, 14). The areas of EAT were delineated on consecutive short-axis cine images. Epicardial border and visceral pericardial border on each slice from the level of the mitral valve to the apical slice were manually traced (**Figure 2**). Then the EAT volume was calculated by summation of the results of each slice's area multiplied by the slice thickness based on the modified Simpson's rule.

Morphological LA and LV parameters and the EAT volume were indexed to body surface area (BSA). Reproducibility was assessed for EAT volume and LA and LV strain parameters. To determine the intra-observer reproducibility, one observer (SH) performed all the measurements at first and repeated in 30 randomly selected CMR scans 1 month later. And inter-observer reproducibility was evaluated by comparing the measurements from the same collection of images by another experienced observer (KS).

Statistical analysis

Statistical analyses were conducted with SPSS (Version 19; IBM, Armonk, NY, USA) and Graphpad Prism (Version 7.0a, GraphPad Software Inc., San Diego, CA, USA). Baseline characteristics and CMR indices were all summarized across the quartile of EAT volume. Continuous data are expressed as the means ± SDs or medians with interquartile ranges. Categorical data are expressed as numbers (percentages). Continuous variables were compared among the four groups of EAT volume using one-way analysis of variance (ANOVA). Dichotomous variables were compared among groups by using χ test. Pearson's or Spearman correlation analyses were performed to evaluate the bivariable correlations among EAT volume and other CMR parameters as appropriate. Multivariable linear regression analyses were conducted using body mass index (BMI), EAT and clinical factors as independent variables and LA and LV myocardial longitudinal strain as dependent variables. Candidate variables with no collinearity and a p-value < 0.1 in the univariate analyses as well as factors based on clinical grounds were included in the multivariable models. The intraclass correlation coefficient (ICC) was used to assess the inter- and intra- observer reproducibility. Two-sided $p < 0.05$ was considered statistically significant.

Results

Baseline characteristics of the included participants

In total, 283 postmenopausal women were enrolled in this study. Baseline demographic and clinical characteristics were summarized across the quartiles of EAT volume in **Table 1**. The ranges of EAT volume of the four groups were Q1: <37.5 ml/m^2, Q2: 37.5∼48.9 ml/m^2, Q3: 48.9∼62.0 ml/m^2, and

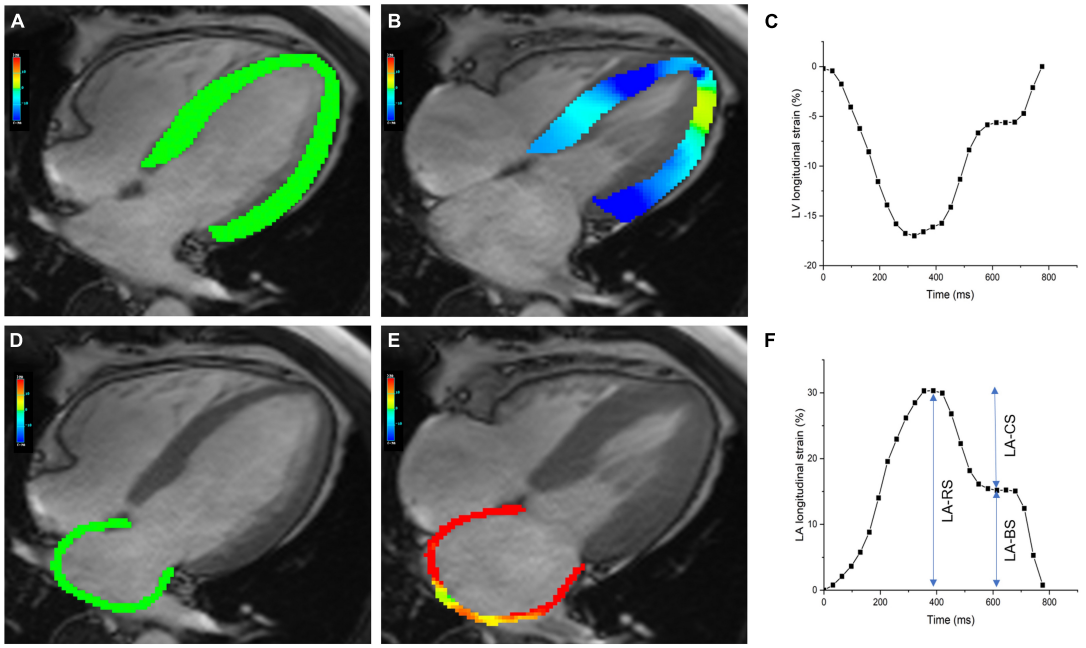

FIGURE 1
Cardiac magnetic resonance (CMR)-derived left ventricular and atrial longitudinal strain. Panels **(A,B)** show the pseudocolor maps of LV longitudinal strain in the four-chamber view at the end-diastolic and end-systolic phases. Panel **(C)** shows representative plot of LV longitudinal strain. Panels **(D,E)** show the pseudocolor maps of LA longitudinal strain in the four-chamber view at the end-diastolic and end-systolic phases. Panel **(F)** shows a plot of LA longitudinal strain, along with measures of reservoir, conduit, and booster strain. LA-RS, LA reservoir strain; LA-CS, LA conduit strain; LA-BS, LA booster strain.

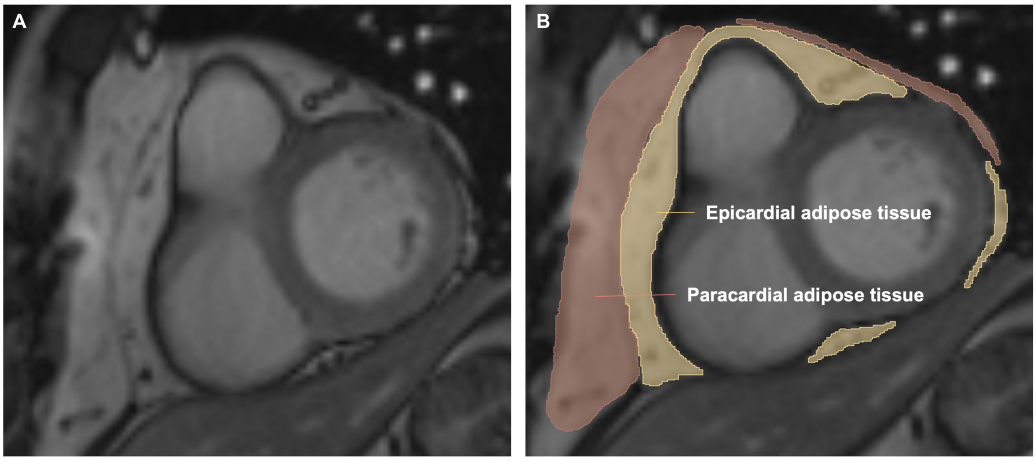

FIGURE 2
Volumetric assessment of the epicardial adipose tissue (EAT) on short-axis slices. Panels **(A,B)** are representative images of one short-axis slice. Epicardial adipose tissue is shown in yellow. Paracardial adipose tissue is shown in red. Pericardial adipose tissue is epicardial adipose tissue plus paracardial adipose tissue. The EAT volume was calculated by summation of the results of each slice's area multiplied by the slice thickness based on the modified Simpson's rule.

Q4: > 62.0 ml/m^2, respectively. The average age of the study cohort was 61.5 ± 9.1 years. Six women in the study population had surgical menopause. There were graded increases in BMI and TG/HDL across the quartiles of EAT. And BMI was significantly correlated with EAT volume (r = 0.354). EAT was inversely correlated with the level of HDL cholesterol (r = −0.214). Age was found to be related to EAT volume (r = 0.399). Women with higher EAT volumes were significantly older than those in the lower quartile. Presence of hypertension was more frequent in participants with a larger EAT volume.

The presence of diabetes mellitus had a graded increase from the lowest to the highest quartile of EAT, but the difference was not statistically significant.

Comparisons of cardiac magnetic resonance-derived cardiac structure and function among quartiles of epicardial adipose tissue volume

Cardiac structural and functional parameters by CMR according to the quartile distribution of EAT volume are presented in **Table 2** and **Figure 3**. The mean EAT volumes of the four groups were Q1 = 29.7 ± 5.9 ml/m^2 vs. Q2 = 42.7 ± 3.3 ml/m^2 vs. Q3 = 54.8 ± 4.1 ml/m^2 vs. Q4 = 73.3 ± 9.6 ml/m^2. LVM and LV remodeling index were both increased in the group with the highest EAT volume, compared to those in the lowest quartile. LV-EDV and LV-ESV did not show any difference across the four groups. There was no significant difference in LVEF among the groups. The LV-GLS and LV-GCS, but not LV-GRS, was significantly reduced in the highest quartile of EAT.

LAV_{min} and LAV_{ac} were markedly enlarged in participants with larger EAT volumes. But no significant difference was found in LAV_{max} among the groups. Regarding volume-based LA function, LAEFT and LAEFP were markedly decreased in the higher EAT group. No significant difference was observed in LAEFB among the four groups. The strain-based LA function indices, including LA-RS, LA-CS, and LA-BS, all progressively decreased from the lowest quartile of EAT volume to the highest.

Associations between epicardial adipose tissue and cardiac structural and functional indices

Univariate correlation analyses of EAT and other CMR indices are presented in **Table 2**. EAT volume had a weak correlation with LVM (r = 0.204) and the remodeling index (r = 0.242). LV-GLS (r = −0.250), LV-GCS (r = −0.174), and LV-GRS (r = −0.134) were inversely correlated with EAT volume. Volume-based LA function indices were negatively related to EAT volume, with only LAEFT (r = −0.346) and LAEFP (r = −0.442) being statistically significant. LA-RS (r = −0.424) and LA-CS (r = −0.527), and LA-BS (r = −0.169) were also correlated with EAT volume.

In the multivariable linear regression analyses, age, systolic blood pressure, heart rate, hypertension, diabetes, dyslipidemia, menopausal age, surgical menopause, TG/HDL, BMI, and EAT volume were included as independent variables. Among them, BMI (β = −0.261), EAT volume (β = −0.149) and diabetes (β = −0.286) were found to be independently associated with LV-GLS. Furthermore, EAT volume was also found to be independently correlated with LA-RS (β = −0.277), LA-CS (β = −0.324), and LA-BS (β = −0.210) (**Table 3**).

Intra- and inter-observer reproducibility of cardiac magnetic resonance parameters

The intra-observer and inter-observer reproducibility of EAT volume, and LA and LV strains were considered excellent (ICCs ranged from 0.882 to 0.952) (**Supplementary Table 1**).

Discussion

In this study, we used CMR to explore the associations of EAT with cardiac functional and structural parameters. First, we found that LV global longitudinal strain was progressively reduced with the increasing of EAT volume. Second, the phasic emptying function and deformation of LA were also found to be gradually decreased from the lowest quartile of EAT volume to the highest. Third, EAT was correlated with LV GLS and LA strains independent of age, systolic blood pressure, heart rate, hypertension, diabetes, dyslipidemia, menopausal age, surgical menopause, TG/HDL, and BMI.

Previous studies on EAT mainly focused on EAT thickness around the right ventricular free wall or pericardial adipose tissue (epicardial adipose tissue plus paracardial adipose tissue) measured by echocardiogram or CT. Kim et al. found that pericardial adipose tissue (PAT) was more strongly associated with the subclinical LV dysfunction than BMI and waist circumference (15). However, EAT is embryologically different from paracardial adipose tissue. And EAT is anatomically more closely connected to the coronary arteries and myocardium than paracardial adipose tissue (16). The proinflammatory cytokines released by EAT can directly impair the myocardium, due to the absence of a fascial plane between the two structures (17). A previous echocardiographic study that included 1,004 participants found that only EAT was significantly correlated with diastolic dysfunction, whereas, PAT was not associated with the decreased diastolic function (18). Therefore, we focused on investigating the specific association of EAT, not PAT, with the cardiac structure and function during the same CMR examination.

Association of epicardial adipose tissue with volumetric- and strain-based phasic left atrial function

Impairment of LA function has been proposed to precede the development of heart failure in a large longitudinal population of asymptomatic participants (7). In our study,

TABLE 1 Baseline characteristics of the included participants.

Variable	Q1 ($n = 72$)	Q2 ($n = 71$)	Q3 ($n = 70$)	Q4 ($n = 70$)	*P*-value
EAT ranges, ml/m^2	<37.5	37.5∼48.9	48.9∼62.0	>62.0	–
Age, years	57.3 ± 8.5	59.5 ± 7.4	63.0 ± 9.1	66.4 ± 9.0	**<0.001**
Height, cm	1.57 ± 0.05	1.57 ± 0.05	1.57 ± 0.06	1.56 ± 0.06	0.325
Weight, kg	55.5 ± 7.8	59.4 ± 9.6	60.7 ± 9.9	62.1 ± 8.1	**<0.001**
BSA, m^2	1.64 ± 0.12	1.69 ± 0.15	1.70 ± 0.15	1.72 ± 0.12	**0.009**
BMI, kg/m^2	22.4 ± 2.7	24.0 ± 3.3	24.7 ± 3.5	25.6 ± 3.2	**<0.001**
SBP, mmHg	127.9 ± 20.4	132.1 ± 18.8	137.6 ± 17.9	134.0 ± 17.9	**0.045**
DBP, mmHg	79.3 ± 14.3	78.0 ± 11.1	81.7 ± 14.2	78.7 ± 11.4	0.483
Heart rate, min^{-1}	79.1 ± 15.5	77.5 ± 13.5	78.1 ± 15.9	77.4 ± 11.7	0.976
Menopausal age, years	50 (48, 51)	49.5 (46.7, 51.2)	50 (48, 50)	49 (47, 50.5)	0.813
Hypertension, *n* (%)	18 (25)	31 (43.7)	41 (58.6)	45 (64.3)	**<0.001**
Diabetes, *n* (%)	22 (30.5)	25 (35.2)	28 (40.0)	31 (44.3)	0.322
Dyslipidemia, *n* (%)	13 (18.1)	20 (28.2)	21 (30.0)	23 (32.8)	0.214
TG, mmol/L	1.32 (0.98, 1.81)	1.29 (0.80, 1.76)	1.50 (1.12, 1.85)	1.58 (1.17, 1.86)	0.055
TC, mmol/L	4.19 (3.45, 4.83)	4.55 (3.82, 5.17)	4.62 (4.03, 5.44)	4.76 (4.21, 5.46)	**0.005**
HDL, mmol/L	1.42 (1.26, 1.54)	1.47 (1.27, 1.71)	1.28 (1.12, 1.51)	1.29 (1.03, 1.53)	0.001
LDL, mmol/L	2.63 (1.96, 3.34)	2.71 (2.21, 3.33)	2.69 (1.85, 3.16)	2.35 (1.83, 2.80)	0.060
eGFR, ml/min/1.732 m^2	89.4 ± 15.5	91.2 ± 16.4	85.6 ± 16.7	79.1 ± 16.2	**0.002**
TG/HDL	0.55 (0.45, 0.97)	0.61 (0.36, 0.97)	0.80 (0.50, 1.15)	0.79 (0.59, 1.28)	**0.005**
EAT volume, ml/m^2	29.7 ± 5.9	42.7 ± 3.3	54.8 ± 4.1	73.3 ± 9.6	**<0.001**
LV-EDV, ml/m^2	73.8 ± 10.2	75.1 ± 14.1	74.5 ± 14.1	80.5 ± 23.7	0.756
LV-ESV, ml/m^2	29.1 ± 6.3	30.6 ± 9.2	29.6 ± 8.1	35.7 ± 21.3	0.825
LVEF,%	61.1 ± 4.9	59.9 ± 6.6	60.3 ± 7.3	57.9 ± 11.0	0.514

The values are the mean ± SD, median (interquartile ranges) and numbers (percentages). EAT, epicardial adipose tissue; BSA, body surface area; BMI, body mass index; SBP, systolic blood pressure; DBP, diastolic blood pressure; TG, plasma triglycerides; TC, total cholesterol; HDL, high-density lipoprotein; LDL, low-density lipoprotein; eGFR, estimated glomerular infiltration rate; LV-EDV, left ventricular end-diastolic volume; LV-ESV, LV end-systolic volume; LVEF, left ventricular ejection fraction. *P*-values of statistical significance are shown in bold.

TABLE 2 Cardiac structural and functional parameters by cardiac magnetic resonance (CMR) and their correlations with epicardial adipose tissue (EAT) volume.

Variable	Q1 ($n = 72$)	Q2 ($n = 71$)	Q3 ($n = 70$)	Q4 ($n = 70$)	Correlation coefficients		
					R	95% CI	*P*-value
LVM, g/m^2	35.1 ± 7.2	36.2 ± 8.4	38.9 ± 10.5	42.2 ± 13.7	0.204	0.084–0.318	**0.001**
Remodeling index[#]	0.48 ± 0.09	0.49 ± 0.11	0.53 ± 0.11	0.53 ± 0.10	0.242	0.123–0.353	**<0.001**
LV-GRS, %	34.3 ± 8.1	33.3 ± 9.1	32.0 ± 9.7	30.5 ± 10.8	−0.134	−0.257—0.009	**0.031**
LV-GCS, %	−21.0 ± 2.3	−20.6 ± 2.6	−20.0 ± 3.1	−18.9 ± 4.5	−0.174*	−0.307—0.028	**0.005**
LV-GLS, %	−15.5 ± 3.0	−14.7 ± 3.0	−13.5 ± 3.4	−12.9 ± 4.1	−0.250*	−0.379—0.108	**<0.001**
LAV_{max}, ml/m^2	32.6 (27.9, 41.2)	37.4 (25.5, 42.3)	37.6 (27.8, 46.9)	38.0 (27.5, 48.2)	0.136	0.006–0.261	**0.035**
LAV_{ac}, ml/m^2	20.8 (17.5, 26.8)	25.6 (17.2, 31.6)	27.7 (20.0, 33.7)	28.5 (20.3, 43.6)	0.270	0.145–0.387	**<0.001**
LAV_{min}, ml/m^2	12.2 (9.4, 16.7)	13.6 (7.9, 16.6)	14.9 (10.4, 21.2)	16.6 (11.7, 26.7)	0.224	0.097–0.344	**<0.001**
LAEFT, %	0.63 ± 0.07	0.62 ± 0.10	0.55 ± 0.14	0.51 ± 0.17	−0.346	−0.453—0.230	**<0.001**
LAEFP, %	0.34 ± 0.10	0.30 ± 0.09	0.25 ± 0.10	0.21 ± 0.11	−0.442	−0.538—0.334	**<0.001**
LAEFB, %	0.43 ± 0.09	0.46 ± 0.11	0.41 ± 0.15	0.39 ± 0.16	−0.126	−0.248–0.001	0.051
LA-RS, %	43.6 ± 13.3	42.7 ± 14.3	33.9 ± 13.4	27.2 ± 13.0	−0.424	−0.522—0.315	**<0.001**
LA-CS, %	26.2 ± 9.7	24.3 ± 9.9	17.8 ± 8.3	11.6 ± 7.5	−0.527	−0.614—0.426	**<0.001**
LA-BS, %	17.4 ± 5.7	18.7 ± 7.1	16.2 ± 8.2	14.5 ± 7.9	−0.169	−0.289—0.044	0.008

[#]LV remodeling index was calculated as LVM/ LV-EDV. *LV-GCS and LV-GLS were calculated as absolute value in the correlation analyses. LVM, LV mass; LV-GRS, LV global radial strain; LV-GCS, LV global circumferential strain; LV-GLS, LV global longitudinal strain; LAV_{max}, maximum left atrial volume; LAV_{ac}, pre-atrial contraction LA volume; LAV_{min}, minimum LA volume; LAEFT, total LA emptying fraction; LAEFP, passive LA emptying fraction; LAEFB, booster LA emptying fraction; LA-RS, LA peak longitudinal reservoir strain; LA-CS, LA peak longitudinal conduit strain; LA-BS, LA peak longitudinal booster strain. *P*-values of statistical significance are shown in bold.

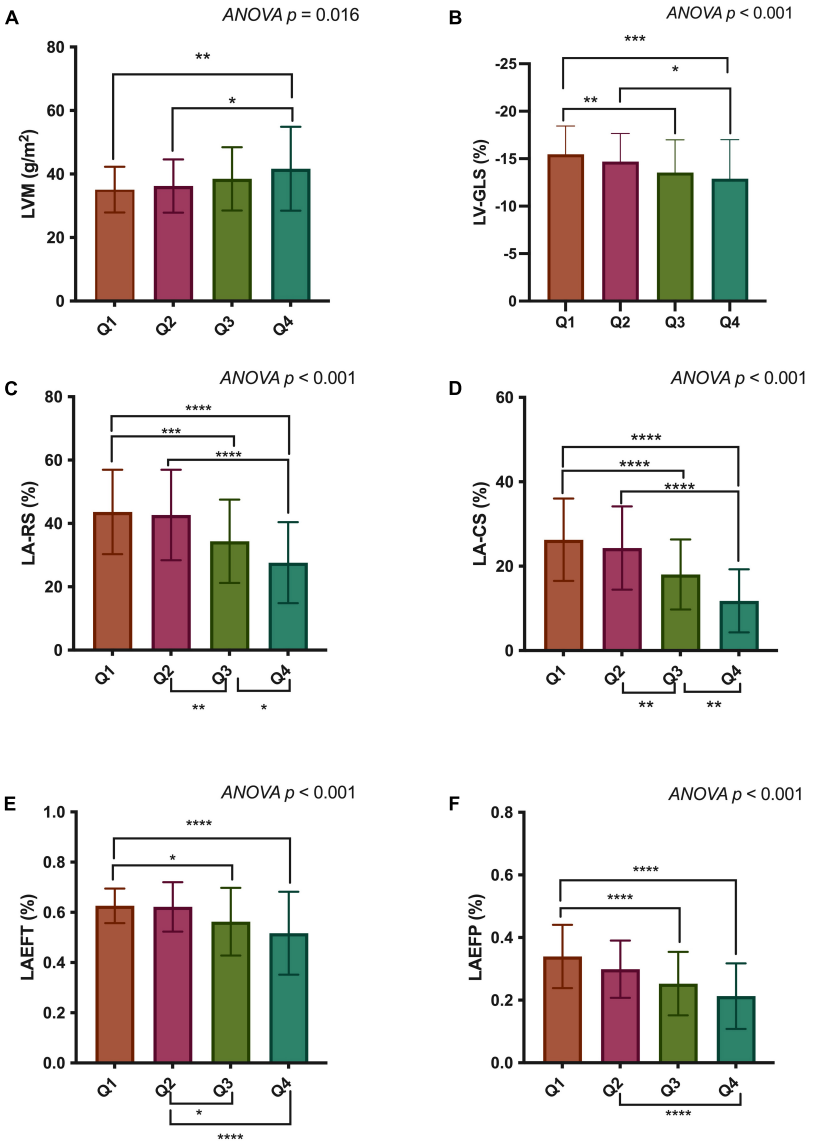

FIGURE 3
Comparisons of LVM **(A)**, LV-GLS **(B)**, LA-RS **(C)**, LA-CS **(D)**, LAEFT **(E)**, and LAEFP **(F)** among quartiles of epicardial adipose tissue (EAT) volume. LVM, left ventricular mass; LV-GLS, LV global longitudinal strain; LA-RS, left atrial reservoir strain; LA-CS, LA conduit strain; LAEFT, total LA emptying fraction; LAEFP, passive LA emptying fraction. *$p < 0.05$; **$p < 0.01$, ***$p < 0.001$; ****$p < 0.0001$.

we found that LAEFT and LAEFP, but not LAEFB, gradually decreased as the EAT volume accumulated. Evidence about the booster function of LA is still conflicting (19, 20). Even though the volumetric booster function was not significantly different among the groups, the booster strain along with the other two components of LA strain, demonstrated significant differences across the quartile of EAT in our study. This is because that strain-based indices are more sensitive in evaluating atrial mechanics than volumetric indices (21). As for the reservoir function, it is an indicator for LA compliance, reflecting the relaxation of LA during LV systole. The reservoir strain has been previously demonstrated to be correlated with LV filling pressure (22) and the incidence of heart failure (7). The LA-CS of the conduit phase also had a strong association with EAT volume. Considering that conduit function is mainly influenced by the LV relaxation, the abnormality of conduit strain could indicate an early stage of LV diastolic dysfunction.

In a prior study, the researchers demonstrated that LA strain was correlated with EAT in patients with coexisting obesity and diabetes (23). However, possibly due to the small sample size of this study, no significant correlation was observed between EAT and LA function when the patient group and control group were evaluated separately. The researchers assumed that this might indicate that abnormal LA function only occurs when the

TABLE 3 Multivariable linear regression of epicardial adipose tissue (EAT) and cardiac function parameters.

Variables	LV-GLS		LA-RS		LA-CS		LA-BS	
	Univariable β	Multivariable β	Univariable β	Multivariable β	Univariable β	Multivariable β	Univariable β	Multivariable β
Age, years	−0.123*		−0.479*	−0.381	−0.546*	−0.374	−0.191*	−0.213
SBP, mmHg	−0.189*		−0.125		−0.148*		−0.044	
HR, min^{-1}	−0.039		0.015		−0.007		0.052	
Hypertension	−0.150*		−0.220*		−0.282*		−0.077	
Diabetes	−0.312*	−0.286	−0.175*	−0.159	−0.178*	−0.166	−0.083	
Dyslipidemia	−0.066		−0.087		−0.109		−0.015	
Menopausal age, years	−0.022		−0.106		−0.099		−0.057	
Surgical menopause	0.056		0.093		0.089		0.065	
TG/HDL	−0.025		−0.081		−0.126		0.004	
BMI, kg/m^2	−0.243*	−0.261	−0.182*		−0.200*		−0.093	
EAT volume, ml/m^2	−0.250*	−0.149	−0.424*	−0.277	−0.527*	−0.324	−0.169*	−0.210

Multivariable regression models were constructed with LV and LA myocardial longitudinal strain as dependent variables and age, SBP, HR, hypertension, diabetes, dyslipidemia, menopausal age, surgical menopause, TG/HDL, BMI, and EAT as independent variables. Abbreviations as in Table 2. *$p < 0.05$ in the univariable linear regression analyses.

EAT volume is over a certain amount. Our study was supportive of this assumption. The volume- and strain-based LA function were all significantly reduced in the highest amount of EAT compared to the low quartile of EAT volume.

Association of epicardial adipose tissue with left ventricular systolic function

The relationship between EAT and LV diastolic function has been well-established in several echocardiographic studies (24). However, evidence about the association between EAT and LV systolic function remains to be elucidated. Several studies using speckle tracking strain analysis by echocardiography demonstrated that EAT is inversely correlated with LV global longitudinal strain (25, 26). Consistent with these results, we observed that longitudinal strain was reduced in the high EAT group. We assumed that the link between EAT and longitudinal strain could be explained by microvascular dysfunction and interstitial fibrosis induced by adipokines and cytokines secreted by EAT (25). These abnormalities mainly affect the subendocardial layer of the myocardium, leading to a reduction in longitudinal LV mechanics in the subclinical stage of disease.

Potential mechanisms underlying the influence of epicardial adipose tissue on cardiac structure and function

Several relevant mechanisms have been proposed to explain the associations between EAT and cardiac structure and function (27). The first is that EAT could impair LV diastolic filling by a regional mechanical force. Findings of impaired diastolic function and enlarged LA volume in the absence of LV hypertrophy observed in uncomplicated obesity suggest the mechanical role of local adipose depot around the ventricles (28).

Furthermore, EAT could also affect LV structure and function by a paracrine pathway due to the anatomic proximity of EAT to the myocardium (29). A recent study by Ng et al. which quantified the intramyocardial fat content and myocardial interstitial fibrosis by CMR, suggested that the redundant EAT might impair the contractile function by mediating an increase in myocardial fat accumulation and interstitial fibrosis (25).

Third, in our diverse population of postmenopausal women with a relatively high presence of hypertension, obesity and diabetes, there was a possible systemic inflammatory effect induced by these comorbidities that caused the expansion of EAT volume and abnormalities in the heart (30, 31). Under the influence of systemic inflammation, EAT can release various pro-inflammatory cytokines. Thus, the EAT can further

aggravates these systemic inflammatory influences on the myocardium and has a deleterious impact on cardiac structure and function. However, a prior clinical study by Woerden et al. did not observe significant association between EAT and the level of C-reactive protein or leucocytes (32). Possibly because the effect of EAT is too small to be reflected *via* peripheral venepuncture. Also, the sample size is relatively small.

As our correlation analyses showed, age and EAT were both independent factors that inversely correlated with LV-GLS and LA strains. Several previous studies also found a strong relation between age and EAT (14, 33). In the study by de Vos et al. age-adjusted regression analyses showed that EAT was positively related to weight, BMI, waist circumference, waist-to-hip ratio and subclinical coronary atherosclerosis (34). However, we were unable to examine the effect of aging process on EAT expansion and other cardiac abnormalities in this study.

Limitations

This study has several limitations. First, this was a cross-sectional study. Therefore, we were unable to demonstrate a causal relationship between the increased EAT, laboratory biomarkers, co-morbidities and abnormalities in cardiac structure and function. Second, data on waist circumference, waist to hip ratio or abdominal visceral adipose fat are lacking in the majority of included participants, since this was a retrospective study. Inclusion of these data would have made our study more comprehensive. Third, this study only included postmenopausal women. Whether these results could also be applied to men or premenopausal women needs to be elucidated. Finally, due to the lack of long-term follow-up data, we were unable to evaluate the prognostic role of EAT in our study population. Further longitudinal studies are required to examine the potential of EAT in predicting cardiovascular outcomes.

Conclusion

The accumulation of EAT is independently associated with LV and LA function in postmenopausal women. These associations support the role of EAT in mediating deleterious effects on cardiac structure and function. The assessment of EAT volume may facilitate clinicians to have added information on the impairment of cardiac function. Researchers could commit themselves to developing medicine targeting the epicardial fat tissue to prevent the cardiac remodeling and dysfunction.

Data availability statement

The raw data supporting the conclusions of this article will be made available by the authors, without undue reservation.

Ethics statement

The studies involving human participants were reviewed and approved by West China Hospital of Sichuan University Biomedical Research Ethics Committee. Written informed consent for participation was not required for this study in accordance with the national legislation and the institutional requirements.

Author contributions

SH and Z-GY designed the study. SH was the major contributor to the manuscript drafting and revisions. LJ and JW were responsible for data collecting and sorting. SH and KS analysed the CMR parameters and interpreted the results. W-FY and W-LQ performed the statistical analyses and prepared the tables and figures. YL and YR helped to revise the manuscript critically for important intellectual content. Z-GY supervised the whole work and revised the manuscript. All authors approved the final manuscript.

Funding

This work was supported by the 1·3·5 project for disciplines of excellence, West China Hospital, Sichuan University (ZYGD18013).

Conflict of interest

The authors declare that the research was conducted in the absence of any commercial or financial relationships that could be construed as a potential conflict of interest.

Publisher's note

Supplementary material

The Supplementary Material for this article can be found online at: https://www.frontiersin.org/articles/10.3389/fcvm.2022.1015983/full#supplementary-material

References

1. Kim S-A, Kim M-N, Shim W-J, Park S-M. Epicardial adipose tissue is related to cardiac function in elderly women, but not in men. *Nutr Metab Cardiovasc Dis.* (2017) 27:41–7. doi: 10.1016/j.numecd.2016.11.001

2. Baragetti A, Pisano G, Bertelli C, Garlaschelli K, Grigore L, Fracanzani AL, et al. Subclinical atherosclerosis is associated with Epicardial Fat Thickness and hepatic steatosis in the general population. *Nutr Metab Cardiovasc Dis.* (2016) 26:141–53. doi: 10.1016/j.numecd.2015.10.013

3. Alam MS, Green R, de Kemp R, Beanlands RS, Chow BJW. Epicardial adipose tissue thickness as a predictor of impaired microvascular function in patients with non-obstructive coronary artery disease. *J Nucl Cardiol.* (2013) 20:804–12. doi: 10.1007/s12350-013-9739-6

4. Shim IK, Cho K-I, Kim H-S, Heo J-H, Cha TJ. Impact of gender on the association of epicardial fat thickness, obesity, and circadian blood pressure pattern in hypertensive patients. *J Diabetes Res.* (2015) 2015:924539. doi: 10.1155/2015/924539

5. Kararigas G, Dworatzek E, Petrov G, Summer H, Schulze TM, Baczko I, et al. Sex-dependent regulation of fibrosis and inflammation in human left ventricular remodelling under pressure overload: Sex-specific LV gene regulation in pressure overload. *Eur J Heart Fail.* (2014) 16:1160–7. doi: 10.1002/ejhf.171

6. Regitz-Zagrosek V, Kararigas G. Mechanistic pathways of sex differences in Cardiovascular Disease. *Physiol Rev.* (2017) 97:1–37. doi: 10.1152/physrev.00021.2015

7. Habibi M, Chahal H, Opdahl A, Gjesdal O, Helle-Valle TM, Heckbert SR, et al. Association of CMR-measured LA function with heart failure development: results from the MESA study. *JACC Cardiovasc Imaging.* (2014) 7:570–9. doi: 10.1016/j.jcmg.2014.01.016

8. Aquaro GD, Pizzino F, Terrizzi A, Carerj S, Khandheria BK, Di Bella G. Diastolic dysfunction evaluated by cardiac magnetic resonance: the value of the combined assessment of atrial and ventricular function. *Eur Radiol.* (2019) 29:1555–64. doi: 10.1007/s00330-018-5571-3

9. Peters DC, Lamy J, Sinusas AJ, Baldassarre LA. Left atrial evaluation by cardiovascular magnetic resonance: sensitive and unique biomarkers. *Eur Heart J Cardiovasc Imaging.* (2021) 23:14–30. doi: 10.1093/ehjci/jeab221

10. Nelson AJ, Worthley MI, Psaltis PJ, Carbone A, Dundon BK, Duncan RF, et al. Validation of cardiovascular magnetic resonance assessment of pericardial adipose tissue volume. *J Cardiovasc Magn Reson.* (2009) 11:1–8. doi: 10.1186/1532-429X-11-15

11. Zhao Q, Cheng Y-J, Xu Y-K, Zhao ZW, Liu C, Sun TN, et al. Comparison of various insulin resistance surrogates on prognostic prediction and stratification following percutaneous coronary intervention in patients with and without type 2 diabetes mellitus. *Cardiovasc Diabetol.* (2021) 20:190. doi: 10.1186/s12933-021-01383-7

12. Shi K, Yang M-X, Huang S, Yan WF, Yan WF, Li Y, et al. Effect of diabetes mellitus on the development of left ventricular contractile dysfunction in women with heart failure and preserved ejection fraction. *Cardiovasc Diabetol.* (2021) 20:185.

13. Zhang Y, Li X-M, Shen M-T, Huang S, Li Y, Yang Z-G. Atrioventricular coupling and left atrial abnormality in type 2 diabetes mellitus with functional mitral regurgitation patients verified by cardiac magnetic resonance imaging. *Cardiovasc Diabetol.* (2022) 21:100. doi: 10.1186/s12933-022-01536-2

14. Huang S, Li Y, Jiang L, Ren Y, Wang J, Shi K, et al. Impact of Type 2 diabetes mellitus on epicardial adipose tissue and myocardial microcirculation by MRI in postmenopausal women. *J Magn Reson Imaging.* (2022) 56:1404–13.

15. Kim J-S, Kim SW, Lee JS, Lee SK, Abbott R, Lee KY, et al. Association of pericardial adipose tissue with left ventricular structure and function: a region-specific effect? *Cardiovasc Diabetol.* (2021) 20:26. doi: 10.1186/s12933-021-01219-4

16. Sacks HS, Fain JN. Human epicardial fat: what is new and what is missing? *Clin Exp Pharmacol Physiol.* (2011) 38:879–87. doi: 10.1111/j.1440-1681.2011.05601.x

17. Packer M. Epicardial adipose tissue may mediate deleterious effects of obesity and inflammation on the myocardium. *J Am Coll Cardiol.* (2018) 71:2360–72. doi: 10.1016/j.jacc.2018.03.509

18. Christensen RH, Hansen CS, Scholten BJ, Jensen MT, Pedersen BK, Schnohr P, et al. Epicardial and pericardial adipose tissues are associated with reduced diastolic and systolic function in type 2 diabetes. *Diabetes Obes Metab.* (2019) 21:2006–11. doi: 10.1111/dom.13758

19. Tadic M, Ilic S, Cuspidi C, Ivanovic B, Bukarica L, Kostic N, et al. Left and right atrial phasic function and deformation in untreated patients with prediabetes and type 2 diabetes mellitus. *Int J Cardiovasc Imaging.* (2015) 31:65–76. doi: 10.1007/s10554-014-0536-3

20. Steele JM, Urbina EM, Mazur WM, Khoury PR, Nagueh SF, Tretter JT, et al. Left atrial strain and diastolic function abnormalities in obese and type 2 diabetic adolescents and young adults. *Cardiovasc Diabetol.* (2020) 19:163. doi: 10.1186/s12933-020-01139-9

21. Chirinos JA, Sardana M, Ansari B, Satija V, Kuriakose D, Edelstein I, et al. Left atrial phasic function by cardiac magnetic resonance feature tracking is a strong predictor of incident cardiovascular events. *Circ Cardiovasc Imaging.* (2018) 11:e007512. doi: 10.1161/CIRCIMAGING.117.007512

22. Cameli M, Lisi M, Mondillo S, Padeletti M, Ballo P, Tsioulpas C, et al. Left atrial longitudinal strain by speckle tracking echocardiography correlates well with left ventricular filling pressures in patients with heart failure. *Cardiovasc Ultrasound.* (2010) 8:14. doi: 10.1186/1476-7120-8-14

23. Evin M, Broadhouse KM, Callaghan FM, McGrath RT, Glastras S, Kozor R, et al. Impact of obesity and epicardial fat on early left atrial dysfunction assessed by cardiac MRI strain analysis. *Cardiovasc Diabetol.* (2016) 15:164. doi: 10.1186/s12933-016-0481-7

24. Mancio J, Azevedo D, Fragao-Marques M, Falcao-Pires I, Leite-Moreira A, Lunet N, et al. Meta-Analysis of relation of epicardial adipose tissue volume to left atrial dilation and to left ventricular hypertrophy and functions. *Am J Cardiol.* (2019) 123:523–31. doi: 10.1016/j.amjcard.2018.10.020

25. Ng ACT, Strudwick M, van der Geest RJ, Ng ACC, Gillinder L, Goo SY, et al. Impact of epicardial adipose tissue, left ventricular myocardial fat content, and interstitial fibrosis on myocardial contractile function. *Circ Cardiovasc Imaging.* (2018) 11:e007372. doi: 10.1161/CIRCIMAGING.117.007372

26. Cho D-H, Joo HJ, Kim M-N, Lim D-S, Shim WJ, Park S-M. Association between epicardial adipose tissue, high-sensitivity C-reactive protein and myocardial dysfunction in middle-aged men with suspected metabolic syndrome. *Cardiovasc Diabetol.* (2018) 17:95. doi: 10.1186/s12933-018-0735-7

27. Fox CS, Gona P, Hoffmann U, Porter SA, Salton CJ, Massaro JM, et al. Pericardial fat, intrathoracic fat, and measures of left ventricular structure and function: the framingham heart study. *Circulation.* (2009) 119:1586–91. doi: 10.1161/CIRCULATIONAHA.108.828970

28. Iacobellis G, Ribaudo MC, Leto G, Leto G, Zappaterreno A, Vecci E, et al. Influence of excess fat on cardiac morphology and function: Study in uncomplicated obesity. *Obes Res.* (2002) 10:767–73.

29. Fitzgibbons TP, Czech MP. Epicardial and perivascular adipose tissues and their influence on cardiovascular disease: basic mechanisms and clinical associations. *J Am Heart Assoc.* (2014) 3:e000582. doi: 10.1161/JAHA.113.000582

30. Nakanishi K, Fukuda S, Tanaka A, Otsuka K, Taguchi H, Yoshikawa J, et al. Epicardial adipose tissue accumulation is associated with renal dysfunction and coronary plaque morphology on multidetector computed tomography. *Circ J.* (2015) 80:196–201. doi: 10.1253/circj.CJ-15-0477

31. Cheng K, Chu C, Lee K, Lin TH, Hsieh CC, Chiu CC, et al. Adipocytokines and proinflammatory mediators from abdominal and epicardial adipose tissue in patients with coronary artery disease. *Int J Obes.* (2008) 32:268–74. doi: 10.1038/sj.ijo.0803726

32. van Woerden G, Gorter TM, Westenbrink BD, Willems TP, van Veldhuisen DJ, Rienstra M. Epicardial fat in heart failure patients with mid-range and preserved ejection fraction: Epicardial fat in heart failure. *Eur J Heart Fail.* (2018) 20:1559–1566. doi: 10.1002/ejhf.1283

33. Cosson E, Nguyen MT, Rezgani I, Tatulashvili S, Sal M, Berkane N, et al. Epicardial adipose tissue volume and coronary calcification among people living with diabetes: a cross-sectional study. *Cardiovasc Diabetol.* (2021) 20:35. doi: 10.1186/s12933-021-01225-6

34. de Vos AM, Prokop M, Roos CJ, Meijs MF, van der Schouw YT, Rutten A, et al. Peri-coronary epicardial adipose tissue is related to cardiovascular risk factors and coronary artery calcification in post-menopausal women. *Eur Heart J.* (2008) 29:777–83. doi: 10.1093/eurheartj/ehm564

frontiers | Frontiers in Cardiovascular Medicine

TYPE Review
PUBLISHED 09 December 2022
DOI 10.3389/fcvm.2022.1052068

OPEN ACCESS

EDITED BY
Claudia Prieto,
King's College London,
United Kingdom

REVIEWED BY
Julio Sotelo,
Universidad de Valparaíso, Chile
Angela Lungu,
Technical University of Cluj-Napoca,
Romania

*CORRESPONDENCE
Eva S. Peper
evaspeper@gmail.com

SPECIALTY SECTION
This article was submitted to Cardiovascular Imaging, a section of the journal Frontiers in Cardiovascular Medicine

RECEIVED 23 September 2022
ACCEPTED 22 November 2022
PUBLISHED 09 December 2022

CITATION
Peper ES, van Ooij P, Jung B, Huber A, Gräni C and Bastiaansen JAM (2022) Advances in machine learning applications for cardiovascular 4D flow MRI.
Front. Cardiovasc. Med. 9:1052068.
doi: 10.3389/fcvm.2022.1052068

Advances in machine learning applications for cardiovascular 4D flow MRI

Eva S. Peper[1,2]*, Pim van Ooij[3,4], Bernd Jung[1,2], Adrian Huber[1], Christoph Gräni[5] and Jessica A. M. Bastiaansen[1,2]

[1]Department of Diagnostic, Interventional and Pediatric Radiology (DIPR), Inselspital, Bern University Hospital, University of Bern, Bern, Switzerland, [2]Translational Imaging Center (TIC), Swiss Institute for Translational and Entrepreneurial Medicine, Bern, Switzerland, [3]Department of Radiology and Nuclear Medicine, Amsterdam University Medical Centers, Amsterdam, Netherlands, [4]Department of Pediatric Cardiology, Wilhelmina Children's Hospital, University Medical Center Utrecht, Utrecht, Netherlands, [5]Department of Cardiology, Inselspital, Bern University Hospital, University of Bern, Bern, Switzerland

Four-dimensional flow magnetic resonance imaging (MRI) has evolved as a non-invasive imaging technique to visualize and quantify blood flow in the heart and vessels. Hemodynamic parameters derived from 4D flow MRI, such as net flow and peak velocities, but also kinetic energy, turbulent kinetic energy, viscous energy loss, and wall shear stress have shown to be of diagnostic relevance for cardiovascular diseases. 4D flow MRI, however, has several limitations. Its long acquisition times and its limited spatio-temporal resolutions lead to inaccuracies in velocity measurements in small and low-flow vessels and near the vessel wall. Additionally, 4D flow MRI requires long post-processing times, since inaccuracies due to the measurement process need to be corrected for and parameter quantification requires 2D and 3D contour drawing. Several machine learning (ML) techniques have been proposed to overcome these limitations. Existing scan acceleration methods have been extended using ML for image reconstruction and ML based super-resolution methods have been used to assimilate high-resolution computational fluid dynamic simulations and 4D flow MRI, which leads to more realistic velocity results. ML efforts have also focused on the automation of other post-processing steps, by learning phase corrections and anti-aliasing. To automate contour drawing and 3D segmentation, networks such as the U-Net have been widely applied. This review summarizes the latest ML advances in 4D flow MRI with a focus on technical aspects and applications. It is divided into the current status of fast and accurate 4D flow MRI data generation, ML based post-processing tools for phase correction and vessel delineation and the statistical evaluation of blood flow.

KEYWORDS

4D flow cardiovascular magnetic resonance, 4D flow, four-dimensional flow imaging, artificial intelligence, machine learning (ML)

Introduction

Since its emergence in 1993 (1–3), four-dimensional (4D) flow magnetic resonance imaging (MRI) has evolved as a non-invasive imaging technique to visualize and quantify blood flow and has been used for clinical imaging since the early 2000s (4, 5). 4D flow MRI is based on a time-resolved 3D phase contrast MRI sequence and is widely applied to the heart and vessels.

The quantification of net flow and peak velocities from 4D flow MRI has shown to be of diagnostic relevance for cardiovascular diseases such as the grading of stenoses, aortic coarctation, or aortic- and mitral valve regurgitation (6–9). Also, the visualization of the direction of the blood flow is important, for example in aortic aneurysms, aortic dissections and coarctations, in hypertrophy cardiomyopathy (6, 10), as well as in congenital heart disease, such as univentricular hearts or transposition of the great arteries (11, 12). Moreover, 4D flow MRI allows the direct quantification of regurgitant flow compared to traditional indirect methods (i.e., subtracting stroke volume calculated from aortic 2D flow MRI from stroke volume measured by left ventricular segmentation) in mitral valve insufficiency (13). Furthermore, 3D visualization of the blood flow using pathlines can help interpreting complex flow patterns pre- and post-surgery, such as the Fontan procedure (14). Also, other biomarkers such as kinetic energy (KE) (15, 16), turbulent kinetic energy (TKE) (17, 18), viscous energy (VE) loss (16), wall shear stress (WSS) (19, 20) or pulse wave velocity (PWV) (21) have shown significant differences in patients with cardiovascular disease compared to normal subjects.

Four-dimensional flow MRI, however, has several limitations. Due to its velocity encoding scheme, 4D flow MRI takes at least four times as long as cine MRI scans (i.e., around 10 min). This poses limits on the clinical application due to additional costs, patient discomfort and motion artifacts. Additionally, limited spatio-temporal resolutions, constrained by the signal-to-noise-ratio (SNR) and scan time, lead to inaccuracies in velocity measurements in small vessels, low-flow venous vessels and near the vessel wall due to partial volume effects (14). This in turn creates inaccurate grading of stenoses and inaccuracies in WSS estimation (22, 23). Additionally, 4D flow MRI is subject to inherent inaccuracies of the MRI measurement process such as residual phase errors, induced by eddy currents, concomitant fields, or even mechanical vibrations (24), which can lead to errors in velocity estimations. Although tuning of the scanners' pre-emphasis can help to correct for non-linearities in the gradient field, these inaccuracies, as well as phase aliasing effects, must be corrected for retrospectively, creating long post-processing times using dedicated software. The post-processing times are prolonged as net flow and peak velocities are typically evaluated by (manually) placed 2D planes and contours at the location of the corresponding vessel or valve within the 3D acquisition. Parameters such as KE, VE, TKE and WSS require even a careful delineation of the 3D vessel lumen.

Various machine learning (ML) techniques have been proposed to overcome these limitations. Existing scan acceleration methods, such as compressed sensing (CS) (25–27) have been extended using ML reconstructions which are able to speed up the image reconstruction time up to a couple of seconds (28). Also, ML super-resolution methods can assimilate high-resolution computational fluid dynamic (CFD) simulations and 4D flow MRI, which leads to more realistic velocity results. ML based techniques, such as U-Nets, used to localize vessels and segment vessel boundaries, have been applied to 4D flow MRI to automate contour drawing and 3D segmentation. ML efforts have also focused on the automation and acceleration of other post-processing steps, by learning phase corrections and anti-aliasing.

This review summarizes the latest ML advances in 4D flow MRI with a focus on technical aspects and applications, including all original research articles published on the topics of (4D) flow MRI and ML published until November 2022. It is divided into the current status of (1) scan acceleration and image reconstruction, (2) super resolution and data assimilation for fast and accurate 4D flow MRI data generation, as well as ML based post-processing methods for (3) phase corrections, (4) vessel segmentation and (5) the statistical evaluation of blood flow.

Scan acceleration and image reconstruction

4D flow MRI uses additional magnetic field gradients to encode the velocity of moving blood. These gradients are applied to each spatial direction separately, which results in four different images, the reference image and three flow encoded images, also called 4-point encoding (**Figure 1A**). As the scan time is therefore four times as long, various acceleration techniques have been proposed (25, 29–32). These acceleration methods skip datapoints in k-space (undersampling), which creates aliasing artifacts in the image when using a conventional reconstruction. Most image reconstruction algorithms of these techniques take advantage of information redundancies – similar to those used for image compression – such that the full information content can be derived (27). However, the runtimes for those (iterative) reconstruction algorithms range between 10 and 60 mins, a drawback that can be tackled with machine learning (ML) approaches.

Most approaches for ML image reconstruction are based on artifact-removal of undersampled data in image space, rather than training a network to retrieve the full image content directly from the undersampled k-space. In 2019, Vishnevsky et al. (28) implemented a variational neural network (FlowVN) for fast, automatic image reconstruction of undersampled 4D

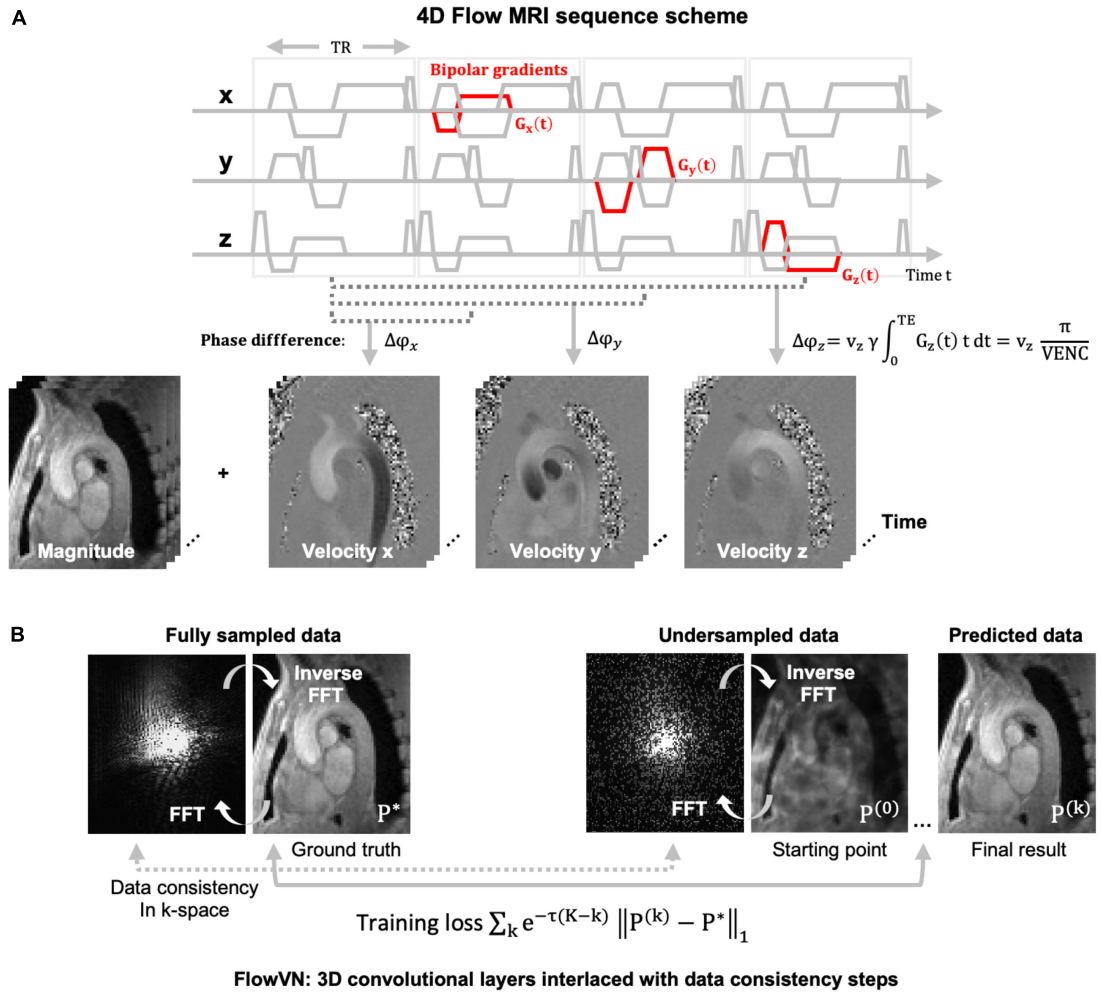

FIGURE 1
(A) 4D flow MRI image acquisition scheme using a spoiled gradient echo sequence with additional bipolar gradients for motion encoding (red). The velocity maps of this exemplary 4D flow MRI dataset of the aortic arch are obtained by subtracting the phase ϕ of the reference and the three flow encoded images. Magnitude images for the four acquired images are averaged, or in other applications, used for turbulence encoding. All images are time-resolved, representing one cardiac cycle. The velocity encoding strength (VENC) in [cm/s] is set by the user and is inversely proportional to the area of the bipolar gradient. The VENC is usually chosen in the range of the maximum expected velocity to prevent velocity aliasing. **(B)** Fully sampled and randomly undersampled k-space and their corresponding images. The undersampled data displays incoherent artefacts in image space ($P^{(0)}$). In data recovery training with the FlowVN (28). $P^{(0)}$ is the Fourier transform of the undersampled k-space and the starting point of the training. The training loss is defined by the difference of the reconstructed image with the fully sampled data (P*). The data consistency is calculated in k-space as the difference between the sampled datapoints. After k iterations image $P^{(k)}$ is achieved. Abbreviations: TR = repetition time, TE = echo time, x,y,z = spatial dimension, v = velocity, γ = gyromagnetic ratio, FFT = fast Fourier transform, P = image, k = iteration steps.

flow MRI data. During training, fully sampled data served as a ground truth and was retrospectively undersampled using a random undersampling pattern as used in CS (33–37) applications (see **Figure 1B**). The starting point of the FlowVN training was an image with random, noise-like undersampling artifacts (the Fourier transform of a randomly undersampled k-space) as shown in **Figure 1B**. The network used this image, the undersampled k-space data (real and imaginary parts), and the coil sensitivity maps as inputs for training. It consisted of 3D convolutional layers and data consistency steps. This design [similar to Hammerik et al. (38)] enabled that (1) the network learns differences between the ground truth and the artifact image and (2) that the data points in k-space for sampled and undersampled data match. The output were artifact-free images close to the fully sampled data. The network could demonstrate its similar performance to a regular CS image reconstruction; however, the runtime was 21 s for the FlowVN vs. 10 min for the CS reconstruction. Also, when applied to 13 times undersampled patient data, the FlowVN was 30 times faster and systolic peak velocity errors were only marginally lower (–1.59% for FlowVN and –1.18% for CS). In a different study, Haji-Valiyadeh et al. (39) used a 3D U-Net to remove aliasing

artifacts from undersampled radial 2D flow MRI data for the purpose of fast, real-time data acquisition. They developed a network trained on 510 radial, real-time 2D flow datasets, which were artificially created from the images of Cartesian 2D flow dataset. The undersampling artifact removal of the network was then tested in an actual free-breathing real-time 2D flow sequence for acceleration factors up to 28. In a comparison to a CS reconstruction of the real-time data the 3D U-net filtering was almost 5 times faster and could recover higher peak velocity values than the CS reconstruction. Peak velocity values were also closer to the ground truth of non-real-time image acquisition, represented by an average heartbeat composed of by all the heartbeats throughout the acquisition, when compared with the CS reconstruction. Another way of 4D flow MRI scan acceleration was recently suggested by Kim et al. (40). The proposed network learns to recover velocity maps as obtained by regular 4-point encoding (referring to 4 acquisitions, as illustrated in **Figure 1A**) by replacing it with a sampling scheme that requires only three acquisitions and learning the phase reconstruction subsequently. Velocity results demonstrated a good agreement between both encoding schemes (regression slope = 0.96 and R^2 = 0.992).

Super resolution and data assimilation

To increase the spatio-temporal resolution of 4D flow MRI, which is limited by SNR and scan time, ML super-resolution techniques can be applied. These techniques learn on paired high- and low-resolution datasets to resolve an image resolution higher than the input resolution. As there is typically a lack of high-resolution *in vivo* data, most super-resolution approaches for 4D flow MRI rely on synthetic images created by CFD simulations. These simulations solve the Navier Stokes equation in a given vessel geometry and under given inflow conditions and can be computed at resolutions much higher than the maximum achievable resolutions with 4D flow MRI, while maintaining correct physics.

In 2020, Ferdian et al. (41) developed a framework to derive synthetic high-resolution 4D flow MRI images from CFD simulations in the aorta for training a super-resolution network. They used three aortic geometries to generate simulations with high spatial resolution and a temporal resolution of 71 cardiac frames, using inlet and outlet conditions at the ascending and descending aorta. From the simulations synthetic 4D flow MRI images were generated by deriving the velocity fields and dividing them into their spatial v_x, v_y, and v_z components, similar to a 4D flow MRI acquisition (**Figure 2**). Then, a complex signal was created with the velocity maps as the signals phase and a simulated magnitude, followed by a fast Fourier transform (FFT) to generate a synthetic k-space (**Figure 2**). To mimic MRI characteristics the CFD data was down-sampled in k-space i.e., high frequency components were cut off, and Gaussian noise was added to the complex signal to achieve a pre-defined SNR. After inverse fast Fourier transform (IFFT) the image represented a complex, MRI-like low-resolution signal. A super-resolution residual network (4DFlowNet), based on the generator of the SRResNet network (42), was then trained to recover the high-resolution data. Training was performed on the paired synthetic high- and low-resolution 4D flow MRI data. The input layers consisted of two parts, the anatomical one (with channels: phase-contrast magnetic resonance angiogram and magnitude image), and the velocity one (with channels: v_x, v_y, and v_z velocity maps). In this setup, the anatomical channels selected the vessel regions and supported de-noising. As only three aortic geometries were available, the network training was patch-based, that means 16 × 16 × 16 randomly selected voxel patches, with a flow region of at least 20%, were used for training. The super-resolution network could successfully recover simulated data with a resolution down-sampled by a factor of 2 and at varying SNR levels. The network was then applied to high-resolution phantom and high- (2 mm) and low-resolution (4 mm) volunteer 4D flow MRI datasets. The study showed that the super-resolution network had smaller flow rate errors averaged in an ROI at in- (–0.6%) and outlet (5.8%) than interpolated data at in- (7%) and outlet (5.8%) in the phantom and (1.1%) and (3.8%) *in vivo*. In a similar study, Rutkowski et al. (43) used high-resolution, CFD-derived vector fields to create synthetic, MRI like, high- and low-resolution data pairs. CFD simulations were calculated on cerebrovascular flow models of five patient-specific aneurysms on which data augmentation (changes in diameter size, aneurysm geometry, synthetic vessel creation) was applied. The vessels had rigid walls and a time-resolved inflow profile as an inlet condition. Simulations were repeated 6 times with different inflow profiles, which led to 180 unique time-varying velocity fields. For training, a CNN similar to standard super-resolution networks (44) was used. 32 × 32 × 32 velocity field blocks were extracted from the simulated MRI acquisition. The loss function was based on magnitude weighted least squares and the network was tested in retrospectively down-sampled phantom data, allowing for a comparison against the original high-resolution dataset. Also, the network was applied to 20 time-averaged 4D flow MRI patient datasets (0.4–0.6 mm isotropic spatial resolution, 20 frames). As a result, the network could remove background noise up to 64%. Overall, the 4D flow MRI derived velocities had lower noise and a higher spatial resolution when enhanced with the CNN. Vessel boundaries could be delineated better, and the velocities close to the walls were estimated more accurately, including smoother velocity gradients near the wall. In the future, these simulations and ML frameworks might be extended to more advanced 4D flow MRI acquisition schemes, including turbulence induced signal dephasing in the magnitude images. Dirix et al. (45) developed a similar framework for synthesized

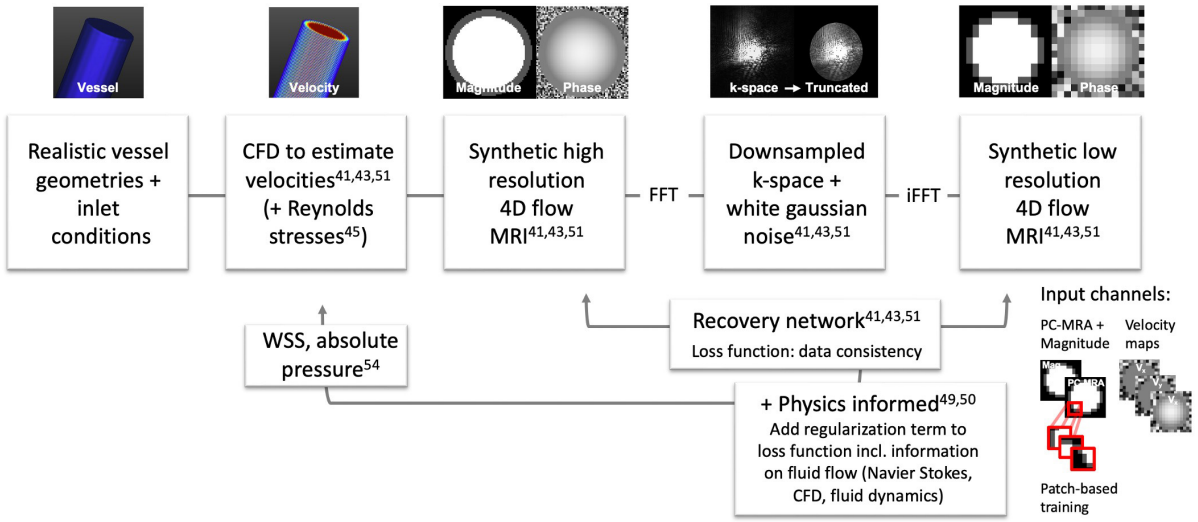

FIGURE 2
Overview of frameworks for 4D flow MRI super-resolution training and data assimilation for 4D flow MRI and CFD data: Ferdian et al. (aortic simulation) (41), Rutkowski et al. (cerebrovascular simulations) (43), Kissas et al. (49), Fathi et al. (50), Dirix et al. (45), Ferdian et al. (54). Exemplary data in this figure was created with GTFlow (Gyrotools, Zürich, Switzerland).

4D flow MRI images using multipoint encoding to achieve turbulence assessment (45).

For ML it can be advantageous (faster, more accurate, less training data) to restrict the space of solutions. Generally, data fidelity terms in the loss function of neural networks minimize the distance between the predicted output and the measured data. Physics-informed networks include a regularization part that enforces the underlying physical principles of a given dataset. For 4D flow MRI this can for example be the conservation of mass and momentum in the flow domain, which leads to a correct solution even with limited training data (46). In contrast, other non-machine learning-, but physics-based methods use divergence free velocity fields as a constraint to 4D flow MRI data (47) and CFD based velocity field optimizations to inform the 4D flow MRI data about CFD physics (48). The physics informed neural network introduced by Raissi et al. (46) was picked up by Kissas et al. (49) and Fathi et al. (50) in 2020 for 4D flow MRI implementations. The network from Kissas et al. (49) solves partial differential equations using a neural network to predict flow and pressure from 4D flow MRI measurements of the carotid bifurcation. It was trained on simulations with 1D Navier Stokes equations. Fathi et al. (50) trained a deep neural network with the aim to remove noise and to increase the resolution of 4D flow MRI data. They restricted the space of solutions of the applied network by a regularization term on the Navier Stokes equations within a pre-defined region inside the blood flow. The data fidelity term (the same as in (46)) was applied to the entire data. The network then output v_x, v_y, and v_z velocity components, pressure, and the magnitude image. The network was trained using synthetic 4D flow MRI data and tested on 4D flow MRI scans of a silicon phantom. For their workflow only a rough segmentation of the blood flow region was necessary (in which Navier Stokes was valid), and in contrast to other techniques, no strict boundaries or inflow conditions had to be defined, which made it less error prone. They could demonstrate a significant reduction in velocity errors during simulation, however, phantom measurements showed marginal improvements of velocity estimation. Very recently, a super resolution 4D flow network (SRflow) has been published by Shit et al. (51) in which they achieved a higher velocity-to-noise ratio in images with a 4-times increased resolution using their super-resolution approach than using a regular cubic B-spline interpolation.

4D flow derived biomarkers, such as WSS, have been associated with endothelial cell remodeling, for regions of low WSS (or high oscillatory WSS) in particular. Also, high WSS has been associated with disease patterns such as in aortic stenosis and aortic dissection. However, limited spatial resolution, partial volume effects and segmentation inaccuracy do not allow for accurate WSS, which is typically solved with curve-fitting and interpolation (52, 53). 4D flow MRI derived WSS therefore typically results in an underestimation when compared to CFD (22). Ferdian et al. (54) developed a U-Net based ML network (WSSNet) to directly estimate WSS from 4D flow MRI, trained on patient-specific CFD simulations and synthetic 4D flow MRI. The datasets consisted of 37 aortic geometries and simulated velocities. The input of the WSSNet were 2D maps of simulated velocities close to the vessel border and their coordinates with respect to the border. The network learned the connection between geometry, velocity and WSS, and the output were estimated WSS values (which were compared to WSS values calculated from the CFD data). To generalize better to 4D flow

MRI, synthetic low-resolution 4D flow MRI was created from the CFD data and the training repeated. Then the network was applied to 43 real, *in vivo* 4D flow MRI datasets and compared against the fitting algorithms for WSS estimation. The mean absolute error of the estimated WSS using the network was 0.55 ± 0.60 Pa (relative error 4.34 ± 4.14%). The values correlated well with the WSS from the CFD simulations, reporting a correlation coefficient of $r = 0.92 \pm 0.05$. The estimated WSS showed 2–3 times higher WSS values when compared to regular fitting methods and more robustness to artificially introduced noise.

Phase corrections

Since velocity maps are derived from the phase of the 4D flow MRI signal, sources that introduce phase offsets, such as eddy currents, can impair the data quality. Phase corrections and anti-aliasing can be performed retrospectively to the acquisition but are user-dependent and time-consuming. ML techniques, however, can learn and apply these corrections.

Eddy current induced background phase can be corrected for by linear or polynomial fits of the phase in static tissue regions. The calculated phase error fields can then be applied the flow regions to correct the estimated velocities. You et al. (55) used 139 (85 training, 14 validation, 40 testing) abdominopelvic 4D flow MRI datasets to train a multichannel 3D U-Net that automatically generates phase error fields for correction. Flow analysis was performed on the testing datasets and compared against a regular background phase correction as a reference, which included a manual detection of static tissue regions using dedicated software. Assuming in- and outflow values to be the same, non-corrected images showed an offset due to background fields and a low correlation between in- and outflow values. The Pearson's correlation coefficient r was reported to be $r = 0.5$, with a p-value of $p < 0.001$. After manual correction this increased to $r = 0.98$, $p < 0.001$ and after automatic ML correction to $r = 0.91$, $p < 0.001$. Flow differences reduced from uncorrected −0.14 L/min to corrected 0.05 L/min for regular and ML correction. This technique demonstrated the use of a fast, automated correction and the feasibility of ML training for this task, demonstrating similar results as manual correction. However, also (semi-) automatic algorithms for the selection of static tissue regions and fitting exists (and usually perform well), which were not included as a reference in the study.

Aliasing effects, or phase-wraps, can occur if the velocity encoding, defined by the VENC, was chosen too low. High velocities, higher than the VENC value, will appear as wrapped phases (transitioning from $+\pi$ to $-\pi$) in the velocity map (**Figure 3A**), which must be corrected for retrospectively. The correction, however, requires the identification of the aliased voxel in 3D and for all time frames. There are several semi-automatic solutions that support 2D voxel wise un-wrapping by region-merging and graph cut optimization (56, 57), which, however, require a start point for unwrapping or rely on spatio-temporal smoothness (58, 59). These methods were also adapted to be applicable to 4D flow MRI by using a Laplacian algorithm (60). Robust, automatic detection of all aliased voxel in all time frames, however, remains challenging and large, aliased regions or regions with multiple wraps remain a problem. In Berhane et al. (61) a U-Net CNN was used to automatically detect and correct aliasing in 667 4D flow dataset (VENCs ranging between 60 and 500 cm/s, 534 with contrast agent, 321 bicuspid aortic valve (BAV), 247 tricuspid aortic valve, 99 controls). Aliasing was either introduced during acquisition or retrospectively added. An additional 10 subjects were acquired with three different VENC settings (60, 100, 175 cm/s) to show the accuracy of the unwrapping method. From all datasets static segmentations of the thoracic aorta were created. Datasets without aliasing ($N = 305$) were used to introduce aliasing in predefined regions, serving as labeled pairs of ground truth and aliased voxels. The data was split up in training (and validation) and testing, with a binary mask for the aliased voxels as a network output. Test results provided much better correction when compared to an automated method (from Salfity (58, 59)). The difference of the performance of the techniques was significant with a Dice score (DS) between 0.89 and 0.99 (for the different VENCs) for the CNN and between 0.84 and 0.90 for the conventional algorithm. Ten datasets scanned with different VENCs showed similar peak velocity, net and peak flow rates for the conventional anti-aliasing algorithm and the CNN corrected datasets. However, no comparison against a 4D Laplacian algorithm was done and also multiple phase wrapping was not taken into account. Also, phase-unwrapping at the vessel wall was limited, which leaves the phase-unwrapping problem open to find a fully automatic solution.

Vessel segmentation

4D flow MRI requires accurate delineation of the vessel lumen for calculation of mean velocities, flow and WSS. The blood-tissue contrast of the sequence is low, especially without the use of contrast-agents, which is why for segmentation angiogram-like images are generated from the absolute velocity. These PC-MRAs can be calculated in a time-resolved way, but do not have sufficient signal in regions and time frames with low velocities, which is why they cannot be used for accurate, fully automated segmentations (see **Figure 3B**). 3D segmentation is therefore done in a semi-automatic way for static images and there is a strong need for fast, robust and automatic delineations.

Classifying machine learning tasks like the U-Net (62) have been used broadly to define labels and their location in 2D or 3D images. They are built up by an encoder part, so the down-sampling of spatial information, and a decoder part, restoring the spatial information. The networks are trained on paired

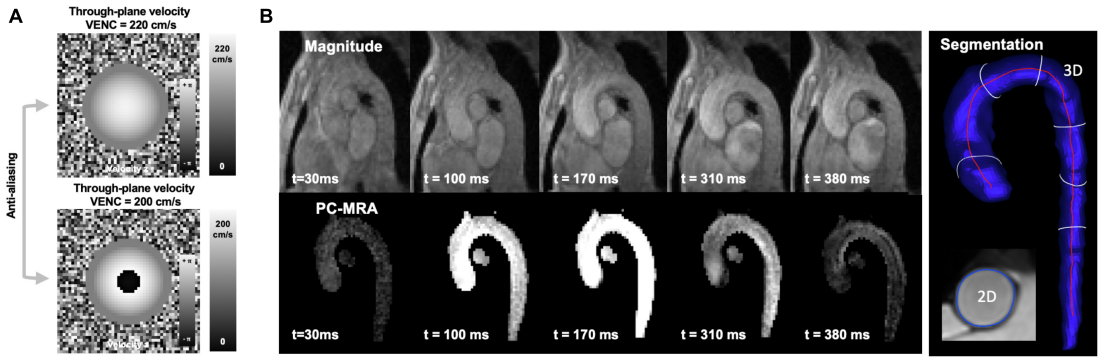

FIGURE 3
(A) Simulated parabolic flow with a central peak velocity of 220 cm/s and the aliasing effect create in the phase-difference image and the velocity map when a lower VENC e.g., of 200 cm/s is chosen. **(B)** Temporal evolution of the magnitude and PC-MRA signal in an aortic 4D flow MRI dataset. Magnitude images do not allow for fast segmentations based on thresholding as blood and tissue have a similar contrast. PC-MRA images lose their signal when there is no apparent blood flow e.g., during diastole.

datasets of the original image and the matching voxel-based segmentation. To compare the geometric segmentation results the DS and the Hausdorff distance (HD) are used. The DS ranges from zero to one and calculates the voxel-based match between learned and ground truth geometry. The HD is the maximum value of all (Euclidian) distances calculated between each point of a geometry and the closest point of another geometry.

Bratt et al. (63) trained a U-Net to segment the aortic valve from 2D flow MRI magnitude images, based on manual, time-resolved segmentations. They achieved a DS of 0.94 using 150 aortic datasets for training. In 190 additional testing datasets (patients with coronary artery disease) the ML based segmentation demonstrated high correlations in the analysis of net forward flow through the aortic valve when compared to a manual delineation (r = 0.99, $p < 0.001$) and it performed better than a commercial automatic segmentation [significant differences in flow 1.85 ± 1.8 ml (U-Net) vs. 3.33 ± 3.18 ml (automatic)]. Also, in a different patient cohort with BAV and stenotic aortic valves acquired at a different scanner and vendor the network performed equally well in comparison to manual segmentations (correlation r = 0.99, $p < 0.001$). In a similar study, Garcia et al. (64) trained a network to detect and track the movement of the aortic and the mitral valve in 3-chamber cine (bSSFP) images. The resulting position of a 2D plane through the valve was interpolated onto 4D flow MRI data acquired in the same scan session in 106 subjects resulting in significant differences in flow and peak velocity between aortic- and mitral valve disease patients and controls (no comparison between manual and ML segmentation was conducted). Tsou et al. (65) trained two networks, a MultiResUNet (66) and a U-Net to perform 2D contour delineations of the cerebral aqueduct on 333 (266 training, 67 validation) cerebral 2D flow MRI datasets. Cerebrospinal fluid flow through the aqueduct was similar for both segmentation approaches when compared to segmentations of a radiologist. The DS was slightly higher for the MulitResUNet than for the U-Net (DS = 0.933 vs. DS = 0.928, respectively) and the MulitResUNet was less prone to segmentation errors than the U-Net.

In 2020, Berhane et al. (67) used 4D flow MRI scans of a wide range of age, body mass index and aortic valve types of 1,018 subjects (528 BAV and 376 tricuspid aortic valves, 114 healthy controls) to train a CNN based 3D U-Net (62) segmentation network for labeling the aorta in a systolic timeframe. Training datasets were constituted from manually labeled images, done by >20 operators. The segmentations resulted in a DS of 0.951 and HD of 2.8 mm for the testing dataset (499 training, 101 validation, 418 testing). Additionally, a centerline was automatically detected, and perpendicular slices were chosen with the vessel boundary being the segmentation. These values were then compared against each other in peak velocity (< 0.001 m/s, LOA 0.01% for the CNN at all regions) and net flow (−0.2 to 0.1 mL/cycle, LOAs 6.4–9.2%) to quantify differences. Interestingly, most deviations in the testing cohort with a DS below 0.9 were around the aortic outflow tract or at the superior extend of the aortic branches, indicating a difference in the segmentations extend. Also, the CNN achieved DS similar to the interobserver values (DS = 0.95). This ML workflow can certainly be used on a wide range of 4D flow MRI images, eventually it requires retraining if different PC-MRA calculation methods are used. Similarly, Garrido-Oliver et al. (68) trained a 3D nnU-Net (69) for static segmentations of the aorta and a Deep Q-Network (DQN) (70), based on reinforcement learning, for landmark detection on 323 patients (BAV, genetic syndrome, aneurisms) who received 4D flow MRI scans. For the aortic segmentations they achieved a DS of 0.949. The landmark detection algorithm performed well in the identification of the supra-aortic vessels, and it performed less good in the detection of the sinotubular junction and the pulmonary artery bifurcation. The sinotubular junction, however, was also challenging to be identified by human

observers. Both studies, (67) and (68), did not take the motion of the aorta into account but included only time-averaged images.

So far, only limited studies exist on training time-resolved segmentations from 4D flow MRI. However, time-resolved segmentations are of interest when investigating stiffness by PWV (71–74), and to avoid inaccuracies in flow estimation, as the aortic root can move up to 8 mm within one heartbeat (75). Segmentation of time-resolved images is very time-consuming as it requires a 3D segmentation for each of 10–40 timeframes. In 2022, Bustamante et al. (76) created a framework to segment all 4 cardiac chambers, the aorta, and pulmonary arteries for all time frames from contrast-enhanced 4D flow MRI data. A 3D U-net was developed on 205 4D flow dataset (144 training, 20 validation, 41 testing), which contained a variety of cardiac disorders (N = 165). Forty cardiac frames were acquired and treated as independent segmentations. The segmentations were compared against ground truth, manually corrected, atlas-based segmentations also developed by Bustamante et al. (77). This method registers a general segmentation mask onto the image, which is, however, computationally expensive. The results showed good overall scores, the best scores achieved in the aorta. Time-averaged DS were >0.9 for all anatomies, similar to Berhane et al. (67).

To avoid the problem of poor myocardium-to-blood contrast in 4D flow MRI and time intensive pre-registration on atlases, Corrado et al. (78) used a stack of 2D time-resolved short-axis cine (bSSFP) images acquired at the same scan session to segment 4D flow MRI of mainly healthy subjects (N = 105). They used a pretrained fully convolutional network (FCN) from Bai et al. (79) trained on 4,875 short axis bSSFP images of the UK biobank study to create a 3D segmentation of the left and right ventricle. Then a 3D-to-3D registration of the time-averaged bSSFP and 4D flow data was done to map the segmentation results onto the 4D flow dataset. The automated segmentation (LV: DS = 0.92, RV: DS = 0.86) showed good agreement with manual segmentations (LV: DS = 0.91, RV: DS = 0.87).

Corrado et al. (80) also developed a ML based plane selection (80), which automatically defines measurement planes perpendicular to the 8 great vessels: ascending aorta, main pulmonary artery, superior and inferior vena cava, and the 4 pulmonary veins. The training was done on 323 subjects (241 training, 42 validation, 40 testing; in total 186 healthy controls, 123 patients and 14 with unknown health status). A 3D CNN predicted the probability of a predefined patch (32 × 32 × 32 voxels) containing a vessel and also location, size and a double oblique plane on that vessel. The CNN was based on residual learning [ResNet (81)] with residual blocks for feature extraction and convolutional blocks for downsampling. At each plane either done by ML or manual selection, a segmentation of the vessel was performed automatically based on the PC-MRA and net flow was calculated and compared. As a result, the correlation between the ML algorithm and two manual observers was slightly lower (observer 1 vs. algorithm: r = 0.68 and observer 2 vs. algorithm: r = 0.72) that the difference between the two observers (r = 0.81). Also, the algorithm was more accurate on straighter vessels such as the SVC and worse in the ascending aorta. The performance was stable for all flow estimations (as this was probably insensitive to small variation in measurement plane). Also, the patient datasets were an additional challenge for the network suggesting more diverse datasets. Overall, the ML method was faster than atlas-based approaches. Processing times when applying the ML were 18s vs. 300–400 s for a manual observer. The study suggested a reinforcement learning approach for measurement plane planning in the future.

Contrast enhanced 4D flow MRI is used for many clinical examinations and creates a better blood-tissue contrast than conventional 4D flow MRI. In medical imaging, realistic but fictitious images can be produced by generative adversarial networks (GANs), and CycleGANs (82, 83) in particular. Bustamante et al. (84) used a cyclic GAN, to artificially transform non-contrast cardiac enhanced scans into contrast enhanced data. The cyclic GAN can be considered as unsupervised learning which needs two images sets as input, which do not have to be exact pairs. It consists of two generators or data transformation functions that transform (1) non-contrast data into contrast data and (2) contrast data into non-contrast data. It also consists of two discriminators that distinguishes (1) artificial from real contrast data and (2) artificial from real non-contrast data. They used 69 with and 72 datasets without contrast agents for training a 2D GAN. In total additional 81 non-contrast aortic datasets were used for testing and were converted into artificially enhanced datasets using the GAN. For training, the data was cropped and rearranged as 120 2D slices in a coronal view, using only the magnitude image as an input. The quantitative evaluation of the artificially enhanced test data showed an increase in contrast-to-noise ratio (CNR) by 88%, and an increase in SNR by 48%. This was achieved while maintaining a structural similarity index, describing structural information, of 0.82 ± 0.01 and a mean relative error of 0.09 ± 0.01 between enhanced and original images. Also, segmentation on artificially enhanced data performed better than on regular data.

Statistical evaluation of blood flow

ML has the potential to support the statistical classification of healthy controls and patients with cardiovascular disease based on 4D flow MRI data using supervised or unsupervised learning. For classification, typically a set of hemodynamic features is derived from the data (such as velocity, vorticity, etc.), then the number of features is reduced by a feature-selection step e.g., using a sequential forward search. A set of different classifiers is then tested during (supervised/unsupervised) training and the best performing features, feature-selection steps and classifiers might be used for future predictions.

Niemann et al. (85) developed a method for feature-based classification of patients with BAV and healthy controls, based on aortic 4D flow MRI. They trained a network to classify between (1) BAV (N = 22) and healthy controls (N = 90), (2) BAV and "older" healthy controls (N = 30) and (3) male and female subjects. Their framework included hemodynamic feature selection, model training and hyperparameter tuning. Selected features were parameters such as minimum, maximum and mean velocities derived from planes perpendicular to the aortic centerline. Classifiers used for training were methods such as random forest (RF) and support vector machine (SVM). The results for classifying the task were for (1) an accuracy of 93% with features time-to-peak vorticity, time-to-peak in-plane velocity and peak-systolic in-plane mean velocity using sequential forward search (SFS) as a feature-selection method and RF as a classifier, for (2) an accuracy of 100% with features peak-systolic mean velocity, time-to-peak-systolic-through-plane mean velocity and diastolic median right rotation volume using SFS as a feature selection method and SVM a classifier, and for (3) an accuracy of 69% with features peak velocity, peak systolic velocity and time-to-peak-systolic-through-plane velocity using SFS as a feature selection method and RF as a classifier. The results of the classification model demonstrated a good distinction between BAV and controls and only moderate distinction between male and female subjects. Also, in Franco et al. (86) the hemodynamics of the thoracic aorta in 4D flow MRI data of patients with BAV was analyzed searching for new biomarkers. The aim was to find a ML model that distinguishes three classes: BAV patients with (N = 49) and without (N = 18) dilated ascending aorta and healthy controls (N = 48). A total of 17 hemodynamic features such as e.g., forward velocity, velocity angle, vorticity, KE, TKE and WSS were extracted from 4D flow MRI data in two parts of the aorta. Then a set of classifiers (linear discriminant analysis, k-nearest neighbors, quadratic discriminant, Mahalanobis distant, SVM, neural network, RF) were tested and used to train a neural network with multiple layers. The performance was evaluated with repeated cross-validation and Pearson correlation between the hemodynamic features. Overall, the model classifying the data showed, that linear discriminant analysis (96.3% accuracy) and random forest (96.0% accuracy) were the best performing classifiers using the features: velocity angle, forward velocity, vorticity, and backward velocity in the ascending aorta.

TABLE 1 Available code for all original research papers screened for this review.

References	Topic	Code
Vishnevsky et al. (28)	Reconstruction of undersampled Cartesian 4D flow MRI data (aorta)	https://codeocean.com/capsule/0115983/tree
Haji-Valizadeh et al. (39)	Reconstruction of radial 2D flow MRI data (aorta)	https://dataverse.harvard.edu/dataset.xhtml?persistentId=doi:10.7910/DVN/N97M6H
Kim et al. (40)	Fast 4D flow MRI by estimating velocity maps from 3-point encoding	https://github.com/uwmri/ThreePoint4DFlow
Ferdian et al. (41)	4D flow MRI super-resolution framework	https://github.com/EdwardFerdian/4DFlowNet
Kissas et al. (49)	1D flow physics informed DNN	https://github.com/PredictiveIntelligenceLab/1DBloodFlowPINNs
Ferdian et al. (54)	WSS estimation from 4D flow MRI	https://github.com/EdwardFerdian/WSSNet
Berhane et al. (61)	Anti-aliasing correction of 4D flow MRI data	https://github.com/hberhane/4D-flow-Velocity-Aliasing-CNN
Bratt et al. (63)	Segmentation on 2D flow MRI data	https://github.com/akbratt/PC_AutoFlow
Tsou et al. (65)	Segmentation on 4D flow MRI data	Uses MultiResUNet from (66): https://github.com/nibtehaz/MultiResUNet
Corrado et al. (80)	Automatic measurement plane selection on 4D flow MRI data	https://github.com/pcorrado/DL-Vessel-Localization
Corrado et al. (78)	Ventricular segmentation on 4D flow MRI data	Using the FCN from (79): https://github.com/baiwenjia/ukbb_cardiac
Garrido-Oliver et al. (68)	3D segmentation and landmark detection 4D flow MRI data (aorta)	Uses the nnU-Net (69): https://github.com/MIC-DKFZ/nnUNet Reinforcement learning and landmark detection: https://github.com/CardiovascularImagingVallHebron/4D_flow_landmark_detection

Conclusion

Current 4D flow MRI acquisitions are constrained by their scan time, spatio-temporal resolution, and SNR, limiting their accuracy and clinical application. Semi-automatic post-processing steps, including phase corrections and segmentation for vessel delineation are time-consuming and in need for automation. This review shows various ways of accelerating image reconstruction times and post-processing tasks using ML, when compared to the current state-of-the-art approaches. Code and data have been made publicly available for many ML applications reviewed for this article (as summarized in **Table 1**), which supports their reproducibility, applicability and development. A table summarizing all papers reviewed and their technical details can be found in the **Supplementary Table 1**.

In the future, it will be essential that accurate cardiovascular 4D flow MRI can be performed in a single, fast scan. That includes an easy choice of VENCs (by retrospective correction of anti-aliasing and phase offsets) and spatio-temporal resolutions

that might be increased by super-resolution approaches retrospectively to the scan and for vessels with slow flow and small geometries. It is important, that the analysis of the data is performed in an automated, operator independent and robust way, to allow accurate assessment of biomarkers such as peak velocities and WSS for diagnosis and clinical decision making. Classification of disease by 4D flow MRI-derived biomarkers has the potential to be reinforced by ML technologies.

Author contributions

EP conceptualizing of the manuscript, literature research for manuscripts included in the review, and manuscript writing. PO, BJ, and JB conceptualizing of the manuscript, technical feedback and discussion, and manuscript reviewing. AH and CG clinical feedback and discussion and manuscript reviewing. All authors contributed to the article and approved the submitted version.

Funding

This study was supported by funding received from the Swiss National Science Foundation (grant #PCEFP2_194296) and the Swiss Heart Foundation (grant #FF18054).

Conflict of interest

The authors declare that the research was conducted in the absence of any commercial or financial relationships that could be construed as a potential conflict of interest.

Publisher's note

Supplementary material

The Supplementary Material for this article can be found online at: https://www.frontiersin.org/articles/10.3389/fcvm.2022.1052068/full#supplementary-material

SUPPLEMENTARY TABLE 1
All papers reviewed and their technical details.

References

1. Firmin DN, Gatehouse PD, Konrad JP, Yang GZ, Kilner PJ, Longmore DB. Rapid 7-dimensional imaging of pulsatile flow. *Proceedings of computers in cardiology conference*. London: *IEEE* (1993). p. 353–6.

2. Wigstrom L, Sjoqvist L, Wranne B. Temporally resolved 3D phase-contrast imaging. *Magn Reson Med.* (1996) 36:800–3. doi: 10.1002/mrm.1910360521

3. Wigström L, Ebbers T, Fyrenius A, Karlsson M, Engvall J, Wranne B, et al. Particle trace visualization of intracardiac flow using time-resolved 3D phase contrast MRI. *Magn Reson Med.* (1999) 799:793–9. doi: 10.1002/(SICI)1522-2594(199904)41:4<793::AID-MRM19>3.0.CO;2-2

4. Kozerke S, Hasenkam JM, Pedersen EM, Boesiger P. Visualization of flow patterns distal to aortic valve prostheses in humans using a fast approach for cine 3D velocity mapping. *J Magn Reson Imaging.* (2001) 13:690–8.

5. Markl M, Chan F, Alley M, Wedding K, Draney M, Elkins C, et al. Time-resolved three-dimensional phase-contrast MRI. *J Magn Reson Imaging.* (2003) 17:499–506. doi: 10.1002/jmri.10272

6. Hope M, Meadows A, Hope T, Ordovas K, Saloner D, Reddy G, et al. Clinical evaluation of aortic coarctation with 4D flow MR imaging. *J Magn Reson Imaging.* (2010) 31:711–8. doi: 10.1002/jmri.22083

7. Hsiao A, Tariq U, Alley MT, Lustig M, Vasanawala SS. Inlet and outlet valve flow and regurgitant volume may be directly and reliably quantified with accelerated, volumetric phase-contrast MRI. *J Magn Reson Imaging.* (2015) 41:376–85. doi: 10.1002/jmri.24578

8. Feneis J, Kyubwa E, Atianzar K, Cheng J, Alley M, Vasanawala S, et al. 4D flow MRI quantification of mitral and tricuspid regurgitation: reproducibility and consistency relative to conventional MRI. *J Magn Reson Imaging.* (2018) 48:1147–58. doi: 10.1002/jmri.26040

9. Adriaans BP, Westenberg JJ, Cauteren YJ, Gerretsen S, Elbaz MS, Bekkers SC, et al. Clinical assessment of aortic valve stenosis: comparison between 4D flow MRI and transthoracic echocardiography. *J Magn Reson Imaging.* (2020) 51:472–80. doi: 10.1002/jmri.26847

10. Schnell S, Ansari SA, Vakil P, Hurley M, Carr J, Batjer H, et al. Characterization of cerebral aneurysms using 4D FLOW MRI. *J Cardiovasc Magn Reson.* (2012) 14:W2. doi: 10.1186/1532-429X-14-S1-W2

11. Vasanawala SS, Hanneman K, Alley MT, Hsiao A. Congenital heart disease assessment with 4D flow MRI. *J Magn Reson Imaging.* (2015) 42:870–86. doi: 10.1002/jmri.24856

12. Callaghan FM, Burkhardt B, Valsangiacomo Buechel ER, Kellenberger CJ, Geiger J. Assessment of ventricular flow dynamics by 4D-flow MRI in patients following surgical repair of d-transposition of the great arteries. *Eur Radiol.* (2021) 31:7231–41. doi: 10.1007/s00330-021-07813-0

13. Fidock B, Archer G, Barker N, Elhawaz A, Al-Mohammad A, Rothman A, et al. Standard and emerging CMR methods for mitral regurgitation quantification. *Int J Cardiol.* (2021) 331:316–21. doi: 10.1016/j.ijcard.2021.01.066

14. Dyverfeldt P, Bissell M, Barker A, Bolger A, Carlhäll C, Ebbers T, et al. 4D flow cardiovascular magnetic resonance consensus statement. *J Cardiovasc Magn Reson.* (2015) 17:72. doi: 10.1186/s12968-015-0174-5

15. Sjöberg P, Bidhult S, Bock J, Heiberg E, Arheden H, Gustafsson R, et al. Disturbed left and right ventricular kinetic energy in patients with repaired tetralogy of Fallot: pathophysiological insights using 4D-flow MRI. *Eur Radiol.* (2018) 28:4066–76. doi: 10.1007/s00330-018-5385-3

16. Han QJ, Witschey W, Fang-Yen C, Arkles J, Barker A, Forfia P, et al. Altered right ventricular kinetic energy work density and viscous energy dissipation in patients with pulmonary arterial hypertension: a pilot study using 4D flow MRI. *PLoS One.* (2015) 10:e0138365. doi: 10.1371/journal.pone.0138365

17. Dyverfeldt P, Kvitting J, Sigfridsson A, Engvall J, Bolger A, Ebbers T. Assessment of fluctuating velocities in disturbed cardiovascular blood flow: in vivo

feasibility of generalized phase-contrast MRI. *J Magn Reson Imaging.* (2008) 28:655–63. doi: 10.1002/jmri.21475

18. Binter C, Gülan U, Holzner M, Kozerke S. On the accuracy of viscous and turbulent loss quantification in stenotic aortic flow using phase-contrast MRI. *Magn Reson Med.* (2016) 76:191–6. doi: 10.1002/mrm.25862

19. van Ooij P, Potters W, Nederveen A, Allen B, Collins J, Carr J, et al. methodology to detect abnormal relative wall shear stress on the full surface of the thoracic aorta using four-dimensional flow MRI. *Magn Reson Med.* (2015) 73:1216–27. doi: 10.1002/mrm.25224

20. Potters W, van Ooij P, Marquering H, vanBavel E, Nederveen AJ. Volumetric arterial wall shear stress calculation based on cine phase contrast MRI. *J Magn Reson Imaging.* (2015) 41:505–16. doi: 10.1002/jmri.24560

21. Markl M, Wallis W, Strecker C, Gladstone B, Vach W, Harloff A. Analysis of pulse wave velocity in the thoracic aorta by flow-sensitive four-dimensional MRI: reproducibility and correlation with characteristics in patients with aortic atherosclerosis. *J Magn Reson Imaging.* (2012) 35:1162–8. doi: 10.1002/jmri.22856

22. Cibis M, Potters W, Gijsen F, Marquering H, van Ooij P, vanBavel E, et al. The effect of spatial and temporal resolution of cine phase contrast MRI on wall shear stress and oscillatory shear index assessment. *PLoS One.* (2016) 11:e0163316. doi: 10.1371/journal.pone.0163316

23. van Ooij P, Potters WV, Nederveen AJ, Collins JD, Carr JC, Malaisrie S, et al. Thoracic aortic wall shear stress atlases in patients with bicuspid aortic valves. *J Cardiovasc Magn Reson.* (2014) 16:161. doi: 10.1186/1532-429X-16-S1-P161

24. Dillinger H, Kozerke S, Guenthner C. Direct comparison of gradient Fidelity and acoustic noise of the same MRI system at 3 T and 0.75 T. *Magn Reson Med.*. (2022) 88:1937–47. doi: 10.1002/mrm.29312

25. Tsao J, Boesiger P, Pruessmann KP. k-t BLAST and k-t SENSE: dynamic MRI with high frame rate exploiting spatiotemporal correlations. *Magn Reson Med.* (2003) 50:1031–42. doi: 10.1002/mrm.10611

26. Cheng, JY, Alley M, Lustig M, Vasanawala S, Pauly J. Variable-density radial view-ordering and sampling for time-optimized 3D Cartesian imaging. *Proceedings of the ISMRM workshop on data sampling and image reconstruction*. Sedona, AZ. (2013).

27. Lustig M, Donoho D, Pauly JM. Sparse MRI: the application of compressed sensing for rapid MR imaging. *Magn Reson Med.* (2007) 58:1182–95. doi: 10.1002/mrm.21391

28. Vishnevskiy V, Walheim J, Kozerke S. Deep variational network for rapid 4D flow MRI reconstruction. *Nat Mach Intell.* (2020) 2:228–35. doi: 10.1038/s42256-020-0165-6

29. Pruessmann KP, Weiger M, Scheidegger MB, Boesiger P. SENSE: sensitivity encoding for fast MRI. *Magn Reson Med.* (1999) 42:952–62. doi: 10.1002/(SICI)1522-2594(199911)42:5<952::AID-MRM16>3.0.CO;2-S

30. Tsao J, Kozerke S. MRI temporal acceleration techniques. *J Magn Reson Imaging.* (2012) 36:543–60. doi: 10.1002/jmri.23640

31. Pedersen H, Kozerke S, Ringgaard S, Nehrke K, Won YK. k-t PCA: temporally constrained k-t BLAST reconstruction using principal component analysis. *Magn Reson Med.* (2009) 62:706–16. doi: 10.1002/mrm.22052

32. Lustig M, Donoho D, Santos J, Pauly J. Compressed sensing MRI. *IEEE Signal Process Mag.* (2008) 25:72–82. doi: 10.1109/MSP.2007.914728

33. Prieto C, Doneva M, Usman M, Henningsson M, Greil G, Schaeffter T, et al. Highly efficient respiratory motion compensated free-breathing coronary MRA using golden-step Cartesian acquisition. *J Magn Reson Imaging.* (2015) 41:738–46. doi: 10.1002/jmri.24602

34. Han F, Zhou Z, Han E, Gao Y, Nguyen K, Finn J, et al. Self-gated 4D multiphase, steady-state imaging with contrast enhancement (MUSIC) using rotating cartesian K-space (ROCK): validation in children with congenital heart disease. *Magn Reson Med.* (2017) 78:472–83. doi: 10.1002/mrm.26376

35. Zhu Y, Guo Y, Lingala S, Lebel R, Law M, Nayak K. GOCART: GOlden-angle CArtesian randomized time-resolved 3D MRI. *Magn Reson Imaging.* (2016) 34:940–50. doi: 10.1016/j.mri.2015.12.030

36. Peper ES, Gottwald LM, Zhang Q, Coolen B, van Ooij P, Nederveen A, et al. Highly accelerated 4D flow cardiovascular magnetic resonance using a pseudo-spiral Cartesian acquisition and compressed sensing reconstruction for carotid flow and wall shear stress. *J Cardiovasc Magn Reson.* (2020) 22:7. doi: 10.1186/s12968-019-0582-z

37. Gu T, Korosec F, Block W, Fain S, Turk Q, Lum D, et al. PC VIPR: a high-speed 3D phase-contrast method for flow quantification and high-resolution angiography. *Am J Neuroradiol.* (2005) 26:743–9.

38. Hammernik K, Klatzer T, Kobler E, Recht MP, Sodickson DK, Pock T, et al. Learning a variational network for reconstruction of accelerated MRI data. *Magn Reson Med.* (2018) 79:3055–71. doi: 10.1002/mrm.26977

39. Haji-Valizadeh H, Guo R, Kucukseymen S, Paskavitz A, Cai X, Rodriguez J, et al. Highly accelerated free-breathing real-time phase contrast cardiovascular MRI via complex-difference deep learning. *Magn Reson Med.* (2021) 86:804–19. doi: 10.1002/mrm.28750

40. Kim D, Jen M-L, Eisenmenger LB, Johnson KM. Accelerated 4D-flow MRI with 3-point encoding enabled by machine learning. *Magn Reson Med.* (2022). [Epub ahead of print]. doi: 10.1002/mrm.29469

41. Ferdian E, Suinesiaputra A, Dubowitz D, Zhao D, Wang A, Cowan B, et al. 4DFlowNet: super-resolution 4D flow MRI using deep learning and computational fluid dynamics. *Front Phys.* (2020) 8:138. doi: 10.3389/fphy.2020.00138

42. Ledig C, Theis L, Huszár F, Caballero J, Cunningham A. Photo-realistic single image super-resolution using a generative adversarial network. *Proceedings of the IEEE conference on computer vision and pattern recognition*. Honolulu, HI: IEEE (2017). p. 4681–90. doi: 10.1109/CVPR.2017.19

43. Rutkowski DR, Roldan-Alzate A, Johnson K. Enhancement of cerebrovascular 4D flow MRI velocity fields using machine learning and computational fluid dynamics simulation data. *Sci Rep.* (2021) 11:10240. doi: 10.1038/s41598-021-89636-z

44. Medero R, Ruedinger K, Rutkowski D, Johnson K, Roldán-Alzate A. In vitro assessment of flow variability in an intracranial aneurysm model using 4D flow MRI and tomographic PIV. *Ann Biomed Eng.* (2020) 48:2484–93. doi: 10.1007/s10439-020-02543-8

45. Dirix P, Buoso S, Peper ES, Kozerke S. Synthesis of patient-specific multipoint 4D flow MRI data of turbulent aortic flow downstream of stenotic valves. *Sci Rep.* (2022) 12:16004. doi: 10.1038/s41598-022-20121-x

46. Raissi M, Perdikaris P, Karniadakis GE. Physics-informed neural networks: a deep learning framework for solving forward and inverse problems involving nonlinear partial differential equations. *J Comput Phys.* (2019) 378:686–707. doi: 10.1016/j.jcp.2018.10.045

47. Busch J, Giese D, Wissmann L, Kozerke S. Reconstruction of divergence-free velocity fields from cine 3D phase-contrast flow measurements. *Magn Reson Med.* (2013) 69:200–10. doi: 10.1002/mrm.24221

48. Töger J, Zahr M, Aristokleous N, Bloch K, Carlsson M, Persson P. Blood flow imaging by optimal matching of computational fluid dynamics to 4D-flow data. *Magn Reson Med.* (2020) 84:2231–45. doi: 10.1002/mrm.28269

49. Kissas G, Yang Y, Hwuang E, Witschey WR, Detre JA. Machine learning in cardiovascular flows modeling: predicting arterial blood pressure from non-invasive 4D flow MRI data using physics-informed neural networks. *Comput Methods Appl Mech Eng.* (2020) 358:112623. doi: 10.1016/j.cma.2019.112623

50. Fathi M, Perez-Raya I, Baghaie A, Berg P, Janiga G, Arzani A, et al. Super-resolution and denoising of 4D-flow MRI using physics-informed deep neural nets. *Comput Methods Programs Biomed.* (2020) 197:105729. doi: 10.1016/j.cmpb.2020.105729

51. Shit S, Zimmermann J, Ezhov I, Paetzold J, Sanches A, Pirkl C, et al. SRflow: deep learning based super-resolution of 4D-flow MRI data. *Front Artif Intell.* (2022) 5:928181. doi: 10.3389/frai.2022.928181

52. Stalder AF, Russe MF, Frydrychowicz A, Bock J, Hennig J, Markl M. Quantitative 2D and 3D phase contrast MRI: optimized analysis of blood flow and vessel wall parameters. *Magn Reson Med.* (2008) 60:1218–31. doi: 10.1002/mrm.21778

53. Potters W, Marquering HA, VanBavel E, Nederveen AJ. Measuring wall shear stress using velocity-encoded MRI. *Curr Cardiovasc Imaging Rep.* (2014) 7:9257. doi: 10.1007/s12410-014-9257-1

54. Ferdian E, Dubowitz DJ, Mauger CA, Wang A, Young AA. WSSNet: aortic wall shear stress estimation using deep learning on 4D flow MRI. *Front Cardiovasc Med.* (2022) 8:769927. doi: 10.3389/fcvm.2021.769927

55. You S, Masutani E, Alley M, Vasanawala S, Taub P, Liau J, et al. Deep learning automated background phase error correction for abdominopelvic 4D flow MRI. *Radiology.* (2022) 302:584–92. doi: 10.1148/radiol.2021211270

56. Jenkinson M. Fast, automated, N-dimensional phase-unwrapping algorithm. *Magn Reson Med.* (2003) 49:193–7. doi: 10.1002/mrm.10354

57. Untenberger M, Hüllebrand M, Tautz L, Joseph A, Voit D, Merboldt K, et al. Spatiotemporal phase unwrapping for real-time phase-contrast flow MRI. *Magn Reson Med.* (2015) 74:964–70. doi: 10.1002/mrm.25471

58. Xiang Q-S. Temporal phase unwrapping for CINE velocity imaging. *J Magn Reson Imaging.* (1995) 5:529–34. doi: 10.1002/jmri.1880050509

59. Salfity MF, Huntley JM, Graves MJ, Marklund O, Cusack R, Beauregard DA. Extending the dynamic range of phase contrast magnetic resonance velocity

imaging using advanced higher-dimensional phase unwrapping algorithms. *J R Soc Interface.* (2006) 3:415–27. doi: 10.1098/rsif.2005.0096

60. Loecher M, Schrauben E, Johnson KM, Wieben O. Phase unwrapping in 4D MR flow with a 4D single-step laplacian algorithm. *J Magn Reson Imaging.* (2016) 43:833–42. doi: 10.1002/jmri.25045

61. Berhane H, Scott MB, Barker A, McCarthy P, Avery R, Allen B, et al. Deep learning–based velocity antialiasing of 4D-flow MRI. *Magn Reson Med.* (2022) 88:449–63. doi: 10.1002/mrm.29205

62. Çiçek Ö, Abdulkadir A, Lienkamp SS, Brox T, Ronneberger O. 3D U-Net: learning dense volumetric segmentation from sparse annotation. In: Ourselin S, Joskowicz L, Sabuncu M, Unal G, Wells W editors. *Medical image computing and computer-assisted intervention – MICCAI 2016.* Cham: Springer (2016). p. 424–32. doi: 10.1007/978-3-319-46723-8_49

63. Bratt A, Kim J, Pollie M, Beecy A, Tehrani N, Codella N, et al. Machine learning derived segmentation of phase velocity encoded cardiovascular magnetic resonance for fully automated aortic flow quantification. *J Cardiovasc Magn Reson.* (2019) 21:1. doi: 10.1186/s12968-018-0509-0

64. Garcia J, Beckie K, Hassanabad AF, Sojoudi A, White JA. Aortic and mitral flow quantification using dynamic valve tracking and machine learning: prospective study assessing static and dynamic plane repeatability, variability and agreement. *JRSM Cardiovasc Dis.* (2021) 10:2048004021999900. doi: 10.1177/2048004021999900

65. Tsou C, Cheng Y, Huang C, Chen J, Chen W, Chai J, et al. Using deep learning convolutional neural networks to automatically perform cerebral aqueduct CSF flow analysis. *J Clin Neurosci.* (2021) 90:60–7. doi: 10.1016/j.jocn.2021.05.010

66. Ibtehaz N, Rahman MS. MultiResUNet: rethinking the U-Net architecture for multimodal biomedical image segmentation. *Neural Netw.* (2020) 121:74–87. doi: 10.1016/j.neunet.2019.08.025

67. Berhane H, Scott M, Elbaz M, Jarvis K, McCarthy P, Carr J, et al. Fully automated 3D aortic segmentation of 4D flow MRI for hemodynamic analysis using deep learning. *Magn Reson Med.* (2020) 84:2204–18. doi: 10.1002/mrm.28257

68. Garrido-Oliver J, Aviles J, Córdova M, Dux-Santoy L, Ruiz-Muñoz A, Teixido-Tura G, et al. Machine learning for the automatic assessment of aortic rotational flow and wall shear stress from 4D flow cardiac magnetic resonance imaging. *Eur Radiol.* (2022) 32:7117–27. doi: 10.1007/s00330-022-09068-9

69. Isensee F, Jaeger PF, Kohl SAA, Petersen J, Maier-Hein KH. nnU-Net: a self-configuring method for deep learning-based biomedical image segmentation. *Nat Methods.* (2021) 18:203–11. doi: 10.1038/s41592-020-01008-z

70. Mnih V, Kavukcuoglu K, Silver D, Rusu A, Veness J, Bellemare M, et al. Human-level control through deep reinforcement learning. *Nature.* (2015) 518:529–33. doi: 10.1038/nature14236

71. Kim H-L, Kim S-H. Pulse wave velocity in atherosclerosis. *Front Cardiovasc Med.* (2019) 6:41. doi: 10.3389/fcvm.2019.00041

72. Wentland AL, Grist TM, Wieben O. Review of MRI-based measurements of pulse wave velocity: a biomarker of arterial stiffness. *Cardiovasc Diagn Ther.* (2014) 4:193–206.

73. Rogers WJ, Hu YL, Coast D, Vido DA, Kramer CM, Pyeritz RE, et al. Age-Associated Changes in Regional Aortic Pulse Wave Velocity. *J Am Coll Cardiol.* (2001) 38:1123–9. doi: 10.1016/S0735-1097(01)01504-2

74. Ma Y, Choi J, Hourlier-Fargette A, Xue Y, Chung H, Lee J, et al. Relation between blood pressure and pulse wave velocity for human arteries. *Proc Natl Acad Sci USA.* (2018) 115:11144–9. doi: 10.1073/pnas.1814392115

75. Kozerke S, Scheidegger MB, Pedersen EM, Boesiger P. Heart motion adapted cine phase-contrast flow measurements through the aortic valve. *Magn Reson Med.* (1999) 42:970–8. doi: 10.1002/(SICI)1522-2594(199911)42:5<970::AID-MRM18>3.0.CO;2-I

76. Bustamante M, Viola F, Engvall J, Carlhäll C-J, Ebbers T. Automatic time-resolved cardiovascular segmentation of 4D flow MRI using deep learning. *J Magn Reson Imaging.* (2022). [Epub ahead of print]. doi: 10.1002/jmri.28221

77. Bustamante M, Petersson S, Eriksson J, Alehagen U, Dyverfeldt P, Carlhäll C, et al. Atlas-based analysis of 4D flow CMR: automated vessel segmentation and flow quantification. *J Cardiovasc Magn Reson.* (2015) 17:87. doi: 10.1186/s12968-015-0190-5

78. Corrado PA, Wentland AL, Starekova J, Dhyani A, Goss K, Wieben O. Fully automated intracardiac 4D flow MRI post-processing using deep learning for biventricular segmentation. *Eur Radiol.* (2022) 32:5669–78. doi: 10.1007/s00330-022-08616-7

79. Bai W, Sinclair M, Tarroni G, Oktay O, Rajchl M, Vaillant G, et al. Automated cardiovascular magnetic resonance image analysis with fully convolutional networks. *J Cardiovasc Magn Reson.* (2018) 20:65. doi: 10.1186/s12968-018-0471-x

80. Corrado PA, Seiter DP, Wieben O. Automatic measurement plane placement for 4D Flow MRI of the great vessels using deep learning. *Int J Comput Assist Radiol Surg.* (2022) 17:199–210. doi: 10.1007/s11548-021-02475-1

81. He K, Zhang X, Ren S, Sun J. Deep Residual Learning for Image Recognition. *2016 IEEE conference on computer vision and pattern recognition (CVPR).* Las Vegas, NV: IEEE (2016). p. 770–8. doi: 10.1109/CVPR.2016.90

82. Zhu J-Y, Park T, Isola P, Efros AA. Unpaired image-to-image translation using cycle-consistent adversarial networks. *Proceedings of the IEEE international conference on computer vision.* Venice: IEEE (2017). p. 2223–32. doi: 10.1109/ICCV.2017.244

83. Wolterink JM, Dinkla AM, Savenije MHF, Seevinck PR, van den Berg CAT, Išgum I. Deep MR to CT synthesis using unpaired data. In: Tsaftaris S, Gooya A, Frangi A, Prince J editors. *International workshop on simulation and synthesis in medical imaging.* Cham: Springer (2017). p. 14–23. doi: 10.1007/978-3-319-68127-6_2

84. Bustamante M, Viola F, Carlhäll C-J, Ebbers T. Using deep learning to emulate the use of an external contrast agent in cardiovascular 4D flow MRI. *J Magn Reson Imaging.* (2021) 54:777–86. doi: 10.1002/jmri.27578

85. Niemann, U, Neog A, Behrendt B, Lawonn K, Gutberlet M, Spiliopoulou M, et al. Cardiac cohort classification based on morphologic and hemodynamic parameters extracted from 4D PC-MRI data. *arXiv.* [Preprint]. (2020). Available online at: https://arxiv.org/abs/2010.05612 (accessed September 15, 2022).

86. Franco P, Sotelo J, Guala A, Dux-Santoy L, Evangelista A, Rodríguez-Palomares J, et al. Identification of hemodynamic biomarkers for bicuspid aortic valve induced aortic dilation using machine learning. *Comput Biol Med.* (2022) 141:105147. doi: 10.1016/j.compbiomed.2021.105147

frontiers | Frontiers in Cardiovascular Medicine

TYPE Review
PUBLISHED 04 January 2023
DOI 10.3389/fcvm.2022.984326

OPEN ACCESS

EDITED BY
Adelina Doltra,
Hospital Clinic of Barcelona, Spain

REVIEWED BY
Sarah Moharem-Elgamal,
NIHR Bristol Cardiovascular Biomedical Research Unit, United Kingdom
Monique Bernard,
UMR 7339 Centre de Résonance Magnétique Biologique et Médicale (CRMBM), France
Frank Kober,
Aix-Marseille Université, France

*CORRESPONDENCE
Lilia M. Sierra-Galan
lilisierra@wdevel.net
W. Patricia Bandettini
ingkanisorn@nih.gov

SPECIALTY SECTION
This article was submitted to Cardiovascular Imaging, a section of the journal Frontiers in Cardiovascular Medicine

RECEIVED 01 July 2022
ACCEPTED 12 December 2022
PUBLISHED 04 January 2023

CITATION
Sierra-Galan LM, Aggarwal NR, Stojanovska J, Raman SV, Han Y, Ferreira VM, Thomas K, Seiberlich N, Parwani P, Bucciarelli-Ducci C, Baldassarre LA, Mavrogeni S, Ordovas K, Schulz-Menger J and Bandettini WP (2023) Women physicians in cardiovascular magnetic resonance: Past, present, and future. *Front. Cardiovasc. Med.* 9:984326. doi: 10.3389/fcvm.2022.984326

Women physicians in cardiovascular magnetic resonance: Past, present, and future

Lilia M. Sierra-Galan[1]*, Niti R. Aggarwal[2], Jadranka Stojanovska[3], Subha V. Raman[4], Yuchi Han[5], Vanessa M. Ferreira[6], Katharine Thomas[6], Nicole Seiberlich[7], Purvi Parwani[8], Chiara Bucciarelli-Ducci[9], Lauren A. Baldassarre[10], Sophie Mavrogeni[11], Karen Ordovas[12], Jeanette Schulz-Menger[13] and W. Patricia Bandettini[14]*

[1]Cardiology Department of the Cardiovascular Division at the American British Cowdray Medical Center, Mexico City, Mexico, [2]Department of Cardiovascular Disease, Mayo Clinic, Rochester, MN, United States, [3]New York University Langone Health, New York, NY, United States, [4]Indiana University School of Medicine, Indianapolis, IN, United States, [5]The Ohio State University Wexner Medical Center, Columbus, OH, United States, [6]University of Oxford Centre for Clinical Magnetic Resonance Research, Oxford British Heart Foundation Centre of Research Excellence, The National Institute for Health Research Oxford Biomedical Research Centre at the Oxford University Hospitals NHS Foundation Trust, Division of Cardiovascular Medicine, Radcliffe Department of Medicine, University of Oxford, Oxford, United Kingdom, [7]Department of Radiology, University of Michigan, Ann Arbor, MI, United States, [8]Division of Cardiology, Department of Medicine, Loma Linda University Health, Loma Linda, CA, United States, [9]Royal Brompton and Harefield NHS Foundation Trust, London, United Kingdom, [10]Section of Cardiovascular Medicine, Yale School of Medicine, New Haven, CT, United States, [11]Onassis Cardiac Surgery Center, Athens, Greece, [12]Department of Radiology, University of Washington, Seattle, WA, United States, [13]Charité - Universitätsmedizin Berlin, Corporate Member of Freie Universität Berlin, Humboldt-Universität zu Berlin, ECRC Cardiology, Helios-Clinics Berlin-Buch, Clinic of Cardiology and Nephrology, DZHK Partnersite Berlin, Berlin, Germany, [14]National Heart, Lung, and Blood Institute, National Institutes of Health, Bethesda, MD, United States

Women's engagement in medicine, and more specifically cardiovascular imaging and cardiovascular MRI (CMR), has undergone a slow evolution over the past several decades. As a result, an increasing number of women have joined the cardiovascular imaging community to contribute their expertise. This collaborative work summarizes the barriers that women in cardiovascular imaging have overcome over the past several years, the positive interventions that have been implemented to better support women in the field of CMR, and the challenges that still remain, with a special emphasis on women physicians.

KEYWORDS

women, cardiovascular MRI, cardiovascular imaging, gender diversity, leadership, CMR, inclusion, equity

Introduction

Women have long struggled for equal footing in many aspects of society. While, in recent years, their unique value in some areas traditionally dominated by men has become better understood, women still work to achieve recognition in many professional fields. Expressly, women in medicine often have not been granted the privileges that are afforded to men with the same degrees and training. In cardiovascular imaging and cardiovascular MRI (CMR), in particular, the challenges faced by women make it difficult for them to enter the field and reduce their likelihood of staying.

The first barrier to entry in the field of cardiovascular imaging is the long and challenging training, consisting of medical school and residency (in either diagnostic radiology or internal medicine), followed by cardiology and dedicated cardiac imaging or cardiovascular fellowships. Those who choose to engage in cardiovascular imaging research, either as a scientist pursuing a Ph.D. or a physician-scientist, must take on additional training. This lengthy process may cause women to hesitate when making the decision to pursue a career in cardiovascular imaging. The long career process is a gender-neutral consideration; however, in parallel, in the current era, women in some societies bear more responsibility for the family. As such, they must be capable of contributing more substantially to the support of their families and the inevitable family circumstances, including birth, death, divorce, relocation, and consequences of financial troubles. The long educational process before becoming fully-trained in cardiovascular imaging, along with the gender pay gap, may contribute to these obstacles.

Once this training is completed, women may still face challenges in clinical cardiovascular imaging practice. In many countries, cardiology and radiology have traditionally been viewed as "male" specialties, making it difficult for women to excel (if they even select these specialties in the first place). Among CMR experts, more men hold tenured academic positions than women (68% vs. 32%).[1] As a result, women are outnumbered by men in the fields of cardiology and radiology (1). Although institutions may seemingly accept the female presence in their respective departments, they may still underappreciate the contributions of women colleagues and are more likely to appoint men to leadership positions.

These lower numbers of women physicians in fields such as cardiovascular imaging may reduce the quality of care offered to patients, as the presence of women in multi-disciplinary teams has resulted in improved outcomes measured by lower patients' 30-day mortality and readmission rates (2, 3). Modern medical practice requires many individuals with different areas of expertise, and the advanced imager is an essential part of the team taking care of cardiovascular patients. Advanced imaging using approaches including cardiovascular magnetic resonance (CMR) has revolutionized the field of cardiology with high spatial resolution and three-dimensional capabilities. CMR is now indicated for various cardiovascular conditions, with extensive evidence available to showcase its impact on overall outcomes and clinical practice (4, 5). Unfortunately, as described above, women in the field of CMR—among other subspecialties—face the challenge of balancing personal life, family responsibilities, and career demands. Specialized training inherent to CMR adds to this challenge. Unfortunately, only a few dedicated centers provide advanced CMR training, the competition is hard, and a strong biographic sketch is necessary to be accepted.

This manuscript is meant to provide an understanding of the current state of women in cardiovascular imaging and CMR and to suggest some practical changes that could be enacted to help recruit and retain women in CMR. To this end, the historical role of women in cardiovascular imaging, the challenges women face in CMR, the current state of the field by the numbers, the importance of the presence of women in CMR, and the potential solutions to these challenges are discussed. While the importance of women in all aspects of CMR is acknowledged, this work is meant primarily to highlight those challenges faced by female cardiologists and radiologists in the field of cardiovascular imaging.

History of women in CMR

Women have played an essential role in the development of medical imaging. A prime example is Marie Curie, an early pioneer of "in-the-field" medical imaging. While best known for her research on radioactivity, Professor Curie was pivotal in implementing mobile x-ray units during World War I (6).

Compared to x-ray, cardiovascular magnetic resonance (CMR) is a relatively recent addition to the medical imaging toolbox, with its origins in the early 1980s. However, women were among the early developers of this emerging technology. For example, Dr. Joanne Ingwall was instrumental in promoting cardiovascular spectroscopy (7) and served as the first female president of the International Society for Magnetic Resonance in Medicine (ISMRM). In the 1990s, Daisy Chien, Ph.D., developed MRI pulse sequences for cardiovascular imaging, including magnetic resonance angiography, spin-echo T2 MRI for the detection of acute myocardial infarction, perfusion imaging, and left ventricular segmental TrueFISP imaging (8–11). Her scientific status led to a position on the ISMRM Board of Trustees. Katherine Wu, M.D. demonstrated microvascular obstruction as a predictor of adverse outcomes. Her work using CMR to predict sudden cardiac death outcomes helped push CMR into mainstream clinical use (9). Similarly, Brigitte Poncelet-Belliveau, Ph.D., developed a broad spectrum of CMR sequences and applications, including blood oxygen level-dependent contrast (BOLD), echo planar imaging, myocardial

1 Sierra-Galan LM, Estrada-Lopez E, Ferrari VA, et al. *Worldwide Variation in Cardiovascular Magnetic Resonance Practice Models.* (In Review).

perfusion, and T2-TrueFISP (12–14). In the 2000s, Dr. Vivian Lee, a radiologist and ISMRM Gold Medal Winner, developed the MRI research program at New York University. She worked to improve methods of assessing vascular disease with 3D gadolinium MRA and non-contrast methods. She also developed CMR viability imaging (15–17) and served on the Board of Trustees and later as President of the ISMRM.

By the early-to-mid 2000s, an increasing number of women from many fields (physicists, cardiologists, radiologists, and technologists) had entered the field of CMR. Critical work in translating the CMR methods into cardiovascular applications was carried out by key individuals, such as Jeanette Schulz-Menger, M.D. with her work in inflammatory disease and myocarditis (18–20)—and the first female president of the Society for Cardiovascular Magnetic Resonance (SCMR), as well as a member of the ISMRM Board of Trustees, Subha Raman, M.D., the second female president of the SCMR, with her innovative treadmill CMR research (21), Chiara Bucciarelli-Ducci, M.D.'s—the second chief executive officer (CEO) and first female CEO of the SCMR—contributions to better understanding myocardial infarction in the setting of non-obstructive coronary arteries (MINOCA) (22) and many other women imaging experts. While CMR has become more widespread over the past 15 years, new methods are continuously being developed, validated, and deployed for patient care through integrated technological, translational, and clinical development.

Barriers to entering and remaining in the CMR field

Professional women in all careers face layered challenges. CMR is a physically and mentally demanding and fast-paced specialty. Here we describe some aspects of CMR that deter women from entering the field and the challenges of remaining engaged in the field. Although the field of CMR benefits from multi-disciplinary collaboration between specialists in cardiology, radiology, and physics/engineering, these different groups face different obstacles. While many similar challenges are experienced by women scientists in cardiovascular imaging, portions of this section are more applicable to women physicians, as the pathways for cardiologists and radiologists overlap more than that of the technical experts.

Absence of female physicians

Historically, women were not allowed to train as doctors. As a result, parity in medical school intake has only been achieved in the last few decades (23, 24) with some countries continuing to lag (25). Fortunately, this recruitment barrier appears now largely resolved, with medical school graduates comprising an equal number of males and females. Improved female representation of women in medical schools is promising for increased representation of women in cardiology, diagnostic radiology, and cardiac imaging.

Even with this growing number of women in medical schools, it is interesting how medical professionals may mistakenly infer that women are now broadly well-represented, overestimating the true representation. The misperception could produce growing reservations or less support for gender equality initiatives and political support (26).

In reality, there is a progressive decline in female representation from each training step to clinical practice in cardiology. In the United States, women comprise 51% of medical school graduates and 43% of internal medicine residents, yet they are underrepresented in cardiology training and practice (27). Currently, 12–28% of cardiology trainees (23, 24, 28) and 24–30% of radiology trainees are female (29). In comparison, only 12–14% of fully trained cardiologists are women. Worldwide, women are less likely to reach the highest levels of cardiology (23, 24, 27, 28, 30–32). Though some of this disparity will inevitably improve as current trainees complete their training, the attrition rate remains high.

Literature reports that many women have been actively discouraged from becoming cardiologists. For example, numerous female cardiologists were told as young doctors not to become cardiologists because they are female (33) and sometimes because they were too "nice," an assertion male doctors rarely encounter. Women also report being denied consultant, i.e., attending, cardiologist jobs, as other consultants would not work with women (33). In addition, although challenging to quantify formally, many women experience discrimination when applying for medical training posts or other career opportunities during their reproductive years, as it is often perceived that they may become pregnant and unavailable for clinical duties and call schedules. A male candidate is thus often preferred. When faced with these attitudes, many women will simply choose a specialty that demonstrates that they want them.

Work–life balance and the risk of burn-out

The demands of cardiology make an appropriate work-life balance difficult to maintain. Women looking to choose their specialty often consider this aspect carefully and are more likely than men to value family-friendly specialties, female-friendly specialties, and stable hours (34). Prospective trainees see the reality of life as a cardiologist: 38% of prospective female cardiology trainees report their female mentors not having a reasonable work-life balance (35). There is also the issue of long hours: in Japan, 50% of female cardiologists work more than 960 h of overtime a year, with more than 60% considering leaving the field due to gender discrimination, pregnancy, and children (36). Once within the cardiology specialty, trying to

maintain a reasonable work-life balance can hinder training and career opportunities (35).

Similarly, for radiology, the rigors of rotations, an ever-increasing workload, and call schedule make at least half of the female radiology trainees and junior faculty prone to burn-out stemming from a poor work-life balance (37). In fact, burn-out is more prevalent among female radiology trainees entering parenthood because the radiology and cardiothoracic radiology training and early junior faculty years occur during the prime childbearing ages (38). Given this inference and the demographic shift of increasing mean childbearing age, radiology trainee-parents become a minority, with only 21% having one or more children (39). Additionally, 27% of radiology trainees are women likely experiencing work-life imbalance during early motherhood, thus precipitating burn-out among female diagnostic radiologists, making the specialty unattractive to women.

In an American College of Cardiology (ACC) life survey, female cardiologists and cardiology trainees had a 7% higher burn-out prevalence than male peers (40). Based on a Medscape survey of physicians from June to September 2021, radiology was the seventh most common medical specialty to be associated with burn-out (49%), with the highest level occurring among women compared to men (65% vs. 44%) (41). This results in low self-esteem, decreased career satisfaction, social dysfunction, poor well-being, and inevitable attrition from the profession.

Lack of female role models

Despite improvement over the decades, there remains a paucity of female role models and mentors within cardiology. Women cite a lack of female role models that creates hesitancy to apply for cardiology specialty training (34). However, simply being able to see that female cardiologists exist and succeed may be sufficient to encourage young women to pursue cardiology training (42). The value of female role models for diagnostic radiology and engineering sciences also holds true.

Discrimination, harassment, and bullying

Women face discrimination, bullying, and harassment more frequently than men. Discrimination occurs across the world and is reported by female cardiologists 62% of the time in the UK, 65% in the US, and 68% worldwide. In the US, this figure has changed little over the past two decades (31, 43–45). Examples of gender-based discrimination include women not being introduced by their professional titles, patients transferring their care to male colleagues, and an implicit assumption by some men that women are simply not up to the pressures of cardiology with a corresponding loss in career opportunities (46, 47).

Regarding bullying, surveys of both trainees and consultants in the UK found that women were significantly more likely to have experienced bullying than men, and this bullying was usually sexist in nature. Women also report high levels of sexual harassment (36% of British and 12% of worldwide female cardiologists) (43, 44, 48).

Women may turn to senior female role models to seek advice to deal with these problems; however, the limited number of women in leadership of institutions, professional societies, and editorial boards limits availability. Additionally, many of these female role models face impossible pressures to succeed themselves and, at times, may adopt a more stereotypically masculine behavior and shun other women, keeping solidarity with their male peers (49). Improved networking among women professionals might provide another level of support.

Family planning

Female cardiologists frequently express concern about how to plan their family while also having a career (34). This is not helped by perceived unfriendliness from their employer—43% of female cardiologists in the US have been asked about family planning in an interview setting.

Female cardiologists are less likely to be married (75% women vs. 89% men) and less likely to have children (72% women vs. 87% men). Many factors contribute to this discrepancy: in addition to institutional hostility, women who adopt part-time work patterns or take more extended periods of maternity leave are frowned upon and miss out on opportunities at work (50). Female cardiologists are also more likely to require paid childcare, whereas male cardiologists often have spouses that care for their children (46, 51). The outdated yet prevalent cultural norm of the female shouldering most of the childcare burden appears to prevail even when the female is the primary salary earner.

Maternity leave policies differ significantly worldwide. In the US, an outlier in parental leave policies, 50% of female cardiologists took eight weeks or less of maternity leave, with only 3% taking more than 6 months. One-quarter reported that their maternity leave was unpaid, and more than half felt pressured to return to work early. Cardiologists in training felt particularly pressured compared to those that had completed training. One-third of female cardiologists in the US also reported being asked to do extra service or call prior to their maternity leave (50, 52).

Maternity leave of female cardiologists outside of the US has not been studied in as much detail as in the US; however, in a worldwide survey of female surgeons (a similar cohort to female cardiologists), average maternity leave was between 7 and 12 months. However, in this worldwide survey, only half felt that their employer was generally supportive, and 80% of

female surgeons reported being told that a surgical career was incompatible with parenthood (53).

Radiation exposure

Likely for safety reasons, pregnant people were often excluded from any place where radiation exposure could occur. While CMR *per se* does not involve radiation, advanced imagers often train in both CMR and cardiovascular computed tomography (CCT), using X-rays for imaging. More recently, this level of extreme caution around pregnant people has been replaced by warnings coupled with more monitoring. For example, there are now guidelines regarding radiation exposure that set strict limits and include using a fetal monitoring badge (54, 55). These guidelines are not overly restrictive and allow training and career progression to continue even when pregnant safely. Despite this added vigilance, women are increasingly more concerned about radiation exposure than previous cohorts (50, 51, 54, 55). This concern may potentially result in less exposure to training or scanning involving radiation and fewer opportunities due to this reduced experience.

Responsibilities outside of work

With arduous long hours, overnight calls, and at times, a competitive, cutthroat work environment, the fields of radiology or cardiology are often not conducive to family life, discouraging women from considering these fields as a career. As mentioned, female cardiologists often have more domestic responsibilities than their male counterparts, spending around 8.5 h more on household tasks per week than their male peers. They also shoulder more caretaking—for sick children and parents in need—compared to their male counterparts (56, 57). With average work weeks of 40–60 h, these extra responsibilities outside of work can quickly create unsustainable pressure (58). Flexible work patterns can help, but these can be difficult to negotiate and achieve (23, 51). Part-time working patterns are often unavailable to trainees, who are most likely to have very young children. Where part-time work is allowed, there is still very low uptake: only 4% of cardiology trainees in the UK work part-time (59). Once fully trained, working part-time is also uncommon: only 10% of female cardiologists in the UK work part-time as opposed to 4% of men (44). Part-time work brings its own challenges: lower pay, fewer career opportunities, and loss of status. A recent British survey showed that cardiologists who work part-time are perceived as having lower status (44).

Academia

Women are underrepresented in cardiovascular academia: only 17% of faculty appointments are women. Women have significantly lower rates of the first authorship, particularly in high-impact journals, and are cited less often (60–63). Female cardiologists are often neither involved in the high-impact trials nor on the writing committees of clinical guidelines (64–66). Women in academia also have less success in career development awards, with gender differences persisting in a number of awards for clinician-researchers in the US, even when adjusting for confounders (67). Similarly, women in radiology are under-represented, with only 34% of women joining academia in the US. However, this number declines at higher levels of leadership, reaching just 25% among section chiefs and vice chairs and 9% among chairs (68).

Salary

Significant gender inequity persists when it comes to compensation. Female cardiologists continue to earn, on average, $32,000 less than male cardiologists in both private practice and academia, even after controlling for location, subspecialty, and full-time status (65, 66, 69). This disparity in earnings is exacerbated by the cost of children, both in fewer work hours or hired child care: either women are predominantly responsible for looking after their children (and thus not able to work and earn), or they must arrange paid childcare, which will cost around 11–20% of their salary (44, 53, 56).

Political dimension

As mentioned above in their independent sections, societal habits and traditions, such as family planning, marriage, divorce, relocation, work-life balance and the risk of burn-out, lack of female role models, discrimination, harassment, and bullying, radiation exposure, responsibilities outside of work, academia and salary, among others, where women are submitted to more substantial constraints than men, have reached a political dimension in some countries in the world, leading to action and legislation specifically to help women with these aspects for better professional equity (70).

Current CMR practice in the world

Utilizing the data obtained by a survey launched by the Society for Cardiovascular Magnetic Resonance (SCMR) in 2017 that is currently under review by the Journal of Cardiovascular Magnetic Resonance (see text footnote 1), an analysis was performed to identify women's participation in CMR practice around the world. Of 1,086 respondents, 337 (31%) were women, as shown in **Figure 1**.

The percentage of female CMR practitioners who responded to the survey varied significantly depending on the geographical

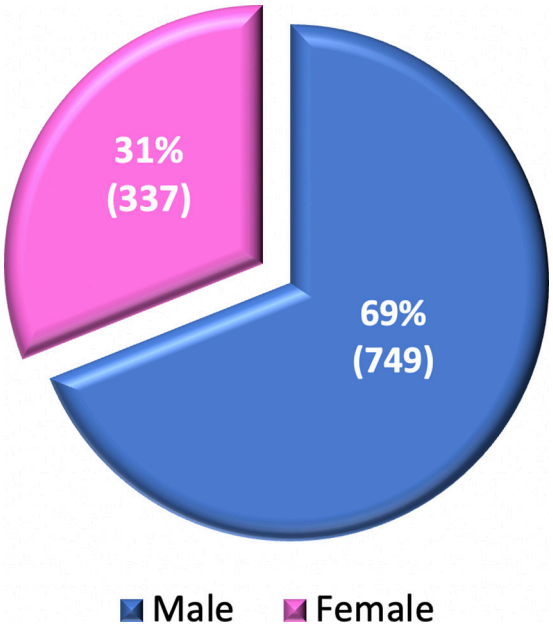

FIGURE 1
Gender distribution of CMR surveyed practitioners.

location (Figure 2). Female respondents were as follows: in New Zealand, Thailand, Romania, Indonesia, Egypt, Uruguay, and Kuwait, women represented 67–80% of respondents; in Norway, Malaysia, Sweden, Hong Kong, Lithuania, Algeria, Republic of Korea, and Finland, 50–57% of respondents were women; in Mexico, India, Canada, the UK, Italy, Singapore, Denmark, Spain, China, South Africa, Australia, Argentina, Colombia, Austria, South Korea, Chile, and Switzerland, 32–47% of respondents were women; in Saudi Arabia, the Czech Republic, Brazil, Germany, and the US, Greece, and Hungary, only 20–25% of respondents were women; in Portugal, Ireland, and Japan, 14–17% of respondents were women; and only 3% of the Netherlands respondents were women.

In the Philippines, El Salvador, Nicaragua, Iran, Georgia, Russia, Panama, Myanmar, Morocco, and Monaco, there were 1–3 respondents, and all of them were only women.

There were no responses from Turkey, France, Belgium, United Arab Emirates, Qatar, Bangladesh, Slovakia, Poland, Pakistan, Ecuador, Andorra, Venezuela, Oman, Mongolia, Lebanon, Vietnam, and Kazakhstan women.

The age distribution by ranges showed almost a consistent trend of 30% of women respondents for ages less than 60 years; women made up a smaller percentage of older respondents (8% in the range of 61 to 70 years old, and 0% older than 70 years). This is concordant with the history of CV imaging and CMR, mainly dominated by males in the past. However, an exciting and encouraging fact revealed is that the highest percentage of women respondents was in the youngest surveyed range (from 21 to 30 years old), demonstrating an apparent increase in women joining the field in recent years (Figure 3).

When examining the most common practice types of those working in CMR, it is interesting to note that for both men and women, there is more CMR practice in the academic and government scenarios compared to private practice, as displayed in Figures 4, 5. One might speculate that the economics of performing, interpreting, and reimbursement of CMR may contribute to this difference. However, there may also be less representation of private practices and small private hospitals within the SCMR; thus, the data should not be overinterpreted.

Recruiting and retaining women in cardiovascular imaging

Both recruiting women and retaining women physicians and scientists in cardiovascular imaging are essential to increasing their numbers. Progress is slow, but it is also encouraging: the proportion of women is increasing in medical school and in cardiology and radiology training programs (23, 27). Likewise, the number of women physicists and engineers is growing. However, over the past decade, the percentage of women in diagnostic radiology training has remained steady at 30% (29, 71). As women's numbers and leverage increase, they will begin to assert themselves to negotiate more favorable conditions: good parental leave policies, flexible work patterns, and equal pay (51, 72). These should be available for both women and men to help eliminate tendencies to avoid hiring female candidates. Those running training programs should consider optimizing work conditions for everyone to continue attracting the best candidates.

To increase the number of women entering cardiology, diagnostic radiology, and cardiac imaging, it is essential to target women interested in medicine or a biomedical career early in the process while in high school, college, or medical school. Additionally, there are too few mentors targeted explicitly toward working with women. Imaging societies must provide avenues for trainees and early career professionals to interact with expert advanced cardiovascular imagers. In addition to increasing the number of mentors from both genders, educating and engaging those in leadership about gender disparities and biases are essential. Professional societies should create initiatives to ensure that diversity is a priority and that women advanced imagers are supported to increase representation. This should happen both at the level of societal leadership, societal committees, and core groups.

Despite rising awareness of women's unique challenges, the need for flexible working patterns, and better family planning policies, barriers remain. The recent global pandemic has shown how quickly progress can be eroded: women have faced a disproportionate impact, taking on increased domestic and childcare responsibility, affecting jobs and salaries (73, 74).

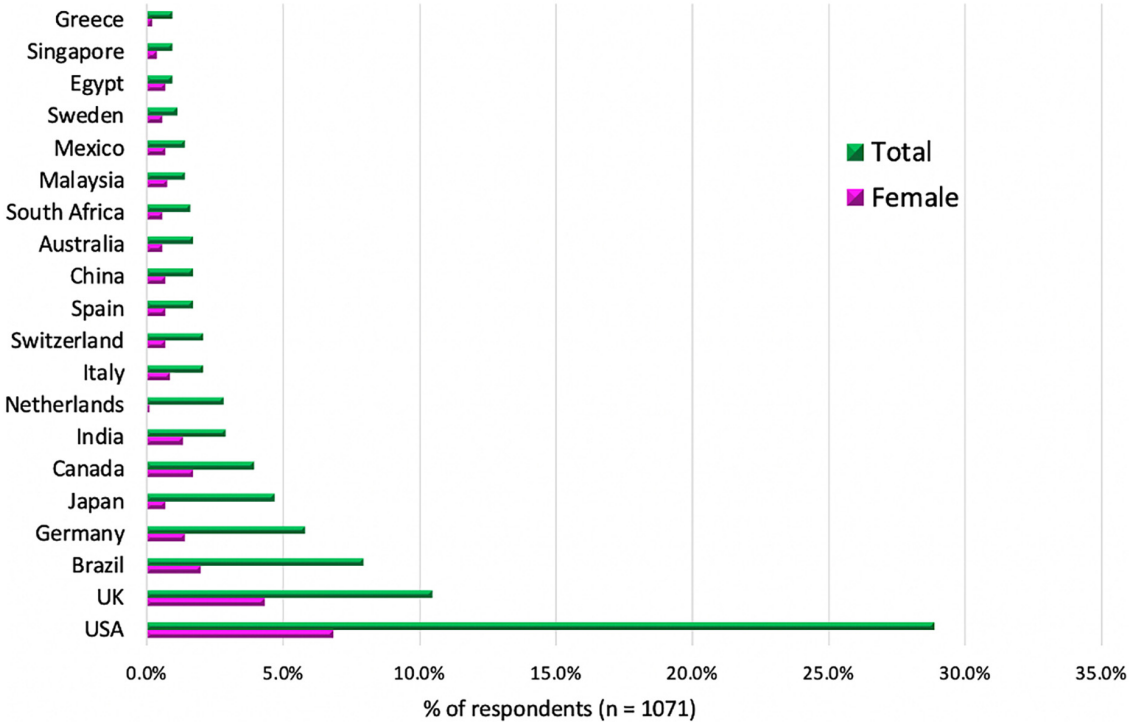

FIGURE 2
Top 20 countries of origin of surveyed respondents (n = 1,071). The top 20 countries with the most respondents are shown. The data from all other respondent countries are not displayed in the graph. The detailed description of the responders and their gender (within parentheses) were as follows, for USA 309 (F:73/M:236), UK 112 (F:46/M:66), Brazil 85 (F:21/M:64), Germany 62 (F:15/M:47), Japan 50 (F:7/M:43), Canada 42 (F:18/M:24), India 31 (F:14/M:17), the Netherlands 30 (F:1/M:29), Switzerland 22 (F:7/M:15), Italy 22 (F:9/M:13), China 18 (F:7/M:11), Australia 18 (F:6/M:12), Spain 18 (F:7/M:11), South Africa 17 (F:6/M:11), Malaysia 15 (F:8/M:7), Mexico 15 (F:7/M:8), Sweden 12 (F:6/M:6), Egypt 10 (F:7/M:3), Greece 10 (F:2/M:8), Singapore 10 (F:4/M:6). The rest of the surveyed countries are described in the **Supplementary material**.

The early career remains a challenging period for female professionals due to the tension between job requirements and additional family responsibilities, including childbearing. Supporting female physicians and scientists during this difficult time by instituting policies for maternity leave and ensuring flexible work hours (including part-time positions, telework, and different adaptable strategies) can help retain women as advanced imagers in the field. The increasing burn-out rate among female physicians should serve as an impetus for many institutions to adopt and support physician-parent wellness, such as a prolonged family leave policy and sustaining gender diversity and parity in advancements and leadership for female faculty. Establishing and supporting groups, such as women in radiology or parenting mentorship, will pay dividends in the form of improved retention of female faculty and well-being. This premise is based on the literature that radiology trainees and junior faculty reported increased networking (94%) compared to senior faculty (69%) and increased research involvement, which accelerated the professional development and contributed to a more diverse and enabled workforce (75).

Institutions and professional societies must enforce a no-tolerance policy for sexual harassment or bullying in the workplace. Institutional leadership's responsibility is to create a culture to promote a safe environment where victims of sexual harassment and gender bias feel empowered to report it.

Additionally, institutions should regularly conduct reviews and analyses of faculty salaries to uncover any unconscious biases in salary negotiation.

The empowerment strategies in cardiovascular imaging parallel women's empowerment in cardiology, diagnostic radiology, and physics/engineering, which include increasing opportunities for leadership training and women in leadership positions who can serve as role models such as advocates, coaches, and mentors for other women (**Figure 6**).

To improve retention rates of women in cardiology, societies such as the British Cardiac Society (BCS) and American College of Cardiology (ACC) have created Women in Cardiology (WIC) groups that serve as important leadership, career development, and advocacy forums for female cardiologists (76). In addition, the ACC has introduced several initiatives, including courses such as "Upping your game – clinical trials training," aimed at providing opportunities for learning and networking for underrepresented minorities and women in the field. Furthermore, the Association of American Medical

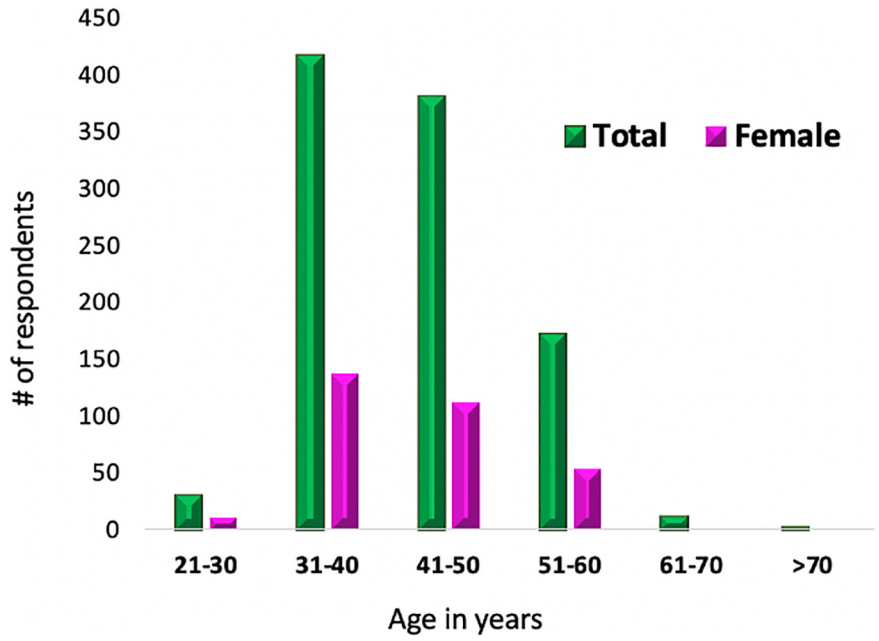

FIGURE 3
Age distribution of surveyed CMR practitioners. This graph displays the age range distribution of the CMR surveyed practitioners with the breakdown of the percentage of women respondents.

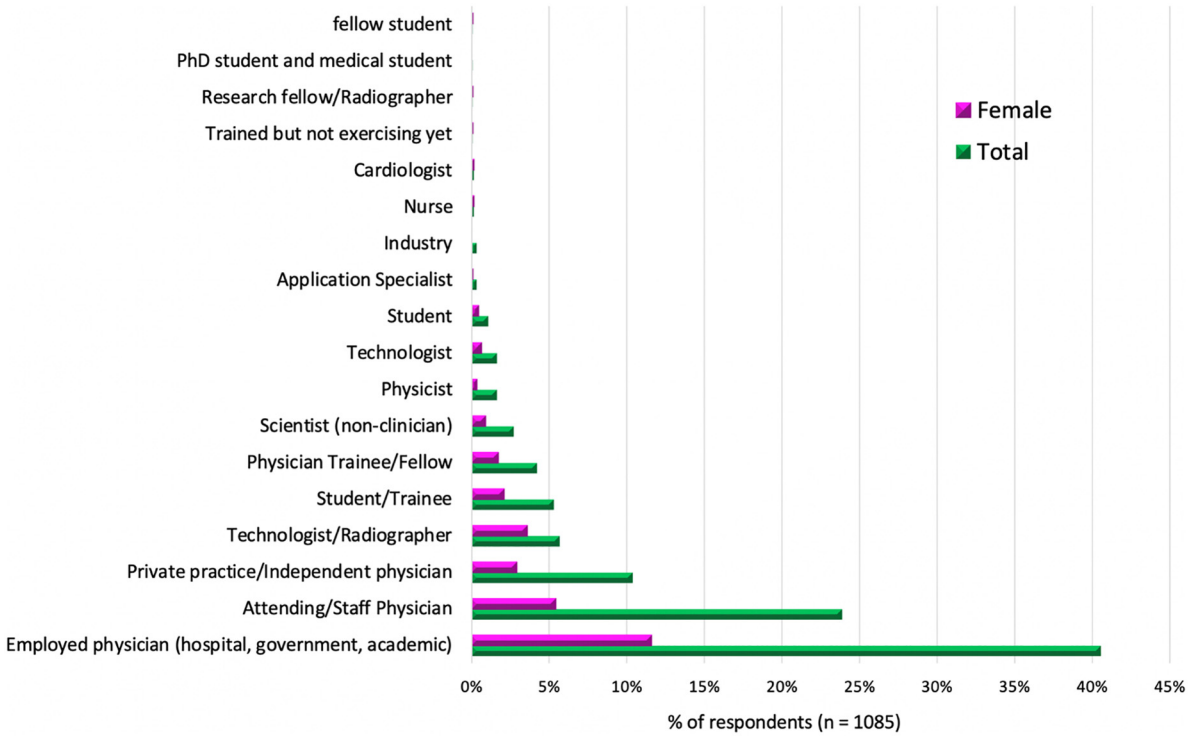

FIGURE 4
Stage of training or primary practice type of the CMR survey practitioners. This bar graph shows the different types of primary practice or stages of training of those CMR surveyed practitioners. The distribution is shown in percentages of total (male and female) in green and just female respondents in pink.

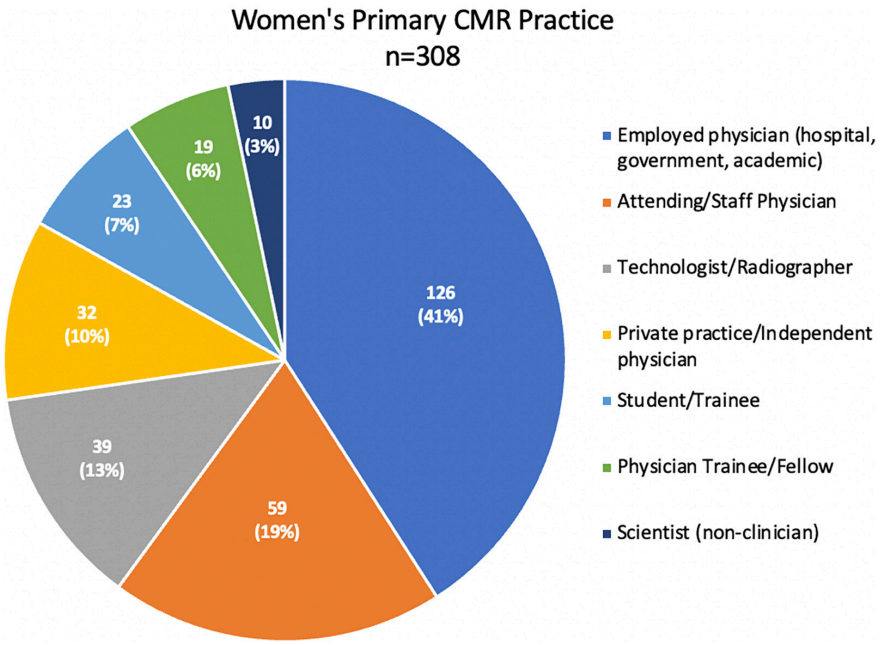

FIGURE 5
Women's primary CMR practice of the CMR survey practitioners. Responses in this category = 308. This pie graph shows the distribution of the women's primary CRM practice as employed physicians at different kinds of institutions such as academic, community, or government hospitals (*n* = 126, 41%), attending or staff physicians (*n* = 59, 19%), technologists or radiographers (*n* = 39, 13%), private practice or independent physicians (32, 10%), pre-grade students or trainees (23, 7%), physician trainees, residents or fellows (19, 6%), and scientist (non-clinician) (10, 3%).

Colleges (AAMC) offers a "Mid Mid-Career Women Faculty Leadership Development Seminar" every year for mid-career women faculty who have been at the associate professor level for at least two years with "the knowledge and skills necessary to support their continued progress along the path to leadership in academic medicine and science." The seminar includes organizational leadership topics and career-advancing strategies considered highly important for effective leadership throughout "various mission-critical activities."

Some institutions have programs to mentor and promote women faculty. For example, at the University of Pennsylvania, there is a program called FOCUS (77) that focuses on the health and leadership of women with separate sections for medical students, residents and fellows, junior faculty, and senior faculty. This program addresses the key national issue of the underrepresentation of women in senior levels of academic medicine. Moreover, with the support from the Dean of the Medical School, FOCUS launched initiatives including seminars, workshops, and conferences related to career development and mentoring; faculty research seed grants and recognition awards, and medical student fellowships in mentored projects involving women's health research to recruit, retain, and promote female leadership. These kinds of institutional and medical societal programs are crucial to providing leadership training and empowerment for female academic physicians.

Similarly, on the radiology side, there is a very active American Association for Women Radiologists (AAWR) that educates and enhances the professional fulfillment of female radiologists. In addition, almost every academic radiology department in the United States has adopted and supported women in radiology groups providing bona fide opportunities for mentorship and leadership growth (75). The Radiological Society of North America (RSNA) has embraced several committees empowering women across subspecialties. One such example is the Committee for Diversity, Equity, and Inclusion (DEI), whose member efforts are geared toward increasing the visibility of women in the field. For example, 57% of RSNA committee chairs are women; nine women have served on the RSNA Board of Directors, and seven women have served as RSNA President. Recognizing the need for women's empowerment in radiology, the AAWR was formed 25 years ago to promote, educate, and advocate for women radiologists. The AAWR holds regular meetings and workshops tailored to meet women's needs in radiology.

While there are no explicitly tailored programs/workshops for women empowerment in the cardiovascular imaging subspecialty, the North American Society of Cardiovascular Imaging (NASCI) has worked diligently to increase the representation and visibility of women within the society. In terms of women's reputation in leadership (as tabulated below), NASCI follows closely with the Society for Cardiovascular

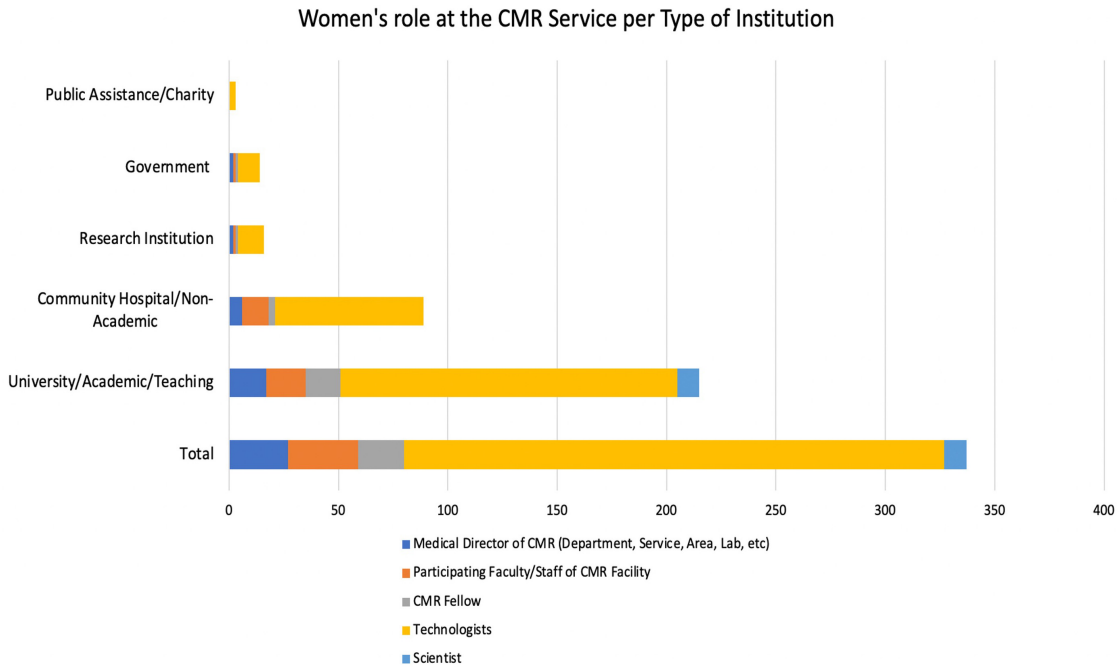

Women's role at the CMR Service per Type of Institution	Total n=337 (%)	University/Academic/ Teaching n=215 (%)	Community Hospital/Non-Academic n=89 (%)	Research Institution n=16 (%)	Government n=14 (%)	Public Assistance/ Charity n=3 (%)
Medical Director of CMR (Department, Service, Area, Lab, etc)	27(8)	17(8)	6(7)	2(13)	2(14)	0(0)
Participating Faculty/Staff of CMR Facility	32(9)	18(8)	12(13)	1(6)	1(7)	0(0)
CMR Fellow	21(6)	16(7)	3(3)	1(6)	1(7)	0(0)
Technologists	247(73)	154(72)	68(76)	12(75)	10(71)	3(100)
Scientist	10(3)	10(5)	0(0)	0(0)	0(0)	0(0)

FIGURE 6
Women's role at the CMR Service per Type of Institution of the CMR survey practitioners. Responses in this category = 337. This stacked bar graph shows the women's role at the CMR service per type of institution, where 64% practice in the university, academic, or teaching environment. Although it is where women primarily participate in leadership roles, 26% of women develop their professional activities in the community or non-academic institutions, where 76% participate as technologists. Women scientists are working only in universities or academic institutions. Detailed data shown in the graph description is in the table at the bottom of the figure.

TABLE 1 Female leadership participation in the major US-based cardiovascular imaging societies.

	ASE [Ref (76–78)]	ASNC [Ref. (82, 83)]	NASCI [Ref. (79–81)]	SCCT [Ref. (84, 85)]	SCMR [Ref. (86, 87)]
Presidents over the past 10 years No. of women (% women)	4 (40)	1 (10)	3 (30)	1 (10)	2 (20)
Current executive officers** No. of women/#positions (% women)	4/8 (50)	2/7 (28.5)	3/6 (50)	1/7 (14)	2/5 (40)
Current committee chairs No. of women/#positions (% women)	9/18 (50)*	4/20 (20)	8/19 (42)	4/10 (40)	8/18 (44)

ASE, American Society of Echocardiography; ASNC, American Society of Nuclear Cardiology; NASCI, North American Society for Cardiovascular Imaging; SCCT, Society of Cardiovascular Computed Tomography; SCMR, Society for Cardiovascular Magnetic Resonance.
*These data reflect what was reported on the specific society's public website on 26 June 2022.
**The "Executive Officers" varied slightly between societies but most often included a president, vice-president, treasurer, secretary, and past-president, among other roles.

Magnetic Resonance (SCMR). Table 1 (78–89) shows a current year comparison of the women's participation in main US-based international cardiovascular imaging societies, using the leadership roles in executive officer positions and committees chairs as a surrogate of female involvement in the field. Note that the comparison is limited by what was available

on each society's publicly available website and differences between each organizational governance rule and represents more of an "at-a-glance" assessment of women's representation in these societies. The American Society of Echocardiography (ASE) seems to be particularly successful in elevating women to leadership roles.

Although women are well-represented in NASCI, gender parity has not been reached in all reaches of the society. The number of women speakers and moderators (n = 35; 33%) at the 2021 annual meeting indicates that we need to understand women's needs better and increase their engagement in future meetings. These findings are reproduced at other organizations' meetings. Improved support for women's engagement may include providing childcare during the meeting, lactation rooms, work and life integration workshops, one-on-one mentor-mentee sessions, and/or short-term coaching sessions, which describe how to navigate through the system to offset any future decline of leadership role or active participation during the annual meetings.

From the highest leadership perspective, women are still underrepresented in imaging, as shown in **Table 1**. In addition, the percentage of female presidents of the imaging societies was lower than its female membership. However, in the executive officers (defined differently among societies but typically in addition to the president, including positions like the vice president, treasurer, and secretary, among other offices) and committee chairs, there is a higher representation of women than traditionally seen. To increase female leadership at the top, a pipeline of leaders must be developed through leadership education and mentoring. Both the American Society of Echocardiography (ASE) and the American Society of Nuclear Cardiology (ASNC) have leadership programs, although not explicitly geared toward women.

Recently, in 2020, The European Association of Cardiovascular Imaging (EACVI) formed its Task Force of Women in CV Imaging. The task force represents an initiative within the EACVI to connect members interested in promoting women's representation both in the career setting and leadership roles and in clinical research development in CV diseases in women. This task force intends to unite women in CV imaging worldwide and provide opportunities that may not be available to all women professionals. The main goal intends to help low-to-middle-income country women imagers train within a European country with strong CV imaging expertise with a plan to then return to their home country and serve the community, providing continuous support by addressing challenging cases via remote communication (88).

The increasing involvement of women in the SCMR also corresponds to the initiation and sustained activities of the SCMR Women in CMR Group, which was the brainchild of Dr. Dara Kraitchman (**Figure 7**). The Women in CMR group meets at the annual SCMR Scientific Sessions and throughout the year. Since the advent of this group, a steady increase in women's engagement in leadership positions within the SCMR over the past decade has been evident (**Figure 7**). In addition, women leaders have also stimulated and founded new interest groups like those focused on cardio-rheumatology and cardio-oncology, as well as the CMR translation working group that has advocated for the translation of key CMR documents into other languages to promote international dissemination of the field. These data indicate a shift in thinking and demonstrate positive support for women's engagement within the CMR community. Intersocietal joint activities (e.g., between the SCMR and ISMRM or other imaging societies) may help to amplify awareness of women's issues within the field of CMR and imaging, as well as help to jointly work on action items to solve some of the ongoing challenges.

How CMR has made an impact on women's cardiovascular health

Even as women have become more involved in the field of CMR, CMR has likewise impacted women's cardiovascular health (90). Among the cardiovascular diagnoses affected are myocardial infarction in the setting of non-obstructive coronary arteries (MINOCA), small vessel disease ischemia, ischemic heart disease in general, rheumatological disorders, and cardio-oncology.

Historically, women with acute coronary syndrome exhibit symptoms that differ from men. Chest pain may be vague or completely absent. Women may present with fatigue or shortness of breath as a primary symptom. In the past, when women presented with an acute coronary syndrome with elevated cardiac enzymes but non-obstructive coronary arteries or MINOCA, the next steps in management were unclear. Implementing CMR in this diagnosis has helped to elucidate an underlying etiology clarifying if a patient has myocarditis, stress cardiomyopathy (Takotsubo), coronary dissection, or coronary spasm (22, 91). CMR's strengths in comprehensively evaluating the myocardium and its pathophysiologic health (e.g., looking for edema, inflammation, and fibrosis), as well as other cardiac structures like the coronary arteries, elevate its importance in being used early in the patient presenting with chest pain.

In the non-acute chest pain setting, CMR is exceptional in identifying small vessel ischemia using vasodilator perfusion. In newer methods, myocardial perfusion may be quantified, and endocardial-to-epicardial myocardial blood flow ratios assessed. Dr. Noel Bairey Merz, a Professor of Medicine at the Cedars Sinai Heart Institute, and others demonstrated the utility of CMR in evaluating women with chronic chest pain who have non-obstructive coronary arteries (22). With a diagnosis of small vessel disease, clinicians then have a therapeutic target; whereas, in the past, without a definitive diagnosis, treatment was directed as a "best guess," or worse yet, women were told that their chest pain was non-cardiac.

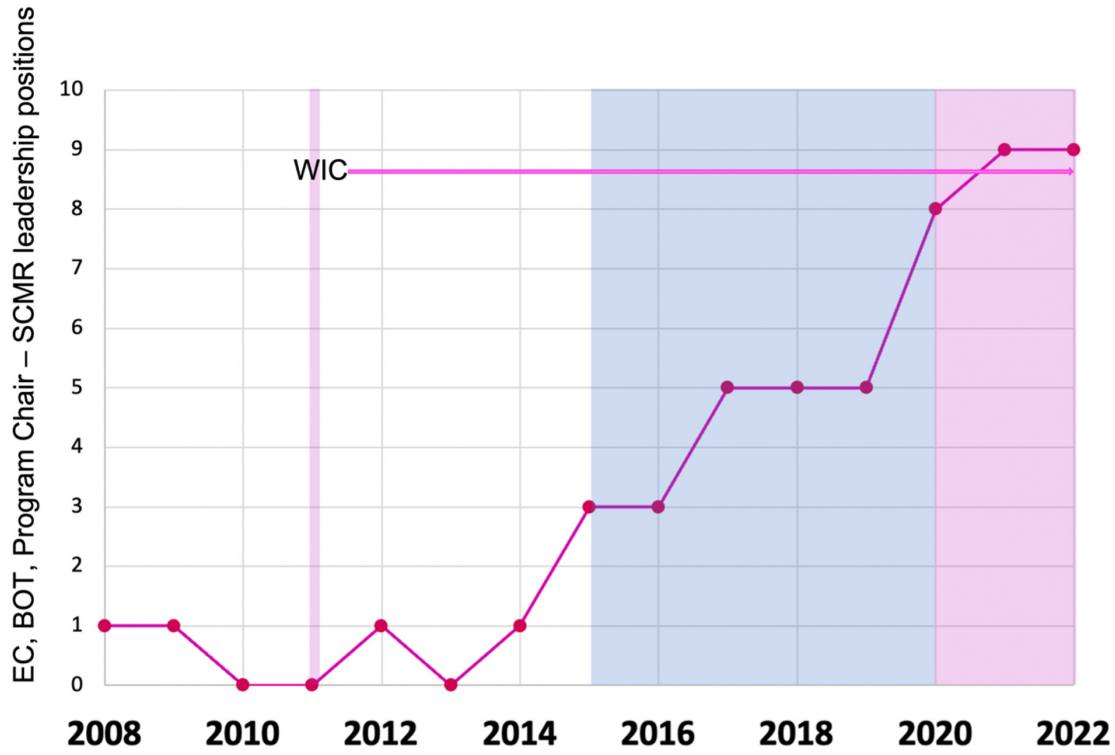

FIGURE 7
Women's representation in SCMR leadership. The blue background represents the first CEO (male) and the pink the second and current CEO (female) of SCMR. The thick pink line marks the Women in CMR (Special group of SCMR) establishment as a Task Force by Dara L. Kraitchman, Ph.D., and supported by the E.C. leadership by Victor A. Ferrari, MD. EC, Executive Committee; BOT, Board of Trustees; WIC, women in CMR (Special group of SCMR).

Diagnosing epicardial coronary artery disease in women has also not been straightforward. Exercise treadmill has a notoriously high false-negative rate in women; nuclear stress testing may yield false positive or equivocal results with breast attenuation. However, CMR stress testing provides a comprehensive assessment of myocardial ischemia, independent of a woman's body mass index or body habitus (92).

Another field that CMR has changed is that of cardio-rheumatology. Rheumatological disorders such as systemic lupus erythematosus, dermatomyositis, and polymyositis affect women greater than men (e.g., 90% of patients with lupus are women between the ages of 15 and 45 years of age). Again, the ability to discern when the heart is actively affected helps guide the management of the rheumatological patient. Newer parametric mapping methods now offer the ability to serially follow patients, even without contrast, to monitor patients' response to therapy (93, 94).

Cardio-oncology and a host of therapeutic-related adverse events affect both men and women. However, breast cancer cardio-toxicities have mainly utilized CMR effectively to monitor anthracycline toxicities. Active research is ongoing, using CMR to monitor chemo- and immunotherapeutic toxicities, parametric mapping, and myocardial strain. Beyond identification of cardiomyopathy, CMR may also detect therapy-related acute myocarditis. In women who have undergone chest irradiation and are at risk for premature atherosclerosis, CMR provides a comprehensive assessment of ischemic heart disease using pharmacologic or exercise stress testing (95, 96).

The aforementioned uses of CMR are not meant to comprise an exhaustive list but rather demonstrate a few common examples in which CMR has impacted women's cardiovascular health. Research and clinical translation are ongoing in a multitude of disease processes. MRI pulse sequences and technology are continuously developing, and new CMR applications are constantly evolving.

It is of particular relevance to highlight the role of CMR in improving cardiovascular care since women are under-represented in clinical trials (97–99), limiting biological understanding and contributing to health inequities, social injustice (99), and impacting their health directly as the state-of-the-art treatments and recommendations have been historically mainly male-oriented (100). Within CMR clinical studies and trials, dedicated emphasis in understanding sex as a biologic variable also needs additional attention and should be a goal for current and future studies.

Conclusion

While there have been challenges to entering and remaining in the field, recent data show that women have become an integral part of the cardiovascular imaging workforce. However, additional work remains to support and increase women's representation in cardiovascular imaging, academia, and multidisciplinary societies. Recognition of the need for diversity is more widespread, as well as recognition of the need to better support women in all career stages. For example, women's representation on moderator and speaking panels requires additional mindfulness and work on the part of the organizers, not simply to fulfill a quota but to add to the depth, breadth, and richness of the meetings as there are qualified women who have valuable and unique expertise to share in the scientific sessions. Similarly, active women's participation in leadership roles within professional societies adds valuable insights and diversity to the growing field. It should be restated clearly that the entire effort to help engage women in cardiology and radiology is not only fair and proper but also enhances the field—increasing the resilience and level of care.

There has been significant progress in advancing cardiovascular magnetic resonance and cardiovascular imaging. Translational applications of cardiovascular imaging make a difference in cardiovascular diagnosis, management, and prognosis. While the initial involvement of women professionals was low, the engagement of creative, thoughtful physicists, engineers, cardiologists, and radiologists within the field has grown and continues to grow. At this moment, we are just beginning to bend the curve. However, sustained vigilance and creative effort will ensure that the future of women in cardiovascular imaging is hopeful and bright.

Author contributions

LS-G designed the project. LS-G, NA, JS, SR, YH, VF, KT, NS, PP, CB-D, LB, SM, KO, JS-M, and WB discussed the content, wrote the manuscript, reviewed, and approved the final version.

Conflict of interest

The authors declare that the research was conducted in the absence of any commercial or financial relationships that could be construed as a potential conflict of interest.

Publisher's note

All claims expressed in this article are solely those of the authors and do not necessarily represent those of their affiliated organizations, or those of the publisher, the editors and the reviewers. Any product that may be evaluated in this article, or claim that may be made by its manufacturer, is not guaranteed or endorsed by the publisher.

Author disclaimer

The views expressed in this manuscript are those of the authors and do not necessarily represent the views of the National Heart, Lung, and Blood Institute, the National Institutes of Health, nor the U.S. Department of Health and Human Services.

Supplementary material

The Supplementary Material for this article can be found online at: https://www.frontiersin.org/articles/10.3389/fcvm.2022.984326/full#supplementary-material

References

1. Association of American Medical Colleges. *Workforce. Physician Specialty Data Report. Active Physicians by Sex and Specialty*. Washington, DC: AAMC (2019).

2. Tsugawa Y, Jena A, Figueroa J, Orav E, Blumenthal D, Jha A. Comparison of hospital mortality and readmission rates for medicare patients treated by male vs female physicians. *JAMA Intern Med.* (2017) 177:206–13. doi: 10.1001/jamainternmed.2016.7875

3. Greenwood B, Carnahan S, Huang L. Patient–physician gender concordance and increased mortality among female heart attack patients. *Proc Natl Acad Sci U.S.A.* (2018) 115:8569–74. doi: 10.1073/pnas.1800097115

4. Budoff M, Achenbach S, Blumenthal R, Carr J, Goldin J, Greenland P, et al. Assessment of coronary artery disease by cardiac computed tomography: a scientific statement from the American heart association committee on cardiovascular imaging and intervention, council on cardiovascular radiology and intervention, and committee on cardiac imaging, council on clinical cardiology. *Circulation.* (2006) 114:1761–91. doi: 10.1161/CIRCULATIONAHA.106.178458

5. Leiner T, Bogaert J, Friedrich M, Mohiaddin R, Muthurangu V, Myerson S, et al. SCMR Position Paper (2020) on clinical indications for cardiovascular magnetic resonance. *J Cardiovasc Magn Reson.* (2020) 22:76. doi: 10.1186/s12968-020-00682-4

6. Jorgensen T. *Marie Curie and her X-ray Vehicles' Contribution to World War I Battlefield Medicine*. (2017). Available online at: https://theconversation.com/marie-curie-and-her-x-ray-vehicles-contribution-to-world-war-i-battlefield-medicine-83941?xid=PS_smithsonian (accessed May 22, 2022).

7. Goldman M, Pohost G, Ingwall J, Fossel E. Nuclear magnetic resonance imaging: potential cardiac applications. *Am J Cardiol.* (1980) 46:1278–83. doi: 10.1016/0002-9149(80)90299-4

8. Edelman R, Chien D, Atkinson D, Sandstrom J. Fast time-of-flight MR angiography with improved background suppression. *Radiology.* (1991) 179:867–70. doi: 10.1148/radiology.179.3.2028008

9. Lim T, Hong M, Lee J, Mun C, Park S, Park S, et al. Novel application of breath-hold turbo spin-echo T2 MRI for detection of acute myocardial infarction. *J Magn Reson Imaging.* (1997) 7:996–1001. doi: 10.1002/jmri.1880070611

10. Rosen B, Belliveau J, Chien D. Perfusion imaging by nuclear magnetic resonance. *Magn Reson Q.* (1989) 5:263–81.

11. Hänicke W, Merboldt K, Chien D, Gyngell M, Bruhn H, Frahm J. Signal strength in subsecond FLASH magnetic resonance imaging: the dynamic approach to steady state. *Med Phys.* (1990) 17:1004–10. doi: 10.1118/1.596452

12. Niemi P, Poncelet B, Kwong K, Weisskoff R, Rosen B, Brady T, et al. Myocardial intensity changes associated with flow stimulation in blood oxygenation sensitive magnetic resonance imaging. *Magn Reson Med.* (1996) 36:78–82. doi: 10.1002/mrm.1910360114

13. Poncelet B, Koelling T, Schmidt C, Kwong K, Reese T, Ledden P, et al. Measurement of human myocardial perfusion by double-gated flow alternating inversion recovery EPI. *Magn Reson Med.* (1999) 41:510–9. doi: 10.1002/(SICI)1522-2594(199903)41:3<510::AID-MRM13>3.0.CO;2-G

14. Huang T, Liu Y, Stemmer A, Poncelet B. T2 measurement of the human myocardium using a T2-prepared transient-state TrueFISP sequence. *Magn Reson Med.* (2007) 57:960–6. doi: 10.1002/mrm.21208

15. Pandharipande PV, Lee V, Reuss P, Charles H, Rosen R, Krinsky G, et al. Two-station bolus-chase MR angiography with a stationary table: a simple alternative to automated-table techniques. *Am J Roentgenol.* (2002) 179:1583–9. doi: 10.2214/ajr.179.6.1791583

16. Miyazaki M, Lee V. Nonenhanced MR angiography. *Radiology.* (2008) 248:20–43. doi: 10.1148/radiol.2481071497

17. Lee V, Resnick D, Tiu S, Sanger J, Nazzaro C, Israel G, et al. MR imaging evaluation of myocardial viability in the setting of equivocal SPECT results with (99m)Tc sestamibi. *Radiology.* (2004) 230:191–7. doi: 10.1148/radiol.2301030070

18. Schulz-Menger J, Abdel-Aty H. Use of integrated biomarkers in inflammatory disease of the heart: new insights applying cardiovascular magnetic resonance potential as a biomarker. *Expert Opin Med Diagn.* (2008) 2:883–9. doi: 10.1517/17530059.2.8.883

19. Wagner A, Schulz-Menger J, Dietz R, Friedrich M. Long-term follow-up of patients paragraph sign with acute myocarditis by magnetic paragraph sign resonance imaging. *MAGMA.* (2003) 16:17–20. doi: 10.1007/s10334-003-0007-7

20. Abdel-Aty H, Boye P, Zagrosek A, Wassmuth R, Kumar A, Messroghli D, et al. Diagnostic performance of cardiovascular magnetic resonance in patients with suspected acute myocarditis: comparison of different approaches. *J Am Coll Cardiol.* (2005) 45:1815–22. doi: 10.1016/j.jacc.2004.11.069

21. Raman SV, Dickerson J, Mazur W, Wong T, Schelbert E, Min J, et al. Diagnostic performance of treadmill exercise cardiac magnetic resonance: the prospective, multicenter exercise CMR's accuracy for cardiovascular stress testing (EXACT) trial. *J Am Heart Assoc.* (2016) 5:e003811. doi: 10.1161/JAHA.116.003811

22. Occhipinti G, Bucciarelli-Ducci C, Capodanno D. Diagnostic pathways in myocardial infarction with non-obstructive coronary artery disease (MINOCA). *Eur Heart J Acute Cardiovasc Care.* (2021) 10:813–22. doi: 10.1093/ehjacc/zuab049

23. Sinclair H, Joshi A, Allen C, Joseph J, Sohaib S, Calver A, et al. Women in cardiology: the British junior cardiologists' association identifies challenges. *Eur Heart J.* (2019) 40:227–31. doi: 10.1093/eurheartj/ehy828

24. Oza N, Breathett K. Women in cardiology: fellows' perspective. *J Am Coll Cardiol.* (2015) 65:951–3. doi: 10.1016/j.jacc.2015.01.011

25. Ramakrishnan A, Sambuco D, Jagsi R. Women's participation in the medical profession: insights from experiences in Japan, Scandinavia, Russia, and Eastern Europe. *J Womens Health.* (2014) 23:927–34. doi: 10.1089/jwh.2014.4736

26. Begeny C, Grossman R, Ryan M. Overestimating womens representation in medicine: a survey of medical professionals estimates and their(un)willingness to support gender equality initiatives. *BMJ Open.* (2022) 12:e054769. doi: 10.1136/bmjopen-2021-054769

27. Khan M, Mahmood S, Khan S, Fatima K, Khosa F, Sharma G, et al. Women training in cardiology and its subspecialties in the United States: a decade of little progress in representation. *Circulation.* (2020) 141:609–11. doi: 10.1161/CIRCULATIONAHA.119.044693

28. Segan L, Vlachadis Castles A. Women in cardiology in Australia-are we making any progress? *Heart Lung Circ.* (2019) 28:690–6. doi: 10.1016/j.hlc.2018.12.010

29. Association of American Medical Colleges. *Radiology-Diagnostic. ERAS 2014.* Washington, DC: AAMC (2018).

30. Raymundo-Martínez G, Alanis-Estrada G, Araiza-Garaygordobil D, Delgado-Cruz IV, Gopar-Nieto R, Cabello-López A, et al. Gender differences in cardiology professionals: a Latin American survey. *Arch Cardiol Mex.* (2022) 92:11–8. doi: 10.24875/ACME.M22000294

31. Farhan H, Dakhil Z. Women in cardiology: critical status and a call to move forward. *Egypt Heart J.* (2020) 72:45. doi: 10.1186/s43044-020-00078-w

32. Kubik-Huch R, Vilgrain V, Krestin G, Reiser M, Attenberger U, Muellner A, et al. Women in radiology: gender diversity is not a metric-it is a tool for excellence. *Eur Radiol.* (2020) 30:1644–52. doi: 10.1007/s00330-019-06493-1

33. Timmis A, Baker C, Banerjee S, Calver A, Dornhorst A, English K, et al. Women in UK cardiology: report of a Working Group of the British cardiac society. *Heart.* (2005) 91:283–9. doi: 10.1136/hrt.2004.047340

34. Douglas P, Rzeszut A, Bairey Merz C, Duvernoy C, Lewis S, Walsh M, et al. Career preferences and perceptions of cardiology among US internal medicine trainees: factors influencing cardiology career choice. *JAMA Cardiol.* (2018) 3:682–91. doi: 10.1001/jamacardio.2018.1279

35. Yazdani M, Kotronias R, Joshi A, Camm C, Allen C. British cardiology training assessed. *Eur Heart J.* (2019) 40:2475–7. doi: 10.1093/eurheartj/ehz545

36. Fukue N, Ishida M, Taniyama M, Mukai-Yatagai N, Sakamoto T, Tamada T, et al. Current diversity issues in cardiovascular workplaces in the chugoku district results from 2 questionnaire surveys. *Circ Rep.* (2022) 4:59–65. doi: 10.1253/circrep.CR-21-0111

37. Bin Dahmash A, Alorfi F, Alharbi A, Aldayel A, Kamel A, Almoaiqel M. Burnout phenomenon and its predictors in radiology residents. *Acad Radiol.* (2020) 27:1033–9. doi: 10.1016/j.acra.2019.09.024

38. Stentz N, Griffith K, Perkins E, Jones R, Jagsi R. Fertility and childbearing among American female physicians. *J Womens Health.* (2016) 25:1059–65. doi: 10.1089/jwh.2015.5638

39. Guenette J, Smith S. Burnout: prevalence and associated factors among radiology residents in New England with comparison against United States resident physicians in other specialties. *Am J Roentgenol.* (2017) 209:136–41. doi: 10.2214/AJR.16.17541

40. Mehta L, Lewis S, Duvernoy C, Rzeszut A, Walsh M, Harrington R, et al. Burnout and career satisfaction among U.S. Cardiologists. *J Am Coll Cardiol.* (2019) 73:3345–8. doi: 10.1016/j.jacc.2019.04.031

41. Kane L. *Physician Burnout & Depression Report 2022: Stress, Anxiety, and Anger.* The Heart.org Medscape Cardiology (2022). Available online at: https://www.medscape.com/slideshow/2022-lifestyle-burnout-6014664 (accessed Jun 12, 2022).

42. Curtis A, Rodriguez F. Choosing a career in cardiology: where are the women? *JAMA Cardiol.* (2018) 3:691–2. doi: 10.1001/jamacardio.2018.1286

43. Sharma G, Douglas P, Hayes S, Mehran R, Rzeszut A, Harrington R, et al. Global prevalence and impact of hostility, discrimination, and harassment in the cardiology workplace. *J Am Coll Cardiol.* (2021) 77:2398–409. doi: 10.1016/j.jacc.2021.03.301

44. Jaijee S, Kamau-Mitchell C, Mikhail G, Hendry C. Sexism experienced by consultant cardiologists in the United Kingdom. *Heart.* (2021) 107:895–901. doi: 10.1136/heartjnl-2020-317837

45. Lewis S, Mehta L, Douglas P, Gulati M, Limacher M, Poppas A, et al. Changes in the professional lives of cardiologists over 2 decades. *J Am Coll Cardiol.* (2017) 69:452–62. doi: 10.1016/j.jacc.2016.11.027

46. Files J, Mayer A, Ko M, Friedrich P, Jenkins M, Bryan M, et al. Speaker introductions at internal medicine grand rounds: forms of address reveal gender bias. *J Womens Health.* (2017) 26:413–9. doi: 10.1089/jwh.2016.6044

47. Kittleson M. The trials of women in cardiology. *J Am Coll Cardiol.* (2020) 76:1931–3. doi: 10.1016/j.jacc.2020.09.014

48. Camm C, Joshi A, Moore A, Sinclair H, Westwood M, Greenwood J, et al. Bullying in UK cardiology: a systemic problem requiring systemic solutions. *Heart.* (2022) 108:212–8. doi: 10.1136/heartjnl-2021-319882

49. Salles A, Choo E. Queen bee phenomenon: a consequence of the hive. *Lancet.* (2020) 395:940. doi: 10.1016/S0140-6736(20)30597-3

50. Sarma A, Nkonde-Price C, Gulati M, Duvernoy C, Lewis S, Wood M. Cardiovascular medicine and society: the pregnant cardiologist. *J Am Coll Cardiol.* (2017) 69:92–101. doi: 10.1016/j.jacc.2016.09.978

51. Lau E, Wood M. How do we attract and retain women in cardiology? *Clin Cardiol.* (2018) 41:264–8. doi: 10.1002/clc.22921

52. Gulati M, Korn R, Wood M, Sarma A, Douglas P, Singh T, et al. Childbearing among women cardiologists: the interface of experience, impact, and the law. *J Am Coll Cardiol.* (2022) 79:1076–87. doi: 10.1016/j.jacc.2021.12.034

53. Au S, Bellato V, Carvas J, Córdoba C, Daudu D, Dziakova J, et al. Global parental leave in surgical careers: differences according to gender, geographical regions and surgical career stages. *Br J Surg.* (2021) 108:1315–22. doi: 10.1093/bjs/znab275

54. Best P, Skelding K, Mehran R, Chieffo A, Kunadian V, Madan M, et al. SCAI consensus document on occupational radiation exposure to the pregnant cardiologist and technical personnel. *EuroIntervention.* (2011) 6:866–74. doi: 10.4244/EIJV6I7A148

55. Wood A, Hussain S. Working with radiation in pregnancy: a guide for cardiologists. *Heart.* (2021) 107:1182–3. doi: 10.1136/heartjnl-2021-318993

56. Jolly S, Griffith K, DeCastro R, Stewart A, Ubel P, Jagsi R. Gender differences in time spent on parenting and domestic responsibilities by high-achieving young physician-researchers. *Ann Intern Med.* (2014) 160:344–53. doi: 10.7326/M13-0974

57. Tsukada Y, Tokita M, Kato K, Kato Y, Miyauchi M, Ono I, et al. Solutions for retention of female cardiologists: from the survey of gender differences in the work and life of cardiologists. *Circ J.* (2009) 73:2076–83. doi: 10.1253/circj.CJ-09-0206

58. Vlachadis Castles A, Burgess S, Robledo K, Beale A, Biswas S, Segan L, et al. Work-life balance: a comparison of women in cardiology and other specialties. *Open Heart.* (2021) 8:e001678. doi: 10.1136/openhrt-2021-001678

59. Dobson R, Joshi A, Allen C, Sinclair H. Less than full-time training in cardiology. *Heart.* (2019) 105:1445–6. doi: 10.1136/heartjnl-2019-315226

60. Lerchenmüller C, Lerchenmueller M, Sorenson O. Long-term analysis of sex differences in prestigious authorships in cardiovascular research supported by the National Institutes of Health. *Circulation.* (2018) 137:880–2. doi: 10.1161/CIRCULATIONAHA.117.032325

61. Holman L, Stuart-Fox D, Hauser C. The gender gap in science: how long until women are equally represented? *PLoS Biol.* (2018) 16:e2004956. doi: 10.1371/journal.pbio.2004956

62. Blumenthal D, Olenski A, Yeh R, DeFaria Yeh D, Sarma A, Stefanescu Schmidt A, et al. Sex differences in faculty rank among academic cardiologists in the United States. *Circulation.* (2017) 135:506–17. doi: 10.1161/CIRCULATIONAHA.116.023520

63. Chatterjee P, Werner R. Gender disparity in citations in high-impact journal articles. *JAMA Netw Open.* (2021) 4:e2114509. doi: 10.1001/jamanetworkopen.2021.14509

64. Whitelaw S, Thabane L, Mamas M, Reza N, Breathett K, Douglas P, et al. Characteristics of Heart failure trials associated with under-representation of women as lead authors. *J Am Coll Cardiol.* (2020) 76:1919–30. doi: 10.1016/j.jacc.2020.08.062

65. Rai D, Kumar A, Waheed S, Pandey R, Guerriero M, Kapoor A, et al. Gender differences in international cardiology guideline authorship: a comparison of the US, Canadian, and European cardiology guidelines from 2006 to 2020. *J Am Heart Assoc.* (2022) 11:e024249. doi: 10.1161/JAHA.121.024249

66. Tong I, Griffin B, Trott J, Romano M, Stein A, Madsen T. The proportion of women authors and the inclusion of sex and gender content among the American college of cardiology clinical practice guidelines, 2008-2018. *J Womens Health.* (2021) 30:1616–25. doi: 10.1089/jwh.2020.8454

67. Jagsi R, Griffith K, Jones R, Stewart A, Ubel P. Factors associated with success of clinician-researchers receiving career development awards from the National institutes of health: a longitudinal cohort study. *Acad Med.* (2017) 92:1429–39. doi: 10.1097/ACM.0000000000001728

68. Kapoor N, Blumenthal D, Smith S, Ip I, Khorasani R. Sex differences in radiologist salary in U.S. public medical schools. *Am J Roentgenol.* (2017) 209:953–8. doi: 10.2214/AJR.17.18256

69. Jagsi R, Biga C, Poppas A, Rodgers G, Walsh M, White P, et al. Work activities and compensation of male and female cardiologists. *J Am Coll Cardiol.* (2016) 67:529–41. doi: 10.1016/j.jacc.2015.10.038

70. Biden J. *Executive Order on Diversity, Equity, Inclusion, and Accessibility in the Federal Workforce.* Washington, DC (2021). Available online at: https://www.whitehouse.gov/briefing-room/presidential-actions/2021/06/25/executive-order-on-diversity-equity-inclusion-and-accessibility-in-the-federal-workforce/ (accessed October 4, 2022).

71. Baker S, Barry M, Chaudhry H, Hubbi B. Women as radiologists: are there barriers to entry and advancement? *J Am Coll Radiol.* (2006) 3:131–4. doi: 10.1016/j.jacr.2005.10.001

72. Sharma G, Sarma A, Walsh M, Hayes S, Sahni S, Brown S, et al. 10 recommendations to enhance recruitment, retention, and career advancement of women cardiologists. *J Am Coll Cardiol.* (2019) 74:1839–42. doi: 10.1016/j.jacc.2019.08.016

73. Jones Y, Durand V, Morton K, Ottolini M, Shaughnessy E, Spector N, et al. Collateral damage: how COVID-19 is adversely impacting women physicians. *J Hosp Med.* (2020) 15:507–9. doi: 10.12788/jhm.3470

74. Nishida S, Nagaishi K, Motoya M, Kumagai A, Terada N, Kasuga A, et al. Dilemma of physician-mothers faced with an increased home burden and clinical duties in the hospital during the COVID-19 pandemic. *PLoS One.* (2021) 16:e0253646. doi: 10.1371/journal.pone.0253646

75. Gaetke-Udager K, Knoepp U, Maturen K, Leschied J, Chong S, Klein K, et al. A women in radiology group fosters career development for faculty and trainees. *Am J Roentgenol.* (2018) 211:W47–51. doi: 10.2214/AJR.17.18994

76. Sharma G, Lewis S, Singh T, Mehta L, Mieres J, Poppas A, et al. The pivotal role of women in cardiology sections in medical organizations: from leadership training to personal enrichment. *CJC Open.* (2021) 3(12 Suppl.):S95–101. doi: 10.1016/j.cjco.2021.07.015

77. Focus. *Center for Clinical Epidemiology and Biostatistics (CCEB) at the University of Pennsylvania Perelman School of Medicine (PSOM). FOCUS On Health & Leadership for Women.* (2004). Available online at: https://www.focusprogram.org/ (accessed June 22, 2022).

78. American Society of Echocardiography. *ASE Past Presidents*. Durham, NC: American Society of Echocardiography (2022).

79. American Society of Echocardiography. *ASE Board of Directors*. Durham, NC: American Society of Echocardiography (2022).

80. Society for Cardiovascular Magnetic Resonance. *SCMR Past Presidents*. (2022). Available online at: https://scmr.org/page/PastPresidents/Past-Presidents.htm (accessed June 27, 2022).

81. Society for Cardiovascular Magnetic Resonance. *SCMR Committees*. (2022). Available online at: https://scmr.org/page/SCMRCommittees (accessed June 27, 2022).

82. American Society of Echocardiography. *ASE Committees*. (2022). Available online at: https://www.asecho.org/about-ase/standing-committees-and-councils/ (accessed June 27, 2022).

83. North American Society for Cardiovascular Imaging. *NASCI Committees*. (2022). Available online at: https://nasci.org/about-nasci/committees/ (accessed June 27, 2022).

84. North American Society for Cardiovascular Imaging. *NASCI Past Presidents*. (2022). Available online at: https://nasci.org/about-nasci/past-presidents/ (accessed June 27, 2022).

85. North American Society for Cardiovascular Imaging. *NASCI Executive Committee*. East Dundee, IL: NASCT (2022).

86. American Society of Nuclear Cardiology. *ASNC Board of Directors*. (2022). Available online at: https://www.asnc.org/governance (accessed June 27, 2022).

87. American Society of Nuclear Cardiology. *ASNC Committees*. (2022). Available online at: https://www.asnc.org/committees (accessed June 27, 2022).

88. Society of Cardiovascular Computed Tomography. *SCCT Past Presidents*. (2022). Available online at: https://scct.org/page/PastPresidents (accessed June 27, 2022).

89. Society of Cardiovascular Computed Tomography. *SCCT Committees & Board of Directors*. (2022). Available online at: https://scct.org/page/About_SCCT#a4 (accessed June 27, 2022).

90. Ordovas K, Baldassarre L, Bucciarelli-Ducci C, Carr J, Fernandes J, Ferreira V, et al. Cardiovascular magnetic resonance in women with cardiovascular disease: position statement from the society for cardiovascular magnetic resonance (SCMR). *J Cardiovasc Magn Reson.* (2021) 23:52. doi: 10.1186/s12968-021-00746-z

91. Assomull R, Lyne J, Keenan N, Gulati A, Bunce N, Davies S, et al. The role of cardiovascular magnetic resonance in patients presenting with chest pain, raised troponin, and unobstructed coronary arteries. *Eur Heart J.* (2007) 28:1242–9. doi: 10.1093/eurheartj/ehm113

92. Cardona A, Zareba K, Raman SV. The role of stress cardiac magnetic resonance in women. *J Nucl Cardiol.* (2016) 23:1036–40. doi: 10.1007/s12350-016-0597-x

93. Markousis-Mavrogenis G, Bonou M, Vartela V, Kolovou G, Venetsanopoulou A, Markatseli T, et al. Cardiovascular magnetic resonance detects inflammatory cardiomyopathy in symptomatic patients with inflammatory joint diseases and a normal routine workup. *J Clin Med.* (2022) 11:1428. doi: 10.3390/jcm11051428

94. Lagan J, Schmitt M, Miller C. Clinical applications of multi-parametric CMR in myocarditis and systemic inflammatory diseases. *Int J Cardiovasc Imaging.* (2018) 34:35–54. doi: 10.1007/s10554-017-1063-9

95. Soufer A, Baldassarre L. The role of cardiac magnetic resonance imaging to detect cardiac toxicity from cancer therapeutics. *Curr Treat Options Cardiovasc Med.* (2019) 21:28. doi: 10.1007/s11936-019-0732-5

96. Saunderson C, Plein S, Manisty C. Role of cardiovascular magnetic resonance imaging in cardio-oncology. *Eur Heart J Cardiovasc Imaging.* (2021) 22:383–96. doi: 10.1093/ehjci/jeaa345

97. Brown S, Sparapani R, Osinski K, Zhang J, Blessing J, Cheng F, et al. Establishing an interdisciplinary research team for cardio-oncology artificial intelligence informatics precision and health equity. *Am Hear J plus Cardiol Res Pract.* (2022) 13:100094. doi: 10.1016/j.ahjo.2022.100094

98. Blakemore E. *Women are Still Underrepresented in Clinical Trials.* Washington, D.C: Washington Post (2022).

99. Bierer B, Meloney L, Ahmed H, White S. Advancing the inclusion of underrepresented women in clinical research. *Cell Rep Med.* (2022) 3:100553. doi: 10.1016/j.xcrm.2022.100553

100. Bird C. Women and health research: ethical and legal issues of including women in clinical studies: Volume 2: Workshop and commissioned papers. In: Mastroianni A, Faden R, Federman D editors. *Women's Representation as Subjects in Clinical Studies: A Pilot Study of Research Published in JAMA in 1990 and 1992.* Washington, DC: National Academies Press (1999). p. 151–73.

frontiers | Frontiers in Cardiovascular Medicine

TYPE Original Research
PUBLISHED 12 June 2023
DOI 10.3389/fcvm.2023.1048927

OPEN ACCESS

EDITED BY
Sebastian Kelle,
German Heart Center Berlin, Germany

REVIEWED BY
Yousef Shahin,
The University of Sheffield, United Kingdom
Brett David Hambly,
Torrens University Australia, Australia

*CORRESPONDENCE
Xia Lu
lxgf2222@163.com
Jie Du
jiedu@ccmu.edu.cn

†These authors have contributed equally to this work and share first authorship

RECEIVED 20 September 2022
ACCEPTED 29 May 2023
PUBLISHED 12 June 2023

CITATION
Lu X, Zhu M, Zhao L, Qi F, Zou H, He P, Zhou H, Shi K and Du J (2023) ^{68}Ga-labeled WVP peptide as a novel PET probe for molecular biological diagnosis of unstable thoracic aortic aneurysm and early dissection: an animal study. Front. Cardiovasc. Med. 10:1048927. doi: 10.3389/fcvm.2023.1048927

^{68}Ga-labeled WVP peptide as a novel PET probe for molecular biological diagnosis of unstable thoracic aortic aneurysm and early dissection: an animal study

Xia Lu[1*†], Meilin Zhu[2†], Lingzhou Zhao[3], Feiran Qi[4,5], Heng Zou[6], Peng He[7], Haizhong Zhou[1], Kuangyu Shi[8,9] and Jie Du[5*]

[1]Department of Nuclear Medicine, Northern Jiangsu People's Hospital, Yangzhou, China, [2]School of Basic Medical Sciences, Ningxia Medical University, Yinchuan, China, [3]Department of Nuclear Medicine, Shanghai General Hospital, Shanghai Jiao Tong University School of Medicine, Shanghai, China, [4]Beijing Anzhen Hospital, Capital Medical University, Beijing, China, [5]Beijing Institute of Heart, Lung and Blood Vessel Diseases, Beijing Anzhen Hospital, Capital Medical University, Beijing, China, [6]Department of Clinical Medicine, Cellomics (Shenzhen) Co., Ltd, Shenzhen, China, [7]Department of Medical Research, Xiangpeng Youkang (Beijing) Technology Co., Ltd, Beijing, China, [8]Department of Nuclear Medicine, University of Bern, Bern, Switzerland, [9]Department of Informatics, Technical University of Munich, Munich, Germany

Objective: Type IV collagen (Col-IV) is a prospective biomarker for diagnosing and treating of unstable thoracic aortic aneurysm and dissection (TAAD). This study aims to evaluate the feasibility of ^{68}Ga-labeled WVP peptide (^{68}Ga-DOTA-WVP) as a novel Col-IV-targeted probe for TAAD biological diagnosis using PET/CT.
Methods: WVP peptide was modified with bifunctional chelator DOTA for ^{68}Ga radiolabeling. Immunohistochemical staining was used to evaluate the expression and location of Col-IV and elastin in aortas treated with 3-aminopropionitrile fumarate (BAPN) at different time points (0, 2, and 4 weeks). The imaging performance of ^{68}Ga-DOTA-WVP was investigated using Micro-PET/CT in a BAPN-induced TAAD mouse model. The relationship between ^{68}Ga-DOTA-WVP uptake in aortic lesions and the serum levels of TAAD-related biomarkers including D-dimer, C-reactive protein (CRP), and serum soluble suppression of tumorigenicity–2 (sST2) was also analyzed.
Results: ^{68}Ga-DOTA-WVP was readily prepared with high radiochemical purity and stability *in vitro*. ^{68}Ga-DOTA-WVP Micro-PET/CT could detect Col-IV exposure of unstable aneurysms and early dissection in BAPN-induced TAAD mice, but little ^{68}Ga-DOTA-WVP uptake was shown in the control group at each imaging time point. The differences of Col-IV expression and distribution of ^{68}Ga-DOTA-WVP both in TAAD and control groups further verified the imaging efficiency of ^{68}Ga-DOTA-WVP PET/CT. Additionally, a higher sST2 level was found in the imaging positive ($n = 14$) than the negative ($n = 8$) group (9.60 ± 1.14 vs. 8.44 ± 0.52, $P = 0.014$).
Conclusion: ^{68}Ga-DOTA-WVP could trace the exposure and abnormal deposition of Col-IV in enlarged and early injured aortas, showing a potential for biological diagnosis, whole-body screening, and progression monitoring of TAAD.

KEYWORDS

molecular biological diagnosis, type IV collagen detection, WVP peptide, PET/CT imaging, thoracic aortic aneurysm and dissection

Introduction

Thoracic aortic aneurysm and dissection (TAAD) is a life-threatening vascular disease, especially when unstable aneurysms with inflammatory conditions progress to aortic dissection, which starts from a tear in the intimal layer of the aorta and bleeding within the media (1, 2). Dissection expands rapidly, leading to serious complications such as rupture or organ ischemia (3). Current clinical guidelines suggest surgical intervention for aortic aneurysm and dissection when the vessel reaches >5–5.5 cm or a growth rate of >0.5 cm/year (4, 5). Unfortunately, this approach oversimplifies complex aortopathy. Up to 50% of ascending thoracic dissections occur in vessels with diameters below the threshold for surgical intervention (6). It has been pointed out that misdiagnosis and delayed management often occurs in clinical workflow even among transfers to aortic referral centers and dramatically worsens the outcomes of patients with TAAD (7, 8). On the other hand, in individuals with thoracic aortic disease, elective endovascular aortic repair and replacement surgery have improved and may be lifesaving; however, these conditions are still associated with increased risk of failure and adverse outcomes (9). Detailed information on the associated findings of the structural and functional biological characteristics are helpful in selecting the best management plan and repeatedly assessing the patient's response to treatment. Therefore, a multidisciplinary approach and earlier and more precise molecular biological diagnosis of unstable aneurysms are imperative to screen the high-risk patients who can benefit from appropriate surgical timing and correct surgical treatment strategy in clinical scenarios to optimize outcomes of TAAD patients.

Molecular imaging, such as hybrid positron emission tomography (PET)/computed tomography (CT), as an adjunctive tool to conventional structural imaging technology, can be used to non-invasively assess anatomic, hemodynamic, and molecular biological features of the aorta, providing a more accurate selection of patients who can benefit from preventative surgical intervention and different options of surgery (10). The complexity of aortic disease is more fully revealed with new functional imaging techniques than with conventional anatomic analysis alone by using a suitable probe to personalize a surveillance regimen or define a more precise intervention threshold to prevent aortic complications (11, 12).

It has been demonstrated that progressive endothelial injury occurs before intimal tearing, including endothelial cell (EC) loss, increased permeability, and subsequent exposure of the subendothelial basement membrane (11, 13). Type IV collagen (Col-IV), a major component of the subendothelial basement membrane, is initially exposed at the sites of EC loss and vessel injury. Patients with TAAD exhibit significantly increased exposure of aortic collagen into the arterial lumen, which may present a novel target for molecular imaging and therapy (14). In our previous studies, a multimodal Col-IV-DOTA-Gd-rhodamine targeted Col-IV by peptide WVP (KLWVLPK) probe was designed to identify the exposed Col-IV in the degenerated aorta for early detection of TAAD via magnetic resonance imaging (MRI) and monitor disease progression in TAAD (15). We also reported a multifunctional nanosystem for delivery (TP-Gd/miRNA-Col-IV) that targets the exposed Col-IV by peptide WVP for nucleic acid therapy to treat TAAD and found such targeted therapy could stabilize the vascular structures, preventing the deterioration of TAAD (16). However, there is still a lack of research on radionuclide-based probes for Col-IV imaging that would be more sensitive to monitor TAAD progression than MRI owing to priority of molecular functional detection and whole-body imaging. Thus, the capability for making a biological diagnosis of TAAD remains to be assessed.

Herein, the Col-IV-targeted WVP peptide was radiolabeled with ^{68}Ga (^{68}Ga-DOTA-WVP) as a novel PET probe for TAAD imaging. This study aims to evaluate the feasibility of ^{68}Ga-DOTA-WVP as a Col-IV-targeted probe for PET/CT of unstable thoracic aneurysms and early TAAD biological diagnosis. To the best of our knowledge, this is the first example regarding the development of a WVP-based PET probe for TAAD imaging.

Materials and methods

Materials

WVP peptide was manufactured using the solid-phase peptide synthesis method by ChinaPeptides Co., Ltd. (Shanghai, China). During the synthesis process, the C-terminus of WVP was modified with DOTA to obtain DOTA-WVP. Sodium acetate (NaOAc), hydrogen chloride (HCl), 3-aminopropionitrile fumarate salt (BAPN), Sirius red, and picric acid were supplied by Sigma-Aldrich (St. Louis, MO, USA). Rabbit anti-mouse Col-IV and elastin were purchased from Abcam, Inc. (Cambridge, UK). Other chemicals and solvents were supplied by Sinopharm Chemical Reagent Co., Ltd. (Shanghai, China).

Preparation of ^{68}Ga-DOTA-WVP and quality control

^{68}Ga was eluted from a ^{68}Ge/^{68}Ga generator (ITG, Baden-Württemberg, Germany) with 4 ml of 0.5 M HCl solution and collected in a 10 ml sterile vial. One milliliter of eluted $^{68}GaCl_3$ was mixed with 65 µl of DOTA-WVP (1 mg/mL) dissolved in 1 M NaOAc. Then the reaction mixture was incubated at 95°C for 15 min. After being cooled to room temperature, the formed ^{68}Ga-DOTA-WVP was analyzed using the Agilent 1260 high-performance liquid chromatography (HPLC) system (Agilent Technologies, Santa Clara, CA, USA) equipped with a UV-Vis detector ($\lambda = 220$ nm) and radioactive flow detector (BioScan, Poway, CA, USA). The SunFire C18 column (5 µm, 4.6 × 250 mm, Waters, Osaka, Japan) was used at a flow rate of 1 ml/min using the following gradient method: 0.1% trifluoroacetic acid in water and acetonitrile (CH_3CN) (0–20 min, 15%–45% CH_3CN). The final product was diluted with 0.9% saline and filtered through a 0.22 µm Millipore filter. To assess *in vitro* stability, 500 µl of ^{68}Ga-DOTA-WVP (4 mCi) was mixed with 500 µl of phosphate-buffered saline (PBS, 0.1 M, pH = 7.4) at room

temperature. The radiochemical purities (RCPs) were tested using HPLC at different time intervals (1, 2, and 3 h).

Animal experiment and experimental model of TAAD

All animal experiments complied with the Guidelines for the Care and Use of Research Animals established by the ethical committee of Shanghai General Hospital. C57BL/6J male mice were purchased from the Shanghai Laboratory Animal Center of the Chinese Academy of Sciences (Shanghai, China). Three-week-old male mice (weight: 8–12 g) were fed a normal diet (control) or 0.1% Wt/Vol BAPN in drinking water for 6 weeks to establish the TAAD disease model. The lower dose of BAPN used in this study to extend the survival of the mice to monitor the whole process of TAAD formation and evaluated the efficiency of ^{68}Ga-DOTA-WVP for early detection of unstable aortic aneurysm and diagnose early dissection (17, 18). Animals grouped TAAD ($n = 62$) and control ($n = 10$) performed PET/CT imaging and immunohistochemistry staining in different pathogenesis to compare ^{68}Ga-DOTA-WVP uptake in aorta and expression of Col-IV on aortic lesions.

PET procedures

The ^{68}Ga-DOTA-WVP solution (100 µl, 200 μCi) was administered as an intravenous bolus to mice with TAAD and the control mice. PET images were acquired at 0.5, 1, and 2 h after injection using a Micro-PET/CT scanner (Siemens Inveon PET/CT scanner, Siemens Healthineers, Erlangen, Germany). All PET studies were reconstructed as a series of three-dimensional (3D) PET images using a two-dimensional-ordered subsets expectation maximization algorithm (four iterations, six subsets), resulting in a voxel size of $0.86 \times 0.86 \times 0.79$ mm. Whole-body CT was used for attenuation correction, and PET studies were corrected for random coincidences, dead time, scatter, and decay.

Image analysis

PMOD software 3.8 (PMOD Technologies, Ltd., Zurich, Switzerland) was used to perform image analysis. The CT and PET images were co-registered using the "Fuse it" toolkit. Abnormal findings that visually matched the characteristics of TAAD were outlined in transverse slices and automatically adapted to 3D volume. Volumetric regions of interest (VROIs) were placed on the anatomical CT images to identify the thoracic aorta and drawn around the high uptake area within the aortic wall lesions. Additional VROIs were drawn in other important organs, including the liver, muscle, heart, brain, bone, lung, and intestine, to measure the *in vivo* biodistribution of the novel peptide probe. The VROIs in the control group were created in the same manner.

The ^{68}Ga-DOTA-WVP uptake was analyzed in the VROI with respect to the maximum standardized uptake value (SUV_{max}). To determine the probe uptake in the early and late phases (static) in the defined TAAD regions, data were compared and analyzed at three time points (0.5, 1, and 2 h) in the TAAD group to explore the *in vivo* dynamic information of the novel peptide probe.

Immunohistochemistry

After imaging, the aortas of mice were excised, embedded in an optimal cutting temperature compound, sectioned, and stained for immunohistochemistry using rabbit anti-mouse Col-IV and elastin antibodies and the secondary antibody was goat antirabbit IgG. Elastin on sections of the aorta in the control mice and mice with TAAD was incubated for 5 min in Lugol's iodine solution, washed twice with PBS, and then incubated with sodium thiosulfate for 5 min. Next, sections were washed for 5 min with running tap water, followed by 70% ethanol, incubated with aldehyde-fuchsin for 10 min, washed with 70% ethanol until they no longer bleached, and stained with Acid Orange G for 10 s.

Collagen was stained directly with Sirius red and saturated aqueous picric acid (1.3% in water). Nuclei were stained with Weigert's hematoxylin for 8 min, washed with running tap water for 10 min, stained with picric-Sirius red for 1 h, and then washed in two changes of acidified water. This achieved near-equilibrium staining that did not increase with longer staining times as shorter times were not sufficient, even when the colors appeared adequate. The slides were then dehydrated in three changes of 100% ethanol, cleared in xylene, and mounted in a resinous medium. The results were observed using a digital slide scanner (3DHISTECH. Ltd).

Enzyme-linked immunosorbent assay analysis of blood

All collected blood samples were divided into positive ($SUV_{TAAD} \geq 1.6\ SUV_{liver}$) and negative ($SUV_{TAAD} < 1.6\ SUV_{liver}$) imaging groups based on the data from ^{68}Ga-DOTA-WVP PET/CT imaging. Blood samples were collected in anticoagulant tubes and centrifuged for 10 min. The supernatant was used to measure the levels of serum D-dimer, C-reactive protein (CRP), and serum soluble suppression of tumorigenicity-2 (sST2) using enzyme-linked immunosorbent assay.

Statistical analysis

Data were expressed as mean ± standard deviation. The differences between the two groups were analyzed using unpaired Student's t-tests, and comparisons between more than two groups were conducted using one-way analysis of variance, followed by Bonferroni's *post hoc* test. For normally distributed data, we used Pearson's correlation test, and we used Spearman's correlation test for data with skewed distribution. Statistical

analysis was performed using SPSS 24.0 (IBM Corp., Armonk, NY, USA). *P*-values < 0.05 were considered statistically significant.

Results

Radiochemistry

The WVP peptide was effectively radiolabeled with ^{68}Ga via the bifunctional chelator DOTA in 15 min. As shown in **Figures 1A,B**, the HPLC results of ^{68}Ga-DOTA-WVP had a single radioactive peak with a retention time of 10.16 min, which was consistent with that of the corresponding DOTA-WVP (10.13 min). The RCP of ^{68}Ga-DOTA-WVP was calculated to be more than 99% without further purification. No obvious changes in the labeling peptide were found in PBS at room temperature within 3 h, suggesting good stability of ^{68}Ga-DOTA-WVP *in vitro*.

Exposure of Col-IV at the site of EC loss in the early stage of TAAD

Three-week-old C57BL/6J mice ($n = 12$, weight: 8–10 g) were fed 0.1% Wt/Vol BAPN in drinking water for 4 weeks and observed EC loss occurred as early as the first week of BAPN administration by Evans blue staining, and the area of EC loss increased with progressive TAAD development, as reported in a previous study (15). Elastin staining revealed slight disordering and disruption of elastic fibers that could be detected in the aortic arch after 2 weeks of BAPN administration (**Figures 2A,B**). Col-IV located under the aortal intima was exposed and gradually increased with BAPN administration during the development and worsening of TAAD from 2 weeks to 4 weeks confirmed using Sirius red staining (**Figures 2A,C**). These results demonstrated that exposure of Col-IV is a crucial characteristic of early stage of TAAD and high-risk TAAD.

Micro-PET/CT imaging and biodistribution on early stage of TAAD

Following BAPN administration for 2 weeks (early stage of TAAD), the mice ($n = 12$) were intravenously injected with 100 μl of the ^{68}Ga-DOTA-WVP solution [(^{68}Ga) = 2 mCi/ml] and PET/CT imaging was performed at 0.5, 1, and 2 h after injection. Significantly increased uptake was observed in the thoracic aortic region, followed by the heart (**Figure 3**). The thoracic aortic lesions were visualized by PET/CT imaging at 0.5 h after injection and signals decreased fast at 1 h and 2 h imaging after injection ^{68}Ga-DOTA-WVP owning to good wash-out dynamics *in vivo*. ^{68}Ga-DOTA-WVP was excreted through the urinary system; thus, the kidneys and bladder retained abundant tracers. The *in vivo* biological distribution analysis verified the spatial distribution of the images within the analyzed tissues. The ^{68}Ga-DOTA-WVP peptide probe focused on injured aortic lesions and had low background signals. In addition, the brain exhibited barely tracer uptake, and the intestine exhibited little tracer uptake, which is important to facilitate accurate diagnosis and reduce radiation dose.

Molecular biological detection of TAAD by serial PET/CT imaging

We evaluated the efficacy of ^{68}Ga-DOTA-WVP in detecting unstable TAAD lesions using PET/CT (TTAD group: $n = 20$ and

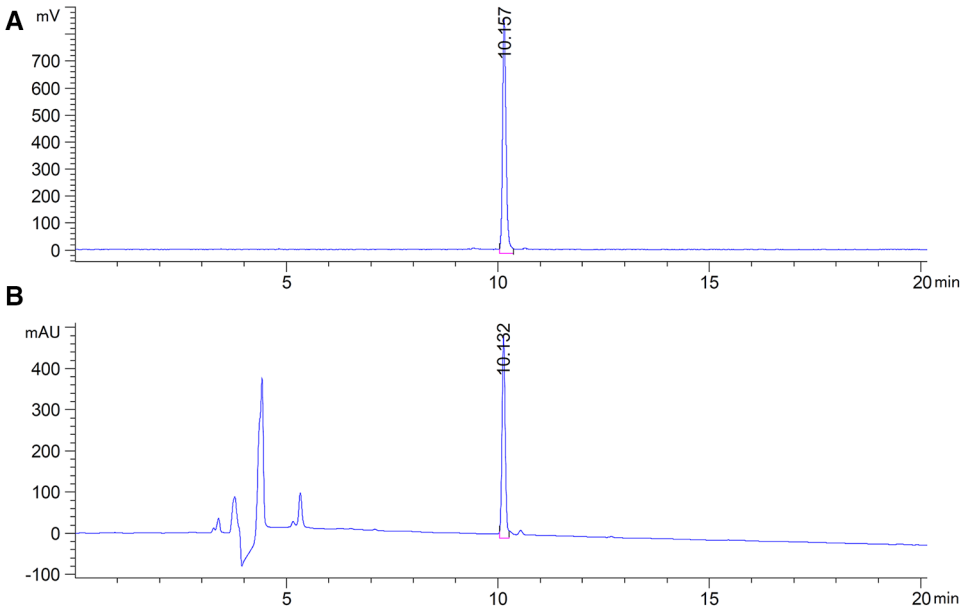

FIGURE 1
HPLC results of ^{68}Ga-DOTA-WVP. (**A**) The radioactive peak shows the position of ^{68}Ga-DOTA-WVP. (**B**) The UV peak shows the position of DOTA-WVP peptide, which is consistent with the ^{68}Ga-DOTA-WVP, indicating that the precursor was successfully radiolabeled with ^{68}Ga.

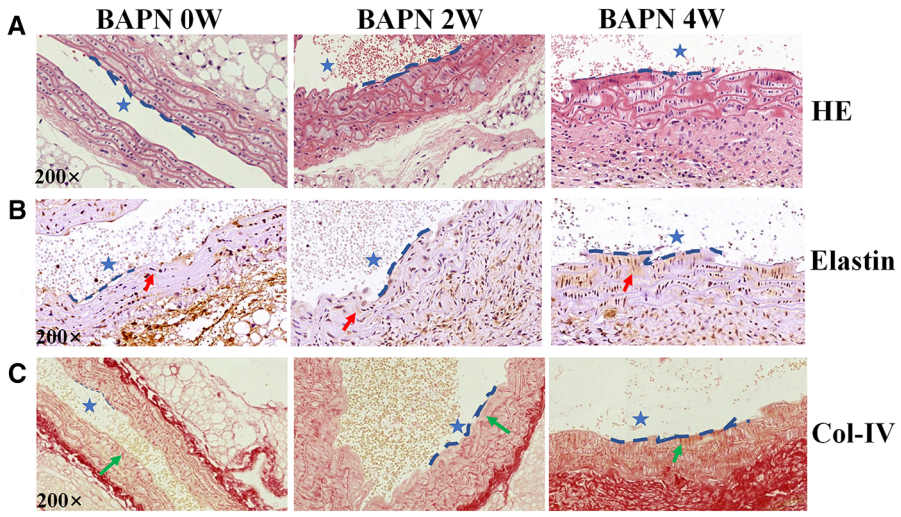

FIGURE 2
Pathological features of TAAD at different stages (0, 2 and 4 weeks). Mice were fed 0.1% BAPN for 4 weeks to simulate the different stages of TAAD development. (A) H&E staining on the aortic arch. (B) Elastin staining on the aortic arch (red arrow). (C) Sirius red staining of collagen on the aortic arch (green arrow indicates Collagen). The scale bars on the three panels are 50 μm. The blue dashed line is the intima, indicating the vascular lumen (blue asterisk indicates lumen of aorta).

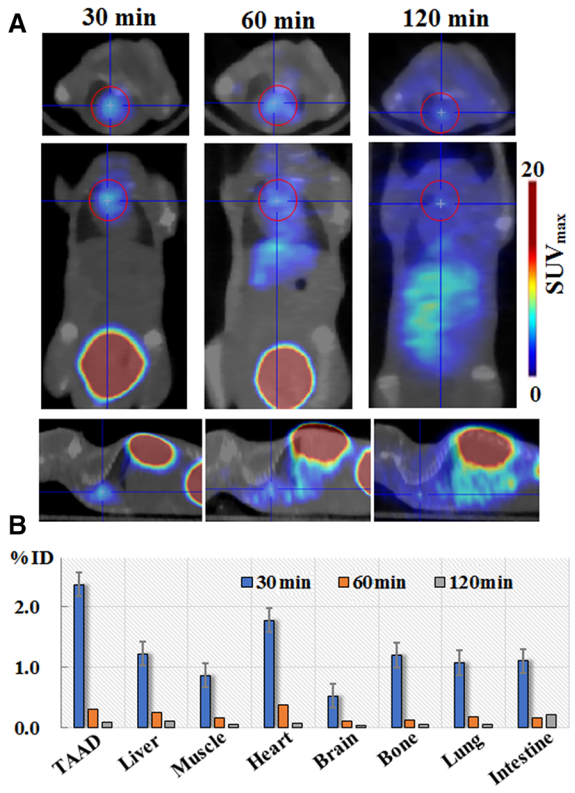

FIGURE 3
(A) Micro-PET/CT imaging and (B) biodistribution of ^{68}Ga-DOTA-WVP in mice with early stage of TAAD. The thoracic aorta and other tissues of interest were analyzed to determine the uptake levels of ^{68}Ga-DOTA-WVP. Data are expressed as SUV_{max} and the percentage of injection dose (% ID).

control group $n = 10$). The aortic diameters of thoracic aneurysm become progressively enlarged with prolonged BAPN administration shown by representative photographs thoracic aorta. Whole-body static images were compared at 0.5 h after injection of ^{68}Ga-DOTA-WVP in mice with TAAD and control mice group in different pathologic stage (Figure 4). The thoracic aortic wall with Col-IV abnormal deposition and exposure presented markedly higher uptake of the peptide probe in the TAAD group as early as 2 weeks compared with that in the control group, which was consistent with the results of Elastin and Col-IV staining. Additionally, the ^{68}Ga-DOTA-WVP uptake in thoracic aortic lesions gradually increased with the longed BAPN administration, which could be visualized clearly at 4 weeks on serial PET/CT images and accompanied by TAAD progression and marked by more exposure of Col-IV. This was also in agreement with the immunohistochemical staining results (Figure 4). The retention of ^{68}Ga-DOTA-WVP in kidneys was significantly higher in the TAAD group than in the control group at 0.5 h after injection (11.53 ± 6.56 vs. 1.21 ± 0.35, $P < 0.001$). Moreover, the ^{68}Ga-DOTA-WVP uptake in the heart was also significantly increased in the TAAD group compared to that in the control group at 0.5 h after injection (1.74 ± 1.23 vs. 0.19 ± 0.08, $P < 0.001$).

Predictive value of ^{68}Ga-DOTA WVP uptake for assessing the severity of TAAD

The weight of the TAAD mice decreased significantly compared to the normal ones (11.60 ± 2.18 vs. 22.31 ± 1.91, $P < 0.001$) (Figure 5A). In contrast, the ^{68}Ga-DOTA-WVP uptake in thoracic aortic lesions increased significantly in TAAD mice (2.14 ± 1.64 vs. 0.23 ± 0.11, $P < 0.001$) (Figure 5B). The uptake value of ^{68}Ga-DOTA-WVP in thoracic aortic lesions showed an obvious increase with the progression of TAAD after BAPN administration using serial PET/CT imaging (Figure 5C). The

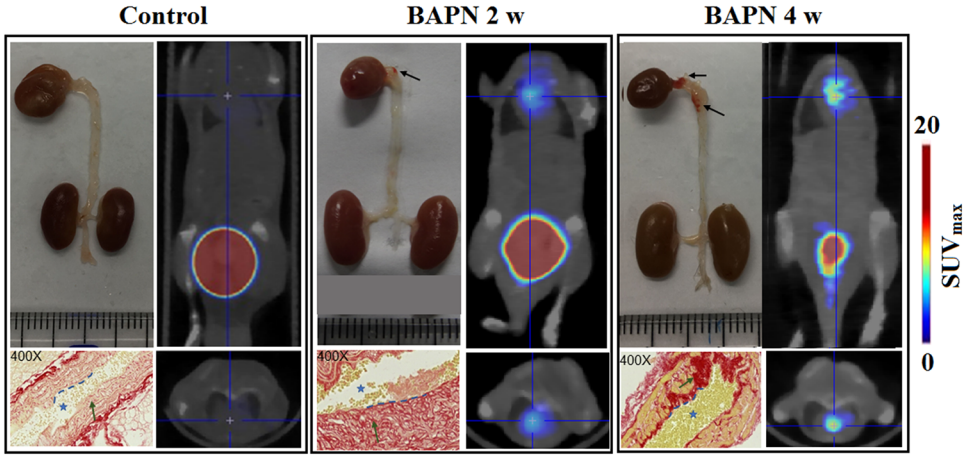

FIGURE 4
^{68}Ga-DOTA-WVP PET/CT images of mice with TAAD in different stages and control mice. The *in vivo* images were verified by photographs of macroscopic features of the thoracic aorta and histological staining (blue asterisk = lumen of aorta; blue dashed line = intima; green arrow = collagen expression; black arrow = TAAD lesions).

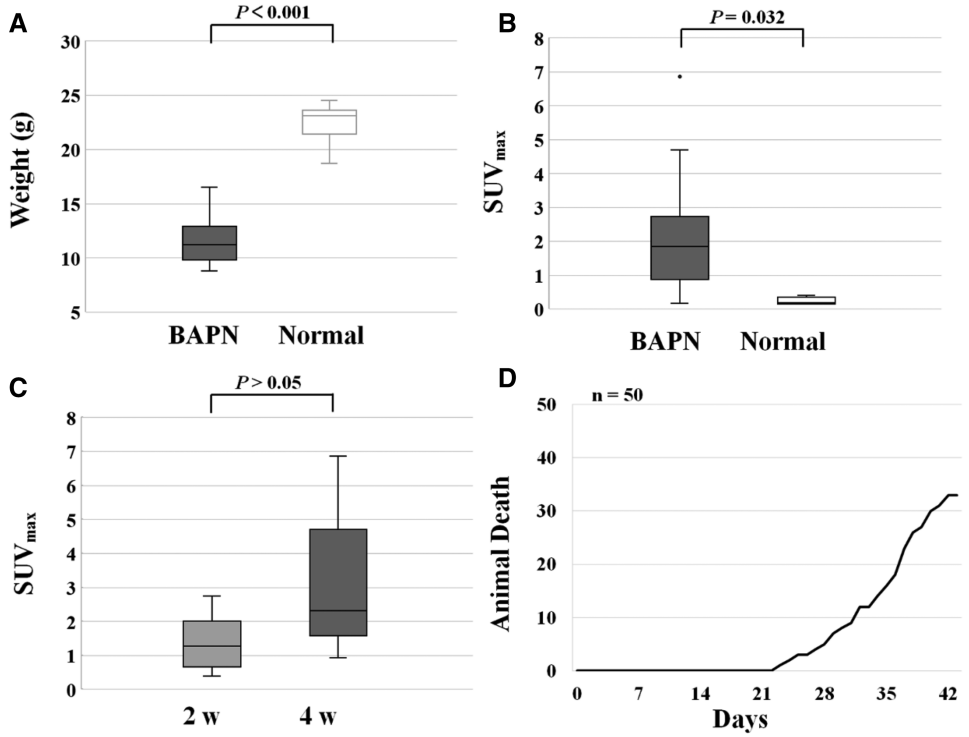

FIGURE 5
(A) Changes in body weight of mice control and TAAD treated mice. (B) Increased uptake of ^{68}Ga-DOTA-WVP in mice with TAAD in thoracic aortic lesions. (C) The comparison of ^{68}Ga-DOTA-WVP uptake in thoracic aortic lesions between 2 and 4 weeks after BAPN treatment. (D) Ruptures in mice with progressive TAAD (n = 50).

mice did not die from rupture of TAAD until 3 weeks of BAPN administration. The first dead TAAD mouse died from rupture was found 23 days after BAPN administration and gradually increased until 66% (33/50) of TAAD mice died from rupture at 6 weeks after BAPN administration (Figure 5D).

We also present a case report of a TAAD mouse dying from rupture which indicates the predictive value of ^{68}Ga-DOTA-WVP PET/CT imaging when assessing the severity of vascular damage after BANP administration. The body weight of this mouse increased slowly and was lighter than other mice in group 2 from 2 to 4 weeks post BAPN administration. When imaged at 4 weeks, the mouse had the lowest body weight among all surviving TAAD mice and was subsequently euthanized by overexposure to isoflurane and found blood clot in chest cavity after dissected.

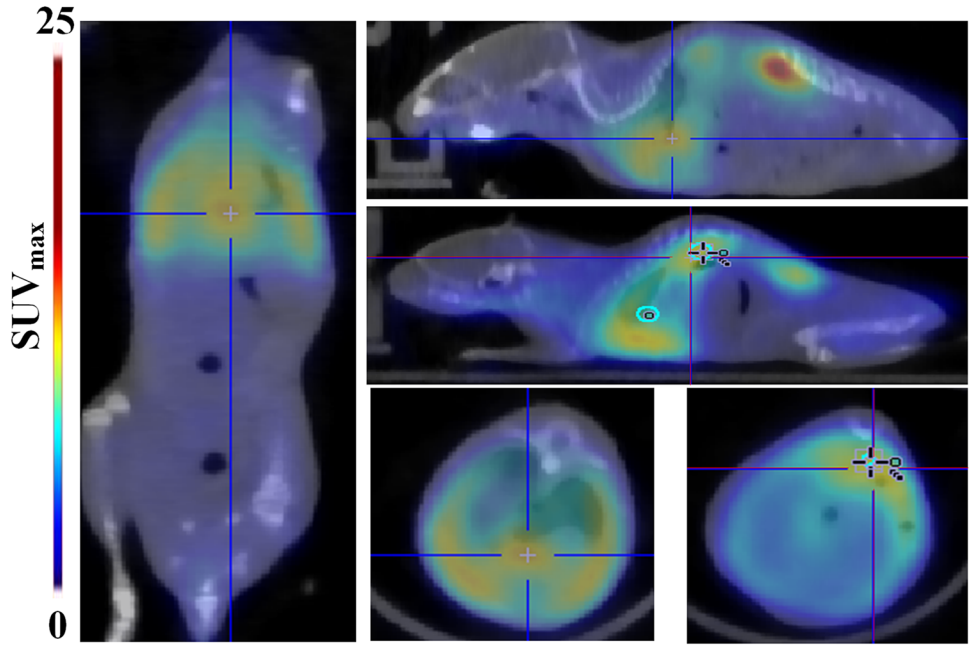

FIGURE 6
A case of rupture among the TAAD mice. Whole-body ^{68}Ga-DOTA-WVP PET/CT images showed significant high uptake of the probe in the aorta, heart, and lung, indicating the large extent and severity of vascular damage caused by BAPN administration. Thoracic aortic dissection is showed in the blue cross and abdominal aortic dissection is shown in the blue cross.

Whole-body images showed a significantly intense concentration of probe was detected in the thoracic and abdominal aorta, heart, and lung. This possibly demonstrated whole body vasculature damage from BAPN administration (Figure 6).

Relationship between ^{68}Ga-DOTA-WVP uptake and serum biomarkers

The relationship between ^{68}Ga-DOTA-WVP uptake on the thoracic aortic wall and serum levels of CRP, D-dimer, and sST2 were analyzed. There was no significant association between ^{68}Ga-DOTA-WVP accumulation and serum levels of those biomarkers. We then compared the levels of these biomarkers between the ^{68}Ga-DOTA-WVP PET/CT positive ($n = 14$) and negative imaging groups ($n = 8$). The sST2 level was significantly higher in the positive imaging group than in the negative group (9.60 ± 1.14 vs. 8.44 ± 0.54, $P = 0.014$); however, the levels of CRP and D-dimer did not differ significantly between the groups (Figure 7).

Discussion

In the present study, the novel probe ^{68}Ga-DOAT-WVP was designed and successfully prepared for PET imaging, and we found that ^{68}Ga-DOAT-WVP PET/CT imaging could extensively detect unstable aneurysms and enable early diagnosis of TAAD (after 2 weeks of BAPN administration) by targeting Col-IV, which was exposed to a small tear site of the intimal aorta. During TAAD development, Col-IV exposure gradually increased with BAPN administration and processive TAAD, owing to the compensatory repair of the degenerated aorta, which was consistent with the gradual increase in ^{68}Ga-DOTA-WVP uptake and intensive signal on thoracic aortic wall lesions *in vivo* PET/CT imaging. Importantly, the *in vivo* biodistribution results showed high ^{68}Ga-DOTA-WVP uptake in the heart, but lower uptake in the liver, brain, lung, bone, muscle, and intestine, which was beneficial to acquire good imaging quality and have robust potential applications in clinical screening of high risk TAAD patients.

The accuracy of diagnosing unstable aneurysms and early TAAD has varied in each trial, and the appropriate imaging technique to apply in each at-risk population remains unclear. Molecular imaging techniques, such as PET/CT, have shown promise in detecting vessel wall instability at an early stage (19, 20). Our results suggest that ^{68}Ga-DOTA-WVP PET/CT imaging could provide whole-body molecular information on Col-IV exposure and expression as an ideal biological characteristic target of unstable TAAD lesions. We showed firstly that ^{68}Ga-DOTA-WVP administration resulted in a clear and significantly high uptake in aortic lesions in whole body imaging, which was confirmed by the high SUV_{max} after 2 and 4 weeks following BAPN administration, whereas no obvious uptake was observed in the control group at the same time points. Patients with TAAD reportedly exhibit significantly increased expression of collagen, which may be a new target molecule in the molecular imaging of TAAD (21). This finding concurs with the current study's finding. In the early stages of aneurysm, the basement membrane components that contain collagen increased in the thickened area, and the basement membrane becomes thin from

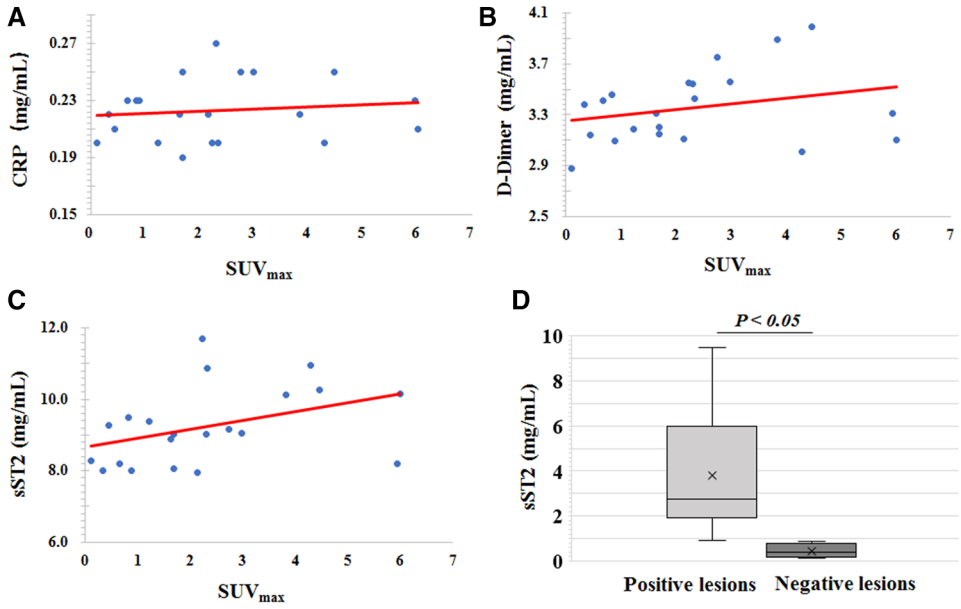

FIGURE 7
Scatter diagrams of the association analysis of ^{68}Ga-DOTA-WVP uptake on thoracic aortic wall and serum levels of (A) CRP, (B) D-dimer, and (C) sST2. (D) Comparison of the serum level of sST2 between the positive and negative imaging groups.

the degeneration of elastin and depletion of smooth muscle cells in the later stages. Smooth muscle cells in unstable aortic aneurysms and dissected aortic media exhibit phenotypic switching from the contractile to synthetic type. Synthetic smooth muscle cells increase collagen synthesis and matrix metalloproteinase-2 production, both of which can promote abnormal collagen deposition and elastin degradation in TAAD and support the intense accumulation of ^{68}Ga-DOTA-WVP trace Col-IV expression in high-risk aneurysms and the early stages of dissection (22).

Col-IV can not only be exposed and posited on the intima beneath the TAAD, but also in the pathological tissues of renal fibrosis, atherosclerosis, and hepatic fibrosis, which is consistent with our results that the heart and kidneys also showed high uptake of ^{68}Ga-DOTA-WVP (23). On one hand, the most reasonable explain of high accumulation of ^{68}Ga-DOTA-WVP observed in heart and kidney in TAAD mice was caused of systematic aortic pathologies induced from BAPN administration in this TAAD model. But in the other hand, we should also pay an attention to the relationship of TAAD and heart as well as renal disease based on common pathogenesis. Renal injury was indicated by prolonged excretion time in mice with TAAD compared to that of the normal mice in the control group. However, previous studies demonstrated that type IV collagen that accumulates in the glomerular mesangium and renal interstitium contributes to the progression of chronic renal disease via the TGF-β signal path (24). Therefore, the importance of evaluation heart and renal abnormal function should be emphasized in patients with TAAD based on the common pathological change of type IV collagen deposition. Additionally, Kurata demonstrated that the severity of atherosclerosis and number of renal cysts were correlated with thoracic aortic circumference. Type IV collagen was noted in background renal tissue in cases with numerous renal cysts and suggests that a syndrome that affects the aorta and renal tubules, as well as atheroma, may exist (25). Therefore, abnormal exposure and deposition of Col- IV involving dysfunction of other important organs might be an target for noninvasive molecular imaging and nanosystem therapy for patients with TAAD. Whole-body PET/CT imaging and systematic evaluation using ^{68}Ga-DOTA-WVP may play an important role in systematic assessing function changes of heart, renal and atherosclerosis in patients with TAAD. Reportedly, immune responses against collagen type IV contributed to vascular injury, affecting the development of atherosclerosis (26). Steffensen and Rasmussen summarized the important role causal involvement of collagen type IV in macrovascular diseases as the marker of intact basement membrane and stability of cellular homeostasis (27). The progression of atherosclerosis and other macrovascular diseases is accompanied by degrading collagen type IV and an increased production of abnormal interstitial collagen in the intima (28). Col-IV exposure is a prospective target to biological diagnosis and therapy and the application of ^{68}Ga-DOTA-WVP PET/CT imaging targeted Col-IV detection in various other diseases accompanied by Col-IV deposition and exposure should be studied in future research.

Reportedly, the sST2 level was significantly elevated in patients with severe aortic valve stenosis who presented with pulmonary hypertension and associated with earlier death and high mortality (29). Another study demonstrated the prognostic value of sST2, which is an independent predictor of adverse outcomes in different aortic diseases (30). Additionally, sST2 can act as a heart damage biomarker because it acts as a decoy receptor for interleukin (IL)-33 and blocks the binding of IL−33 to

membrane-bound ST2 to interrupt myocardial and vascular benefits (31). Our results showed that the level of sST2 was significantly increased in the ^{68}Ga-DOTA-WVP PET/CT positive imaging group compared to the negative imaging group, which reflected the damage caused by sST2 in the heart and thoracic aortic wall. However, no relationship was observed between probe uptake and sST2 levels. CRP and D-dimer are systemic laboratory diagnostic biomarkers have been investigated and linked to the risk for aortic aneurysms or its outcomes but not sensitive and specific enough in clinical application. Reportedly, CRP is an independent risk factor in detection of vascular inflammation was associated with abdominal aortic aneurysm progression but few studies in TAAD (32). Inflammation and coagulopathy are non-specific characteristic in aortic aneurysm and dissection, while ^{68}Ga-DOTA-WVP was designed to target imaging exposure of Col-Ⅳ to detect aorta damage earlier and specifically in unstable TAAD in this study. Therefore, no significant association between ^{68}Ga-DOTA-WVP accumulation and the serum levels of these non-specific biomarkers in PET/CT positive and negative imaging groups of TAAD mice (33). The negative association also could be caused by insufficient sample size in this study and further research is needed on the topic.

The main limitation of this pilot study is the lack of reliable binding and inhibition experiments to quantify the quantitative-efficacy relationship between the uptake of ^{68}Ga-DOTA-WVP and Col-IV expression, which will be studied further. Secondly, this pilot study lacks sufficient sample size for serial visualization of TAD progression using PET/CT to quantitatively analyze the relationship between probe uptake *in vivo* and Col-IV exposure at different time points as well as lack of confocal microscope photography scanning due to the COVID-19 pandemic. In our timeframe of experimentation, most aorta samples did not develop dissection. However, we observed that many animals with significant accumulation of ^{68}Ga-DOTA-WVP in the aorta died from TAAD rupture. In our future study, we will continue analyzing the relationship between probe uptake and formation of dissection as well as the specificity of the probe for TAAD detection. Another limitation is that, although we showed that ^{68}Ga-DOTA-WVP could be used to detect early TAD in a mouse model, this agent needs to be investigated further in large animals and eventually confirmed in humans. Furthermore, we should also visualize the aorta using CT-enhanced scans to co-locate TAAD lesions from structural information of size and functional imaging of Col-IV exposure via hybrid PET/CT imaging, which will be conducted in our following study.

Conclusions

In summary, we prepared ^{68}Ga-DOTA-WVP through a simple method with a high RCP and stability and demonstrated its ability to detect the biological characteristics of unstable aneurysms and early TAAD. Biological diagnosis of dissection plays an important role in clinical management. Thus, the current study proposes a promising method for dissection screening in high-risk patient populations, monitoring disease progression and assessing therapeutic response. Therefore, clinicians may benefit from PET-based whole-body risk assessments in guiding patient management and surgical decisions.

Data availability statement

The original contributions presented in the study are included in the article, further inquiries can be directed to the corresponding authors.

Ethics statement

All animal experiments complied with the Guidelines for the Care and Use of Research Animals established by the ethical committee of Shanghai General Hospital.

Author contributions

XL and MZ: design, methodology, investigation, analysis, and writing initial manuscript. LZ: methodology, analysis and writing initial manuscript. FQ, HZ and PH: methodology and analysis. KS: analysis. JD: design and supervision. All authors contributed to the article and approved the submitted version.

Funding

This work was supported by Capital Medical University Research Development Fund (1200020106), Ningxia Key Research and Development Program (2020BFG03005), Ningxia Natural Science Foundation (2022AAC03136) and Yangzhou Science Foundation for Leading Talent Researchers (LYJF00040).

Conflict of interest

Author HZ is employed by Cellomics (Shenzhen) Co., Ltd and PH is employed by Xiangpeng Youkang (Beijing) Technology Co., Ltd.

The remaining authors declare that the research was conducted in the absence of any commercial or financial relationships that could be construed as a potential conflict of interest.

Publisher's note

References

1. Nienaber CA, Clough RE. Management of acute aortic dissection. *Lancet.* (2015) 385:800–11. doi: 10.1016/S0140-6736(14)61005-9

2. Golledge J, Eagle KA. Acute aortic dissection. *Lancet.* (2008) 372:55–66. doi: 10.1016/S0140-6736(08)60994-0

3. Katzen B, Dake M, MacLean A, Wang D. Endovascular repair of abdominal and thoracic aortic aneurysms. *Circulation.* (2005) 112:1663–75. doi: 10.1161/circulationaha.105.541284

4. Adriaans B, Wildberger J, Westenberg J, Lamb H, Schalla S. Predictive imaging for thoracic aortic dissection and rupture: moving beyond diameters. *Eur Radiol.* (2019) 29:6396–404. doi: 10.1007/s00330-019-06320-7

5. Chau K, Elefteriades J. Natural history of thoracic aortic aneurysms: size matters, plus moving beyond size. *Prog Cardiovasc Dis.* (2013) 56:74–80. doi: 10.1016/j.pcad.2013.05.007

6. Elefteriades J, Mukherjee S, Mojibian H. Discrepancies in measurement of the thoracic aorta: JACC review topic of the week. *J Am Coll Cardiol.* (2020) 76:201–17. doi: 10.1016/j.jacc.2020.03.084

7. Huang F, Wu H, Lai Q, Ke X. Application value of preoperative dual-source computed tomography in assessing the rupture site of thoracic aortic dissection. *J Cardiothorac Surg.* (2021) 16:346. doi: 10.1186/s13019-021-01729-y

8. Arnaoutakis G, Ogami T, Aranda-Michel E, Dai Y, Holmes R, Beaver T, et al. Misdiagnosis of thoracic aortic emergencies occurs frequently among transfers to aortic referral centers: an analysis of over 3700 patients. *J Am Heart Assoc.* (2022) 11:e025026. doi: 10.1161/jaha.121.025026

9. Tcheandjieu C, Xiao K, Tejeda H, Lynch J, Ruotsalainen S, Bellomo T, et al. High heritability of ascending aortic diameter and trans-ancestry prediction of thoracic aortic disease. *Nat Genet.* (2022) 54:772–82. doi: 10.1038/s41588-022-01070-7

10. Lu X, Calabretta R, Wadsa W, Haug AR, Mayerhöfer M, Raderer M, et al. Imaging inflammation in atherosclerosis with CXCR4-directed [68 Ga] PentixaFor PET/MRI—compared with [18F] FDG PET/MRI. *Life.* (2022) 12(7):1039–50. doi: 10.3390/llife12071039

11. Shiga T, Wajima Z, Apfel C, Inoue T, Ohe Y. Diagnostic accuracy of transesophageal echocardiography, helical computed tomography, and magnetic resonance imaging for suspected thoracic aortic dissection: systematic review and meta-analysis. *Arch Intern Med.* (2006) 166:1350–6. doi: 10.1001/archinte.166.13.1350

12. Salmasi M, Al-Saadi N, Hartley P, Jarral O, Raja S, Hussein M, et al. The risk of misdiagnosis in acute thoracic aortic dissection: a review of current guidelines. *Heart.* (2020) 106:885–91. doi: 10.1136/heartjnl-2019-316322

13. Malm B, Sadeghi M. Multi-modality molecular imaging of aortic aneurysms. *J Nucl Cardiol.* (2017) 24:1239–45. doi: 10.1007/s12350-017-0883-2

14. Reeps C, Pelisek J, Bundschuh R, Gurdan M, Zimmermann A, Ockert S, et al. Imaging of acute and chronic aortic dissection by 18F-FDG PET/CT. *J Nucl Med.* (2010) 51:686–91. doi: 10.2967/jnumed.109.072298

15. El-Hamamsy I, Yacoub M. Cellular and molecular mechanisms of thoracic aortic aneurysms. *Nat Rev Cardiol.* (2009) 6:771–86. doi: 10.1038/nrcardio.2009.191

16. Xu K, Xu C, Zhang Y, Qi F, Yu B, Li P, et al. Identification of type IV collagen exposure as a molecular imaging target for early detection of thoracic aortic dissection. *Theranostics.* (2018) 8:437–49. doi: 10.7150/thno.22467

17. Xu C, Zhang Y, Xu K, Nie J, Yu B, Li S, et al. Multifunctional cationic nanosystems for nucleic acid therapy of thoracic aortic dissection. *Nat Commun.* (2019) 10:3184. doi: 10.1038/s41467-019-11068-1

18. Sawada H, Beckner Z, Ito S, Daugherty A, Lu H. *β*-Aminopropionitrile-induced aortic aneurysm and dissection in mice. *JVS Vasc Sci.* (2022) 3:64–72. doi: 10.1016/j.jvssci.2021.12.002. eCollection 2022.

19. Ren W, Liu Y, Wang X, Jia L, Piao C, Lan F, et al. *β*-Aminopropionitrile monofumarate induces thoracic aortic dissection in C57BL/6 mice. *Sci Rep.* (2016) 6:28149. doi: 10.1038/srep28149

20. Blasi F, Oliveira B, Rietz T, Rotile N, Day H, Looby R, et al. Effect of chelate type and radioisotope on the imaging efficacy of 4 fibrin-specific PET probes. *J Nucl Med.* (2014) 55:1157–63. doi: 10.2967/jnumed.113.136275

21. Wang L, Zhang J, Fu W, Guo D, Jiang J, Wang Y. Association of smooth muscle cell phenotypes with extracellular matrix disorders in thoracic aortic dissection. *J Vasc Surg.* (2012) 56:1698–709, 709.e1. doi: 10.1016/j.jvs.2012.05.084

22. Fredman G, Kamaly N, Spolitu S, Milton J, Ghorpade D, Chiasson R, et al. Targeted nanoparticles containing the proresolving peptide Ac2-26 protect against advanced atherosclerosis in hypercholesterolemic mice. *Sci Transl Med.* (2015) 7:275ra20. doi: 10.1126/scitranslmed.aaa1065

23. Karsdal M, Nielsen S, Leeming D, Langholm L, Nielsen M, Manon-Jensen T, et al. The good and the bad collagens of fibrosis - their role in signaling and organ function. *Adv Drug Deliv Rev.* (2017) 121:43–56. doi: 10.1016/j.addr.2017.07.014

24. Matsuda T, Yamamoto T, Muraguchi A, Saatcioglu F. Cross-talk between transforming growth factor-beta and estrogen receptor signaling through Smad3. *J Biol Chem.* (2001) 276:42908–14. doi: 10.1074/jbc.M105316200

25. Kurata A, Inoue S, Ohno S, Nakatsubo R, Takahashi K, Ito T, et al. Correlation between number of renal cysts and aortic circumferences measured using autopsy material. *Pathol Res Pract.* (2013) 209:441–7. doi: 10.1016/j.prp.2013.04.012

26. Vallejo J, Dunér P, To F, Engelbertsen D, Gonçalves I, Nilsson J, et al. Activation of immune responses against the basement membrane component collagen type IV does not affect the development of atherosclerosis in ApoE-deficient mice. *Sci Rep.* (2019) 9:5964. doi: 10.1038/s41598-019-42375-8

27. Steffensen LB, Rasmussen LM. A role for collagen type IV in cardiovascular disease? *Am J Physiol Heart Circ Physiol.* (2018) 315:H610–H25. doi: 10.1152/ajpheart.00070.2018

28. Baumert J, Schmidt K, Eitner A, Straube E, Rödel J. Host cell cytokines induced by Chlamydia pneumoniae decrease the expression of interstitial collagens and fibronectin in fibroblasts. *Infect Immun.* (2009) 77:867–76. doi: 10.1128/iai.00566-08

29. Boxhammer E, Mirna M, Bäz L, Bacher N, Topf A, Sipos B, et al. Soluble ST2 as a potential biomarker for risk assessment of pulmonary hypertension in patients undergoing TAVR? *Life (Basel).* (2022) 12:389. doi: 10.3390/life12030389

30. Stundl A, Lünstedt N, Courtz F, Freitag-Wolf S, Frey N, Holdenrieder S, et al. Soluble ST2 for risk stratification and the prediction of mortality in patients undergoing transcatheter aortic valve implantation. *Am J Cardiol.* (2017) 120:986–93. doi: 10.1016/j.amjcard.2017.06.033

31. Chen W, Hong J, Gannon J, Kakkar R, Lee R. Myocardial pressure overload induces systemic inflammation through endothelial cell IL-33. *Proc Natl Acad Sci U S A.* (2015) 112:7249–54. doi: 10.1073/pnas.1424236112

32. Hellenthal F, Buurman W, Wodzig W, Schurink G. Biomarkers of abdominal aortic aneurysm progression. Part 2: inflammation. *Nat Rev Cardiol.* (2009) 6:543–52. doi: 10.1038/nrcardio.2009.102

33. Kordzadeh A, Parsa A, Askari A, Maddison B, Panayiotopoulos Y. Presenting baseline coagulation of infra renal ruptured abdominal aortic aneurysm: a systematic review and pooled analysis. *Eur J Vasc Endovasc Surg.* (2016) 51:682–9. doi: 10.1016/j.ejvs.2016.02.009

Frontiers in
Cardiovascular Medicine

Innovations and improvements in cardiovascular treatment and practice

Focuses on research that challenges the status quo of cardiovascular care, or facilitates the translation of advances into new therapies and diagnostic tools.

Discover the latest Research Topics

See more →

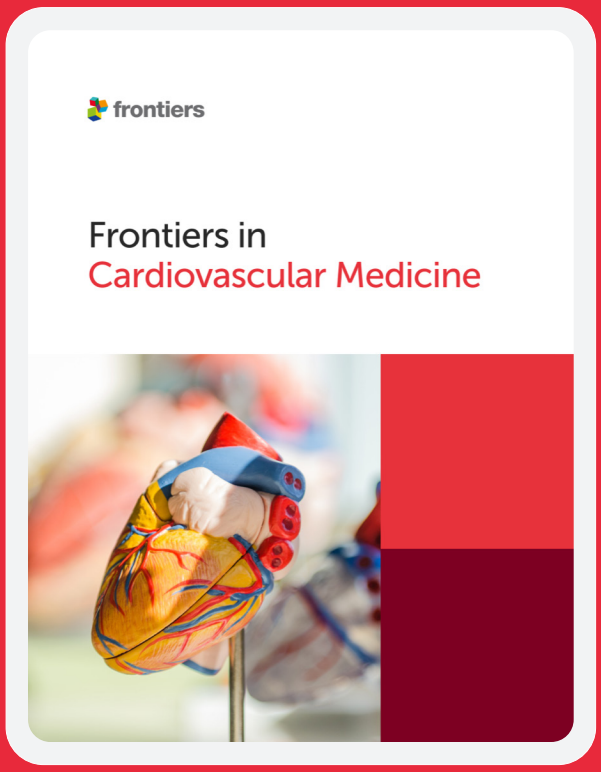

Frontiers

Avenue du Tribunal-Fédéral 34
1005 Lausanne, Switzerland
frontiersin.org

Contact us

+41 (0)21 510 17 00
frontiersin.org/about/contact